THE UNIVERSITY *of* EDINBURGH

Thermal Analysis and Air Flow Modelling of Electrical Machines

Yew Chuan Chong

Doctor of Philosophy

The University of Edinburgh

2015

Abstract

Thermal analysis is an important topic that can affect the electrical machine performance, reliability, lifetime and efficiency. In order to predict the electrical machine thermal performance accurately, thermal analysis of electrical machines must include fluid flow modelling. One of the technologies which may be used to estimate the flow distribution and pressure losses in throughflow ventilated machines is flow network analysis, but suitable correlations that can be used to estimate the pressure losses in rotor ducts due to fluid shock is not available. The aim of this work is to investigate how the rotation affects the pressure losses in rotor ducts by performing a dimensional analysis.

Apart from the additional friction loss due to the effects of rotation, other rotational pressure losses that appear in a rotor-stator system are: duct entrance loss due to fluid shock and combining flow loss at the exit of the rotor-stator gap. These losses are analysed using computational fluid dynamics (CFD) methods. The CFD simulations use the Reynolds-averaged Navier Stokes (RANS) approach. An experimental test rig is built to validate the CFD findings. The investigation showed that the CFD results are consistent with the experimental results and the rotational pressure losses correlate well with the rotation ratio (a dimensionless parameter). It shows that the rotational pressure loss generally increases with the increase in the rotation ratio. At certain operating conditions, the rotational pressure loss can contribute over 50 % of the total system loss.

The investigation leads to an original set of correlations for the pressure losses in air ducts in the rotor due to fluid shock which are more suitable to be applied to fluid flow modelling of throughflow ventilated machines. Such correlations provide a significant contribution to the field of thermal modelling of electrical machines. They are incorporated into the air flow modelling tool that has been programmed in Portunus by the present author. The modelling tool can be integrated with the existing thermal modelling method, lumped-parameter thermal network (LPTN) to form a complete analytical thermal-fluid modelling method.

Declaration

I hereby declare that this thesis was composed by myself, that the work contained herein is my own except where explicitly stated otherwise in the text, and that this work has not been submitted for any other degree or professional qualification except as specified.

_____

Yew Chuan Chong

Acknowledgements

Firstly, I would like to thank my supervisor, Professor Markus Mueller for giving all kinds of support, guidance and encouragement to me to carry out my research. I really appreciate that he took me of becoming a member of his prestigious electrical machine group despite that fact that I had provided no much contribution towards his group. I also would like to thank my main supervisor Dr. John Chick who is always supportive and encouraging. He kept me motivated towards a solution every time I encountered a bottleneck.

Secondly, I am very grateful to Energy Technology Partnership, Institute for Energy Systems and Motor Design Ltd. for providing funding, facility, software, training and guidance of this research. I would also like to express my warmest gratitude to my industrial supervisor Dr. Dave Staton for his guidance, help and idea during this project.

I would also like to thank the following people who have helped me to the completion of this dissertation: Dr. Prashant Valluri and Professor David Ingram for helping me to understand the core of computational fluid dynamics; Mike Galbraith for building my experimental test rig; Other lecturers such as Dr. Jonathan Shek, Dr. Tom Bruce, Dr. Ewen Macpherson, etc. for their kindness; My lovely colleagues: Ozan Keysan, Estanislao Juan Pablo Echenique Subiabre, Nissar Ahmed, Douglas Carmichael, Li Bin, Isaac Portugal, Aris Zavvos, Leong Kit Gan, Xiao Yun Rong, Lathan Sethuraman, Marios Sousounis, Tom Wood, Yao Zhou, etc.

Finally, my special thanks are given to the most important person in my life, my lovely wife, Jue Wang for her love, patience and support during the difficult last four years. Also, our little son, Ian Tian Yi Chong, who lets me know the meaning of the life. I am also very grateful to my parents and parents-in-law.

Table of Contents

List of Figures

List of Tables

Nomenclature

Mechanical symbols

Roman

a	Inner radius of an annular gap (m).
A	Cross sectional area of a flow path (m^2).
b	Outer radius of an annular gap (m).
C	Discharge coefficient (dimensionless).
c_p	Specific heat (J/kgK)
d, D	Diameter (m).
ΔT_{coil}	Temperature rise in coils above ambient temp. (ºC or K).
e	Internal energy per unit mass (J/kg), roughness height (m).
E	Energy (J).
f	Friction factor (dimensionless).
F	Force (N).
g	Gravitational acceleration (m/s^2).
G	Gap ratio, s/R (dimensionless).
Gr	Rotational Grashof number (dimensionless).
Gz	Graetz number (dimensionless).
$\bar{h}$	Mean convection heat transfer coefficient (W/m^2K).
H	Radius of rotation, Pitch-circular radius of rotor ducts (m).
J	Rotational Reynolds number (dimensionless), Jacobian matrix.
k	Turbulent kinetic energy (m^2/s^2).
K	Pressure loss coefficient (dimensionless).
L	Length (m).
$\dot{m}$	Mass flow rate (kg/s).
Ma	Mach number (dimensionless).
N_r	Rotational speed (rpm).
$\overline{Nu}$	Mean Nusselt number (dimensionless).
Δp	Pressure drop (Pa).
p_s	Fan pressure (Pa).
p, p_{tot}	Static and total gauge pressures (Pa).
Pr	Prandtl number (dimensionless).
P'	Perimeter (m).
q''	Heat flux (W/m^2).
Q	Volumetric flow rate (m^3/s).
Q_{conv}	Convective heat transfer (W).
r	Radius, local radius (m).
R	Rotor outer radius (m), thermal resistance (K/W), flow resistance (kg/m^7).

R_{th}	Thermal contact resistance per unit area (m^2K/W).
Ra_τ	Rotational Rayleigh number (dimensionless).
Re	Axial flow Reynolds number (dimensionless).
Re_θ, Re_ω	Rotational Reynolds number (dimensionless).
s	Gap size (m).
S_m	Momentum source per unit volume (N/m^3)
S_T	Heat generation per unit volume (W/m^3).
S_{ij}	Strain-rate tensor (s^{-1}).
t	Time (s).
T, T_w, T_{ref}	Temperature, wall and reference temperature (°C or K).
T_q	Torque (Nm).
Ta	Taylor number (dimensionless).
U	Axial flow velocity (m/s).
V	Velocity (m/s).
V_T	Tangential velocity (m/s).
u^+	Dimensionless velocity (dimensionless).
u^*	Friction velocity (m/s).
w	Duct spacing (m).
W_{in}, W_{out}	Work transfer to and from a system (J).
y	Normal distance from the wall (m).
y^+	Dimensionless wall distance (dimensionless).
z	Elevation above a reference plane (m).

Greek

α	Thermal diffusivity (m^2/s), flow rate coefficient (dimensionless).
β	Coefficient of volumetric expansion (K^{-1}), diameter ratio.
Δ	Finite difference.
δ_{ij}	Kronecker delta function.
ε	Turbulent dissipation rate (m^2/s^3), eccentricity parameter.
ϵ	Expansibility factor (dimensionless).
η	Radius ratio (dimensionless).
Γ	Inertia to body force ratio (dimensionless).
κ	Exponent of Prandtl number (dimensionless).
λ	Thermal conductivity (W/mK)
μ, μ_t	Dynamic viscosity and turbulent viscosity (Pa.s).
ν	Kinematic viscosity (m^2/s).
ω	Specific dissipation rate (s^{-1}).
ω_m	Angular velocity (rad/s).
Φ	Dissipation function.

ρ	Density (kg/m^3).
σ	Standard deviation.
$\sigma_{\bar{x}}$	Standard deviation of the mean.
τ_{turb}	Reynolds stress tensor.
τ_w	Wall shear stress (Pa).
ζ	Thermal to hydrodynamic boundary layer thickness ratio (dimensionless).

Subscripts

CF	Combining flow.
Cu	Copper.
e	Effective.
exp	Experiment.
f	Friction.
f_0	Stationary friction factor.
f_r	Rotational friction factor.
h	Hydraulic.
i	Inner, inlet.
∞	Fully developed flow.
o	Stationary, outer, outlet.
r	Rotational.
rms	Root mean square.
s	Stationary.
SC	Sudden contraction.
SE	Sudden expansion.
sol	Solid.
t	Turbulence.
w	Water.

Electrical symbols

Roman

B	Magnetic loading (T).
B_g	Peak value of air-gap flux density due to the permanent magnets.
d_w	Wire diameter (m).
EMF	Back electromotive field, open circuit phase voltage.
f, f_q	Electric frequency (Hz).
I	Phase current (A).

k_{circ}, k_{eddy}	Constants for circulating and eddy current losses (Nm·(rad/s)$^{-1}$).
k_m	Constant for mechanical losses (Nm).
L_s	Synchronous phase inductance (H).
L_m	Mean turn length covered by magnet (m).
N_t	Number of turns per coil.
P	Power (W), number of poles.
P_{Cu}	Copper loss in coils (W).
$P_{eddy-coils}$	Eddy current loss in coils (W).
P_{load}	Output power dissipated into the resistive load (W).
P_{magnet}	Magnet loss (W).
P_{mech}	Mechanical input power (W).
$P_{mech-loss}$	Mechanical loss (W).
$P_{no-load}$	No-load loss (W).
P_{rotor}	Rotor loss (W).
P_{steel}	Core back iron loss (W).
P_w	Loss due to eddy and circulating currents in the coils (W).
q	Electric loading (A/m).
R	Electric resistance (Ω).
R_{circ}	Equivalent winding resistance to represent circulating current loss (Ω).
R_{core}	Equivalent core resistance (Ω).
R_{Cu}^{amb}	Copper phase resistance at ambient temperature (Ω).
R_{eddy}	Equivalent resistance to represent eddy current loss in coils (Ω).
R_{eq}	Thevenin resistance of the generator seen by the load (Ω).
R_{load}	Load resistance (Ω).

Greek

α_{Cu} , α_{core}	Copper and core thermal resistivity coefficient (K^{-1}).
ρ_{Cu}	Copper resistivity (Ω-m).
ω_s	Electric angular frequency (rad/s)

1 Introduction

1.1 Thermal Issues

Electrical machine design is a multi-physics problem including electromagnetic, thermal and structural designs, which are all interrelated. Thermal analysis is an important topic that can affect the machine's electrical performance. According to equation (1.1), the electric loading (q) determines the power output (P) of an electrical machine. However, the maximum permissible current (I) in the armature windings is limited by the maximum temperature limit of wire insulation which significantly affects the life time of a machine as shown in Figure 1.1.

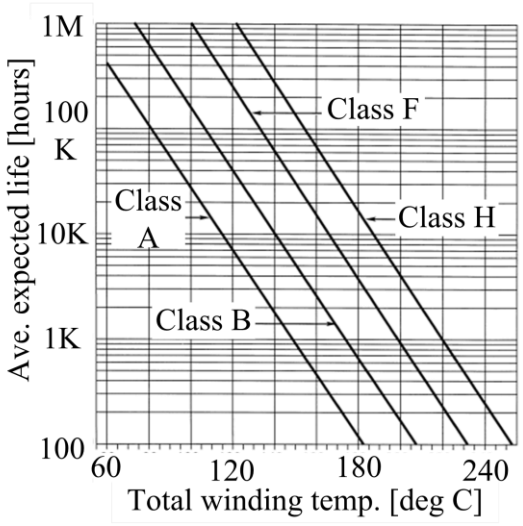

Figure 1.1: The impact of winding temperature on the electrical machine life time, in terms of different insulation classes, Electrical Apparatus Service Association [2000]

The power output (P) of an electrical machine can be defined as, Hughes [2006]:

$$P = \frac{\pi}{2}(Bq)D_{ag}^2 L\omega_m \tag{1.1}$$

where B is the magnetic loading which is limited by the magnetic properties of materials, q is the electric loading is mainly as a function of current (I) in the conductors, D_{ag} is the rotor-stator gap diameter, L is the length of the rotor and ω_m is the rotor speed.

Furthermore, the machine temperature can affect the electrical efficiency because some electromagnetic losses are temperature dependent. For example, the electrical

resistance of copper windings increases with temperature and hence too high operating temperature may lead to unnecessary power losses. Temperature rise will change material properties which can cause severe failure. For permanent magnet machines, the performance of magnets decreases with temperature and the magnets will be demagnetized if they are overheated. From a structural point of view, elevated temperatures can induce mechanical stresses due to thermal expansion, and even thermal fatigue if the machine is operated at variable speed. Thus, effective cooling is ultimately essential to ensure machine reliability, life time and efficiency.

Existing cooling design techniques have been developed mostly for conventional radial flux machines and at a time when power density was not so much of an issue. There is a challenge applying those techniques to modern machines because of the use of new topologies such as axial flux machines, and new materials such as polymers used in stator. In addition to that, cooling is more of a challenge for machines with very high power density and compactness. As the power rating of the electrical machine increases, the corresponding increase in the surface area of the machine for cooling which is equal to πDL is less than the relative increase in the power losses because the power losses are directly proportional to the volume, $\pi D^2 L$ by assuming D and L are the diameter and length of the machine respectively.

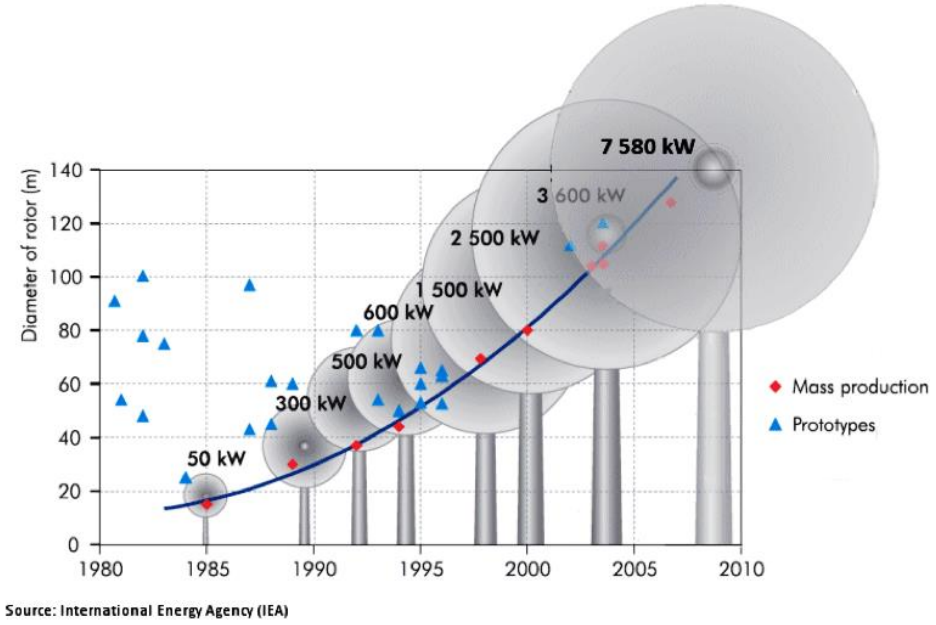

Figure 1.2: Size and power evolution of wind turbines over time. (Source: International Energy Agency, IEA)

The rapid growth of the renewable energy sector has brought about an increased demand for generators with high power output. For instance, the average size of wind turbines has been increasing rapidly over the last 3 decades as illustrated in Figure 1.2. Modern wind turbines are typically connected to generators of multi-megawatts. The 7.5 MW Enercon E126 is the world's most powerful wind turbine. Some international projects (such as European's Sixth Framework Programme – FP6 UpWind, The European Wind Energy Association [2011] and European's Seventh Framework Programme – FP7 DeepWind, Technical University of Denmark, [2010]) are looking towards the design of very large wind turbines, up to 20 MW, both onshore and offshore. Although the generators nowadays are very efficient, mostly more than 95%, the power losses from the process of transforming mechanical energy into electricity turns into heat, the amount of heat generated per unit volume is very significant. Thus, appropriate cooling must be provided to remove the heat in order to ensure reliable operation.

Figure 1.3: Stator assembly of Enercon E126 7.5MW wind turbine (direct drive) generator, (Courtesy of Enercon)

For example, by assuming electrical efficiency of 95 %, 7.5 MW Enercon E126 electrical machine with turbine blade diameter of 126 m, Enercon [2014] would provide 375 kW of power loss whereas 3 MW Enercon E101 electrical machine with turbine blade diameter of 101 m, Enercon [2014] would provide 150 kW of power loss. Hence, the heat generation of E126 is 2.5 times of E101. This also means the

required cooling is increased by that ratio, but cooling is normally limited by the surface area of the machine. According to the trend of size and power evolution in Figure 1.2, the difficult of machine cooling can be clearly imagined.

1.2 Cooling Methods for Electrical Machines

Below are the common cooling methods used for electrical machines. The method of cooling depends upon the application and the machine topology. The following issues should be considered to choose the most suitable cooling method for a machine:

1. Cooling power requirement
2. Operational environment
3. Constant, or adjustable speed applications
4. Cost
5. Space and weight limitations
6. Machine protection: totally-enclosed, or throughflow ventilation

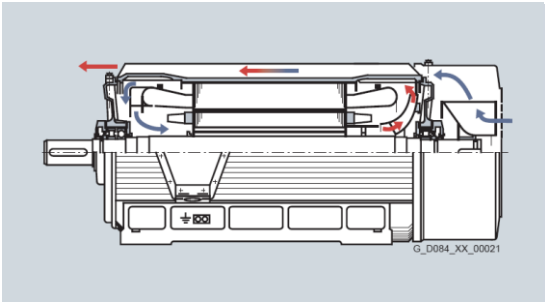

(a) Self-cooled

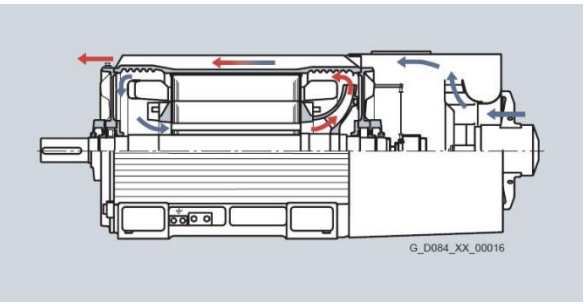

(b) Forced-cooled

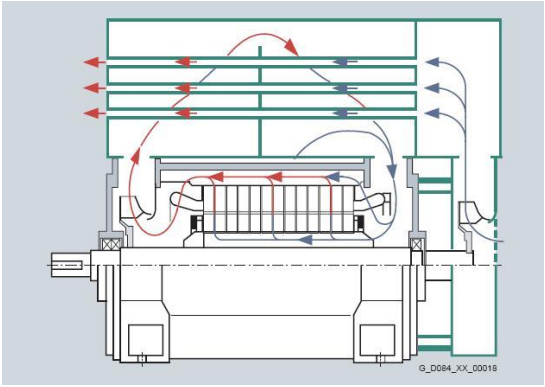

(c) Air-to-air heat exchanger

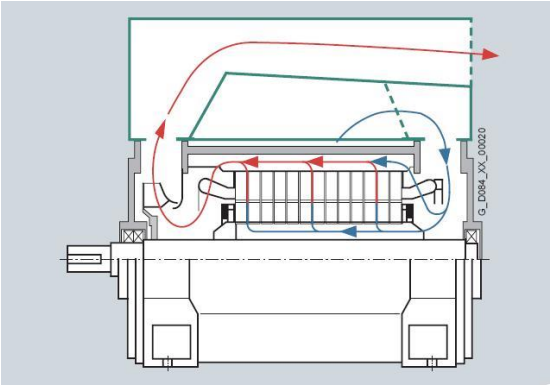

(d) Throughflow ventilation

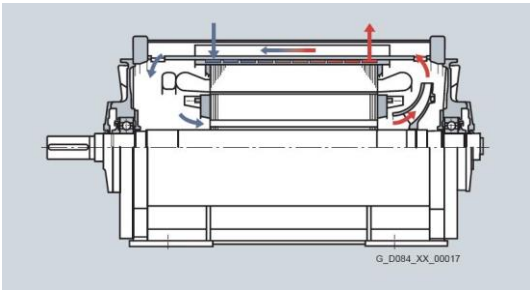

(e) Water-jacket-cooled

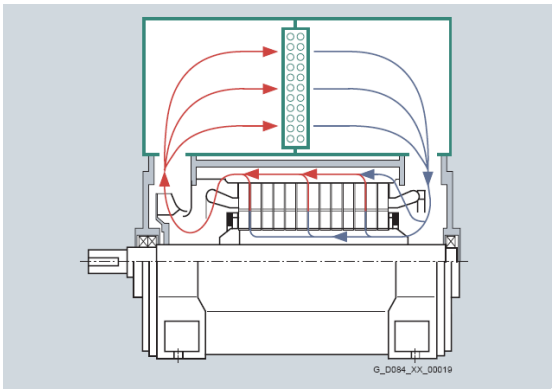

(f) Air-to-water heat exchanger

Figure 1.4: Cooling methods for electrical machine, Siemens AG [2013].

For self-cooled machines (Figure 1.4 (a)), there is a fan at the non-drive end, drawing the surrounding air to pass over the fins on the housing. As the machines are totally-enclosed, to improve the cooling, some self-cooled machines also have an internal fan circulating the air inside the machines to exchange the heat from the inner to the housing. Both internal and external fans are shaft-mounted. As the cooling power is fixed by the fan speed, the self-cooled method is unsuitable for machines that require higher fan pumping pressures, and for machines with variable operational speed. Consequently, forced-cooled methods (Figure 1.4 (b)) become an option because the external fan is driven separately. So, the pressure difference generated by the fan can be controlled, and hence deliver the required cooling power for adjustable speed applications.

As the cooling power of totally-enclosed fan-cooled machines, Figure 1.4 (a) and (b), is restricted by the surface area of housing fins, air-to-air heat exchanger (e.g. Figure 1.4 (c)) can be employed to increase the surface area of heat exchange. High power rating machines normally have a big heat exchanger placed on the top of the machine for corresponding cooling requirements. The inner cooling air circuit is important to ensure uniform temperature distribution in the active areas because the rotor does not have direct contact with the stator. Throughflow ventilation (Figure 1.4 (d)) is a very effective air cooling method. Unlike the totally-enclosed fan-cooled machines, the cooling air of throughflow ventilated machines has direct contact with the heat generating parts such as stator and rotor windings, magnets, etc. Because of high temperature differences between the cooling air and heat surface, throughflow

ventilation improves heat transfer considerably which meets the cooling requirements of large electrical machines. However, throughflow ventilation is inappropriate for the electrical machines that operate in corrosive and explosive environments, and the machine that needs protection from contaminations.

Although more costly to implement, the physical properties of water make it a much more effective fluid for heat transfer, this makes water-jacket-cooling (Figure 1.4 (e)) an attractive cooling solution for the electrical machines with high power losses. Water-jacket-cooled machines normally have some spiral grooves in the housing to allow the water circulating around the machines and to remove heat. Since the water cooling is restricted only to the water duct, it is aided in cooling by internally circulating air to ensure a uniform temperature distribution in the active parts. Water-jacket-cooling can be improved by using air-to-water heat exchanger (Figure 1.4 (f)) to increase the surface area of heat exchange between inner air and water duct. However, the cost of water cooling can be prohibitively expensive. In addition, if the cooling water is recycled, the water cooling system needs extra room for a heat exchanger to cool the water before pumping it back to the machine.

1.3 Steady Flow Energy Equation

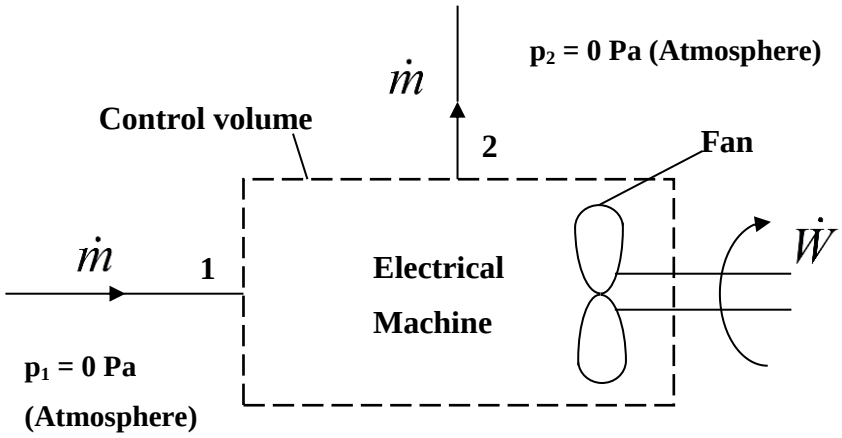

Figure 1.5: Electrical machine is represented by a control volume. $\dot{W}$ is the work transfer by a fan. $\dot{m}$ is a mass flow rate driven by the fan into the control volume at position 1 and exit at position 2. p_1 and p_2 are pressure at the gauge position 1 and position 2.

Considering only the work done by the fan on the cooling air, Figure 1.5 shows a control volume representing an electrical machine. The ambient air passes through at

a steady rate of mass flow $\dot{m}$, entering at position 1 and leaving at position 2. Based on the conservation of mass, the flow into the open system must be equal to the flow out of the system. The air density ρ is assumed constant and Q is the volumetric flow rate through the control volume. Based on the principle of conservation of energy, the fluid flow condition in an electrical machine can be analysed using the Steady Flow Energy Equation (SFEE), Douglas et al. [1995]:

$$W_{in} - W_{out} = \Delta E_{1-2} \tag{1.2}$$

ΔE_{1-2} is the change of energy from state 1 to 2, W_{in} and W_{out} are the energy supplied to and leaving the system respectively. It is assumed that the thermal effects due to pressure variation of flow through the control volume are negligible and hence SFEE can be expanded and expressed in terms of pressure as:

$$p_s - (p_2 - p_1) = \frac{\rho\left(V_2^2 - V_1^2\right)}{2} + \rho g(z_2 - z_1) + \rho(e_2 - e_1) \tag{1.3}$$

As the fan is rotated at a given speed, p_s is the fan pressure that drives Q through the control volume. V_i (where i = {1, 2}) is the air velocity, z_i is the elevation above datum, e_i is the internal energy per unit mass and p_i is static pressure.

Equation (1.3) is in the form of Bernoulli equation with shear forces being present. The pressure term p_1 and p_2 can be ignored as both inlet and outlet boundaries are atmospheric. By assuming the boundaries of the control volume are located sufficiently far from the entry and periphery of the electrical machine and the area of the inlet and outlet of the control volume are the same, thus V_1 and V_2 are equal, the kinetic energy terms $\rho V^2/2$ can be then cancelled out. Since the working fluid is air, the potential energy term $\rho g z$ is negligible. Hence, the SFEE can be reduced to:

$$p_s = \rho \Delta e \tag{1.4}$$

The term $\rho \Delta e$ represents the energy loss per unit volume, i.e. the additional work done on the fluid. This term is commonly known as the system pressure loss as a result of friction and separation of the flow and is usually defined in the form of $K\rho V^2/2$, where K is the pressure loss coefficient and V is the mean local flow velocity. From equation (1.4), the total pressure loss of the system can be written as:

$$p_s = \frac{1}{2}\rho \sum_{i=1}^{n} \left(\frac{K_i}{A_i^2}\right) \times Q^2 \qquad (1.5)$$

A_i is the local cross-sectional area of the flow paths. Here, the main purpose of simplification of the steady flow energy equation is to demonstrate that fan pressure is mainly used to maintain a fluid motion against a system flow resistance and a system pressure loss strongly depends on the flow rate in the system.

1.4 Fan Engineering

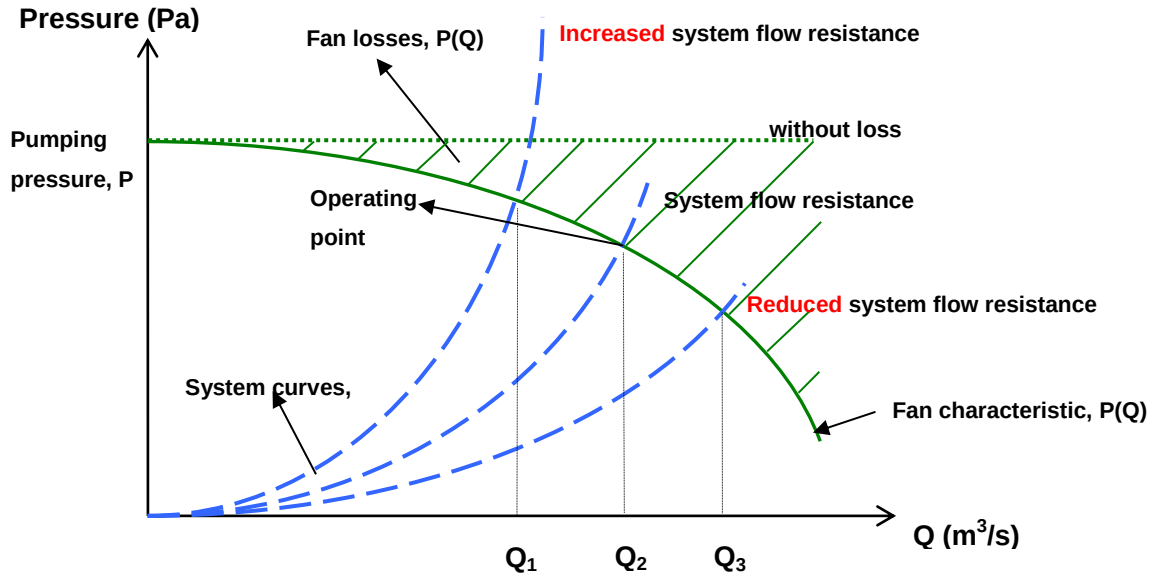

Figure 1.6: The relationship between fan characteristic, system resistance curve and the operating point

In general, all cooling methods rely on a pressure difference to drive the motion of cooling medium. The flow rate through a system is commonly determined from the intersection between the fan (or pump for liquid) characteristic and system resistance curves. The pumping pressure produced by the fan at this "operating point" matches the pressure requirements of the system at that flow rate.

Figure 1.6 illustrates a typical fan characteristic curve. The fan pressure is not constant; it reduces with the flow rate passing across the fan due to energy losses. However, the system characteristic curve is proportional to the square of flow rate. As fan pressure is normally limited by the fan speed, reduced flow resistance can

give a higher flow rate whereas increased flow resistance can reduce the flow rate in a system. Flow rate in an electrical machine is emphasized in the preceding sections because it is an important parameter that links to convective heat transfer through Reynolds number. Besides the traditional friction loss and flow separation loss (e.g. contraction, expansion, bending, etc.), the operation of electrical machines involves rotation will cause additional flow resistance to the system. As a result, for the same pressure, the flow rate through the system will be less than that of the stationary condition.

1.5 Convection Heat and Mass Transfer

Convection is the main heat transfer mechanism to remove the heat from electrical machines in the presence of coolant motion. Convection heat transfer is generally expressed as:

$$Q_{conv} = hA\Delta T \tag{1.6}$$

where h is the convective heat transfer coefficient, A is the surface area and ΔT is the temperature difference between heat transfer surface and coolant normal to that surface. In thermal resistance analysis, the equation (1.6) can be rewritten into a form of Ohm's law.

$$Q_{conv} = \frac{\Delta T}{R} \tag{1.7}$$

The thermal resistance, heat transfer and temperature difference are being in the same way analogous to that of electrical resistance, current and voltage respectively. Thus, the convection thermal resistance (R) is equivalent to the reciprocal of the product of heat transfer coefficient and surface area, which indicates that the higher the heat transfer coefficient, the lower the thermal resistance. Convection heat transfer coefficient is not a fluid property, but it is a complex parameter, depending on the types of flow regime, physical properties of the fluid, thermodynamic and heating conditions, geometry of heat transfer surface, surface roughness and etc.

When an electrical machine reaches steady-state operating temperature, the heating condition the electrical machines can be approximated as constant surface heat flux heating as shown in Figure 1.7. The mean fluid temperature (T_{fluid}) varies linearly

with x along the duct. The duct entrance effect results in larger value of h at the duct entrance than that of the fully developed flow region. Therefore, the temperature difference between the wall and fluid (ΔT) is initially small but increases with increasing x. As the value of h is independent of x in the fully developed flow region, hence the ΔT is also independent of x in the region.

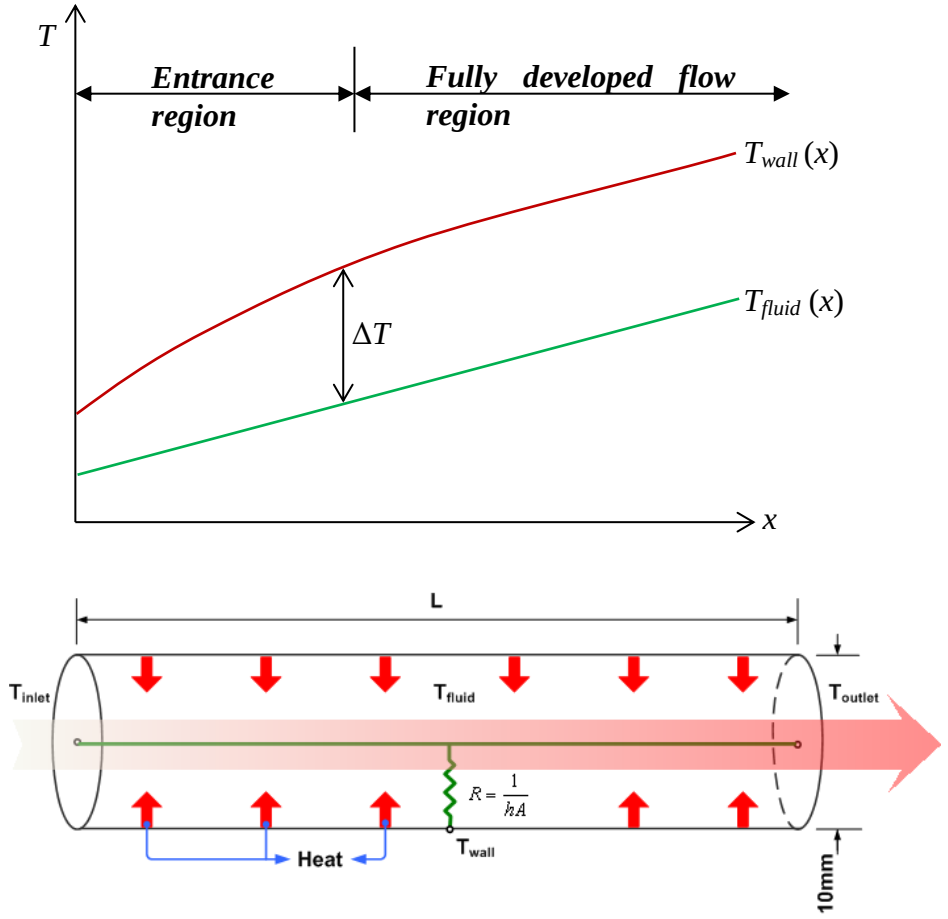

Figure 1.7: Axial variations of fluid and wall temperature in a duct for constant surface heat flux (T – temperature, *R* – thermal resistance, *h* – convective heat transfer coefficient, *A* – surface area, L – duct length, *x* – axial distance)

Based upon the characteristics of laminar and turbulent flows, the level of convective heat transfer is non-dimensionalized with Nusselt number. The Nusselt number (Nu) is a measure of the ratio of convective to conductive heat transfer normal to the boundary. Turbulent flow leads to a larger Nusselt number which corresponds to higher level of convective heat transfer due to the lateral mixing of fluid particle of turbulent flow. For laminar flow, each fluid particle moves along a streamline

parallel to the duct wall. Heat can only be transferred by means of heat conduction from layer to layer. For fully developed laminar flow, the Nusselt number is a constant and is equal to 4.36 for constant heat flux. Based upon empirical method, the Nusselt number for turbulent flow is normally correlated with Reynolds number and Prandtl number and is expressed as:

$$Nu = \frac{hd}{\lambda} = f(Re, Pr) \tag{1.8}$$

The Reynolds number (*Re*) is used to quantify whether flow conditions lead to laminar or turbulent flow. It is a measure of the ratio of inertial forces to viscous forces which is defined as:

$$Re = \frac{\rho V d}{\mu} \tag{1.9}$$

where V is fluid velocity, d is the diameter of a duct. ρ and μ are the density and dynamic viscosity of a fluid respectively. The Prandtl number (*Pr*) is basically a measure of the ratio of momentum diffusivity to heat diffusivity (or the relative thickness of the velocity and the thermal boundary layers) which is defined as:

$$Pr = \frac{\mu c_P}{\lambda} \tag{1.10}$$

where λ and c_p are the thermal conductivity and specific heat of a fluid respectively. The Prandtl number depends on the type of fluid. The Prandtl numbers of gases are about unity, which means that both momentum and heat diffusive rates of gases are about the same. For water and oils, *Pr* is greater than 1, the thermal boundary layer is thinner relative to the velocity boundary layer. Thus, liquid coolant tends to provide higher convection heat transfer under the same Reynolds number.

As shown Figure 1.8, Reynolds number and Prandtl number increase the Nusselt number significantly and give more active convection. The empirical Nusselt number correlations for various geometries are widely available. One only needs to look for the most appropriate correlation that fits the flow condition. Chapter 2 gives a more detailed discussion on heat transfer correlations that are most applicable to electrical machines.

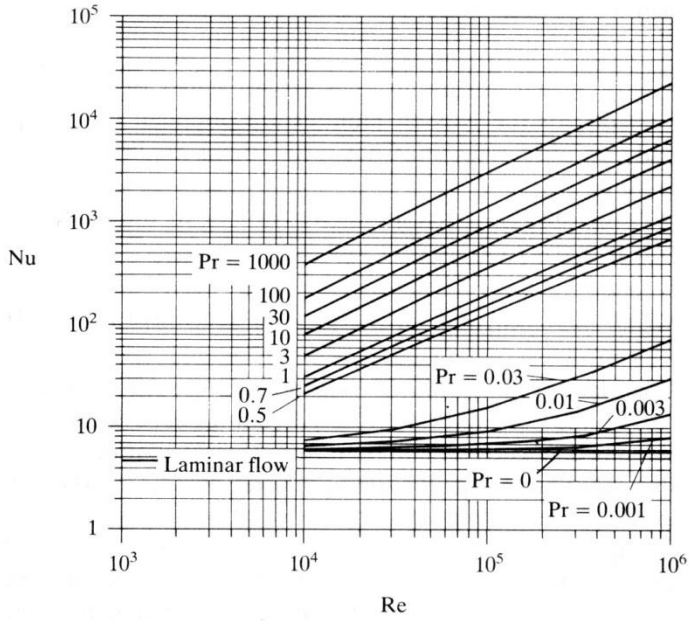

Figure 1.8: Nusselt number for fully developed velocity and temperature profiles, circular duct and constant heat flux, Kays and Crawford [1993]

In general, air and water are the most common coolant for electrical machines. The fluid properties of air and water at ambient temperature are tabulated in Table 1-1. The comparison between water cooling and air cooling at Reynolds number at 3×10^4 and duct diameter of 10 mm is shown in Table 1-2. Water gives higher convective heat transfer, but it needs to be compensated by higher pumping pressure mainly due to the density of water.

Fluid properties	Water	Air
Prandtl number, *Pr*	6.59	0.72
Density, ρ [kg/m^3]	998	1.2
Dynamics viscosity, μ [kg/(m.s)]	9.77×10^{-4}	1.82×10^{-5}
Thermal conductivity, λ [W/(m.K)]	0.6048	0.0256
Specific heat, c_p [J/(kg.K)]	4076	1006

Table 1-1: Fluid properties of water and air at 20 °C

Cooling	Water	Air	Water/air ratio
Nusselt number, Nu	187	77	2.4
Heat transfer coefficient, h [W/(m^2.K)]	11310	197	57.4
Mean velocity, V [m/s]	2.94	45.5	0.065
Pressure drop, Δp [Pa]	$K\rho_w V_w^2/2$	$K\rho_{air} V_{air}^2/2$	$\frac{\rho_w V_w^2}{\rho_{air} V_{air}^2} = 3.5$

Table 1-2: Comparison between water and air coolings for Re = 3×10^4 and duct diameter of 10 mm

1.6 Rotation Effects in Electrical Machines

In fact, the operation of electrical machines involves rotation which complicates the fluid flow and heat transfer problem in cooling ducts, as described in the previous section. The effects of rotation introduce additional forces to the system due to Coriolis and centrifugal accelerations.

In electrical machine, the fluid motion is influenced by the Coriolis force from a rotating reference frame. The Coriolis force is directly proportional to the mass of the fluid particle (m), angular velocity vector of the rotating frame (ω_m) and also the velocity vector of the fluid particle (V) with respect to the rotating frame. The vector equation of Coriolis force can be expressed as follows:

$$F_{coriolis} = -2m(\omega_m \times V) \tag{1.11}$$

The cross product operator (i.e. ×) in the equation (1.11) multiplies only the ω_m and V vectors that are orthogonal. The ω_m vector is directed along the axis of the rotating reference frame. It is important to note that the resulting Coriolis force is also orthogonal to both ω_m and V. Within throughflow ventilated electrical machine, the fluid around a duct is subjected to pressure gradient force and tends to flow towards the duct. At the same time, the fluid is being dragged to rotate about the rotation axis. Hence, the fluid tangential velocity component above the duct is higher than the one below. Therefore, the flows from each side get deflected to the left of their initial direction due to the Coriolis effect which is represented by red arrows in Figure 1.9. This results in a swirling flow in the rotating duct entrance region. The Coriolis force

becomes less inside the duct because of the decrease in the fluid velocity vector that orthogonal to the rotation axis. Instead, the flow tends to be parallel to the rotation axis inside the duct.

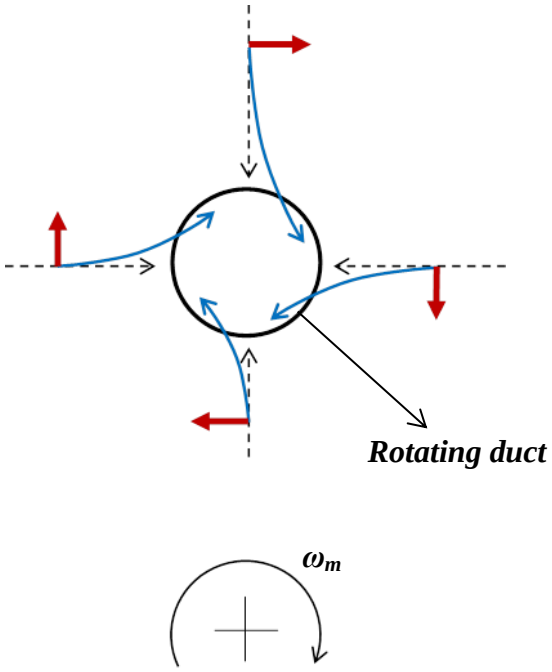

Figure 1.9: The flow pattern at the duct entrance in rotating reference frame is represented by blue arrows. The dashed arrows represent the flow direction due to the pressure gradient force. The red arrows indicate the direction of Coriolis force acting on the fluid particles.

Inside the duct, the fluid motion is relatively dominated by centrifugal force in a rotating reference frame. The centrifugal force is directly proportional to the square of angular velocity (ω_m), mass of the fluid particle (m) and the distance of the body from the axis of the rotating reference frame (r) which can be written as:

$$F_{centrifugal} = -m\omega_m \times (\omega_m \times r) \tag{1.12}$$

The centrifugal force acts outwards in the radial direction. In electrical machine, the fluid adjacent to the duct wall is less dense than the fluid at the centre of the duct due to the heating effect. The density variation in the centrifugal field results in a centrifugal buoyancy which further enhance the temperature exchange between the hot and cold fluid particles.

As described above, the fluid in straight circular ducts which rotate about a parallel axis are strongly influenced by rotating effects. Consequently, the heat transfer in rotor ducts cannot be estimated using the same correlations for the stationary case. On the other hand, the rotating effects will also affect the pressure loss of fluid passing through the duct. The additional pressure losses due to rotation need to be characterised before the convection heat transfer can be estimated accurately. Therefore, the Coriolis and centrifugal effects will be taken into account in the fluid flow and heat transfer analysis in electrical machines.

1.7 Focus and aims of research

A machine's electrical performance is strongly limited by the machine's thermal performance. This heat dissipation of electrical machines becomes more and more important issue nowadays because of the demand of machine of higher power density but smaller in physical size. In order to effectively remove the heat generated inside an electrical machine, air is commonly forced through the cooling ducts of the machine. Therefore, accurate prediction of air flow distribution and associated pressure losses is crucial to the accurate prediction of heat transfer in electrical machines. In this topic, the effects of rotation to the air flow and heat transfer analysis in electrical machines still remain a great challenge.

The main objective of the present research is to investigate the pressure losses of air passing through circular ducts in rotor. The ducts rotate about the rotor axis parallel to the axis of the ducts. A dimensional analysis will be performed to identify the dimensionless groups that are important to the problem. This investigation will lead to an original set of correlations for pressure losses in air ducts in the rotor due to fluid shock. For the first time, the pressure losses arisen from the Coriolis and centrifugal effects in rotating reference frame will be taken into account in the analysis of the problem. The problem will be investigated using CFD and experimental methods. An experimental test rig will be built for this investigation.

The proposed correlations will be suitable to be applied to fluid flow modelling of electrical machines. The correlations are aimed to be incorporated into the flow

network analysis, an analytical fluid flow modelling method that can outperform the existing lumped-parameter thermal network method in terms of accuracy.

1.8 Outline of Thesis

Chapter 2 reviews the advantages and weaknesses of the methods used for thermal analysis of electrical machines. The correlations that can be used to model convective heat transfer and fluid flow in the ventilation paths in the throughflow ventilated electrical machines are presented.

Chapter 3 describes the application of computational fluid dynamics (CFD) in thermal modelling of electrical machines.

Chapter 4 investigates the impact of configurations of air inlet ducts on the convective heat transfer and operating temperatures of a 25 kW 100 rpm axial flux permanent magnet prototype. Conjugate heat transfer analysis of the machine was performed using a CFD method.

Chapter 5 develops an analytical design tool that is suitable to perform flow network analysis of throughflow ventilated electrical machines.

Chapter 6 performs a dimensional analysis to identify the geometric and fluid dynamic parameters that influence the rotational pressure losses using CFD simulations.

Chapter 7 explains how the experimental apparatus is constructed to investigate the effects of rotation on the flow resistance of a rotor-stator system.

Chapter 8 presents the experimental results obtained using the experimental apparatus in Chapter 7 and compares them with the CFD and analytical results. Correlations that can be used to characterise the rotational pressure losses in throughflow ventilated machines are proposed.

Chapter 9 summarises the work undertaken in this thesis and finally suggestions for further work are provided.

2 Literature Review

In the design of electrical machines, the heat generation inside a machine mainly depends on the electromagnetic characteristics of the machine. The cooling system not only determines the temperature distribution within the machine, but also influences the electromagnetic performance. Severe thermal conditions can lead to insulation failure and permanent magnet demagnetization for permanent magnet machines. Therefore, thermal issues must be considered in the design process to ensure that the machine performance meets the required application.

In this chapter, a survey of literature of the thermal analysis of electrical machines is presented. It can be categorised into analytical methods and numerical methods. The advantages and weaknesses of these methods are described through their application to various electrical machines. Because of the high power density of electrical machines, the coolant is often forced to pass over the heated surface for removing the undesired heat. Hence, an understanding of the flow distribution in electrical machines and flow characteristics in the ventilation passages is essential to improve machine thermal performance. Experimentally determined heat transfer coefficients may be applied at the solid-fluid boundaries of thermal models based upon past experience of manufacturing and design. For those machines which rely heavily on forced convection cooling, a flow network analysis is coupled with the equivalent thermal circuit to compute the mean flow rate in the ventilation passages (e.g. stator ducts, airgap, rotor ducts, etc.) so that the convective heat transfer coefficients can then be derived from published empirical correlations.

The problems of heat transfer and fluid mechanics are normally studied using dimensional analysis. Dimensional analysis groups the variables of these problems into a set of dimensionless groups and translates the experimental investigation into a form of systematic empirical approach, which allows the investigation of one prototype to be applied to other models having geometric and dynamic similarities. This chapter reviews the published literature highlighting the effects of rotation in convection heat transfer and flow resistance, which is an effect that needs to be considered in electrical machine thermal modelling. However, the review of existing literature also reveals that the literature describing how the rotating effects increase

the pressure loss is very limited. More research needs to be carried out on this topic, and is the aim of the present study.

2.1 Thermal Analysis Methods for Electrical Machines

2.1.1 Analytical method

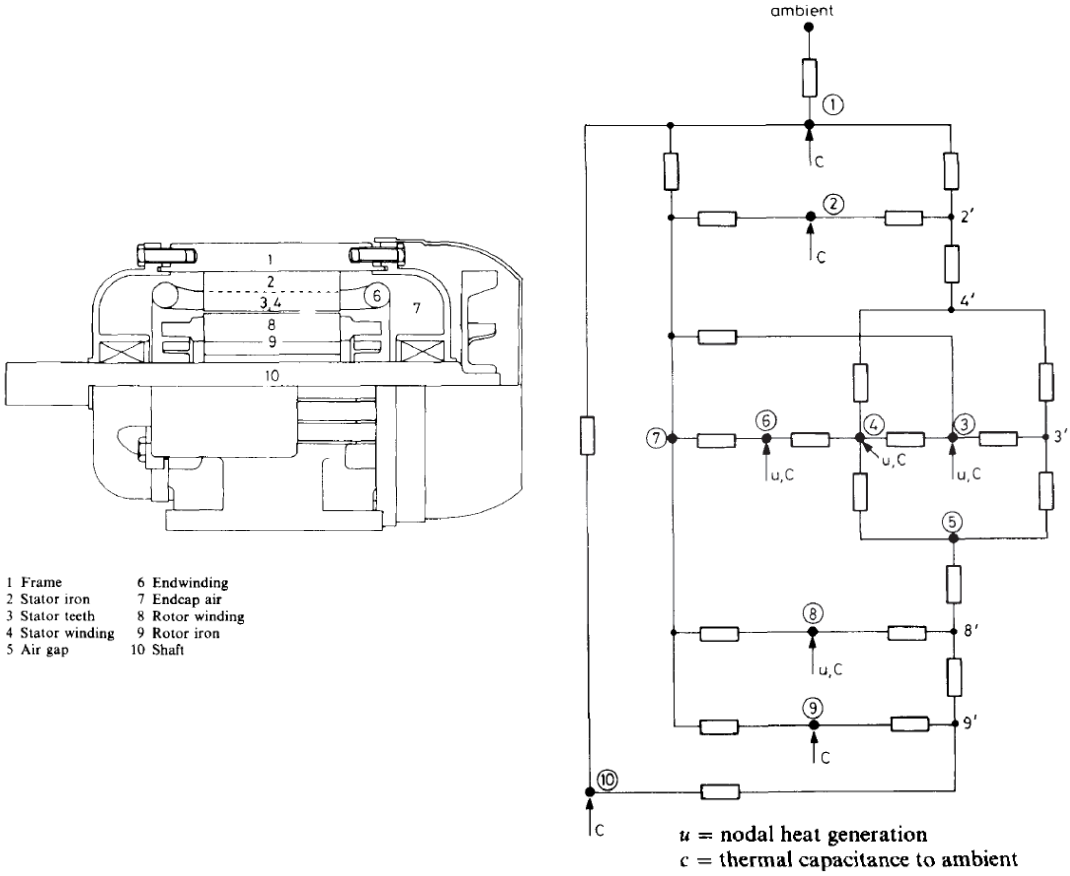

Figure 2.1: Equivalent thermal network of an induction motor, Mellor et al. [1991]

The lumped parameter thermal network (LPTN) is an analytical thermal modelling method for estimating electrical machine thermal performance based on finite difference method. The lumped parameter thermal network is an equivalent circuit for thermal domain based on the so-called lumped element modelling technique. This lumped element modelling technique is first used for electrical domain and represents the domain by an equivalent electrical circuit. Then, this technique is also applied to mechanical, fluid and electromagnetic domains. The application of LPTN method on electrical machine thermal modelling is found to be first published by Mellor et al. [1991]. An equivalent thermal model reduces an electrical machine to a

number of discrete elements and assumes that the temperature difference inside each element is negligible. The heat flow between the lumps is modelled using conduction, convection and radiation thermal resistances. The approximation is useful to simplify the complex heat transfer problem of the electrical machine. The LPTN method results in very fast computational speed for temperature prediction. Hence, the LPTN method is widely used for electrical machine thermal analysis for steady-state solution and even transient solution.

Mellor et al. [1991] built lumped parameter thermal models for 75kW and 5.5kW totally enclosed fan cooled (TEFC) induction motors. As shown in Figure 2.1, the thermal model is sufficiently detailed to identify the temperatures at most locations in the machine. The calculation of thermal resistances and thermal capacitances of the thermal models were presented. Steady-state and transient solutions were obtained from eight linear differential heat balance equations. The transient results showed good agreement with the experimental temperatures obtained from varying load tests. To analyse the thermal performance of a high-energy-density wound component using a lumped parameter thermal network, Wrobel et al. [2010] integrated the loss predictions from electromagnetic finite element analysis and experimentally determined convective heat transfer coefficients with the equivalent thermal network and used to determine the operating temperature of the wound component.

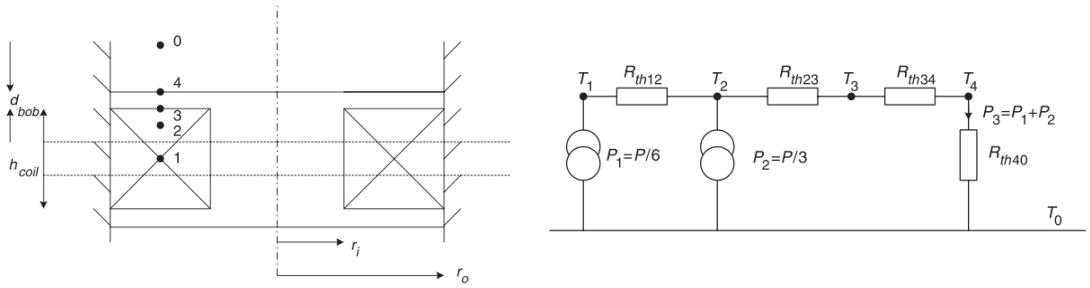

Figure 2.2: Cross section through stator coil (left) and thermal network (right), Bumby and Martin [2005]

In order to determine the maximum current density in the winding due to the temperature limit, Bumby and Martin [2005] made use of a simple thermal model (see Figure 2.2) based on the LPTN method for stator (losses dominant) section to

calculate the maximum temperature in the copper winding for the design and development of an axial flux permanent magnet air-cored generator. An estimated convective heat transfer of 50 W/m^{2}K from previous experience was used in the calculation, while an average value of 60 W/m^{2}K was measured from the prototype.

A lumped parameter thermal model is also used for the design of a 50 kW air-cored permanent magnet linear generator to predict coil temperatures. Hodgins et al. [2012] demonstrated that the convective heat transfer is the dominant component of the thermal network, but it involves a less-defined area and heat transfer coefficients may need to be modified to suit the conditions in the convection region.

Wrobel et al. [2010] developed a general cuboidal element for three-dimensional conduction modelling based on the LPTN method (see Figure 2.3). This technique is able to account for internal heat generation and anisotropic thermal conductivity, in contrast to the commonly used two resistor network. It is more appropriate for accurate temperature predictions in transient thermal analysis. The results from the cuboidal element thermal network showed good agreement with 3D finite element analysis (FEA) model values.

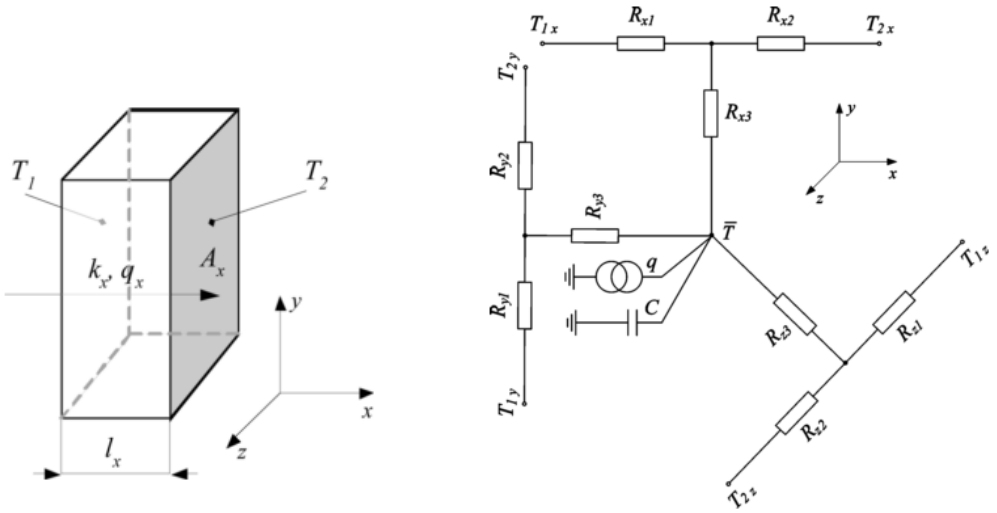

Figure 2.3: Three-dimensional network representation of the general cuboidal element comprising of heat generation source, thermal capacitance and resistances, Wrobel [2010]

Motor-CAD is a commercial software package developed by Motor Design Ltd. based on this thermal modelling technique, which is able to model most standard radial flux machine topologies. It provides the crucial link between electromagnetic

design and the thermal analysis of electrical machines. Extensive investigations were carried out by Staton et al. [2005] to address the complex thermal phenomena that occur in electrical machines and how they can be modelled using Motor-CAD. Staton et al. [2008] addressed the suitable formulations and empirical correlations that are used in Motor-CAD for convective heat transfer calculation in electrical machines. Boglietti et al. [2004] employed Motor-CAD to model the thermal performance of TEFC induction motors. Sensitivity analysis was performed to investigate the variation in temperature rise for changes in selected thermal parameters and to identify the parameters that have most influence on the temperature rise. The important parameters are the focus for thermal performance improvement. Mejuto et al. [2006] performed a thermal optimisation of a TEFC synchronous generator using Motor-CAD. The temperatures predicted by the thermal model showed good agreement with the experimental results. A sensitivity analysis was implemented using the validated thermal model to optimise the machine for a required application. As the electromagnetic and thermal designs are interdependent, Motor-CAD was employed by Al'Akayshee and Williams [2003] together with an analytical electromagnetic equivalent circuit to obtain an optimum design of a throughflow ventilated induction motor for oil field drilling application. Figure 2.4 shows the lumped parameter thermal network of the machine using Motor-CAD.

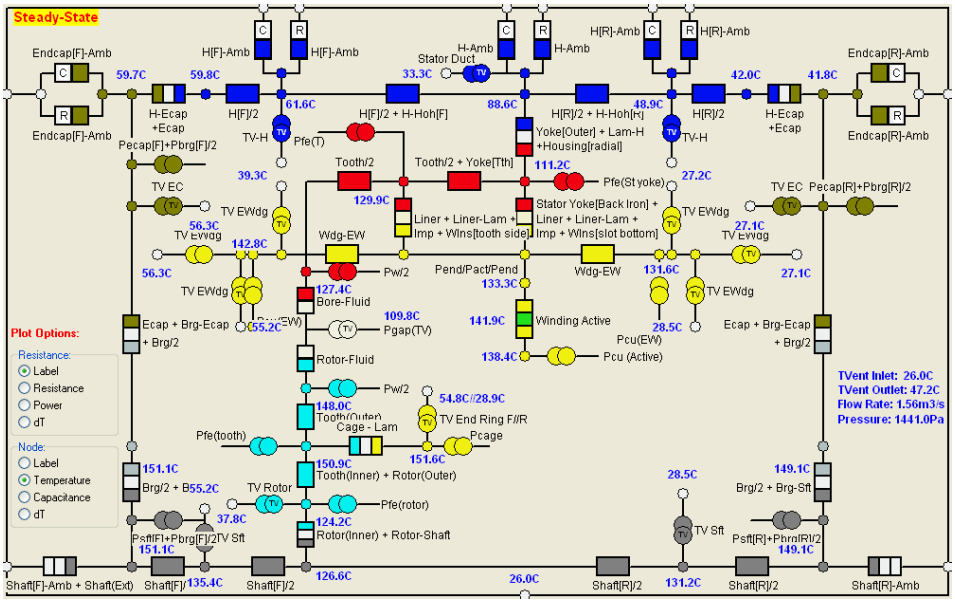

Figure 2.4: Lumped parameter thermal network of Al'Akayshee [2003] throughflow ventilated induction motor using Motor-CAD

Convection is a major heat transfer mechanism in electrical machines due to fluid motion. In the analytical thermal model, the convective heat transfer coefficient is commonly based on empirical correlations, which can be found in Section 2.2. These empirical heat transfer correlations typically require the local flow velocity as an input. In order to predict the local flow velocity, a flow network analysis is required to be incorporated into the thermal network of throughflow ventilated electrical machines. A general method for conducting flow network analysis on a throughflow ventilated electrical machine is presented in Taylor [1960]. The author used a correction factor to account for the effect of rotating ducts to the pressure drop, but no related reference can be found to show how the proposed correction factor is obtained. A flow network analysis of ventilation system for large hydro generator using a computing solving algorithm is presented by Chen [2001]. Due to the nonlinear relationship between pressure loss and flow rate, the flow distribution within the complex flow network was obtained using a successive iterative method. A computer program was developed for this by the author. However, Chen [2001] did not account for rotating effects on the pressure loss.

Basically, the movement of cooling medium through the ventilation paths of an electrical machine is caused by the differential pressure normally provided by fan, blower or pump. The flow rate of the cooling medium passing through the electrical machine is strongly dependent on the flow resistances of the ventilation system. The flow resistances are commonly known to be due to friction loss and separation losses arising from flow disturbance caused by changes of direction, changes in flow cross-sectional area and interaction with other pipe fittings. They are quantified using empirical pressure loss coefficients based on the flow kinetic energy, which are available in Idelchik [2007] and Miller [1978]. Since the differential pressure provided by a fan is practically limited by the fan speed, the cooling performance of an electrical machine in practice is determined from the obtainable flow rate through the electrical machine based on the system flow resistance. In order to determine the temperature distribution of a throughflow ventilated axial flux permanent magnet (AFPM) machine, a fluid flow model was built by Scowby et al. [2004] and incorporated into the thermal model. The results obtained from the flow model and experimental measurement showed reasonable agreement. The pumping pressure is

mainly created by the rotor hub blades and channels between the magnets due to rotation, which is used to drive the cooling air to pass through the air flow paths. Wang et al. [2005] developed a thermofluid model for typical AFPM machines by combining a lumped parameter thermal network (see Figure 2.5) and a fluid flow model. The fluid flow model calculates the air flow rate through the machine by taking into account the pumping pressure induced by the protruding magnets and the pressure losses within the machine. However, the effects of rotation was neglected which may significantly affect the accuracy of the thermofluid model.

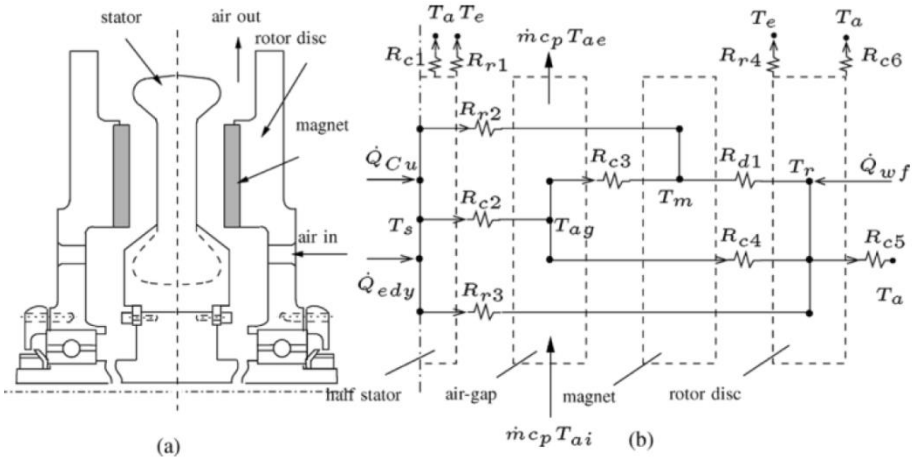

Figure 2.5: Lumped parameter thermal network of an AFPM machine, Wang et al. [2005]

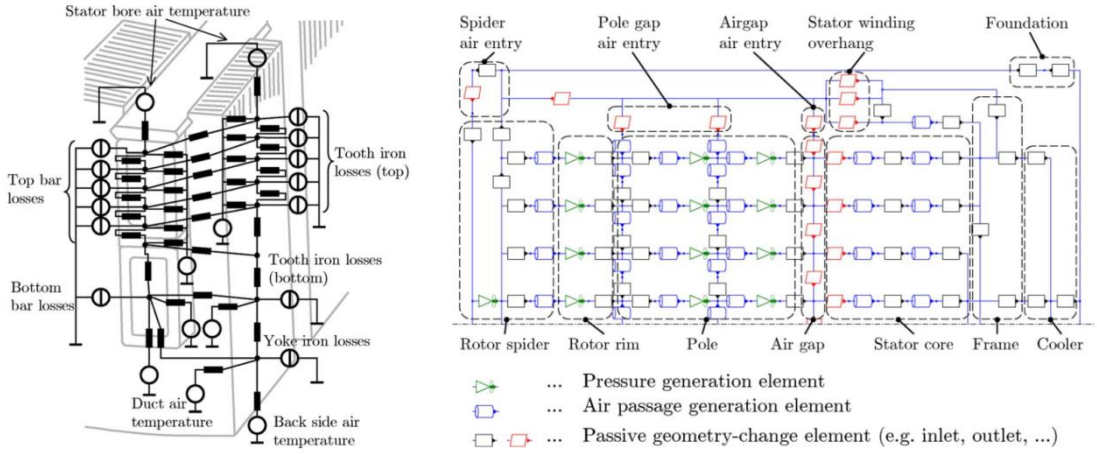

Figure 2.6: Thermal network of stator core (left) and flow network of half of an air-cooled machine (right), Traxler-Samek et al. [2010]

Traxler-Samek et al. [2010] developed a computational method for the calculation of temperatures in the active parts of large air-cooled synchronous generators. As the electrical losses, temperature and cooling air are interdependent in nature, the computational method couples an analytical power loss calculation, an automated air flow and air temperature network calculation, and a set of linked thermal networks. The thermal network of stator core and airflow network are shown in Figure 2.6. The calculations were performed by software developed by the authors. The computational method is fine-tuned with a set of 60 hydro generators to guarantee the reliability of predicted values regarding the commissioning tests.

Due to the operating temperatures inside the large machines varying significantly depending on location, thermal modelling using only a lumped parameter thermal model is not sufficient to predict the temperature distribution precisely. Centner et al. [2012] developed a coupled thermal-fluid model for a 6 MW cylindrical rotor synchronous machine which is capable of predicting the temperature variation of an excitation winding from the centre of the rotor to the end winding for directly cooled conductors and indirectly cooled conductors. By using indirect cooling, an increase of relative temperature of 20% was found at the centre of the rotor when compared to direct cooling.

2.1.2 Numerical method

Two common numerical methods for thermal analysis of electrical machines are computational fluid dynamics (CFD) and finite element analysis (FEA). The main advantage of thermal modelling using FEA is that it can predict the conductive heat transfer accurately, particularly when coupled with electromagnetic FEA models for detailed and accurate loss determination, making it suitable to obtain thermal solution for solid regions of high temperature gradient such as the winding. However, convective heat transfer correlations need to be adapted for convective boundaries. As convection is associated with fluid motion, CFD is applied to electrical machine thermal analysis to determine the flow rate and velocity distribution, and pressure drop along the cooling passages. If solid regions are included, CFD can perform conjugate heat transfer analysis combining heat transfer by conduction and

convection, predicting the rate of heat transfer at convective boundaries and temperature distribution in the solid regions. CFD software programmes commonly used for electrical machine thermal modelling are STARCCM+, Ansys CFX, and Fluent. The details of CFD method used in this thesis are given in Chapter 3.

2.1.3 Hybrid method

As described in the preceding section, the fluid flow and its distribution within a throughflow ventilated electrical machine is an important issue that must be considered in the electrical machine thermal analysis.

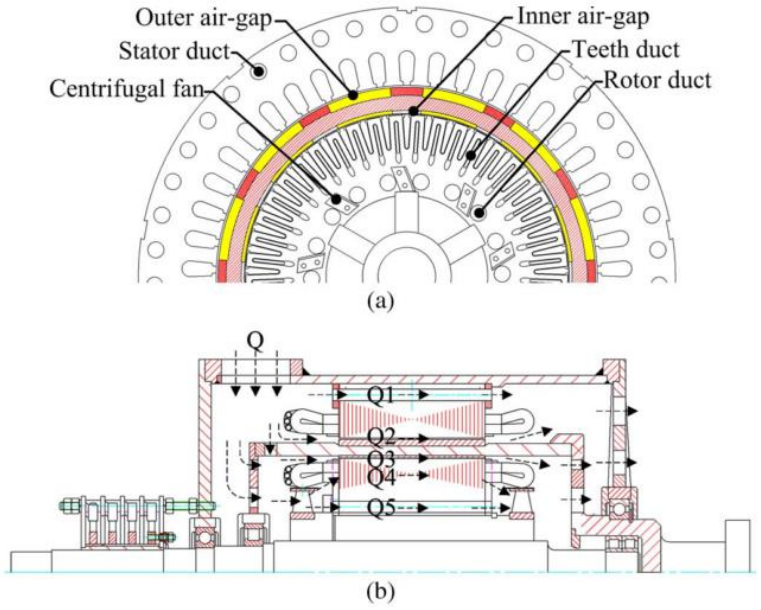

Figure 2.7: Ventilation system of DMP machine, (a) radial cross section, (b) flow distribution between the ventilation paths, Sun et al. [2013]

Sun et al. [2013] performed thermal analysis of a dual mechanical port (DMP) machine for wind power application using FEA method. The thermal FEA model was coupled with the electromagnetic FEA model for the heat sources in real operation. The initial cooling arrangement of the machine consists of four cooling paths, namely, the stator duct (Q1), the outer air gap (Q2), the inner air gap (Q3), and the rotor ducts (Q5). A centrifugal fan is used to force the air flow through the cooling paths. The original cooling arrangement was improved by introducing inner rotor teeth ducts (Q4) as illustrated in Figure 2.7 in order to dissipate the heat generated in the inner rotor more effectively. Although the iron loss in the inner rotor teeth increases 9% compared with the original cooling system due to the increase in

the flux density, the temperature of the inner rotor winding drops significantly. A simple flow network analysis was implemented to deduce the convective heat transfer coefficients that need to be applied to the convective boundaries of the thermal FEA model. The validity of the FEA model was verified by a 10 kW DMP prototype.

Hey et al. [2010] developed a hybrid thermal model for an AFPM machine. Because of geometric complexities and limited literature in the relevant topic, CFD was used to determine the average values of convective heat transfer coefficient at the solid-fluid boundaries within the machine. As a result, the hybrid thermal model based upon the LPTN method allows fast computation and provides high level of accuracy for transient temperature prediction, which was confirmed with experimental results.

In order to accurately estimate claw pole machine temperatures, Jeremie et al. [2010] combined an analytical lumped-parameter thermal network with a CFD model. Convective thermal resistances between the machine components and the flow rate of cooling air as a function of the machine speed were obtained using CFD method. This information was used in the analytical LPTN model to compute the machine temperatures.

2.2 Convective heat transfer in rotor-stator systems

For throughflow ventilation cooling methods, a differential pressure drives the cooling medium passing through the ventilation paths to remove the undesired heat from electrical machines. Heat transfer in the ventilation paths of electrical machines is similar to heat transfer in closed conduits. In order to limit the scope of this section to a manageable size, a focus is given to the literature that deals with heat transfer in straight coolant paths rotating about a parallel axis. However, a brief survey of heat transfer in stationary ducts is presented to indicate some important heat transfer characteristics that have been mostly ignored in analytical methods, and also to highlight the difference between rotating and stationary conditions.

2.2.1 Stator ducts

Heat transfer correlations that are suitable for stator ducts are widely presented in engineering textbooks such as Incropera et al. [2002], Burmeister [1993], Kays and

Crawford [1993]. However, they cannot be applied directly to compute the convective heat transfer as they are mostly for ideal conditions (e.g. fully developed flow, uniform heating, smooth surface, etc.). They need to be tuned according to the actual geometric and dynamic conditions. When heating begins in a duct, Nusselt numbers would be large at the start of the heated section and would asymptotically approach the value for fully developed flow occurring in long ducts further downstream. The investigation of the effect of thermal entry length on the mean Nusselt number with respect to duct length was performed by Deissler [1953]. This heat transfer characteristic is more appropriate for practical use in electrical machines, but it is rarely applied to the analytical thermal modelling.

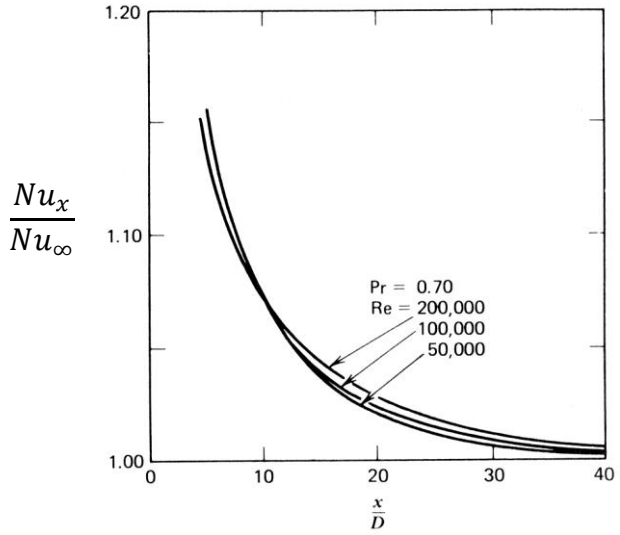

(a) Influence of Reynolds numbers at *Pr* = 0.7 (air)

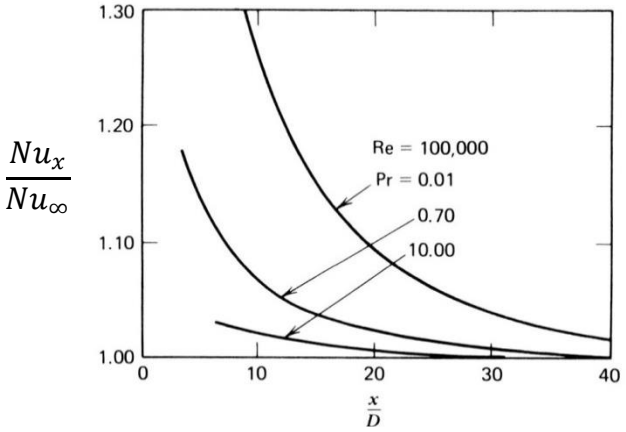

(b) Influence of Prandtl numbers at *Re* = 100,000

Figure 2.8: Nusselt numbers in the thermal entrance region of a circular duct for constant wall heat flux, Kays and Crawford [1993]

As illustrated in Figure 2.8, the thermal-entry-length effect is pronounced at small *Pr*, but is small for large *Pr*. The thermal-entry-length effect is independent of Reynolds number for *Pr* = 0.7, i.e. air. The heat transfer correlations for air that take the thermal-entry-length effect into account are given in Burmeister [1993], which are dependent on entrance configuration.

For fully developed turbulent flow, the average heat transfer in a stationary smooth circular duct can be estimated using the Dittus-Boelter equation, Winterton [1998]:

$$Nu_0 = 0.023Re^{0.8}Pr^{0.4} \tag{2.1}$$

The Sieder-Tate equation can be used for fluids of temperature-sensitive viscosity as:

$$Nu_0 = 0.027Re^{0.8}Pr^{0.33}\left(\frac{\mu}{\mu_s}\right)^{0.14} \tag{2.2}$$

where μ is the fluid viscosity at the bulk fluid temperature and μ_s is the fluid viscosity at the heat transfer boundary surface temperature. For a more accurate heat transfer correlation, Gnielinski's heat transfer correlation should be applied, which covers a wide range of Reynolds number from 3000 to 5×10^6, *Pr* from 0.5 to 2000 and takes the Darcy friction factor (f) into account from Moody chart. The correlation is expressed as:

$$Nu_0 = \frac{(f/8)(Re-1000)Pr}{1+12.7(f/8)^{1/2}(Pr^{2/3}-1)} \tag{2.3}$$

These equations can be found in Incropera et al. [2002]. Since manufacturing and operating conditions often lead to rough walls, duct surface roughness may cause significant effect on the heat transfer. According to Kays and Crawford [1993], a simple empirical correlation considering the influence of surface roughness on heat transfer is suggested by Norris [1971]:

$$\frac{Nu_{rough}}{Nu_{smooth}} = \left(\frac{f}{f_{smooth}}\right)^{0.68Pr^{\,0.215}} \tag{2.4}$$

When (f/f_{smooth}) > 4, the Nusselt number was found no longer increases with increase in roughness.

Moreover, a great extent of heat transfer analysis is based upon the circular duct, but the ventilation paths in electrical machines may not be circular. A noncircular duct can be treated as a "circular duct" having a hydraulic diameter, White [1986]. The heat transfer in a noncircular duct can be accurately approximated by the use of the hydraulic diameter as the characteristic dimension in circular duct heat transfer correlations. The hydraulic diameter, D_h is defined as:

$$D_h = \frac{4A}{P'} \tag{2.5}$$

A is the cross-sectional area of a noncircular duct and P' is the wetted perimeter of the noncircular duct.

2.2.2 Rotor ducts

Due to the high power density of electrical machines nowadays, this causes the heat generation per unit volume to increase. To solve this problem, ventilation ducts can be created in the rotor-yoke to enhance the convective heat transfer. Onuki [1999] presented a novel approach for the design optimisation of ventilation ducts in the rotor-yoke of a squirrel-cage induction motor while maintaining the magnetic flux density in the airgap. The flow and heat transfer characteristics of coolant in straight circular ducts which rotate about a parallel axis are influenced by rotating effects. Rotation causes a secondary flow, which is perpendicular to the direction of the main flow, induced by Coriolis and centrifugal forces. Consequently, the heat transfer in rotor ducts cannot be estimated using the same correlations for the stationary case. Based on the dimensional analysis of this problem, more dimensionless groups are required to correlate the convective heat transfer in rotor ducts. The centrifugal buoyancy may be quantified by means of the rotational Grashof number (which measures the centrifugal buoyancy based on the duct centre line centrifugal acceleration to viscosity acting on a fluid), Mori and Nakayama [1976] and Nakayama [1968]. In rotor ducts of electrical machine, the fluid adjacent to the duct wall is heated and thus the fluid adjacent to the duct wall is less dense than the fluid at the centre of the duct. Here, the gravitational acceleration of Grashof number for a natural convection is replaced by a centrifugal acceleration. Due to density change in

the centrifugal field, the buoyant force brings the cooler fluid into contact with the outer duct wall. The product of rotational Grashof number and Prandtl number forms the rotational Rayleigh number which is given by:

$$Ra_\tau = Gr \times Pr = \frac{H\omega_m^2 \beta d^4 \tau_a}{2\nu^2} Pr \tag{2.6}$$

H is the radius of rotation, ω_m is the angular velocity, β is the coefficient of volumetric expansion, τ_a is the temperature gradient along the duct axis and ν is the kinematic viscosity of a fluid.

The Coriolis effect may be quantified by means of a rotational Reynolds number, J (the ratio of Coriolis force to viscous force) as:

$$J = \frac{\omega_m d^2}{8\nu} \tag{2.7}$$

An eccentricity parameter (ε) is a geometric description of radius of rotation to duct diameter ratio.

$$\varepsilon = \frac{H}{d} \tag{2.8}$$

Table 2-1 and Table 2-2 summarise relevant heat transfer correlations that account for the secondary flow induced by the centrifugal buoyancy and Coriolis effects. The methodologies of how these correlations were obtained and also the important insight into the influence of secondary flow on the heat transfer characteristics will be then described in more detail.

Flow regime	Flow condition	Approach	Validity	Formula	Authors
Laminar	Fully developed	Analysis	Constant axial temperature gradient	For Pr ≤1, $\zeta_{Pr\leq1}=\frac{1}{5}\left[2+\left(\frac{10}{Pr^2}-1\right)^{1/2}\right]$ $\frac{Nu}{Nu_0}=\frac{0.273}{\zeta_{Pr\leq1}}\left(\zeta_{Pr\leq1}-1+\frac{1}{3\zeta_{Pr\leq1}}\right)^{1/5}\frac{(Ra_\tau Re)^{1/5}}{1+[1/(10\zeta_{Pr\leq1}Pr)]}$ For Pr > 1, $\zeta_{Pr>1}=\frac{2}{11}\left[1+\left(\frac{77}{4Pr^2}+1\right)^{1/2}\right]$ $\frac{Nu}{Nu_0}=\frac{0.191}{\zeta_{Pr>1}}(3\zeta_{Pr>1}-1)^{1/5}\frac{(Ra_\tau Re)^{1/5}}{1+[1/(10\zeta_{Pr\leq1}Pr)]}$	Mori and Nakayama [1967]
Laminar	Fully developed	Numerical, Experimental	$4\times10^3 < Re\,Ra_\tau\,Pr < 1\times10^8$, $0.7 \leq Pr \leq 1\times10^4$	$\frac{Nu}{Nu_0}=0.262(ReRa_\tau Pr)^{0.173}$	Woods and Morris [1974]
Laminar	Developing	Experimental	$L/d = 20$, $162 \leq Re \leq 2.7\times10^3$, $Ra_b \leq 2\times10^7$	$\frac{\overline{Nu}}{Nu_0}=\left(1+0.03\frac{Ra_b}{Gz}\right)^{1/3}$ $Gz=\frac{\pi}{4}RePr\frac{d}{L}$	Sakamoto and Fukui [1971]

Table 2-1: Relevant heat transfer correlations for laminar flow in rotating duct

Flow regime	Flow condition	Approach	Validity	Formula	Authors
Turbulent	Fully developed	Analysis	Constant axial temperature gradient	For Pr ≈ 1, $$Nu_4 = \frac{0.043Pr}{Pr^{2/3} - 0.05}\frac{Re^{4/5}}{\Gamma^{1/10}}\left[1 + \frac{0.061}{(Re/\Gamma^2)^{1/5}}\right]$$ For Pr > 1, $$Nu_5 = 0.028Pr^{2/5}\frac{Re^{5/6}}{\Gamma^{1/12}}\left[1 + \frac{0.032}{(Re/\Gamma^{2.5})^{1/6}}\right]$$	Nakayama [1968]
Turbulent	Developing	Experimental	Pr = 0.7, $5\times10^3 \le Re \le 4\times10^4$, ε = 10.67, $1.4 \le \frac{w}{d} \le 2.09$, $0.255 \le \frac{V_T}{U} \le 3.07$	For L/d = 6.4, $$\frac{\overline{Nu}}{Nu_0} = 1.58\left(\frac{w}{d}\right)^{-0.3}\left(\frac{V_T}{U}\right)^{0.21}$$ For L/d = 10.7, $$\frac{\overline{Nu}}{Nu_0} = 1.44\left(\frac{w}{d}\right)^{-0.2}\left(\frac{V_T}{U}\right)^{0.19}$$	Le Feuvre [1968]
Turbulent	Developing	Experimental	Pr = 0.7, $1.3\times10^3 \le Re \le 2\times10^4$, L/d = 34.65 and 69.30, ε = 24 and 48, $15 \le J \le 150$,	$$\overline{Nu} = 0.015Re^{0.78}J^{0.25}$$	Morris and Woods [1978]
Turbulent	Developing	Experimental	Pr = 0.7, $5\times10^3 \le Re \le 4\times10^4$, ε = 6 and 10.67, $6.4 \le L/d \le 12$, $50 \le J \le 600$,	$$\overline{Nu} = 0.012Re^{0.78}J^{0.18}$$	Morris [1981]

Table 2-2: Relevant heat transfer correlations for turbulent flow in rotating duct

2.2.2.1 Heat transfer for laminar flow in rotating duct

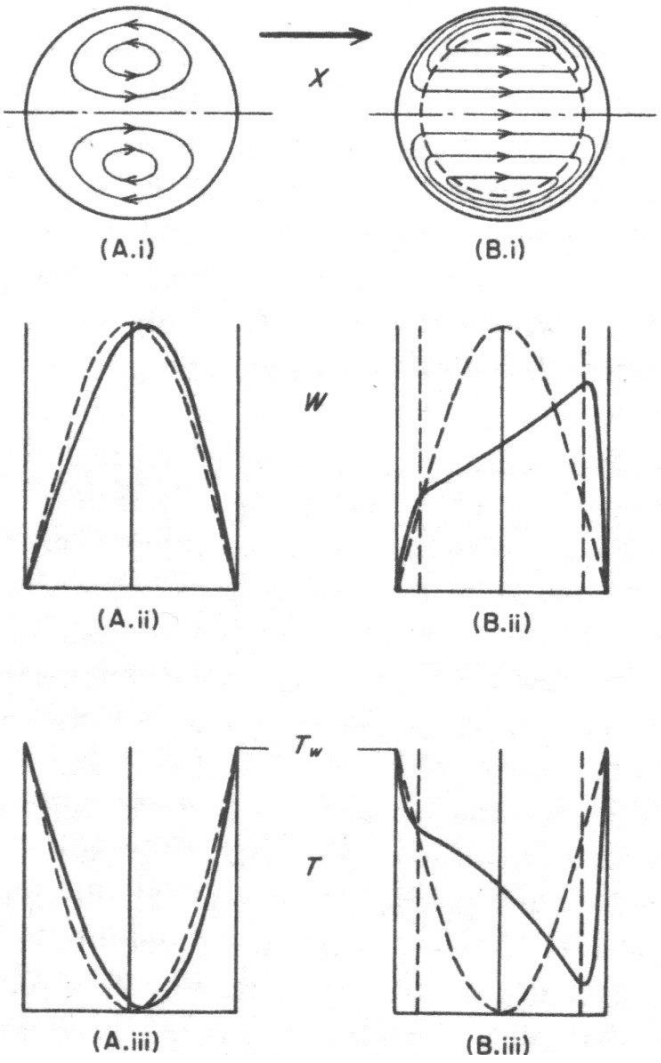

(A) weak secondary flow **(B) strong secondary flow**

Figure 2.9: Stream lines of secondary flow, flow field (*W*) and temperature field (*T*) respectively (top to bottom) driven by a body force in the *X* direction in a centrifugal field, Mori and Nakayama [1967]

Mori and Nakayama [1967] presented a theoretical analysis for convective heat transfer of a fully developed laminar flow in a straight circular pipe rotating about a parallel axis under a constant wall temperature gradient condition. Flow field and temperature field in the pipe were analysed by assuming a strong secondary flow perpendicular to the pipe axis. The secondary flow is driven by a body force caused by density difference in a centrifugal field. As shown in Figure 2.9, the growth of a

secondary flow to a sufficient extent distorts velocity profile (A.ii and B.ii) and temperature profiles (A.iii and B.iii) considerably from the symmetrical profile of the stationary case. The fields were divided into a flow core region and a thin boundary layer along the wall. As the influences of viscosity and heat conduction are mainly limited in the thin boundary layer adjacent to the pipe wall, the authors analysed the present problem using boundary layer approximations. The effect of secondary flow is predominant in the core region and it increases the heat transfer coefficient markedly. Thermal to hydrodynamic boundary-layer thickness ratios (ζ) were obtained for the calculations of Nusselt number. A specific relation was obtained from the boundary-layer momentum integral equation in the circumferential direction for force balance between the body force in centrifugal field and viscous resistance against the secondary flow at the pipe wall. The heat transfer correlations proposed by Mori and Nakayama [1967] can be found in Table 2-1.

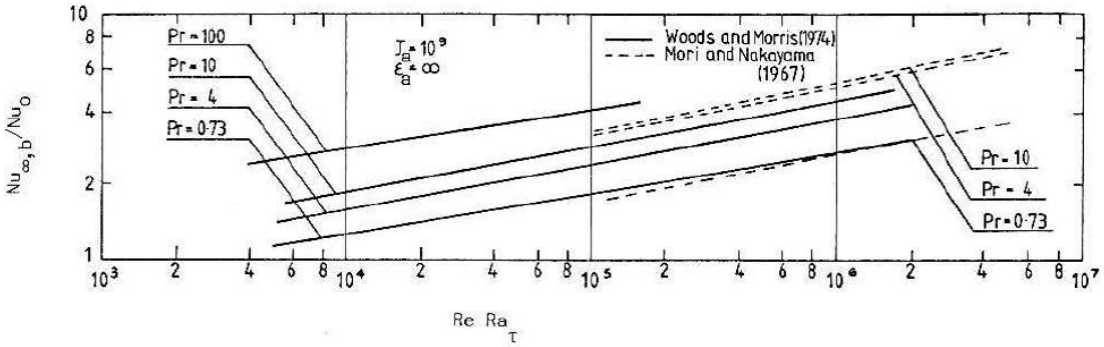

Figure 2.10: Comparison between the influence of rotation on the heat transfer of Mori and Nakayama [1967] and Woods and Morris [1974], Morris [1981]

Woods and Morris [1974] investigated the effects of rotation on heat transfer for a uniformly heated and fully developed laminar flow based on numerical methods by solving the differential equations of mass, momentum and energy conservation without making any assumption concerning the secondary flow field suggested by Mori and Nakayama [1967]. They obtained a numerical model to characterise the influence of rotation on heat transfer. The Nusselt number was determined by numerical integration. The comparison between the predictions of Mori and Nakayama [1967] and Woods and Morris [1974] is illustrated in Figure 2.10. Both predictions are in good agreement only when *Pr* is equal to 0.73, but there are

significant discrepancies for *Pr* is greater than unity. The authors also performed a comparison between the numerical predictions and experimental results obtained with air and water, demonstrating that the theoretical model is capable of predicting the effects of rotation. This led Woods and Morris [1981] to propose a theoretically generated heat transfer correlation for fully developed laminar flow. The heat transfer enhancement relative to the stationary case (Nu_0) is dependent on the product of Reynolds Number (*Re*), rotational Rayleigh number (Ra_τ) and Prandtl number (*Pr*). The heat transfer correlation can be found in Table 2-1. The authors found that the eccentricity parameter (ε) had negligible influence on the heat transfer.

Sakamoto and Fukui [1971] investigated experimentally the influence of rotation on heat transfer for developing laminar flow in the entrance region using air, oil and Naphthalene as the test fluids. A tube of length-to-diameter (*L/d*) ratio of 20 was revolved in the range of speed between 420 and 2700 rpm. The authors found that rotation produces a marked improvement on heat transfer in the laminar flow range. A correlation of average heat transfer improvement in the entrance region of rotating tube was proposed, which is a function of the rotational Rayleigh number (Ra_b) based on the tube wall to bulk fluid temperature difference and the Graetz number (*Gz*). The Graetz number is a dimensionless number that characterises thermally developing laminar flow in a tube.

2.2.2.2 Heat transfer for turbulent flow in rotating duct

Nakayama [1968] performed a theoretical analysis of turbulent heat transfer in a pipe rotating about a parallel axis by assuming an effective secondary flow due to density difference in a centrifugal field. Flow and temperature fields are fully developed under the condition of constant wall temperature gradient and they are analysed by dividing them into a flow core region and a thin boundary layer along the wall. The analysis was performed using an identical solution technique to that used for the laminar counterpart reported by Mori and Nakayama [1967]. The main additional physical effect which was included in the analysis is the incorporation of the turbulent fluctuations of velocity and temperature into the basic conservation equations of momentum and energy. The Nusselt number is expressed by use of an integer m which forms the exponents of parameter $Re/\Gamma^{m/2}$ in the analysis. The

correlations for Nusselt number due to secondary flow were obtained in terms of Prandtl number, Reynolds number and inertia force to the body force ratio (Γ) by setting $m = 4$ for gases and $m = 5$ for liquids.

$$\Gamma = \left[\frac{Re^{2m+1}}{(GrPr^{1-\kappa})^{m+1}}\right]^{2/(2m+3)} \tag{2.9}$$

κ is the exponent of Pr in the formula for Nussult number at stationary case, $\kappa = 0.33$ for gases and $\kappa = 0.4$ for liquids. The effect of Coriolis force due to secondary flow was found to be negligible in fully developed turbulent flow.

Humphreys et al. [1967] experimentally studied the turbulent heat transfer characteristics of air flowing through a uniformly heated circular duct rotating about a horizontal axis parallel to the duct axis. The duct has length-to-diameter (L/d) ratio of 12 and eccentricity parameter (ε) of 6. The experiments were conducted with axial Reynolds number from 5×10^3 to 2×10^4, with rotational speed of 0, 200 and 500 rpm. The experimental results showed significant increases in heat transfer arisen from the combined effects of inherent entry swirl and centrifugal buoyancy due to rotation. Their experimental investigation demonstrated that in the entrance region increased heat transfer is more marked with respect to increase in the rotational Reynolds number, but the influence of rotational Rayleigh number on heat transfer is small and only noticeable at low axial Reynolds number. Although the test rig can only spin up to 500 rpm due to its limitation, the study has provided useful insight into how rotational Reynolds number and rotational Rayleigh number increase the convective heat transfer. Since electrical machines operate at speed higher than 500 rpm, higher rotational speed will be investigated in the present research.

Le Feuvre [1968] performed a dimensional analysis to investigate the enhancement of heat transfer for air passing through the axial cooling ducts in a rotor due to the rotation. The dimensional analysis includes dimensionless groups to indicate the relative importance of the effects of rotor duct geometry, centrifugal buoyancy and inherent entry swirl on the flow and heat transfer in the rotor ducts. The rotor ducts were uniformly heated. The rotor was driven at a fixed speed of 1500 rpm and the axial Reynolds number ranges from 5×10^3 to 4×10^4. The measurements were carried out for a range of duct spacing, pitch-circle diameter and length-to-diameter ratio.

His experimental data was presented in a form much more suitable for electrical machines and show quantitative agreement with those proposed by Humphreys et al. [1967]. Heat transfer correlations were proposed for the length-to-diameter (L/d) ratios of 6.4 and 10.7 as functions of the duct spacing ratio (w/d) and the rotor duct tangential velocity to the axial flow velocity ratio (V_T/U) as shown in Table 2-2.

Morris and Woods [1978] investigated the effects of rotation on heat transfer in the entrance region of uniformly heated circular ducts that are constrained to rotate about a parallel axis up to 1000 rpm. The ducts have length-to-diameter (L/d) ratios of 34.65 and 69.30, eccentricity parameters (ε) of 24 and 48 respectively. The experiments were performed for air flow rates in the laminar and turbulent flow regimes, for axial Reynolds numbers between 1300 and 2×10^4. Their experimental results demonstrated that the rotation produced a significant improvement in local and mean heat transfers in the entrance region of ducts. Similar to Humphreys et al. [1967], the authors suggested that the Coriolis effect is more dominant in the thermal entrance region. The centrifugal effect is more likely to dominate at distances well downstream of the entry plane. Therefore, the rotational Reynolds number (J) and axial Reynolds number (Re) were used to correlate the experimental heat transfer data. For laminar flow, the authors were only able to correlate the mean heat transfer data for duct of L/d = 34.65 and ε = 24, and for duct of L/d = 69.30 and ε = 48. In contrast, the authors found that the mean heat transfer data for the turbulent flow conditions can be correlated in an equation which appears to be relatively insensitive to the L/d and ε of the rotating ducts. The equation can be found in Table 2-2, which is valid for a range of rotational Reynolds number from 15 to 150, but does not apply to zero speed case.

Using the manner suggested by Morris and Woods [1978], Morris [1981] correlated the experimental data reported by Humphreys et al. [1967] and Le Feuvre [1968]. This gives an equation having similar characteristics to that proposed by Morris and Woods [1978], but less improvement in heat transfer due to different velocity profiles at the immediate entry planes of the test sections and lower length-to-diameter (L/d) ratio from 6.4 to 12.

2.2.2.3 Summary of heat transfer in rotor ducts

In general, the effects of rotation can induce two types of secondary flow to the flow passing through a rotor duct, Coriolis-induced secondary flow and centrifugal-induced secondary flow, which they can enhance the heat transfer above the stationary case. The Coriolis-induced secondary flow is predominant in the entrance region because of the variation of flow velocity vector due to the entrance effect. The centrifugal-induced secondary flow is predominant is the region where the Coriolis-induced secondary flow becomes insignificant, this secondary flow is caused by the density difference in a centrifugal field. Although a large amount of investigations have been done for the heat transfer in rotor ducts, the literature that describes the use of heat transfer correlations for estimating the thermal performance of throughflow ventilated electrical machines is very limited. Due to the complexity of flow phenomenon in rotor duct which involves a large number of geometric and dynamic variables, these heat transfer correlations need to be applied with care. Therefore, a machine design engineer needs to ensure the selected correlation fulfils the geometric and dynamic similarities of the design machine.

2.2.3 Rotor-stator gap

As the topologies of radial flux electrical machine form an annular gap between the rotor and stator, the heat transfer in the rotor-stator gap is focused on literature that mainly deals with concentric cylinders, with rotating inner cylinder and stationary outer cylinder. There is a huge amount of literature on convective heat transfer in annulus with the mixed axial and rotational flow. Apart from the common dimensionless groups, the influence of rotation on heat transfer in an annulus may be characterised by means of additional dimensionless groups as following:

The Rotational Reynolds number based on the rotor radius,

$$Re_\theta = \frac{\rho \omega_m a^2}{\mu} \tag{2.10}$$

The rotational Reynolds number based on the rotor-stator gap size, i.e. $s = b - a$,

$$Re_\omega = \frac{\rho \omega_m a(2s)}{\mu} \tag{2.11}$$

where a and b are the inner and outer radius of an rotor-stator gap. The hydraulic diameter (D_h) of an annulus is equal to two times of gap size (s).

Radius ratio,

$$\eta = \frac{a}{b} \tag{2.12}$$

Taylor number based on mean annulus radius (r_m),

$$Ta = \frac{\rho \omega_m r_m^{0.5} s^{1.5}}{\mu} \tag{2.13}$$

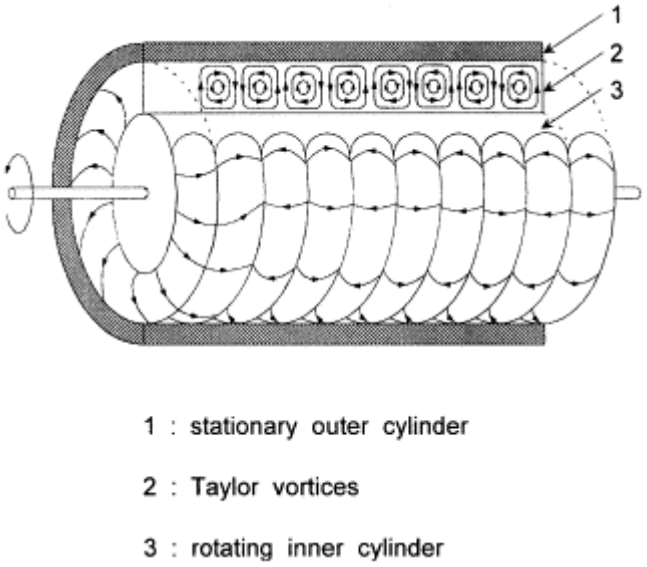

Figure 2.11: Taylor vortices, Jung et al. [2000]

Taylor [1923] studied theoretically the stability of the laminar flow between concentric cylinders and revealed an unstable flow structure with the formation of complex toroidal vortices. This unstable flow structure occurs when the angular velocity of the inner cylinder exceeds a critical value. The centrifugal forces due to rotation overcome the viscous forces which dominate in Couette flow, set off flow instability and result in a secondary flow. The secondary flow is in the form of regularly spaced vortices, rotating in opposite direction along the annulus, as illustrated in Figure 2.11. These steady alternate vortices are known for certain flow conditions as "Taylor vortices". The Taylor number is commonly used to quantify Taylor vortex flow. For the case of a narrow annulus (i.e. radius ratio is equal to unity), the critical Taylor number ($Ta_{critical}$) is equal to 41.19. However, for annulus

with the radius ratio less than unity, the critical Taylor number needs to be corrected by a geometrical factor. Then, the critical Taylor number becomes greater than 41.19.

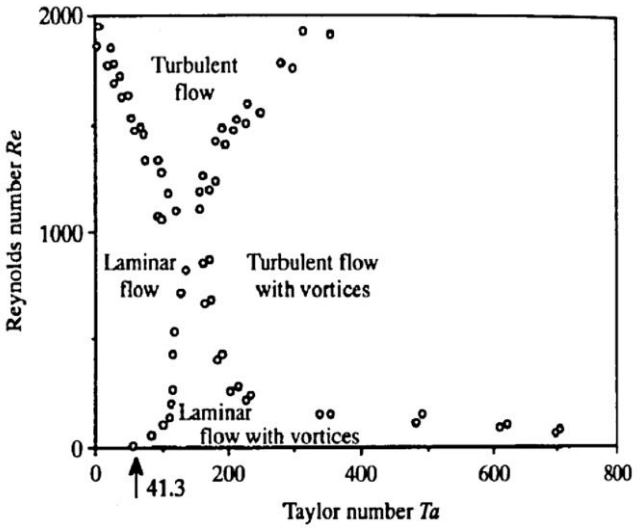

Figure 2.12: Modes of mixed axial and rotational flow in an annulus between concentric cylinders, (radius ratio, $\eta \approx 1$), Kaye and Elgar [1958]

For throughflow ventilation cooling methods, the fluid flow in a rotor-stator gap is similar to the fluid flow in an annulus between concentric cylinders (with rotating inner cylinder and stationary outer cylinder) but is superimposed with an axial flow. Kaye and Elgar [1958] revealed the existence of four possible modes in this flow condition. They can be distinguished and categorised based upon the Taylor number and axial Reynolds number as illustrated in Figure 2.12. These four modes are:

- Purely laminar flow
- Laminar flow with Taylor vortices
- Turbulent flow
- Turbulent flow with Taylor vortices

The convective heat transfer in the annular gap was also presented by the authors, which is dependent on the axial Reynolds number and Taylor number. It is strongly influenced by the mode of flow it belongs to.

Goldstein [1937] investigated the stability of laminar flow between concentric cylinders with axial flow. His theoretical results showed that the stability of purely rotational laminar flow is increased by the addition of axial flows. This can be seen

in Figure 2.12, the onset of instability increases monotonically with axial Reynolds number.

Coney and Simmers [1979] presented a correlation for the critical Taylor number with axial throughflow by means of shear stress measurements at the outer wall of the annular gap. The values of critical Taylor number that were obtained using these experimental measurements are well in excess of those found by other investigators because the onset of Taylor vortices initially occurs at the inner rotating boundary. Hence, the values of the critical Taylor number obtained using this correlation are likely to be for fully developed Taylor vortex flow. The correlation is valid up to axial Reynolds number of 1600. The critical Taylor numbers form a demarcation line between the flow regions with and without Taylor vortices for the annular radius ratio of 0.833. The original correlation does not account for the critical Taylor number when there is no axial throughflow (i.e. Re = 0). Hence, it was modified to include the critical Taylor number for the given radius ratio, which is 48.4. The modified correlation can be expressed as:

$$Ta_{critical} = \sqrt{166.75 Re^{0.913}} + 48.4 \tag{2.14}$$

2.2.3.1 Heat transfer for mixed axial and rotational flow in rotor-stator gap

Heat transfer for purely laminar flow and turbulent flow are not the focus of this section because they can be found in many engineering textbook, such as Incropera et al. [2002]. A survey of heat transfer for the mixed axial and rotational flow with the existence of the Taylor vortices in annulus is presented in this section. The relevant empirical correlations that could be used to predict the heat transfer in rotor-stator gap is summarised in Table 2-3. They are mainly applicable for air. These correlations have been recently incorporated in Motor-CAD. Due to the complexity of fluid dynamics and heat transfer in rotor-stator gap, these correlations need to be applied with care. Rotor-stator gap of similar radius ratio and operating conditions (Ta and Re) to the correlations should only be chosen. The methodologies of how these correlations were obtained and also the important insight into the influence of mixed flow on the heat transfer characteristics will be then described in more detail.

Mode of flow	Approach	Radius ratio, η	Validity	Correlation	Authors
Turbulent flow with Taylor vortices	Experimental	0.904	$600 < Ta < 5500$, $2\times10^3 < Re_e < 1.5\times10^4$	$1.3\times10^3 \le Re \le 2\times10^4$ $\overline{Nu} = 0.03Re_e^{0.8}$, $Re_e = \frac{\rho D_h V_e}{\mu}$, $V_e = \sqrt{U^2 + \left(\frac{V_T}{2}\right)^2}$	Gazley et al. [1958]
Laminar flow and turbulent flow with Taylor vortices	Experimental	0.75 – 0.937	$380 < Re < 4220$, $71 < Ta < 3415$	$\overline{Nu} = \overline{Nu}_{rotation} + \overline{Nu}_{axial}$ $\overline{Nu}_{rotation} = 0.092(Ta^2 Pr)^{1/3}$ $\overline{Nu}_{axial} = 0.015\left(1 + 4.6\frac{s}{L}\right)\left(\frac{r_i}{r_o}\right)^{0.45} Re^{0.8} Pr^{1/3}$	Tachibana and Fukui [1964]
Turbulent flow with Taylor vortices	Numerical, Experimental	0.57	$1.5\times10^4 < Re < 6.5\times10^5$, $7\times10^4 < Ta < 9.3\times10^4$	$\overline{Nu} = Nu_0\left[1 + \left(\frac{2sV_T}{\pi r_i U}\right)^2\right]^{0.8714}$	Kuzay and Scott [1977]
Laminar flow with Taylor vortices	Analysis, Experimental	0.8 and 0.955	$65 \le L/D_h \le 288$, $400 < Re < 1200$, $100 < Ta < 1414$	$\overline{Nu} = \frac{APrRe^{0.5}Ta^{0.735}}{B\left(\frac{A}{1-\eta}\right)^{0.5}\left(\frac{\eta}{1-\eta}\right)^{0.25} Ta_{critical}^{1.235}}$ $A = \frac{1 + \eta^2 + (1-\eta^2)/ln\,\eta}{2 + (1-\eta^2)/\ln\eta}$ $B = Pr + \ln\{1 + Pr \times \exp C - Pr\}$ $C = \frac{2}{3}\left(\frac{1-\eta}{\eta}\right)^{0.25}\left(\frac{\eta A}{(1-\eta)^2}\right)^{0.5} Re^{-0.5}Ta^{0.265}Ta_{critical}^{0.235} - 1$	Simmers and Coney [1979]
Turbulent flow with Taylor vortices	Experimental	0.87	$1.7\times10^5 < Re < 3.7\times10^5$, $8\times10^3 < Ta < 1.6\times10^5$	$\overline{Nu} = Nu_0\left[1 + 0.068\left(\frac{V_T}{2U}\right)^2\right]$	Childs and Turner [1994]

Table 2-3: Relevant heat transfer correlations for rotor-stator gap

Gazley et al. [1958] investigated the convective heat transfer characteristics of the mixed rotational and axial flow between concentric cylinders for a range of smooth and slotted surfaces with particular application to electrical machines. Their experiments were conducted for axial Reynolds number up to 1.2×10^4 and rotational Reynolds number up to 1.1×10^4. An effective velocity for the fluid flow in the annulus combining the average axial velocity (U) and the peripheral velocity of the inner cylinder (V_T) was proposed and is expressed as:

$$V_e = \left[U^2 + \left(\frac{V_T}{2}\right)^2\right]^{1/2} \tag{2.15}$$

A heat transfer correlation was proposed in terms of the effective Reynolds number (Re_e) based upon the effective fluid velocity. The Nusselt numbers were compared between the cases with and without axial flow. Lower values of Nusselt number were obtained for the cases with axial flow in laminar and transition flow regimes due to the stabilising effect of axial flow, which agree with Goldstein [1937]. The slotted surfaces were found to have no appreciable effect on the heat transfer characteristics in the annulus.

Tachibana and Fukui [1964] performed a comprehensive study of convective heat transfer in the annulus with superimposed axial flow. The experimental results demonstrated that the rate of dissipated heat from the inner rotating cylinder to the air is the sum of the rate of heat transferred by the axial flow and the rate of heat transferred by rotation. The heat transfer correlation by irregular vortices due to rotation was obtained from the experimental measurements using air, water and methanol. For the heat transfer correlation by the axial flow, the entrance effect was considered using the parameter, $1+4.6(s/L)$. The experiments were performed with either inner cylinder or outer cylinder being heated, or both inner and outer cylinders being heated. The experimental results demonstrated no difference in heat transfer whether inner cylinder or outer cylinder being heated and the other side is cooled. But, an increase of 15% of heat transfer was observed for both cylinders being heated. The experimental apparatus gave a range of radius ratio from 0.75 to 0.937. They were operated for the axial Reynolds number between 380 and 4220, and the Taylor number between 71 and 3415.

Kuzay and Scott [1977] presented an experimental study of fully developed turbulent heat transfer in an annulus with inner cylinder rotating in air. Their experiments were performed using a heated outer cylinder and an insulated inner cylinder, with a large-gap annulus (i.e. radius ratio of 0.57), for the axial Reynolds number up to 6.5×10^4, and the rotational Reynolds number up to 4×10^4. The obtained correlation of the Nusselt number is a function of the equivalent Nusselt number without rotation and a "rotation parameter". The rotation parameter is a physical quantity characterising the flow helix in the annulus as follows:

$$\alpha = \frac{2sV_T}{\pi r_i U} \tag{2.16}$$

In the rotation parameter, the rotation ratio, $\zeta = V_T/U$, is used to identify the strength of rotation by the ratio of the peripheral velocity of the rotating inner cylinder to the mean axial flow velocity. In Figure 2.13, the rotational Nusselt numbers were non-dimensionlised with respect to pure axial flow Nusselt numbers. The experimental results demonstrated that the heat transfer increases in a near parabolic relationship with the rotation ratio. The influence of the rotation ratio on the Nusselt number is particularly significant at lower Reynolds number because of the stabilising effect of axial flow in the annulus as described in Gazley et al. [1958].

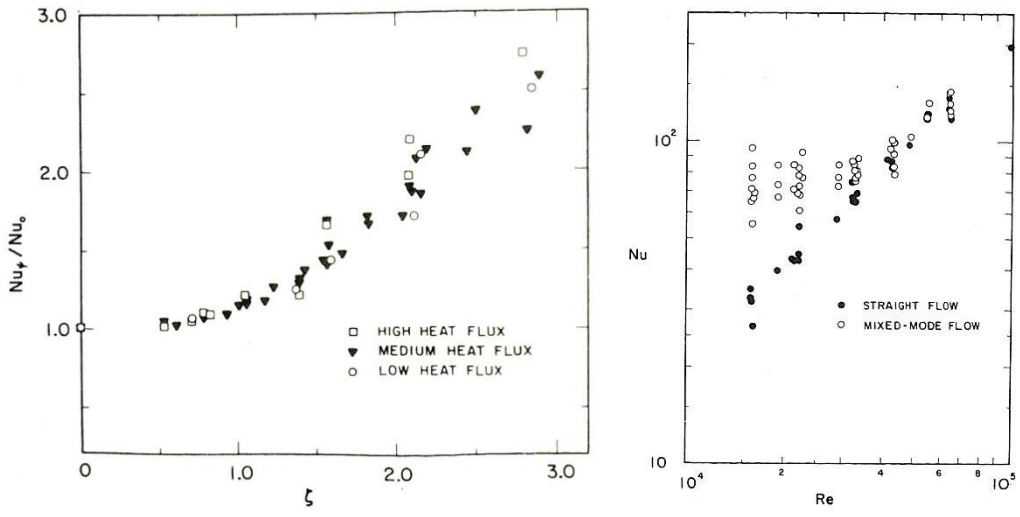

Figure 2.13: Nusselt number versus rotation ratio for mixed flow (left), Nusselt number versus axial Reynolds number (right), where rotation ratio is the variable at fixed axial Reynolds number, Kuzay and Scott [1977]

Gardiner and Sabersky [1978] measured the heat transfer from a heated inner cylinder to the fluid in the annulus between the rotating inner cylinder and a stationary outer cylinder in the presence of axial flow of the fluid's Prandtl number equal to 2.5, 4.5 and 6.5. The experiments were conducted for the axial Reynolds number and Taylor number up to 7000 and 1100 respectively. The authors found that the Nusselt number increases with the Prandtl number for laminar and transitional flows, but the heat transfer in the annular gap is less influenced by the Prandtl number for turbulent flow. The motion of rotation has no influence on the heat transfer before the onset of the Taylor vortices in the mixed axial and rotational flow, but the heat transfer increases with the Taylor number after the onset of the Taylor vortices. Also, a decrease in heat transfer with increasing axial Reynolds number was observed which is similar to the previous investigators.

For the case of combined Taylor vortices and laminar axial flow, Simmers and Coney [1979] developed a solution for heat transfer between the outer surface of an annulus and the air in the annulus using the Reynolds analogy solution for momentum and heat transfer. The heat transfer correlation derived using the analogy solution was compared with the Nusselt numbers obtained using experimental methods. Reasonable agreement was achieved between the predicted and experimental results for radius ratios of 0.8 and 0.955.

Since the previous investigators mainly concerned with the fully developed flow heat transfer characteristics using long annuli, Lee and Minkowycz [1989] investigated experimentally the heat transfer characteristics using relatively short annulus of the annular hydraulic diameter to axial annular gap length ratio less than 12.5 with inner cylinder rotating and outer cylinder stationary. The superimposed axial flow is in the range of laminar flow with the axial Reynolds number from 50 to 1000 and the Taylor number range from 32 to 4500. Besides smooth cylinders, grooved cylinders were also used to represent the slotted features in electrical machines. The investigation was conducted using four different configurations of inner and outer cylinders. For a smooth outer cylinder with smooth inner cylinder rotating, their experimental results demonstrated that the entrance effect is negligible at high Taylor number because the heat transfer is dominated by the Taylor vorticity effect. For a

smooth outer cylinder with grooved inner cylinder rotating, the heat transfer results are insensitive to the axial Reynolds number and entrance effect due to the existence of grooves. The presence of grooves on the rotating inner cylinder significantly increases Nusselt number over the smooth cylinder. For a grooved outer cylinder with smooth inner cylinder rotating and grooved inner cylinders with grooved outer cylinder rotating, the experimental results are similar to that of grooved inner cylinder rotating of similar radius ratio, but the axial Reynolds number shows minor effect.

Childs and Turner [1994] performed an experimental study of annulus heat transfer with fully hydrodynamic developed axial flow encountering a heated rotating inner cylinder. Measurements were taken using heat flux meters located along the surface of the inner cylinder. Their experimental rig has a radius ratio of 0.87, atmospheric air was drawn through the annulus giving an axial Reynolds number up to 3.7×10^5, and the inner cylinder can rotate up to 10000 rpm, giving a rotational Reynolds number up to 2.8×10^6. An experimental correlation was presented for the averaged Nusselt number which is proportional to the equivalent Nusselt number without rotation and to the square of rotation ratio as proposed by Kuzay and Scott [1977]. Their experimental results also showed the enhancement of annulus heat transfer with increasing axial and rotational Reynolds number, but the influence of rotation is less marked at higher axial Reynolds number.

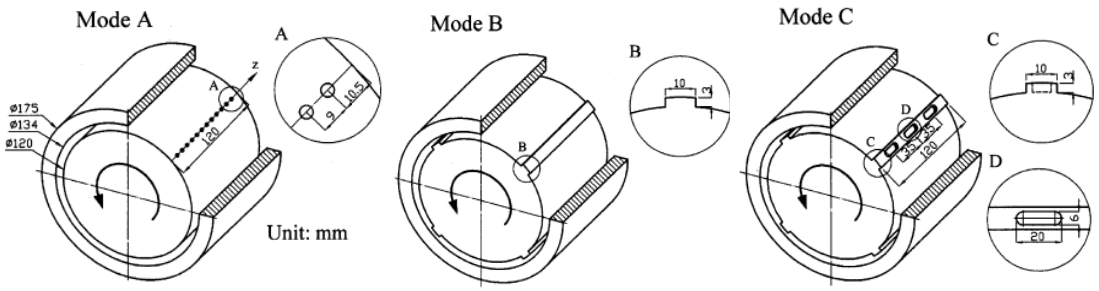

Figure 2.14: Modes of inner cylinder, Jeng et al. [2007]

Jeng et al. [2007] experimentally investigated the heat transfer characteristics of Taylor-Couette-Poiseuille flow in an annulus by mounting longitudinal ribs on the rotating inner cylinder. Three modes of the inner cylinder were tested as illustrated in Figure 2.14: mode A with a smooth surface, modes B and C with four equally spaced

longitudinal ribs on the outer surface of the inner cylinder, but mode C with three cavities on the top surface of each rib. The experiments were conducted for the axial Reynolds number from 30 to 1200 and the rotational Reynolds number up to 2922. Overall, the experimental data demonstrated that Nusselt number increases more with rotational Reynolds number at low axial Reynolds number than at higher axial Reynolds number. The heat transfer is typically enhanced by the longitudinal ribs, but the presence of cavities showed little influence. When the axial Reynolds number is equal to 300 and 600, and the rotational Reynolds number is higher than 2000, the Nusselt number of modes B and C is about 1.4 times that of mode A.

2.2.3.2 Summary of heat transfer in rotor-stator gap

In throughflow ventilated electrical machines, when the Taylor number exceeds the critical Taylor number of the finite rotor-stator gap, the formation of Taylor vortices can significantly enhance the heat transfer above the stationary condition. High Taylor number can diminish the thermal-entry-length effect that occurs in stationary condition because the Taylor vorticity effect becomes dominant. However, superimposed axial flow can reduce or suppress the formation of Taylor vortices and consequently may reduce the heat transfer in the rotor-stator gap. Moreover, a further increase in superimposed axial flow gives higher axial Reynolds number and results in a strong turbulent flow which dominates the heat transfer. Therefore, the heat transfer in rotor-stator gap is determined by the combined effects of mixed axial and rotational flow.

2.2.4 Section summary

In rotor-stator systems, the effects of rotation on convective heat transfer can be characterized using dimensionless numbers. For rotor ducts, the rotating effect can be mainly characterized using the rotational Grashof number and rotational Reynolds number. For rotor-stator gap, the rotating effect can be mainly characterized using the Taylor number. These dimensional numbers can be determined directly from the rotor speed. As the heat transfer correlations for both rotor ducts and rotor-stator gap involving the axial Reynolds number or axial flow velocity, the axial Reynolds number is an essential parameter in convective heat transfer. Although the axial

Reynolds number is derived from the mean axial flow velocity, it cannot be determined directly because the flow velocity is normally unknown. The flow distribution needs to be obtained using iterative method. In the perspective of fluid mechanics, it is important to determine how the effects of rotation affect the flow distribution in a rotor-stator system before the heat transfer correlations can be applied.

2.3 Fluid mechanics in ventilation paths

The preceding section demonstrates that the understanding of flow field in throughflow ventilated electrical machines is very important to improve machine thermal management. Cooling media flowing through the ventilation passage are subjected to the rotating effect. In practice, it is necessary to find out the flow resistance and heat transfer rate under the effect of the secondary flow due to rotation. A number of studies in this section have demonstrated that the rotating effect increases the flow resistance, causes an additional pressure loss to the ventilation system and reduces the obtainable coolant flow rate through the cooling system. Consequently, this must be included in the flow network to determine the flow rates and pressure drops in the individual sections of the network. This is the core of the present research. Some dimensionless groups in the preceding section of convective heat transfer are also used in this section to account for the effects of rotation.

2.3.1 Stator ducts

Friction loss is one of the major loss components in electrical machines. The frictional loss along a stationary duct is commonly calculated using the Darcy-Weisbach equation, Douglas et al. [1995], which is valid for duct flows of any cross section and for laminar and turbulent flows. The dimensionless friction factor in the equation can be determined from the Moody chart for smooth and rough walls. However, the frictional loss obtained using this equation only accounts for fully developed flow. It does not account for developing flow, which is the case in most electrical machines mainly due to the change in flow cross section area. As shown in Figure 2.15, the friction loss in the entrance region is much higher than the friction loss for fully developed flow. After the entrance region, the friction loss is in a linear

relation with the duct length. Since the Prandtl number is a measure of the relative thickness of the momentum and thermal boundary layers, thermal entrance length can relate to the fluid dynamic entrance length through Prandtl number. Hence, friction factors can be corrected for developing duct flows.

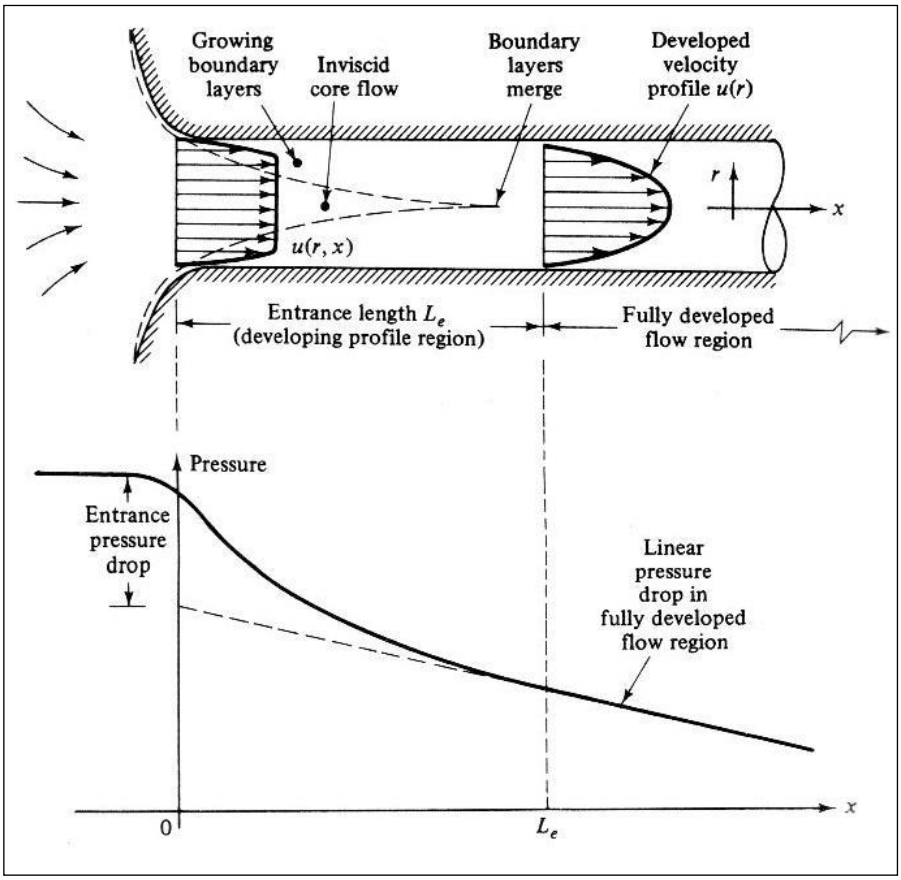

Figure 2.15: Developing velocity profiles and pressure changes in the entrance of a duct, White [1986]

2.3.2 Rotor ducts

Morris [1981] performed an experimental investigation into the flow resistance characteristics of adiabatic laminar flow in a circular tube of length-to-diameter ratio of 64. The tube was constrained to rotate about a parallel axis up to 600rpm. The author found that the flow remains laminar even though the axial Reynolds numbers were in the turbulent flow region because of the hypothesis that the transition from laminar flow to turbulent flow is suppressed due to the rotation. Rotation significantly increased the friction factor in the laminar flow region. The experimental results suggested that the rotating friction factor is simply the sum of

the stationary friction factor and the "excess friction factor" due to rotation. This excess friction factor can be correlated in terms of the Rossby number (*Ro*). The Rossby number here is a measure of Coriolis force to inertial force ratio concerning Coriolis-induced secondary flow.

In the theoretical analysis of Mori and Nakayama [1967] for convective heat transfer from a rotating duct wall to a fully developed laminar flow under a constant wall temperature gradient condition, which can be found in Section 2.2.2.1, the analysis of flow characteristics in the duct was also included. Similar to the temperature field, the flow field was analysed by assuming a strong secondary flow due to centrifugal buoyancy. The field was divided into a flow core region and a thin boundary layer along the wall. The analysis was performed using boundary-layer approximation as the influence of viscosity is mainly limited in the thin boundary layer. A relation was obtained from the boundary-layer momentum integral equation in the circumferential direction for force balance between the body force in centrifugal field and viscous resistance against the secondary flow at the pipe wall. The analysis demonstrated that the rotation increases the friction factor in laminar flow significantly. An increase in friction factor with rotation was expressed by the ratio of rotating to non-rotating conditions as shown in Figure 2.16. For fluids with *Pr* less than unity,

$$\frac{f}{f_0} = 0.149\left(\zeta_{Pr\leq 1} - 1 + \frac{1}{3\zeta_{Pr\leq 1}}\right)^{1/5} (Ra_\tau Re)^{1/5} \tag{2.17}$$

For fluids with *Pr* greater than unity,

$$\frac{f}{f_0} = 0.104(3\zeta_{Pr>1} - 1)^{1/5}(Ra_\tau Re)^{1/5} \tag{2.18}$$

Since convective heat transfer is a function of fluid mechanics, Woods and Morris [1974] also modelled the effects of rotation on friction factor in laminar flow based on numerical method by solving the governing equations of conservation of mass, momentum and energy. The comparison between Mori and Nakayama [1967] and Woods and Morris [1974] predictions is illustrated in Figure 2.16. Both investigations on the present problem show the same qualitative influence of Prandtl number on friction factor. The numerical model was validated with experimental

data for convective heat transfer. Fluids with higher Prandtl number were found to have less of an increase in friction factor due to rotation.

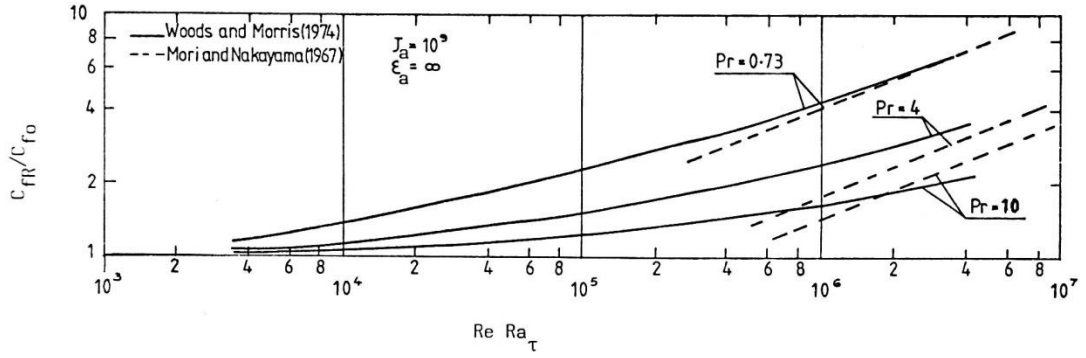

Figure 2.16: Comparison between the influence of rotation on the friction factor of Mori and Nakayama [1967] and Woods and Morris [1974], Morris [1981]

In the theoretical analysis of Nakayama [1968] for fully developed turbulent heat transfer in a pipe rotating about a parallel axis under a constant wall temperature gradient condition, which can be found in Section 2.2.2.2, the analysis of turbulent flow characteristics due to rotation was also included. Similar to the temperature field, the flow field was analysed by assuming an effective secondary flow, induced mainly by centrifugal buoyancy. The analysis was performed using an identical solution technique to that used for the laminar counterpart reported by Mori and Nakayama [1967]. The main additional physical effect which was included in the analysis is the incorporation of the turbulent fluctuations of velocity and temperature into the basic conservation equations of momentum and energy. Theoretical correlations of friction factor under the influence of rotation were proposed in terms of parameter $Re/\Gamma^{m/2}$ (m = 4 for gases and m = 5 for liquids). In fully developed turbulent flow, the Coriolis effect was found to be negligible.

Friction factor for gases with *Pr* of about unity,

$$f_4\sqrt{\Gamma} = \frac{0.338}{(Re/\Gamma^2)^{1/5}}\left[1 + \frac{0.07}{(Re/\Gamma^2)^{1/5}}\right] \tag{2.19}$$

Friction factor with *Pr* greater than unity,

$$f_5\sqrt{\Gamma} = \frac{0.22}{(Re/\Gamma^{2.5})^{1/6}}\left[1 + \frac{0.035}{(Re/\Gamma^{2.5})^{1/6}}\right] \tag{2.20}$$

The suffixes 4 and 5 denote the value of *m* used in the analysis.

As equation (2.17) to (2.20) are for fully developed flow, Johnson and Morris [1992] performed an experimental investigation into the influence of rotation on the flow resistance of adiabatic developing air flow in circular tubes rotating about a parallel axis. The experimental apparatus allowed the author to conduct pressure drop measurement at the length-to-diameter (*L/d*) ratio of 10.6, 21.2, 31.8 and 42.3 from the tube entrance. The eccentricity parameter (ε) of the tube could be adjusted between 21.5 and 32.3 using rotor arms. The authors found that in the entrance region the Coriolis effect induces secondary flow, provided there are variation of air velocity vector. It increases the flow resistance above the normal stationary condition. The influence of rotation was confined in the entrance region and decay away when the flow became fully developed. The eccentricity parameter had no effect on the friction factor. Empirical correlations for friction factor for tube of *L/d* = 10.6 and *L/d* = 31.8 were proposed by Johnson and Morris [1992], which as functions of rotational Reynolds number (*J*) and axial Reynolds number (*Re*).

Webb [1964] performed an experimental investigation into the pressure drop of air passing through axial rotor ducts of a mock-up throughflow ventilated machine. The author found that the ventilation system experienced additional pressure drop because of the abrupt change of flow direction of the air entering into the rotor ducts due to rotation, namely "shock loss". A correlation for shock loss coefficient was proposed as a function of the ratio of the tangential velocity of the rotor ducts to the average axial flow velocity, which is similar to the rotation ratio, V_T/U. The shock loss increases in a parabolic relationship with this velocity ratio, but it is independent of duct spacing, duct pitch circle diameter and duct length. However, the correlation was obtained based upon two inappropriate assumptions. First, the author assumed the flow rate passing through the rotor-stator gap is the same for the cases with the rotor ducts blocked and unblocked. The CFD simulations in Chapter 6 show that the fluid flow from rotating ducts can interfere with the flow rate in the rotor-stator gap. Second, the author did not consider the effects of rotation on the friction loss. Therefore, the correlation for the shock loss will be corrected in this research by taking these factors into account.

Taylor [1960] introduced an adjustment factor to the entry loss (i.e. contraction loss) to account for the increase in pressure drop with rotational speed of rotor ducts (V_T), which is given by:

$$K_{adj} = 1 + \left(\frac{V_T}{U}\right)^2 \tag{2.21}$$

But, no relevant literature can be found to reveal the truth of the adjustment factor and its details.

2.3.3 Rotor-stator gap

Cornish [1933] presented an experimental study on the flow resistance of water through smooth and fine annular gaps between concentric cylinders with inner cylinder rotating. In the laminar flow, the author found that the rotation has no or little effect on the flow resistance at low rotational speed, but the rotation increases the flow resistance when the angular velocity of the inner cylinder rises above a critical value. In the region of turbulent flow, the influence of rotation on the flow resistance for a given rotor speed diminishes with an increase of axial Reynolds number.

Goldstein [1937] performed a theoretical analysis of the laminar flow characteristics in an annular gap with mixed axial and rotational flows. The analysis indicated that the axial flow and rotational flow characteristics are independent of each other. The friction factor of axial flow in the annular gap with rotating inner cylinder was found to be the same with the case of stationary cylinders. This is agreed with Cornish [1933] when the rotational speed is below the critical value.

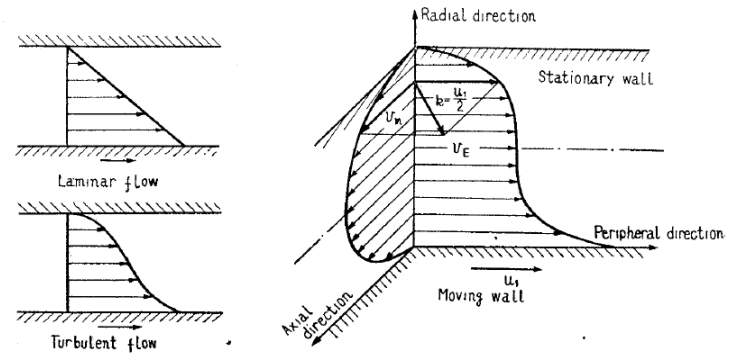

Figure 2.17: Velocity distribution in annular gap, Yamada [1962]

Yamada [1962] performed a theoretical study and experimental investigation into the resistance of a flow through concentric cylinders with the inner cylinder rotating and outer cylinder stationary. A theoretical correlation of the friction factor was proposed for turbulent flow based upon an analogy solution for the shear stress acting on the wall by the "resultant velocity" due to flow helix in the annulus as illustrated in Figure 2.17. The 1/7 power law was employed for the velocity distribution in the wall boundary layer. The author assumed the tangential velocity of the flow in the middle of the annulus is the half of the peripheral velocity of the inner cylinder, ignored the secondary flow and neglected the curvature of the cylinder wall as the annular gap is small compared to the rotor radius. The validity of the proposed correlation was verified with experimental results as shown in Figure 2.18. The resistances were measured for gap-to-rotor-radius ratio from 0.0136 to 0.115. A considerable amount of data in the laminar flow and turbulent flow regions for various combinations of axial and rotational flow was obtained. The author confirmed that when the axial flow is laminar, the friction factor in the annular gap is not affected by the rotational flow up to a certain rotating speed (i.e. critical speed as mentioned in Cornish [1933]), but beyond this speed the flow resistance increases significantly with an increase in rotational Reynolds number.

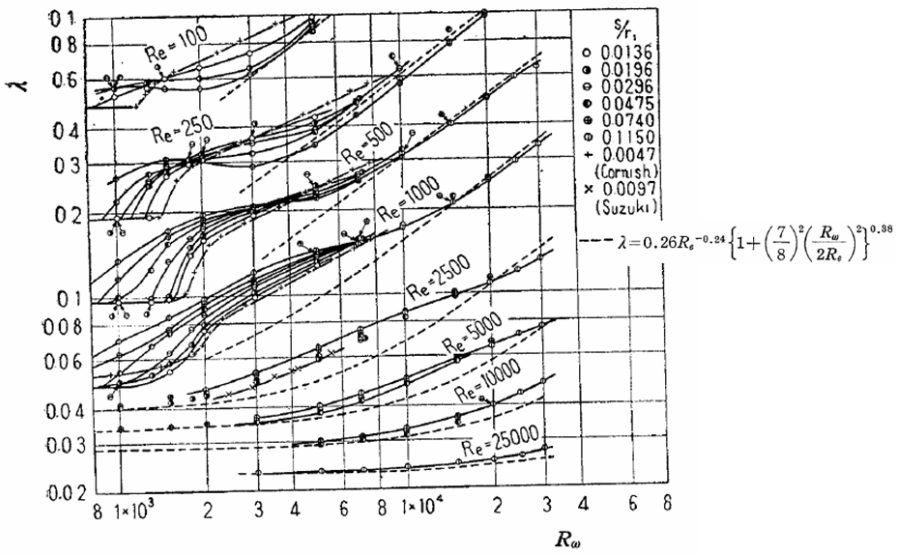

Figure 2.18: Relation between friction coefficient and rotational Reynolds number for various gap ratios, Yamada [1962]

Gardiner and Sabersky [1978] performed some measurements of pressure drop of superimposed axial flow between the inlet and discharged reservoir of concentric cylinders. The measurements were compared with the smooth and slotted rotors. At the same axial Reynolds number, the frictional pressure loss of the slotted rotor was generally higher than the smooth rotor. The rotation was found to have no noticeable influence on friction factor at low Taylor number, but the friction factor increased in a near parabolic relationship with the Taylor number.

Yanagida and Kawasaki [1987] experimentally investigated the pressure drop of axial flow in an annulus with inner cylinder rotating. The experiments were conducted with smooth or slotted outer cylinder and smooth inner cylinder. The authors found that the friction factor can be characterised as a function of a dimensionless number *X*, which is a ratio of the square of axial Reynolds number to rotating Reynolds number (Re^2/Re_ω). For smooth outer cylinder, the friction factor can be expressed as $f = 2.2X^{-0.5}$ for $X \leq 5000$ and as $f = 0.072X^{-0.1}$ for $X > 5000$. For slotted outer cylinder, the friction factor can be expressed as $f = 3.25X^{-0.5}$ for $X \leq 4000$ and as $f = 0.275X^{-0.2}$ for $X > 4000$.

Lee and Minkowycz [1989] carried out an experimental study on the pressure drop characteristics of air flow through an annulus between two concentric cylinders. The pressure loss characteristics are expressed in terms of the friction coefficient. The experimental results based on rotating grooved inner cylinder demonstrated that the rotational speed has a significant impact on the pressure drop characteristics. The friction coefficient always increases with the rotational speed. However, the influence is small at low rotational speeds, which is similar to Gardiner and Sabersky [1978]. A preliminary comparison between the heat transfer and pressure drop ratios of the rotating to non-rotating cases for a given Reynolds number was obtained for the rotor-stator system. The heat transfer and pressure drop ratios do not give the same value. The friction coefficient is increased by a factor, which is much higher than the factor obtained by the increased Nusselt number.

2.3.4 Section Summary

Besides the influence on heat transfer as described in Section 2.2.2, the Coriolis-induced and centrifugal-induced secondary flows increase the friction loss of the flow passing through a rotating duct. In the present research, the empirical correlations obtained by Johnson and Morris [1992] will be employed to account for the friction factor of adiabatic developing flow in rotor ducts. Due to the flow helix in rotor-stator gap, the friction factor increases in a near parabolic relationship with the rotor speed. The experimentally validated correlation proposed by Yamada [1962] will be used for the present research to account for the friction factor in rotor-stator gap. From the survey on literature of fluid mechanics and heat transfer of rotor-stator systems, the rotation ratio, V_T/U is an important parameter which could be used to characterise the additional pressure loss for combined axial and rotational flow, e.g. friction loss, shock loss of rotor ducts and rotor-stator gap, etc.

2.4 Summary of literature review

From the literature review of electrical machine thermal analysis, the lumped parameter thermal network is shown to be a well-established method to predict thermal performance of electrical machines. LPTN has the advantages of fast computation speed even for thermal transients, making it suitable for electrical machine design optimisation. Sensitivity analysis is more easily implemented using LPTN when compared to other numerical methods. However, the accuracy of LPTN is limited by the appropriateness of how the thermal resistance components are set. Convective heat transfer is still the most complex issue which needs to have better understanding of fluid flow within electrical machines. As described in the preceding section, rotation significantly influences flow resistance and hence the convective heat transfer rate in electrical machines. Rotational pressure losses could cause a redistribution of the fluid flow through electrical machines. Consequently, the effects of rotation on pressure loss must be considered and included in the flow network analysis, which is the main objective of the present study. CFD and experimental methods are used for the characterisation of the rotational pressure losses.

3 Computational Fluid Dynamics

Due to recent improvements in CFD capabilities and computer power, the CFD method is becoming very popular in industry and is now widely used for electrical machine thermal analysis. The application of CFD in thermal modelling of electrical machines can be found in Section 3.5. The current chapter presents the fundamental governing equations of fluid flow which all CFD codes are based on. It is important to understand the physical phenomena of fluid motion and how these phenomena are modelled in CFD. All the theories presented in this chapter are referred to CFD textbooks, Tu et al. [2013], Versteeg et al. [2007], Saatdjian [2000] and White [1986]. The assumptions and techniques that suit the CFD modelling of electrical machines are explained and justified. In common with many engineering fluid flow problems, turbulence is the main interest and is the focus of this chapter.

3.1 Governing Equations of Fluid Flow

Fluid motion is fundamentally governed by conservation equations based upon the basic physical laws of fluid mechanics. The purpose of this section is to introduce these equations, where the following physical laws are adopted:

1. Conservation of mass (i.e. continuity equation)
2. Conservation of momentum (i.e. Newton's second law)
3. Conservation of energy (i.e. first law of thermodynamics)

The governing equations are presented in the differential form, which have been derived by considering an infinitesimal fixed control volume. As these conservation equations are nonlinear partial differential equations, the differential analyses of the fluid flow and heat transfer phenomena of electrical machines can only be solved numerically using a CFD code (e.g. STAR-CCM+, ANSYS-FLUENT or ANSYS-CFX). In a CFD study, the domain of electrical machine is created and the domain is divided into computational cells and nodes. After mesh is generated, the governing equations are numerically discretized using a finite volume method to a system of linear algebraic equations. They are normally used to solve for the velocity field,

fluid density and one of the pressure field, temperature field and internal energy in the system.

For thermal fluid analysis of electrical machine, the governing equations are coupled. The continuity equation is used as the transport equation for density and the energy equation is the transport equation for temperature. The density in the flow field varies with temperature due to heat transfer. In thermodynamics, an equation of state describes the relationships between state variables in thermodynamic equilibrium. The fluid density is obtained using the equation of state (i.e. ideal gas law) as:

$$\rho = \frac{p}{RT} \tag{3.1}$$

where R is the ideal gas constant, p is pressure and T is the temperature in Kelvin. The equation of state provides the linkage between the energy equation and the continuity and momentum equations. The resulting velocity field that satisfy mass conservation is obtained through pressure-velocity coupling algorithm.

The discrete linear system is solved using iterative method (e.g. algebraic multi-grid method). In the CFD solver, the fluid properties, the boundary conditions and the flow regime (laminar or turbulent) are specified. The simulation is started with initial conditions until a converged solution is obtained.

3.1.1 Continuity equation

In general, the mass conservation equation represents the rate of change of mass in a fluid element and is equal to the net flow rate of mass into the fluid element governed by:

$$\frac{\partial \rho}{\partial t} + \nabla \cdot \rho V = 0 \tag{3.2}$$

V is a velocity vector. For steady flow, equation (3.2) can be simplified to:

$$\nabla \cdot \rho V = 0 \tag{3.3}$$

The above equation (3.3) is used in Chapter 4 because conjugate heat transfer analysis is performed for electrical machine operated at constant speed.

3.1.2 Navier-Stokes equation

Based on Newton's second law, the rate of change of momentum of a fluid particle is equal to the sum of the forces acting on the fluid particle. The general momentum conservation equation can be written in vector notation as:

$$\frac{D(\rho V)}{Dt} = -\nabla p + \nabla \cdot \tau_{ij} + \rho g \tag{3.4}$$

The terms ∇p, $\nabla \cdot \tau_{ij}$ and ρg on the right hand side of equation (3.4) are pressure force, viscous force and gravitational force components respectively. The viscous force is due to viscous stress components acting on the fluid element. The term DV/Dt is the fluid particle acceleration which can be divided into local acceleration and convective acceleration, describing the rate of change of the vector quantity subjected to a space-and-time-dependent velocity field.

$$\frac{DV}{Dt} = \frac{\partial V}{\partial t} + u\frac{\partial V}{\partial x} + \mathrm{v}\frac{\partial V}{\partial y} + w\frac{\partial V}{\partial z} = \frac{\partial V}{\partial t} + V \cdot \nabla V \tag{3.5}$$

As the cooling media (e.g. air, water, oil and etc.) used for the machine cooling are normally Newtonian in behaviour, the governing equations presented in this chapter are solely concerned with the linear relation between shear stress and velocity gradient (i.e. strain rate) perpendicular to the direction of the shear. In the case of constant viscosity and steady flow, equation (3.4) is represented by:

$$V \cdot \nabla \rho V = -\nabla p + \mu \nabla^2 V + \rho g \tag{3.6}$$

If the working fluid is a gas, e. g. air, the gravitational term ρg is negligible and can be ignored mostly for forced convection cases.

3.1.3 Energy equation

Based on the first law of thermodynamics, the rate of change of energy of a fluid particle is equal to the sum of the net rate of heat added to the fluid particle and the net rate of work done on the fluid particle. For a Newtonian compressible viscous flow, the energy conservation equation can be expressed as:

$$\frac{D\left(\rho c_p T\right)}{Dt} = \nabla \cdot (\lambda \nabla T) + \Phi \tag{3.7}$$

The term $\nabla \cdot (\lambda \nabla T)$ relates heat conduction through the boundaries of fluid element, where λ is the thermal conductivity. The conversion of mechanical energy into heat is taken into account by the term Φ, (i.e. viscous dissipation function) and is given by:

$$\Phi = \mu \left[2\left(\frac{\partial u}{\partial x}\right)^2 + 2\left(\frac{\partial \mathrm{v}}{\partial y}\right)^2 + 2\left(\frac{\partial w}{\partial y}\right)^2 + \left(\frac{\partial \mathrm{v}}{\partial x} + \frac{\partial u}{\partial y}\right)^2 + \left(\frac{\partial w}{\partial y} + \frac{\partial \mathrm{v}}{\partial z}\right)^2 + \left(\frac{\partial u}{\partial z} + \frac{\partial w}{\partial x}\right)^2 \right] \tag{3.8}$$

This term describes the change of mechanical energy into thermal energy, which can be neglected because it is only important when the fluid viscosity is very high and when the velocity gradients of the fluid motion are very large. In the case of steady flow, constant specific heat and thermal conductivity, the energy equation is simplified as:

$$c_p V \cdot \nabla \rho T = \lambda \nabla^2 T \tag{3.9}$$

These governing equations are solved for laminar flow in Cartesian coordinates. However, similar to many other engineering problems, the operation of electrical machines mainly involves turbulent flows. Consequently, these equations are modified to form the Reynolds-Averaged Navier-Stokes (RANS) approach for turbulence modelling. This will be explained in a later section.

3.2 Turbulence Flows

CFD simulations of turbulent flows are much more difficult than those of laminar flows because of the fine features of the turbulent flow field, which are known as turbulent eddies. They are always unsteady, three-dimensional-random, chaotic and swirling. The ratio of inertia force to viscous force (which is normally referred to as the Reynolds number) is used to indicate if a flow is considered to be a turbulence condition. A turbulent flow occurs at higher Reynolds number, as the inertia forces are sufficiently large to trigger the turbulent eddies in a flow. Also, in many engineering problems, disturbances in the flow may also generate turbulence.

Direct Numerical Simulation (DNS) is a technique that resolves all the scale unsteady turbulent eddies (i.e. large-scale and small-scale turbulent eddies) in the

flow field. To obtain DNS solutions, extremely fine and fully three-dimensional mesh is essential. Even with current processing power, DNS solutions are rarely used because they are computationally very expensive.

Large Eddy Simulation (LES), only large-scale turbulent eddies are resolved while small-scale dissipative turbulent eddies are modelled with the assumption that these smaller turbulent eddies are isotropic and behave in a statistically similar and predictable way. Consequently, LES requires less computational cost than DNS. However, neither DNS nor LES are suitable for electrical machine thermal analysis because they provide too detailed information that is not of interest and requires high computational resources.

3.2.1 Reynolds-Averaged Navier-Stokes (RANS) equations

Nevertheless, the Reynolds-Averaged Navier-Stokes (RANS) approach is widely used for most practical applications because in general the effects of turbulence on the mean flow are usually sufficient to quantify the turbulent flow characteristics. It is the method most commonly employed for the thermal analysis of electrical machines as shown in Section 3.5. To obtain the RANS equations, the velocity and all other variables in a turbulent flow field are decomposed into time-averaged and fluctuating components.

For the flow velocity,

$$u = \bar{u} + u', \qquad \mathrm{v} = \bar{\mathrm{v}} + \mathrm{v}', \qquad w = \bar{w} + w'$$

For the pressure and temperature,

$$p = \bar{p} + p', \quad T = \bar{T} + T'$$

The RANS approach adopts the time-averaging operation on the Navier-Stokes equations (3.2)-(3.6) and discards all details concerning the state of flow contained in the instantaneous fluctuations, resulting in the equations with the mean quantities and an additional term in the momentum transport equation due to the fluctuations of flow velocity. The additional term is known as the Reynolds stress tensor and it can be defined as:

$$\tau_{turb} = -\rho\overline{u_i' u_j'} = -\rho \begin{bmatrix} \overline{u'u'} & \overline{u'v'} & \overline{u'w'} \\ \overline{u'v'} & \overline{v'v'} & \overline{v'w'} \\ \overline{u'w'} & \overline{v'w'} & \overline{w'w'} \end{bmatrix} \tag{3.10}$$

For steady and turbulent flow motion using the ensemble-averaged variables, the governing equations (3.3), (3.6) and (3.9) are written as:

Continuity:

$$\nabla \cdot \rho\bar{V} = 0 \tag{3.11}$$

Momentum:

$$\bar{V} \cdot \nabla\rho\bar{V} = \rho g - \nabla\bar{p} + \nabla \cdot \tau_{ij} \tag{3.12}$$

where

$$\tau_{ij} = \mu\left(\frac{\partial u_i}{\partial x_j} + \frac{\partial u_j}{\partial x_i}\right) - \rho\overline{u_i' u_j'} \tag{3.13}$$

Energy:

$$c_p\bar{V} \cdot \nabla\rho\bar{T} = \nabla \cdot \left(\lambda\nabla\bar{T} - \rho c_p\overline{u_i' T'}\right) \tag{3.14}$$

In the RANS equations, the viscous force term of the momentum equation consists of viscous stresses of the working fluid and turbulent stresses. These extra turbulent stresses are known as the Reynolds stresses. Since the Reynolds stress tensor is symmetric, it creates additional 6 unknowns to the RANS approach. So, it is necessary to have the same number of closure equations to obtain a solution. Similar to the momentum equation, turbulent eddy motion also generates an extra turbulent transport term (i.e. turbulent heat flux) in the energy equation.

In order to solve for the Reynolds stresses, eddy viscosity models are applied, which are based on the Boussinesq approximation to relate the Reynolds stresses to the mean rates of deformation.

$$-\rho\overline{u_i' u_j'} = 2\mu_t S_{ij} - \frac{2}{3}\rho k\delta_{ij}, \qquad S_{ij} = \frac{\partial u_i}{\partial x_j} + \frac{\partial u_j}{\partial x_i} \tag{3.15}$$

where μ_t is the turbulent viscosity, S_{ij} is the mean strain rate tensor and δ_{ij} is the Kronecker delta function (i.e. the function is 1 if the variables are equal, or otherwise is 0). *k* is the turbulent kinetic energy, which is expressed as:

$$k = \frac{1}{2}\left(\overline{u'^2} + \overline{v'^2} + \overline{w'^2}\right) \tag{3.16}$$

Turbulent heat flux can be modelled similarly. By analogy, the turbulent transport of heat is taken to be proportional to the gradient of the mean value of the temperature as:

$$-\overline{u_i' T'} = \alpha_t \frac{\partial \bar{T}}{\partial x_j} \tag{3.17}$$

where α_t is the turbulent thermal diffusivity, $\alpha_t = \lambda_t / \rho c_p$. The turbulent viscosity μ_t and turbulent thermal conductivity λ_t mathematically take the enhanced mixing and diffusion due to the turbulent eddies into account and hence provide closure of the Reynolds stresses and turbulent heat flux. These are related through the turbulent Prandtl number Pr_t. Hence, the momentum and energy transport equations (3.12) and (3.14) can be simplified to:

$$\bar{V} \cdot \nabla \rho \bar{V} = \rho g - \nabla \bar{p} + (\mu + \mu_t) \nabla^2 \bar{V} \tag{3.18}$$

$$\bar{V} \cdot \nabla \bar{T} = (\alpha + \alpha_t) \nabla^2 \bar{T} \tag{3.19}$$

There is a variety of turbulence models developed to compute turbulent flows using the RANS approach. These can be categorised into algebraic, one-equation, two-equation and Reynolds stress models. However, one has to know that the turbulence model only provides an approximation to the problem being calculated, which heavily depends on empirical constants for mathematical closure of the model equations. The validity of the turbulence models is mainly supported through the calibration of experimental data. As a result, a CFD user needs to be very careful when making use of a turbulence model. According to Cengel and Cimbala [2006],

> "No turbulence model is universal, and a turbulent flow CFD solution is only as good as the appropriateness and validity of the turbulence model used in the calculation"

It is important that only the model that has been calibrated with similar flows should be employed, to obtain a physically correct solution caused by the physical accuracy of the turbulence model.

3.2.2 Turbulence Models

When a turbulence model is used to compute a turbulent flow, the field of turbulent modelling is essentially concerned with employing a series of mathematical equations to account for the enhanced mixing and diffusion caused by turbulent fluctuations on the mean flow and the turbulent effects on mean flow properties. All relevant turbulent eddies are not resolved, not even for the large-scale turbulent eddies such as those are implemented in DNS and LES. The turbulence models are basically predicting the unknowns (e.g. Reynolds stresses and turbulent transport of scalar properties) in the turbulent flow field and provide closure to the system of mean flow equations. Consequently, the accuracy and complexity of RANS turbulence models are associated with the number of additional transport equations that need to be solved along with the RANS flow equations.

Two-equation turbulence models are most commonly used for turbulence modelling in industry. The k-ε and k-ω models are the most common two-equation models because they are well-established and widely validated. They are capable of predicting the mean flow trends and successfully lend themselves as design tools that can provide a qualitative understanding of the flow physics. Two-equation models include the transport equations for the turbulence kinetic energy k and turbulence dissipation rate ε for k-ε models, and the specific turbulence dissipation rate ω for k-ω models. In words, the general transport equations are:

Rate of change of k, ε or ω	+	Transport of k, ε or ω by convection	=	Transport of k, ε or ω by diffusion	+	Rate of production of k, ε or ω	-	Rate of dissipation of k, ε or ω

Model constants are given which have been calibrated against comprehensive experiment data for a wide range of turbulent flows.

Compared to the standard *k-ε* model, the two-layer *k-ε* model and low Reynolds number *k-ε* model have improved the solution for near-wall regions. The renormalized group (RNG) version of *k-ε* model includes a modification to the transport equation of *ε* to account for the effects of rapid strain rate and streamline curvature. The Realizable *k-ε* model consists of a model coefficient expressed as a function of mean flow and turbulence properties and hence allows the model to satisfy certain mathematical constraints on the normal Reynolds stresses consistent with the physics of turbulence.

The standard *k-ω* model is an alternative to the standard *k-ε* model because it is more suitable to account for the flow problem with boundary layers under adverse pressure gradient. The shear stress transport (SST) *k-ω* model overcomes the free stream sensitivity problem in the standard *k-ω* model and makes the model stable in the free stream and viscous-affected region. However, based on Boussinesq's isotropic eddy viscosity assumption, two-equation models have limitations in modelling strong swirling flows, flows with large rapid changes in strain rate, and secondary flows driven by anisotropic normal Reynolds stresses.

Reynolds Stress Transport Model (RSM) also known as the second-moment closure model, it has the advantage over the two-equation models to predict turbulent flows with complex strain fields because it discards the Boussinesq's isotropic turbulence assumption. The directional effects of Reynolds stress field are computed with the exact Reynolds stress transport equations, which include two new terms for pressure-strain interactions and rotation. Hence, six equations for Reynolds stress transport are solved along with a model equation for the dissipation rate of turbulent kinetic energy ε. This allows anisotropic turbulence to be modelled. Due to the extra closure equations, this turbulence model is more computationally expensive than two-equation turbulence models.

3.2.3 Turbulent Boundary Layer (Wall Treatment)

As the turbulence models described in the previous section are mostly valid only outside the viscous-affected region of the boundary layer, wall treatment models

must be adopted to resolve the viscous-affected region. In the viscous-affected region close to solid walls, the flow field is dominated by shear due to wall friction and damping of turbulent velocity fluctuations perpendicular to the boundary. This results in a complex flow structure characterised by rapid changes in the mean and fluctuating velocity component within the near-wall boundary layer. As shown in Figure 3.1, the near-wall boundary layer can be divided into three regions, e.g. a viscous sub-layer, buffer layer and log-law layer, depending on whether the viscous shear or turbulent shear dominates in that layer. To apply the law of the wall, the flow velocity and wall distance in the wall velocity profiles are expressed in dimensionless form as:

$$u^+ = \frac{\bar{u}}{u^*} \tag{3.20}$$

$$y^+ = \frac{yu^*}{\nu} \tag{3.21}$$

$$u^* = \sqrt{\frac{\tau_w}{\rho}} \tag{3.22}$$

u^* is called the friction velocity, τ_w is the wall shear stress, $\bar{u}$ is the mean velocity parallel to the wall and y is normal distance from the wall.

For $y^+ < 5$, viscous shear dominates in the inner most layer, namely the laminar viscous sublayer. A linear relationship between u^+ and y^+ can be obtained in this layer as:

$$u^+ = y^+ \tag{3.23}$$

For $y^+ > 30$, turbulent shear dominates in the outer turbulent layer, namely log-law layer. The outer turbulent layer velocity varies logarithmically with y. For a smooth wall,

$$u^+ = \frac{1}{0.41} lny^+ + 5 \tag{3.24}$$

For $5 < y^+ < 30$, a buffer layer exists where both types of shear are important. The buffer region can be solved by setting the $y^+ = 11$ as a boundary to distinguish the laminar profile from the turbulent profile. Alternatively, blended wall laws can be

used by blending the linear and logarithmic laws of the wall to represent the buffer layer, e.g. Reichardt's law.

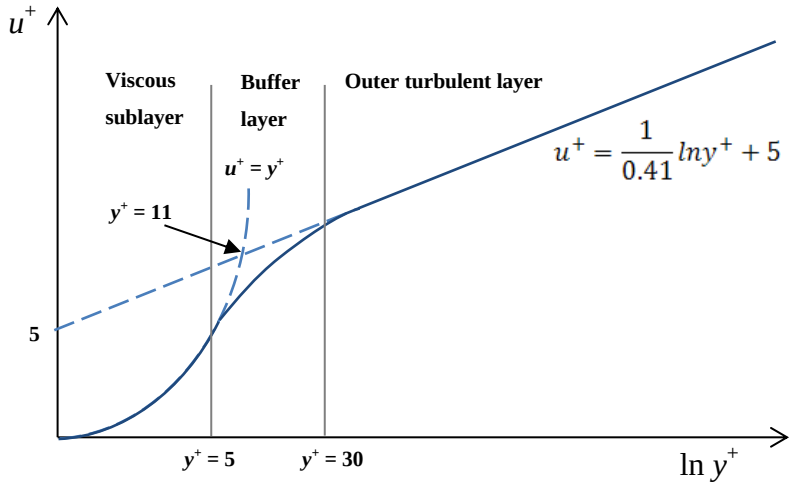

Figure 3.1: The wall laws

As shown in Figure 3.2, there are two main wall treatment models, *high* y^+ *wall treatment* (also known as wall functions) and *low* y^+ *wall treatment* approaches. The *high* y^+ *wall treatment* approach does not resolve the viscous sublayer and buffer layer. The distributions of velocity, temperature, turbulence and other scalar quantities are derived as functions of wall distance through the wall laws and then blended smoothly with the values computed in the log-law layer (turbulent core region). Since a high mesh resolution in the viscous-dominated region is not required (i.e. the wall-cell centroid, $y^+ > 30$), this approach is less computationally expensive.

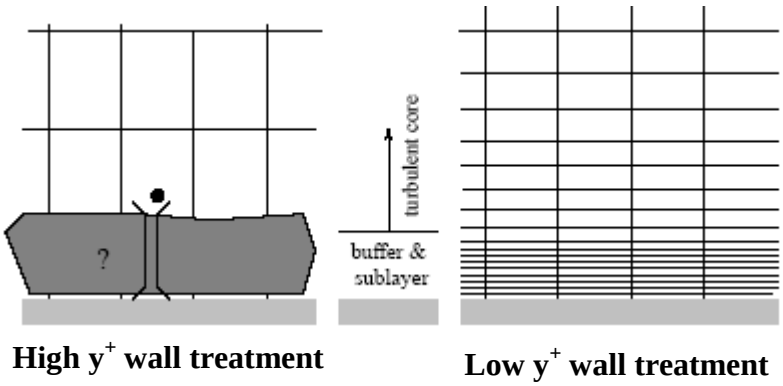

Figure 3.2: Wall treatment approaches, CD-adapco [2011]

A *low y^+ wall treatment* approach is necessary for low-Reynolds number problems because the fluid viscosity dominates in the turbulent boundary layer. The viscous sublayer is properly resolved without using any wall law assumptions and hence the turbulence models can be applied throughout the wall boundary layer. This approach demands more computer resources than the wall function approach because a sufficient boundary-layer mesh resolution is required in the viscous-affected region (i.e. the wall-cell centroid, $y^+ \approx 1$).

The wall-cell y^+ is strongly related to the local Reynolds number. Due to the geometric complexity of electrical machines, the full low y^+ type meshes in the CFD fluid domain is hard to achieve and it is usual to have some high y^+ type meshes in the fluid domain. An *All y^+ wall treatment* is a hybrid approach that allows the chosen turbulence models to be applied throughout the boundary layer for low y^+ type meshes and the wall function approach based on the wall laws assumptions to be applied for high y^+ type meshes (i.e. wall-cell centroid, $y^+ > 30$).

3.3 Modelling Rotation

As mentioned in Chapter 1, the operation of electrical machines involves rotation which strongly influences the flow field and pressure distribution. Therefore, it is crucial that the rotating effects are appropriately modelled using the CFD method. There are two main approaches that can be used: moving reference frame (MRF) and sliding mesh.

The MRF approach is also referred to “frozen rotor”. In a frozen rotor simulation, a rotating reference frame is applied to the region of mesh containing the rotor. The remainder of the mesh is static. As the rotor is frozen in space with respect to the stator, the flow field that the stator sees depends on the relative position of the stages. Different relative positions result in different solutions, which is a major disadvantage of this approach. This approach gives a solution that represents the time-averaged behaviour of the flow, rather than the time-accurate behaviour. The region where MRF is applied does not move physically, but rotation of all walls in the MRF region is taken into account to generate a constant grid flux. The grid flux is calculated based on the properties of the reference frame and hence forces due to

rotation (Coriolis and centrifugal forces) in rotating reference frame are introduced to the MRF region as illustrated in Figure 3.3. This approach is suitable for a steady state analysis and it can resolve most flow behaviour like mass flow rate and pressure rise/drop across rotating components. Furthermore, the MRF approach requires much less computational resources when compared with sliding mesh. This makes it an attractive solution for investigation involving a vast number of simulations. Consequently, the MRF approach is used for performing fluid flow and heat transfer analysis of electrical machines throughout this thesis.

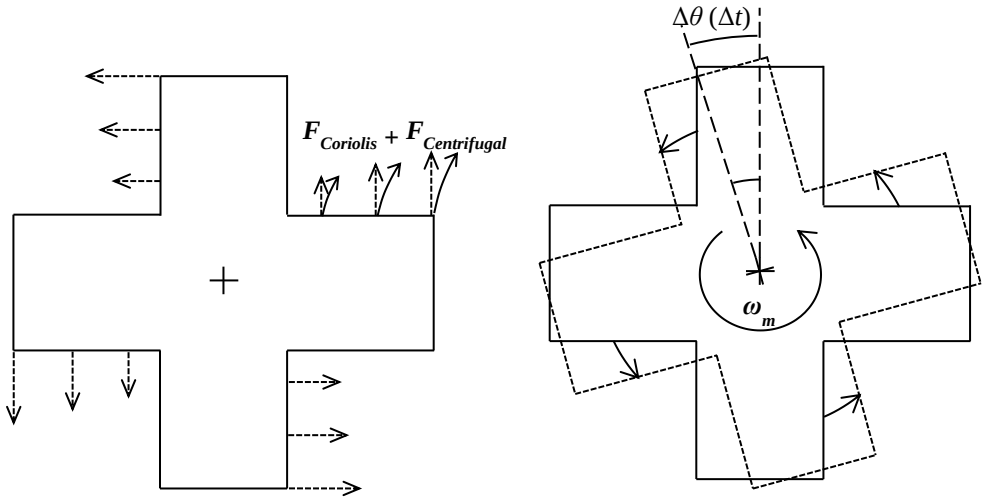

(a) Moving reference frame approach (b) Sliding mesh approach

Figure 3.3: The region of a salient pole rotor modelled using MRF and sliding mesh ($F_{Coriolis}$ is Coriolis force, $F_{centrifugal}$ is centrifugal force, ω_m is the angular velocity, $\Delta\theta$ is the angular displacement and Δt is the time step)

However, if transient effects such as vortex shedding or the wake coming off rotating components are investigated, then the sliding mesh approach is suitable for resolving those flow structures. The sliding mesh approach allows the components in the rotating domain to physically rotate around a specified axis. This is achieved by rotating the region through a small increment at each time step as shown in Figure 3.3. Thus, the interfaces between rotating and stationary domains slide relative to each other and hence the interaction between the rotor and stator is modelled exactly. This approach is required for flow problems involving strong rotor-stator interaction such as blade passing effects. Since this involves transient solutions, the sliding mesh

approach is computationally much more intensive and time-consuming than the MRF approach. In a sliding mesh simulation, the setting of the time steps is very important and is controlled by the rotor peripheral speed, e.g. 1° rotation per time step.

For best practice, the rotation of an electrical machine should be modelled using the MRF approach for steady state solutions before switching to the sliding mesh approach so that the initial condition of the sliding mesh simulation will be then well-defined. Thus, this procedure reduces the required computational time for a converged solution.

3.4 Convective Heat Transfer

CFD is a well-known technique for resolving numerous thermofluid problems which involve convection heat transfer phenomena, such as electronic device cooling, heat exchangers, cooling of turbine blades, etc. CFD can also be applied to the cooling of electrical machines by coupling the energy equation with the classical flow equations. Additional boundary conditions related to heat transfer need to be specified. For instance, the active parts of electrical machines generate thermal energy during their operation. The thermal energy generation rate per unit volume (W/m^3) within the corresponding active parts may be specified in order to obtain CFD results that closely mimic the actual thermal performance. Both the temperature field and the heat transfer rate at the solid-fluid interface converge to values that match the specified thermal energy generation rate. Since this conjugate heat transfer analysis combines heat transfer processes by conduction and convection, it involves both solid and fluid regions and requires conservation of energy equations to be solved for each region. As convective heat transfer is the transfer of thermal energy between a solid surface and fluid in motion, the boundary condition of heat flux at the solid-fluid interface is given by equation (3.25).

$$\lambda_{solid} \frac{\partial T}{\partial n} = \lambda_{fluid} \frac{\partial T}{\partial n} \tag{3.25}$$

When an electrical machine involves forced convective cooling, heat transfer by radiation is insignificant, Pyrhonen et al. [2008]. This is also demonstrated through the numerical investigation performed by Chirila et al. [2010]. Moreover, electrical

machines nowadays are fitted with fan, housing water jacket and heat exchanger for heat removal as shown in Section 1.2. Therefore, the radiation heat transfer is neglected in equation (3.25).

3.5 CFD Modelling of Electrical Machines

This section mainly reviews the application of CFD in thermal modelling of thermal modelling of electrical machines.

Liao et al. [1999] carried out conjugate heat transfer analysis over the entire totally enclosed fan cooled induction motor. Challenges of applying CFD include issues of heat generation which is non-uniformly distributed throughout the active components of the machine, anisotropic thermal conductivity and meshing of airgap and housing fins. The temperature distribution solution was compared with thermal imaging and thermocouple data and good agreement was achieved. The validated CFD model was used for design optimisation. The CFD model was rerun by replacing the material of housing from cast iron to aluminium and this reduced the average stator temperature by 8 °C.

As the CFD allows the detailed visualisation of fluid flow distribution, Mugglestone et al. [1998] simulated the influence of end winding porosity on the ventilation losses and flow field within the end region of a totally enclosed fan cooled induction machine using CFD method. In order to save the computational cost to fit with the available computer resources, only a periodic one-eighth section of the end region with simplified end winding was modelled. A k-ε turbulence model was employed. Since the end region includes wafters, causing transient rotor-stator interaction, a sliding mesh approach was used to obtain the flow solution. The computed flow velocity components agreed with the measured velocity components within the experimental error tolerance. The validated CFD model provided detailed flow visualisation in the experimentally inaccessible areas which is useful for design optimisation.

Pickering et al. [2001] [2002] performed heat transfer and ventilation analysis of an air-cooled four-pole synchronous machine with a salient-pole rotor using MRF, standard k-ε turbulence model and wall function approach for wall treatment. As the

machine was symmetrically ventilated, only a periodic quarter section was modelled. To compare CFD with experimental results of heat transfer coefficient, heat flux and surface temperature were measured from the machine. The variable parameters in the experiments were rotor speed, air flow rate and angle of inlet guide vanes. The comparison indicated that the CFD results follow all the trends experienced in the experimental measurements in response to the parameter variations. However, the heat transfer coefficients predicted by CFD are up to about 30% lower than the measured values. Agreement was also found on the prediction of the velocity profiles at the outlets of stator radial ducts. Therefore, the authors suggested that CFD could be a potential design tool used to examine the effects of operating parameters and geometric modifications on the cooling performance of salient pole machines.

By including copper losses at the field coil, Shanel et al. [2003] computed temperatures in the salient pole rotor of an air-cooled, four-pole synchronous machine using CFD. The standard k-ε turbulence model, MRF and wall function approach for wall treatment were employed. The authors suggested that knowing the conduction heat transfer paths could lead to an improvement in the rotor cooling by modifying the air flow appropriately and increasing convective heat transfer at the heat generated places. This was demonstrated through the modifications of the coil-supporting V-blocks in the inter-polar spaces which successfully reduce the average field coil temperature. Besides, the authors found that modelling the coils as a homogeneous material with an equivalent anisotropic thermal conductivity was sufficient for accurate approximation of coil temperature distribution.

Airoldi et al. [2008] presented a CFD investigation of the effects of geometric variation (running clearance, rotor groove depth and rotor speed) on temperature distribution and convective heat transfer of a self-ventilated axial flux permanent magnet (AFPM) machine. In the CFD simulations, only a periodic one-eighth section of AFPM machine was modelled. A Realizable k-ε model, two-layer enhanced wall treatment approach and MRF method were employed to compute the fluid flow and heat transfer solutions. The experimental measurements were used to validate the CFD models. The present study provides useful insight into how those geometric variations affect the mass flow rate, windage loss and also heat transfer coefficient.

Due to the limitations of numerical method for thermal transient and limitations of analytical method for accurate convective heat transfer modelling of novel topology machine, Hey et al. [2010] developed a thermal hybrid model for transient thermal modelling of an AFPM machine. Conjugate heat transfer analysis was performed using a CFD method to obtain the average heat transfer coefficients at the convective boundary. As the computation involved for thermal transient is relatively low using lumped parameter thermal network, the values of heat transfer coefficient obtained using the CFD method were used to calculate for the convective thermal resistances in the analytical model.

Due to the advantages of AFPM machine offering high power density and efficieny, Howey et al. [2010] [2011] studied the heat transfer in an air-cooled disc-type electrical machine using experimental and CFD methods. The SST k-ω turbulence model was chosen for modelling turbulent fluid flow and the MFR method was used to model rotation. The investigation was performed using a simplified rotor-stator system with a flat rotor and a flat stator, and also replacing the flat rotor with a rotor with protrusions to mimic the permanent magnets of the AFPM machine. The rotor with protrusions was found to create different radial flow patterns compared to that of the flat rotor and gave higher heat transfer. Stator heat transfer correlations for flat rotor and rotor with protrusions over a range of gap ratio were proposed. They can be used to predict the convective heat transfer of throughflow ventilated disc-type machines with similar rotor geometry.

Jungreuthmayer et al. [2012] performed conjugate heat transfer analysis of a water cooled radial flux permanent magnet synchronous machine. The entire machine was modelled in three dimensions for simulating flow and heat transfer. The heat sources of the CFD model were provided by a separate finite element analysis of the machine. MRF, SST k-ω turbulence model and all y^+ wall treatment approaches were employed. The main objective of the investigation is to obtain a better understanding of convective process in the machine for design optimisation. The authors found that the amount of air motion inside the machine can be increased by fan blades attached to the mounting plates of the rotor, leading to an increased heat transfer at the convective boundaries and thus lower machine temperatures.

3.6 Chapter Summary

Based upon the review of the existing literature for turbulence modelling of electrical machines, the k-ε and k-ω turbulence models are shown to be sufficient to estimate the fluid flow and heat transfer problem of electrical machines, in spite of the fact that these two-equation turbulence models are based on the Boussinesq's isotropic eddy viscosity assumption that the Reynolds stress is proportional to the mean rate of deformation of the fluid element. The Boussinesq's assumption may not be valid for complex flows such as rotating flows and other flows where curvature effects are significant. As already described in the previous sections, no single turbulence model is universally accepted as being the superior for all classes of problems. The choice of turbulence model depends on the fluid flow physics, established practices for specific classes of fluid flow, the level of accuracy, available computational resources and time constraint. So, the Realizable k-ε and SST k-ω turbulent models are used in the present research. In CFD, verification and validation together constitute the procedure of checking the accuracy of numerical experiments, AIAA [1998]. Verification will be performed to assess the numerical accuracy of the solution through mesh refinement study. Validation will be performed by comparing experimental measurements with numerical results.

Due to the literature regard the fluid dynamic aspect of electrical machines is limited, CFD is used to investigate the fluid flow problem of electrical machines. From the application of CFD in electrical machines, the understanding of the flow phenomena of cooling medium inside and outside the electrical machines is the primary concern for accurate thermal modelling and even for design optimisation. However, CFD method is computationally expensive. Therefore, the analytical lumped parameter thermal network has the advantage over CFD because of its fast computational speed. This makes it a much more feasible method for modelling thermal transient. Therefore, there is a need of interpreting the understanding of the effects of rotation on the fluid properties (pressure drop, velocity, heat transfer, etc.) obtained using CFD method into a way which can be applied to the analytical method. Consequently, CFD method is employed to develop some generic correlations which can be used to account for the rotational pressure losses of rotor ducts and rotor-stator gap flows.

4 The Ventilation Effect on Stator Convective Heat Transfer of an Axial Flux Permanent Magnet Machine

As described in Chapter 1, the cooling of an electrical machine strongly depends on the effectiveness of the cooling medium in removing undesired heat. The flow rate of the cooling medium through the machine is one of main parameters that affects the cooling performance. The amount of the cooling medium passing through ventilation paths of the machine is restricted by the system flow resistance. By reducing the system pressure losses, an increase in mass flow rate is obtainable for a given input pressure. In this chapter, the ventilation effect on the cooling of a novel AFPM machine is presented. CFD is employed to investigate the impact of inlet configuration on the convective heat transfer and temperature distribution in the stator.

4.1 Introduction

Due to the development in high performance rare-earth permanent magnet technology, AFPM machines are an attractive solution for many applications such as hybrid and electric vehicles, Hey et al. [2010], and wind turbine generators Di Gerlando et al. [2011]. Owing to the high remanent magnetic field, the use of Neodymium magnets (NdFeB) can meet industry demands such as high power density, efficiency and cost reduction. This has opened up great opportunities for novel machine topologies to be developed, Mueller and McDonald [2009], Hodgins et al. [2012]. AFPM machines have noticeably short axial length because the disc-shaped stator and rotor are placed face to face coaxially. However, if proper cooling is not considered in the design process, the compact construction of AFPM machines can result in a high temperature rise. Existing cooling design techniques have been developed mostly for conventional radial flux machines and at a time when power density was not so much of an issue. More effort should be given to the thermal analysis to fully exploit new topologies, Sun et al. [2013] and materials, Marignetti et al. [2008]. Indeed, overheating can cause detrimental effects to machine lifetime, reliability, electrical efficiency, demagnetization of magnets and insulation failure.

Effective ventilation can be a very economical cooling method for electrical machines because of the high temperature difference between the cooling air and heated surface. For a self-cooled AFPM machine, the air adjacent to the rotor is dragged by the rotor due to the no-slip condition and driven radially outwards by the centrifugal force, as demonstrated by Childs [2011]. Hence, the rotor movement creates a pressure difference to draw the air from the surroundings towards the rotor centre to replace the cooling air which has been pumped out. Moreover, the protruding magnets on the rotor assist the pumping effect. Heat generated in the machine is transferred to the radial outflow by forced convection. However, due to the topologies of AFPM machines, this flow phenomenon is subjected to a degree of restriction.

Two main flow regimes are exhibited in a flat rotating disc facing a stationary disc: Batchelor flow as defined by Batchelor [1951] and Stewartson flow as defined by Stewartson [1953]. The Batchelor flow normally describes the flow structure with the radial outflow adjacent to the rotor, replaced by the radial inward flow adjacent to the stator from the periphery to satisfy the conservation of mass. The distinction between Batchelor flow and Stewartson flow is that Batchelor flow has an inviscid rotating fluid core between separate tangential boundary layers of the rotating and stationary discs respectively, and at almost zero radial velocity. Batchelor flow is more likely to occur in enclosed systems, whereas Stewartson flow tends to appear in open and throughflow ventilated systems. Convective heat transfer has been investigated for open rotor-stator systems in Owen and Rogers [1989], Boutarfa and Harmand [2004], Howey et al. [2011]; and enclosed rotor-stator systems in Daily and Nece [1960]. The convective heat transfer correlations that have been developed for these systems show that the Nusselt number mainly depends on the rotational Reynolds number, $Re_\theta = \rho\omega_m R^2/\mu$ and the gap ratio, $G = s/R$.

In Chong et al. [2012] the authors studied the cooling performance of an AFPM machine by blocking the ventilation holes at the rotor inner radius. It was demonstrated that the measured temperatures were higher than the cases with ventilation holes unblocked. Throughflow ventilated AFPM machines are usually designed with a degree of ventilation to provide a pathway for the surrounding air.

However, the literature that describes the effect of inlet configuration of AFPM machine on cooling in detail is limited. A rotor hub with radial blades to assist in pumping air through an AFPM machine was proposed in Scowby [2004]. In fact, both Batchelor and Stewartson flows can coexist in the rotor-stator gap of throughflow ventilated AFPM machines; at the outer radius, there will be both inflow and outflow of air; at the inner radius, there will be just radial outflow, Howey et al. [2011]. This occurs as the supply of air to the rotor-stator gap provided from the flow entry at or near the rotating axis does not match the net radial outflow exiting from the rotor-stator gap. The mode of flow in the rotor-stator gap is mainly dependent on the machine speed and ventilation design.

For surface-mounted permanent magnet machines (i.e. rotor with protrusions), linear correlations based only on rotational Reynolds number and gap ratio for mean Nusselt number were proposed in Howey et al. [2011]. They were based upon the experimental measurements for stator convective heat transfer using a mock-up throughflow ventilated rotor-stator system. In Airoldi [2010], the effects of variation of rotor-stator gap spacing, magnet depth and rotational speed to convective heat transfer were investigated through CFD modelling with experimental verification on mass flow rate and temperatures. Also, a complex correlation was proposed to predict their influences on stator convective heat transfer variation with radial position. Wang et al. [2005] used simplified free rotating disk correlations for AFPM machines, the lumped-parameter thermal network developed shows reasonable temperature estimation. However, in surface-mounted permanent magnet machines, correlations such as the ones proposed in Airoldi [2010] can give better agreement.

Since the stator is commonly sandwiched between two rotor discs in AFPM machine topologies, the subject of this thesis is to investigate the effect of inlet configuration at the rotor on convective heat transfer between air and the stator, facing two moving rotors with protruding magnets at a distance s from the stator; with no air flow imposed on the system. This study provides an important insight to machine designers of how convective cooling can be enhanced for AFPM machines with improved ventilation design. Since the electromagnetic and thermal aspects are linked, a detailed power loss distribution in the machine is presented in section 4.3. The electrical losses provide the heat sources and inputs to the CFD models.

Additionally, the simulation of heat transfer is coupled with air flow modelling for conjugate heat transfer analysis. Measured temperatures from a 25 kW AFPM prototype are used to validate the CFD models.

4.2 Experimental Test Facility

4.2.1 AFPM Machine

(a) C-core rotor (b) Partially assembled rotor

(c) Assembly of stator blocks (d) Fully assembled rotor

Figure 4.1: Assembly of AFPM prototype

The machine that used for this investigation is a 25 kW 100 rpm AFPM prototype. This is an air-cooled AFPM machine with three axial stages developed by NGenTec for direct-drive applications, McDonald et al. [2011]. The AFPM machine is assembled from c-core rotor and stator modules as shown in Figure 4.1. For each stator module, there are 3 coils potted in epoxy. Stator modules are supported within a permanent magnet c-core rotor structure. The inner and outer radii of the rotor are

220 mm and 460 mm respectively. The running clearance between the rotor and stator is 3.5 mm providing a gap ratio of 0.0076. During experiment, the AFPM generator is driven by means of an inverter fed induction machine through a step down gearbox as shown in Figure 4.2.

Figure 4.2: 25 kW AFPM prototype at the experimental test facility

4.2.2 Machine Ventilation

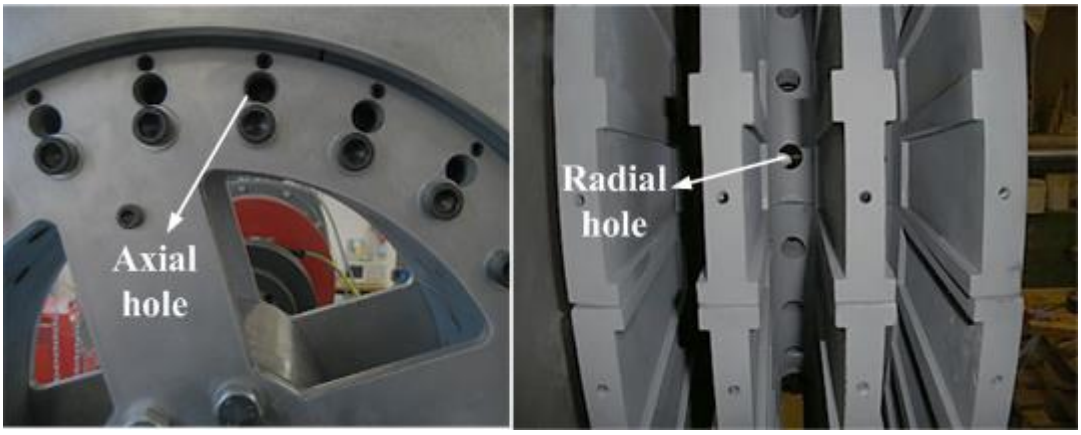

Figure 4.3: Ventilation holes

The prototype is ventilated by 24 radial and axial holes respectively on the rotor at the inner radius as illustrated in Figure 4.3. The outer edge of the AFPM machine is unshrouded. Both axial and radial holes have the same diameter of 20 mm, and the axial holes are located at a radius of 272 mm. Different arrangements of the air inlet holes can be tested by blocking the unnecessary holes using tape. Three cases were considered:

1. All holes unblocked
2. Only radial holes unblocked
3. Only axial holes unblocked

4.2.3 Temperature Measurement

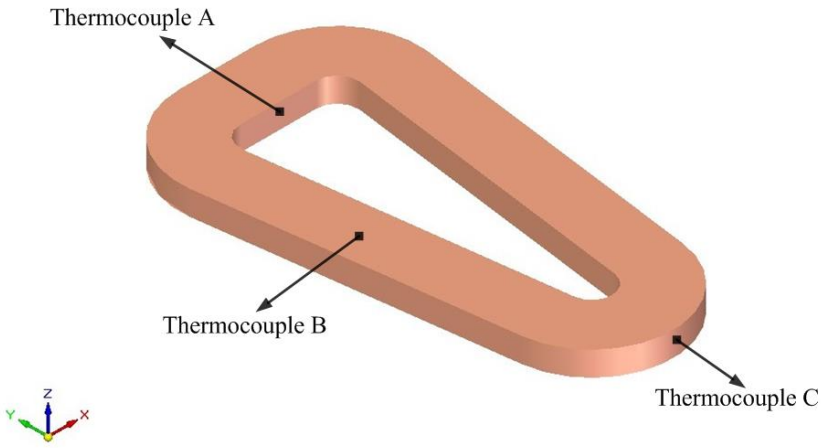

Figure 4.4: Locations of thermocouples on stator coil

Since copper loss is the major loss component in this machine topology, the temperature rise of stator coils was recorded during the tests. The temperature is measured using type K thermocouple. The measurement range is from -100°C to 250°C with an accuracy of ±1.5°C. Thermocouples were embedded in the stator to measure the local temperatures at the coils. Thermocouples A, B, and C measure the coil surface temperature at the outer radius, mid and inner radius respectively as shown in Figure 4.4. Four coils were monitored and each coil is located at a different angle in the stator disc. No significant difference in temperature rise was found between the coils. The experimental heating curves are illustrated in Figure 4.5 and Figure 4.6. The heating curves of thermocouple A, B and C are taking the averaged value of those four coils. Since the generator is stator-critical, temperature measurement was not performed on the rotor. In addition, the electrical resistance of the coils after steady-state was reached, was also measured.

The non-drive end stage of the generator was loaded with a three-phase resistive load during the tests, because in this stage all stator modules were of the same construction. Since this prototype was also assembled with different stator module designs, loading the drive end and middle stages may affect the consistency of temperature measurement. The machine was warmed up at full load before the ventilation tests were carried out until steady-state was achieved. There was an interval of 20 minutes of cooling (disconnecting the load) after warm-up and testing. The heating curve profiles for the warm-up period in Figure 4.5 and Figure 4.6 are different because in Figure 4.6 the generator was warmed up with all the ventilation holes blocked, whereas in Figure 4.5 the generator was warmed up with all the ventilation holes unblocked. However, this does not affect the ventilation tests conducted after the warm-up period.

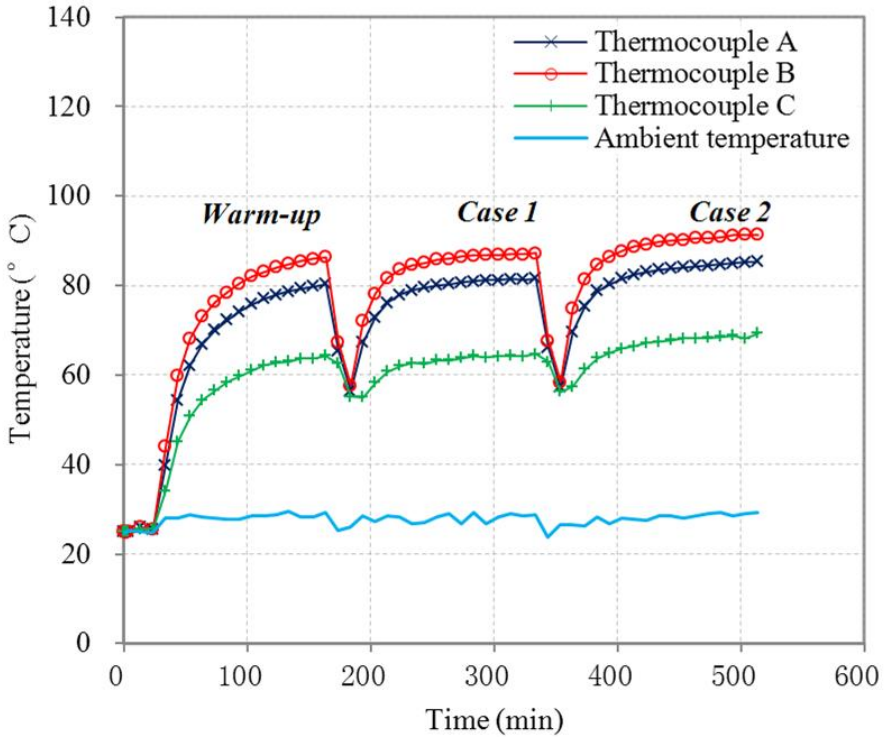

Figure 4.5: Heating curves of warm-up, Case 1 and Case 2 respectively

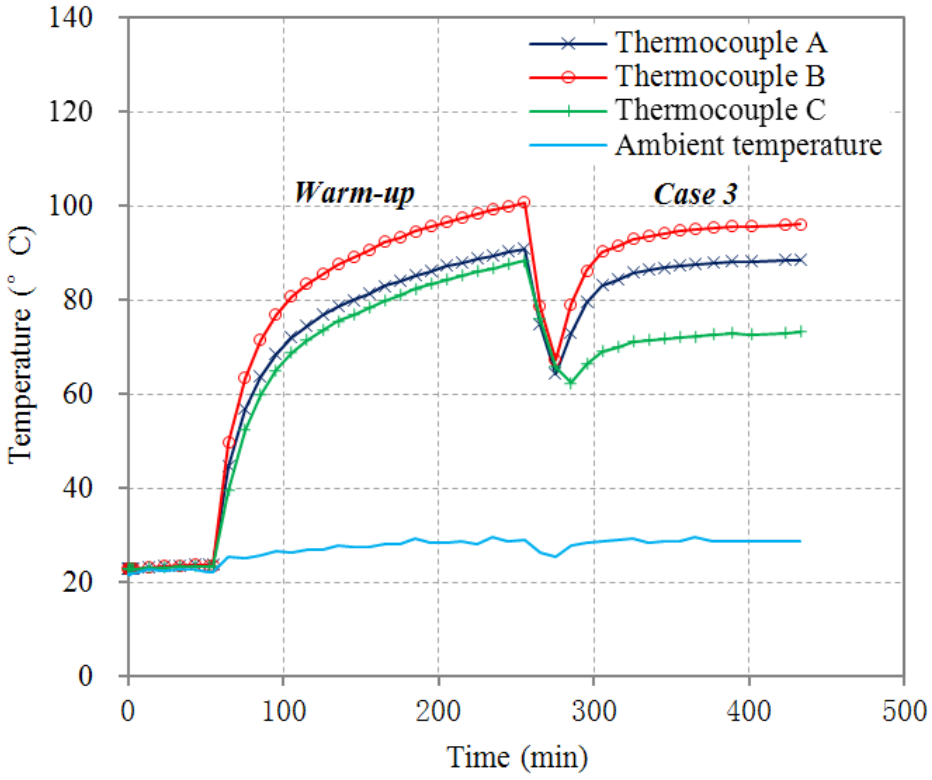

Figure 4.6: Heating curves of warm-up and Case 3 respectively

4.3 Power Losses

Heat generation in an electrical machine depends on the machine power losses. Therefore, detailed evaluation of the power losses of the prototype is very important to give an accurate estimation of the machine operating temperature. Losses in the electrical machine are in mechanical and electrical forms. Since direct drive topologies rotate at low speed, the mechanical losses (bearing and windage losses) have a negligible contribution to the machine power losses. Moreover, due to the use of an air cored stator, the cogging torque is zero. Hence, the electrical losses can be considered as the main losses and they are fed into the CFD model as the inputs of heat sources. (See Appendix A for the power losses calculation)

In the stator, which is ironless, all losses are therefore in the copper coils. The power losses in the stator can be divided into no-load and load losses. No-load losses are caused by the action of the rotating field of the magnets inducing eddy and circulating currents in the coils. Circulating currents exist in coils connected in parallel because of the induced voltage differences between the coils. They behave

like additional Joule heating in the windings even when the machine is running at no load. In this machine topology, the temperature rise is dominated by the resistive heating. The phase current produces copper loss in the windings. At ambient temperature, eddy current, circulating current and copper losses in the windings contribute approximately 84% of total electrical losses.

The power losses in the rotor are smaller than those in the stator. They are distributed in the magnets and core-back iron, occurring only when the machine is loaded. The reaction field from the windings (armature reaction) creates asynchronous time-varying fluxes on the rotor causing eddy current losses in the magnets and the iron supporting them. At rated speed, the rotor losses account for only 16% of the total electrical losses at ambient temperature. The distribution of the electrical losses described in this section is shown in Figure 4.7.

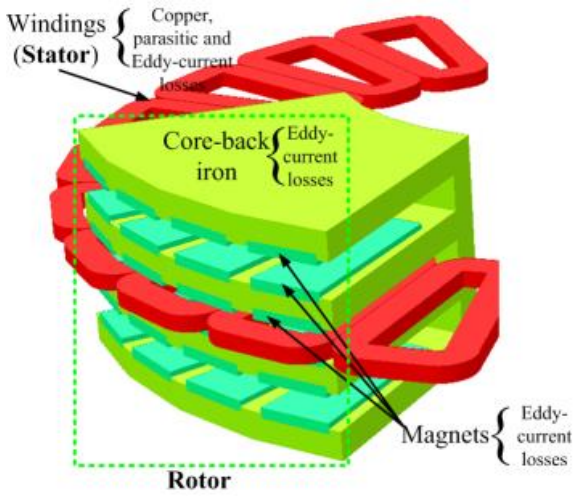

Figure 4.7: Distribution of electrical losses in the AFPM machine

A breakdown of the electrical losses at 100 rpm is shown in Figure 4.8. The copper loss is the major loss accounting for 71% of the total electrical losses, whereas the eddy current loss in the windings represents only 3% of the total losses. The losses were measured at ambient temperature, i.e. ΔT_{coil} = 0, using the methodology described in the Appendix A. The variation of the losses with coil temperature rise ΔT_{coil} is obtained through extrapolation. It can be seen that the coil temperature rise only gives significant influence to the copper loss ($3I_{rms}R^2$) and circulating current loss as the resistivity of the copper increases with temperature. Figure 4.9 illustrates

the dynamic integration between the input losses and CFD. The CFD model updates the steady state input loss in each iteration until the temperature of the coil converges.

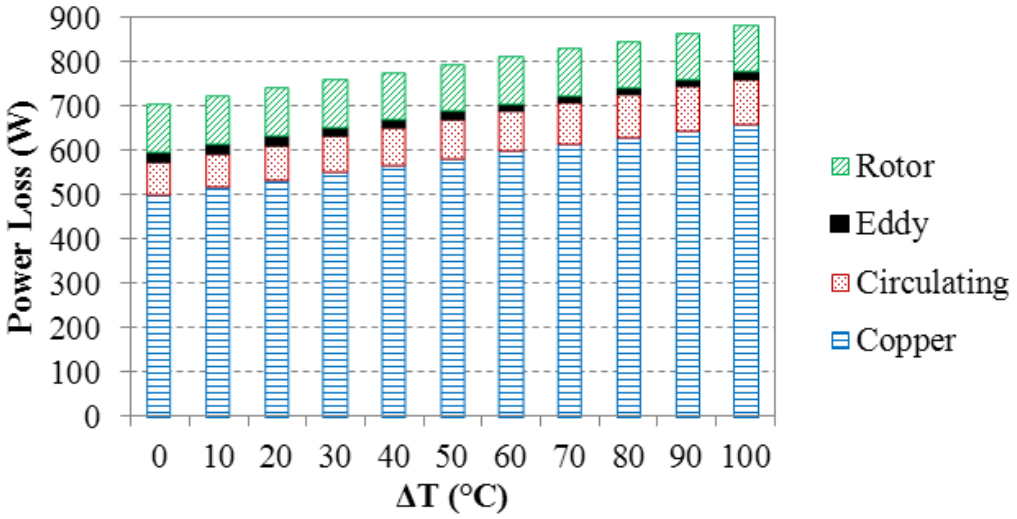

Figure 4.8: Input losses for CFD model at 100 rpm for single stage

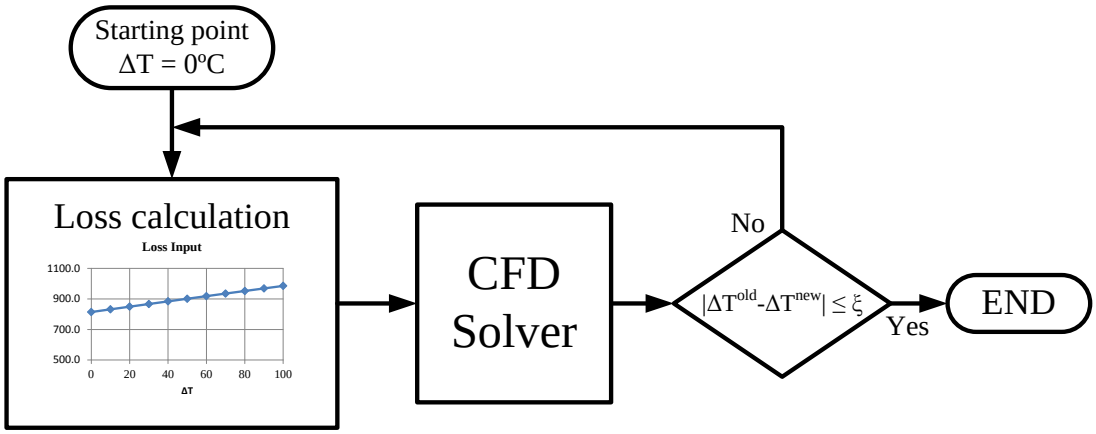

Figure 4.9: Flow diagram of loss integration: CFD heat sources are mapped from the power losses as a function of ΔT_{coil}, allowing the simulation to upgrade the steady state input loss in each iteration.

4.4 Computational Fluid Dynamics

Due to the improvement of numerical methods and computer power, modelling using CFD methods is now popular for electrical machine thermal analysis. The CFD software programme STAR-CCM+, CD-adapco [2011] was used in the present study.

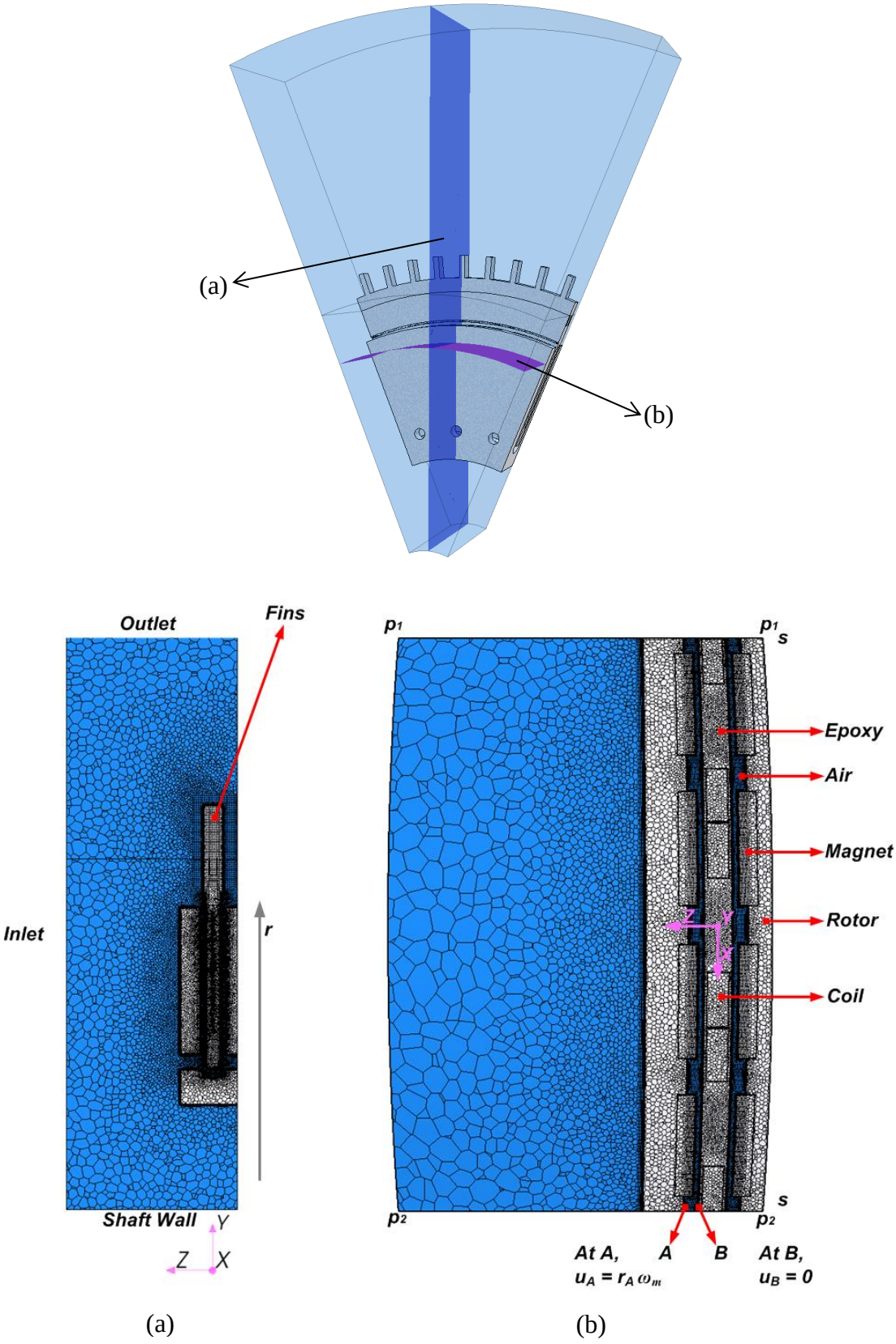

Figure 4.10: Geometry (top) and mesh (bottom) of CFD domain. Mesh is shown on plane section (a) and cylinder section at radius = 0.43 m (b) extracted from the CFD domain.

4.4.1 Model Definition and Mesh

Since the AFPM machine is assembled from eight c-core rotor and stator modules arranged circumferentially to give one stage, only one-eighth (45º) segment was modelled in three dimensions for simulating flow and heat transfer. As shown in Figure 4.10, symmetry and periodic planes of this segment are represented by *s*-*s*, p_1-p_1 and p_2-p_2 respectively. Alongside the fluid domain, the solid domain representing the rotor and stator was also included to calculate power dissipation via conduction. All material properties specified in the CFD model were the same as those of the prototype machine (i.e. magnets – NdFeB, coils – copper, fins – aluminium, rotor – cast iron, stator core – epoxy resin). Conformal mesh interfaces between solid and fluid domains were created to maintain the continuity of heat flux and temperature.

Polyhedral and prism layer meshers were employed. Within the fluid regions, the minimum mesh size was set to be 0.0178 mm close to the walls, which corresponds to one-hundredth of the fluid boundary layer. However, the minimum mesh size for the solid regions was set to be 1 mm, which corresponds to one-twelfth of the coil thickness sufficient to calculate conductive heat transfer. The maximum mesh sizes of the fluid and solid regions were set to 12 mm and 5 mm respectively to save the computational cost. The total number of computational cells of the fluid is about 6 million, whereas for the solid is about 2 million. The mesh in the fluid region is denser because of the advection term in the flow equations, which is more difficult to resolve than pure conduction in the solid domain.

Mesh refinement study has been performed in Appendix B to verify and assess the numerical accuracy of the CFD solutions. This ensures that the CFD solutions are mesh-independent. Besides, the residuals and key variables (i.e. temperature) are monitored (as shown in Appendix B) in order to confirm convergence of CFD solutions.

4.4.2 Turbulent Flow and Energy Modelling

As steady state operation of the machine was investigated, steady state models were chosen for CFD simulation. The present study had made use of a rotating reference frame to simulate the relative motion of the rotor and stator for time-averaged steady-

state solutions. As the rotor speed gives the peripheral Reynolds number of 1.4×10^5, a turbulence model was necessary. Two kinds of turbulence models, Realizable *k-ε* and SST (Menter) *k-ω* were used to provide closure of the Reynolds-Averaged Navier-Stokes (RANS) equations in the present study and these will be compared against each other. The effect of gravity is ignored. The air was assumed to be an ideal gas with constant viscosity, thermal conductivity and specific heat. The governing equations of a steady fully turbulent flow can be represented in vector form as:

Fluid continuity:

$$\nabla \cdot \rho \bar{V} = 0 \tag{4.1}$$

Fluid momentum:

$$\bar{V} \cdot \nabla \rho \bar{V} = -\nabla \bar{p} + (\mu + \mu_t)\nabla^2 \bar{V} + S_m \tag{4.2}$$

Fluid energy:

$$c_p \bar{V} \cdot \nabla \rho \bar{T} = (\lambda_{air} + \lambda_t)\nabla^2 \bar{T} \tag{4.3}$$

Solid energy:

$$\lambda_{sol}\nabla^2 T + S_T = 0 \tag{4.4}$$

where S_m and S_T are the momentum and energy source terms respectively. They will be defined in the next section. The enhanced diffusion due to the turbulent eddies is taken into account by the turbulent viscosity μ_t and turbulent conductivity λ_t. They are related through the turbulent Prandtl number, Pr_t = 0.7. Turbulence kinetic energy is caused by velocity fluctuations and is dissipated by viscosity. The transport equations of turbulent kinetic energy, *k* and dissipation rate, *ε* for Realizable *k*-ε model are:

$$\bar{V} \cdot \nabla \rho k = \nabla \cdot \left[\left(\mu + \frac{\mu_t}{\sigma_k}\right)\nabla k\right] + P_k - \rho\varepsilon \tag{4.5}$$

$$\bar{V} \cdot \nabla \rho \varepsilon = \nabla \cdot \left[\left(\mu + \frac{\mu_t}{\sigma_\varepsilon}\right)\nabla \varepsilon\right] + C_1 \rho \sqrt{2S_{ij}S_{ij}}\varepsilon - C_2 \rho \varepsilon^2 / \left[k + \left(\frac{\mu_t \varepsilon}{\rho}\right)^{1/2}\right] \tag{4.6}$$

The turbulent viscosity μ_t for Realizable *k-ε* model is computed as:

$$\mu_t = \rho C_\mu \frac{k^2}{\varepsilon} \tag{4.7}$$

$$P_k = 2\mu_t S_{ij} \cdot S_{ij} - \frac{2}{3}\rho k \nabla \cdot V - \frac{2}{3}\mu_t (\nabla \cdot V)^2 \tag{4.8}$$

S_{ij} is the strain rate tensor. The turbulence model coefficients, σ_k, σ_ε, C_2 and auxiliary relations of C_1 and C_μ are described in CD-adapco [2011].

The transport equations of turbulent kinetic energy, *k* and specific dissipation rate, ω for SST *k*-ω model are:

$$\bar{V} \cdot \nabla \rho k = \nabla \cdot [(\mu + \sigma_k \mu_t) \nabla k] + P_k - \rho \beta^* k \omega \tag{4.9}$$

$$\begin{aligned} \bar{V} \cdot \nabla \rho \omega = {} & \nabla \cdot [(\mu + \sigma_\omega \mu_t) \nabla \omega] + \rho \gamma G_\omega - \rho \beta \omega^2 \\ & + 2(1 - F_1) \frac{\rho \sigma_{\omega 2}}{\omega} \nabla k \cdot \nabla \omega \end{aligned} \tag{4.10}$$

For SST *k*-ω model, the Durbin's realizability constraint ($C_T = 0.6$) was applied and imposed on the turbulent viscosity formula (4.11) to overcome an unexpectedly large growth of *k* in stagnation point flows. Hence, the turbulent viscosity μ_t is computed as:

$$\mu_t = \rho k \min \left[\frac{1}{\max\left(\omega,\ F_2 \sqrt{2 S_{ij} S_{ij}} / a_1\right)}, \frac{C_T}{\sqrt{6 S_{ij} S_{ij}}} \right] \tag{4.11}$$

$$G_\omega = 2 S_{ij} \cdot S_{ij} - \frac{2}{3}\omega \nabla \cdot V - \frac{2}{3}(\nabla \cdot V)^2 \tag{4.12}$$

The turbulence model coefficients and auxiliary relations of a_1, β^*, β, F_1, F_2, γ, σ_k, σ_ω and $\sigma_{\omega 2}$ are described in CD-adapco [2011].

4.4.3 Boundary Conditions

The governing equations are subjected to the following boundary conditions:

At the inlet, the total gauge pressure, p_{tot} = 0 Pa and inlet temperature = 29°C (ambient). At the outlet, the static pressure, p = 0 Pa and opening entrainment temperature = 29°C. At both the inlet and outlet, the turbulent kinetic energy and

dissipation rate were set at default to be 0.001 Jkg^{-1} and 0.1 $Jkg^{-1}s^{-1}$ respectively, whereas the specific dissipation rate was set to be 1×10^{-4} s^{-1}.

Both rotor and stator surfaces are smooth and there is no-slip. The local speed of the rotor surface is equal to $r_{rotor}\,\omega_m$. In the rotating fluid region, additional momentum source is added in the momentum equation (4.2) which is represented by S_m. This momentum source is the sum of the Coriolis force and centrifugal force due to the effects of rotation as:

$$S_m = -[2\rho(\omega_m \times \bar{V}) + \rho\omega_m \times (\omega_m \times r)] \tag{4.13}$$

where r is the position vector of a general point in the flow relative to the rotating frame.

At the wall (solid-fluid interface), the air temperature is equal to T_w. Hence,

$$(\lambda_{air} + \lambda_t)\nabla^2 T = \lambda_{sol}\nabla^2 T \tag{4.14}$$

The power loss described in Section 4.3 is coupled with the CFD model as internal heat generation. The heat generation per unit volume, S_T, varies according to the temperature rise of the coils from ambient temperature. Field functions were created in order to specify up-to-date input losses in the CFD simulation. (See Appendix C)

$$S_T = f(\Delta T_{coil}) \tag{4.15}$$

4.4.4 Wall Treatment

As the turbulence models are valid only outside the viscous-affected region of the boundary layer, a wall treatment model was adopted to specify profiles of the mean flow quantities in the wall boundary layers. The flow velocity and wall distance in the near-wall region are expressed in dimensionless form as:

$$u^+ = \frac{u}{\sqrt{\tau_w/\rho}} \tag{4.16}$$

$$y^+ = \frac{y\rho\sqrt{\tau_w/\rho}}{\mu} \tag{4.17}$$

τ_w is the wall shear stress, u is the mean velocity parallel to the wall and y is the normal distance from the wall. The near-wall turbulent boundary layers can be

divided into three layers. In the inner most viscous sublayer ($y^+ < 5$), the velocity profile is:

$$u^+ = y^+ \tag{4.18}$$

In the outer turbulent layer ($y^+ > 30$), u^+ varies logarithmically with y^+ as follows ($E = 9$ for smooth wall):

$$u^+ = \frac{1}{0.42} ln(Ey^+) \tag{4.19}$$

Between these two layers (i.e. a buffer layer), u^+ is obtained using Reichardt's law, blending the viscous sublayer and logarithmic velocity profiles. With the intention of resolving the viscous sublayer, a high boundary-layer mesh resolution was created with the wall cell $y^+ \leq 1$. Due to the low rotor speed, *All y^+ Wall Treatment* approach was used to compute the wall shear stress, turbulent production and turbulent dissipation.

4.4.5 Solution strategy

The governing equations were numerically discretized using a finite volume method to a system of linear algebraic equations. These were solved simultaneously based on the conservation of mass, momentum, energy and turbulence parameters using the second-order upwind discretization scheme. However, only the conservation equation for energy was solved for the solid regions.

In the CFD models, each stator coil was simplified by a bulk copper region. As the materials of insulation and impregnation of windings were not physically modelled, the composite thermal resistance per unit area is computed as:

$$R_{th} = \sum_{i=1}^{n} \left(\frac{l_i}{\lambda_i}\right) + \sum_{j=1}^{n} \left(\frac{l_j}{\lambda_j}\right) \tag{4.20}$$

l_i and l_j are the thickness of insulation and impregnation respectively, λ_i and λ_j are the thermal conductivity of insulation and impregnation respectively and n is the number of winding layers. The conductive resistance was applied as the thermal contact resistance of the interfaces between copper and epoxy regions.

4.5 Comparison between CFD and Experimental Results

As shown in Table 4-1(a), the experimental temperature measurements demonstrate that the inlet configuration at the rotor has considerable influence on machine temperature rise. By comparing the measured temperature of Case 1, Case 2 and Case 3, the inlet configuration of Case 1 results in a cooling better than the inlet configurations of Case 2 and Case 3 due to lower temperature rise. As shown in Table 4-1(b) and (c), the CFD results agree reasonably with the finding obtained from the experimental measurements and follow the trend that the inlet configuration of Case 1 gives the lowest temperature rise while the inlet configuration of Case 3 gives the highest temperature rise. Besides, between the thermocouples A, B and C, CFD results also follow the experimental trend that the location at thermocouple B gives the maximum temperature, the location at thermocouple C gives the minimum temperature and the location at thermocouple A gives an intermediate temperature between thermocouples B and C. This demonstrates that the CFD models using the Realizable k-ε and SST k-ω turbulence models are sufficient to predict the impact of inlet configuration on the machine cooling. The relative errors of the CFD prediction are also shown in Table 4-1(b) and (c). When compared to the measured values, the temperature rises predicted using Realizable k-ε model has 15% error and those predicted using SST k-ω model has 30% error. In CFD models, the power losses obtained in Section 4.3 are evenly distributed throughout the volumes of the machine parts that generated the losses, but in practice this may not be true for the actual electrical machine. Furthermore, the turbulence models that used for the present investigation (they have been widely used for turbulence modelling of electrical machine as discussed in Chapter 3) are based on the Boussinesq's assumption that the Reynolds stress is proportional to the mean rate of deformation of the fluid element. The assumption may not be valid for complex flows like rotating flows. Therefore, these two factors described above mainly lead to the discrepancy between experimental and CFD results.

Temperature Rise	Case 1: Ventilation with radial and axial holes	Case 2: Ventilation with radial holes only	Case 3: Ventilation with axial holes only
Thermocouple A	52.6°C	56.4°C	59.5°C
Thermocouple B	58.2°C	62.4°C	67.0°C
Thermocouple C	35.6°C	40.3°C	44.1°C

(a) Experimental results

Temperature Rise	Case 1: Ventilation with radial and axial holes		Case 2: Ventilation with radial holes only		Case 3: Ventilation with axial holes only	
Thermocouple A	47.3°C	-10.08%	53.3°C	-5.50%	63.4°C	6.55%
Thermocouple B	49.3°C	-15.29%	55.9°C	-10.42%	66.2°C	-1.19%
Thermocouple C	36.5°C	2.53%	39.2°C	-2.73%	46.0°C	4.31%
Rotor $_{mean}$	18.9°C	–	23.7°C	–	31.5°C	–
Magnet $_{mean}$	22.2°C	–	27.4°C	–	36.6°C	–
Coil $_{mean}$	50.3°C	–	56.9°C	–	67.3°C	–

(b) CFD results using Realizable *k-ε* turbulence model

Temperature Rise	Case 1: Ventilation with radial and axial holes		Case 2: Ventilation with radial holes only		Case 3: Ventilation with axial holes only	
Thermocouple A	54.1°C	2.85%	58.7°C	4.08%	72.0°C	21.01%
Thermocouple B	57.0°C	-2.06%	63.7°C	2.08%	77.1°C	15.07%
Thermocouple C	42.3°C	18.82%	47.5°C	17.87%	57.3°C	29.93%
Rotor $_{mean}$	22.3°C	–	27.5°C	–	38.0°C	–
Magnet $_{mean}$	25.9°C	–	31.4°C	–	43.4°C	–
Coil $_{mean}$	57.5°C	–	64.2°C	–	77.5°C	–

(c) CFD results using SST *k-ω* turbulence model

Table 4-1: Measured and simulated temperature rise (°C) of inlet configuration of Case 1, 2 and 3 after steady-state ($T_{ambient}$ = 29 °C, Speed = 100 rpm)

As the stator coils generate the main heat, higher temperatures can be seen around the coils. This forms a coil temperature "loop" as illustrated in Figure 4.11(a). Figure 4.11 shows the temperature contour of stator surface predicted using Realizable k-ε model, whereas Figure 4.12 the temperature contour of stator surface predicted using SST k-ω model. Thermocouple B always gives the highest temperature. Thermocouple A and C recorded lower temperature rises because heat is dissipated through the aluminium fins and higher heat transfer rate due to thermal entrance effect at the inner radius respectively. The experimental results indicate that the maximum temperature rise (thermocouple B) of the Case 3 is about 15.1% higher than the Case 1. This demonstrates that the inlet configuration can substantially affect machine cooling. Though the AFPM prototype performance in the present study is well within the temperature limits, cooling becomes a very important issue for machines with high power density such as large-scale wind turbine generators. Therefore, AFPM machine cooling needs efficient ventilation to avoid overheating.

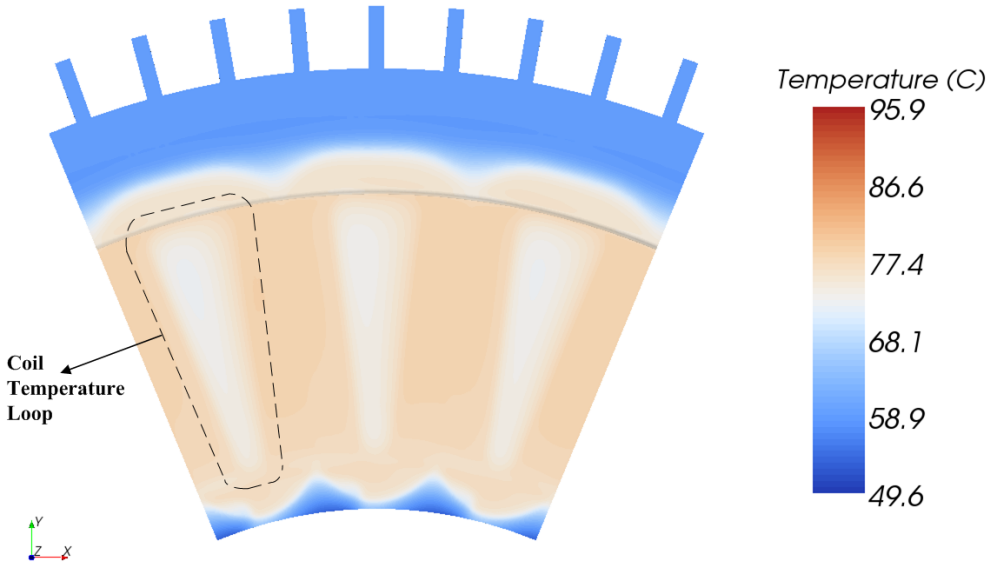

(a) Case 1: Ventilation with radial and axial holes

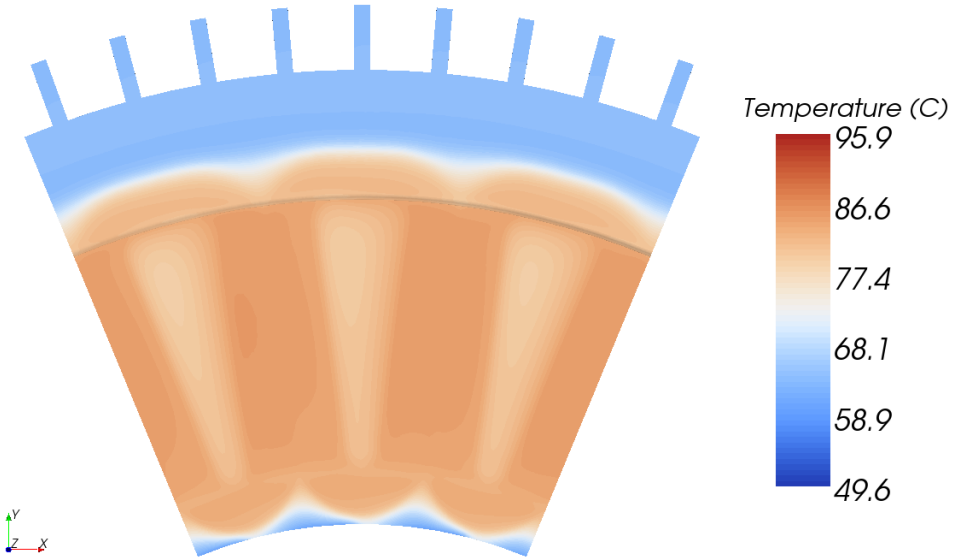

(b) Case 2: Ventilation with radial holes only

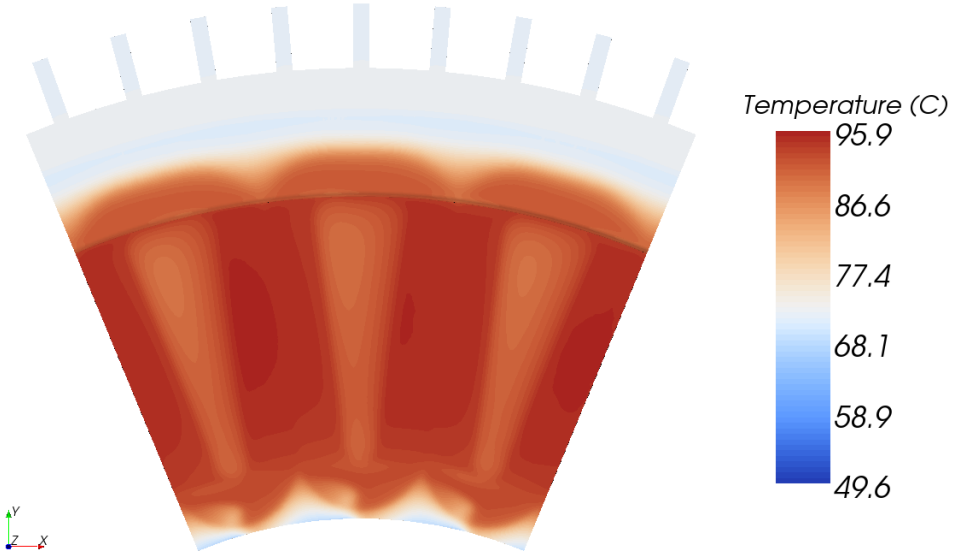

(c) Case 3: Ventilation with axial holes only

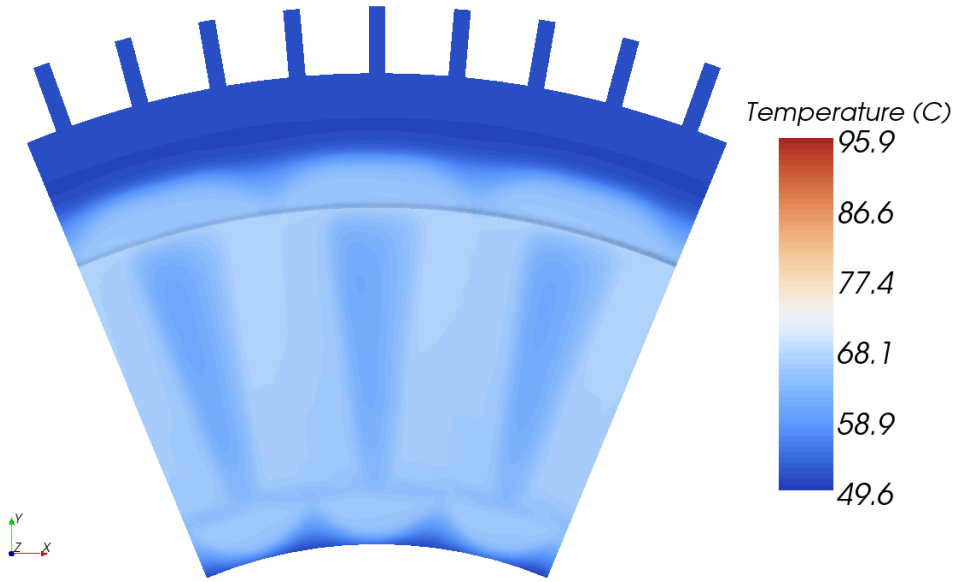

(d) Improved ventilation

Figure 4.11: Temperature contour of stator surface using CFD (Realizable *k*-ε model)

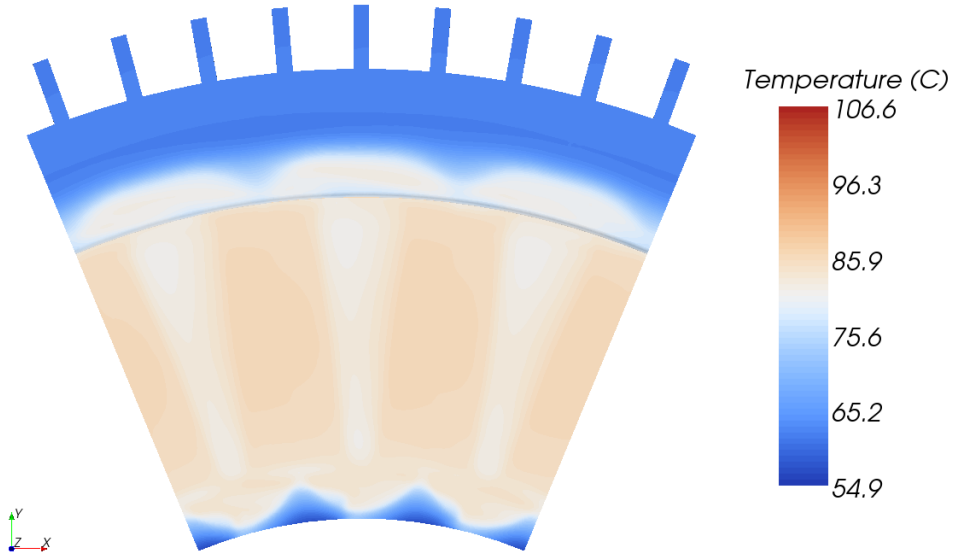

(a) Case 1: Ventilation with radial and axial holes

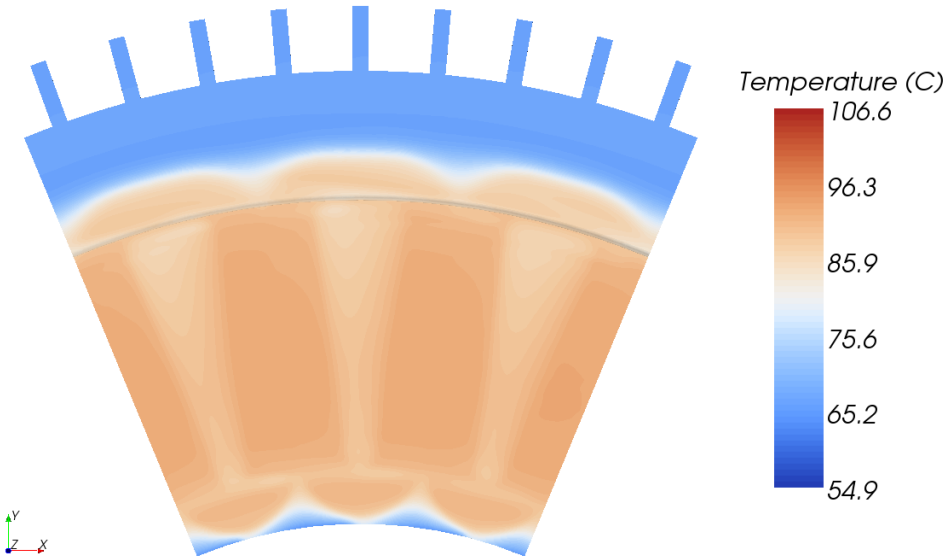

(b) Case 2: Ventilation with radial holes only

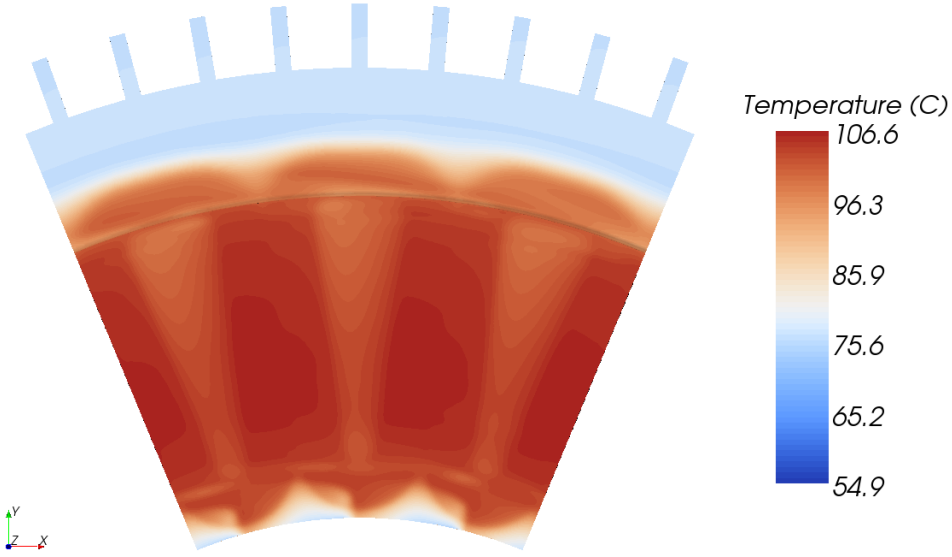

(c) Case 3: Ventilation with axial holes only

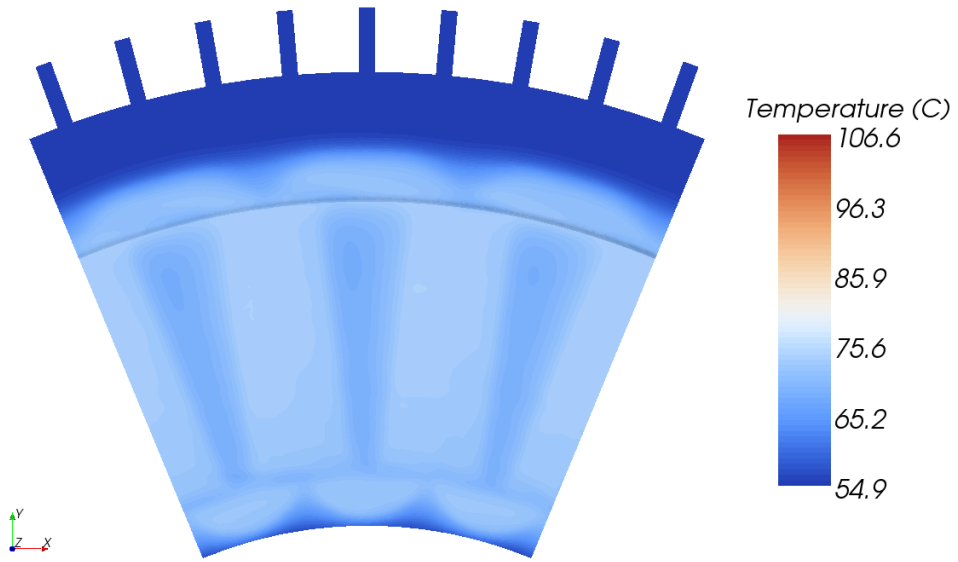

(d) Improved ventilation

Figure 4.12: Temperature contour of stator surface using CFD (SST k-ω model)

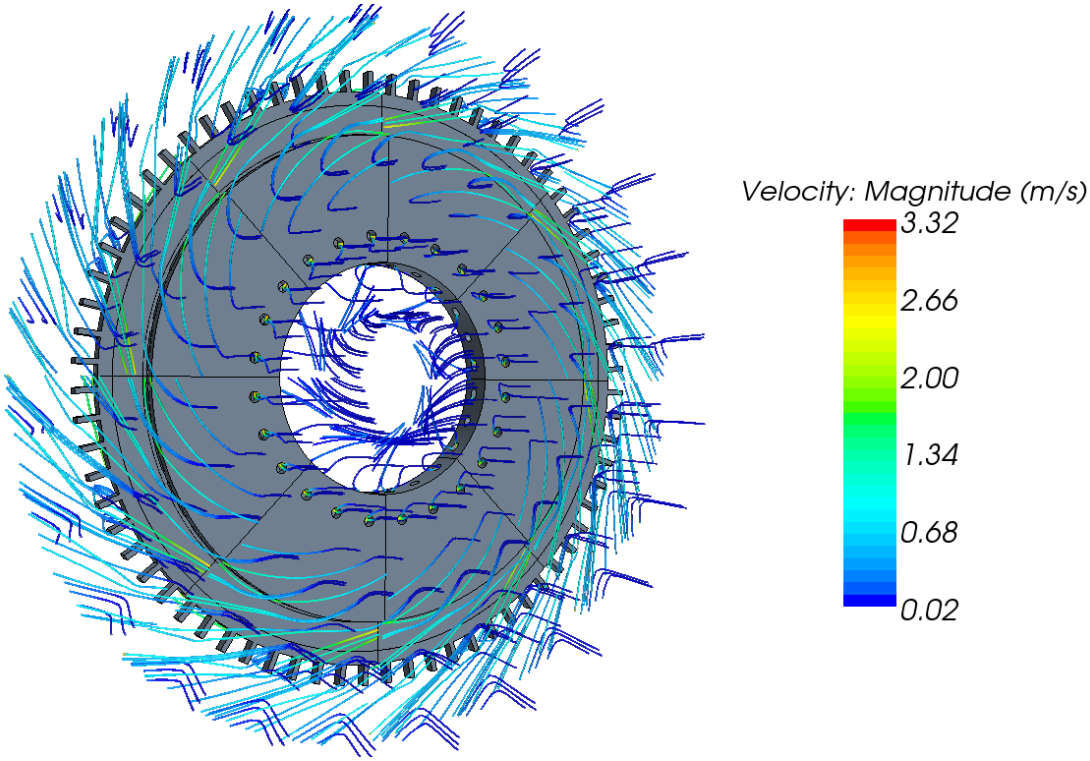

Figure 4.13: Flow pattern induced by the rotor around the AFPM machine for Case 1

Figure 4.13 illustrated the flow pattern induced by rotor spinning at 100 rpm for Case 1 with radial and axial holes. Most of the surrounding air is being drawn into the AFPM machine through the ventilations holes and is expelled radially from the machine. Windage torque of the AFPM generator has a shear and pressure component. Shear torque is used to overcome the air friction for rotating parts while pressure torque is converted into rotor pumping pressure. The windage loss can be calculated using the following equation as:

$$P_{windage} = T_q \omega_m \tag{4.21}$$

where T_q is the moment of force (which is also known as torque) on the rotor surfaces to rotate about the axis of rotation and ω_m is the machine angular velocity. From CFD modelling, the windage losses of the entire AFPM machine for Case 1, 2, and 3 are 1.63, 1.47, and 1.34 W respectively (values of non-drive end stage multiplied by 3); where windage losses are part of the mechanical losses, but negligible compared to the major loss components described in Section 4.3.

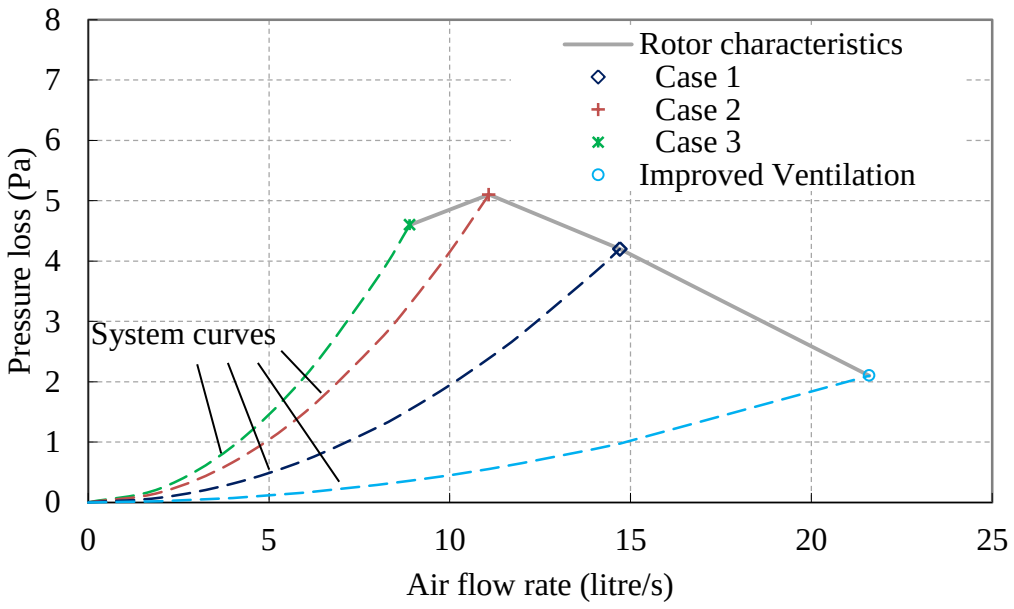

Figure 4.14: System flow resistance for different inlet configurations, CFD (Realizable *k-ε*), rotor speed = 100 rpm.

Figure 4.14 shows the variation of the system pressure loss and total air flow rate through the non-drive end stage for different inlet configurations. The dashed lines

representing system curves were obtained by extrapolating from the CFD results using the equation below.

$$p_s = \frac{1}{2}\rho \sum_{i=1}^{n} \left(\frac{K_i}{A_i^2}\right) \times Q^2 \tag{4.22}$$

$$C = \frac{1}{2}\rho \sum_{i=1}^{n} \left(\frac{K_i}{A_i^2}\right) \tag{4.23}$$

where p_s is the rotor pumping pressure provided by the AFPM machine and Q is the total air flow rate passing through the ventilation holes. C is the coefficient of the system flow resistance. As the flow through axial holes experiences an additional bending loss, the inlet flow rate of Case 2 with radial holes is higher than Case 3 with axial holes. Case 1 shows higher inlet flow rate because the sum of its inlet cross-sectional area is two times bigger than the other two cases. Hence, Case 1 provides the lower flow resistance to the system comparatively. Higher air flow rate results in greater stator convective heat transfer. To obtain a much higher flow rate, an external fan can be connected to the system. However, the corresponding system flow resistance will remain the same. Since the windage loss is negligible at the running speed, it does not result in significant efficiency decease. In contrast, a lower temperature rise may reduce the electromagnetic losses for those losses that are temperature dependent.

4.6 Improved Machine Ventilation

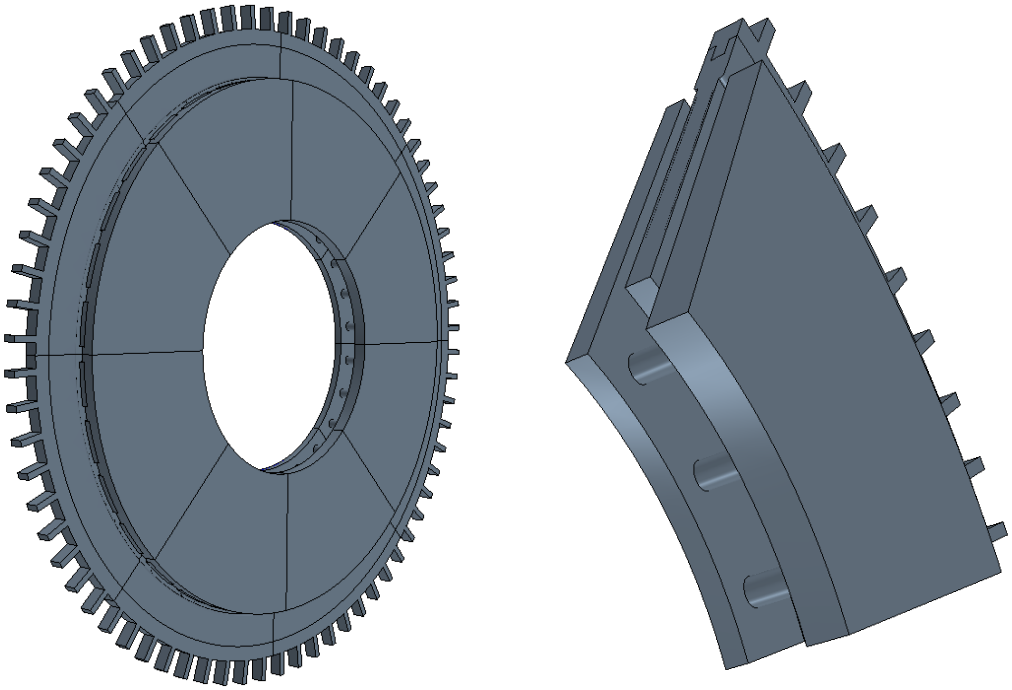

(a) Full non-drive end stage (b) Single rotor-stator module

Figure 4.15: CAD geometry of proposed ventilation

According to the preceding section, the ventilation holes affect the amount of air flow rate passing through the AFPM machine. In theory, the abrupt change in flow cross sectional area will considerably increase the pressure drop. The size of the ventilation hole is important in determining the flow resistance and flow rate passing through the machine. Consequently, the machine ventilation is improved. The rotor module is replaced by rotor plates that are connected by cylindrical bars. This change provides much bigger air inlet as shown in Figure 4.15. It is assumed that the change of machine ventilation does not affect the electromagnetic performance and hence the same heat sources as those of Case 1, 2 and 3 were employed for CFD simulation. The proposed ventilation has lower system flow resistance and allows more air to pass through the machine as illustrated in Figure 4.14. CFD simulation gives an estimation of 21.6 litre/s of cooling air through the stage which is 47% higher than Case 1. Figure 4.16 illustrates the flow pattern induced by the rotor spinning at 100 rpm for improved ventilation. The windage loss of the entire machine is 2.03 W (values of non-drive end stage multiplied by 3). The thermal performance of the

improved ventilation is demonstrated in Table 4-2. When compared to Case 1, there is a reduction in temperature rise of thermocouple B of 10.4 °C using Realizable *k-ε* model and 11.2 °C using SST *k-ω* model.

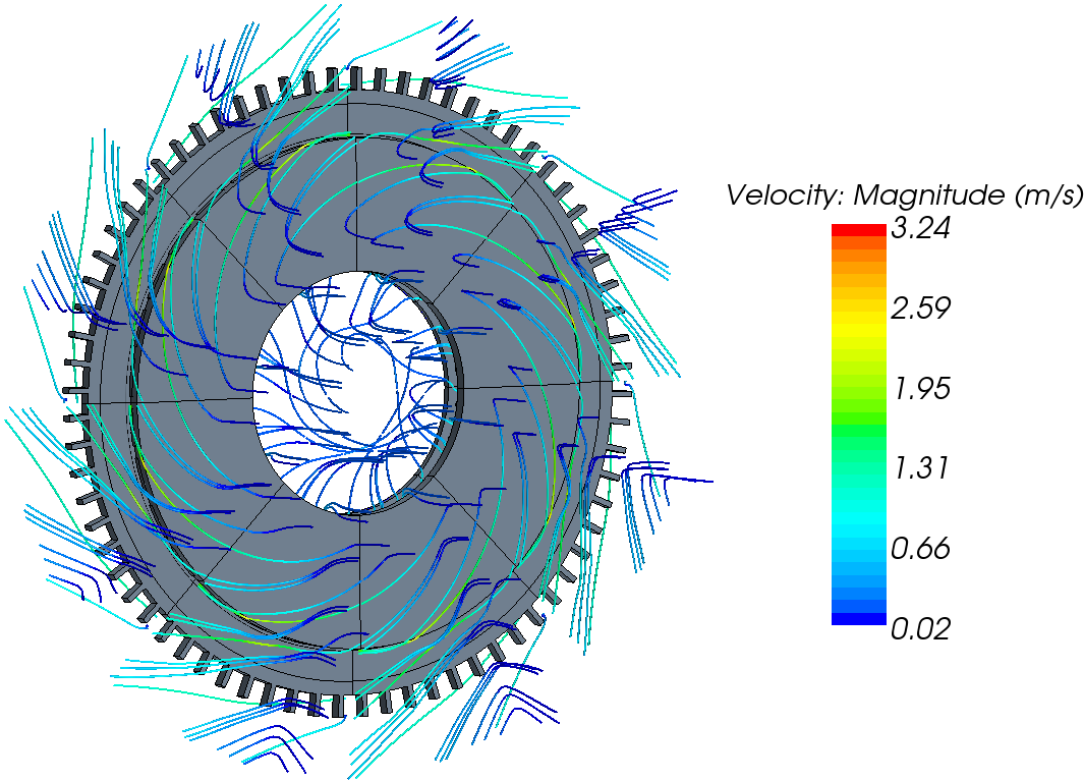

Figure 4.16: Flow pattern induced by the rotor for improved ventilation

Temperature Rise	CFD (Realizable *k-ε* model)	CFD (SST *k-ω* model)
Thermocouple A	37.0	43.7
Thermocouple B	38.9	45.8
Thermocouple C	30.3	36.3
Rotor $_{mean}$	9.9	10.4
Magnet $_{mean}$	11.6	11.9
Coil $_{mean}$	40.1	46.8

Table 4-2 Simulated temperature rise (°C) of the improved ventilation after steady-state ($T_{ambient}$ = 29 °C, Speed = 100 rpm)

4.7 Convective Heat Transfer

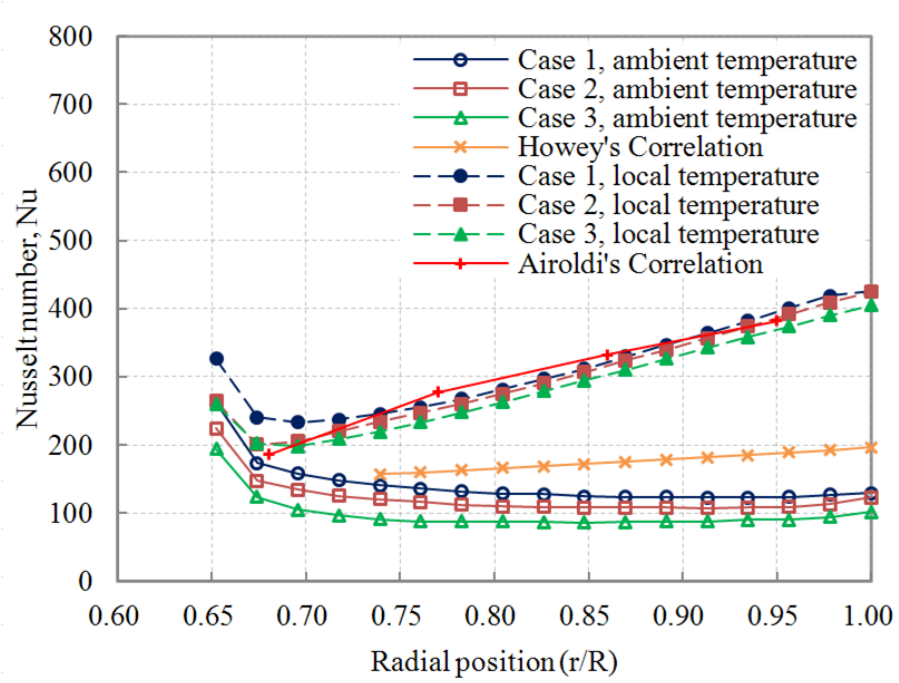

Figure 4.17: Comparison of stator convective heat transfer between CFD (Realizable *k*-ε) and heat transfer correlations.

Convective heat transfer dominates the cooling process of this throughflow ventilated AFPM machine. Since the CFD models have been validated, they are used to obtain heat transfer results and compare to those values of published heat transfer correlations. This may address the suitability of those correlations proposed specifically for AFPM machines. As shown in Figure 4.17, the mean stator convective heat transfer $\overline{Nu}$ at the radial position was calculated for $0.65 \leq r/R \leq 1$ (the area of where the stator facing the magnet protrusions on the rotor) as follows:

$$\overline{h} = \frac{q''}{T_w - T_{ref}} \tag{4.24}$$

$$\overline{Nu} = \frac{\overline{h}r}{\lambda_{air}} \tag{4.25}$$

The predicted CFD results were compared with Howey's correlation which is valid at gap ratio G = 0.0106. Since the empirical correlation is developed based on the convention of using ambient fluid temperature as the reference temperature, this

convention is also followed. In fact, the air entering the machine tends to circulate in the rotor-stator gap in the tangential direction while it is being pumped radially outwards. The air temperature increases along the rotor-stator gap. Hence, using the ambient fluid temperature tends to give conservative estimation of stator convective heat transfer. Based on the heat transfer and fluid dynamic practice, T_{ref} should refer to the local fluid bulk temperature at the radius where the calculation for convective heat transfer coefficient is being made. The Nusselt numbers based on the local air temperature are also shown in Figure 4.17. They were compared with the more comprehensive Airoldi's correlation, which is also based on the local air temperature. It can be seen that they are considerably higher than the values calculated based on the ambient temperature, especially at the outer radii. Overall, the simulated results agree reasonably well with the values obtained from the stator heat transfer correlations. The predicted Nusselt numbers based on ambient temperature are lower than the values obtained from the Howey's correlation because the AFPM machine of the present study has smaller gap ratio of 0.0076.

The limitation of the present study is that the effect of surface roughness on heat transfer was not taken into account. It was assumed here that the decrease in air flow rate due to higher friction was compensated by an increase of heat transfer due to the surface roughness under the given operational conditions. Furthermore, it is common to ignore thermal radiation as it is relatively small under forced convection.

4.8 Conclusion

The detailed distribution of power losses of an AFPM generator has been presented in this chapter. These losses are converted into heat causing the temperature rise of machine parts and this has been modelled through CFD and validated in an actual AFPM direct drive generator with surface-mounted magnets. The present study has demonstrated the impact of inlet configuration on generator cooling for the rated speed. The more efficient the ventilation system can be made, the greater the performance that can be achieved from a given electrical machine, while still maintaining the temperature within proper limits. From a design point of view, a throughflow ventilated electrical machine should not have a degree of enclosure more than the absolutely necessary.

5 Analytical Design Tool for Air Flow Modelling

The development of an analytical design tool for air flow modelling of electrical machines is fundamentally motivated by the limitations of the lumped-parameter thermal network (LPTN) in accurately predicting the convection heat transfer inside electrical machine under the effects of rotation. Therefore, the analytical air flow modelling tool was aimed to be integrated with the existing analytical thermal modelling method, LPTN to form a complete analytical thermal-fluid modelling method to accurately predict electrical machine thermal performance. The analytical air flow modelling tool is based on the flow network analysis technique.

5.1 Flow Network Analysis

The flow network analysis is an analysis of fluid flow through a pipe network involving the process of defining the mathematical model of the fluid transport and distribution in a flow system. It is commonly used for water supply network, heat, ventilation and air conditioning (HVAC) design, hydropower, etc. It is employed for the present study for air flow modelling of electrical machines. Basically, a flow network is composed of various flow components (e.g. friction, expansion, contraction, bend and etc.). Based on the empirical loss coefficients for the corresponding flow components, the flow network analysis is capable of determining the flow rates and pressure drops in the individual flow components of the network. Therefore, the knowledge of flow distribution in the electrical machines, especially for throughflow ventilation cooling method, could benefit the accurate determination of heat transfer coefficients and thus the cooling power that can be obtained.

However, the available flow networks that applied to electrical machines are mainly dependent on the normal stationary correlations and fully developed flow conditions such as those of Sun et al. [2013], David et al. [2008] and Boglietti et al. [2009]. As described in Chapter 2, the effects of rotation could significantly increase the system flow resistance for certain operating conditions. Therefore, the air flow modelling tool developed in this research will include flow components that take into account the effects of rotation and also flow components accounting for developing flow that are more appropriate for practical use in electrical machines. In order to suit the

application of thermal management of electrical machines, the analytical air flow modelling tool that was developed is based upon the following assumptions:

- The compressibility of a fluid flow is determined using Mach number (M), the ratio of the fluid flow velocity and the speed of sound. As the Mach number of the cooling media used in most conventional electrical machines is less than 0.3 (i.e. 100 m/s approximately), thus the flow can be treated as incompressible because the compressibility effects are negligible. Furthermore, the pressure variation of the flow is not large enough to produce significant changes in density due to the thermal effects. This permits the use of the constant density form of the continuity and energy equations in the flow network analysis.
- Steady-state flow condition, in the present study the flow network analysis does not take into account the variations of fluid flow characteristics over time.
- Newtonian fluids, the shear stress that developed in the fluid flow boundary layer is directly proportional to the shear strain and its dynamic viscosity is constant for a given temperature, e.g. air, water, etc.
- The fluid properties, e.g. dynamic viscosity, density, Prandtl number, and specific heat, are temperature dependent only. Their values are constant in the modelling.
- The flow network analysis is not capable of modelling opposite flows in the same pipeline. Thus, it is not able to model the fluid ingress at an outlet (e.g. ambient air) which provides the entrainment flow. For instance, a flow network analysis method is not applicable for the Axial Flux Permanent Magnet (AFPM) machine studied in Chapter 4 because the differential pressure is generated inside the machine by the rotor movement and hence air may be drawn into the machine through its outlet instead. This could happen because of the inappropriateness of ventilation design causing too high flow resistance at the inlet region and hence limiting the amount of air passing into the machine through its inlet, which is not enough to replace the air which has been pumped out.

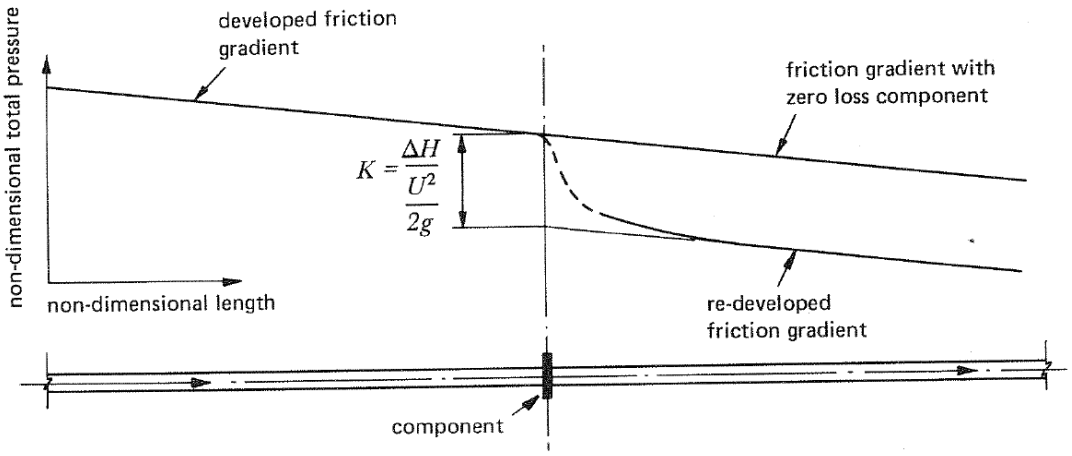

Figure 5.1: Definition of system loss coefficient, Miller [1978]

Besides, it is important to note that the empirical loss coefficient (*K*) of an individual flow component is mostly obtained under fully developed flow condition. Fully developed flow achieved using sufficient long pipes give linear pressure drop due to friction loss as shown in Figure 5.1. Hence, the local pressure drop can be determined by projecting the developed and re-developed friction gradients to the flow component. It can be observed that the pressure loss caused by the flow component not only occurs at the place where it is installed, but also occurs in the downstream. Moreover, in many engineering fluid flow problems flow components could be installed close to each other and there could be more than one type of pressure loss at a same place. According to Idelchik [2007],

> "The total pressure losses in any complex element of the pipeline are inseparable. However, for ease of calculation they are arbitrarily subdivided in each element of the pipeline into local losses and frictional losses. It is also assumed that the local losses are concentrated in one section, although they can occur virtually throughout the entire length."

Based on this, in the flow network analysis the pressure loss caused by a flow component is assumed concentrating at the place of where it is installed. As the total pressure losses in throughflow ventilated electrical machines are intrinsically inseparable in nature, the flow network analysis has one of the main advantages over

CFD and experimental methods to examine the contribution of the individual flow components to the total pressure drop. Hence, the flow network analysis can be very useful for the ventilation design optimisation of electrical machines.

5.2 Methodology of Analysis

The flow network analysis is fundamentally based on Kirchhoff's laws, which is commonly used in electrical engineering. They are adapted for fluid dynamics. It has been proven in many fluid mechanic textbooks that the Darcy-Weisbach equation can phenomenologically relate the pressure loss and fluid flow passing through a pipe. For convenience of network analysis, the Darcy-Weisbach equation, Douglas et al. [1995], is required to express the pressure loss (Δp) in terms of volumetric flow rate (Q) in the pipe and thus equation (1.4) is rewritten into a form of Ohm's law, Hence,

$$\Delta p = RQ^2 \tag{5.1}$$

$$R = \frac{K\rho}{2A^2} \tag{5.2}$$

where R is known as the flow resistance, K is the pressure loss coefficient, ρ is the fluid density and A is the flow cross section area. Therefore, the pressure loss, flow resistance and the square of volumetric flow rate are analogous to that of the voltage, electrical resistance and current respectively.

In the flow network analysis, Kirchhoff's first law means that the sum of flow coming into any intermediate node needs to equal the flow going out of that node and this statement is in line with the principle of conservation of mass. Kirchhoff's second law indicates that the sum of pressure losses around a loop in a flow network is zero. In order to determine the flow rates and pressure drops in the individual flow components of a flow network, the pressures at the nodes and the flow rates in the individual flow components must fulfil the first and second Kirchhoff's laws, and satisfy the flow equations derived from the flow components, see Section 5.4. For instance, the pipe diameter, length, surface roughness and fluid properties at the working temperature are the required inputs for the flow resistance of friction loss.

However, solving the flow distribution within a complex pipe system is complex because it involves the non-linear relationship between pressure loss and flow rate. In fluid dynamics, the most efficient approach for solving a flow network is using the Hardy-Cross technique, Cross [1936]. The Hardy-Cross technique is an iterative method for determining the flow distribution in pipe network systems and the pressure losses throughout the systems when the inputs and outputs are given. The Hardy-Cross technique can be executed using two methods, method of balancing pressure losses and method of balancing flows. For the method of balancing pressure losses, the flows in a network initiate with the condition that the algebraic sum of the flows at each junction is zero, and then the flows are successively corrected to satisfy the condition of zero total change of pressure loss around each loop in the system. In contrast, for the method of balancing flows, the flows in a network initiate with the condition that the total change of pressure loss around each loop in the system is zero, and then the flows are successively corrected so that the algebraic sum of the flows at each junction is zero. As described in Chapter 1, the thermal performance of a throughflow ventilated electrical machine is ultimately dependent upon the flow rates passing through the cooling paths. Therefore, method of balancing pressure losses is selected for the present research because the system pressure requirements are always to match the required cooling power. The computer solving algorithm, Newton-Raphson method is employed for solving non-linear flow network problem. The implementation of Newton-Raphson method on a throughflow ventilated machine can be found in Section 5.6.

5.3 PORTUNUS

PORTUNUS software is a simulation package for the analysis of multi-physics system, cedrat [2012]. It was selected as the simulator for the flow network analysis because of the library and model management of PORTUNUS provides options to create user-defined models. Therefore, the characteristic of the flow components for the stationary and rotating conditions can be described in a new library, namely "Flow Library". As a result, PORTUNUS allows the integration of the flow network analysis with other physical disciplines such as thermal, magnetic, electrical,

mechanical, etc, to the ultimate aim for the full optimisation of electrical machine design.

The flow components were modelled using the VHDL-AMS language in PORTUNUS. VHDL-AMS is a derivative of the hardware description language VHDL (IEEE standard 1076-1993). It includes analog and mixed-signal extensions (AMS) in order to define the behaviour of analog and mixed-signal systems (IEEE 1076.1-1999), cedrat [2012]. The other advantages of VHDL-AMS for the flow network analysis are as follows:

- Standard – The flow models developed using the Flow Library can be exchanged between different simulation tools that adhere to the VHDL-AMS standard, ensuring compatibility between software tools and preserving legacy models.
- Multi-disciplinary modelling – According to Randewijk and Mounton [2006], a further set of extensions to VHDL-AMS was adopted by the IEEE (IEEE 1076.1.1-2004), to support various energy domains to co-exist within a VHDL-AMS simulation. Thus, the flow network constructed using the Flow Library can be coupled with the thermal network for a complete thermal-fluid modelling.
- Implicit equations processing – As the flow network analysis are similar to the electrical and thermal networks in nature, the generalized Kirchhoff's laws are used.
- Graphical user interface – An electrical machine designer can make use of the Flow Library easily because of the graphical model environment, only the machine geometric information, working fluid properties and operating conditions are required as the inputs.

5.4 Pressure Losses of Viscous Flow

In this section, the procedures for determining pressure losses in the passages of throughflow ventilated machines are outlined. Stationary losses are the only focus in this section, whereas the rotational losses are described in Chapter 6 based on CFD method and Chapter 8 based on experimental method.

For real fluids, the flow in a bounded system experiences energy losses due to frictional and separation effects, Douglas et al. [1995]. The frictional effect is associated with shear stresses in the fluid as a result of viscosity. Separation losses arise from flow disturbance due to changes in flow cross section area, changes in flow direction and interaction with other pipe fittings such as a valve, flow measurement device, junction and etc. As a result, the flow separates from the pipe walls as it passes through these disturbances resulting in the formation of turbulence eddies and consequent pressure loss. Based upon the fundamental principles of conservation of mass and energy, the pressure loss between two points in the bounded system is equal to the difference in the total pressure between these two points. The total pressure at a point is the sum of static pressure, kinetic pressure and potential pressure. Hence,

$$\Delta p = (p_1 - p_2) + \frac{1}{2}\rho\left({U_1}^2 - {U_2}^2\right) + \rho g(h_1 - h_2) \tag{5.3}$$

As separation losses associate with the effect of turbulence and the derivation of expressions defines the effect of turbulence is difficult owing to the nature of turbulent flow, a separation loss is usually quantified with empirical loss coefficient based upon the flow kinetic energy as:

$$\Delta p = K \times \frac{1}{2}\rho U^2 \tag{5.4}$$

Therefore, the pumping pressure provided by a fan is mainly used to maintain the motion of bounded flow.

5.4.1 Friction loss

Friction loss is one of the main pressure losses of bounded flow. Darcy-Weisbach equation is the most common formula to estimate the friction loss in a length of duct as:

$$\Delta p = f\frac{L}{d} \times \frac{1}{2}\rho U^2 \tag{5.5}$$

The coefficient of friction loss is a function of friction factor (f), duct length (L) and hydraulic diameter. The friction factor is the Darcy's friction factor.

$$K_f = f\frac{L}{d} \tag{5.6}$$

The friction factor is dependent on the flow regime, e.g. laminar or turbulent. Between the laminar and turbulent flow regime is an area of uncertainty (i.e. transition flow), but the algorithm of turbulent flow is usually applied. Theoretically, the friction loss of laminar flow can be computed using the Hagen-Poiseuille formula, Douglas et al. [1995].

$$\Delta p = \frac{128\mu LQ}{\pi d^4} \tag{5.7}$$

where μ is the dynamic viscosity of the fluid. Equation (5.7) can be expressed into the form of Darcy-Weisbach equation as:

$$\Delta p = \frac{32\mu LU}{d^2} \tag{5.8}$$

$$\Delta p = \frac{64\mu}{\rho Ud} \times \frac{L}{d} \times \frac{1}{2}\rho U^2 \tag{5.9}$$

Hence, by analogy, the friction factor for laminar pipe flow is independent of surface roughness given by:

$$f = \frac{64}{Re} \tag{5.10}$$

However, for annular gap of inner radius to outer radius close to unity, the friction factor is 1.5 times of circular duct as, White [1986]:

$$f = \frac{96}{Re} \tag{5.11}$$

For smooth wall, the friction factor of turbulent pipe flow can be approximated using the empirical relation proposed by Blasius in 1913, Idelchik [2007].

$$f = \frac{0.316}{Re^{0.25}} \tag{5.12}$$

However, the effect of surface roughness to friction factor of turbulent flow can be estimated using Colebrook-White equation, represented by equation (7.5). Besides that, the effect of annulus concentricity to friction factor is often small and can be

neglected, Idelchik [2007]. It is important to note the equation (5.10)-(5.12) and (7.5) are only applicable for fully developed flow. In fact, when a fluid passes through a duct, the friction factor of the flow would be large in the initial section of the duct and would asymptotically approach the value for fully developed flow condition occurring in duct further downstream, Deissler [1953]. According to Kay and Crawford [1993], the length of the entrance region for turbulent flow can be approximated as:

$$\frac{L_{entry}}{d} = 0.623Re^{0.25} \tag{5.13}$$

L_{entry}/d is the number of duct diameters required for the friction factor to approximate to a constant value. In heat transfer, the information of the effect of entrance region to turbulent heat transfer of air is available in Burmeister [1993]. This can be related to momentum transfer of turbulent flow through Prandtl number because Prandtl number is a measure of momentum diffusivity to heat diffusivity ratio. Hence, the actual friction factor of air flow in rotor-stator gap and rotor ducts for a given length is:

$$\begin{aligned} &\frac{L}{d} \geq \frac{L_{entry}}{d}, \qquad \frac{f}{f_\infty} = 1 + \frac{6}{(L/d)Pr} \\ &\frac{L}{d} < \frac{L_{entry}}{d}, \qquad \frac{f}{f_\infty} = 1 + \frac{\frac{1.11Re^{0.2}}{(L/d)^{0.8}} - 1}{Pr} \end{aligned} \tag{5.14}$$

f_∞ is the friction factor for fully developed flow as obtained from equation (5.12) and (7.5).

5.4.2 Sudden expansion loss

Due to a sudden change in flow cross section area, flow separation is generated at the corners of the expansion and turbulence eddies spread through the downstream flow. Reverse flow grows at the separation point followed by intense mixing and flow-reattachment to the main flow, Miller [1978]. This flow phenomenon is associated with significant energy losses. The pressure loss of a sudden expansion flow is based on the mean velocity in the pipe before expansion of smaller cross section area (i.e. inlet).

$$\Delta p = K_{SE} \times \frac{1}{2} \rho {U_{inlet}}^2 \tag{5.15}$$

According to the Borda–Carnot equation, Douglas et al. [1995], the theoretical expression of sudden expansion loss coefficient derived using the momentum principles is given by:

$$K_{SE} = \left(1 - \frac{A_i}{A_o}\right)^2 \tag{5.16}$$

A_i and A_o are inlet and outlet cross section areas respectively.

5.4.3 Sudden contraction loss

For the flow of sudden contraction, flow separation in the downstream pipe forms a *vena contracta*, where the main stream contracts to a minimum diameter before it recovers to occupy the entire pipe cross section area. Hence, turbulence eddies are formed in this region and decay along the downstream pipe. This causes significant pressure loss. The pressure loss of a sudden contraction flow is based on the mean velocity in the pipe after contraction of smaller cross section area (i.e. outlet) as:

$$\Delta p = K_{SC} \times \frac{1}{2} \rho {U_{outlet}}^2 \tag{5.17}$$

The correlation of sudden contraction loss coefficient can be obtained by fitting the empirical data given in Khan [1987] as:

$$K_{SC} = 0.5085 - 0.1979 \left(\frac{A_o}{A_i}\right) - 0.3148 \left(\frac{A_o}{A_i}\right)^2 \tag{5.18}$$

It can be observed that both sudden expansion and contraction losses are strongly dependent on the ratio of cross section area. Hence, the reduction of these losses can be achieved by reducing the ratio of cross section area.

5.4.4 Bending loss

When a fluid flows through a bend, the pressure loss suffered by the flow is higher than the normal friction loss due to change in flow direction. Within the bend, the high velocity core flow deflects towards the outside of the bend because of the centrifugal effects and the adverse pressure gradient causes the flow to move round the walls towards the inside of the bend. Thus, secondary flows in the form of a

double spiral are produced in the radial plane. The change in flow direction results in flow separation at the walls and hence the formation of turbulent eddies. This causes a flow separation loss, namely bending loss. The total pressure losses of a bend are determined as the sum of the loss of the bend and the friction loss due to the axial length of the bend as:

$$\Delta p = \left(K_{bend} + K_f\right) \times \frac{1}{2}\rho U^2 \tag{5.19}$$

where K_f can be computed using equation (5.6) and K_{bend} depends on the angle of the bend (A_1), the relative radius of curvature (B_1), the aspect ratio of bend cross section (C_1), the axial flow Reynolds number (D_1) and the relative surface roughness of walls (E_1). Thus, the bend loss coefficient can be expressed as:

$$K_{bend} = A_1 B_1 C_1 D_1 E_1 \tag{5.20}$$

Correlations for the determination of the value of A_1, B_1, C_1, D_1 and E_1 can be found in Idelchik [2007].

Other pressure losses due to pipe fittings are not presented in this section because they are not relevant to throughflow ventilated machines. However, if this information is required, the handbook of hydraulic resistance, Idelchik [2007] should be consulted.

5.5 Study Case I of a Series Flow Problem: Liquid-Cooled Heat Sink

The application of the analytical design tool to a liquid-cooled heat sink is presented in this section. The relationship between the pressure loss and volumetric flow rate of water passing through the heat sink tube and the tube geometric information provided by the manufacturer (Appendix D) can be used to verify the analytical flow model for a series flow problem. As shown in Figure 5.2, the tube of the 4 pass heat sink continuously passes through the plate and forms four straight sections and three 180° bending sections. This can be represented graphically using the equivalent flow network as illustrated in Figure 5.3 using PORTUNUS Flow Library. The flow network displays the volumetric flow rate passing through the heat sink and also the

pressures at the intermediate nodes between the flow components for the operating point (OP).

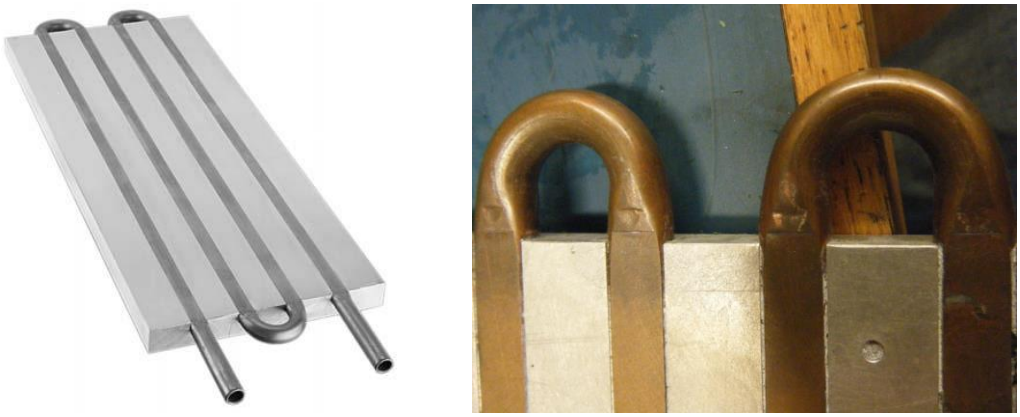

Figure 5.2: Hi-Contact™ Liquid Cold Plate 4 Pass Model, Aavid Thermalloy [2007]

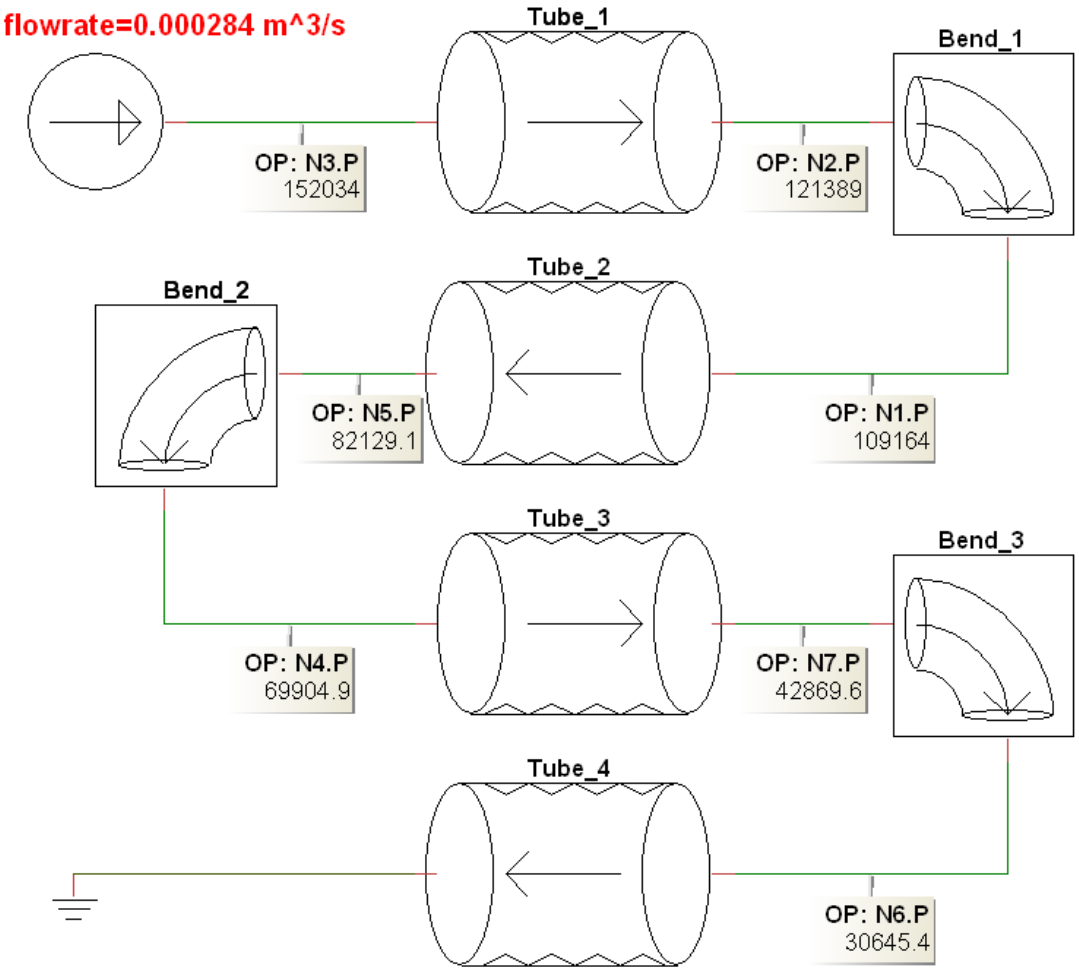

Figure 5.3: Equivalent flow network of 4 pass heat sink model at Q = 0.284 litre/s

The system flow equation can be written as:

$$\Delta p = (R_{tube1} + R_{bend1} + R_{tube2} + R_{bend2} + R_{tube3} + R_{bend3} + R_{tube4})Q^2 \qquad (5.21)$$

The flow problem is simple and hence the iterative process is not required for the solution. The sum of pressure drops in each tube section can be computed directly using equation (5.21) for the given flow rate. As the tube material is copper, wall roughness height of commercial drawn copper pipes of 0.0025 mm was assumed, Miller [1978].

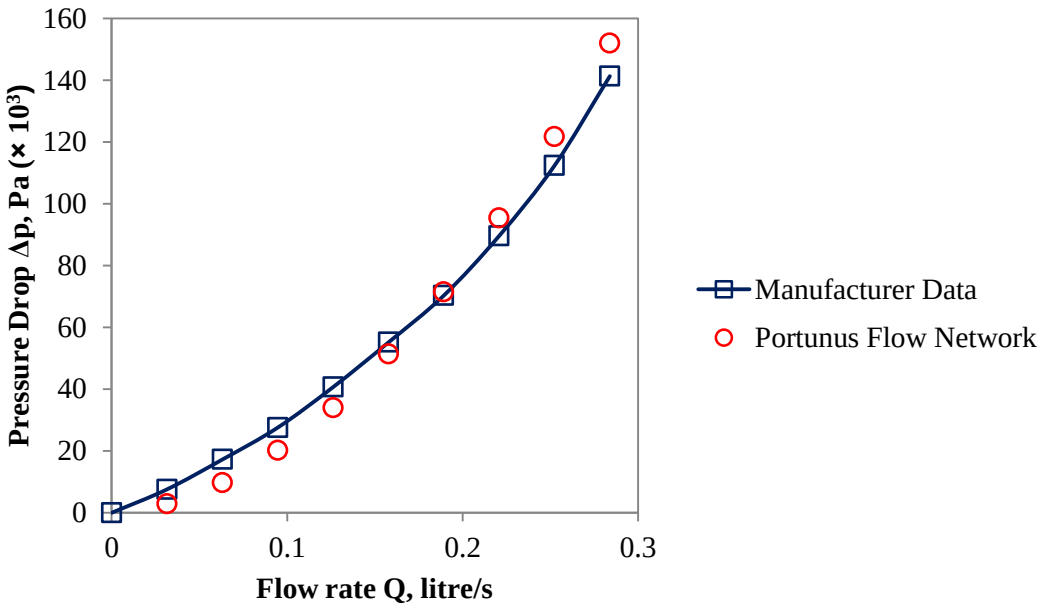

Figure 5.4: The variation of pressure drop with flow rate for 4 pass heat sink

As shown in Figure 5.4, the accuracy of the analytical flow model is acceptable. The discrepancy of the analytical results is due to the fact that the tube was pressed flat on the top surface of the main heat sink plate and distorted from the round cross section as shown in Figure 5.2. This was not considered in the analytical flow network analysis.

5.6 Study Case II of a Parallel Flow Problem: Throughflow Ventilated Induction Machine (Stationary)

In this section, the application of analytical design tool to a throughflow ventilated electrical machine is verified using the CFD method. The throughflow ventilated

electrical machine is one the machines (i.e. Test E) used to investigate the effects of rotation to additional pressure losses in Chapter 6. It involves a parallel flow problem. Since this study case is used to demonstrate the capability of the analytical design tool to model the parallel flow, the stationary pressure losses were only the focus and the pressure losses due to the rotating effects were not included in this section, but the rotating effects were modelled in Chapter 8. The flow distribution in the machine for the stationary condition was solved using the iterative method as described in Section 5.2.

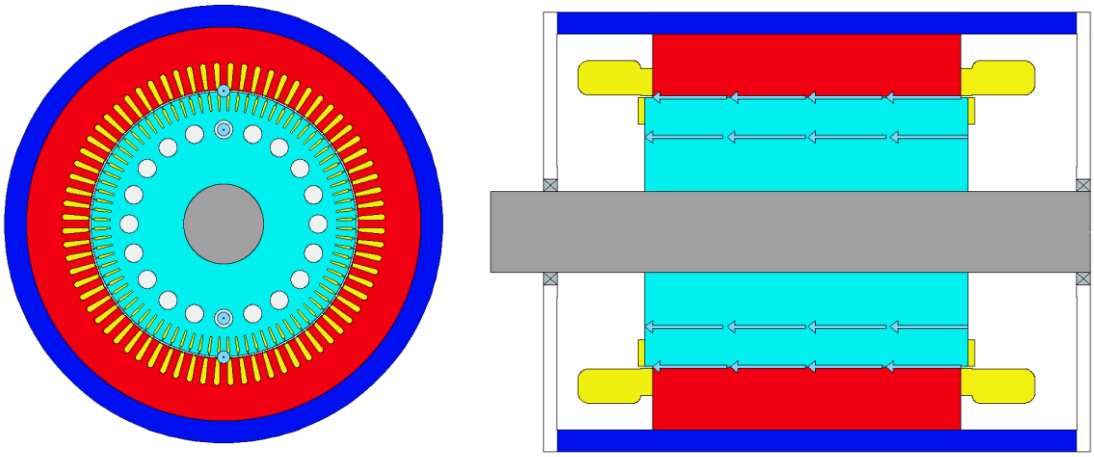

(a) Radial view **(b) Axial view**

Figure 5.5: Throughflow ventilated induction motor adapted from Al'Akayshee [2003] using Motor-CAD

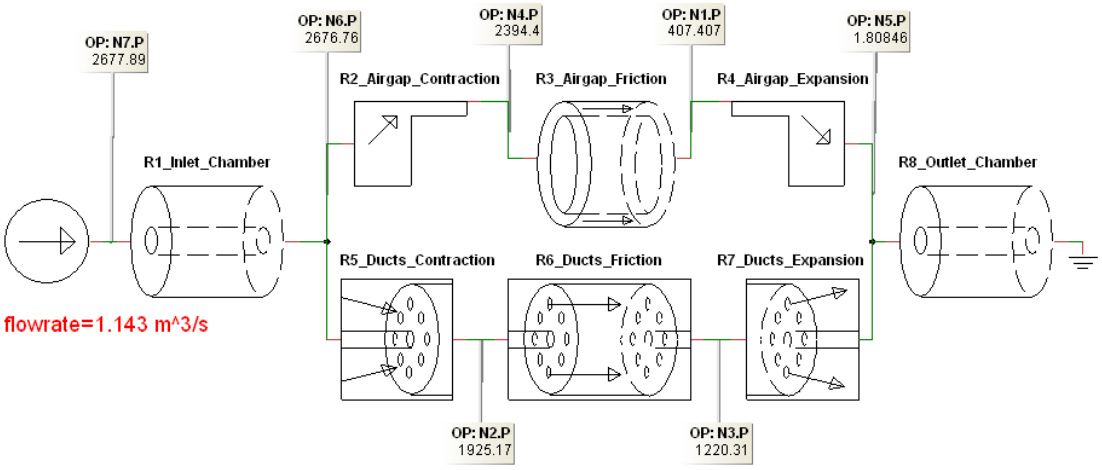

Figure 5.6: Equivalent flow network of adapted throughflow ventilated system at Q = 1.143 m^3/s

As shown in Figure 5.5, the throughflow ventilated electrical machine consists of a number of parallel flow paths, a rotor-stator gap and twenty rotor ducts. This can be represented graphically using the equivalent flow network as illustrated in Figure 5.6 using PORTRUNUS Flow Library.

As the rotor ducts are axisymmetric, they can be simplified as equivalent to a single flow component with an equivalent flow resistance (R_{ducts}) carrying the total flow (Q_{ducts}) passing through the rotor ducts as follows:

$$Q_{ducts} = \sum_{i=1}^{n=20} Q_{duct} \tag{5.22}$$

As equation (5.1) can be represented as $Q = \sqrt{\Delta p / R}$, thus

$$\frac{1}{\sqrt{R_{ducts}}} = 20 \times \frac{1}{\sqrt{R_{duct}}} \tag{5.23}$$

By substituting equation (5.2) into equation (5.23), the following relationship between the equivalent loss coefficient of all the rotor ducts and the loss coefficient of individual rotor ducts can be obtained.

$$K_{ducts} = K_{duct} \tag{5.24}$$

As the contraction, friction and expansion losses of the individual rotor ducts are same in magnitude based on the assumption that the flow rate passing through each rotor duct is the same, they can be represented as a single flow component respectively as illustrated in Figure 5.6.

In the flow network analysis, the Q^2 of equation (5.1) is rewritten into $|Q|Q$ because the square of volumetric flow rate would disregard the sign of the flow rate, where $|Q|$ is the absolute value of Q. Therefore, any change in flow direction can be preserved and reflected appropriately in the mathematical modelling. The flow equations of the equivalent flow network can be represented in matrix form as:

$$\begin{bmatrix} 1 & -1 & -1 \\ 0 & (R_2 + R_3 + R_4)|Q_{airgap}| & -(R_5 + R_6 + R_7)|Q_{ducts}| \\ (R_1 + R_8)|Q| & 0 & (R_5 + R_6 + R_7)|Q_{ducts}| \end{bmatrix} \begin{bmatrix} Q \\ Q_{airgap} \\ Q_{ducts} \end{bmatrix} = \begin{bmatrix} 0 \\ 0 \\ \Delta p \end{bmatrix} \tag{5.25}$$

The suffixes of R denote the flow components used in Figure 5.6.

As described in Section 5.4, the contraction and expansion losses are due to the separation effects and they are mainly affected by the ratio of flow cross section area before and after the contraction or expansion. However, both rotor-stator gap and rotor ducts are sharing the inlet and outlet chambers. Taking the entire cross section area of the inlet and outlet chambers will overestimate the relevant losses. This is solved based on the hypothesis that the area term before or after the contraction or expansion is taken to be a proportion of the geometric area before or after the contraction or expansion, with the ratio being taken from the split in fluid down the rotor-stator gap and rotor ducts as shown by the dashed-line in Figure 5.7.

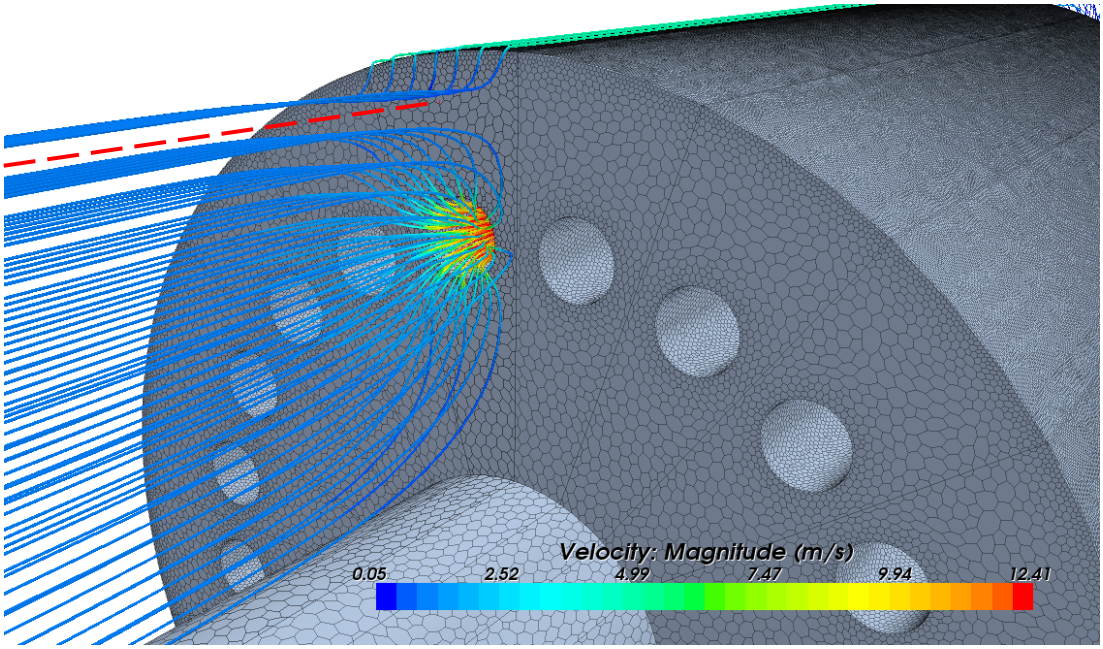

Figure 5.7: Split in air down the rotor-stator gap and rotor ducts for stationary condition using CFD

The equation (5.25) is solved using the Newton-Raphson method in PORTUNUS. For calculating the flow resistance and Jacobian matrices, the coefficients for stationary loss presented in Section 5.4 are used. In the Jacobian matrix, there are only three elements, in which the pressure loss coefficients are dependent on the flow rates in the rotor-stator gap and rotor ducts. The derivative of all the other elements is zero as their loss coefficient is constant. Thus, the Jacobian matrix becomes:

$$J = \begin{bmatrix} 0 & 0 & 0 \\ 0 & \dfrac{\partial(R_2 + R_3 + R_4)|Q_{airgap}|}{\partial Q_{airgap}} & -\dfrac{\partial(R_5 + R_6 + R_7)|Q_{ducts}|}{\partial Q_{ducts}} \\ 0 & 0 & \dfrac{\partial(R_5 + R_6 + R_7)|Q_{ducts}|}{\partial Q_{ducts}} \end{bmatrix} \quad (5.26)$$

The dimensions of the machine can be found in Appendix E, but the passages in the stator are not modelled to simplify the parallel flow problem. Both CFD and analytical flow models assume the surface condition of the flow passages is smooth. The comparisons of system pressure drop and flow distribution are shown in Figure 5.8 and Figure 5.9 respectively. The predicted pressure drop and flow distribution using the analytical flow model agrees with the simulated results obtained using CFD.

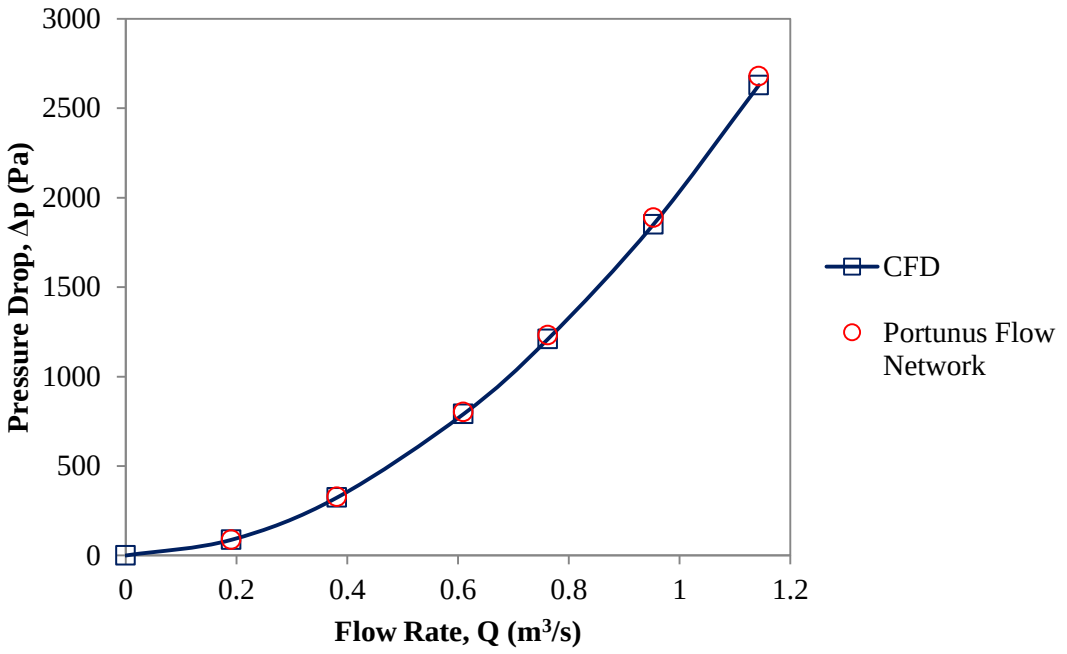

Figure 5.8: The variation of system pressure drop with inlet flow rate for the adapted throughflow ventilated system

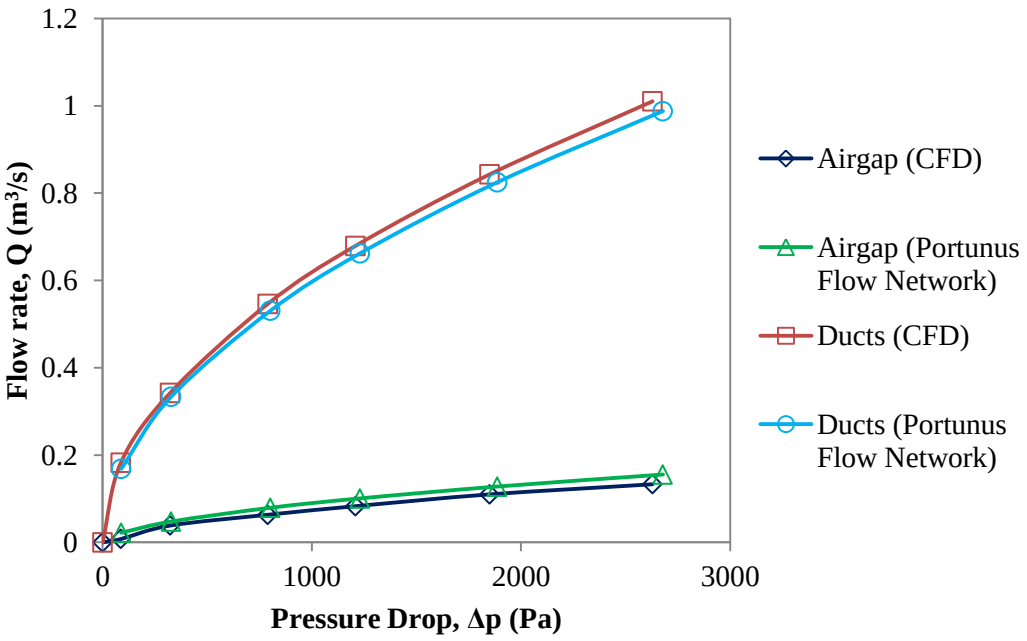

Figure 5.9: The flow distribution between rotor-stator gap and rotor ducts

5.7 Chapter Summary

The limitations of the flow network analysis are addressed. However, the applications of flow network analysis method in a liquid-cooled heat sink and a throughflow ventilated induction machine have demonstrated that the Flow Library developed in PORTUNUS is capable of modelling complex flow problem. As a result, additional flow components based on the correlations of loss coefficient that accounting for rotational pressure losses in electrical machines will be included in the Flow Library. The correlations obtained using the CFD method will be tuned and modified after the validation with an experimental apparatus specially built for the investigation of rotational pressure losses in throughflow ventilated electrical machines in Chapter 7. For rotating conditions, the comparison between the experimental results and the values predicted using equivalent flow models will be presented in Chapter 8.

6 CFD Modelling of Flow Resistances in Rotor-Stator Gap and Rotor Ducts

6.1 Introduction

In Chapter 4, the impact of ventilation on the temperature rise of a throughflow ventilated machine is presented. CFD method is a very useful tool to investigate complex fluid flow problems, especially those problems with flow paths that are difficult to get access for accurate measurement. The existing literature describes that the effects of rotation can increase the pressure loss of flow passing through the ventilation paths, but understanding fluid flow phenomena under rotating effects and suitable correlations that can be applied for electrical machines accounting for the coefficient of pressure loss caused by the rotation are very limited. Therefore, in this chapter, CFD is used to investigate the effects of rotation on the flow passing through the ventilation paths and to characterise the rotational pressure loss. Heat transfer is not modelled in this chapter because convection heat transfer is a function of fluid mechanics.

6.2 Flow Paths of Throughflow Ventilated Machines

Machine topologies can be mainly categorised into radial flux machine and axial flux machine. The radial flux machine is the most common machine topology used in industrial application. A better understanding of flow phenomena will significantly benefit the thermal management of radial flux machines because they are limited by the operating temperature limits. Therefore, the effects of rotation are investigated based upon the topology of radial flux machine.

For radial flux machines, the rotor-stator gap is an inevitable flow path of a throughflow ventilated machine. As the rotor-stator gap is small, this is not favourable for cooling because it considerably limits the amount of cooling medium passing through. Consequently, in order to enhance the cooling, additional pathways are commonly created inside the machine. They can be located at the rotor, stator or both. As the flow phenomenon in stationary passage has been intensively studied and the pressure loss for stationary case can be determined using normal stationary

correlations, the rotor-stator gap and cooling passages in the rotor are the focuses which are mainly modelled using the CFD method because of the following reasons:

- The cross-sectional area of rotor-stator gap and passages in the rotor are relatively small. Due to the conservation of mass, the flow velocity in these passages is much higher than other sections in the throughflow ventilated machines. These passages contribute to the major pressure loss in the system. This will be demonstrated empirically in Chapter 8.
- The rotor-stator gap and passages in rotor are mainly subjected to the rotating effects.
- The electrical losses convert into heat which needed to be removed. The active parts of electrical machines are located mostly at rotor and stator.

6.3 Pressure Losses in Rotor-Stator Gap and Rotor Ducts

The pressure loss of throughflow ventilated machines can be split into stationary and rotational pressure losses. Different forms of stationary pressure loss have been described in Section 5.4. It has been explained in the preceding section that rotation causes the fluid flow passing the rotor-stator gap and rotor ducts to suffer additional pressure loss.

Rotational pressure loss that arises from this flow problem is assumed to be in the form of additional friction loss due to rotation, shock loss and combining flow loss.

With rotation, the characteristics of fluid in the rotor-stator gap change and the flow is in helical form, Kuzay and Scott [1977]. The flow helix is strongly affected by the rotor speed and flow rate passing the rotor-stator gap. As the fluid friction is associated with shear stresses developed between layers within the fluid that are moving relative to each other, the formulas of friction factor for stationary case cannot be applied for rotating case. However, the friction factor of air flow passing through an annular gap with an inner cylinder rotating for turbulent flow can be estimated using the following correction factor proposed by Yamada [1962]:

$$C = \frac{f_r}{f_0} = \left[1 + \left(\frac{7}{8}\right)^2 \left(\frac{Re_\omega}{2Re}\right)^2\right]^{0.38} \tag{6.1}$$

where f_r is the friction factor for rotation and f_0 is the friction factor for stationary.

The correction factor was used to multiply with stationary friction factor in equation (5.14) for friction factor that accounts for the influence of rotation.

For circular cross-sectional passages in the rotor, rotation induces secondary flow at the entrance region of the ducts due to the Coriolis effects and increases the flow resistance in the ducts rotating about a parallel axis, according to Johnson and Morris [1992]. The increases in the friction factor of adiabatic flow under the effects of rotation can be estimated using the empirical correlations proposed by the authors. As the rotation increases the flow resistance above the normal stationary condition, the correction factors were obtained by getting the ratio of rotating case to stationary case for the given duct geometries. In order to take into account the influence of rotation, the stationary friction factor is multiplied by the rotating correction factor. These correlations do not apply to zero rotational speed and thus the correction factor at rotor speed = 0 rpm becomes unity.

For L/d = 10.6 and laminar-like flow (i.e. 900 < Re < 9880),

$$C = \frac{f_r}{f_0} = 0.503 J^{0.16} Re^{-0.03} \tag{6.2}$$

For L/d = 10.6 and turbulent-like flow (i.e. $Re \geq 9880$),

$$C = \frac{f_r}{f_0} = 0.842 J^{0.023} Re^{0.002} \tag{6.3}$$

For L/d = 31.8 and laminar-like flow (i.e. 900 < Re < 7000),

$$C = \frac{f_r}{f_0} = 0.312 J^{0.21} Re^{0.01} \tag{6.4}$$

For L/d = 31.8 and turbulent-like flow (i.e. $Re \geq 7000$),

$$C = \frac{f_r}{f_0} = 0.783 J^{0.058} Re^{-0.01} \tag{6.5}$$

where L/d is the duct length-to-diameter ratio. J is the rotational Reynolds number to account the Coriolis effects and it is defined as:

$$J = \frac{\omega_m d^2}{\nu} \tag{6.6}$$

The relative location of a duct to the axis of rotation (i.e. eccentricity) has been verified theoretically and experimentally that it has no influence on the friction factor. Although the correction factors are limited to specific *L/d* ratios, the difference of the values obtained using the given *L/d* ratios is not significant. These correction factors are more applicable for smoothed inlet configuration, such as bell-mount entry, but they were applied for the rotor ducts because the information regarding the unsmoothed inlet configuration is limited. As the rotor ducts are not heated, the additional friction loss due to centrifugal buoyancy caused by density difference in a centrifugal field is not considered in the present study. The influence of rotation on the diabatic flow in a circular duct rotating about a parallel axis can be found in Mori and Nakayama [1967] and Nakayama [1968].

For rotating duct, the shock loss was first introduced by Webb [1964]. When compared to stationary condition, the fluid suffers additional pressure drop because of the abrupt change of flow direction of the fluid flow entering into the passages in rotor due to rotation. The correlation proposed by the author is not employed in the present study because inappropriate assumptions were made in the investigation as mentioned in Chapter 2. However, the correlation for shock loss coefficient will be corrected using CFD method.

The flow passing through the rotor ducts is restricted to rotate about the axis of rotor. When the flow exits from the confinement of rotor ducts, it will follow the path tangential to the pitch circle of the rotor ducts due to the centrifugal effect. As shown in Figure 6.1, the centrifugal effect causes the flow to deflect radially outwards and it interferes with the flow leaving right from the rotor-stator gap. Thus, these two streams from the rotor ducts and rotor-stator gap "naturally" combine together downstream. This situation is quite similar to the "combining flow" at a junction of pipe network, but the junction combining flow is restricted by pipeline. The combining flow is accompanied by non-recoverable pressure loss arisen from flow separation and subsequent turbulent mixing, namely "combining flow loss". The combining flow loss at the rotor-stator gap is first revealed in the present study with

the aid of the CFD. The combining flow increases the resistance of flow passing through the rotor-stator gap. In this chapter, CFD method is used to investigate the characteristic of combining flow loss in the later section.

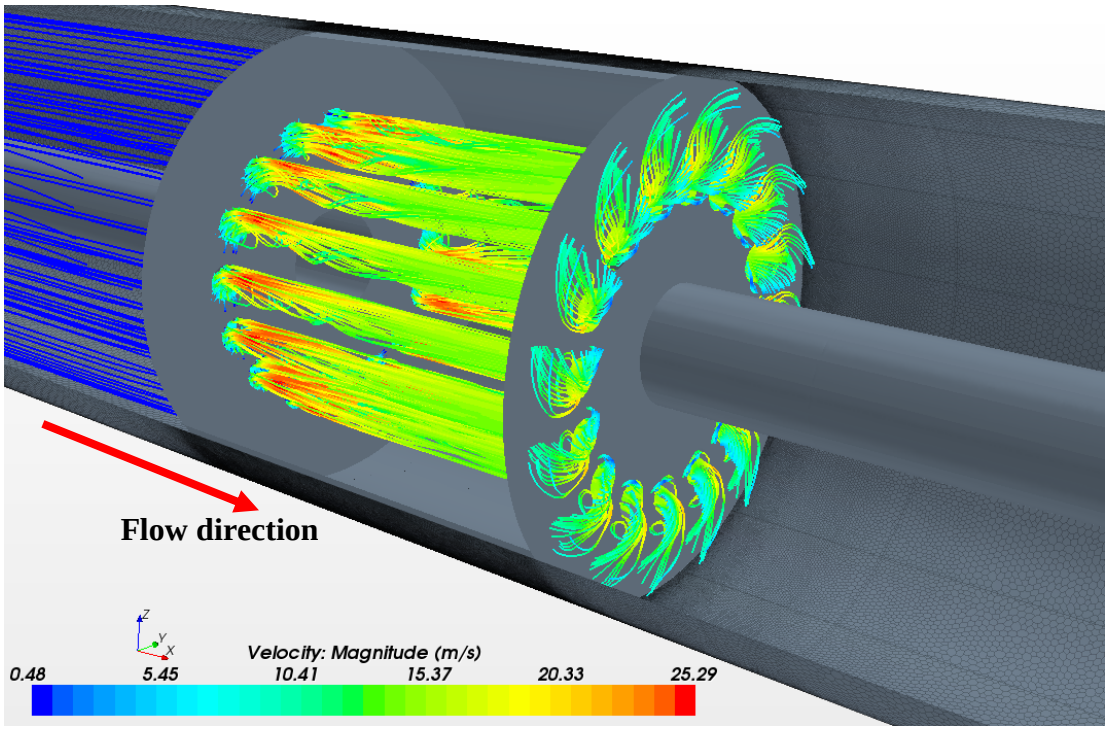

Figure 6.1: Streamlines (velocity observed in a rotating reference frame) of air passing through the ducts in rotating rotor from left to right obtained using CFD method

6.4 Air Flow Tests

Throughflow ventilated machines with such flow paths (e.g. rotor-stator gap and axial ducts in rotor) can be found in Sun et al. [2013] for a dual mechanical port (DMP) machine, Al'Akayshee and Williams [2003] and Onuki et al. [1999] for squirrel-cage induction machines and Webb [1964] for a geometric mock-up throughflow ventilated machine to investigate the shock loss for rotating ducts.

For representatives of throughflow ventilated machine, Al'Akayshee and Williams [2003] and Webb [1964] machines were selected for the investigation of the shock loss and combining flow loss because the rotor geometries are given in the literature. The dimensions of Al'Akayshee and Williams [2003] machine can be found in Appendix E. In addition, the machine geometry of the experimental test rig in

Chapter 8 was also used for CFD modelling, i.e. Chong [2014]. Therefore, the CFD models can be validated by experimental results.

The standard test procedure was carried out on the machine geometries shown in Table 6-1. Figure 6.2 illustrates the schematic diagram of rotor.

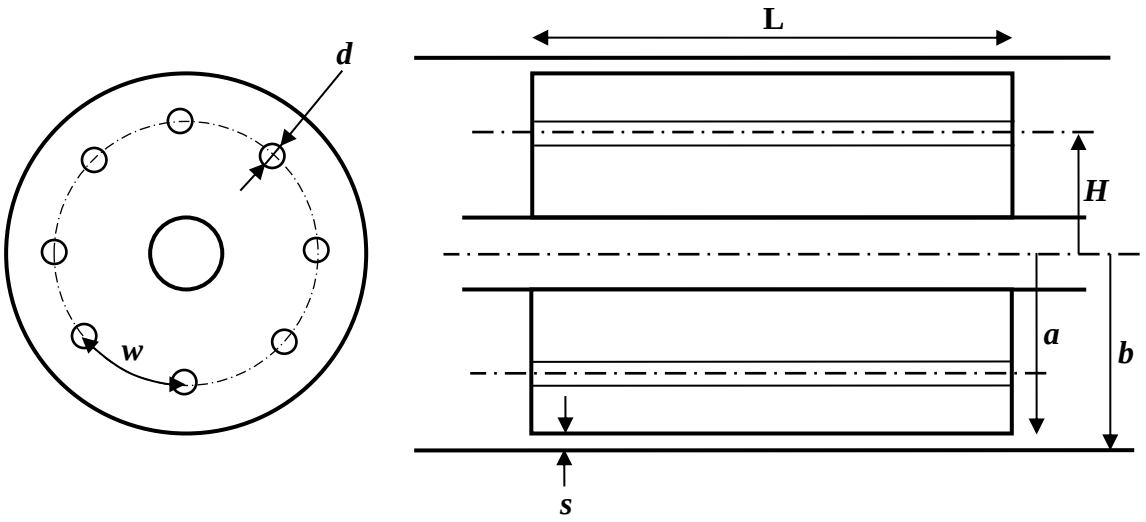

Figure 6.2: Sketch of rotor showing nomenclature

d – Duct diameter,

H – Pitch-circular radius of rotor ducts,

a – Rotor outer radius,

L – Length of airgap and rotor ducts,

n – Number of rotor duct,

s – Gap size,

H/a – Ratio of duct pitch-circular radius to rotor radius,

H/d – Eccentricity ratio,

L/d – Length-to-diameter ratio,

w/d – Duct spacing ratio ($2\pi H/nd$),

s/a – Gap ratio,

L/2s – Length to gap size ratio (hydraulic diameter of rotor-stator gap = 2*s*)

Test	*Dimension of Flow Paths*						*Rotor-Stator Gap*		*Rotor Ducts*				*Machine*
	d (mm)	*n*	*H (mm)*	*a (mm)*	*L (mm)*	*s (mm)*	*s/a ratio*	*L/2s ratio*	*H/a ratio*	*H/d ratio*	*w/d ratio*	*L/d ratio*	
A	12.7	16	76.2	127	228.6	3[i]	0.0236	38.1	0.60	6.00	2.36	18.0	Webb [1964]
B	19.05	16	76.2	127	228.6	3[i]	0.0236	38.1	0.60	4.00	1.57	12.0	Webb [1964]
C	35	20	180	254.8	614	10[ii]	0.0392	30.7	0.71	5.14	1.62	17.5	Al'Akayshee and Williams [2003]
D	35	20	180	254.8	614	5[ii]	0.0196	61.4	0.71	5.14	1.62	17.5	Al'Akayshee and Williams [2003]
E	35	20	180	254.8	614	3[ii]	0.0118	102.3	0.71	5.14	1.62	17.5	Al'Akayshee and Williams [2003]
F	12	6	56.25	75	150	4	0.0533	18.8	0.75	4.69	4.91	12.5	Chong [2014]
G	12	6	37.5	75	150	4	0.0533	18.8	0.50	3.13	3.27	12.5	Chong [2014]
H	-	-	-	75	150	2	0.0266	37.5	-	-	-	-	-

Table 6-1: Machine geometries of air flow tests

[i] Dimension not provided in the literature
[ii] Dimensions modified from the literature

The rotor ducts are in cyclic symmetry. It is important to note that the rotor-stator gap was treated as plain annular gap between concentric cylinders and in order to limit the scope of this investigation to a manageable size the slots were not modelled.

As the annular gap size of Webb [1964] machine is not provided in the literature, it was assumed to be 3 mm. Due to limitations of computational resource, an annular gap of 1.6 mm was not possible to model because the gap is relatively too small compared with the rotor radius. Thus, the annular gap size of Al'Akayshee and Williams [2003] machine was increased to 3 mm, 5 mm and 10 mm. Although the exact gap size of that machine was not modelled, the air flow tests in Table 6-1 with a wide range of gap ratio would sufficient to provide insight into the impact of annular gap size on rotational pressure loss.

6.5 Dimensional Analysis

Due to the complexity of the flow passing through a rotor-stator system, dimensional analysis is performed to identify the factors involved in the fluid flow problem. Dimensional analysis is used to establish the functional relationship between geometric dimensions of flow paths, operating condition (e.g. rotor speed) and flow condition on the rotational pressure loss coefficient (K_r), i.e. shock loss and combining flow loss. According to equation (5.4), the pressure loss coefficient is commonly non-dimensionlized by use of the flow kinetic energy. The functional equation of general coefficient of rotational pressure loss can be written as:

$$K_r = f\left(\frac{L}{D_h}, \frac{e}{D_h}, \frac{s}{a}, \frac{H}{a}, \frac{H}{d}, \frac{w}{d}, \frac{V_T}{U}, Re_\omega, Ta, J, Re, Pr\right) \tag{6.7}$$

To satisfy the principle of dimensional homogeneity, all the terms of equation (6.7) are defined in dimensionless form. The parameters in Table 6-1 are used to compute the dimensionless parameters. This allows the investigations in the present study to be shared through the rule of similarity – geometric similarity and dynamic similarity. According to White [1986],

> "Flow conditions for a model test are completely similar if all relevant dimensionless parameters have the same corresponding values for model and prototype."

D_h is hydraulic diameter. The hydraulic diameter of a rotor-stator gap and rotor duct is $2s$ and d respectively. As the length of the rotor-stator gap and passages in rotor are rather short, the length-to-diameter ratio (L/D_h) is a measure of the equivalent length of a flow path in terms of its hydraulic diameter. It is normally used to account for the developing flow. The surface roughness of the flow paths is also taken into account by the relative roughness (e/D_h). Both L/D_h and e/D_h are assumed to be only important for friction loss. Therefore, they can be discarded from equation (6.7).

The geometric effect of rotor-stator gap is specified by s/a. The gap ratio (s/a) is used to measure the annular gap size relative to the inner cylinder radius. The geometric effect of rotor ducts rotating about a parallel axis is specified by ratios of H/a, H/d and w/d. H is the pitch-circular radius of the rotor ducts, thus H/a is a measure to indicate the proximity of the ducts to rotor periphery and eccentricity parameter (H/d) is a ratio of the pitch-circular radius of the ducts to the duct diameter. Duct spacing ratio (w/d) is a ratio of the spacing between two adjacent rotor ducts to the duct diameter.

Besides the dimensionless geometric parameters, other dimensionless groups in fluid mechanics described in Chapter 2 such as rotation ratio (V_T/U), rotational Reynolds number for annular gap (Re_ω), Taylor number (Ta), rotational Reynolds number for rotating duct (J), axial Reynolds number (Re) and Prandtl number (Pr) are also included in the functional equation. In order to reduce the number of terms in equation (6.7), it is necessary to discard those dimensionless groups which are irrelevant and unimportant for the present study.

As the review of cooling methods for electrical machines reveals that the cooling medium used for rotor-stator gap and passages in rotor is mostly air, hence the Prandtl number can be removed from the functional equation. Both rotational Reynolds number and axial Reynolds number can be combined as follows:

$$\frac{Re_\omega}{Re} = \frac{\frac{\rho \omega_m a D_h}{\mu}}{\frac{\rho U D_h}{\mu}} = \frac{V_T}{U} \tag{6.8}$$

By getting the ratio of the rotational Reynolds number to the axial Reynolds number, equation (6.8) shows that the combination results in a dimensionless parameter,

which is exactly the same as the rotation ratio (V_T/U). In the review of existing literature, the rotation ratio (V_T/U) was already suggested by Childs and Turner [1994], Kuzay and Scott [1977], Le Feuvre [1968], Webb [1964] and Taylor [1960] to account for the effects of rotation on heat transfer and pressure drop for mixed axial and rotational flow. Thus, the equation (6.7) is reduced to:

$$K_r = f\left(\frac{s}{a}, \frac{H}{a}, \frac{H}{d}, \frac{w}{d}, \frac{V_T}{U}, Ta, J\right) \tag{6.9}$$

The Taylor number (Ta) is mainly used to measure the stability of rotational flow between concentric cylinders and the rotational Reynolds number (J) is used to account for the Coriolis-induced secondary flow in the entrance region of a circular duct as suggested by Johnson and Morris [1992], but they do not account for the influence of axial flow on them. Due to this reason, the rotation ratio is the most suitable parameter to characterise the rotating effect with superimposed axial flow. Hence, the dimensionless groups, Ta and J are also discarded. Thus, the equation (6.7) is further simplified to:

$$K_r = f\left(\frac{s}{a}, \frac{H}{a}, \frac{H}{d}, \frac{w}{d}, \frac{V_T}{U}\right) \tag{6.10}$$

After discarding those irrelevant dimensionless parameters for the present study, the number of dimensionless parameter is reduced from twelve to five. This considerably simplifies the process of investigation of the shock loss and combining flow loss.

6.6 Computational Fluids Dynamics

It has been well-known that CFD method is a very useful tool to investigate complex fluid flow problems, especially those problem with flow paths that are difficult to get access for accurate measurement. The CFD software programme STAR-CCM+ was used in the present study to investigate the effects of rotation on the flow passing through the rotor-stator gap and to characterize the rotational pressure loss.

6.6.1 Model Definition and Mesh

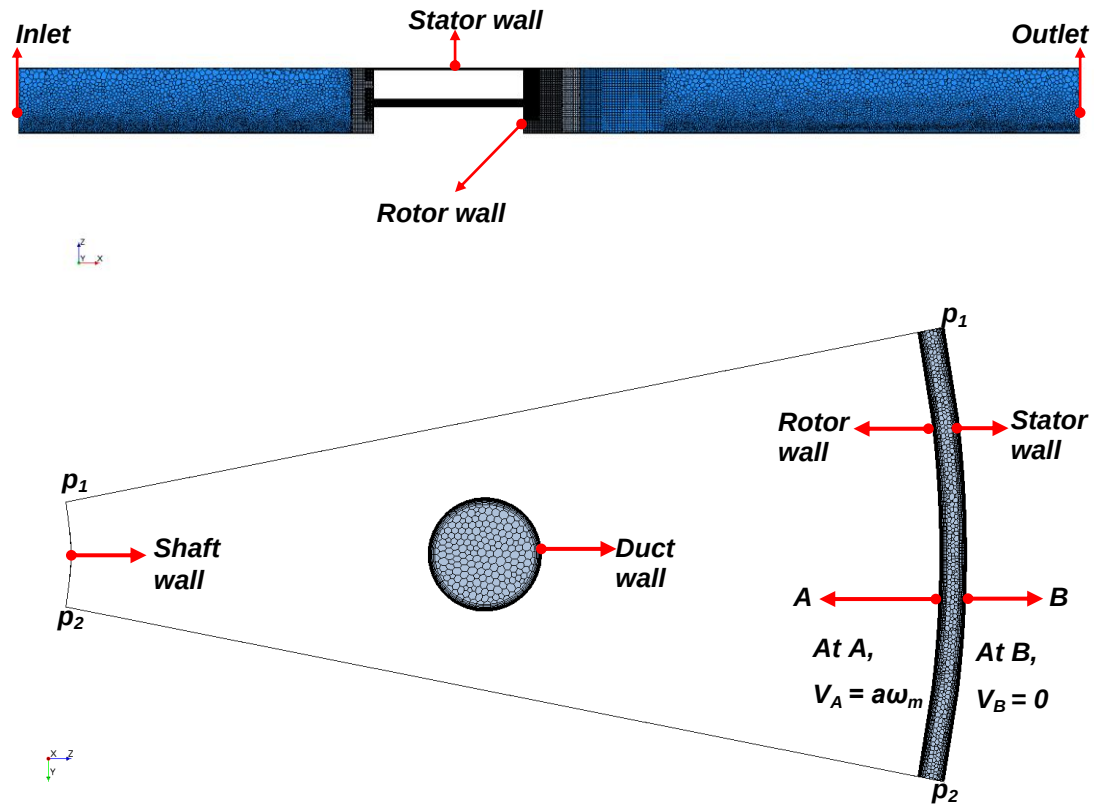

Figure 6.3: Mesh of CFD domain (Test A). Side view (top) and internal view (bottom) of the plane cutting half way through the rotor-stator gap and rotor duct

Since the rotor ducts are spaced regularly and the rotor-stator gap is formed between the rotor and stator, it is cyclic symmetry so only a periodic segment was modelled in three dimensions for simulating flow. For examples, only one-twentieth segment was modelled for Test A and B, one-sixteenth segment for Test C, D and E, one-sixth for Test F and G, etc. As shown in Figure 6.3, periodic planes of the modelled segment are represented by p_1-p_1 and p_2-p_2 respectively. The CFD domain is separated into stationary domain (blue) and rotational domain (grey). Conformal mesh interfaces were created between stationary and rotational domains.

Polyhedral and prism layer meshers were employed. For Test A, within the rotor-stator gap, the minimum mesh size was set to be approximately 3.44×10^{-3} mm close to the walls, which corresponds to 1/440 of the fluid boundary layer (i.e. half of the gap size). The maximum mesh size of the Test A was set to 7.5 mm to save the computational cost. The total number of computational cells of the Test A is about 4

million. The meshes of the other models have similar density. In order to ensure the CFD model for each test provides mesh independent solution, mesh refinement study has been performed in Appendix F.

6.6.2 Turbulent Flow and Energy Modelling

As steady state operations of the machines were investigated, steady state models were chosen for CFD simulation. The present study had made use of a rotating reference frame to simulate the relative motion of the rotor and stator for time-averaged steady-state solutions. The shear stress transport (SST) k-ω (Menter) turbulence model was used to provide closure of the Reynolds-Averaged Navier-Stokes (RANS) equations in the present study. The effect of gravity is ignored. As the Mach number of the cooling media used in most conventional electrical machines is less than 0.3, the air was assumed to be incompressible with constant density (heat transfer is not included) and constant viscosity, thermal conductivity and specific heat. The governing equations of the flow problem are the same with those of the Chapter 4, but the energy equations for solid and fluid regions are not included.

6.6.3 Boundary Conditions

The governing equations are subjected to the following boundary conditions:

At the inlet, a range of flow velocity was set. As the motion of the cooling medium of a fan-cooled system is induced by the fan pressure, therefore it is important to note that the pressure drop of the simulated flow rate was within the pressure range of commercially available fans. Apart from setting the inlet flow rate to predict the pressure drop as illustrated in Figure 6.4, the flow rates passing through the CFD models were also simulated by setting the pressure at the inlet as shown in Figure 6.16 and Figure 6.17. At the outlet, the static pressure, p = 0 Pa. At both the inlet and outlet, the turbulent kinetic energy and specific dissipation rate were set at default to be 0.001 Jkg^{-1} and 1×10^{-4} s^{-1} respectively.

Both rotor and stator surfaces are smooth and no-slip. The local speed of the rotor surface is equal to $a\omega_m$. For incompressible flow, the peripheral speeds of rotor were set below Ma < 0.3 (approximately 100 m/s). Hence, the maximum rotor speed of the

CFD models are tabulated in Table 6-2 and they are determined by the rotor outer radius.

Test	RPM_{max}
A and B	7500 rpm
C to E	3750 rpm
F to H	12700 rpm

Table 6-2: Maximum rotor speed of CFD models

In the rotational domain, additional force terms are added in the momentum equation due to the acting of the Coriolis force and centrifugal force. This is similar to the Section 4.4.3 in Chapter 4.

6.6.4 Wall Treatment

The wall treatment method used in Chapter 4 was also used for the present study.

6.6.5 Solution strategy

The governing equations were numerically discretized using a finite volume method to a system of linear algebraic equations. These were solved simultaneously based on the conservation of mass, momentum and turbulence parameters using the second-order upwind discretization scheme.

6.7 Shock Loss

The total amount of rotational pressure loss was determined from the difference of rotating model and stationary model by assuming the stationary loss preserves in the same amount in the rotating condition.

$$\Delta p = \Delta p_r + \Delta p_s \tag{6.11}$$

where Δp_r is the rotational pressure loss and Δp_s is the stationary pressure loss. For each CFD model, the relationship between the stationary pressure drop and inlet flow rate was first obtained over a range of flow rate. Therefore, for a given flow rate, the

rotational pressure loss of the CFD models can be then determined, which is the excess pressure drop.

In fluid mechanics, the pressure loss between the junctions is the same for each flow path, no matter which flow path the flow is taken.

For CFD models with only an annular gap and CFD models with rotor ducts, the rotational pressure loss of these flow paths is assumed to be comprised of the additional friction loss due to rotation and shock loss. As the additional friction loss can be estimated using the published correlations as described in Section 6.3, the shock loss can be then quantified. The coefficient of shock loss was obtained by non-dimensionlizing the corresponding rotational pressure loss with the kinetic energy of air passing through the flow paths.

$$\Delta p_r = \left[\left(K_{f_r} - K_{f_0}\right) + K_{shock}\right] \times \frac{1}{2}\rho U^2 \tag{6.12}$$

$$K_{shock} = \frac{2\Delta p_r}{\rho U^2} - \left(K_{f_r} - K_{f_0}\right) \tag{6.13}$$

where K_{f_0} is the friction loss coefficient for stationary condition, K_{f_r} is the friction loss coefficient with rotation and U is the mean flow velocity in the flow paths.

6.7.1 Rotor Ducts

For stationary pressure loss of flow passing through a rotor-stator system, the comparison between CFD and analytical methods can be found in Figure 5.8, i.e. Test E. The CFD results showed good agreement with the analytical results. CFD method not only estimated the pressure loss accurately, but also able to predict the flow distribution between the rotor-stator gap and rotor ducts as shown in Figure 5.9.

This section focuses on the shock loss of rotor ducts. Hence, the dimensionless geometric parameter, gap ratio (i.e. s/a) that relate to rotor-stator gap can be discarded from equation (6.10). For a rotor duct, the functional equation of shock loss coefficient can be expressed as:

$$K_{Shock} = f\left(\frac{H}{a}, \frac{H}{d}, \frac{w}{d}, \frac{V_T}{U}\right) \tag{6.14}$$

For the rotation ratio, V_T is the tangential speed of the rotor ducts rotating about a parallel axis and U is the mean axial flow velocity in the rotor ducts. As mentioned earlier, the rotating effects cause additional pressure loss to a ventilation system. This can be demonstrated using CFD method.

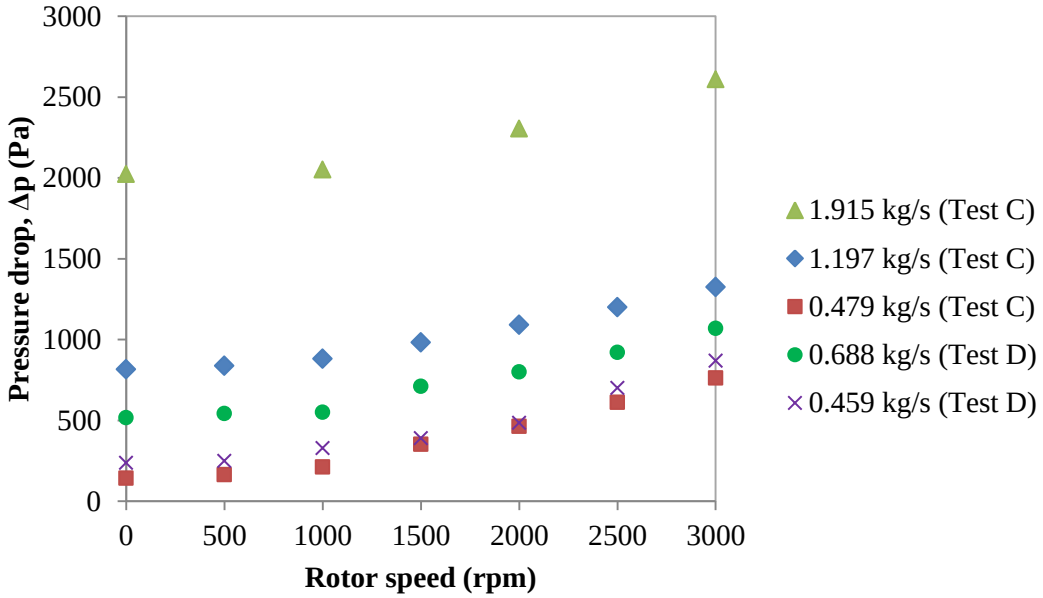

Figure 6.4: Pressure requirement of Test C and Test D over a range of rotor speed

As shown in Figure 6.4, the pressure loss from the model inlet to the outlet for a given flow rate increases with the increase in rotor speed. Thus, the CFD results confirm the existence of rotational pressure loss. In order to ensure the axial Reynolds number has no significant impact on the shock loss coefficient of rotor ducts, a range of flow rate passing through the rotor-stator system was simulated for each CFD model. In general, the motion of the cooling medium of a fan-cooled system is induced by the fan pressure. Therefore, it is important to note that the pressure drop of the simulated flow rate was within the pressure range of commercially available fans.

6.7.1.1 Flow field in rotor duct

Figure 6.5 and Figure 6.6 illustrate the streamlines of air passing through a rotor duct of Test B for stationary and rotating conditions. Their difference is mainly the swirling flow at the entrance region of the rotating duct. This flow phenomenon

agrees with Johnson and Morris [1992] that this Coriolis-induced secondary flow is predominant in the duct entrance region and decay away when the flow becomes fully developed downstream. Therefore, the flow resistance of flow passing through a rotating duct is undoubtedly higher when compared to the normal stationary condition; equations (6.2) to (6.5) are used to account for this additional pressure loss.

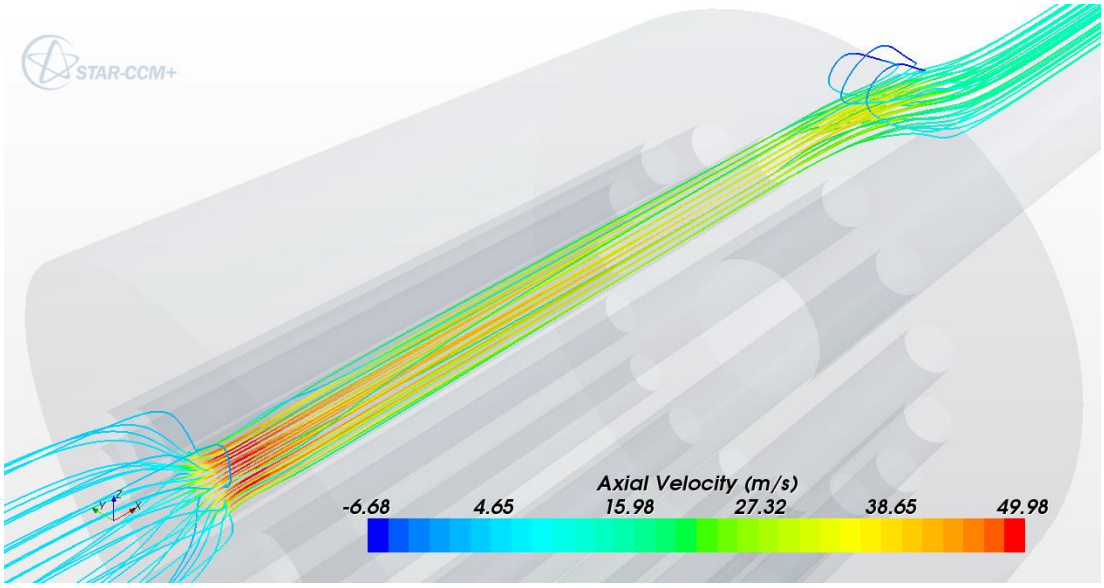

Figure 6.5: Streamlines of air passing through a rotor duct of Test B for stationary case

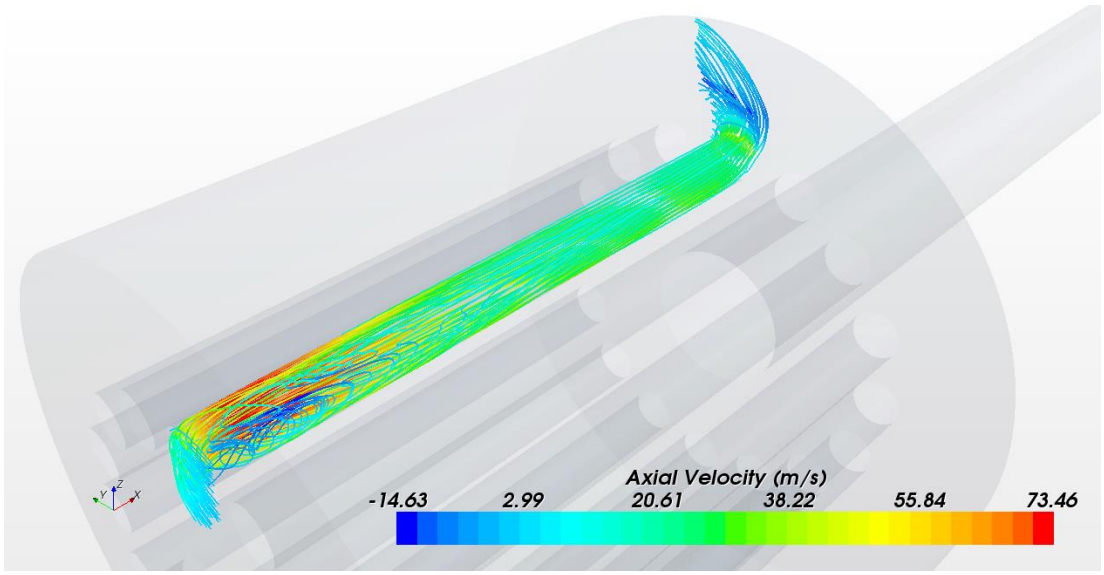

Figure 6.6: Streamlines of air in a rotor duct of Test B for rotating case (velocity observed in a rotating reference frame)

6.7.1.2 Shock loss coefficient of rotor ducts

The mean flow velocity passing the rotor ducts can easily obtained from the CFD models by creating a constrained plane which is perpendicular to the duct axis. Then, the flow kinetic energy and axial Reynolds number can be computed. The rotational pressure loss is the additional pressure drop that requires when compared to the stationary condition. As the rotor speed is known, the shock loss coefficient of the rotor ducts can be calculated using equation (6.13).

Figure 6.7 shows the variation of shock loss coefficient of the rotor ducts with the rotation ratio for Test A and Test B. The shock loss coefficients of Test A and Test B consistently follow the same trend. As the machine geometries of Test A and Test B are exactly the same except the duct size (d), the CFD results demonstrate that the shock loss coefficient of rotor ducts is not affected by the eccentricity parameter (H/d) and the duct spacing ratio (w/d).

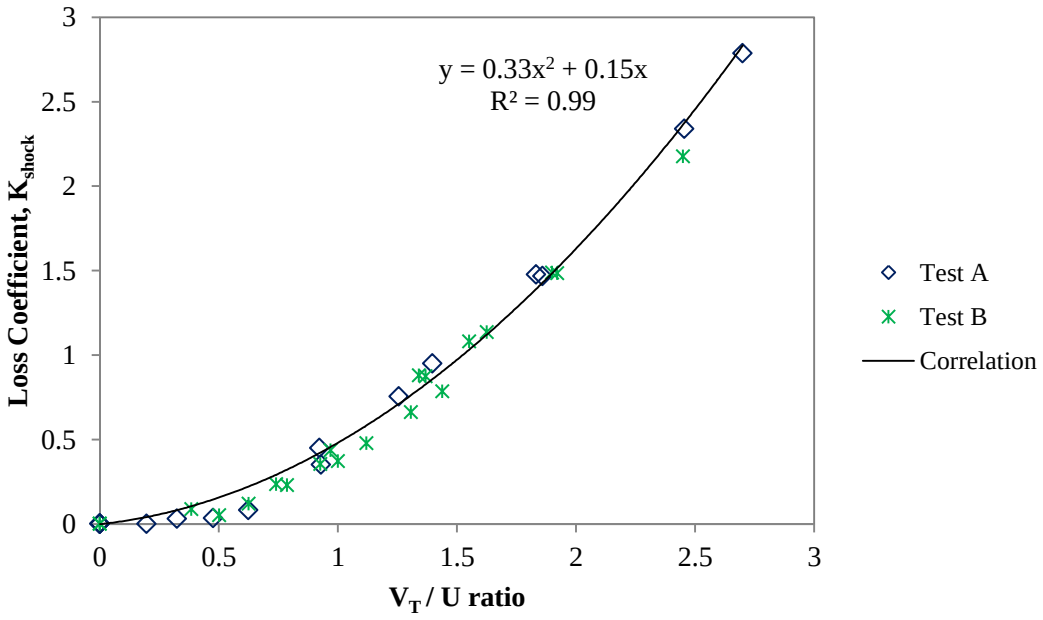

Figure 6.7: The variation of shock loss coefficient of rotor ducts with rotation ratio for Test A and Test B

In order to investigate the influence of rotor-stator gap size on the shock loss of rotor ducts, CFD method was performed on the machine geometries of different gap size. The gap ratios of Test C and Test D are 0.0392 and 0.0196 respectively. The duct

size remained the same in the CFD models. As shown in Figure 6.8, the rotor-stator gap size has no influence on the shock loss coefficient of rotor ducts.

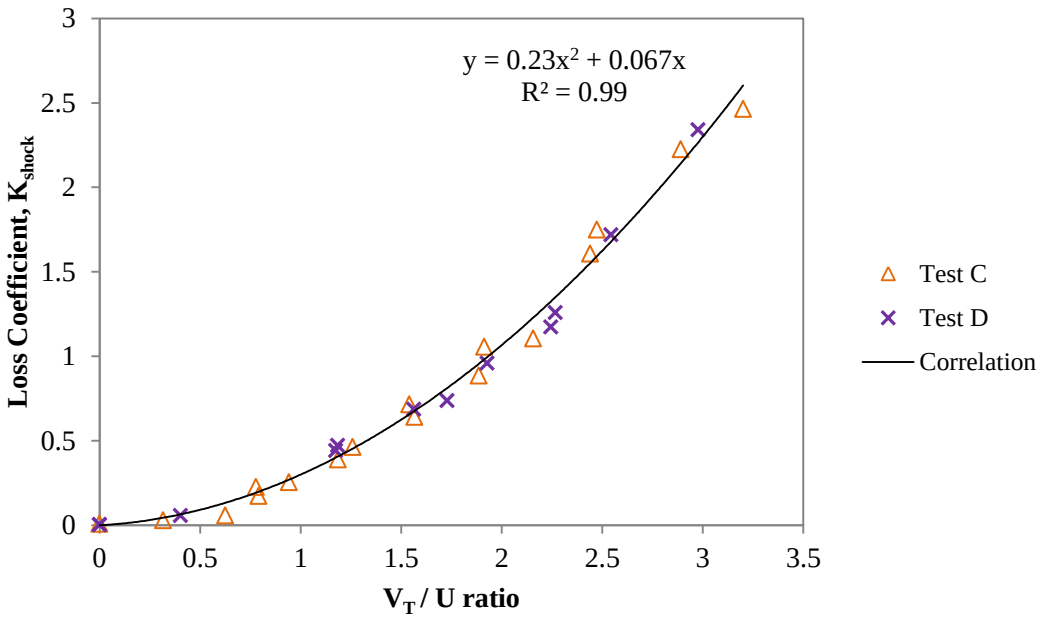

Figure 6.8: The variation of shock loss coefficient of rotor ducts with rotation ratio for Test C and Test D

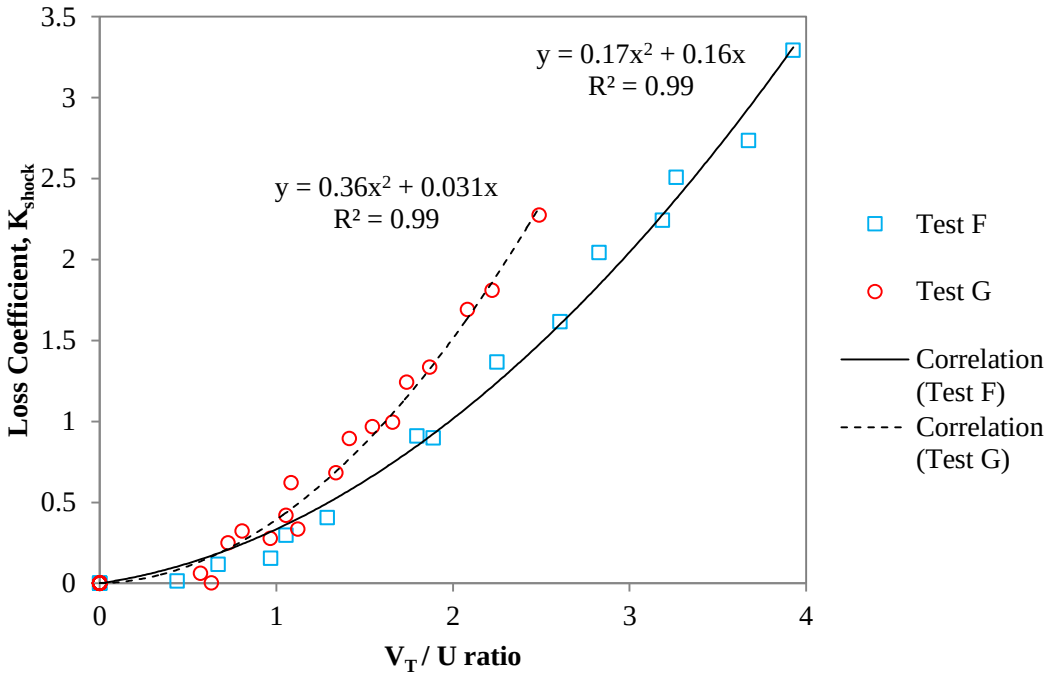

Figure 6.9: The variation of shock loss coefficient of rotor ducts with rotation ratio for Test F and Test G

Finally, CFD modelling was followed to the machine geometries that have different H/a ratios in order to investigate the influence of the proximity of the ducts to rotor periphery on the shock loss of rotor ducts. The H/a ratios of Test F and Test G are 0.75 and 0.5 respectively. Apparently, the CFD results demonstrate that the H/a ratio has significant influence on the shock loss coefficient of rotor ducts as illustrated in Figure 6.9. For a given rotation ratio, the shock loss coefficient of Test G is higher than Test F.

Based upon the CFD results of various machine geometries, the dimensionless geometric parameters (i.e. H/d and w/d) can be discarded from equation (6.14) and thus the functional equation of shock loss coefficient of rotor ducts can be simplified to:

$$K_{Shock} = f\left(\frac{H}{a}, \frac{V_T}{U}\right) \tag{6.15}$$

For the rotor ducts that are of the same H/a ratio, their shock loss coefficients were correlated with the rotation ratio.

For H/a = 0.5,

$$K_{Shock} = 0.36(V_T/U)^2 + 0.031(V_T/U) \tag{6.16}$$

The correlation is valid for the axial Reynolds number in the rotor ducts ranges from 4100 to 12000.

For H/a = 0.6,

$$K_{Shock} = 0.33(V_T/U)^2 + 0.15(V_T/U) \tag{6.17}$$

The correlation is valid for the axial Reynolds number in the rotor ducts ranges from 11000 to 41000.

For H/a = 0.71,

$$K_{Shock} = 0.23(V_T/U)^2 + 0.067(V_T/U) \tag{6.18}$$

The correlation is valid for the axial Reynolds number in the rotor ducts ranges from 17000 to 70000.

For H/a = 0.75,

$$K_{Shock} = 0.17(V_T/U)^2 + 0.16(V_T/U) \quad (6.19)$$

The correlation is valid for the axial Reynolds number in the rotor ducts ranges from 3500 to 10000.

The values of shock loss coefficient obtained from the above correlations were plotted against the rotation ratio in the same graph as shown in Figure 6.10. The shock loss coefficient decreases with the increase in H/a ratio. However, the values obtained from the correlations for the H/a = 0.5 and H/a = 0.6 are identical. Similar to other separation losses as described in Chapter 5, the shock loss arises from flow separation effect due to the change in flow direction. Therefore, it can be concluded that the rotor ducts in close proximity to rotor periphery give less flow separation when compared to the rotor ducts that located further apart from rotor periphery.

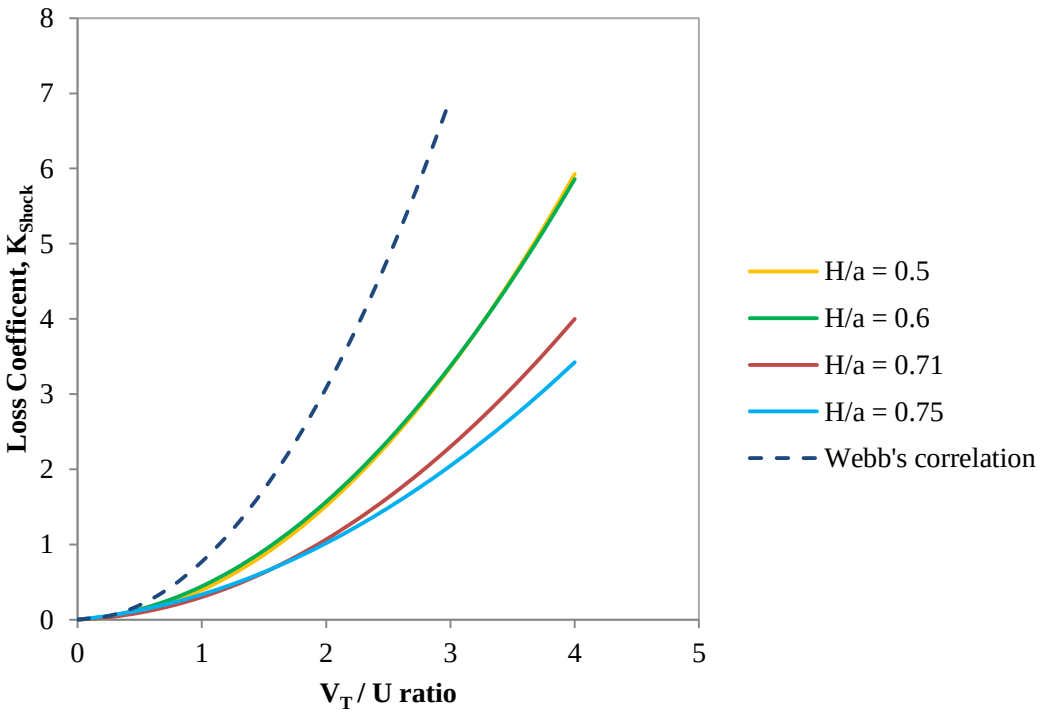

Figure 6.10: The variation of shock loss coefficient with rotation ratio for different *H/a* ratios

On the other hand, the values of shock loss coefficient obtained by the correlation proposed by Webb [1964] for H/a = 0.6 were also plotted in Figure 6.10. They are much higher than the values predicted using CFD method. The reasons of the

discrepancy are: First, the additional friction loss due to the Coriolis effects was also neglected by the author. Second, the author correlated the leakage flow passing outside the rotor with the pressure drop across the rotor by blocking the rotor ducts. With rotor duct unblocked, the leakage flow was assumed to be the same for the same pressure drop. As a result, the author likely overestimated the flow rate passing through rotor-stator gap while underestimated the flow rate passing through the rotor ducts. Thus, due to less flow kinetic energy in the rotor ducts, the shock loss coefficient was probably overestimated. The details of the flow phenomenon will be further explained in Section 6.8.

6.7.2 Rotor-stator Annular Gap

As the rotor-stator gap is formed between two concentric cylinders with inner cylinder rotating, the shock loss of the rotor-stator gap is also investigated in the present study.

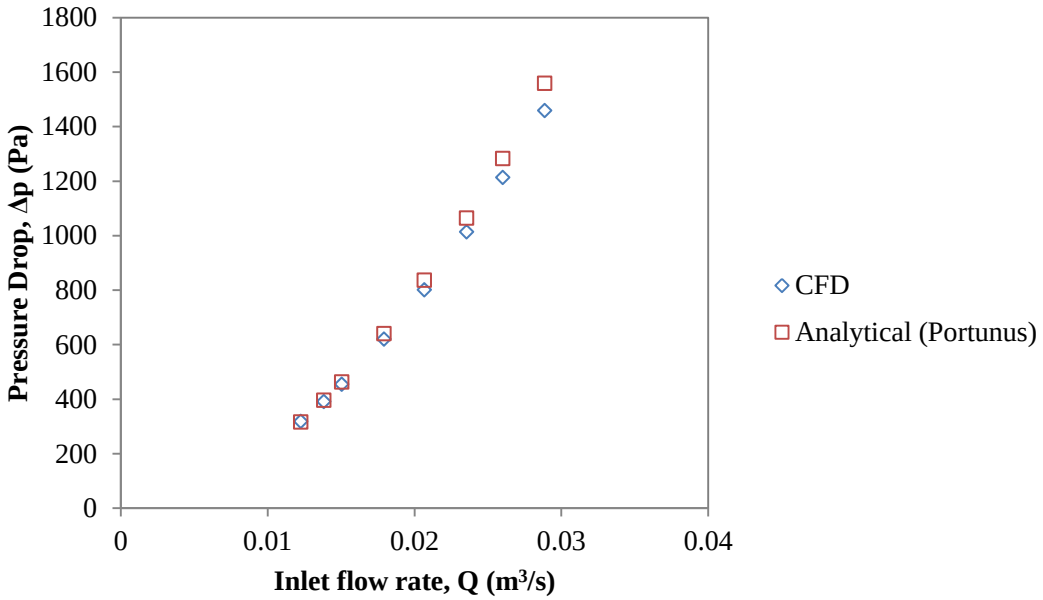

Figure 6.11: Stationary pressure drop of Test H over a range of inlet flow rate

For stationary pressure loss of flow passing through the rotor-stator annular gap, the comparison between CFD and analytical methods is shown in Figure 6.11. The analytical equations for stationary pressure drop (contraction, friction and expansion losses) used in Portunus can be found in Section 5.4. A good agreement was obtained

with the error being less than 6.5 % over the range of flow rate. The relationship between the stationary pressure drop and inlet flow rate was obtained from the CFD results. It was used to isolate the rotational pressure loss from the stationary pressure loss.

This section focuses on the shock loss of rotor-stator annular gap. Hence, those dimensionless geometric parameters (i.e. H/a, H/d and w/d) that relate to rotor ducts can be discarded from equation (6.10). Thus, the functional equation of shock loss coefficient of an annular gap becomes:

$$K_{Shock} = f\left(\frac{s}{a}, \frac{V_T}{U}\right) \tag{6.20}$$

For the rotation ratio, V_T is the peripheral speed of rotor outer surface and U is the mean axial flow velocity in the annular gap. In order to investigate the effect of gap ratio, the pressure loss of the flow passing through the annular gaps of different gap size were simulated. The machines in Table 6-1 were employed, but the rotor ducts were not modelled. The gap ratio of the machines of Test B, Test C, and Test F are 0.0236, 0.0392 and 0.0533 respectively, plus gap ratio of Test H of 0.0266.

As shown in Figure 6.12 and Figure 6.13, the CFD models show that the pressure requirement for a given flow rate increases with the increase in rotor speed. Therefore, it indicates that the resistance of flow passing through the annular gap is higher for the rotating case when compared to the stationary case. However, the influence of rotation is less marked at higher flow rate.

As the peripheral speed of rotor outer surface is limited by the rotor radius of the CFD models, the rotor speeds over 3000 rpm were also modelled in order to predict the values of shock loss coefficient for higher rotation ratio. Consequently, the obtained shock loss coefficient can be applied to those machines of larger rotor radius or higher speed based upon the rule of similarity in dimensional analysis.

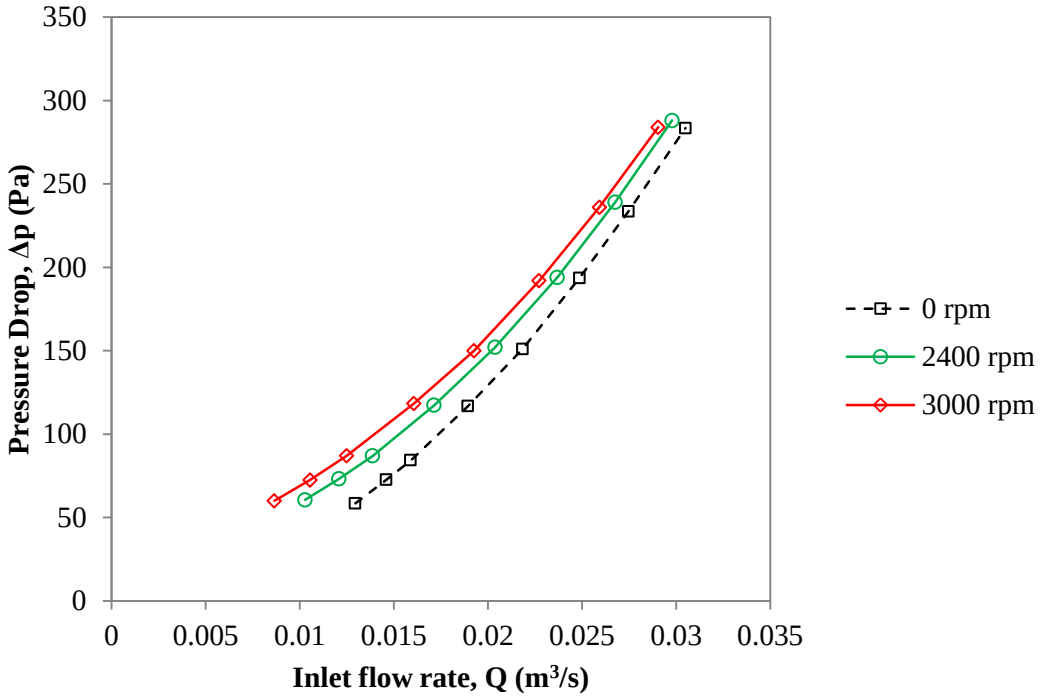

Figure 6.12: System flow resistance curves of Test F for rotor speed at 0, 2400 and 3000 rpm

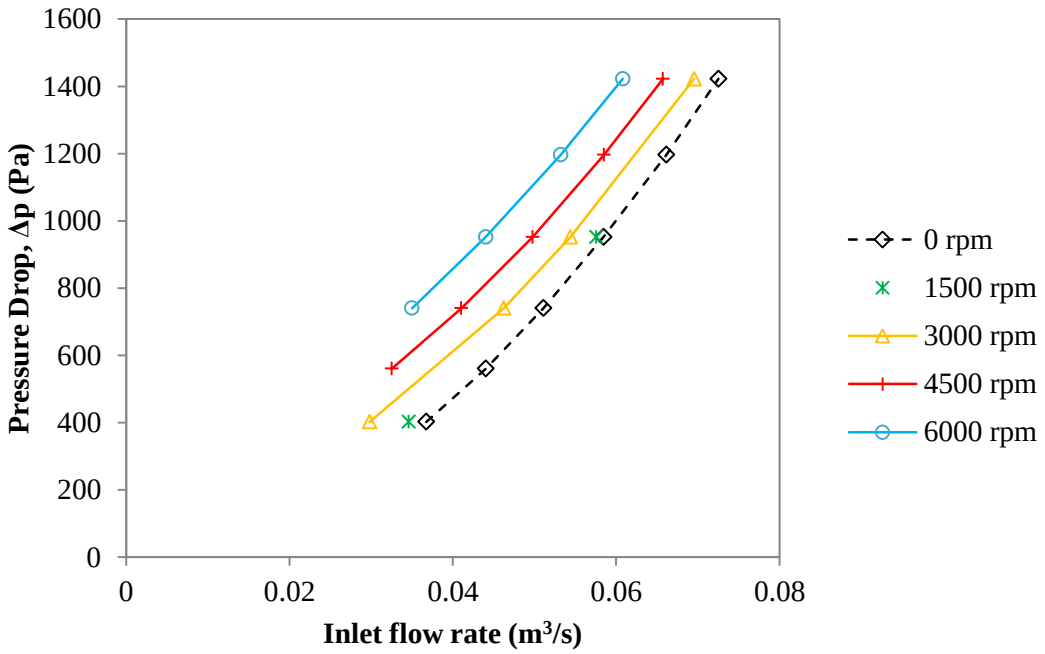

Figure 6.13: System flow resistance curves of Test B for rotor speed up 6000 rpm

6.7.2.1 Flow field in rotor-stator gap

With rotation, the flow passing through the annular gap becomes helical as illustrated in Figure 6.14. As a result, the length of pathway travelled by the rotational flow is longer. This increases the friction loss. Test H was modelled using a periodic sector and also solid rotor, but they have no significant difference. According to Kuzay and Scott [1977], the flow helix can be identified by the rotation ratio because the rotation ratio accounts for the effect of mixed axial and rotational flow. As mentioned in Section 6.5, the rotation ratio is the simplified form of the ratio of the rotational Reynolds number to the axial Reynolds number as shown in equation (6.8). As equation (6.1) is comprised of the ratio of the rotational Reynolds number to the axial Reynolds number, it is suitable to be employed in the present study to calculate the friction factor of flow passing through the rotor-stator annular gap.

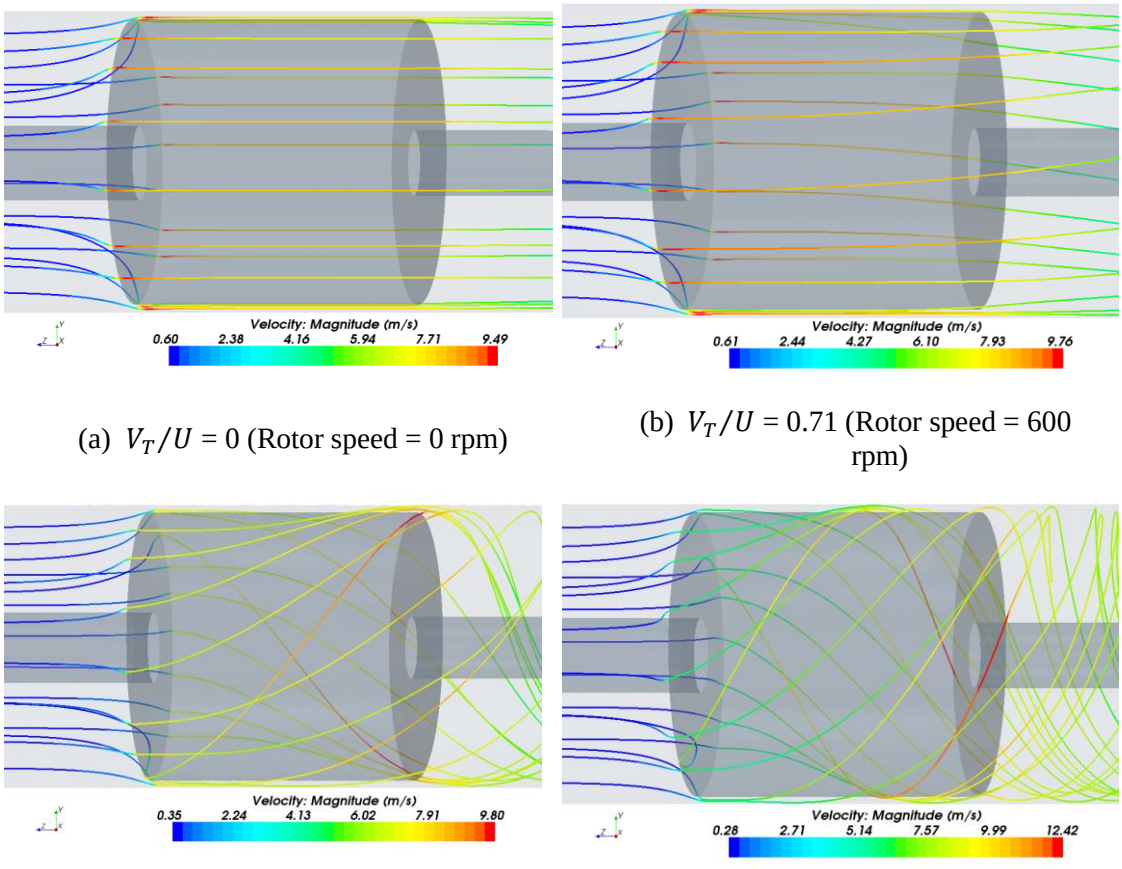

(a) V_T/U = 0 (Rotor speed = 0 rpm)

(b) V_T/U = 0.71 (Rotor speed = 600 rpm)

(c) V_T/U = 3.55 (Rotor speed = 2400 rpm)

(d) V_T/U = 5.27 (Rotor speed = 3000 rpm)

Figure 6.14: Streamlines of air passing through the rotor-stator annular gap of Test F (solid rotor)

6.7.2.2 Shock loss coefficient of rotor-stator gap

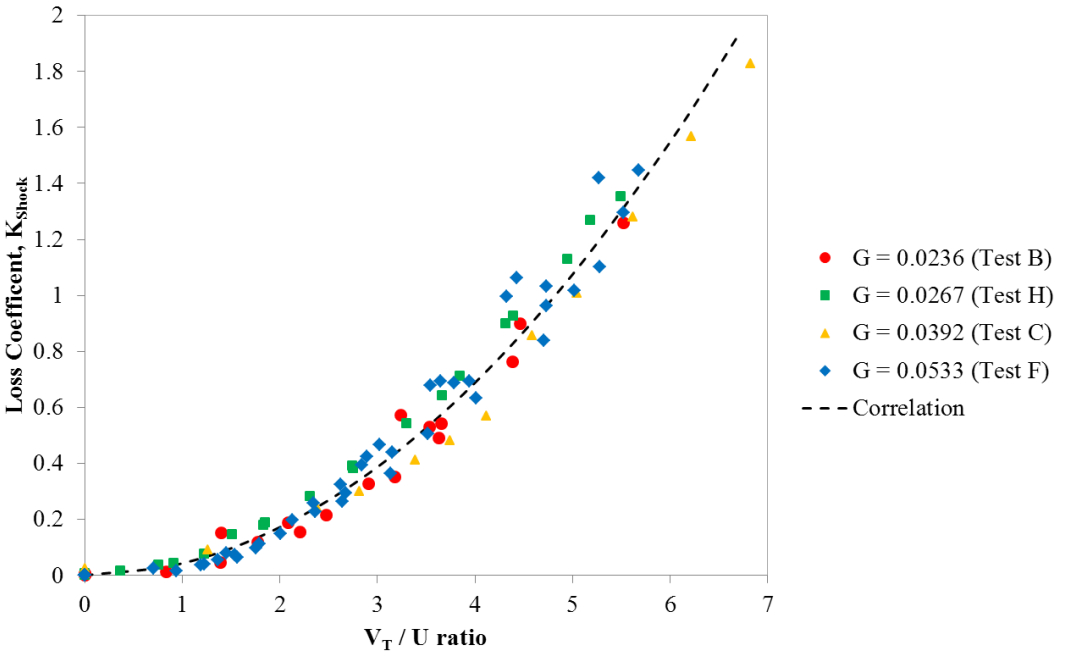

Figure 6.15: The variation of shock loss coefficient of annular gap with rotation ratio

By using equation (6.13), the shock loss coefficient of annular gap of different gap ratio was computed. Figure 6.15 shows that the shock loss coefficient increases in a parabolic relationship with the rotation ratio. However, the CFD results indicate that the values of shock loss coefficient of different gap ratio (i.e. s/a) follow the same trend. Thus, it can be concluded that the gap size has no influence on the shock loss for gap ratio from 0.0236 to 0.0533. The shock loss coefficient of the annular gaps can be correlated as:

$$K_{shock} = 0.043(V_T/U)^2 \tag{6.21}$$

Similar to the rotor ducts, a range of flow rate passing through the rotor-stator annular gap was simulated for each CFD model. Therefore, the correlation is valid for the axial Reynolds number in the annular gap ranges from 2300 to 12000.

6.8 Combining Flow Loss

As mentioned in Section 6.3, the combining flow increases the resistance of flow passing through the rotor-stator gap and thus reduces the flow rate. In order to demonstrate the presence of the combining flow loss within electrical machines, the

flow rates passing through the rotor-stator gap under the same inlet pressure for the models with only rotor-stator gap and with both rotor-stator gap and rotor ducts was compared. The machine of Test B was used in this section. The comparison was performed using inlet pressure of 740 Pa and 952 Pa. As shown in Figure 6.16 and Figure 6.17, the flow rate passing through the rotor-stator gap reduces significantly above certain rotational speed for the case with rotor ducts being modelled. This demonstrates the existence of combining flow loss. For inlet pressure at 952 Pa, the flow reduction becomes noticeable after 4500 rpm whereas for inlet pressure at 740 Pa the flow reduction becomes noticeable after 3000 rpm. Therefore, it is important to note that the combining flow is not only affected by the rotor speed but also affected by the flow rate passing through the flow paths.

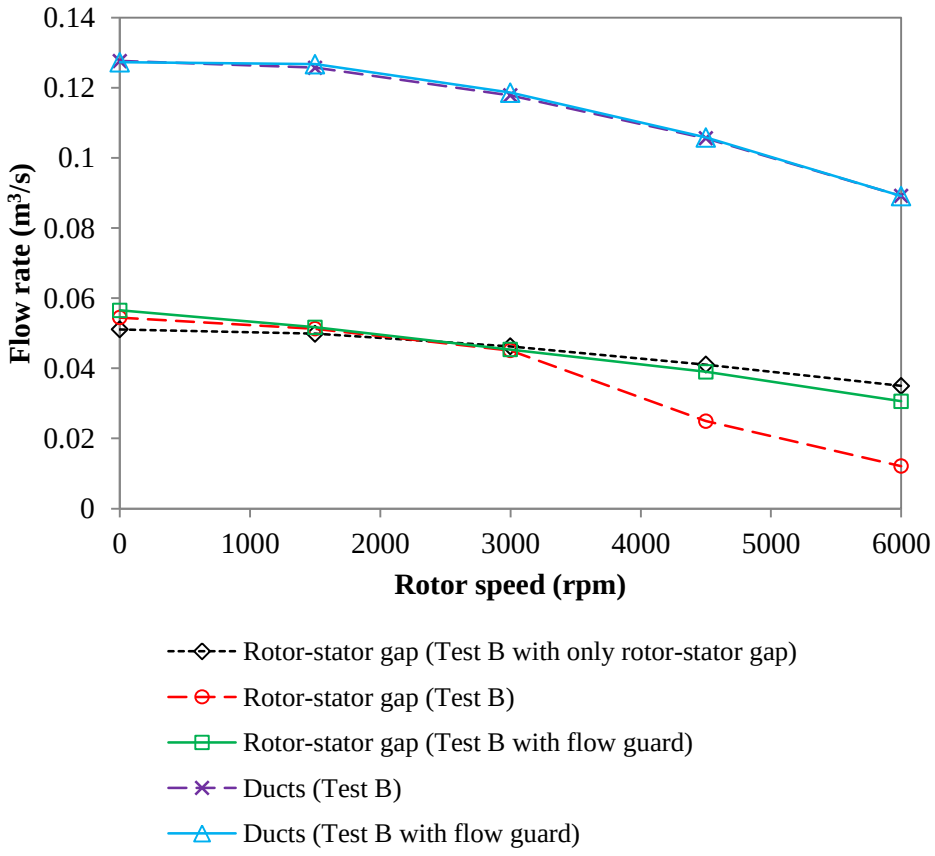

Figure 6.16: Flow rates in rotor-stator gap and rotor ducts for the inlet pressure at 740Pa

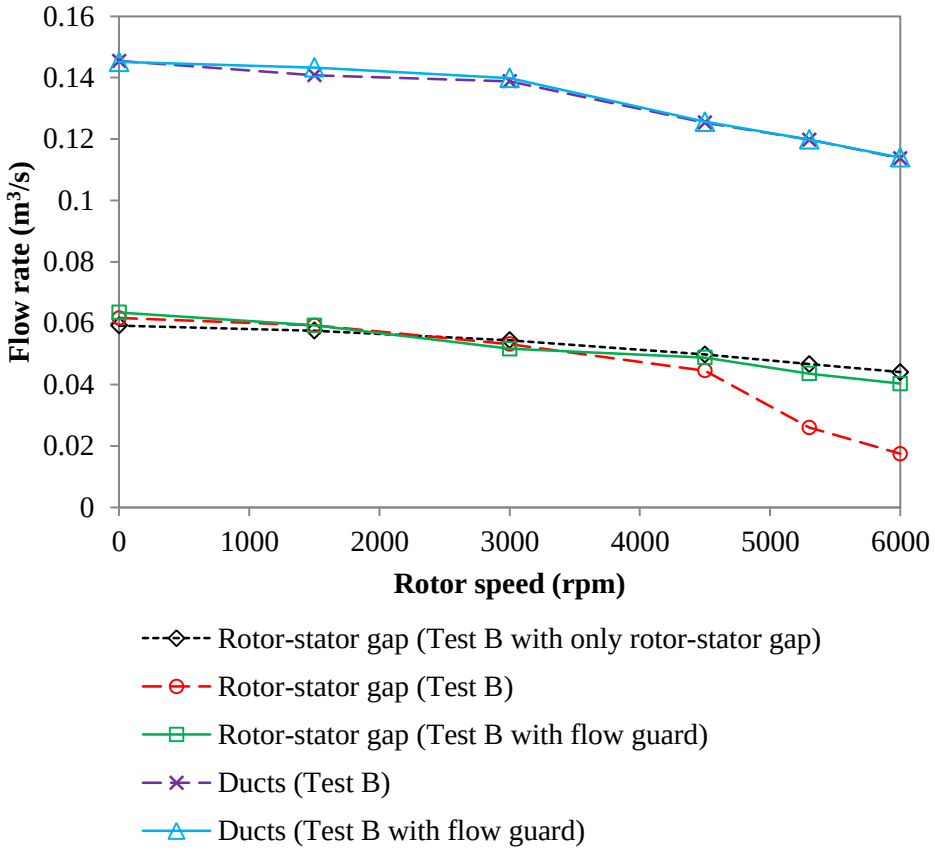

Figure 6.17: Flow rates in rotor-stator gap and rotor ducts for the inlet pressure at 952 Pa

6.8.1 Flow phenomena of combining flow

For Figure 6.17, the flow field inside the rotor-stator system (i.e. Test B) is illustrated in Figure 6.18. With rotation, the air stream exiting from rotor ducts deflects radially from the axis of rotation and the deflection increases with the increase in rotor speed. At 6000 rpm, the air stream of rotor ducts is noticeably perpendicular to the air stream of rotor-stator gap. This results in an additional pressure loss to the flow passing through the rotor-stator gap and thus less flow rate.

Besides the mesh refinement study performed in Appendix F, the solution obtained from the CFD model is also checked. For zero speed case, the velocity profile in the rotor duct is compared with the empirical velocity profile, which is known as "power law velocity profile" for fully developed turbulent flow in a circular pipe, White [1986]. The comparison is performed for the cases with and without flow guard (i.e. Figure 6.18(a) and Figure 6.20(a)). The comparison is shown in Appendix G.

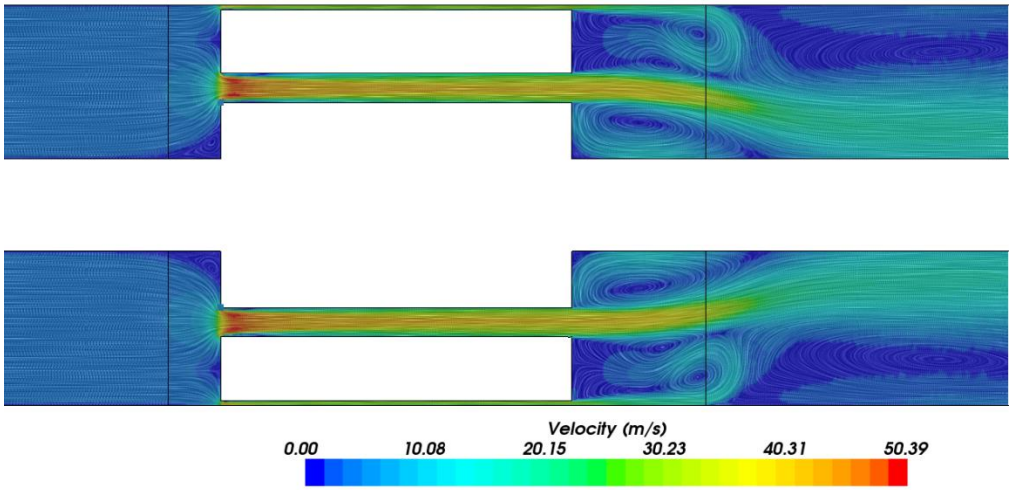

(a) Rotor speed = 0 rpm

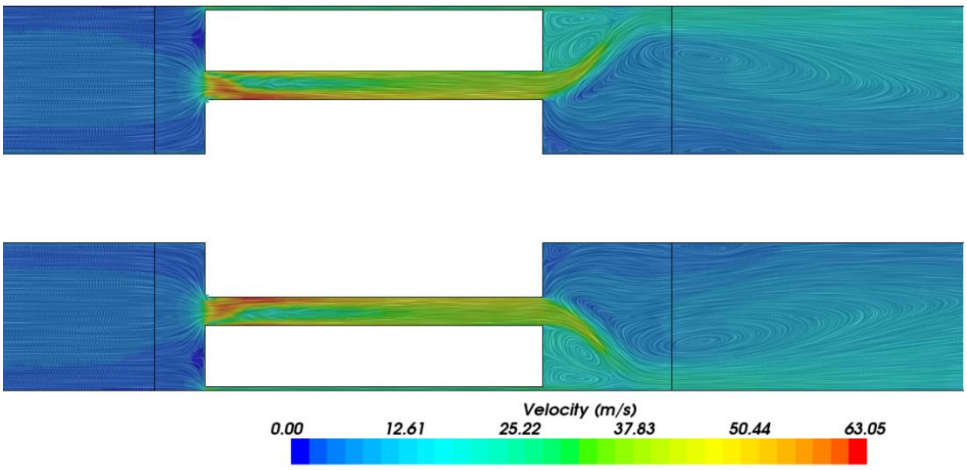

(b) Rotor speed = 3000 rpm

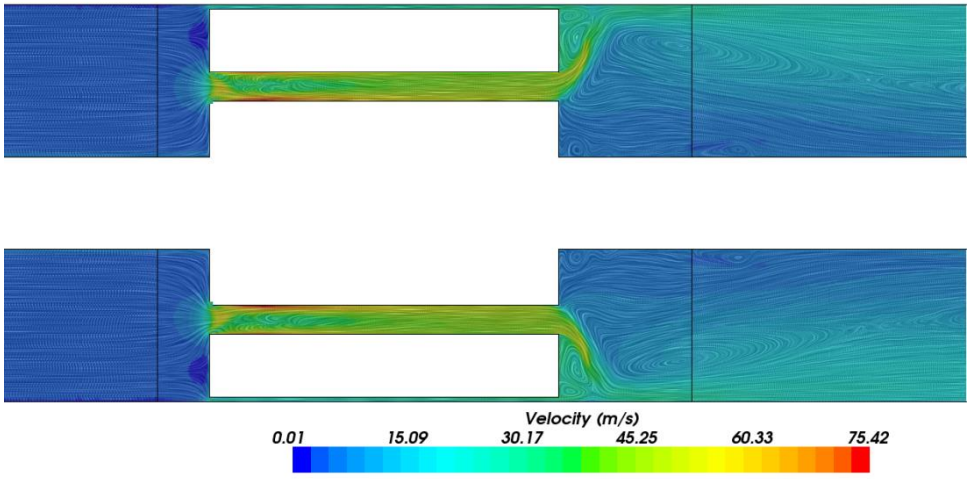

(c) Rotor speed = 4500 rpm

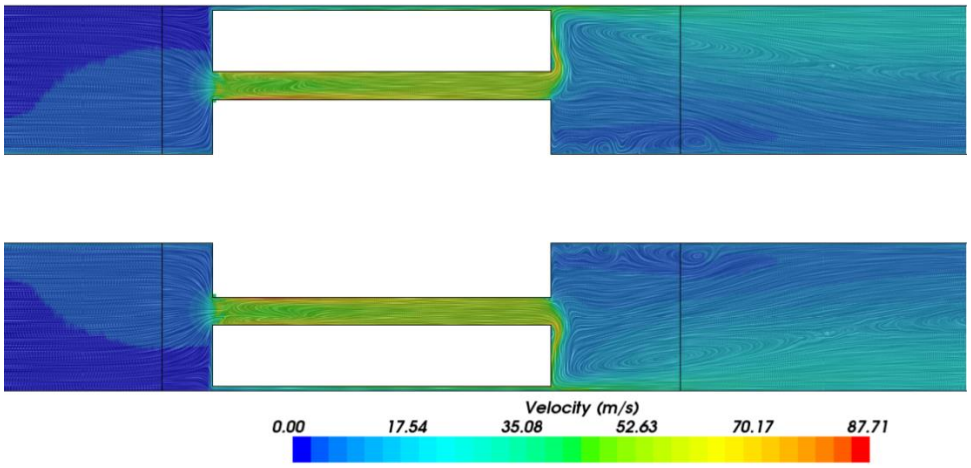

(d) Rotor Speed = 6000 rpm

Figure 6.18: Flow field of Test B for the inlet pressure at 952 Pa

6.8.2 Flow guard

In order to eliminate the combining flow, a flow guard is proposed as shown in Figure 6.19. The flow guard is a tube of thickness equal to 1 mm extended from the rotor end and concentric with the rotor. The length of the flow guard is two rotor duct diameters. It was placed between the rotor ducts and rotor-stator gap.

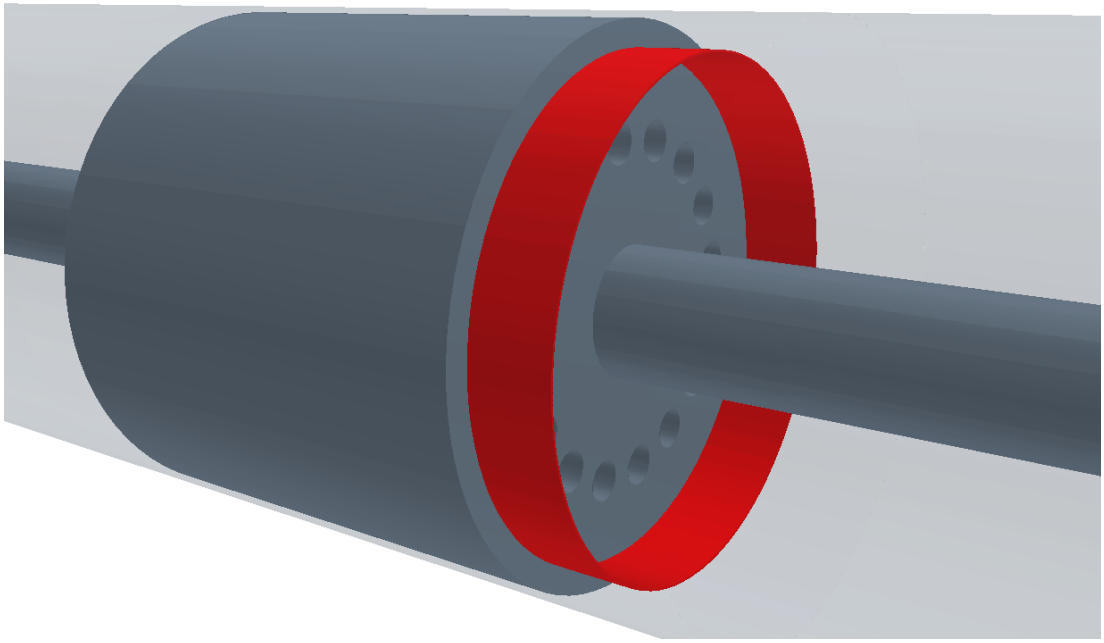

Figure 6.19: Flow guard of Test B at the rotor end, coloured in red

The performance of the flow guard is shown in Figure 6.20. The flow guard stops the interruption of combining flow especially at high rotor speed. The comparison of the flow rates in the rotor-stator gap and rotor ducts for the case with and without the flow guard can be found in Figure 6.16 and Figure 6.17. For the case with only rotor-stator gap and the case with rotor ducts and flow guard, their flow rates passing through the rotor-stator gap are very similar. Hence, the CFD results demonstrate that the proposed flow guard can eliminate the combining flow loss for the testing condition. In addition to that, the flow guard does not lead to extra flow resistance to the flow from the rotor ducts because the flow rates passing through the rotor ducts for the case with and without the flow guard are very similar.

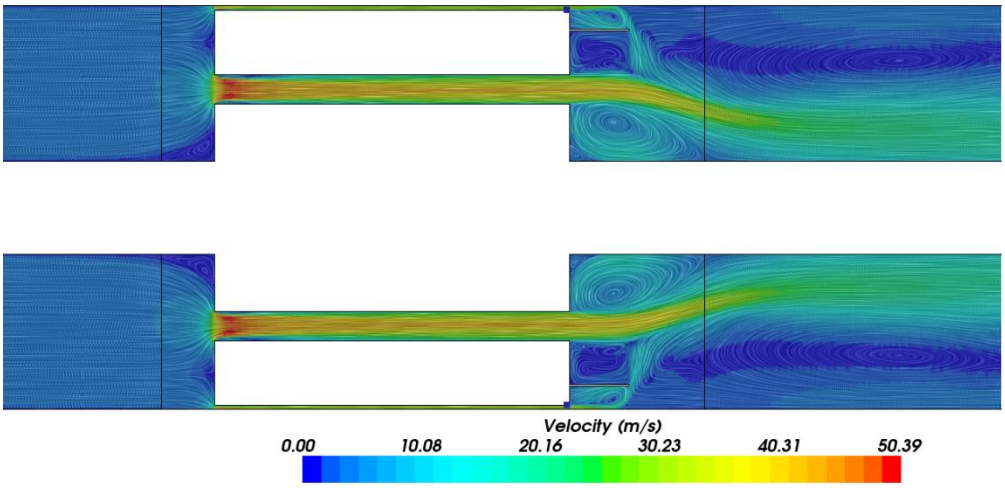

(a) Rotor speed = 0 rpm

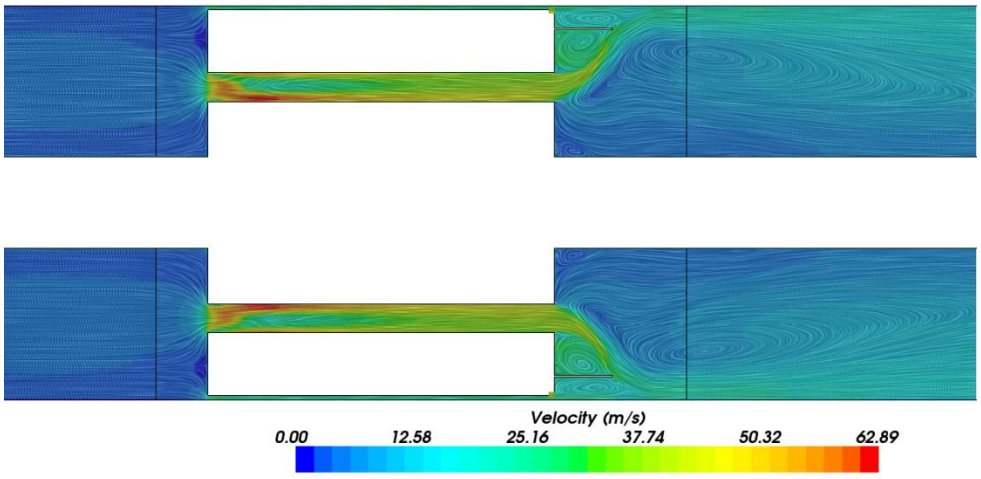

(b) Rotor speed = 3000 rpm

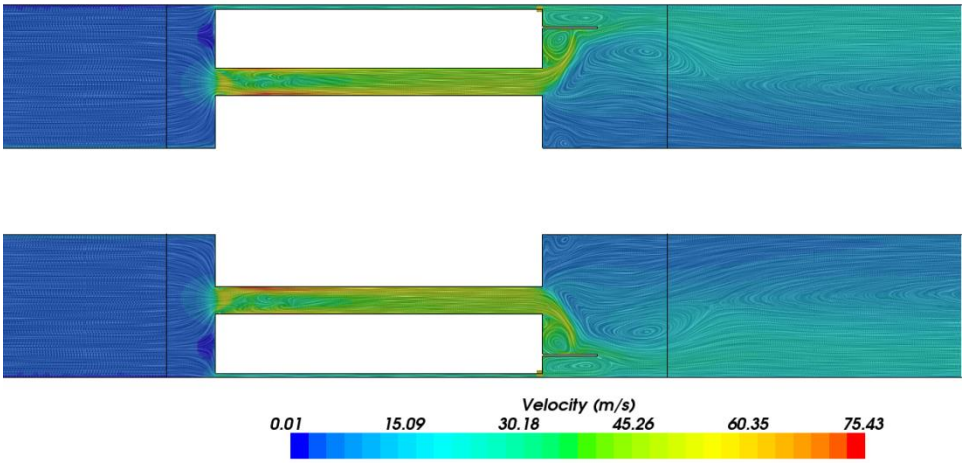

(c) Rotor speed = 4500 rpm

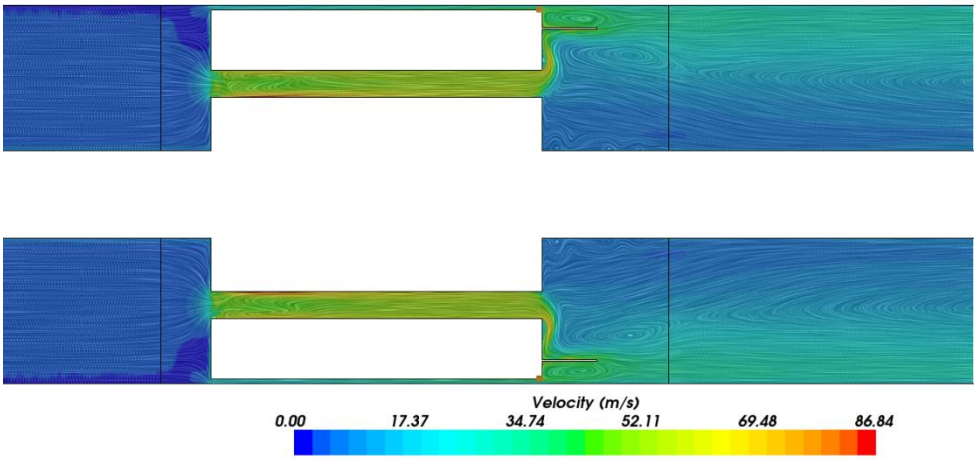

(d) Rotor Speed = 6000 rpm

Figure 6.20: Flow field of Test B with flow guard for the inlet pressure at 952 Pa

6.8.3 Combining flow loss coefficient

In this section, the rotational pressure loss in the rotor-stator gap is assumed to be comprised of the additional friction loss due to rotation, shock loss as described in Section 6.7.2 and combining flow loss. The total rotational loss (Δp_r) can be computed using equation (6.11) because the stationary loss can be calculated using the relationship between the stationary loss and inlet flow rate. As the additional friction loss and shock loss can be computed, the combining flow loss can be determined. Similar to the procedure of getting the shock loss coefficient, the coefficient of combining flow loss (K_{CF}) was obtained by non-dimensionlizing the

corresponding rotational pressure loss with the kinetic energy of air passing through the rotor-stator gap.

$$\Delta p_r = \left[\left(K_{f_r} - K_{f_0}\right) + K_{shock} + K_{CF}\right] \times \frac{1}{2}\rho U^2 \tag{6.22}$$

$$K_{CF} = \frac{2\Delta p_r}{\rho U^2} - \left(K_{f_r} - K_{f_0}\right) - K_{shock} \tag{6.23}$$

where K_{f_0} is the friction loss coefficient for stationary condition, K_{f_r} is the friction loss coefficient with rotation and U is the mean flow velocity in the rotor-stator gap.

As the combining flow is associated with the deflecting flow from rotor ducts, the dimensionless geometric parameters of rotor ducts (i.e. H/a, H/d and w/d) need to be considered in this section. Hence, the functional equation of combining flow loss coefficient can be expressed as:

$$K_{CF} = f\left(\frac{H}{a}, \frac{H}{d}, \frac{w}{d}, \left(\frac{V_T}{U}\right)_{gap}\right) \tag{6.24}$$

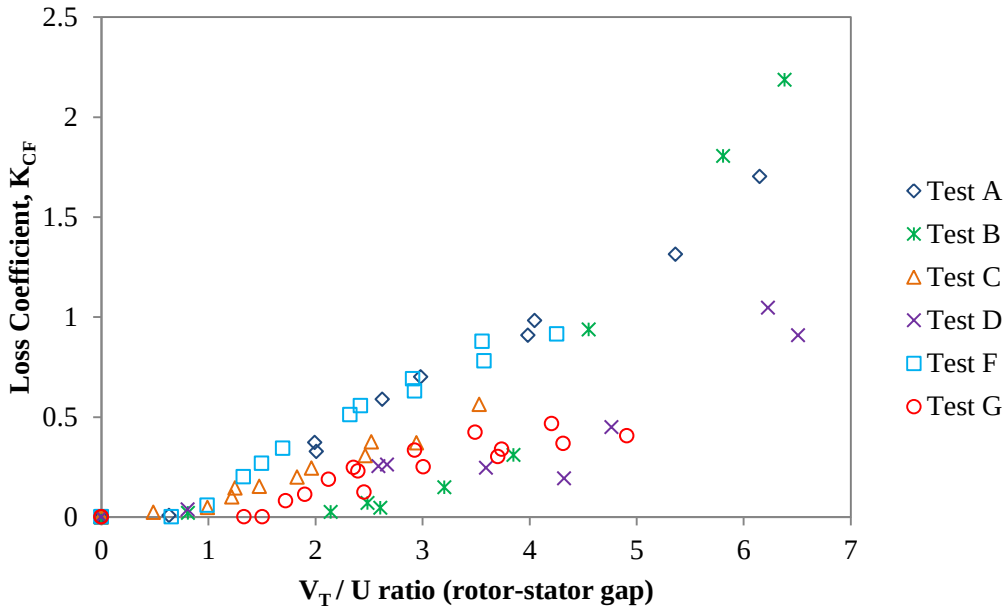

Figure 6.21: The variation of combining flow loss coefficient with rotation ratio

By applying equation (6.23), the combining flow loss coefficients obtained using CFD for Test A, B, C, D, F and G is shown in Figure 6.21. Generally, the loss

coefficient increases with the increase in rotation ratio, but the effects of rotation to each case are different. Therefore, they are analysed individually.

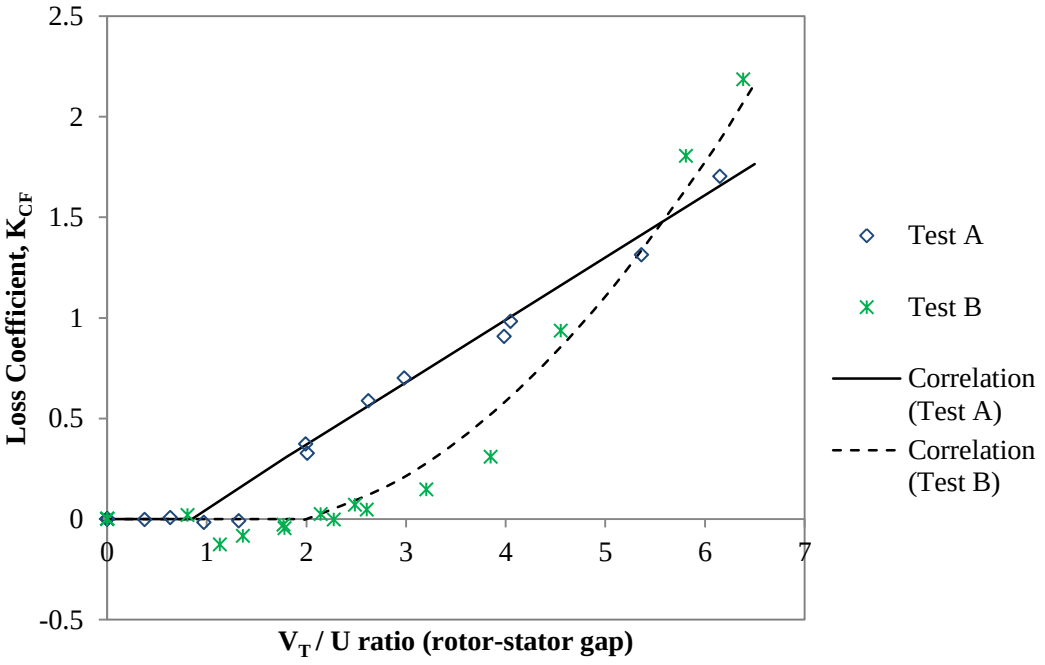

Figure 6.22: The variation of combining flow loss coefficient with rotation ratio for Test A and Test B

The variation of combining flow loss coefficient for Test A and Test B with the rotation is shown in Figure 6.22. The loss coefficient increases linearly with the rotation ratio when the rotation ratio is approximately higher than unity for Test A, while the loss coefficient increases in a second-order polynomial relation with the rotation ratio when the rotation ratio is greater than 2. The difference must be associated with the parameters of H/d and w/d because of different duct size.

Figure 6.23 shows the variation of the combining flow loss coefficient for Test C and Test D with the rotation ratio. For Test C, when the rotation ratio is higher than 0.6 the loss coefficient increase linearly with the rotation ratio. However, the loss coefficients of Test D are inconsistent, consequently appropriate correlation cannot be formed for Test D.

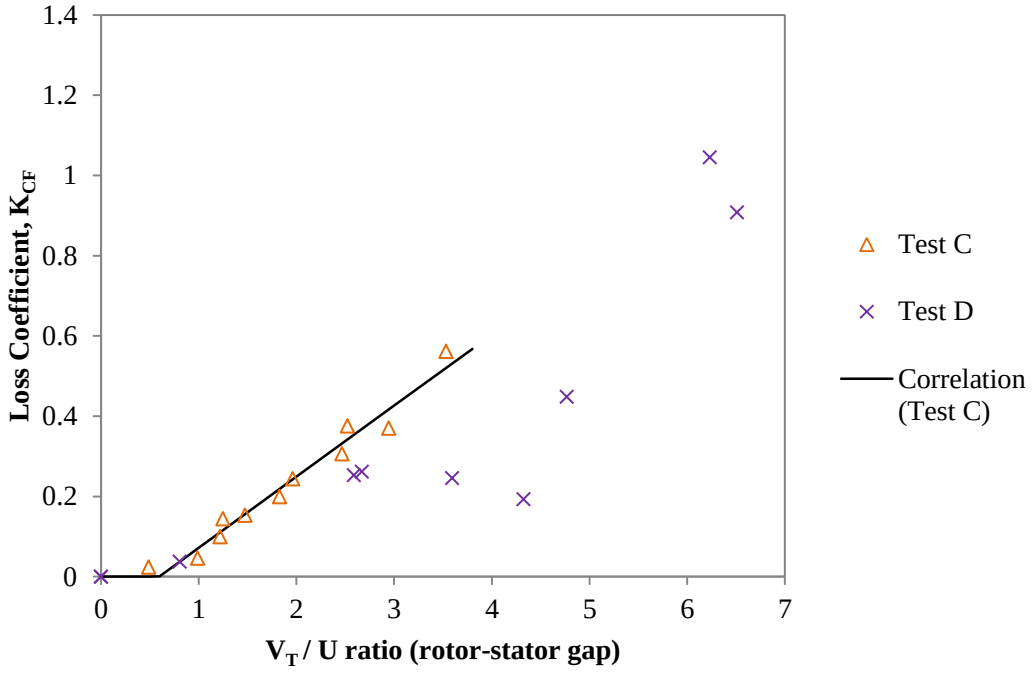

Figure 6.23: The variation of combining flow loss coefficient with rotation ratio for Test C and Test D

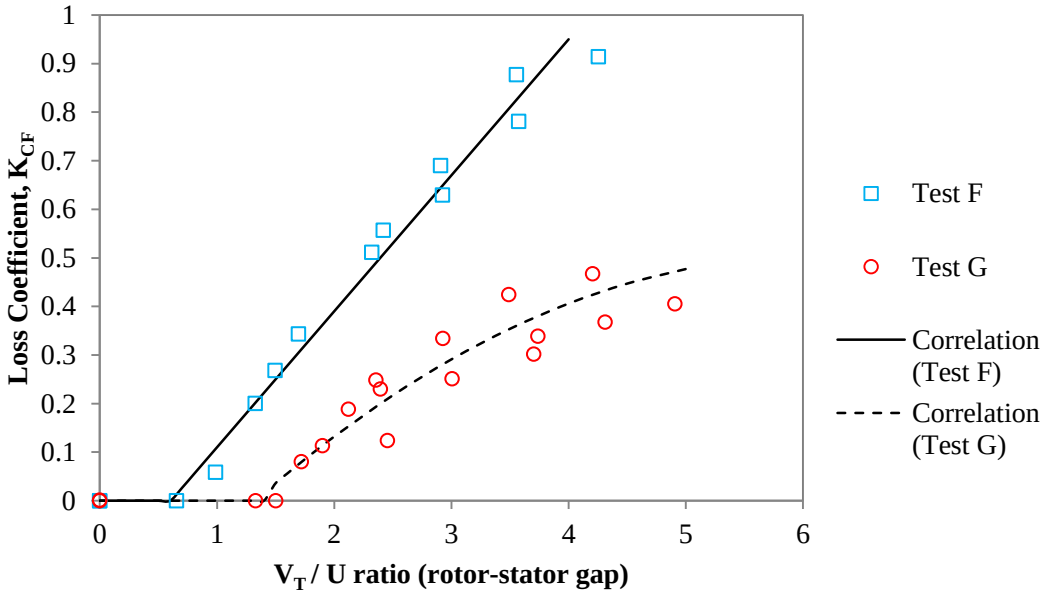

Figure 6.24: The variation of combining flow loss coefficient with rotation ratio for Test F and Test G

Similar to Test A, the combining flow loss coefficient of Test F increases linearly with the rotation ratio. However, the combining flow loss is negligible when the

rotation ratio is below 0.65. For Test G, the combining flow loss coefficient is lower than that of the Test F. This occurs because the rotor ducts of Test F are in closer proximity to the rotor-stator gap. As a result, the combining flow loss of Test G only become significant when the rotation ratio goes above 1.4. However, the increase of the loss coefficient become less gradually when the rotation ratio goes higher because the combining flow reaches its saturated value. This will be further explained in Chapter 8.

As the combining flow loss can be mainly characterised using the rotation ratio of rotor-stator gap, the loss coefficient can be correlated for each case as:

For Test A,

$$\begin{aligned} V_T/U > 1, \quad & K_{CF} = 0.31(V_T/U)_{gap} - 0.25 \\ V_T/U \leq 1, \quad & K_{CF} = 0 \end{aligned} \tag{6.25}$$

The correlation is valid for the axial Reynolds number in the rotor-stator gap ranges from 3900 to 12000.

For Test B,

$$\begin{aligned} V_T/U > 2, \quad & K_{CF} = 0.074(V_T/U)_{gap}{}^2 - 0.146(V_T/U)_{gap} - 0.014 \\ V_T/U \leq 2, \quad & K_{CF} = 0 \end{aligned} \tag{6.26}$$

The correlation is valid for the axial Reynolds number in the rotor-stator gap ranges from 3200 to 8300.

For Test C,

$$\begin{aligned} V_T/U > 0.6, \quad & K_{CF} = 0.177(V_T/U)_{gap} - 0.105 \\ V_T/U \leq 0.6, \quad & K_{CF} = 0 \end{aligned} \tag{6.27}$$

The correlation is valid for the axial Reynolds number in the rotor-stator gap ranges from 13700 to 35000.

For Test F,

$$\begin{aligned} V_T/U > 0.65, \quad & K_{CF} = 0.28(V_T/U)_{gap} - 0.17 \\ V_T/U \leq 0.65, \quad & K_{CF} = 0 \end{aligned} \tag{6.28}$$

The correlation is valid for the axial Reynolds number in the rotor-stator gap ranges from 3000 to 7700.

For Test G,

$$\begin{aligned} &V_T/U > 1.4, \qquad K_{CF} = -0.022(V_T/U)_{gap}{}^2 + 0.269(V_T/U)_{gap} - 0.318 \\ &V_T/U \leq 1.4, \qquad K_{CF} = 0 \end{aligned} \tag{6.29}$$

The correlation is valid for the axial Reynolds number in the rotor-stator gap ranges from 2900 to 7700.

Because of the complexity of the combining flow, the combining flow loss coefficient cannot be simply represented by a single generic correlation. Therefore, equations (6.25) to (6.29) must be applied with great caution and they are only applicable to those machines having geometrically similar rotors to the machines of Test A to G as described in Table 6-1.

6.9 Conclusion

In this chapter, the effects of rotation on the flow passing through the rotor-stator gap and rotor ducts have been successfully studied using the CFD method. The CFD models were first verified using the analytical method for stationary case before they were employed to investigate the influence of rotational speed, configuration of rotor ducts and rotor-stator gap size on the flow resistance. Based upon dimensional analysis, correlations that can be used to characterise the rotational pressure losses (i.e. shock loss and combining flow loss) in the rotor-stator system were proposed. The CFD results have provided very useful insight into how the experiment apparatus should be designed and constructed so that it can validate the findings obtained using the CFD method.

7 Experimental Apparatus for Investigation of the Effects of Rotation on the Flow Resistance in a Rotor-Stator System

7.1 Design of Air Flow Test Rig

In Chapter 6, the preliminary CFD results have demonstrated that the additional flow resistance due to the effects of rotation can be characterised using the rotation ratio. Chapter 5 has shown that the flow network analysis method is applicable for electrical machine air flow modelling. Therefore, the experimental objectives are to validate the findings obtained using the CFD methods in Chapter 6 and also to confirm the validity of the air flow modelling tool as described in Chapter 5.

The main principle of air flow test rig is to measure the pressure requirements of a rotor-stator system of different ventilation configurations for a range of flow rate with rotor rotating. Based on the experimental results, the rotational pressure losses will be characterised and the correlations of the rotational pressure loss coefficient in the rotor-stator gap and rotor ducts are planned to be proposed. To achieve these aims, an air flow test rig was built, shown in Figure 7.1.

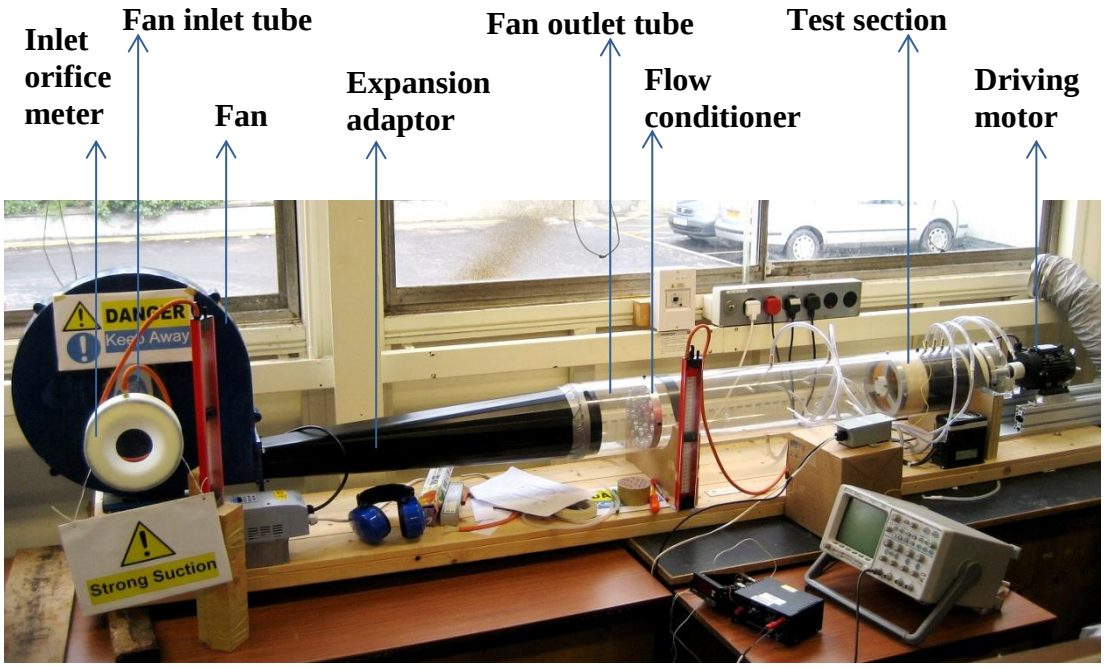

Figure 7.1: Air flow test rig

The air flow test rig mainly consists of a fan inlet tube that connecting between an inlet orifice meter and an adjustable speed fan, a transparent fan outlet tube that connected to the fan through an expansion adaptor and a test section that accommodates a laminated stator and a laminated rotor driven by an inverter drive motor. Functionality of the machine parts will be described in detail in this Chapter and their technical drawings can be found in Appendix H. During operation, air was drawn into the test rig by the fan, passed though the test section and exited from the outlet of the fan outlet tube. The outlet is opened to the atmosphere.

7.2 Sizing of Test Rig

As discussed in Chapter 6, the rotation ratio (i.e. V_T/U) is an important parameter used to characterise the effects of rotation on flow resistance. In order to achieve a qualitative research, the test rig was decided to provide a range of the rotation ratio up to at least 3, the higher the better.

It might be important to review how the airgap size is determined in machine design in order to decide the suitable airgap size for the test rig. According to Pyrhonen et al. [2008], the airgap size of a machine is mainly dependent of the machine type (e.g. synchronous, asynchronous, DC, reluctance, etc.) and the rated speed. In principle, a small air gap gives a low magnetizing current, but increases the eddy current losses of the rotor and stator surface. Although the airgap has significant influence on the characteristics of an electrical machine, the airgap size is usually decided by empirical equations for standard electrical machines based upon experience of mechanical and electromagnetic considerations. As the design of rotating electrical machines is complicated, the airgap size varies for different designs. Nevertheless, most electrical machines have relatively small airgap, for instance, induction machines always use the minimum attainable airgap size in order to reduce the magnetising current to a minimum. For safety reasons and mechanical constraints of the experimental operation, the chosen gap size (s) of rotor-stator system was 4 mm.

As V_T relates to the rotor peripheral velocity and tangential velocity of rotating duct, this can be achieved either by increasing the rotor speed or having a rotor of large diameter. However, for safety reasons and to avoid viscous heating of air, the rotor

speed is limited to a maximum speed of 3000 rpm (i.e. the synchronous speed of 2-pole machine at 50 Hz). Consequently, the rotor size is an important parameter, but the size of rotor must not be too large. The rotor was planned to be removable so that it could easily be assembled or disassembled from the test section. For pragmatic reasons, an unnecessarily heavy rotor is undesired because it makes to the investigation of different rotor duct configurations more difficult. Furthermore, a large rotor will cause an unnecessary increase in cost. Therefore, assuming 20 kg is the maximum mass, by having a rotor of one rotor diameter in length (i.e. $L = 2a$), the rotor radius (a) required is:

$$(\pi a^2) \times 2a \times \rho_{steel} \approx 20kg \tag{7.1}$$

$$a = \sqrt[3]{\frac{20kg}{\rho_{steel}(2\pi)}} \approx 0.075\,m \tag{7.2}$$

The test rig design started with the selection of the rotor radius. This gives a gap ratio (i.e s/a) of 0.0533. Based on the maximum rotor speed and rotor radius, the value of V_T can reach up to 23.6 m/s. To achieve a rotation ratio of 3, the required value of U is 7.9 m/s. As the hydraulic diameter of the airgap and mean axial velocity are known, the axial Reynolds number can be computed as:

$$Re = \frac{U(2s)}{\nu} \approx 4200 \tag{7.3}$$

Although the Re of 4200 falls into transition flow regime (i.e. $2300 < Re < 5000$), the rotation ratio would also cover laminar and turbulent flow regimes because the flow rate can be increased or decreased by adjusting the fan speed.

Mean flow velocity, U	Re	Rotation ratio, V_T/U
12 m/s	6400	2
7.9 m/s	4200	3
4 m/s	2100	5.9

Table 7-1: The relationship of mean flow velocity, Reynolds number and rotation ratio

A higher flow rate gives turbulent flow, but this will reduce the obtainable rotation ratio. While, a lower flow rate gives laminar flow and this will increase the obtainable rotation ratio. For examples, by limiting V_T = 23.6 m/s, the obtainable *Re* and V_T/U over a range of mean flow velocity are shown in Table 7-1. However, the flow rate is limited by the fan performance and flow resistance. Similar procedures were applied for the selection of rotor duct diameter.

7.3 Test Section

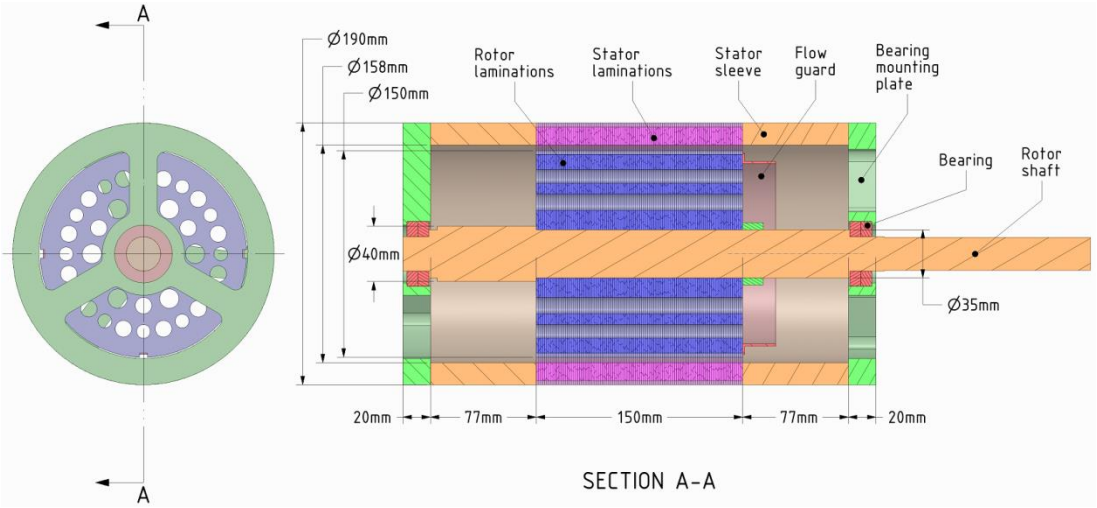

Figure 7.2: Rotor-stator assembly

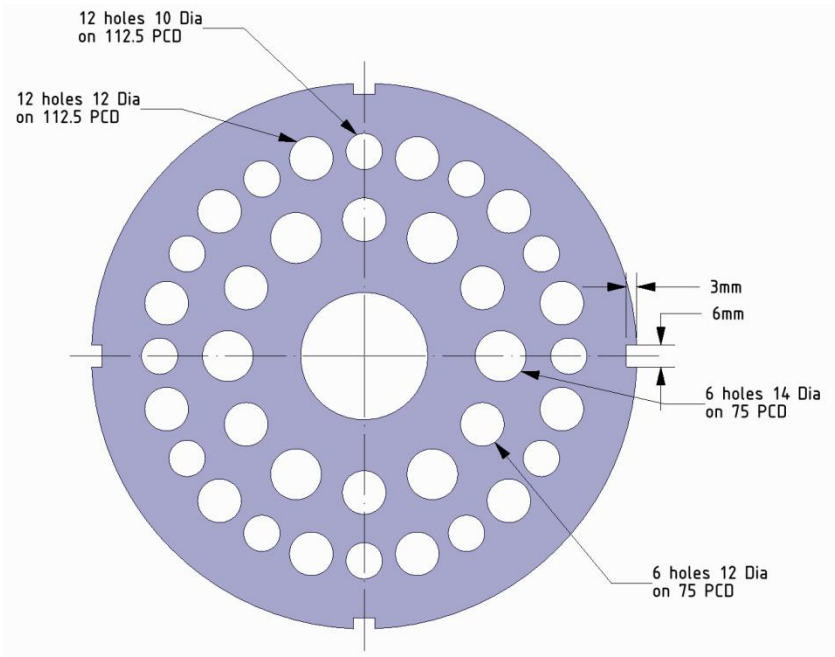

Figure 7.3: Positions and sizes of rotor ducts

In the test section, the stator and rotor are made of steel laminations to simulate the surface condition of electrical machine. They are formed by welding 100 steel laminations of thickness of 1.5 mm together using four 6 mm × 3 mm slots that are arranged at 90° interval. Therefore, the axial length of stator laminations and rotor laminations are approximately equal to 150 mm as shown Figure 7.2. The stator laminations have an inner diameter of 158 mm and outer diameter of approximately 190 mm to suit the inner diameter of fan outlet tube. The stator laminations are positioned by the stator sleeves (of the same inner and outer diameters of stator laminations) to ensure the stator laminations are placed right over the rotor laminations. The rotor laminations have the outer diameter of 150 mm. This forms a rotor-stator annular gap of 4 mm. The rotor laminations are mounted on a shaft and are held in place by 2 bearing mounting plates. The distances between the bearing mounting plate and rotor laminations are approximately 77 mm for the front and rear ends. The rotor has a series of ducts, which is parallel to the axis of the rotor. The details of the rotor ducts in the test rig are as follows:

- 6 ducts of diameter 14 mm on pitch-circular diameter of 75 mm,
- 6 ducts of diameter 12 mm on pitch-circular diameter of 75 mm,
- 12 ducts of diameter 12 mm on pitch-circular diameter of 112.5 mm,
- 12 ducts of diameter 10 mm on pitch-circular diameter of 112.5 mm.

d (mm)	*n*	*H (mm)*	*a (mm)*	*L (mm)*	*H/a ratio*	*H/d ratio*	*L/d ratio*	*w/d ratio*
12	6	56.25	75	150	0.75	4.69	12.5	4.91
12	12	56.25	75	150	0.75	4.69	12.5	2.45
10	12	56.25	75	150	0.75	5.63	15.0	2.95
12	6	37.5	75	150	0.50	3.13	12.5	3.27
14	6	37.5	75	150	0.50	2.68	10.7	2.80

Table 7-2: Configurations of rotor ducts

s (mm)	*a (mm)*	*L (mm)*	*s/a ratio*	*L/2s ratio*
4	75	150	0.0533	18.8

Table 7-3: Configuration of airgap

The purpose of the arrangement of rotor ducts in Figure 7.3 is to investigate the influence of duct size, duct pitch-circular diameter and duct spacing to the additional pressure losses suffered by the air flow passing through the rotating ducts. By blocking some of the rotor ducts, various configurations of rotor ducts can be tested. The configurations of rotor ducts and airgap that were tested are tabulated in Table 7-2 and Table 7-3.

7.3.1 Flow guard

The purpose of introducing a flow guard in the test rig has been described in Chapter 6. Hence, its functionality was demonstrated experimentally. Figure 7.4 shows the arrangement of the flow guard. The flow guard is a thin plate of 1.5 mm with curvature radius of 66.25 mm. The axis of curvature was brought in line with the rotor axis and thus it is located radially above the rotor ducts. The radial distance between the flow guard and rotor outer radius is 8 mm, which is about 2 times the airgap size to reduce the kinetic energy of airgap flow. The flow guard is extended 24 mm (6 times airgap size and 2 times rotor ducts of 12 mm) from the rear end of the rotor for the static pressure recovery.

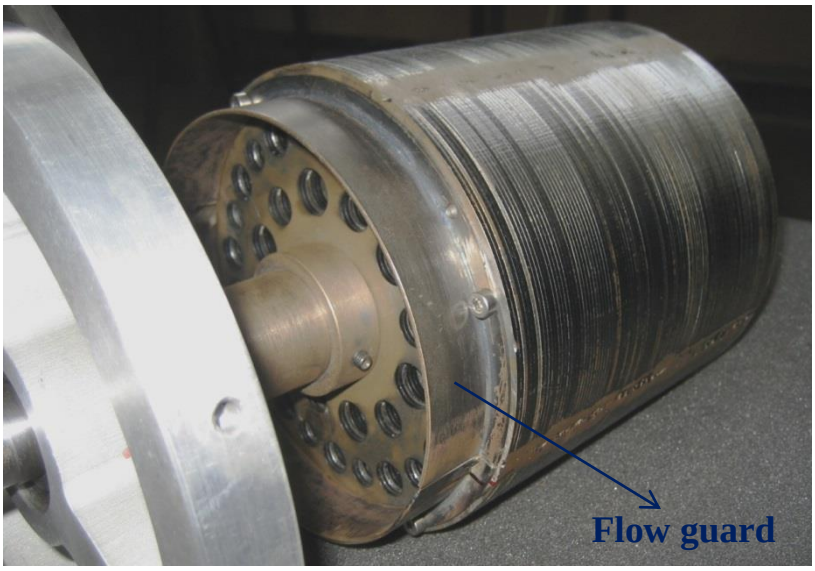

Figure 7.4: Arrangement of flow guard

7.3.2 Surface Roughness Measurement

As friction loss is one of the main system pressure losses, the surface roughness of steel laminations must be determined. In this section, the surface roughness was examined experimentally using two different methods. One is obtained implicitly through the measurements of the pressure drop of fully developed flow for a given duct length. Other measures the surface roughness directly by means of a standardized instrument.

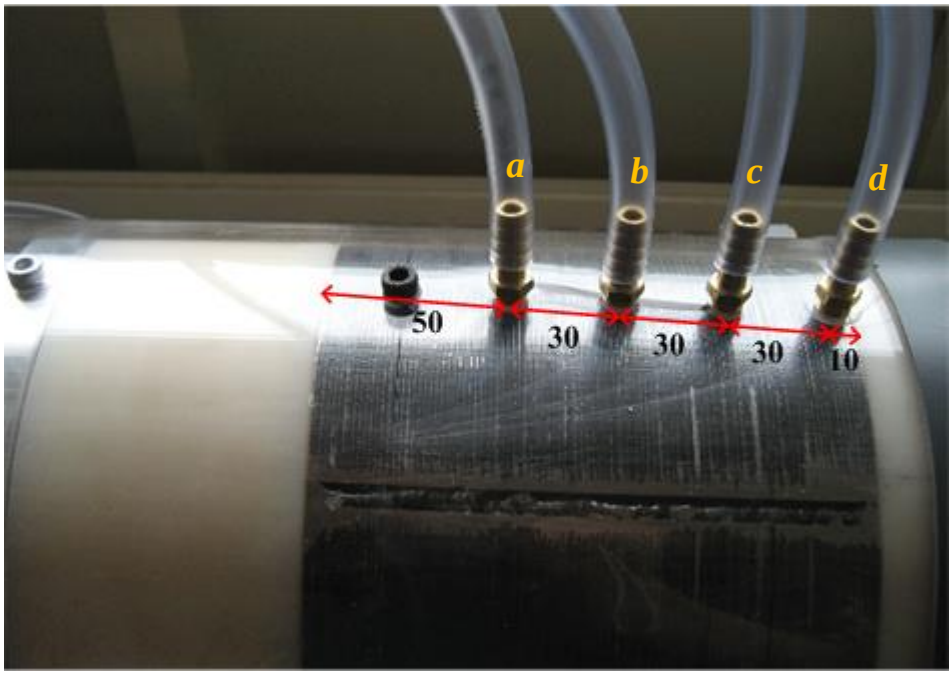

Figure 7.5: Locations of pressure tappings in the annular gap

As shown in Figure 7.5, the pressure drop in the rotor-stator gap is measured using 4 wall pressure tappings at positions *a*, *b*, *c* and *d*, which are spaced at the same interval of 30 mm. The first pressure tapping is located 50 mm away from the front end of rotor-stator gap. As described in section 2.3.1, for a developing flow, the axial gradient of friction loss would be large at the entrance of the rotor-stator gap and would asymptotically approach the gradient for fully developed flow occurring in the rotor-stator gap further downstream. To determine whether the flow in the rotor-stator gap is fully developed, the pressure drop (Δp) between the pressure tappings, *a* – *b*, *b* – *c* and *c* – *d* was measured over a range of Re.

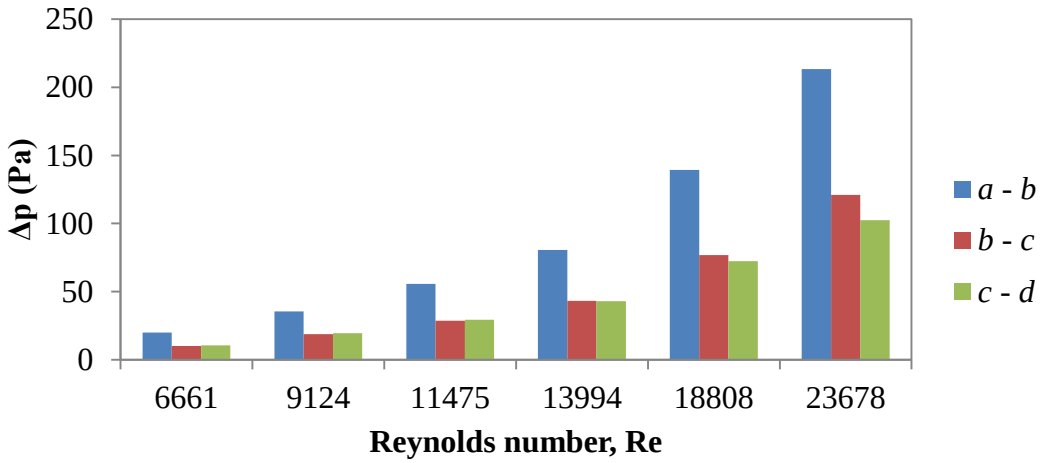

Figure 7.6: Frictional loss between the pressure tappings in the rotor-stator gap

In Figure 7.6, as the magnitudes of friction loss at b – c and c – d are about the same, this indicates that the flow is fully developed after the pressure tapping b, for Re up to 14000. For air flow test with only the rotor-stator gap, the friction factor (f_∞) in the rotor-stator gap based upon fully developed flow can be computed using the Darcy-Weisbach equation as:

$$f_\infty = \frac{2D_h \Delta p}{\rho U^2 L} \tag{7.4}$$

D_h is the hydraulic diameter of rotor-stator gap, U is the mean axial velocity in the rotor-stator gap and L is the distance between the pressure tappings.

According to the well-known Colebrook-White equation, the friction factor in a duct is dependent on the Re and the relative roughness (e/D_h). However, the Colebrook-White equation is an implicit equation, which needs to be solved using an iterative approach. As a result, the Haaland equation (an alternative explicit form of Colebrook-White equation) was used to estimate the surface roughness of the rotor-stator gap. The Haaland equation is accurate to $\pm$15 % and is expressed by:

$$\frac{1}{\sqrt{f_\infty}} = -1.8\log\left[\left(\frac{e/D_h}{3.7}\right)^{1.11} + \frac{6.9}{Re}\right] \tag{7.5}$$

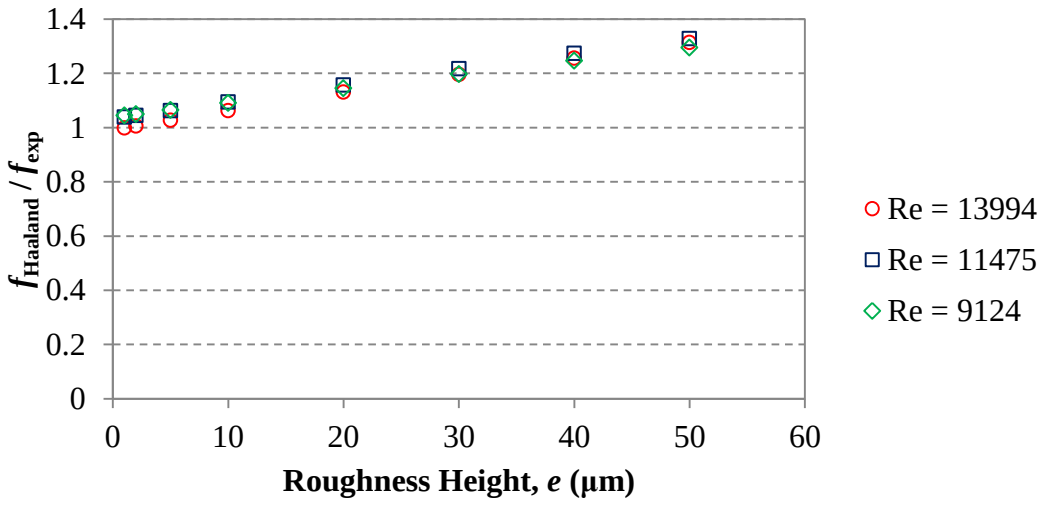

Figure 7.7: The variation of relative friction factor for fully developed flow with roughness height

However, equation (7.5) does not allow back-solve for roughness height by substituting the value of f_∞ obtained experimentally. Instead, arbitrary values of roughness height (e) were substituted into equation (7.5) and solved for the friction factor. The values of friction factor were compared with the experimental data. The relative friction factor ($f_{\text{Haaland}} / f_{\text{exp}}$) for fully developed flow is plotted against roughness height. Figure 7.7 shows that the roughness height up to about 20 µm is still valid within the limits of equation (7.5).

Figure 7.8: Replicating the surface condition of rotor laminations using RepliSet-F5

In order to quantify the pressure loss due to wall friction accurately, the information of surface roughness caused by steel laminations was determined by a standardized

method, namely *RepliSet*. *RepliSet* is a technology of using a fast curing two-part silicon rubber to replicate the micro structure of a surface to a highly accurate and stable replica, Rosendahls [2010]. As *RepliSet* offers a very high resolution down to 0.1 μm and the replica can be removed from the replicated surface without damage and distortion for microscopic examination, *RepliSet* was employed to examine the surface roughness of the steel laminations. Replicas of steel laminations and the surface condition under microscopic examination are shown in Figure 7.8 and Figure 7.9 respectively.

From the surface condition of replicas, the "steps" caused by rotor laminations can be clearly observed under an optical microscope. The mean line of the steps was determined from the scale on the image captured using the optical microscope. Then, the vertical deviations of the step height from the mean line were measured. Thus, the surface roughness based on the arithmetic average of the absolute values can be obtained, Adams et al. [2012]. Figure 7.10 shows the mean surface roughness of 9 replicas ranges between 9.6 μm to 31.5 μm. By taking the mean values of these 9 replicas, the surface roughness of steel laminations is approximately equal to 17.6 μm. The random uncertainties of the surface roughness can be found in Section 7.10.2.

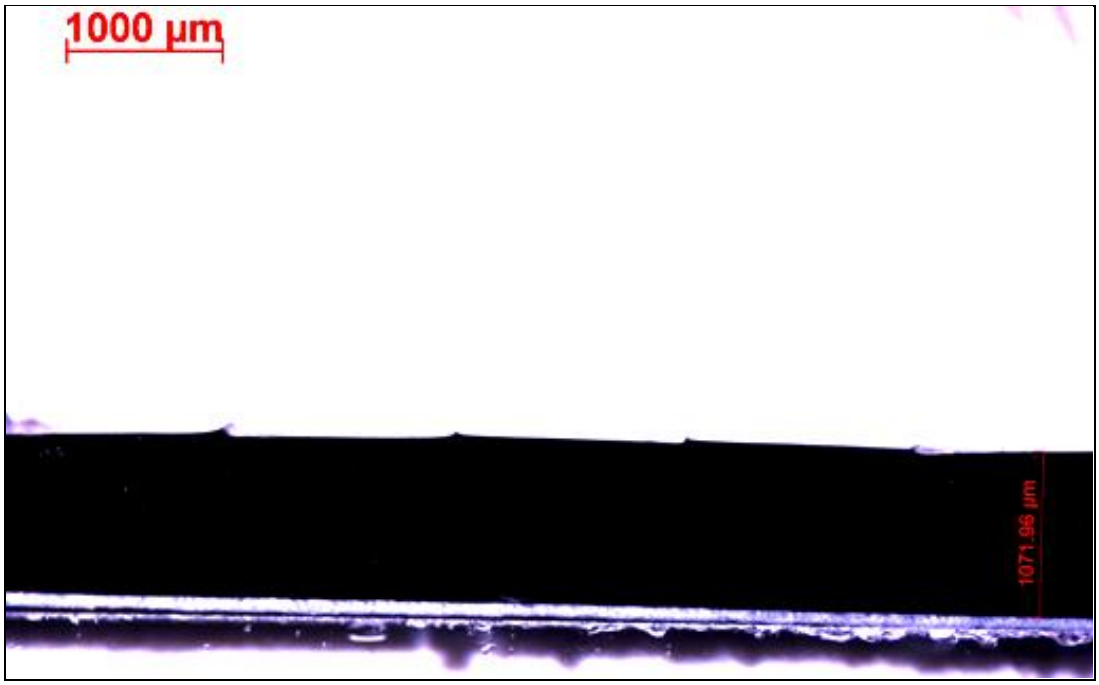

Figure 7.9: Surface condition of a replica viewed from the side under microscopic examination

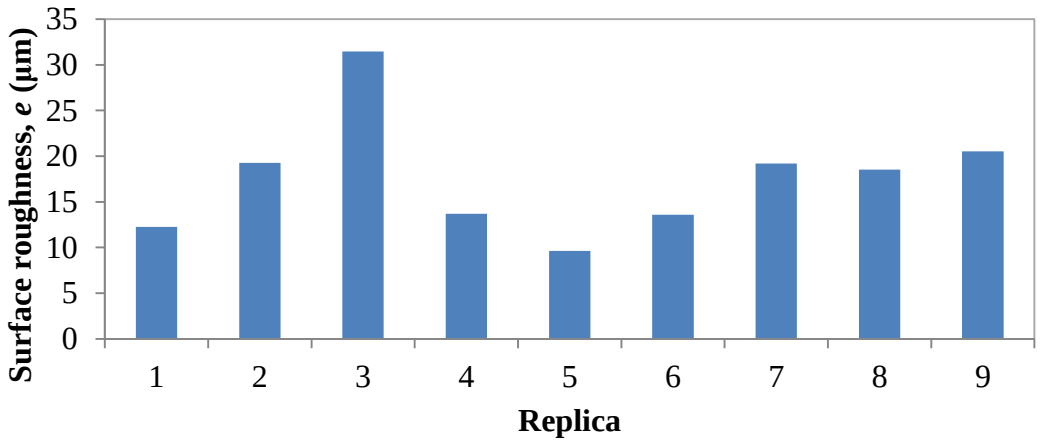

Figure 7.10: Mean surface roughness of 9 replicas

7.4 Rotation of Rotor in the Test Section

The rotor in the test was driven by a 2-pole 0.75 kW AC induction motor. By connecting the motor to an inverter, adjustable rotational speed is allowed to drive the rotor. Hence, the investigation of the rotating effects on additional flow resistance in the ventilation paths (i.e. rotor-stator gap and rotor ducts) can be performed over a range of rotation ratio (i.e. V_T/U). Since the test rig is a geometric mock-up of radial flux machine for fluid dynamic study and it is not loaded, the mechanical torque required is only used to overcome the windage and bearing losses during rotation, which is often small and negligible. The rotor is assumed to rotate at the synchronous speed of the AC motor as follows:

$$N_r = \frac{120 f_q}{P} \tag{7.6}$$

N_r is the rotational speed, f_q is the inverter frequency and P is the number of poles (2, 4, 6…). This synchronous speed is only used for sizing of the test rig. However, the actual speed of the rotor is calibrated in the next section.

It is important to note that the outlet of the fan outlet tube and the motor are separated by a distance of 140 mm and the fan cowling of the motor was removed to avoid counter-flow at the outlet region of the test rig, which may cause unnecessary flow resistance to the flow from the outlet of the test rig.

7.4.1 Calibration of rotor speed

Since the rotor is driven by the motor through a coupling, the speed was measured using a RS TM-2011 Tachometer as shown in Figure 7.11. Based on the calibration, the rotor speed can be expressed as a function of inverter frequency by the following linear relation.

$$N_r = 59.805 f_q \tag{7.7}$$

The measurement data indicates that the rotor was rotating at the synchronous speed of the AC motor. By disconnecting the rotor, the speed of the driving motor was also measured as shown in Figure 7.12. This demonstrates that the windage and bearing losses can be neglected.

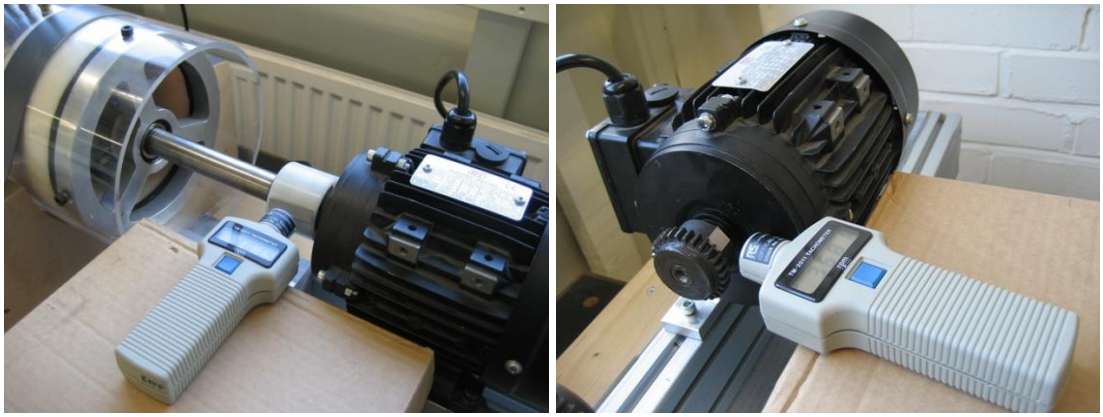

Figure 7.11: Rotor speed measurement using a tachometer

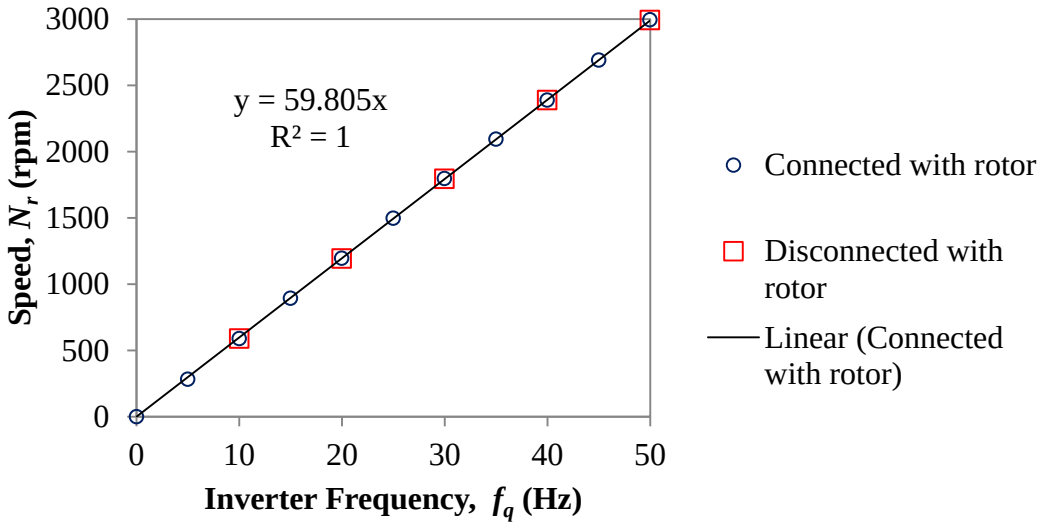

Figure 7.12: Variation of rotor speed with inverter frequency

7.5 Fan Selection

Before selecting a fan for the test rig, a range of system operating points was determined from the geometries of rotor-stator gap and rotor ducts as described in section 7.3. Pressure requirements for the corresponding flow rates in the ventilation system were calculated based on the empirical pressure loss coefficients. For stationary losses, the coefficients can be found in Chapter 5. However, for rotational losses, the loss coefficients obtained using the CFD method in Chapter 6 were applied. The fan selected is a centrifugal fan (K-28-S) manufactured by B.O.B. Stevenson Ltd. At ambient temperature and fan speed of 2850 rpm, the fan is capable of providing a flow rate of 0.094 m^3/s (i.e. 200 c.f.m) at its operating pressure of 2000 Pa (i.e. 8 inches of water column), see Appendix I for the fan performance curve from the original prototype. In order to respond to testing pressure requirements, the fan is driven by means of a CFW080073 inverter to control the fan speed and operated in accordance with the universal fan laws concerning fan speed, flow rate, pressure and power.

The fan has a square cross-sectional outlet (76 mm × 76 mm), which is smaller than the fan outlet tube of inner diameter of 190 mm. An expansion adaptor was fitted in the transition section as a diffuser to eliminate undesirable effects of adverse pressure gradient and flow separation. The length of the expansion adaptor meets the criteria of expansion factor in accordance with the British standard BS 848-1 [1997] as follows:

$$\frac{A_D}{N \times A_{fan}} \leq 1.07 \tag{7.8}$$

where A_{fan} is the fan outlet area and A_D is the fan outlet tube cross-sectional area respectively. N is used to indicate the number of fan outlet tube inner diameter, namely D, required for the adaptor length. As expansion factor of 1.07 is adopted, N is equal to 4.58, which is approximately equivalent to 870 mm.

7.6 Flow Measurement

In this section, the flow meters are reviewed for the determination of the most suitable flow meter for the measurement of air flow rate through the experimental

test rig. The selected flow meter must provide accurate flow measurement, ease to be operated, inexpensive, fit well with the test rig and testing conditions.

Rotating sensors: Rotating sensor is a simple mechanical device. The velocity of fluid motion is directly proportional to the rotational speed of the sensor. As a result, the axis of the rotating sensor must be aligned parallel or perpendicular to the direction of the flow, depending on the types of rotating sensor. Calibration is needed. These sensors are relatively large and their measurements are less accurate.

Pitot-static tube: A pitot-static tube is a pressure measurement instrument which measures local fluid flow velocity by means of a pressure difference. The working principal of a pitot-static tube is based on the Bernoulli equation. It consists of a hole pointing directly to the fluid flow to measure the stagnation pressure (i.e. total pressure) and some holes located on the side wall to measure the static pressure. Therefore, it needs to be connected to a pressure sensor to compute the velocity at a given point in the flow stream. This instrument can provide accurate measurement, but it must be aligned parallel with the flow direction to avoid misalignment error.

Hot-wire and hot-film anemometers: A hot-wire anemometer normally consists of a very fine wire which is electrically heated. The gas passing across the heated wire can remove the heat and influence the electrical resistance of the wire because the resistance is temperature dependent. Hence, the relationship between the wire resistance and the flow velocity can be used to determine the flow velocity at a given point. Calibration is necessary for measurement accuracy. Since hot-wire anemometer has high frequency-response, it is suitable to measure a rapidly fluctuating flow. Hot-wire anemometer is not suitable for liquid flow measurement because of the fine wire; an alternative for liquid flow measurement is hot-film anemometer.

Particle image velocimeter (PIV): PIV is an apparatus based on optical method to track the movement of tracer particles in fluid motion. Hence, the fluid needs to be seeded with sufficiently small tracer particles and these particles must be able to follow the flow of being studied. PIV can provide high quality two-dimensional or three-dimensional velocity field. PIV apparatus consists of a series of integrated devices and they are very expensive.

Laser Doppler anemometer (LDA): LDA is an apparatus detecting the Doppler shift in a laser beam to measure the flow velocity of fluid particles passing through a measuring volume. It must be worked with scattering particles in the fluid. Therefore, scatterers may have to be seeded in certain fluids. It gives very high spatial resolution of a flow field. However, the cost of this method is also very expensive.

Pressure differential devices: Pressure differential devices are widely used for volume-flow measurement. The principal of the measurement method is based on the installation of a pressure differential device into a pipeline. The pressure differential device is treated as a flow obstruction causes a static pressure difference between the upstream side and downstream side of the obstruction. Based on the Bernoulli's equation, continuity equation and device calibration, the volumetric flow rate can be calculated using equation (7.9) from the measured value of pressure difference, the knowledge of the flow characteristics and the type of pressure differential device is being used.

$$Q = \alpha\epsilon\frac{\pi}{4}d'^2\sqrt{\frac{2\Delta p}{\rho}}, \qquad \alpha = \frac{C}{\sqrt{1-\beta^4}} \tag{7.9}$$

where C is the discharge coefficient and β is the diameter ratio (i.e. throat diameter of an orifice (d') to downstream pipe inner diameter). The flow rate coefficients (α), expansibility factor (ϵ), and their corresponding predictable uncertainty limits are specified in ISO 5167-1 [2003]. The pressure differential devices must be manufactured geometrically similar to the one on which calibration has been carried out. The common pressure differential devices are as following:

i. **Orifice meter**: Orifice meter is a plate with a hole, which can be concentric, eccentric or segmental. It is installed in a pipe at a plane perpendicular to the pipe axis to create a pressure difference. The calibration has been mostly carried out for orifice meter with D and $D/2$ tapping, with corner tappings and with flange tappings. Compared with venturi tube and flow nozzle, the pressure loss caused by orifice meter is the highest. But, the construction cost of an orifice meter is very low.

ii. **Venturi tube**: A standard venturi tube consists of three sections: a smooth rounded entrance, a straight throat and a conical expansion. The pressure difference is measured before the venturi effect and at the throat. The fluid velocity increases as it passes through the throat. The gradual change of flow cross-sectional area gives less pressure loss when compared with the orifice meter. However, the cost of a venturi tube is much more expensive than an orifice meter.

iii. **Flow nozzle**: A flow nozzle basically maintains the first half section of a venturi tube, but the inlet of the flow nozzle can be either elliptical, quadrant or conical. The nozzle with smooth rounded entrance convergence gives discharge coefficient near unity. However, the pressure loss is still large because the diffuser section is not provided for gradual expansion. The cost of a flow nozzle is moderate.

7.6.1 Inlet Orifice Meter

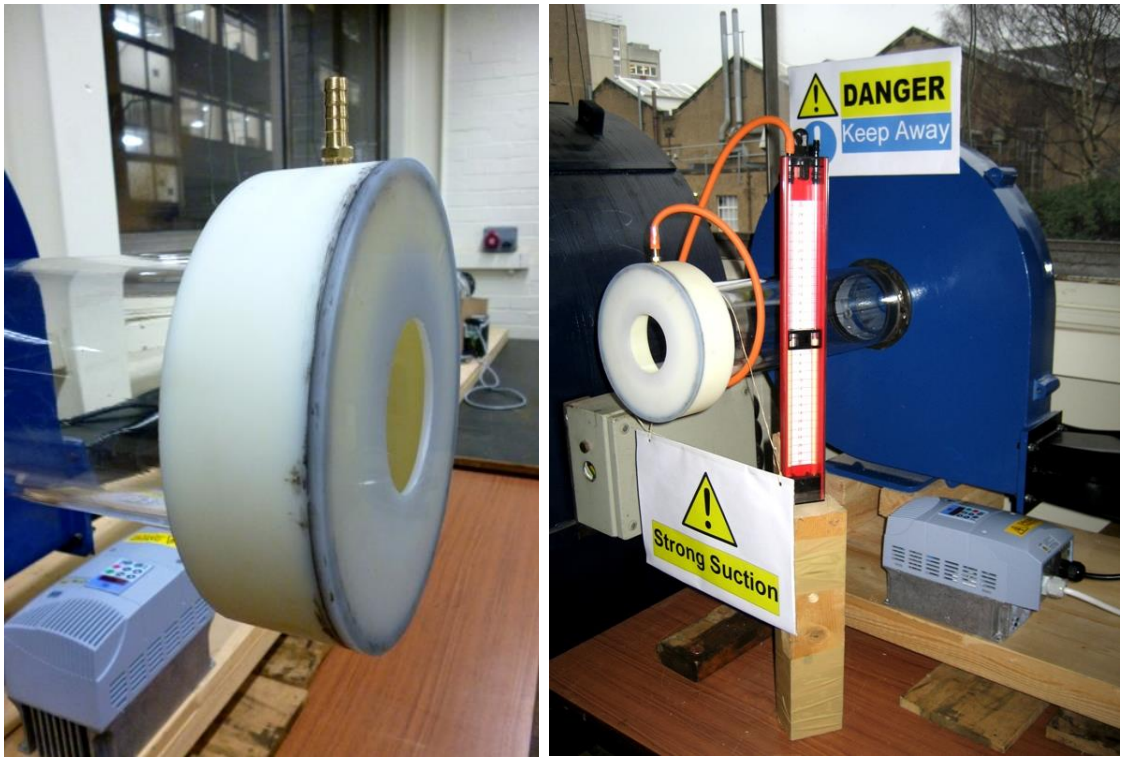

Figure 7.13 Inlet orifice meter with corner tap

Based upon the review of flow meters, an inlet orifice meter was selected because the advantages of using inlet orifice with corner tap are as follows:

- Orifice meter provides volumetric flow rate measurement, rather than local flow velocity measurement.
- Orifice plate is cheap and easy to manufacture. The size is rather flexible to fit the fan inlet.
- Orifice meter provides accurate measurement because the uncertainties that providing a level of confidence of approximately 95 % are given.
- A volumetric flow rate can be calculated directly from a measured pressure difference because the flow rate coefficient (α) is independent of β and is constant and equal to 0.6. In contrast, the flow rate coefficients of certain orifice meter are *Re* dependent, which is itself dependent and hence iteration computation procedure is required.
- Unlike an in-duct orifice meter installed between upstream and downstream pipes of the same diameter, the upstream pipe is deliberately omitted for an inlet orifice. This significantly reduces the overall size and cost of the test rig.

The geometric design, installation and conditions of use of the inlet orifice meter strictly follow the standard specified in BS 848-1 [1997]. It was installed at the inlet of the test rig connected to a centrifugal fan through an Acrylic circular tube of inner diameter of 112 mm. The throat diameter of the orifice meter is 66.6 mm, which gives the diameter ratio (β) of 0.595. The external diameter of the orifice plate is 180 mm (which is more than 1.05 times of inlet pipe inner diameter). The orifice plate is made of PVC.

The difference between atmospheric pressure and pressure right after the orifice plate (Δp) was measured through a piezometer carrier ring with a single pressure tapping connected to a pressure sensor or a manometer as illustrated in Figure 7.13. The carrier ring is made of nylon and manufactured in accordance with geometric requirements as specified in BS 848-1 [1997]. The distance between the orifice plate and fan inlet is more than 3.5 times of connecting tube diameter to eliminate the undesired fan disturbance on the pressure profile in the orifice metering system.

7.7 Flow Conditioning

In fan outlet section, a flow conditioner was installed at a distance of one tube inner diameter (*D*) behind the expansion adaptor. The chosen flow conditioner is the NEL (Spearman) flow conditioner. It has three different sizes of holes on different pitch-circular diameters on a perforated plate. Their dimensions are relative to the tube inner diameter as specified in BS 848-1 [1997]. The perforated plate thickness is 0.12*D*. The use of this unpatented NEL (Spearman) flow conditioner significantly reduces the tube length required for a flow to achieved fully developed condition. Therefore, this gives a reduction in the overall cost and space required for the test rig. Besides, this flow conditioner is easy to manufacture and install compared with many others. Its performance was demonstrated in Spearman et al. [1996]. Based on this, the distance between the flow conditioner and the front bearing mounting plate was set to be 4*D*. This length would be enough for a flow to achieve a nearly fully developed condition. According to ISO 5167-1 [2003], without flow conditioners, a completely fully developed flow may take over 100*D*.

The other main reason of installing the flow conditioner is to remove the swirl that might be introduced by the fan which may affect the level of accuracy of pressure measurement at the downstream. As the air flow velocity profile is redistributed to a condition close to fully developed flow, flow rate determination using Pitot-static tube traverse can be performed in accordance with the British standard BS 848-1 [1997] to calibrate the flow rate determination using inlet orifice meter. The calibration of the inlet orifice meter can be found in the next section. The velocity profiles after the flow conditioner are compared with the 1/7 power law velocity profile as it gives a good general description of the fully developed turbulent velocity profile, White [1986]. The local velocities were normalised with the mean velocity. Figure 7.14 shows that the dimensionless velocity profiles from 2*D* onwards achieving a condition close to fully developed flow.

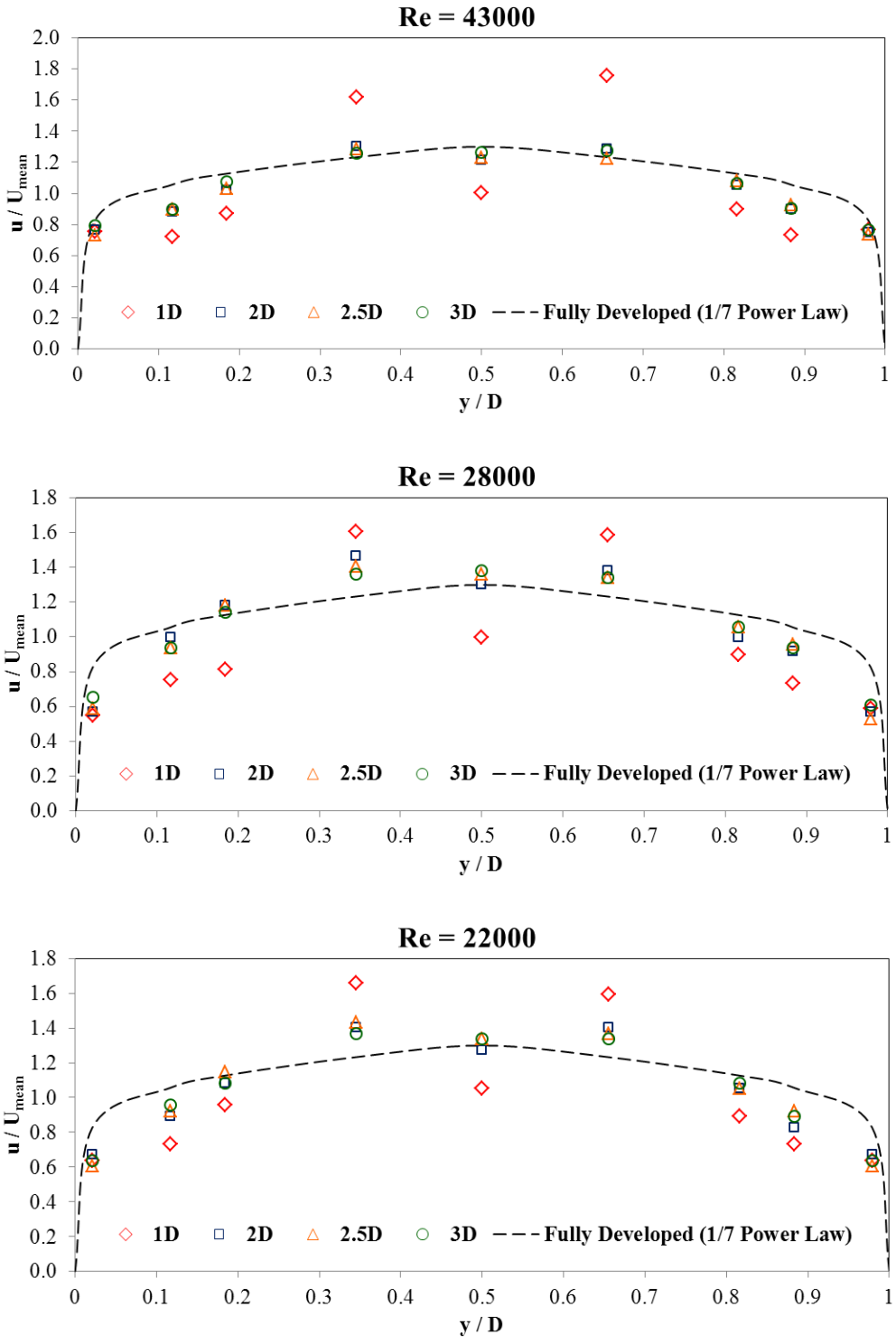

Figure 7.14: Velocity profiles downstream of the NEL (Spearman) flow conditioner

7.7.1 Calibration of inlet orifice meter

By measuring the pressure drop across the inlet orifice, the flow rate through the test rig can be computed using equation (7.9). In equation (7.9), expansibility factor (ϵ) is used to take into account the compressibility of the air. Here, ϵ only depends on the pressure ratio and the isentropic exponent, which is given by:

$$\epsilon = 1 - 0.41\frac{\Delta p}{\kappa p_a}, \qquad \text{valid for } \frac{\Delta p}{p_a} \leq 0.25 \tag{7.10}$$

where κ is the isentropic exponent and is equal to 1.4 for atmospheric air. p_a is the ambient atmospheric absolute pressure. As the operating range of the inlet orifice pressure drop is less than 2000 Pa, ϵ is about unity.

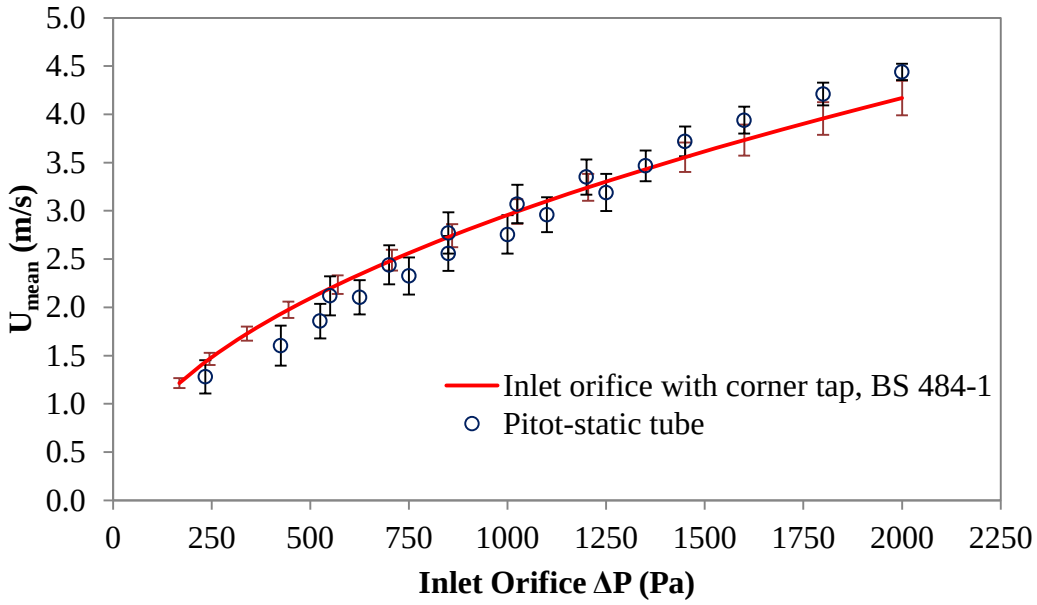

Figure 7.15: Mean air velocity in the fan downstream tube of inner diameter of 190 mm against inlet orifice pressure drop

The flow rate obtained using the inlet orifice is then compared with the mean velocity determined from traverse measurements using Pitot-static tube. The traverse measurements were conducted in accordance with the radial positions as specified in BS 848-1 [1997]. As the Pitot-static tube traverse needs to be performed in a fully developed flow condition, the measurements were taken at three tube diameters behind the flow conditioner as shown in Figure 7.16. However, as shown in Figure 7.14, the flow condition at three tube diameters behind the flow conditioner achieves

only a condition close to fully developed flow condition. Therefore, as indicated by the error bars in Figure 7.15, the level of accuracy of flow rate measurement using Pitot-static tube is low but it is sufficient to check the accuracy of inlet orifice meter. The vertical error bars of measurements using inlet orifice are due to systematic errors. The vertical error bars of measurements using Pitot-static tube are caused by the random errors as detailed in Section 7.10.

Figure 7.15 shows the variation of mean air velocity in the fan outlet tube obtained using the inlet orifice and Pitot-static tube traverse with the inlet orifice pressure drop. A good agreement between these two methods confirmed the validity of the setup of the inlet orifice with corner tap in accurately predicting the volumetric flow rate for the range of the measured flow rate.

7.8 Pressure Measurement

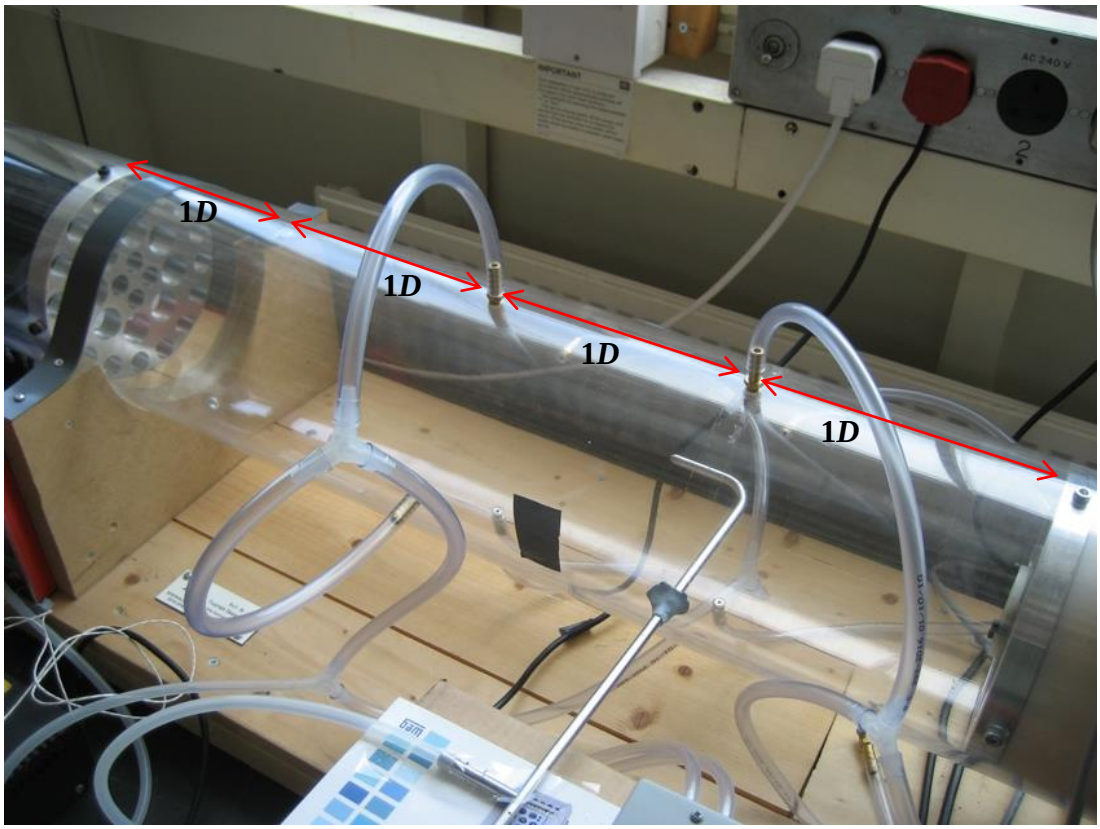

Figure 7.16: Positions of pressure tappings and Pitot-static tube traverse at the downstream of the flow conditioner

In the fan outlet tube, a total of 12 pressure tapping holes were drilled at cross section planes of distance of 1*D*, 2*D* and 3*D* from the flow conditioner. *D* is the fan outlet tube inner diameter. On each cross section plane, four pressure tapping holes are arranged at 90° intervals as shown in Figure 7.16. The static pressure at each cross section plane was measured from four pressure tappings that were connected together in a "triple-T" arrangement. As the static pressure measurement is required to make under developed flow condition, it was conducted at 3*D* unless otherwise specified. The pressure measurements were conducted using an Omega PX277-05D5V differential pressure transducer. Besides pressure measurement, the pressure tapping holes were also used for the Pitot-static tube traverse.

7.9 Temperature Measurement

Because of the quick response of thermocouple to temperature changes, thermocouples were used to monitor the temperature difference between the ambient and air temperature at the outlet. Besides, the measured temperature was used to compute for temperature-dependent air properties for the analysis of system flow resistance.

7.10 Measurement Uncertainties

7.10.1 Systematic errors

Systematic errors come from inherent defects in the equipment or method, and will be repeatable, Bruce [2011].

7.10.1.1 Volumetric flow rate

As equation (7.9) was used to compute the volumetric flow rate obtained, the relative error is given by the following equation:

$$\frac{\delta Q}{Q} = \sqrt{\left(\frac{\delta\alpha}{\alpha}\right)^2 + \left(\frac{\delta\epsilon}{\epsilon}\right)^2 + 4\left(\frac{\delta d'}{d'}\right)^2 + \frac{1}{4}\left(\frac{\delta\Delta p}{\Delta p}\right)^2 + \frac{1}{4}\left(\frac{\delta\rho}{\rho}\right)^2} \qquad (7.11)$$

Since the inlet orifice meter was built, installed and operated in accordance with the BS 848-1, the uncertainty of α and ϵ are given, which are 1.5 % and 0.2 % for Δp of 2000 Pa respectively. The manufacturing tolerance of throat diameter of the orifice

(d') is 2% for the worst case. Δp is measured using a pressure transducer of having an uncertainty of 1 %. Therefore, the uncertainty of flow rate is ± 4.3 %.

The equation (7.11) can also be used to determine the uncertainty of flow rate using Pitot-static tube due to the systematic errors. Based upon the BS 848-1, the uncertainty of α and ϵ are 2.0 % and 0.2 % respectively. Here, the throat diameter of the orifice (d') is replaced with the fan outlet tube inner diameter (D) with the tolerance of 0.2 %. Δp is measured using a pressure transducer of having an uncertainty of 1 %. Therefore, the systematic errors result in uncertainty of ± 2.1 %.

7.10.1.2 Static pressure

When using the manometer, the measurement uncertainty is ± 25 Pa based on half the smallest scale division of the manometer. As manometer measurement error is relatively large, the pressure transducer was mostly used, especially for low pressure measurements.

7.10.2 Random errors

Random errors are statistical fluctuations in the measured data due to extraneous influences in measurement, which cannot be controlled or removed. Since the random errors often have a Gaussian normal distribution, they are commonly evaluated using the standard deviation and can be determined by averaging over a large number of measurements, Taylor [1997]. Thus, the random uncertainties were calculated by taking N measurements in succession and then calculating the mean as follows:

$$\bar{x} = \frac{1}{N}\sum_{i=1}^{N} x_i \tag{7.12}$$

For the sample standard deviation as follows:

$$\sigma = \sqrt{\frac{1}{N-1}\sum_{i=1}^{N}(x_i - \bar{x})^2} \tag{7.13}$$

For the standard deviation of the mean as follows:

$$\sigma_{\bar{x}} = \frac{\sigma}{\sqrt{N}} \tag{7.14}$$

For lamination surface roughness, the total number of measurements, *N* is 45. Thus, $\bar{x}$, σ and $\sigma_{\bar{x}}$ of the lamination surface roughness are 17.6 μm, 13.6 μm and 2.0 μm respectively. Hence, 17.6 ± 4 μm gives a 95% confidence interval for the proportion in the measurements.

In the calibration process of the flow rate measurement by means of Pitot-static tube, besides the systematic errors, the uncertainty was found to be strongly affected by the error arisen from the flow condition (not fully developed flow) within the fan outlet tube, the error arisen from the misalignment of Pitot-static tube beyond ± 2° limit and the error arisen from inaccurate position of Pitot-static tube at the required measurement locations. These errors attribute to the random errors. Therefore, the analysis of standard deviation is performed. The $\bar{x}$, σ and $\sigma_{\bar{x}}$ of each mean air velocity in the fan outlet tube are calculated. For instance, at inlet orifice measured pressure of 425 Pa, 1.63 ± 0.21 m/s gives a 95% confidence interval as shown in Figure 7.15.

8 Experimental Results of Pressure Loss and Flow Resistance in a Rotor-Stator System

The design and setup of the experimental apparatus for the investigation of rotational pressure losses have been described in Chapter 7. In this Chapter, the comparison between experimental, analytical and CFD results of pressure loss and flow distribution under the effects of rotation is presented. The pressure measurement was conducted three tube inner diameters behind the flow conditioner, under fully developed condition. This corresponds to Plane 3 in Figure 8.1. The measured pressure at Plane 3 reflects the total pressure drop of the test section because the test rig outlet was opened to the atmosphere. Based on fan engineering practice, the measured flow rate using the inlet orifice meter and the pressure at Plane 3 were used to plot for the flow resistance curve of rotor-stator system.

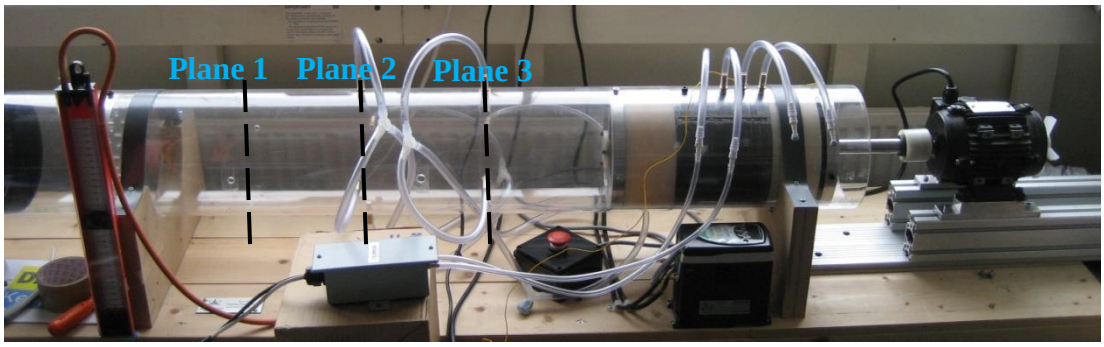

Figure 8.1: Pressure measured at Plane 3 for pressure requirement of the test section

Based upon the Idelchik's quote given in Chapter 5, the pressure losses in the test section are intrinsically inseparable. However, they can be separated using the flow network analysis method. In Figure 8.2, the flow network constructed using the Flow Library corresponds to the ventilation design of the test rig. Therefore, the experimental results were used to verify the system pressure loss for stationary cases and then for rotating cases because all flow components specified in the flow network have the same geometric dimensions and operating condition as those of the experimental test rig. For instance, the friction factor in the airgap and rotor ducts is determined from the measured surface roughness. Consequently, the flow network analysis method can be used to characterise the system pressure loss in detail and to indicate how rotation increases the system flow resistance. Besides, the flow

distribution between the airgap and rotor ducts can be determined experimentally. This can further validate the flow network analysis method in predicting the flow distribution.

It is important to note that no significant temperature difference between the ambient and the air at the outlet was found, less than 2 °C. Therefore, the assumptions of incompressibility and constant fluid properties are acceptable for this research.

8.1 Stationary Tests

The stationary pressure losses from the Plane 3 to the outlet of the test rig can be calculated using the analytical air flow modelling tool presented in Chapter 5. However, the pressure drop caused by the bearing housing in the experimental apparatus is not known. It needs to be determined separately and incorporated into the air flow modelling tool.

As the pressure drop caused by the bearing housing is comparatively too low for the measured flow rates, it was difficult to obtain the loss coefficient accurately using the experimental method. Therefore, the loss coefficient was obtained using the CFD methods under fully developed flow condition. Two different models were simulated. One was modelled with the bearing housing, but the other was modelled without the bearing housing in the same pipeline. As shown in Figure 8.3, the pressure requirement for the case with the bearing housing is apparently higher, which is 11.8 Pa compared to 5.77 Pa for inlet flow rate of 0.05 m^3/s. Hence, the loss coefficient can be determined by dividing the additional total pressure loss due to the bearing housing with the flow kinetic energy in accordance with equation (5.4). By using three kinds of turbulence models (e.g. Realizable k-ε, SST (Menter) k-ω and Reynolds Stress Transport), they simulated a very similar value for the loss coefficient of the bearing housing, which is approximately equal to 2.5.

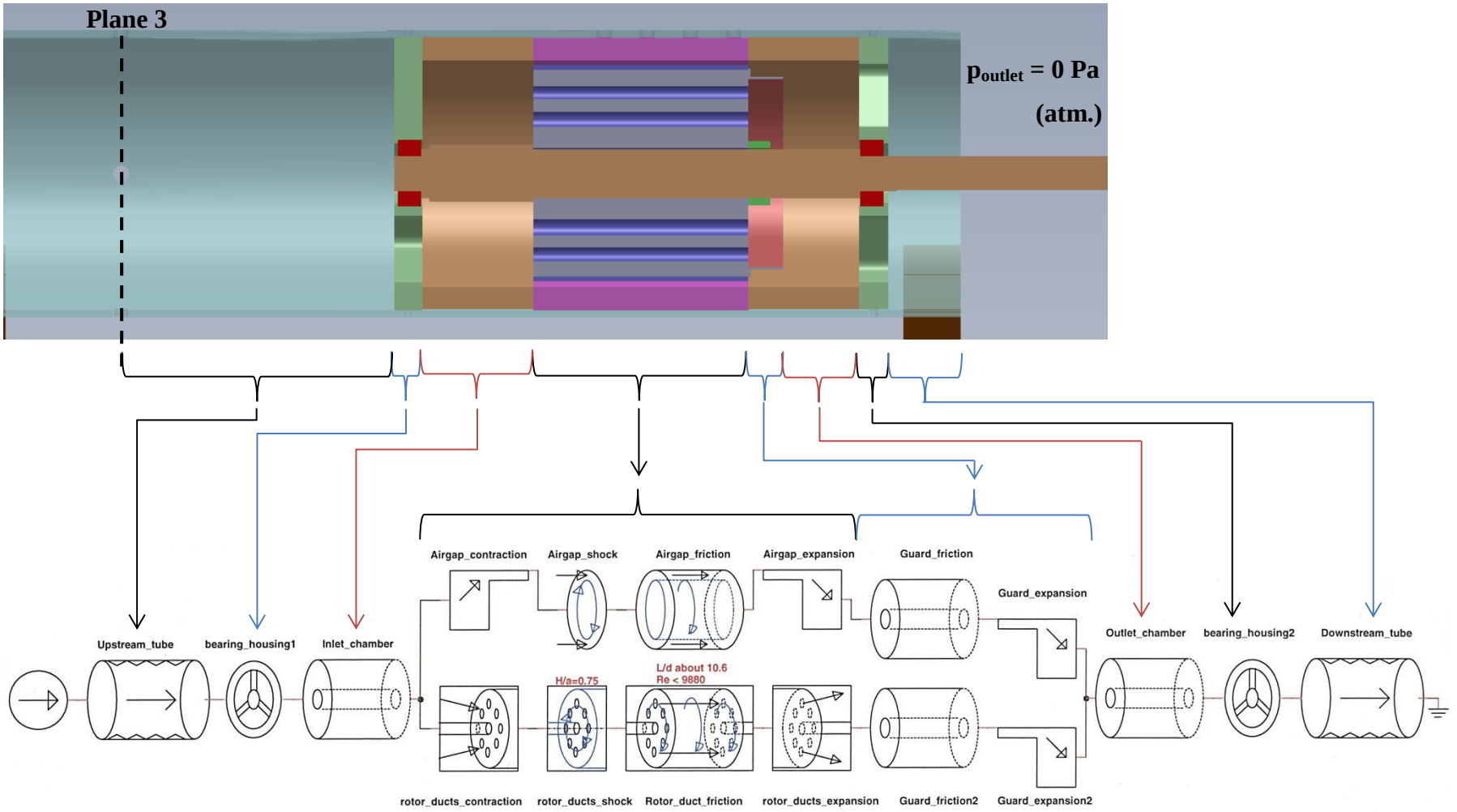

Figure 8.2: Equivalent flow network of experimental test rig using PORTUNUS Flow Library

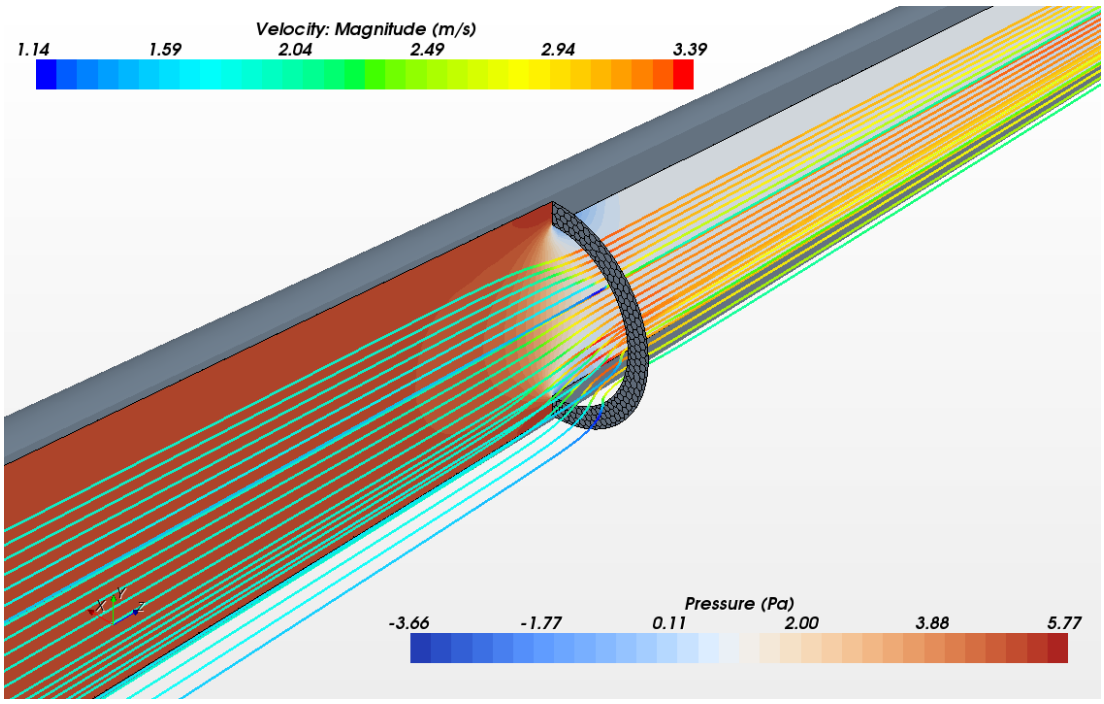

(a) Without bearing housing

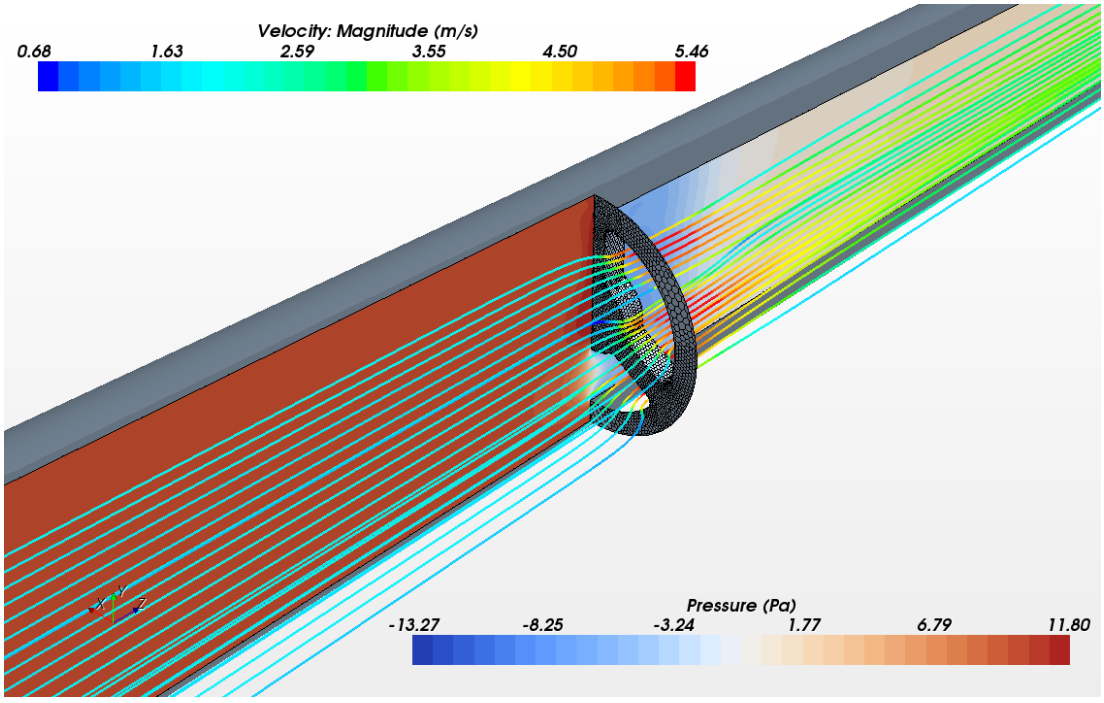

(b) With bearing housing

Figure 8.3: Streamlines and pressure distribution of air within the pipeline

8.2 Stationary Tests with Airgap only

In this section, the pressure losses for the cases with only the airgap are investigated. All the rotor ducts in the rotor were blocked. The experiments were conducted with and without the flow guard. The purpose of the flow guard is already described in Chapter 6. It was fitted at the rear end of rotor and positioned between the annulus and rotor ducts radially to prevent the outflow from rotor ducts interfering with the outflow from annular gap. Figure 8.4 shows the relationship of the air flow rate passing through the test rig and the pressure drop from the Plane 3 to the outlet of the test rig, the system curves of ventilation without flow guard overlap with the system curves of ventilation with flow guard. Apparently, the pressure losses of the airgap with and without flow guard always coincide. Therefore, for the air flow rate from 0.013 m^3/s to 0.040 m^3/s, it can be concluded that the existence of the flow guard has negligible impact on the flow rate passing through the airgap. Furthermore, the experimental measurements for ventilation of airgap with and without flow guard were repeatable as illustrated in Figure 8.4. Due to the consistency of the experimental results, the relationship between the air flow rate and the stationary pressure loss from the Plane 3 to the outlet can be expressed as:

For airgap without flow guard,

$$\Delta p_s = 276392Q^2 + 2229.7Q \tag{8.1}$$

For airgap with flow guard,

$$\Delta p_s = 286087Q^2 + 1201.8Q \tag{8.2}$$

where Q is the inlet flow rate. As the airgap is the only flow path in the rotor-stator system, the airgap flow rate is equal to the inlet flow rate. Equation (8.1) and (8.2) have different coefficients for Q and Q^2. Nevertheless, these two equations will provide similar magnitude of stationary loss as shown in Figure 8.4. These equations were used in Section 8.5 to separate the stationary pressure loss from rotational pressure loss.

In theory, flow is induced by a differential pressure. Therefore, the airgap flow rate as a function of the measured pressure at Plane 3 can be derived from the

experimental results by making the Δp_3 as a variable and Q_{airgap} is a dependence of Δp_3 in the following equation.

$$Q_{airgap} = 7.6 \times 10^{-3} + 8.8 \times 10^{-5}\Delta p_3 - 5.2 \times 10^{-8}(\Delta p_3)^2 \qquad (8.3)$$

In order to obtain a good fitting for the experimental data, the relation is applicable for Δp_3 from 78 Pa to 524 Pa. This equation was used in Section 8.3 to isolate the flow rate in the airgap from the measured inlet flow rate for the case with rotor ducts unblocked.

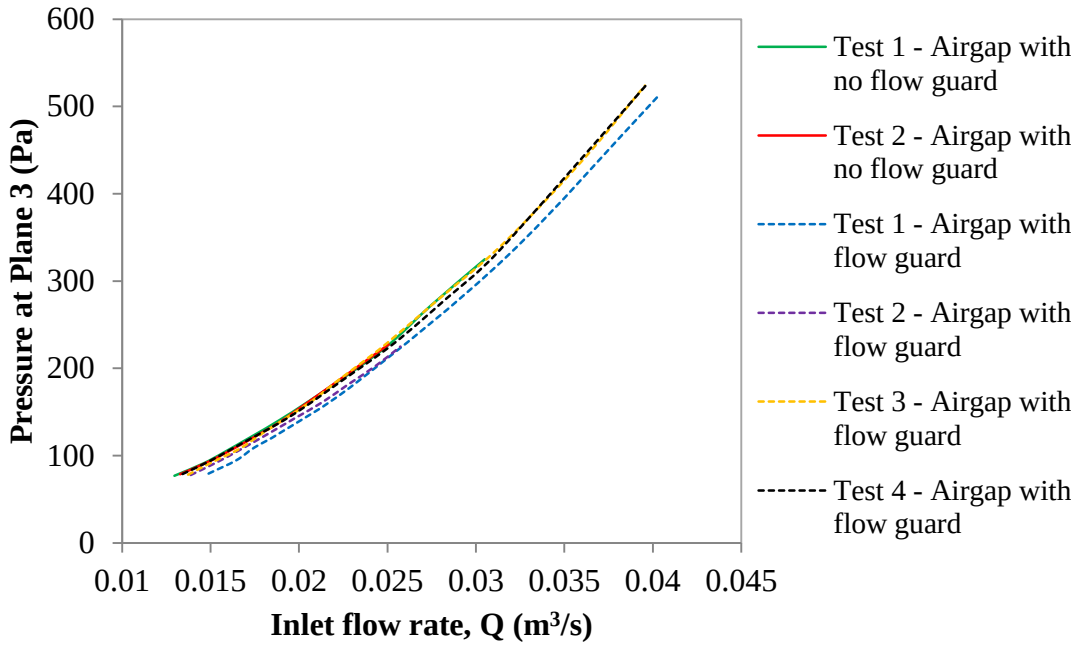

Figure 8.4: System flow resistance curves of ventilation of airgap with and without flow guard for stationary cases

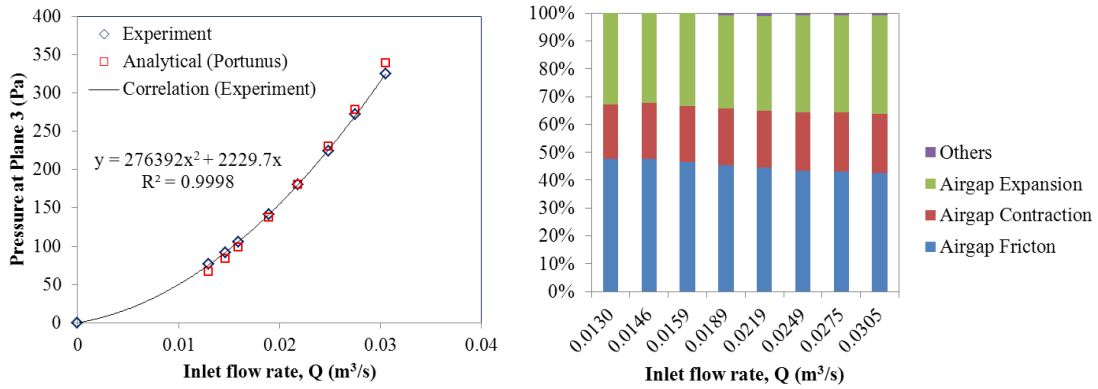

(a) Test 1 without flow guard

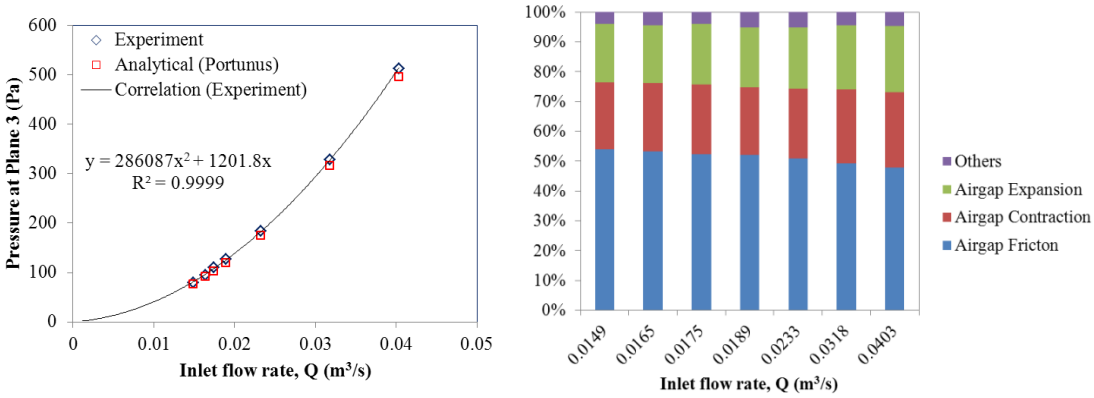

(b) Test 1 with flow guard

Figure 8.5: Pressure drop from the Plane 3 to the outlet versus inlet flow rate for stationary cases of ventilation with airgap only (left) and the contribution of pressure loss components determined using Portunus flow network analysis (right)

The comparison between the experimental results and the values predicted using the analytical flow network analysis is shown on the left hand side of the Figure 8.5 for the case of airgap without flow guard (a) and for the case of airgap with flow guard (b) demonstrates that the flow network analysis is capable of predicting stationary pressure losses for the flow passing through the airgap for a given flow rate. The equivalent flow networks constructed using the Flow Library for the ventilation system of airgap with and without flow guard can be found in Appendix J. Using the flow network analysis, the right hand side of Figure 8.5 indicates the contribution of pressure loss components in percentage from the Plane 3 to the outlet of the test rig. According to the Darcy-Weisbach equation, the pressure drop in a pipe is directly proportional to the square of local flow velocity. As the airgap is the only flow path in the rotor-stator system, the air velocity in the airgap is relatively high compared to other sections from the Plane 3 to the outlet because of small cross-sectional area. Therefore, for the case of airgap without flow guard, approximately 99% of the total pressure loss is caused by contraction, friction and expansion at the airgap. The pressure loss coefficients of contraction and expansion are only geometric dependence. However, for increases in inlet flow rate, the friction pressure loss reduces in terms of percentage because the friction factor of turbulent flow decreases with the increases in *Re* and asymptotically approaches the value for complete

turbulent flow for a given relative roughness according to the Moody chart. Hence, both contraction and expansion losses take the percentage of friction loss.

The existence of the flow guard increases the ratio of cross-sectional area before and after the sudden expansion at the airgap and hence gives lower airgap expansion loss, when compared to the case without the flow guard. However, the loss reduction at the airgap is compensated by the additional friction and expansion losses at the flow guard. Others in the Figure 8.5 consist of pressure losses in bearing housings, friction losses in upstream tube, inlet chamber, outlet chamber and downstream tube for the case of airgap without flow guard, but additional friction and expansion losses at the flow guard for the case of airgap with flow guard.

8.3 Stationary Tests with Rotor Ducts and Airgap

For the stationary tests with rotor ducts and airgap, the annular gap size of 4 mm and flow guard were remained in the test section. The experiments were preceded with rotor ducts unblocked. Figure 7.3 illustrates all the duct holes available in the rotor. In order to distinguish the pressure drop of the ventilation system with specific configuration of rotor ducts as shown in Table 7.1, the following naming system is used:

xx *D*xx *PCD*xx

The number in front of the letter '*D*' indicates the number of unblocked rotor duct. The letter '*D*' stands for the diameter of unblocked rotor ducts and hence the number beside the letter is the value of the duct diameter. The letters '*PCD*' stand for the pitch-circular-diameter of those ducts that are unblocked followed by the value of pitch-circular-diameter for those ducts.

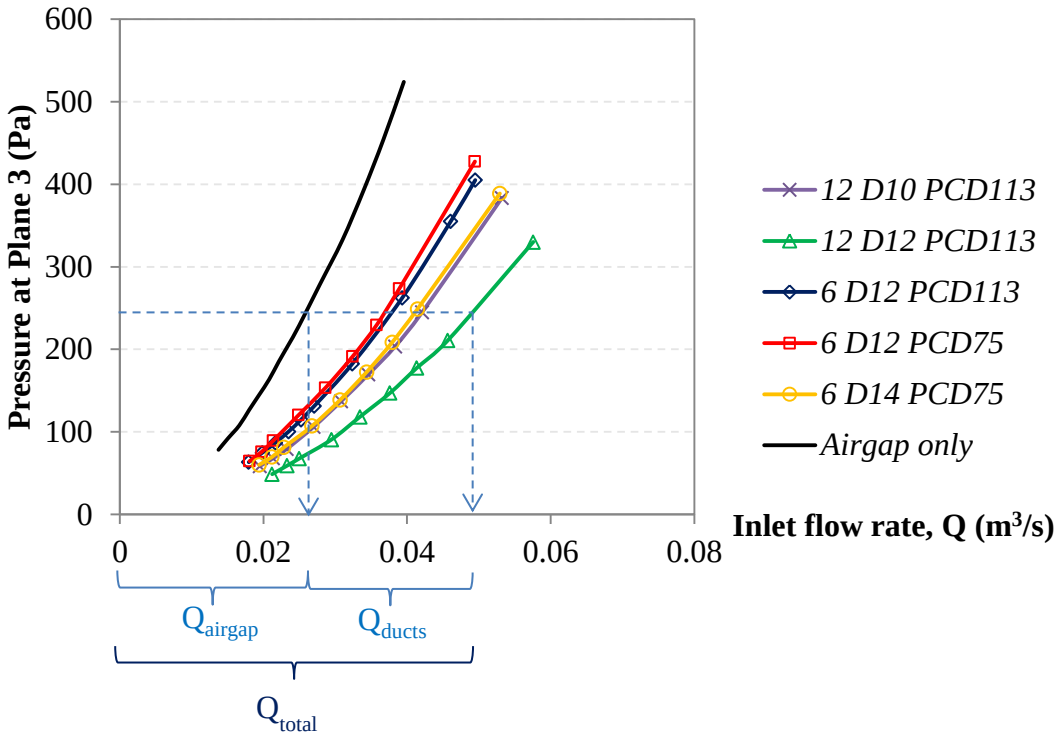

(a) Tests with flow guard

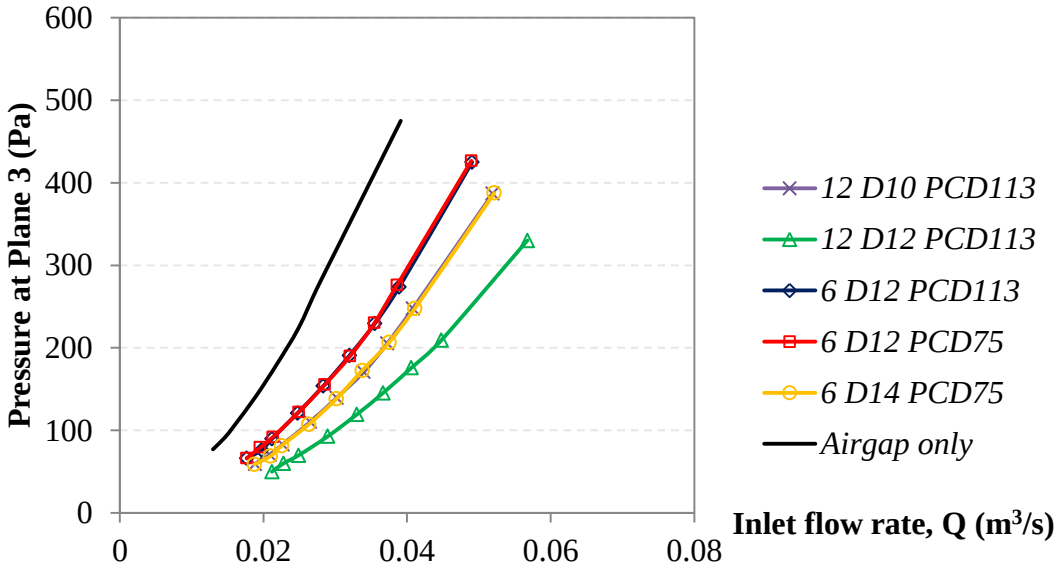

(b) Tests without flow guard

Figure 8.6: System flow resistance curves of ventilation with rotor ducts and airgap for stationary cases

Figure 8.6 shows the system flow resistance curves of ventilation with rotor ducts unblocked. The system curve of ventilation with airgap only is also plotted (i.e. black line). The existence of rotor ducts considerably reduces the flow resistance of the ventilation system. The experimental results demonstrate that the number of rotor ducts and duct size play essential roles in reducing system pressure drop by means of bigger flow cross section area. The comparison between *6 D12 PCD113* and *6 D12 PCD75* demonstrates that the duct *PCD* has no significant influence to the stationary losses. It is interesting to note that *12 D10 PCD113* and *6 D14 PCD75* of having total cross section area of 942 mm^2 and 924 mm^2 respectively give the similar pressure drop. Figure 8.6 shows that ventilation with and without flow guard give the similar system pressure loss.

As the measured values of the flow rate is the total flow rate (Q_{total}) passing through the inlet of the test rig, the flow rate passing through the rotor ducts (Q_{ducts}) can be determined by subtracting the airgap flow rate (Q_{airgap}) from the measured flow rate. In fluid mechanics, the pressure loss between the junctions is the same for each flow path, no matter which flow path the flow is followed. As the information of the obtainable flow rate passing through the airgap for a given pressure is available in the previous section, equation (8.3) was used and hence Q_{airgap} can be computed by substituting the measured Δp_3 of ventilation with rotor ducts and airgap into equation (8.3). Thus, Q_{ducts} can be determined by getting the difference between the measured flow rate Q_{total} and the Q_{airgap} as illustrated in Figure 8.6: (blue-dashed line).

$$Q_{ducts} = Q_{total} - Q_{airgap} \tag{8.4}$$

The comparison between the experimental results and the values predicted using the analytical flow network analysis is shown in Figure 8.7(a) for the case of *6 D14 PCD75* with flow guard and Figure 8.7(b) for the case of *6 D14 PCD75* without flow guard. The comparison for the other cases can be found in Appendix K. The equivalent flow networks constructed using the Flow Library for the ventilation system with rotor ducts and airgap can be found in Appendix J. The flow network analysis assumes that the flow rate passing through the rotor ducts is evenly distributed into each duct. The comparison demonstrates that the flow network

analysis is not only capable of predicting the stationary pressure requirements for the flow passing through the rotor ducts and airgap, but also capable of predicting the flow distribution between the rotor ducts and airgap for a variety of duct sizes and arrangements.

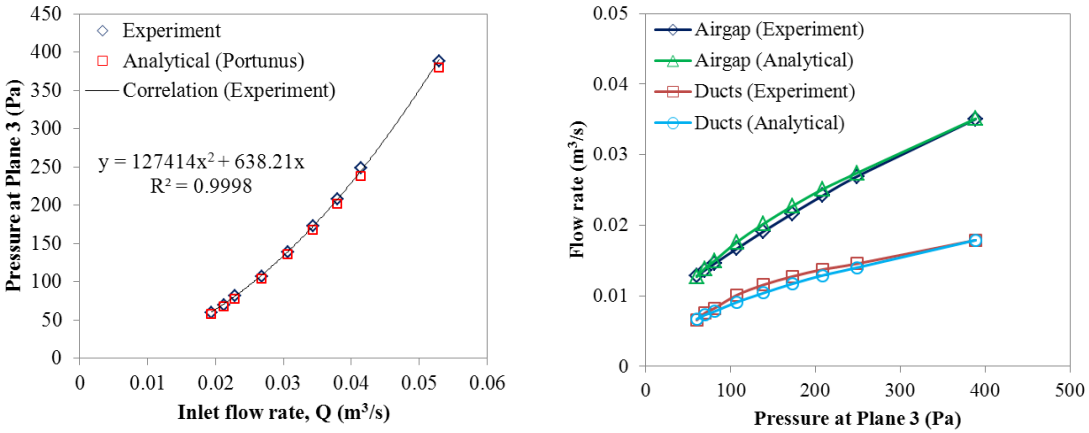

(a) *6 D14 PCD75* with flow guard

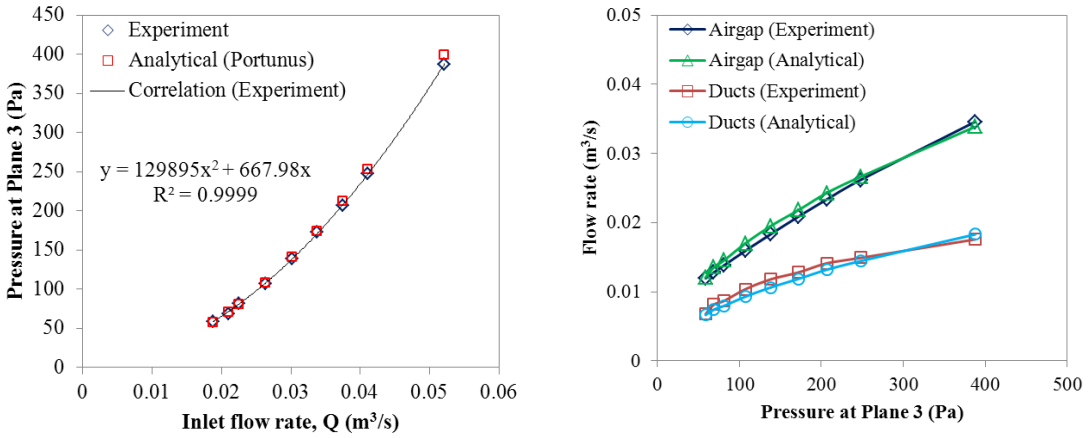

(b) *6 D14 PCD75* without flow guard

Figure 8.7: Pressure drop from the Plane 3 to the outlet versus inlet flow rate (left) and the flow distribution between rotor ducts and airgap (right)

Since the rotor ducts and airgap are in parallel, the pressure difference between the inlet and outlet chamber of the rotor ducts and airgap are theoretically the same. The experimentally validated flow networks were used to investigate the contribution of pressure loss components of the rotor ducts in percentage from the Plane 3 to the outlet of the test rig. The total pressure loss for the cases of rotor ducts and airgap in

Figure 8.8(a) and Figure 8.8(b) corresponds the pressure at Plane 3 for the given flow rate in Figure 8.7(a) and Figure 8.7(b) respectively.

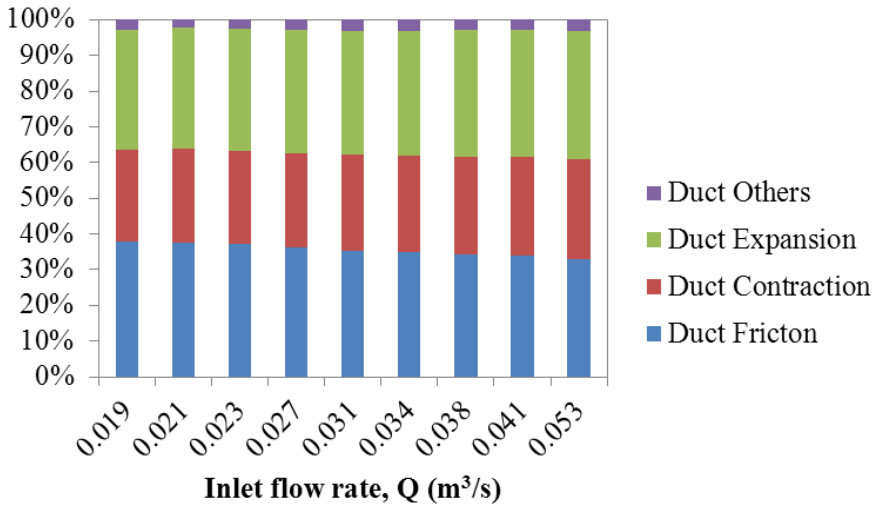

(a) *6 D14 PCD75* with flow guard

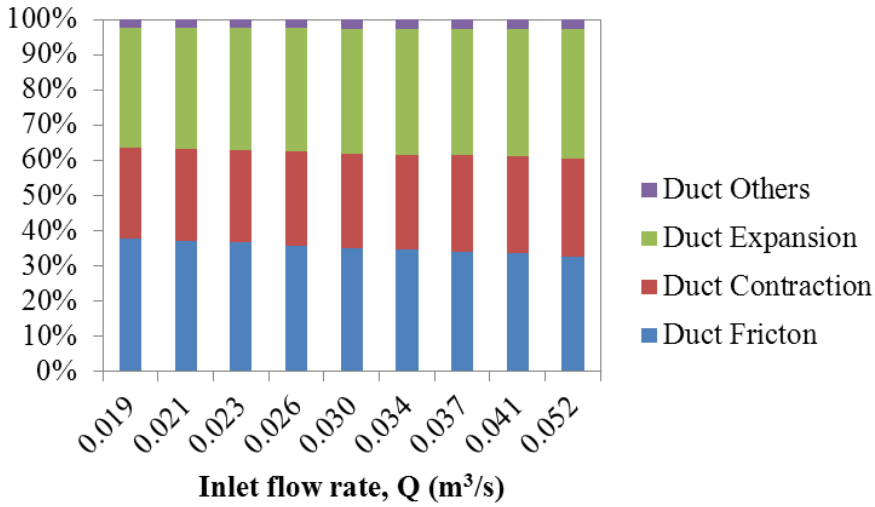

(b) *6 D14 PCD75* without flow guard

Figure 8.8: The contribution of pressure loss components of rotor ducts determined using Portunus flow network analysis

Similar to the case of airgap only, the pressure losses of contraction, friction and expansion of rotor ducts contribute to over 96 % of the total loss because the flow velocity in the duct is relatively high compared to other sections. Again, the pressure loss coefficients of contraction and expansion of the rotor ducts are mainly geometric dependence. Both contraction and expansion losses take the percentage of friction loss because the friction factor of turbulent flow decreases with the increases in *Re* as mentioned in the preceding section. "Duct Others" in Figure 8.8 consist of pressure

losses in bearing housings, friction losses in upstream tube, inlet chamber, outlet chamber and downstream tube, but additional friction and expansion losses at the flow guard for the case with flow guard.

As shown in Figure 8.8, the percentage contribution of pressure loss from "Duct Others" to the total loss is less than 4 %. In addition to that, the values of loss from "Ducts Others" for the cases with and without flow guard are similar. Therefore, for the testing conditions it can be concluded that the additional pressure loss caused by the flow guard to the flow from rotor ducts is negligible.

Due to the excellent agreement between the experimental and analytical results, the relationships between the inlet flow rate and pressure at Plane 3 can be derived from Figure 8.7 for the case of *6 D14 PCD75* and Appendix K for the other cases. The stationary loss as a function of inlet flow rate for various rotor duct configurations is as follows:

For tests with flow guard,

$$\text{For } 12\ D10\ PCD113,\ \Delta p_s = 125169Q^2 + 544.34Q \tag{8.5}$$

$$\text{For } 12\ D12\ PCD113,\ \Delta p_s = 93087Q^2 + 385.22Q \tag{8.6}$$

$$\text{For } 6\ D12\ PCD113,\ \Delta p_s = 149683Q^2 + 786.22Q \tag{8.7}$$

$$\text{For } 6\ D12\ PCD75,\ \Delta p_s = 159739Q^2 + 755.17Q \tag{8.8}$$

$$\text{For } 6\ D14\ PCD75,\ \Delta p_s = 127414Q^2 + 638.21Q \tag{8.9}$$

For tests without flow guard,

$$\text{For } 12\ D10\ PCD113,\ \Delta p_s = 130681Q^2 + 669.98Q \tag{8.10}$$

$$\text{For } 12\ D12\ PCD113,\ \Delta p_s = 94264Q^2 + 473.61Q \tag{8.11}$$

$$\text{For } 6\ D12\ PCD113,\ \Delta p_s = 158365Q^2 + 884.8Q \tag{8.12}$$

$$\text{For } 6\ D12\ PCD75,\ \Delta p_s = 159926Q^2 + 884.71Q \tag{8.13}$$

$$\text{For } 6\ D14\ PCD75,\ \Delta p_s = 129895Q^2 + 667.98Q \tag{8.14}$$

where is Q the inlet flow rate. These equations were used in Section 8.6 and Section 8.7 to separate the stationary and rotational pressure losses.

8.4 Summary for Stationary Tests

- The experimental study provided a better understanding of the effect of rotor duct configurations on the flow resistance of the ventilation system.
- A good agreement with the experimental results confirmed the validity of the equivalent flow network in accurately predicting the pressure requirements as well as the distribution of air between the ventilation passages under stationary condition.
- For the testing conditions, the pressure losses in the annular gap and rotor ducts contribute over 90 % of the total loss.

8.5 Rotational Tests with Airgap only

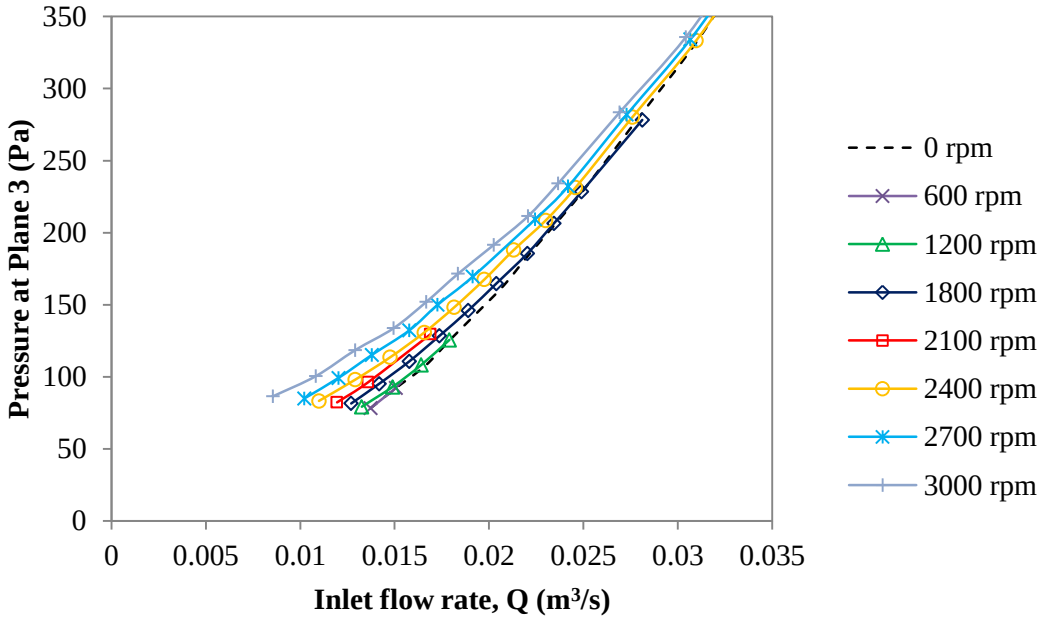

(a) Tests with flow guard

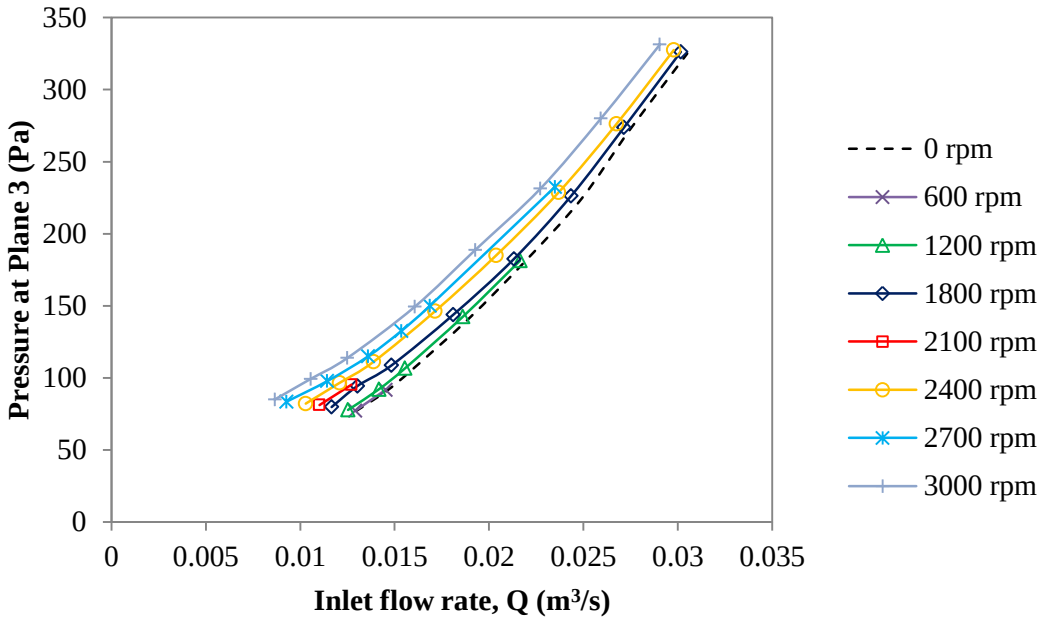

(b) Tests without flow guard

Figure 8.9: System flow resistance curves of ventilation with airgap for speed up to 3000 rpm

For rotating conditions, besides the stationary losses described in the preceding sections, the flow passing through the ventilation paths (e.g. airgap and rotor ducts) in the test rig suffers additional flow resistance due to the rotating effects caused by the rotor. Therefore, the pressure loss in a rotating condition can be expressed as the sum of stationary loss and rotational loss:

$$\Delta p = \Delta p_r + \Delta p_s \tag{8.15}$$

where Δp_r is the rotational pressure loss and Δp_s is the stationary pressure loss, which can be determined using equations (8.1) and (8.2).

The influence of rotation to system flow resistance curves of ventilation with only airgap is shown in Figure 8.9. Rotation affects the system curves and increases the resistance of flow passing through the airgap with rotor rotating. The pressure requirement for a given flow rate is higher for rotating condition. Hence, the experimental results confirm the presence of additional pressure loss due to the effects of rotation. The influence of rotation is less marked at higher flow rate when compared to the lower flow rate. The relationships between Δp_3 and Q_{airgap} can then be derived from the system curves over a range of measured rotor speed (The experimental data can be found in Appendix L). The airgap flow rate as a function of the measured pressure at Plane 3 can be represented by the following equations:

$$RPM = 600, \quad Q_{airgap} = 2.43 \times 10^{-4}(\Delta p_3) - 8.64 \times 10^{-7}(\Delta p_3)^2 \tag{8.16}$$

$$RPM = 1200, \quad Q_{airgap} = 2.10 \times 10^{-4}(\Delta p_3) - 5.37 \times 10^{-7}(\Delta p_3)^2 \tag{8.17}$$

$$RPM = 1800, \quad Q_{airgap} = 1.66 \times 10^{-4}(\Delta p_3) - 2.43 \times 10^{-7}(\Delta p_3)^2 \tag{8.18}$$

$$RPM = 2100, \quad Q_{airgap} = 1.72 \times 10^{-4}(\Delta p_3) - 3.17 \times 10^{-7}(\Delta p_3)^2 \tag{8.19}$$

$$RPM = 2400, \quad Q_{airgap} = 1.34 \times 10^{-4}(\Delta p_3) - 1.15 \times 10^{-7}(\Delta p_3)^2 \tag{8.20}$$

$$RPM = 2700, \quad Q_{airgap} = 1.28 \times 10^{-4}(\Delta p_3) - 1.02 \times 10^{-7}(\Delta p_3)^2 \tag{8.21}$$

$$RPM = 3000, \quad Q_{airgap} = 1.20 \times 10^{-4}(\Delta p_3) - 8.64 \times 10^{-8}(\Delta p_3)^2 \tag{8.22}$$

These equations were used in Section 8.6 to isolate the flow rate in the airgap from the measured inlet flow rate for the ventilation system of rotor ducts and airgap with rotating rotor.

For the case of airgap only, the rotational pressure losses are assumed to be contributed by the additional friction loss due to helical flow and shock loss due to the abrupt change of flow direction into the airgap as described in Chapter 6. Equation (6.1) in the Section 6.3 was used to account for the additional friction loss due to rotation. Therefore, the magnitude of shock loss can be obtained by subtracting the additional friction loss from the total rotational losses. The shock loss coefficient (K_{shock}) can be computed as:

$$\Delta p_r = \left[\left(K_{f_r} - K_{f_0}\right) + K_{shock}\right] \times \frac{1}{2}\rho U^2 \tag{8.23}$$

$$K_{shock} = \frac{2\Delta p_r}{\rho U^2} - \left(K_{f_r} - K_{f_0}\right) \tag{8.24}$$

where K_{f_0} is the friction loss coefficient for stationary annular gap, K_{f_r} is the friction loss coefficient for annular gap with rotation and U is the mean flow velocity in the annular gap. Before the amount of shock loss and its pressure loss coefficient can be obtained, it is necessary to separate the rotational and stationary pressure losses from the measured values. Equation (8.1) and (8.2) were used to compute the stationary loss from the measured inlet flow rate.

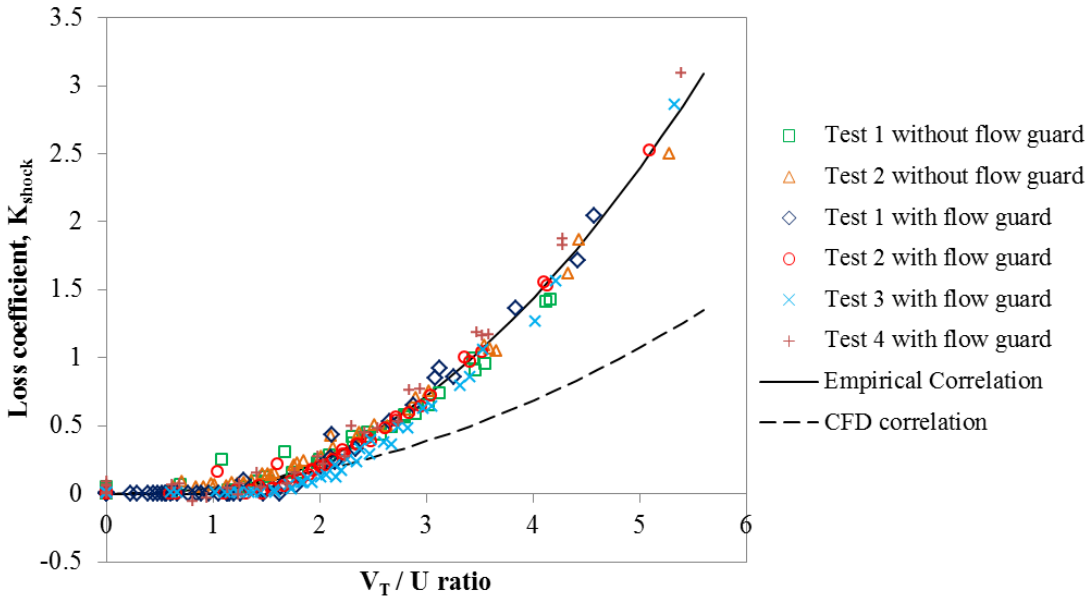

Figure 8.10: The variation of shock loss coefficient for gap ratio of 0.0533 with rotation ratio for tests with and without flow guard

The shock loss coefficient was plotted against the rotation ratio because the rotation ratio (i.e. V_T/U) is a dimensionless number used to identify the strength of rotation as described in Chapter 6. The experiments were repeated for airgap with and without flow guard at least twice to confirm the values of airgap shock loss. The values obtained for the shock loss coefficient were very consistent. The experiments demonstrate that the shock loss for the rotor-stator gap is not influenced by the flow guard. As shown in Figure 8.10, the shock loss can be neglected when the rotation ratio is less than unity and an empirical correlation for the shock loss coefficient can be proposed for the testing conditions. For gap ratio of 0.0533, the shock loss coefficient can be correlated with the rotation ratio as:

$$\begin{aligned} &V_T/U > 1, \qquad K_{shock} = 0.12(V_T/U)^2 - 0.12(V_T/U) \\ &V_T/U \leq 1, \qquad K_{shock} = 0 \end{aligned} \tag{8.25}$$

where V_T is the peripheral speed of rotor outer surface and U is the mean axial flow velocity in the airgap. The correlation is valid for the axial Reynolds number in the airgap ranges from 2400 to 11000, the rotational Reynolds number up to 12700, the Taylor number up to 1470 and the rotation ratio, V_T/U up to 5.4. A flow component was added into the Flow Library to describe the characteristic of the annular gap shock loss.

An analysis of residuals is performed to check if the residuals appear to behave randomly in order to ensure the validity of the proposed correlation. As the shock loss is neglected when V_T/U is less than unity, the difference between the observed value and the estimated value from the correlation (8.25) for V_T/U greater than unity is only plotted. Figure 8.11 shows that the residuals are homoscedastic and unbiased. Therefore, the proposed correlation is verified for the rotational tests.

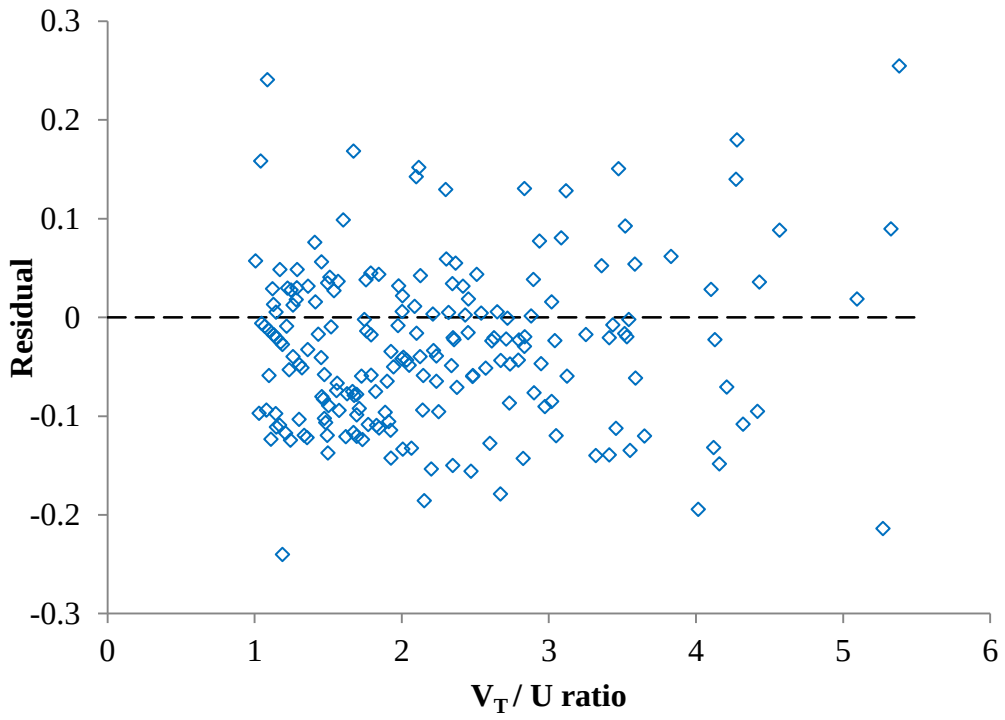

Figure 8.11: Analysis of residuals for airgap shock loss coeffcicient

The comparison between the CFD and experimental results indicated that the CFD results agree with the experimental results, following the trends experienced in measurements in response to the rotation ratio. Discrepancy between the CFD and experimental results is due to the limitations of two-equation turbulence models based on Boussinesq's isotropic eddy viscosity assumption in modelling the flow in rotor-stator gap with large rapid changes in strain rate. This includes SST k-ω model used in Chapter 6. Reynolds Stress Transport (RSM), Direct Numerical Simulation (DNS) or Large Eddy Simulation (LES) of the higher order should provide better accuracy. However, due to the expensive computational cost, the large number of CFD simulations required in the present study is difficult to be finished using DNS or LES approaches. In addition to that, as the shock loss is obtained by subtracting the additional friction loss from the total rotational loss, hence the discrepancy also consists of the uncertainties from equation (6.1).

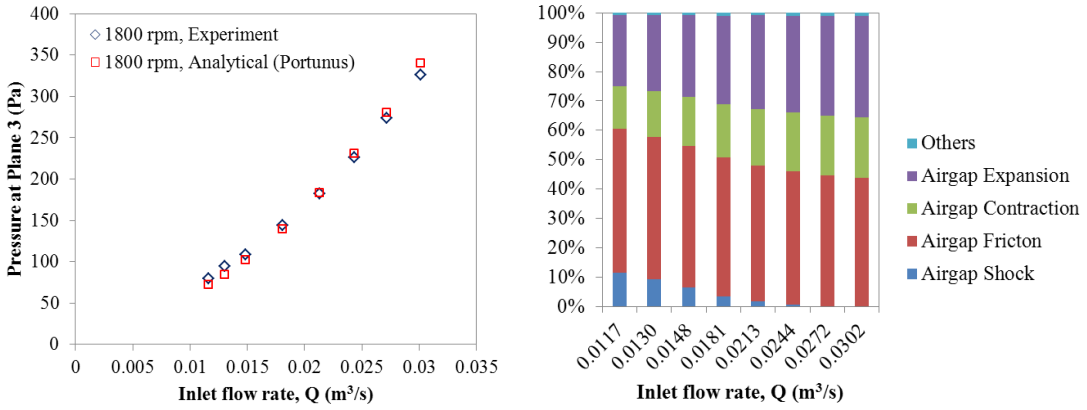

(a) Rotor speed = 1800 rpm

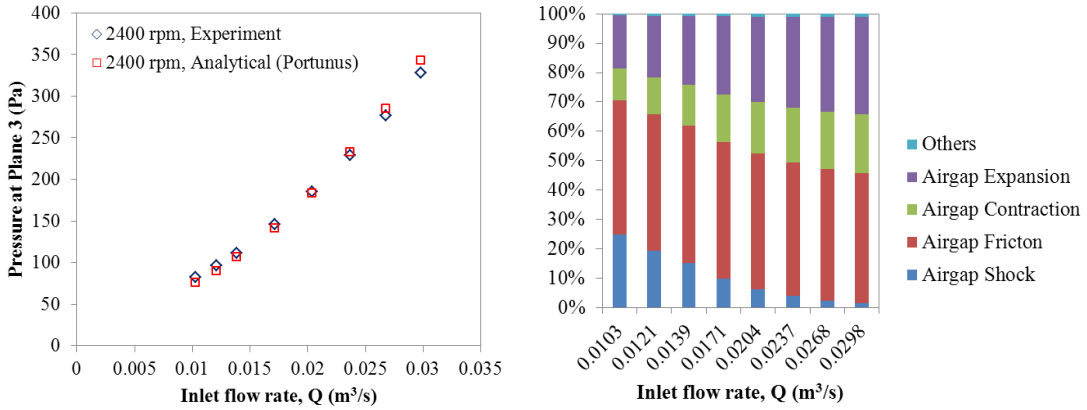

(b) Rotor speed = 2400 rpm

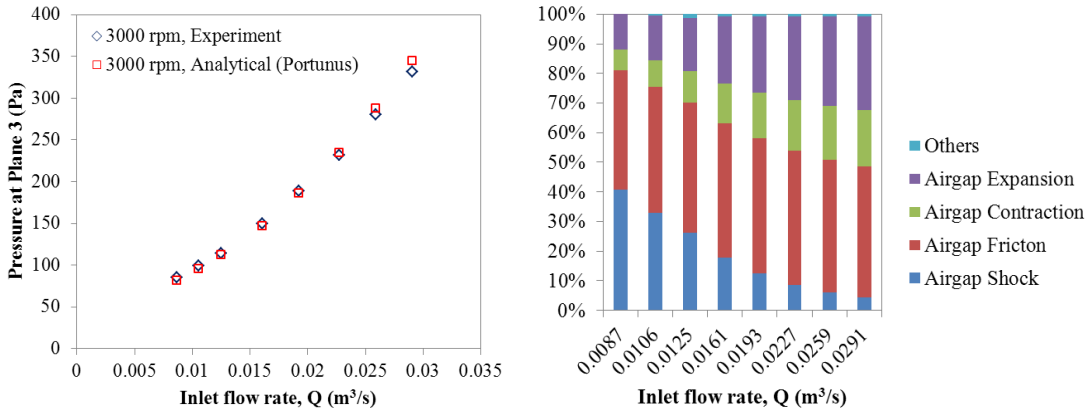

(c) Rotor speed = 3000 rpm

Figure 8.12: Pressure drop from the Plane 3 to the outlet versus inlet flow rate for ventilation system of airgap without flow guard (left), and the contribution of pressure loss components determined using Portunus flow network analysis (right)

The comparison between the experimental results and the values predicted using analytical flow network analysis is shown on the left hand side of Figure 8.12 for the case of airgap without flow guard (see Appendix M for the case of airgap with flow guard). The comparison demonstrates that the flow network analysis is capable of predicting the pressure requirements for the flow passing through the airgap with rotor rotating at 1800 rpm, 2400 rpm and 3000 rpm. The equivalent flow networks constructed using the Flow Library for the ventilation system of airgap with rotating rotor can be found in Appendix J. The contribution of pressure loss components obtained using the the experimentally validated flow network is illustrated on the right hand side of Figure 8.12. The shock loss increases with the increase in rotor speed, but it is less marked for higher flow rate. As the values of loss coefficient of contraction and expansion are mainly geometric dependence, thus the magnitudes of these pressure losses are dependent on the air flow rate only. In Figure 8.12, the stacked columns display the percentage that the main flow components contribute to the total pressure loss over a range of flow rate. At lower flow rate the increases of shock loss and friction loss due to rotation take the percentage. Therefore, the percentage of the contraction and expansion losses become less. The airgap shock, friction, contraction and expansion losses are the major loss components, contributing over 95% of the total loss for the testing conditions.

8.6 Rotational Tests with Rotor Ducts, Airgap and Flow Guard

After the rotational tests with airgap only, the rotational tests were followed with the rotor ducts unblocked to investigate the additional pressure losses of flow passing through the rotor ducts.

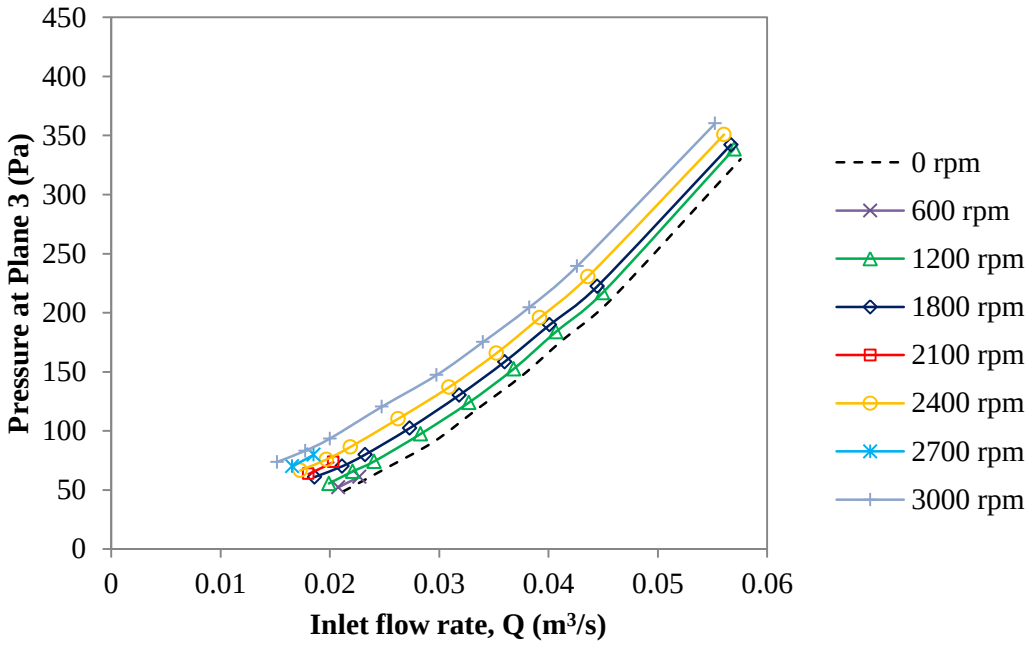

Figure 8.13: System flow resistance curves of *12 D12 PCD113* for rotor speed up to 3000 rpm

The influence of rotation to system flow resistance curves of the case of *12 D12 PCD113* of rotor ducts and airgap in parallel is illustrated in Figure 8.13 (see Appendix N for the other cases). Similar to the case of airgap only, the influence of rotation is less marked at higher flow rate. The effects of rotation apparently increase the flow resistance of ventilation with rotor ducts and airgap. Consequently, the pressure requirement for a given flow is higher for the rotating condition. In other words, for a given differential pressure, the obtainable flow rate is lower in the ventilation system. As the flow passing through the rotor ducts and airgap may suffer different level of the effects of rotation, the flow distribution for the rotating condition may not be the same as the stationary condition. It is necessary to develop a more appropriate approach to separate the flow rate passing through the rotor ducts and the flow rate passing through the airgap. Equations (8.16) to (8.22) obtained in the preceding section were used to compute the flow rate passing through the airgap

(Q_{airgap}) by substituting the values of measured pressure at Plane 3, Δp_3 for the ventilation system of rotor ducts and airgap with rotating rotor. Hence, with rotation, Q_{ducts} can be determined by getting the difference between the measured flow rate Q_{total} and the Q_{airgap} as follows:

$$Q_{ducts} = Q_{total} - Q_{airgap} \tag{8.26}$$

With the flow guard, it is assumed that there was negligible interaction between the airgap outflow and rotor ducts outflow, the flow rate passing through the airgap with the rotor ducts unblocked for a given pressure was the same as that of the rotor ducts blocked. The appropriateness of this assumption was demonstrated in Figure 6.16 and Figure 6.17 using the CFD methods in the Section 6.8.

Figure 8.14 indicates the effects of rotation on flow distribution between the rotor ducts and airgap for the case of *12 D12 PCD113* (see Appendix N for the other cases). In general, Q_{ducts} decreases for the increase in rotor speed.

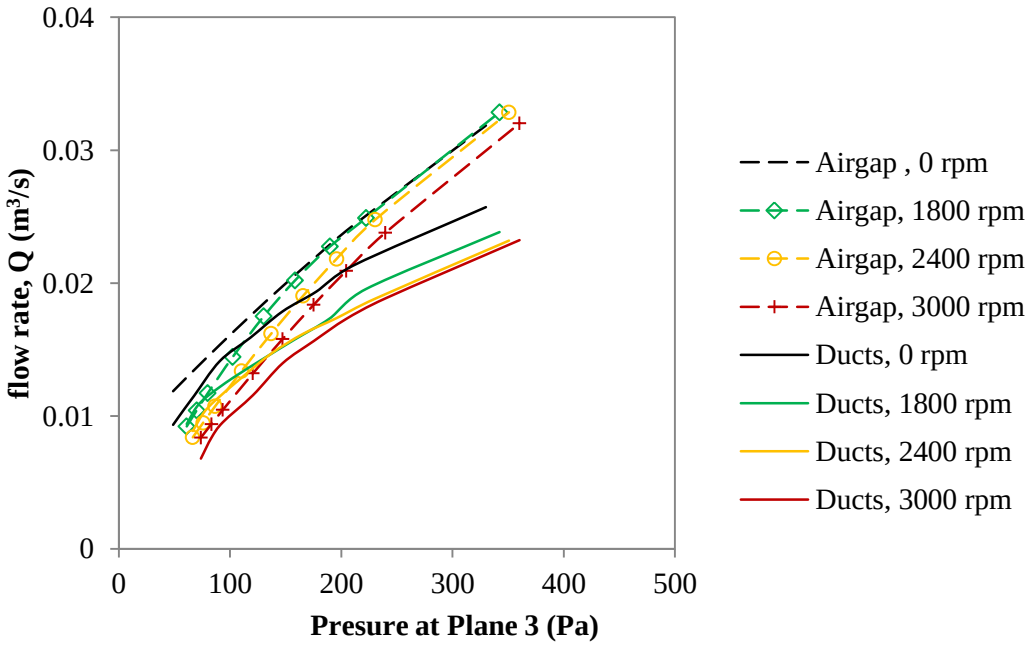

Figure 8.14: Flow distribution between airgap and rotor ducts (*12 D12 PCD113*) with flow guard for rotor speed at 0 rpm, 1800 rpm, 2400 rpm and 3000 rpm

Consequently, the relationships between Δp_3 and Q_{ducts} can be also derived from the experimental data for the rotating conditions. The flow rate passing through the rotor

ducts as a function of the measured pressure at Plane 3 can be represented by the following equations:

For *12 D12 PCD113*,

$$RPM = 1200,\ Q_{ducts} = 4.68 \times 10^{-3} + 9.90 \times 10^{-5}(\Delta p_3) - 1.22 \times 10^{-7}(\Delta p_3)^2 \quad (8.27)$$

$$RPM = 1800,\ Q_{ducts} = 5.39 \times 10^{-3} + 7.80 \times 10^{-5}(\Delta p_3) - 7.03 \times 10^{-8}(\Delta p_3)^2 \quad (8.28)$$

$$RPM = 2400,\ Q_{ducts} = 3.97 \times 10^{-3} + 8.90 \times 10^{-5}(\Delta p_3) - 9.86 \times 10^{-8}(\Delta p_3)^2 \quad (8.29)$$

$$RPM = 3000,\ Q_{ducts} = 1.11 \times 10^{-4}(\Delta p_3) - 1.31 \times 10^{-7}(\Delta p_3)^2 \quad (8.30)$$

For *12 D10 PCD113*,

$$RPM = 1200,\ Q_{ducts} = 3.44 \times 10^{-3} + 6.08 \times 10^{-5}(\Delta p_3) - 6.31 \times 10^{-8}(\Delta p_3)^2 \quad (8.31)$$

$$RPM = 1800,\ Q_{ducts} = 4.10 \times 10^{-3} + 4.73 \times 10^{-5}(\Delta p_3) - 3.45 \times 10^{-8}(\Delta p_3)^2 \quad (8.32)$$

$$RPM = 2400,\ Q_{ducts} = 3.46 \times 10^{-3} + 5.20 \times 10^{-5}(\Delta p_3) - 4.79 \times 10^{-8}(\Delta p_3)^2 \quad (8.33)$$

$$RPM = 3000,\ Q_{ducts} = 7.43 \times 10^{-5}(\Delta p_3) - 8.22 \times 10^{-8}(\Delta p_3)^2 \quad (8.34)$$

For *6 D12 PCD113*,

$$RPM = 1200,\ Q_{ducts} = 2.88 \times 10^{-3} + 4.13 \times 10^{-5}(\Delta p_3) - 3.80 \times 10^{-8}(\Delta p_3)^2 \quad (8.35)$$

$$RPM = 1800,\ Q_{ducts} = 3.50 \times 10^{-3} + 3.04 \times 10^{-5}(\Delta p_3) - 1.76 \times 10^{-8}(\Delta p_3)^2 \quad (8.36)$$

$$RPM = 2400,\ Q_{ducts} = 2.93 \times 10^{-3} + 3.60 \times 10^{-5}(\Delta p_3) - 3.06 \times 10^{-8}(\Delta p_3)^2 \quad (8.37)$$

$$RPM = 3000,\ Q_{ducts} = 5.42 \times 10^{-5}(\Delta p_3) - 5.72 \times 10^{-8}(\Delta p_3)^2 \quad (8.38)$$

For *6 D12 PCD75*,

$$RPM = 1200,\ Q_{ducts} = 4.18 \times 10^{-3} + 2.82 \times 10^{-5}(\Delta p_3) - 1.40 \times 10^{-8}(\Delta p_3)^2 \quad (8.39)$$

$$RPM = 1800,\ Q_{ducts} = 4.52 \times 10^{-3} + 2.85 \times 10^{-5}(\Delta p_3) - 2.09 \times 10^{-8}(\Delta p_3)^2 \quad (8.40)$$

$$RPM = 2400,\ Q_{ducts} = 4.01 \times 10^{-3} + 3.25 \times 10^{-5}(\Delta p_3) - 2.66 \times 10^{-8}(\Delta p_3)^2 \quad (8.41)$$

$$RPM = 3000,\ Q_{ducts} = 6.38 \times 10^{-5}(\Delta p_3) - 7.67 \times 10^{-8}(\Delta p_3)^2 \quad (8.42)$$

For *6 D14 PCD75*,

$$RPM = 1200,\ Q_{ducts} = 4.50 \times 10^{-3} + 5.62 \times 10^{-5}(\Delta p_3) - 5.51 \times 10^{-8}(\Delta p_3)^2 \quad (8.43)$$

$$RPM = 1800,\ Q_{ducts} = 5.75 \times 10^{-3} + 4.30 \times 10^{-5}(\Delta p_3) - 2.98 \times 10^{-8}(\Delta p_3)^2 \quad (8.44)$$

$$RPM = 2400,\ Q_{ducts} = 4.42 \times 10^{-3} + 5.80 \times 10^{-5}(\Delta p_3) - 6.21 \times 10^{-8}(\Delta p_3)^2 \quad (8.45)$$

$$RPM = 3000,\ Q_{ducts} = 9.18 \times 10^{-5}(\Delta P_3) - 1.18 \times 10^{-7}(\Delta p_3)^2 \quad (8.46)$$

In order to obtain a good fitting for the experimental data, the equations for 1200, 1800 and 2400 rpm are mainly applicable for specific range of Δp_3 (The experimental data can be found in Appendix O). These equations were used in Section 8.7 to isolate the flow rate in the rotor ducts of different configurations from the measured inlet flow rate for the ventilation system of rotor ducts and airgap without flow guard.

As shown in Figure 8.13, the pressure obtained from the experiments is the sum of stationary loss and rotational loss for a given inlet flow rate. In order to characterise the rotational loss, it is necessary to separate the rotational and stationary losses from the measured values. The stationary loss can be computed by substituting the inlet flow rate into equations (8.5) to (8.9). The rotational pressure losses (Δp_r) of the rotor ducts are assumed to be contributed by the additional friction loss due to rotation and shock loss due to abrupt change of flow direction entering into the rotor ducts. Equations (6.2) and (6.5) in the Section 6.3 were used to account for the additional friction loss in the rotor ducts due to rotation. Therefore, the magnitude of shock loss of the rotor ducts can be obtained by subtracting the additional friction loss from the total rotational losses. The shock loss coefficient (K_{shock}) of the rotor ducts can be computed as:

$$\Delta p_r = \left[\left(K_{f_r} - K_{f_0}\right) + K_{shock}\right] \times \frac{1}{2}\rho U^2 \quad (8.47)$$

$$K_{shock} = \frac{2\Delta p_r}{\rho U^2} - \left(K_{f_r} - K_{f_0}\right) \quad (8.48)$$

where K_{f_0} is the friction loss coefficient for stationary rotor duct, K_{f_r} is the friction loss coefficient of the rotor duct with rotation and U is the mean flow velocity in the rotor ducts.

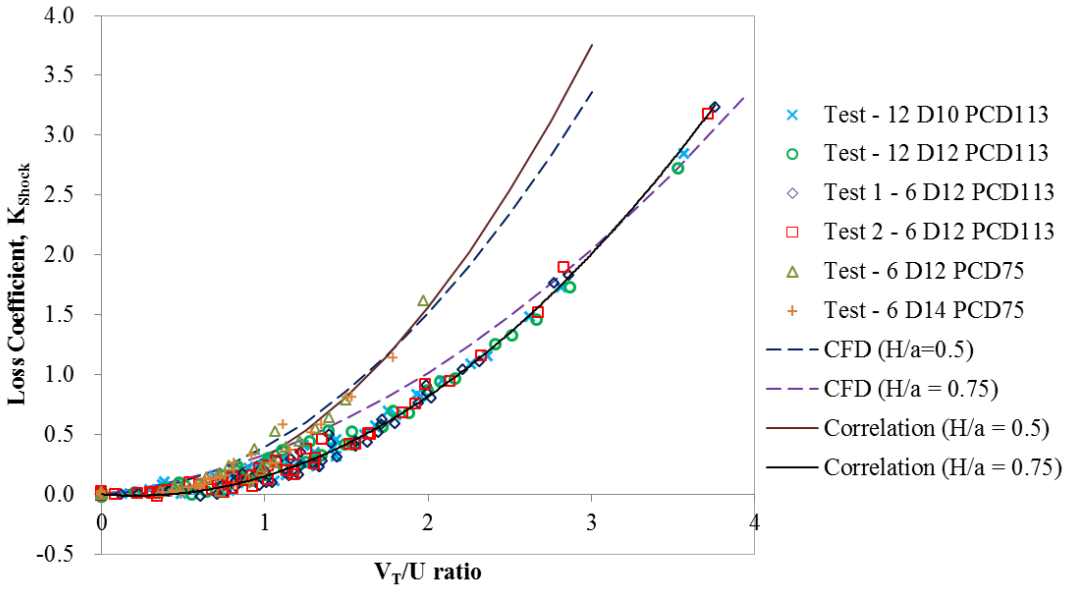

Figure 8.15: The variation of shock loss coefficient of rotor ducts with rotation ratio

As shown in Figure 8.15, the shock loss increases considerably for the increase in rotation ratio, but it can be neglected when the rotation ratio is less than 0.5 approximately. The testing of ventilation system of *6 D12 PCD113* was repeated to ensure the experimental measurements were consistent. The experimental results further validate the findings obtained using the CFD method and demonstrate that the shock loss of the rotor ducts is not influenced by the duct size, duct spacing, duct length-to-diameter ratio and eccentricity parameter over the range of the testing conditions as shown in Table 7.1. This finding agrees with Webb [1964] in some circumstances. However, the shock loss is apparently affected by the ratio of rotating radius to rotor radius (*H/a*), which indicates the proximity of the rotor ducts to rotor periphery. Hence, for *H/a* ratio of 0.75, the shock loss coefficient can be correlated with the rotation ratio as:

$$\begin{aligned} &V_T/U > 0.5, \qquad K_{shock} = 0.234(V_T/U)^2 - 0.043(V_T/U) \\ &V_T/U \leq 0.5, \qquad K_{shock} = 0 \end{aligned} \tag{8.49}$$

For H/a ratio of 0.5, the shock loss coefficient can be correlated with the rotation ratio as:

$$V_T/U > 0.5, \qquad K_{shock} = 0.474(V_T/U)^2 - 0.156(V_T/U)$$
$$V_T/U \leq 0.5, \qquad K_{shock} = 0 \tag{8.50}$$

where V_T is the tangential speed of the rotor ducts rotating about a parallel axis and U is the mean axial flow velocity in the rotor ducts. The correlations are valid for the axial Reynolds number in the rotor ducts ranges from 3200 to 17000, the rotation ratio, V_T/U up to 3.7 for H/a = 0.75, and the rotation ratio, V_T/U up to 2 for H/a = 0.5. The extrapolation of the shock loss correlations must be implemented with care. These shock loss correlations were incorporated into the air flow modelling tool.

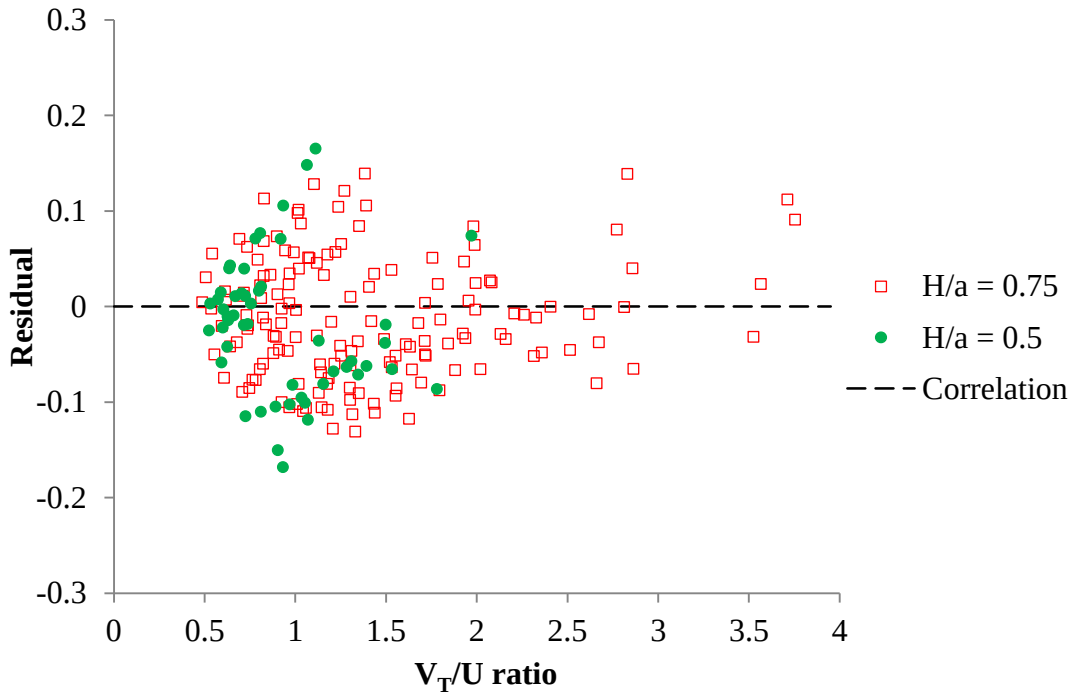

Figure 8.16: Analysis of residuals for rotor duct shock loss coefficient

An analysis of residuals is performed to check if the residuals appear to behave randomly in order to ensure the validity of the proposed correlations. As the shock loss is neglected when V_T/U is less than 0.5, the difference between the observed value and the estimated value from the correlations, (8.49) and (8.50) for V_T/U greater than 0.5 is only plotted. Figure 8.16 shows that the residuals are homoscedastic and unbiased. Therefore, the proposed correlations are verified for the rotational tests.

The comparisons between the experimental results and the values predicted using analytical flow network analysis are shown in Figure 8.17 for *12 D12 PCD113* (see Appendix N for the other cases). The equivalent flow network constructed using the Flow Library for the ventilation system of rotor ducts, airgap and flow guard with rotating rotor can be found in Appendix J. The comparison demonstrates that the flow network analysis is not only capable of predicting pressure requirements for the flow passing through the rotor ducts, airgap and flow guard with rotating rotor at 1800 rpm, 2400 rpm and 3000 rpm, but also capable of predicting the flow distribution between the rotor ducts and airgap under rotating condition. In Figure 8.18, the experimentally validated flow network was used to investigate the contribution of the main pressure loss components in percentage from Plane 3 to the outlet of the test rig. Similar to the case of airgap with rotating rotor, the shock loss of rotor ducts increases with the increase in rotor speed, but it is less marked for higher flow rate. The shock, friction, contraction and expansion losses of rotor ducts are the major loss components contributing over 96% of the total loss for the testing conditions.

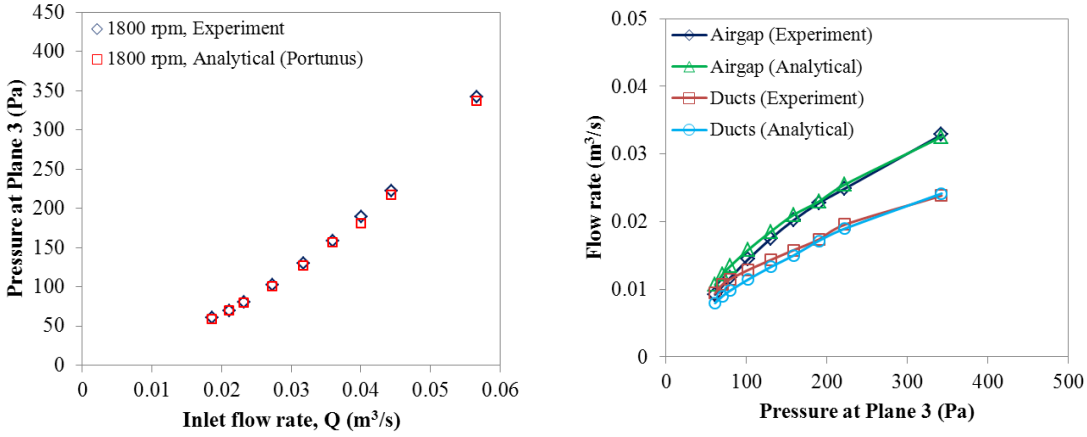

(a) Rotor speed = 1800 rpm

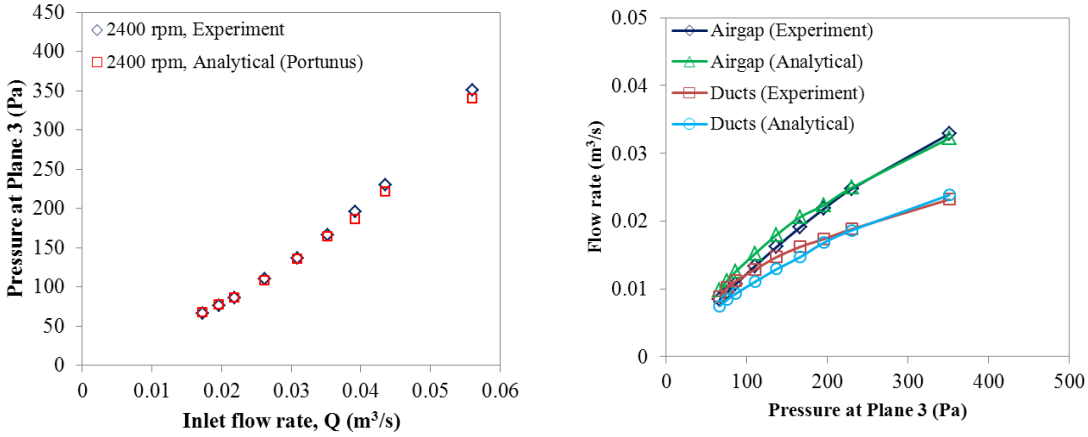

(b) Rotor speed = 2400 rpm

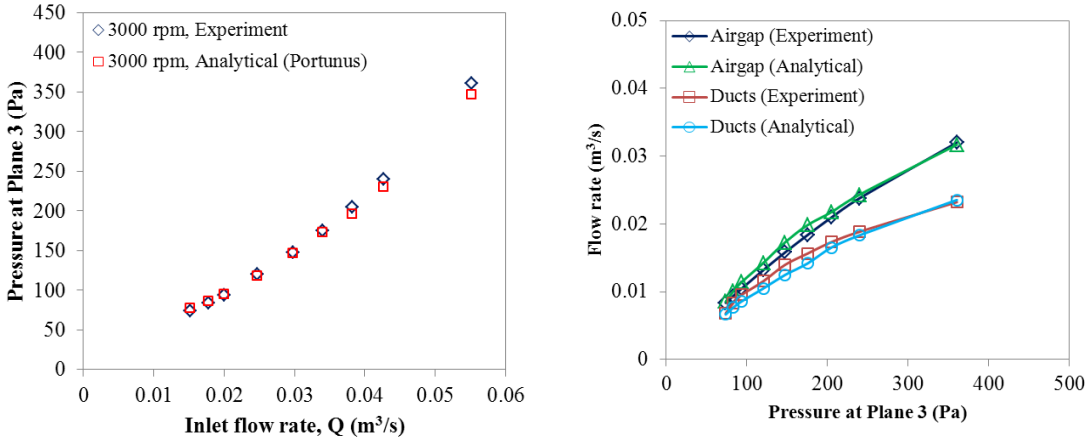

(c) Rotor speed = 3000 rpm

Figure 8.17: Pressure drop from the Plane 3 to the outlet versus inlet flow rate for *12 D12 PCD113* (left) and the flow distribution between rotor ducts and airgap (right)

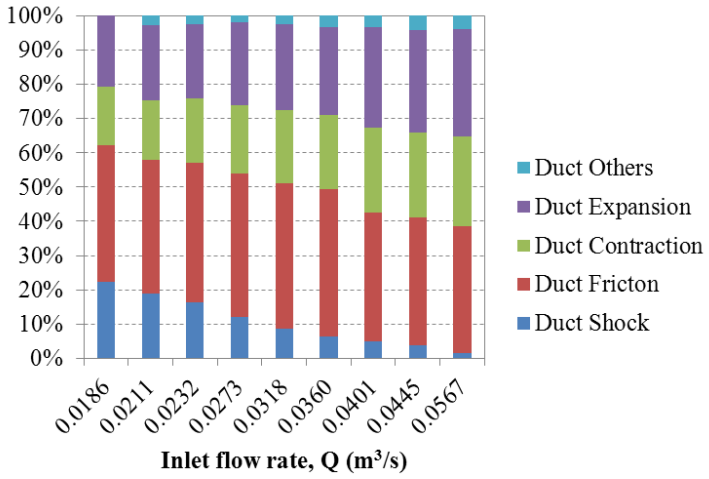

(a) Rotor speed = 1800 rpm

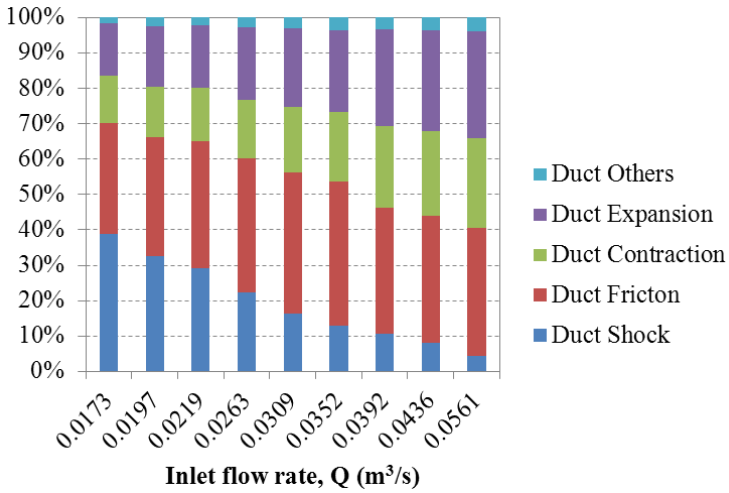

(b) Rotor speed = 2400 rpm

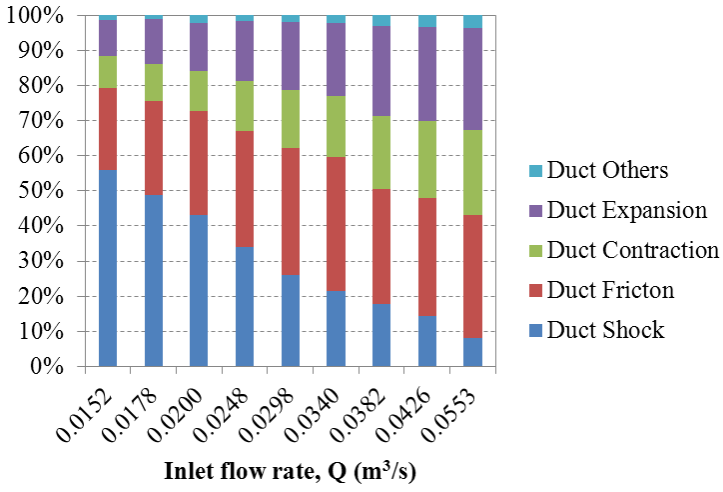

(c) Rotor speed = 3000 rpm

Figure 8.18: The contribution of pressure loss components of rotor ducts for *12 D12 PCD113* obtained using Portunus flow network analysis

8.7 Rotational Tests with Rotor Ducts, Airgap and no Flow Guard

In this section, for the rotational tests with rotor ducts and airgap, the experiments were followed by removing the flow guard to investigate the system pressure loss without the flow guard. The comparison between the system flow resistance curves for the case of rotor ducts and airgap with the flow guard (solid line) and without the flow guard (dashed line) is illustrated in Figure 8.19 for the case of *12 D10 PCD113* (see Appendix P for the other cases). The pressure losses were plotted against the inlet flow rate for rotor speed at 0, 1200, 2400 and 3000 rpm. The experimental results demonstrated the existence of additional pressure loss due to the combining flow loss because the pressure requirement is higher for the case without the flow guard. The combining flow loss is already defined in Chapter 6.

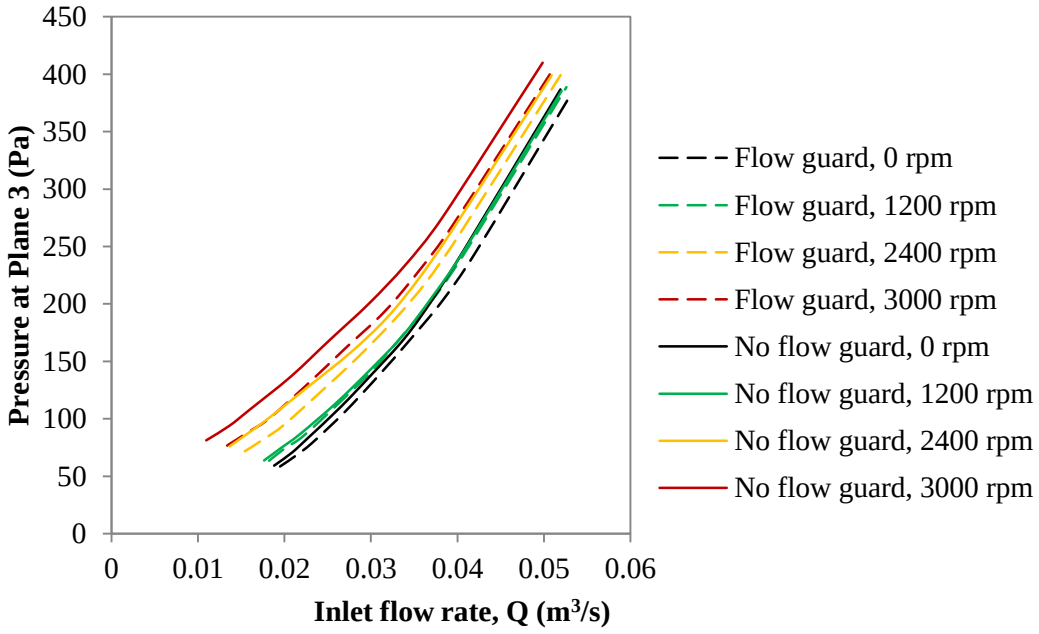

Figure 8.19: System flow resistance curves of *12 D10 PCD113* with and without flow guard for rotor speed up to 3000 rpm

The combining flow loss is more significant for higher rotor speed (e.g. 2400 and 3000 rpm). However, the combining flow loss at 0 and 1200 rpm is negligible because the system flow resistance curves with and without the flow guard coincide with each other. The combining flow loss is significant for the cases of rotor ducts located at *PCD* of 113 mm closer to the rotor periphery (the *H/a* ratio is 0.75),

whereas the combining flow loss for the cases of rotor ducts located at *PCD* of 75 mm (the *H/a* ratio is 0.5) is very small and can be assumed negligible.

Due to the combining flow, the flow passing through the airgap is less than that of the case with the flow guard. However, according to the CFD findings, the combining flow does not affect the flow resistance of the flow passing through the rotor ducts. Therefore, the flow rates passing through the rotor ducts (Q_{ducts}) of different configurations were obtained by substituting the values of measured pressure at Plane 3, Δp_3 into equations (8.27) to (8.46). Hence, Q_{airgap} can be determined by getting the difference between the measured flow rate Q_{total} and the Q_{ducts} as follows:

$$Q_{airgap} = Q_{total} - Q_{ducts} \tag{8.51}$$

Figure 8.20 illustrates the flow distribution between the rotor ducts and airgap for the cases of *12 D10 PCD113* without the flow guard (see Appendix P for the other cases). With rotation, when compared to the ventilation system with airgap only the flow rate passing through the airgap decreases further due to the combining flow loss.

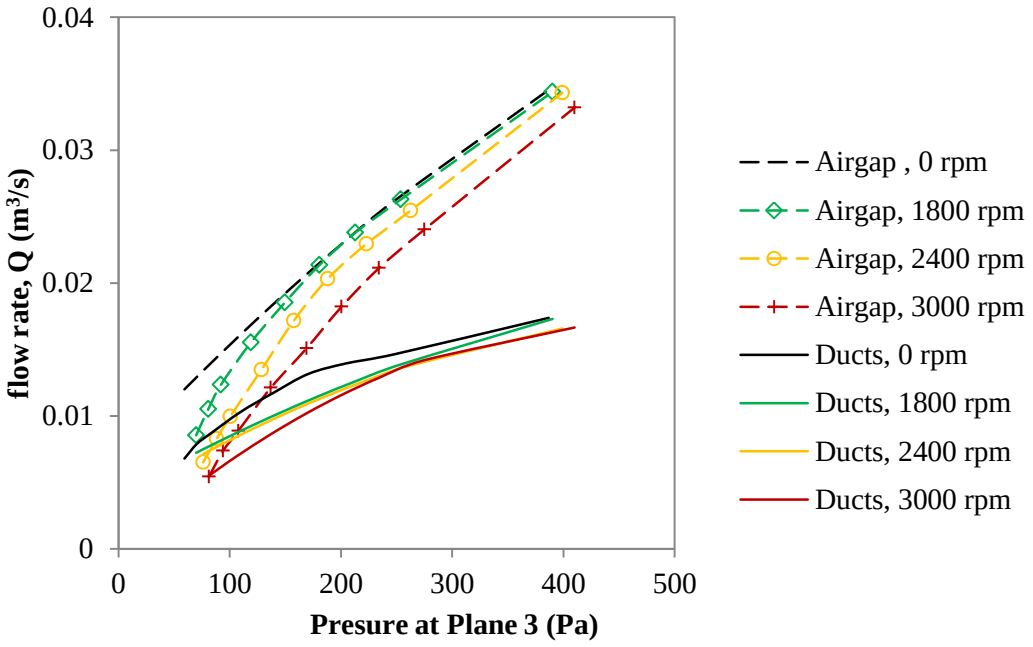

Figure 8.20: Flow distribution between airgap and rotor ducts (*12 D10 PCD113*) without flow guard for rotor speed at 0 rpm, 1800 rpm, 2400 rpm and 3000 rpm

Similar to the tests with the flow guard, the pressure measurements obtained from the tests without the flow guard are the sum of stationary loss and rotational loss for a given inlet flow rate, by taking the combining flow loss into account. In order to isolate rotational loss so that the combining flow loss can be characterised, the measured inlet rates were substituted into equations (8.10) to (8.14) to compute for the stationary loss. For the pathway of the airgap, the rotational pressure losses (Δp_r) are assumed to be contributed by the additional friction loss due to rotation, the shock loss due to abrupt change of flow direction entering into the airgap and the combining flow loss due to the interference with rotor ducts outward flow. The combining flow loss of the airgap can be obtained by subtracting the additional friction loss and shock loss from the total rotational losses. With the information of the flow distribution and magnitude of the combining flow loss, the coefficient (K_{CF}) of combining flow loss can be computed as:

$$\Delta p_r = \left[\left(K_{f_r} - K_{f_0}\right) + K_{shock} + K_{CF}\right] \times \frac{1}{2}\rho U^2 \tag{8.52}$$

$$K_{CF} = \frac{2\Delta p_r}{\rho U^2} - \left(K_{f_r} - K_{f_0}\right) - K_{shock} \tag{8.53}$$

where $K_{f_0}$is the friction loss coefficient for stationary airgap, K_{f_r} is the friction loss coefficient of the airgap with rotation, K_{shock} is the shock loss coefficient of the airgap and U is the mean flow velocity in the airgap.

As shown in Figure 8.21, the coefficients of combining flow loss can also be characterised using the rotation ratio, V_T/U. The loss coefficients for *6 D12 PCD75* and *6 D14 PCD75* are approximately equal to zero because the rotor ducts are located at *H/a* = 0.5. As described in the previous section, *H/a* is a measure to indicate the proximity of the rotor ducts to rotor periphery. Hence, the rotor ducts located at *H/a* = 0.5 allow sufficient distance for the outflow from the rotor ducts to spreads across the outlet chamber to a level that gives less impact of combining flow than that of the rotor ducts located at *H/a* = 0.75 (i.e. *12 D10 PCD 113*, *12 D12 PCD113* and *6 D12 PCD113*). For *H/a* = 0.75, the loss coefficients obtained from the experimental results demonstrate that the combining flow loss is mainly affected by the number of rotor ducts, but is not affected by the duct size for the testing

conditions. The combining flow loss increases linearly with the rotation ratio, but it can be neglected when the rotation ratio is less than 1 approximately. Hence, for 12 rotor ducts at *H/a* = 0.75, the combining flow loss coefficient for the airgap can be correlated with the rotation ratio as:

$$\begin{aligned} V_T/U > 1, \quad & K_{CF} = 0.31(V_T/U)_{gap} - 0.31 \\ V_T/U \leq 1, \quad & K_{CF} = 0 \end{aligned} \tag{8.54}$$

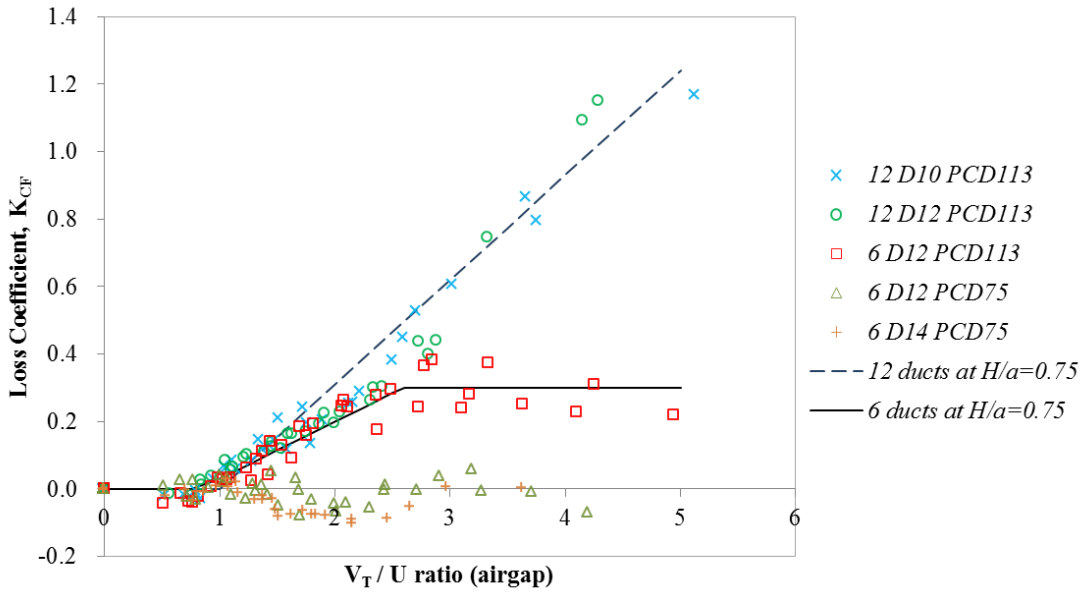

Figure 8.21: The variation of combining flow loss at the airgap with rotation ratio

For 6 rotor ducts at *H/a* = 0.75, the loss coefficient increases for the increase in rotation ratio when the rotation ratio is greater than unity and it becomes constant ($K_{CF} = 0.3$) after the rotation ratio is greater than 2.5. It means the combining flow of *6 D12 PCD113* reach its saturated value at $(V_T/U)_{gap}$ = 2.5 and the flow resistance of the flow passing through the airgap is not affected by any increase in the rotation ratio after that. Thus, the combining flow loss coefficient for the airgap can be correlated with the rotation ratio as:

$$\begin{aligned} V_T/U > 2.5, \quad & K_{CF} = 0.3 \\ V_T/U > 1, \quad & K_{CF} = 0.17(V_T/U)_{gap} - 0.14 \\ V_T/U \leq 1, \quad & K_{CF} = 0 \end{aligned} \tag{8.55}$$

where V_T is the tangential speed of the rotor ducts rotating about a parallel axis and U is the mean axial flow velocity in the rotor ducts. The correlations are valid for the axial Reynolds number in the airgap ranges from 2500 to 10000, the Taylor number up to 1470 and the axial Reynolds number in the rotor ducts ranges from 3800 to 15000. The extrapolation of the combining flow loss correlations must be implemented with care. These combining flow loss correlations were incorporated into the air flow modelling tool.

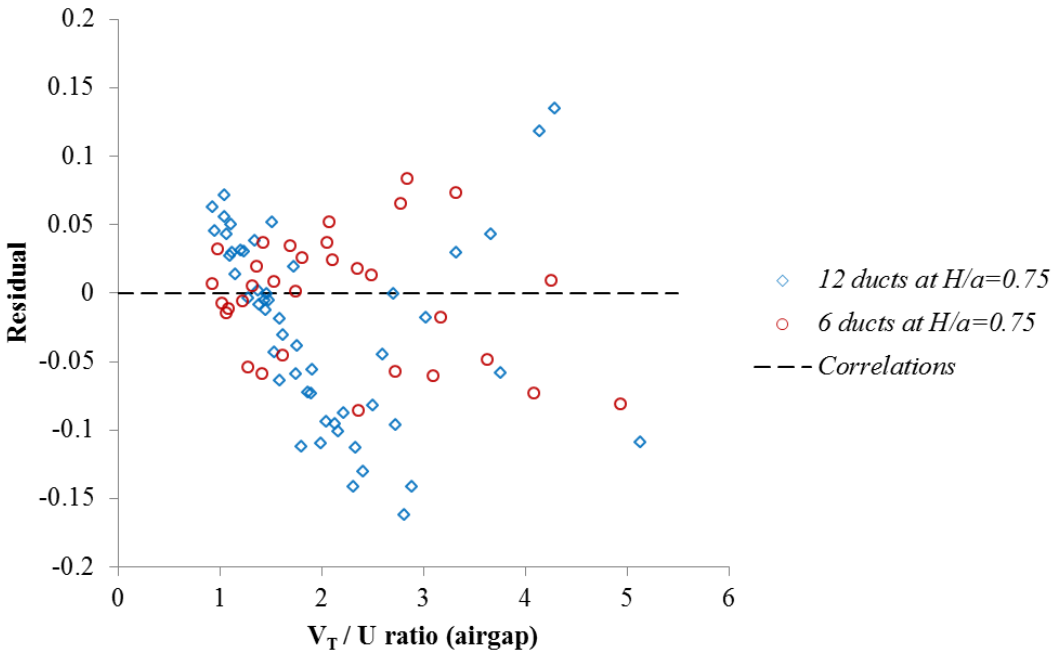

Figure 8.22: Analysis of residuals for combining flow loss coefficient

An analysis of residuals is performed to check if the residuals appear to behave randomly in order to ensure the validity of the proposed correlations. As the combining flow loss is neglected when V_T/U of airgap is less than unity, the difference between the observed value and the estimated value from the correlations, (8.54) and (8.55) for V_T/U greater than unity is only plotted. Figure 8.22 shows that the residuals are homoscedastic and unbiased. Therefore, the proposed correlations are verified for the rotational tests.

As the combining flow loss of the airgap is the remaining loss by subtracting the shock loss and additional friction loss due to rotation from the total rotational loss, the comparison between the experimental and CFD results is meaningless and is not

performed in this section because of the discrepancy of airgap shock loss between the experimental and CFD results.

As the combining flow loss is only significant for the cases where the rotor ducts are located at H/a = 0.75, the comparisons between the experimental results and the values predicted using analytical flow network analysis are only shown in Figure 8.23 for *12 D10 PCD113* (see Appendix P for *12 D12* PCD113 and *6 D12 PCD113*). The analytical results were obtained from the equivalent flow network constructed using the Flow Library, which it can be found in Appendix J. With combining flow, the comparison demonstrates that the flow network analysis is not only capable of predicting pressure requirements for the flow passing through the rotor ducts and airgap with rotating rotor at 1800 rpm, 2400 rpm and 3000 rpm, but also capable of predicting the flow distribution between the rotor ducts and airgap under rotating condition. The experimentally validated flow network was used to investigate the contribution of the pressure loss components from the Plane 3 to the outlet of the test rig. In Figure 8.24, the stacked columns display the percentage that the main flow components contribute to the total pressure loss over a range of inlet flow rate. Before the saturated value of combining flow loss for a corresponding rotor ducts configuration is reached, the percentage of combining flow loss of airgap increases with the reduction in inlet flow rate (i.e. the increase in rotation ratio). However, for *6 D12 PCD113*, once the saturated value is reached, the percentage of combining flow loss is limited by the loss coefficient. Thus, the percentage of combining flow loss of airgap decreases with the reduction in inlet flow rate. The combining flow, shock, friction, contraction and expansion losses of airgap are the major loss components contributing over 96% of the total loss for the testing conditions.

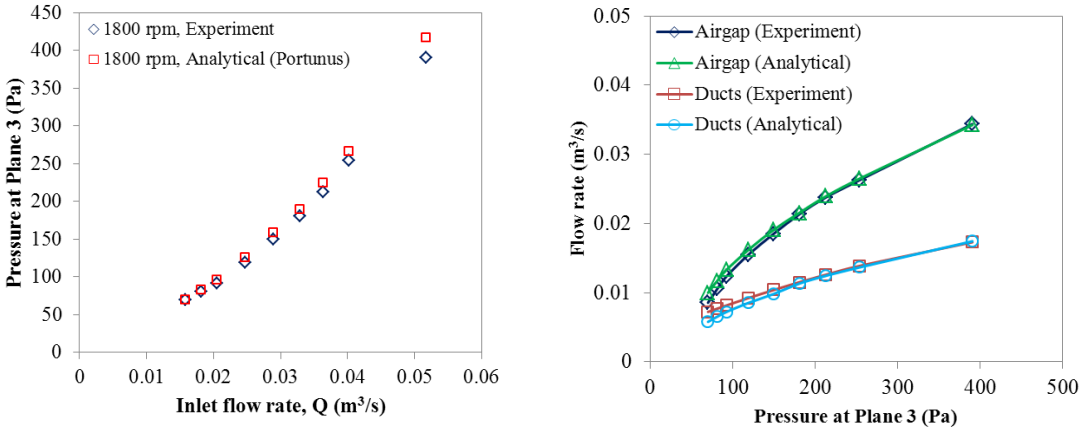

(a) Rotor speed = 1800

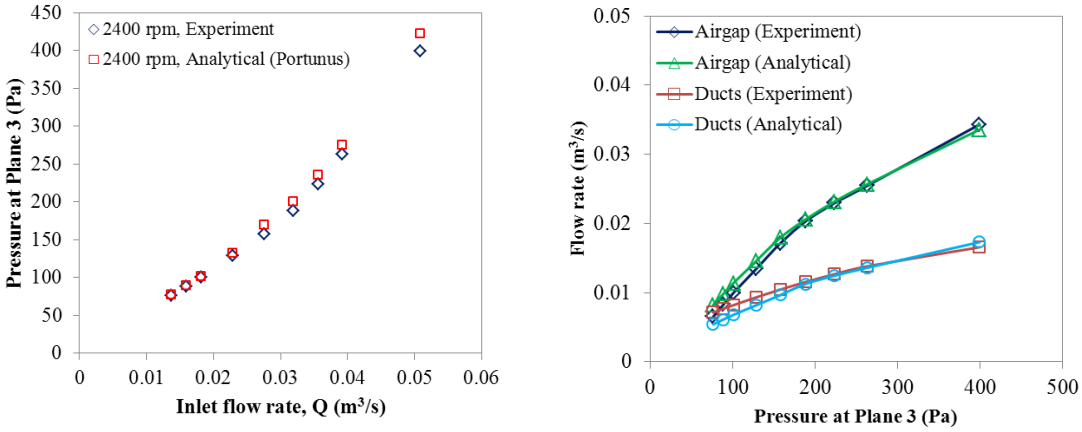

(b) Rotor speed = 2400

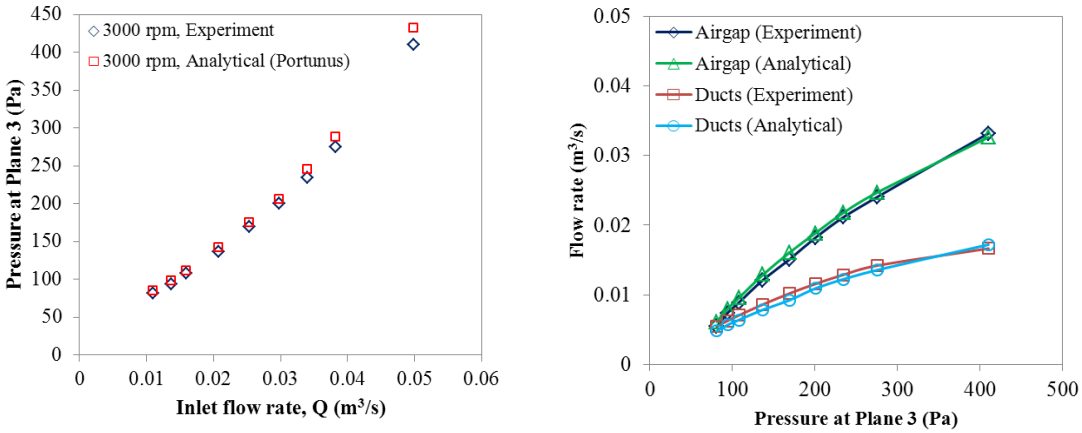

(c) Rotor speed = 3000

Figure 8.23: Pressure drop from the Plane 3 to the outlet versus inlet flow rate (left) and the flow distribution between rotor ducts and airgap (right) for *12 D10 PCD113*

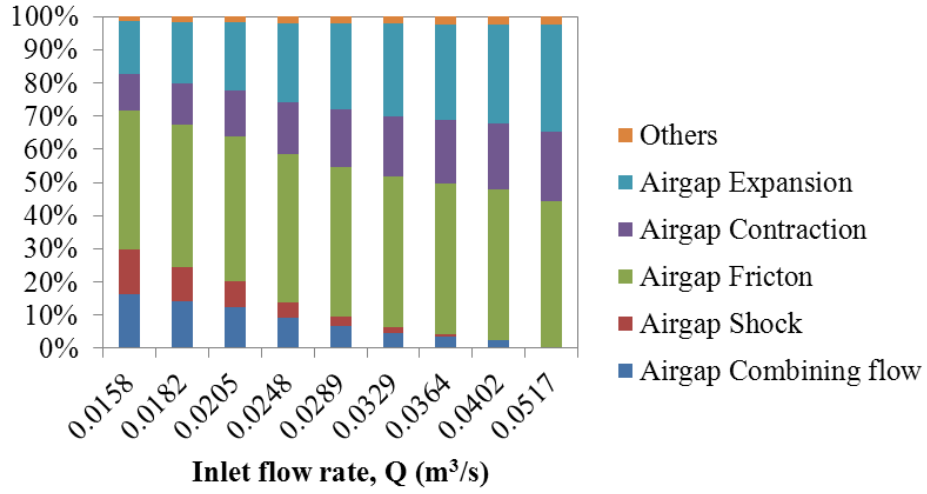

(a) Rotor speed = 1800

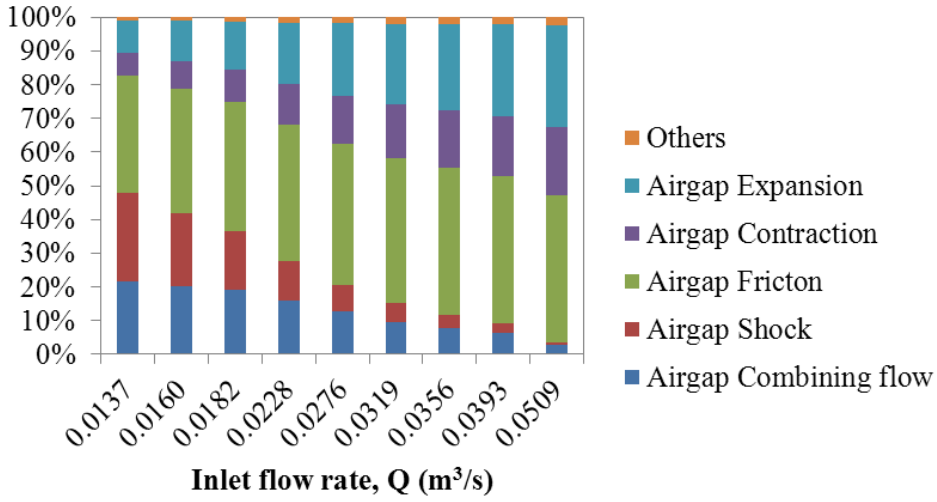

(b) Rotor speed = 2400

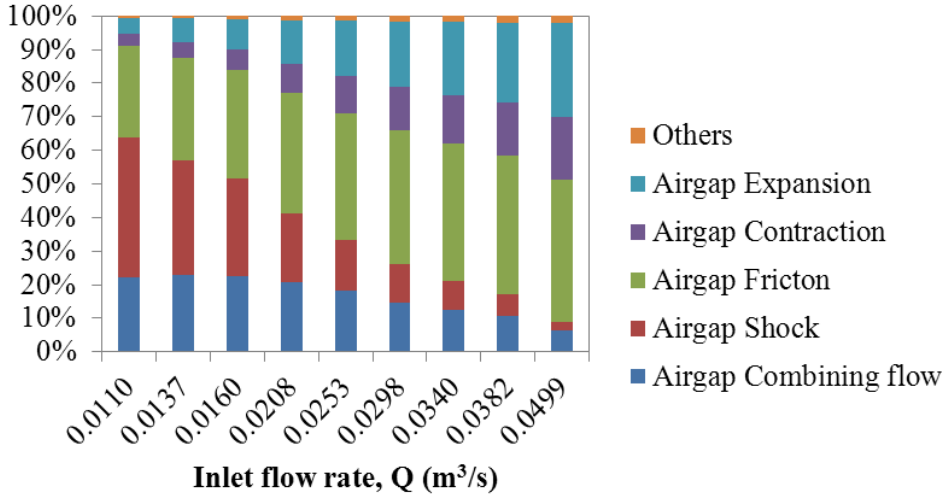

(c) Rotor speed = 3000

Figure 8.24: The contribution of pressure loss components of rotor ducts for *12 D10 PCD113* obtained using Portunus flow network analysis

8.8 Summary for Rotational Tests

- The pressure requirement for air passing through a rotor-stator system is the sum of stationary and rotational pressure losses.
- Rotation can significantly increase the flow resistance of the rotor-stator system above the normal stationary condition.
- The rotational pressure loss in the rotor-stator system consists of additional friction loss due to the rotation induced secondary flows, shock loss and combining flow loss.
- These rotational losses can be mainly characterised using the rotation ratio, V_T/U.
- A good agreement with the experimental results confirmed the validity of the equivalent flow network in accurately predicting the pressure requirements as well as the distribution of air between the ventilation passages under the rotating condition.
- The experimental study provided a better insight into how rotation could affect the flow resistance of a rotor-stator system, e.g. the impact of rotor duct configurations on the rotational losses.

8.9 Conclusion

In this chapter, the experimental investigation of the pressure loss that suffered by the air passing through the ventilation passages of a rotor-stator system (e.g. rotor-stator gap and rotor ducts) is presented. It demonstrates that the flow resistance caused by rotation can be significant, e.g. the rotational pressure loss can be over half of the total pressure loss. Ignoring rotational pressure loss may lead to over estimation of the cooling performance achievable by an electrical machine. Machine design engineers should avoid a machine to be operated at a condition with high rotation ratio to an undesired rotational pressure loss.

Most pressure drop of a system occurs at flow paths of small cross-sectional area such as rotor-stator gap. The existence of rotor ducts can reduce the flow resistance of a rotor-stator system considerably. Different rotor duct configurations were

examined. This investigation highlights the impact of various design parameters on the rotational pressure loss. The geometric parameters that have little or no influence on the rotational loss can be used for cooling design improvement.

The experimental apparatus is used to validate the analytical design tool for air flow modelling and the findings obtained using CFD methods. The analytical results showed good agreement with the experimental measurements, the error being less than 10 % for most of the cases. The correlations of loss coefficient of rotational loss can be applied to other rotating machines that having the geometric and dynamic similarities.

9 Conclusions and Further Work

This chapter summarises the steps taken towards the aim of this work. The conclusions and contributions of this thesis are also presented. Parts of the work in this thesis have been published. Following this, recommendations of areas of potential further research are discussed.

9.1 Conclusions

The importance of cooling of electrical machines is addressed in Chapter 1. The power output of an electrical machine is strongly affected by the machine operating temperature because the maximum permissible current in the armature windings is limited by the maximum temperature limit of wire insulation. Apart from this, effective cooling is ultimately essential to ensure machine reliability, adequate life time and efficiency. Strictly speaking, the effectiveness of electrical machine cooling is determined by how well the undesired heat can be transported out from the machine per unit time while the machine temperature is still within the maximum temperature limit. The most effective way to remove the heat is to force a cooling medium to where the heat is generated. The effectiveness of forced convection heat transfer is associated with the value of convective heat transfer coefficient and the convective heat transfer coefficient is mainly dependent on the dimensionless Reynolds number. The Reynolds number links the fluid flow rate with convective heat transfer because it is a measure of the ratio of inertial forces to viscous forces which determines whether the flow is turbulent or laminar.

In principle, the motion of fluid is driven by the differential pressure created by a fan, blower or pump, but the flow rate passing through the cooling paths is restricted by the flow resistance of the ventilation system. For throughflow ventilated machines, the effects of rotation can affect the pressure losses in the ventilation system and consequent the flow distribution. This introduces extra challenges to the lumped parameter thermal network (LPTN) to predict the thermal performance of throughflow ventilated machines accurately because the LPTN relies strongly on the heat transfer correlations to predict the convective heat transfer. However, as described in Chapter 2, the correlations strongly depend on the axial flow Reynolds

number. Moreover, the interaction between rotational flow and axial flow also gives significant influence on convective heat transfer. Therefore, in order to predict the electrical machine thermal performance accurately, thermal analysis of electrical machines must incorporate accurate fluid flow modelling. The review of existing literature reveals that the literature of describing how the effects of rotation affect the pressure losses in air ducts in rotor due to fluid shock is not available. Therefore, the aim of this work is to investigate the pressure losses of air passing through circular ducts in rotor. The ducts are straight and the axes of the ducts are parallel to the rotor axis. The investigation focuses on the rotor ducts because the rotor ducts are the most common ventilation passages that available in throughflow ventilated machines but they are subjected to the effects of rotation.

Dimensional analysis has carried out in Chapter 6 to identify the geometric and dynamic dimensionless groups that are important to the rotational pressure losses. The problem has been investigated using CFD and experimental methods. An experimental test rig has been built specially for this investigation. Both CFD and experimental results show that the pressure losses in rotor ducts due to fluid shock can be mainly correlated with the rotation ratio, V_T/U (i.e. a simplified form of the rotational Reynolds number to axial flow Reynolds number ratio). The rotational pressure losses increase in a second order polynomial relationship with the rotation ratio. The shock loss of rotor duct is also found to be affected by the *H/a* ratio for the first time. The *H/a* ratio is a measure to indicate the proximity of the rotor duct to rotor periphery. Also, for the first time, the effects of Coriolis and centrifugal forces in rotating reference frame to the friction losses in rotor duct are taken into account in the analysis of the problem. The CFD predictions agree well with the experimental measurements. Consequently, this investigation has led to an original set of correlations for pressure losses in air ducts in the rotor due to fluid shock. The investigation also found that the pressure losses due to fluid shock also appear in the rotor-stator gap. The empirical correlation for rotor-stator gap shock loss is also proposed. The CFD simulations show that the pressure losses in rotor-stator gap due to fluid shock is not affected by the gap ratio. The proposed correlations for pressure losses in rotor ducts and rotor-stator gap due to fluid shock are generic and suitable to be applied to most throughflow ventilated machines.

In the flow problem, apart from the additional friction loss due to the effects of rotation, the pressure losses in rotor ducts and rotor-stator gap due to fluid shock, a new type of pressure loss was found in the rotor-stator system which is so-called "combining flow loss". The additional pressure losses are attributed to the deflection of the flow from the rotor ducts caused by the Coriolis and centrifugal effects. This combining flow loss is first disclosed to the literature on the flow problem of throughflow ventilated electrical machines. It is affected not only by the geometric and dynamic parameters of rotor-stator gap, but also geometric and dynamic parameters of rotor ducts. Due to the complexity of the combining flow which involves intense mixing of rotor duct flow with rotor-stator gap flow, the proposed correlations for the combining flow loss of rotor-stator gap flow are only restricted to the specific flow problems. Based on the CFD predictions of the flow pattern of the combining flow in Chapter 6, a simple mechanical structure "flow guard" is proposed in the present research which successfully minimises and reduces the combining flow loss significantly as demonstrated using CFD and experimental results. The flow guard can be used by other throughflow ventilated machines to improve their cooling performance. The investigation has provided better understanding and very useful insight into how the effects of rotation affect the flow characteristics and pressure losses in the rotor ducts and rotor-stator gap.

Due to the limitation of LPTN method on modelling throughflow ventilation machines, this gives a motivation for this research to develop an analytical design tool to model the air flow in these machines and to be integrated with LPTN model. As the analytical air flow modelling tool is based on the flow network analysis technique, the flow network of an electrical machine is composed of various flow components selecting from "Flow Library" to represent the individual part of the ventilation circuit of the actual machine. Hence, it gives high flexibility to create user-defined models for complex flow problem. The applications of the analytical design tool in a liquid-cooled heat sink and throughflow ventilated induction motor have been demonstrated in Chapter 5. The capability of flow network in calculating the local velocity in the individual part of the machine ventilation circuit is beneficial to thermal model to calculate the correct value for convective heat transfer coefficient.

9.2 Further Work

As the purpose of developing the analytical air flow tool is to be integrated with the established lumped-parameter thermal network for throughflow ventilated machines, an evaluation of the application of the air flow modelling tool in thermal management of electrical machines needs to be performed. By accounting for the effects of rotation, it is expected that the thermofluid model can estimate the thermal performance more accurately and hence yields machine performance enhancement as the power output is limited by maximum temperature. Indeed, the rotational pressure loss is an important issue for high speed machines.

In this thesis, the rotational pressure loss is only accounted for the circular ducts with axes parallel to the axis of rotation and annular gap with inner cylinder rotating about its own axis. In order to model the equivalent flow network of other machine topologies, the Flow Library needs to include more components such as the radial circular and rectangular ducts with axes perpendicular to the axis of rotation, the passage of inter-polar spaces between the salient poles of synchronous machine, etc. Moreover, as the flow passing through the throughflow ventilated machines is induced by a fan, analytical estimation of the fan characteristics (e.g. straight radial blades fan, forward radial blades fan, and backward radial blades fan) may also be incorporated into the Flow Library.

In the experimental investigation, only rotor-stator gap ratio of 0.0533 can be tested using the current experimental apparatus. However, the CFD results show that the shock loss of rotor-stator gap is not affected by the gap ratio. Therefore, it is necessary to conduct another experiment of different gap ratios to ensure this is valid.

In electrical machines, wafters are a rotating arrangement of thin blades located at the ends of rotor, acting like fans used to enhance the flow circulation in the end spaces. There are a variety of wafters of different length, width and design. For most squirrel cage induction machines, wafters are normally attached onto the rotor end rings as the devices that cause a draught for end winding cooling. These wafters are commonly located radially below the rotor-stator gap and above the rotor ducts, which is exactly the same of where the flow guard is introduced in the thesis. Further

work is required to investigate the impact of the wafters on the combining flow and also the flow resistance of a rotor-stator system.

Simulation of flow problem in rotor-stator gap and prediction of rotational pressure loss using two-equation turbulence models leads to the discrepancy between the CFD and experimental results due to the limitations of the turbulence models in modelling the flow of rapid strain rate. Therefore, higher order turbulence models such as Reynolds Stress Transport Model (RSM), Large Eddy Simulation or Direct Numerical Simulation is required for further simulations to see what effect these turbulence models have on rotational pressure loss.

Publications

1. Chong, Y.C, Staton, D.A., Mueller, M.A., & Chick, J., 2014. Pressure Loss Measurement in Rotor-Stator Gap of Radial Flux Electrical Machines. In *XXIth International Conference on Electrical Machines.* Berlin: IEEE. pp.2172 – 2178.

2. Chong, Y.C., Echenique Subiabre, E.J.P., Mueller, M.A., Chick, J., Staton, D.A. & McDonald, A.S., 2014. The Ventilation Effect on Stator Convective Heat Transfer of an Axial-Flux Permanent-Magnet Machine. *IEEE Transactions on Industrial Electronics*, 61(8), pp.4392-4403.

3. Chong Y.C., Chick, J., Mueller, M.A., Staton, D.A. & McDonald, A.S., 2012. Thermal modelling of a low speed air-cooled axial flux permanent magnet generator. In *6th IET International Conference on Power Electronics, Machines and Drives*. Bristol: IET.

4. Chong Y.C., Magahy D.A., Chick, J., Mueller, M.A., Staton, D.A. & McDonald, A.S., 2011. Numerical modelling of an Axial Flux Permanent Magnet machine for convection heat transfer. In *1st IET International Conference on Renewable Power Generation*. Edinburgh: IET.

Bibliography

Aavid Thermalloy, 2007. *Hi-Contact™ liquid cold plates for power applications*. Concord: Aavid Thermalloy, LLC.

Adams, T., Grant, C. & Watson, H., 2012. A Simple Algorithm to Relate Measured Surface Roughness to Equivalent Sand-grain Roughness. *International Journal of Mechanical Engineering and Mechatronics*, 1(1), pp.66–71.

Airoldi, G., Ingram, G.L., Mahkamov, K., Bumby, J.R., Dominy, R.G., Brown, N.L., Mebarki, A. & Shanel, M., 2008. Computations on heat transfer in axial flux permanent magnet machines. In *18th International Conference on Electrical Machines*. Vilamoura. IEEE.

Airoldi, G., 2010. *Numerical Investigations of Air Flow and Heat Transfer in Axial Flux Permanent Magnet Electrical Machines*. Doctoral Thesis, Durham University. Available at: http://etheses.dur.ac.uk/264/ [Accessed May 30, 2011].

Al'Akayshee, Q. & Williams, K., 2003. 1500 hp AC Drive Motor Design for Oil Field Drilling Operations. In *Offshore Technology Conference*. Houston.

American Institute of Aeronautics and Astronautics. 1998. Guide for Verification and Validation of Computational Fluid Dynamics Simulation. Technical Report AIAA-G-077-1998.

Batchelor G., 1951. Note on a class of solutions of the Navier-Stokes equations representing steady rotationally-symmetric flow. *Quart. J. of Mechanics Appl. Math.*, 4(1), pp. 29–41.

Boglietti, A. Cavagnino, A., Staton, D., Shanel, M., Mueller, M. & Mejuto, C., 2009. Evolution and Modern Approaches for Thermal Analysis of Electrical Machines. *IEEE Transactions on Industry Electronics*, 56(3), pp.871–882.

Boglietti, A., Cavagnino, A. & Staton, D.A., 2004. Thermal Sensitivity Analysis for TEFC Induction Motors. In *Second International Conference on Power Electronics, Machines and Drives (Conf. Publ. No. 498)*. pp. 160–165.

Boutarfa, R. & Harmand, S., 2004. Local convective heat transfer for laminar and turbulent flow in a rotor-stator system. *Experiments in Fluids*, 38(2), pp.209–221.

British Standards Institution, 1997. BS 848-1:1997 (ISO 5801:1997) *Fans for general purposes – Part 1: Performance testing using standardized airways*. London: BSI.

Bruce, T., 2011. Treatment of Experimental Error, *SCEE08003 Fluid Mechanics 2*. Edinburgh University, unpublished.

Bumby, J.R. & Martin, R., 2005. Axial-flux permanent-magnet air-cored generator for small-scale wind turbines. *IEE Proceedings-Electric Power Applications*, 152(5), pp.1065–1075.

Burmeister, L. C., 1993. *Convection Heat Transfer*. 2nd Edition, New York: John Wiley & Sons, Inc.

Carter, G.W., 1967. *The Electromagnetic Field in its Engineering Aspect*, 2nd ed. Longman.

CD-adapco, 2011. *User Guide STAR-CCM+ Version 6.04.014*, Melville, NY.

Cengel, Y.A. & Cimbala J.M., 2006. *Fluid Mechanics: Fundamentals and Applications*, New York: McGraw-Hill, pp. 840-853.

Centner, M. & Sabelfeld, I., 2012. Coupled fluid-thermal network modeling approach for electrical machines. In *XXth International Conference on Electrical Machines*, Marseille, pp.1238–1241.

Chen, S., 2001. Network analyses of ventilation system for large hydrogenerator. In *Proceedings of the Fifth International Conference on Electrical Machines and Systems*. Shenyang, pp. 137–140.

Childs, P.R.N., 2011. *Rotating Flow*, 1st ed. Oxford: Butterworth-Heinemann, pp. 81-126.

Childs, P. & Turner, A.B., 1994. Heat transfer on the surface of a cylinder rotating in an annulus at high axial and rotational Reynolds numbers. In *Proc. 10th International Heat Transfer Conference*. Brighton, pp. 13–18.

Chirila, A.-I., Ghita, C., Craciunescu, A., Deaconu, I.-D., Navrapescu, V. & Catrinoiu, M., 2010. Rotating Electric Machine Thermal Study. In *International Conference on Renewable Energies and Power Quality*. Spain: European Association for the Development of Renewable Energies, Environment and Power Quality.

Chong, Y.C., Chick, J., Mueller, M.A., Staton, D.A. & McDonald, A.S., 2012. Thermal modelling of a low speed air-cooled axial flux permanent magnet generator. In *6th IET International Conference on Power Electronics, Machines and Drives*. Bristol: IET.

Chong, Y.C., Echenique Subiabre, E.J.P., Mueller, M.A., Chick, J., Staton, D.A. & McDonald, A.S., 2014. The Ventilation Effect on Stator Convective Heat Transfer of an Axial-Flux Permanent-Magnet Machine. *IEEE Transactions on Industrial Electronics*, 61(8), pp.4392-4403.

Coney, J. & Simmers, D., 1979. A study of fully-developed, laminar, axial flow and Taylor vortex flow by means of shear stress measurements. *Journey Mechanical Engineering Science*, IMechE, 21, pp.19-23.

Cornish, R.J., 1933. Flow of Water through Fine Clearances with Relative Motion of the Boundaries. *Proceedings of the Royal Society A: Mathematical, Physical and Engineering Sciences*, 140(840), pp.227–240.

Cross, H., 1936. Analysis of flow in networks of conduits or conductors. *Engineering Experiment Station*, 34(Bulletin No. 286), pp.1–29.

Daily, J. and Nece, R., 1960. Chamber dimension effects on induced flow and frictional resistance of enclosed rotating dicks. *Trans. ASME, J. Basic Eng.*, 82(1), pp. 217-232.

Deissler, R.G., 1953. *Analysis of turbulent heat transfer and flow in the entrance regions of smooth passages*, Washington. Technical Note 3016. National Advisory Committee For Aeronautics.

Di Gerlando, A., Foglia, G., Iacchetti, M.F. & Perini, R., 2011. Axial flux PM machines with concentrated armature windings: Design analysis and test validation of wind energy generators. *IEEE Transactions on Industrial Electronics*, 58(9), pp.3795–3805.

Douglas, J.F., Gasiorek J.M. & Swaffield J.A., 1995. *Fluid Mechanics*, 3rd ed. Singapore: Longman, pp. 145-189.

Electrical Apparatus Service Association, 2000. *Principles of Large AC Motors*, Missouri: EASA.

Gardiner, S. & Sabersky, R., 1978. Heat transfer in an annular gap. *International Journal of Heat and Mass Transfer*, 21, pp.1459–1466.

Gazley, C., 1958. Heat transfer characteristics of the rotational and axial flow between concentric cylinders. *Transcations of the ASME American Society of Mechanical Engineers*, 80, pp. 79-90.

Goldstein, S., 1937, The stability of viscous fluid flow between rotating cylinders. *Cambridge Philosophical Society*, 33, pp.41-61.

Enercon, 2014. *E101 Optimum yields at low wind sites*. Enercon. Available from: http://www.enercon.de/en-en/65.htm [Accessed 5/04/2014].

Enercon, 2014. *E126 State of the art*. Enercon. Available from: http://www.enercon.de/en-en/2290.htm [Accessed 5/04/2014].

Hey, J., Howey, D. A., Martinez-Botas, R. & Lamperth, M., 2010. Transient Thermal Modeling of an Axial Flux Permanent Magnet (AFPM) Machine Using a Hybrid Thermal Model. *International Journal of Mechanical and Materials Engineering*, pp.150–159.

Hodgins, N., Keysan, Ozan, McDonald, A.S & Mueller, M.A., 2012. Design and Testing of a Linear Generator for Wave-Energy Applications. *IEEE Transactions on Industrial Electronics*, 59(5), pp.2094–2103.

Howey, D.A., Holmes, A.S. & Pullen, K.R., 2011. Measurement and CFD Prediction of Heat Transfer in Air-Cooled Disc-Type Electrical Machines. *IEEE Transactions on Industry Applications*, 47(4), pp.1716–1723.

Howey, D.A., Holmes, A.S. & Pullen, K.R., 2010. Prediction and measurement of heat transfer in air-cooled disc-type electrical machines. In *5th IET International Conference on Power Electronics, Machines and Drives*. IET.

Hughes, A., 2006. *Electric Motors and Drives: Fundamentals, Types and Applications.* 3rd edition, Newnes: Oxford, ISBN 0750647183.

Humphreys, J. F., Morris,W. D. & Barrow, H., 1967. Convection heat transfer in the entry region of a tube which revolves about an axis parallel to itself. *International Journal of Heat & Mass Transfer*, 10, pp. 333-347.

Idelchik, I. E., 2007. *Handbook of Hydraulic Resistance*, 4th edition, Redding: Begell House, Inc.

International Standards Office, 2003. ISO 5167-1:2003(E) *Measurement of fluid flow by means of pressure differential devices inserted in circular cross-section conduits running full – Part 1: General principles and requirements*. Geneva: ISO.

International Standards Office, 2003. ISO 5167-2:2003(E) *Measurement of fluid flow by means of pressure differential devices inserted in circular cross-section conduits running full – Part 2: Orifice plates*. Brussels: ISO.

Jeng, T.-M., Tzeng, S.-C. & Lin, C.-H., 2007. Heat transfer enhancement of Taylor–Couette–Poiseuille flow in an annulus by mounting longitudinal ribs on the rotating inner cylinder. *International Journal of Heat and Mass Transfer*, 50(1-2), pp.381–390.

Incropera, F. P. & DeWitt, D. P., 2002. Fundamental of Heat and Mass Transfer. 5th Edition. New York: John Wiley & Sons, Inc.

Jeremie, L., Foggia, A. & Rakotovao, M., 2010. Thermal and aerolic modeling for air cooled claw pole machines. In *XIX International Conference on Electrical Machines, Rome*.

Johnson, A.R., & Morris, W.D., 1992. An experimental investigation into the effects of rotation on the isothermal flow resistance in circular tubes rotating about a parallel axis, *International journal of heat and fluid flow*, 13(2), pp. 132-140.

Jung, W. M., Kang, S. H., Kim, W. S. & Choi, C. K., 2000. Particle morphology of calcium carbonate precipitated by gas–liquid reaction in a Couette–Taylor reactor, *Chemical Engineering Science*, 55(4), pp. 733–747.

Jungreuthmayer, C., Bauml, T., Winter, O., Ganchev, M., Kapeller, H., Haumer, A. & Kral, C., 2012. A Detailed Heat and Fluid Flow Analysis of an Internal Permanent Magnet Synchronous Machine by Means of Computational Fluid Dynamics. *IEEE Transactions on Industrial Electronics*, 59(12), pp.4568–4578.

Kaye, J. & Elgar, E., 1958. Modes of adiabatic and diabatic fluid flow in an annulus with an inner rotating cylinder," *Transcations of the ASME American Society of Mechanical Engineers*, 80, pp. 753-765.

Kays, W. M. & Crawford, M. E., 1993. *Convection Heat and Mass Transfer*. 3rd Edition. Singapore: McGraw-Hill, Inc.

Khan, I.A., 1987. *Fluid Mechanics*. 1st edition. New York: Holt, Rinehart and Winston.

Knudsen, J. G. & Katz D. L., 1958. *Fluid Dynamics and Heat Transfer*. New York:McGraw-Hill, pp. 361-390.

Kuzay, T. M. & Scott, C. J., 1977. Turbulent heat transfer studies in annulus with inner cylinder rotation. *Transcations of the ASME American Society of Mechanical Engineers, International Journal of Heat & Mass Transfer*, 99, pp. 12-19.

Lee, Y. & Minkowycz, W., 1989. Heat transfer characteristics of the annulus of two coaxial cylinders with one cylinder rotating. *International journal of heat and mass transfer*, 32(4), pp.711–721.

Le Feuvre, R. F., 1968. Heat transfer in rotor cooling ducts. In *Conference Proceedings of the Institution of Mechanical Engineers*, 182(38), pp. 232-240.

Liao, C., Chen, C. & Katcher, T., 1999. Thermal management of AC induction motors using computational fluid dynamics modeling. In *International Electric Machines and Drives Conference*. pp. 189–191.

Marignetti, F., Colli, V.D. & Coia, Y., 2008. Design of Axial Flux PM Synchronous Machines Through 3-D Coupled Electromagnetic Thermal and. *IEEE Transactions on Industrial Electronics*, 55(10), pp.3591–3601.

McDonald, A. S., Benatmane, M., & Mueller, M. A., 2011. A multi-stage axial flux permanent magnet machine for direct drive wind turbines. In *1st IET Conf. Renewable Power Generation*, Edinburgh, U.K.

Mejuto, C., Mueller, M., Staton, D., Mebarki, S. & Al-Khayat, N., 2006. Thermal Modelling of TEFC Alternators. In *32nd Annual Conference on IEEE Industrial Electronics*. Paris: IEEE, pp. 4813–4818.

Mellor, P.H., Roberts, D. & Turner, D.R., 1991. Lumped parameter thermal model for electrical machines of TEFC design. *IEE Proceedings B Electric Power Applications*, 138(5), pp.205–218.

Mellor, P.H., 1991. Estimation of Parameters and Performance of Rare-Earth Permanent-Magnet Motors Avoiding Measurement of Load Angle. *IEE Proc. B Electric Power Appl.*, 138(6), pp. 322–330.

Miller, D.S., 1978. *Internal Flow Systems*, 1st edition. UK: BHRA Fluid Engineering.

Mori, Y. & Nakayama, W., 1967. Forced convection heat transfer in a straight pipe rotating around a parallel axis (1st report, laminar region). *International Journal of Heat & Mass Transfer*, 10, pp. 1179-1194.

Morris, W. D. & Woods, J. L., 1978. Heat Transfer in the Entrance Region of Tubes that Rotate about a Parallel Axis. *Journal of Mechanical Engineering Science*, 20(6), pp. 319-325.

Morris, W. D., 1981. *Heat Transfer and Fluid Flow in Rotating Coolant Channels*, Research Studies Press.

Morris W.D., 1981. A pressure transmission system for flow resistance measurements in a rotating tube," *Journal of Physics E: Scientific Instruments*, 14, pp. 208-214.

Mueller, M.A. & McDonald, A.S., 2009. A lightweight low-speed permanent magnet electrical generator for direct-drive wind turbines. *Wind Energy*, 12(8), pp.768–780.

Mugglestone, J., Lampard, D. & Pickering, S.J., 1998. Effects of end winding porosity upon the flow field and ventilation losses in the end region of TEFC

induction machines. *IEE Proceedings - Electric Power Applications*, 145(5), pp.423–428.

Nakayama, W., 1968. Forced convection heat transfer in a straight pipe rotating around a parallel axis (2nd report, turbulent region). *International Journal of Heat & Mass Transfer*, 11, pp. 1185-1201.

Norris, R.H., 1971, Augmentation of convective heat transfer. *American Society of Mechanical Engineers*, New York.

Onuki, T., Wakao, S., Tokuhisa, M. & Maeda, A., 1999. A novel approach to design optimization of ventilation holes in induction motors. In *International Conference Electric Machines and Drives*. Seattle, WA, pp. 478–480.

Owen, J. & Rogers, R., 1989. *Flow and Heat Transfer in Rotating-Disc Systems, Vol. 1: Rotor–Stator Systems*, 1st ed. Taunton: Res. Stud. Press.

Pickering, S.J., Lampard, D. & Shanel, M., 2001. Modelling ventilation and cooling of the rotors of salient pole machines. In *International Electric Machines and Drives Conference*. IEEE, pp. 806–808.

Pickering, S.J., Lampard, D. & Shanel, M., 2002. Ventilation and heat transfer in a symmetrically ventilated salient pole synchronous machine. In *International Conference on Power Electronics, Machines and Drives*. pp. 462–467.

Press, W.H., Teukolsky, S.A., Vetterling, W.T. & Flannery, B.P., 2007. *"Chapter 9. Root Finding and Nonlinear Sets of Equations Importance Sampling". Numerical Recipes: The Art of Scientific Computing*. 3rd edition. New York: Cambridge University Press.

Pyrhonen, J., Jokinen, T. & Hrabovcova, V., 2008. *Design of rotating electrical machines*. 1st edition, Chichester: John Wiley & Sons, Ltd.

Randewijk, P. & Mouton, H. duT., 2006. Using VHDL-AMS for electrical, electromechanical, power electronic and DSP-algorithm simulations. In *Proceedings of the South African Universities Power Engineering Conference*, Durban.

Rosendahls, 2010. *RepliSet, An advanced replica technique for the inspection of critical surfaces*. Ballerup: Struers.

Saatdjian, E., 2000. *Transport Phenomena: Equations and Numerical Solutions*. 1st edition. Chichester: John Wiley & Sons Ltd.

Sakamoto, M. & Fukui, S., 1971. Convection heat transfer of a rotating tube revolving about an axis parallel to itself. Electrical and Nuclear Lab, Tokyo Shibawa Electric Co. Ltd, Kawasaki, Japan.

Scowby, S., Dobson, R.T. & Kamper, M.J., 2004. Thermal modelling of an axial flux permanent magnet machine. *Applied Thermal Engineering*, 24(2-3), pp.193–207.

Shanel, M., Pickering, S.J. & Lampard, D., 2003. Conjugate heat transfer analysis of a salient pole rotor in an air cooled synchronous generator. In *International Electric Machines and Drives Conference*. IEEE, pp. 737–741.

Siemens AG, 2013. *Three-Phase Induction Motors SIMOTICS HV, SIMOTICS TN Series H-compact Series H-compact PLUS, Catalog D84.1*. [online] Available at: <http://www.automation.siemens.com/mcms/infocenter/content/en/Pages/order_form.aspx?nodeKey=key_516797> [Accessed 2 June 2013].

Simmers, D. & Coney, J., 1979. A Reynolds analogy solution for the heat transfer characteristics of combined Taylor vortex and axial flows. *International Journal of Heat and Mass Transfer*, 22, pp. 679-689.

Spearman, E., Sattary, J. & Reader-Harris, M., 1996. Comparison of velocity and turbulence profiles downstream of perforated plate flow conditioners. *Flow measurement and Instrumentation*, 7(3-4), pp.181–199.

Staton, D.A. & Cavagnino, A., 2008. Convection Heat Transfer and Flow Calculations Suitable for Electric Machines Thermal Models. *IEEE Transactions on Industrial Electronics*, 55(10), pp.3509–3516.

Staton, D., Boglietti, A. & Cavagnino, A., 2005. Solving the More Difficult Aspects of Electric Motor Thermal Analysis in Small and Medium Size Industrial Induction Motors. *IEEE Transactions on Energy Conversion*, 20(3), pp.620–628.

Stewartson, K., 1953. On the flow between two rotating coaxial discs. *Math. Proc. Cambridge Philosph. Soc.*, 49(2), pp. 333–341.

Sun, X. & Cheng, M., 2013. Thermal Analysis and Cooling System Design of Dual Mechanical Port Machine for Wind Power Application. *IEEE Transactions on Industrial Electronics*, 60(5), pp.1724–1733.

Tachibana, F. & Fukui, S., 1964. Convective heat transfer of the rotational and axial flow between two concentric cylinder. *Bulletin of the Japan Society of Mechanical Engineers*, 7 (26), pp. 385-391.

Taylor, G. I., 1923. Stability of a viscous liquid contained between two rotating cylinder," *Proceedings of the Royal Society, London, Series A*, 223, pp. 239-343.

Taylor, J.L., 1960. Calculating Air Flow through Electrical Machines. *Electrical Times*, pp.82–84.

Taylor, J.R., 1997. *An Introduction to Error Analysis: The Study of Uncertainties in Physical Measurements*. 2nd edition. Sausalito: University Science Books.

Technical University of Denmark, 2010. *DeepWind.* [online] Denmark: Seventh Framework Programme, European project. Available at: <http://www.risoecampus.dtu.dk/Research/sustainable_energy/wind_energy/projects/VEA_DeepWind.aspx?sc_lang=en> [Accessed 29 March 2013].

The European Wind Energy Association, 2011. *UpWind Design limits and solutions for very large wind turbines.* [online] Denmark: Sixth Framework Programme, European project. Available at: <http://www.upwind.eu/> [Accessed 29 March 2013].

Traxler-Samek, G., Zickermann, R. & Schwery, A., 2010. Cooling airflow, losses, and temperatures in large air-cooled synchronous machines. *IEEE Transactions on Industrial Electronics*, 57(1), pp.172–180.

Tu J., Yeoh G. & Liu C., 2013. *Computational Fluid Dynamics: A Practical Approach*. 2nd edition. Oxford: Butterworth-Heinemann.

Versteeg, H. K. & Malalasekera, W., 2007. *An Introduction to Computational Fluid Dynamics: The Finite Volume Method*. 2nd edition. Essex: Pearson Education Ltd.

Wang, R.J., Kamper, M.J. & Dobson, R.T., 2005. Development of a Thermofluid Model for Axial Field Permanent-Magnet Machines. *IEEE Transactions on Energy Conversion*, 20(1), pp.80–87.

Wang, R. and Kamper, M. J., 2002. Evaluation of eddy current losses in axial flux permanent magnet (AFPM) machine with an ironless stator. In *37th IAS Annu. Meeting Conf. Rec. IEEE Ind. Appl.*, 2, pp. 1289–1294.

Webb, J.D., 1964. *The Flow of Air Through Axial Cooling Ducts in a Rotor*, Report No. W/M(2A)p.85, The English Electric Company Ltd. Department Mechanical Engineering Laboratory.

White, F.M., 1986. *Fluid Mechanics*. 2nd edition. Singapore: McGraw-Hill.

Winterton, R.H.S., 1998, Where did the Dittus and Boelter equation come from. *International Journal of Heat and Mass Transfer*, 41, pp. 809-810.

Woods, J. L. & Morris, W. D., 1974. An Invesitgation of Laminar Flow in the Rotor Windings of Directly-cooled Electrical Machines. *Journal of Mechanical Engineering Science*, 16(6), pp. 408-417.

Wrobel, R. & Mellor, P., 2010. A General Cuboidal Element for Three-Dimensional Thermal Modelling. *IEEE Transactions on Magnetics*, 46(8), pp.3197–3200.

Wrobel, R., McNeill, N. & Mellor, P.H., 2010. Performance analysis and thermal modeling of a high-energy-density prebiased inductor. *IEEE Transactions on Industrial Electronics*, 57(1), pp.201–208.

Yanagida, T. & Kawasaki, N., 1987. Pressure Drop and Heat Transfer Characteristics of Axial Air Flow Through an Annulus with a Deep-Slotted Outer Cylinder and a Rotating Inner Cylinder : 1st Report, Pressure Drop Characteristics. *Transactions of the Japan Society of Mechanical Engineers. B*, 53(493), pp.2714–2719.

Yamada, Y., 1962. Resistance of a flow through an annulus with an inner rotating cylinder. *Bulletin of the Japan Society of Mechanical Engineers*, 5(18), pp.302–310.

Yamada, Y. & Nakabayashi, K., 1970. Measurements of Pressure Distribution around Eccentric Cylinders, with the Outer Cylinder Rotating. *Bulletin of the Japan Society of Mechanical Engineers*, 13(55), pp.59–68.

Yamada, Y., Nakabayashi, K. & Maeda, K., 1969. Pressure Drop Measurements of the Flow through Eccentric Cylinders with Rotating Inner Cylinders. *Bulletin of the Japan Society of Mechanical Engineers*, 12(53), pp.1032–1040.

Appendix A – Power Losses Calculation

A complete analysis of the power losses of the air-cored AFPM prototype is presented and the procedure of evaluating the power losses of the prototype is described.

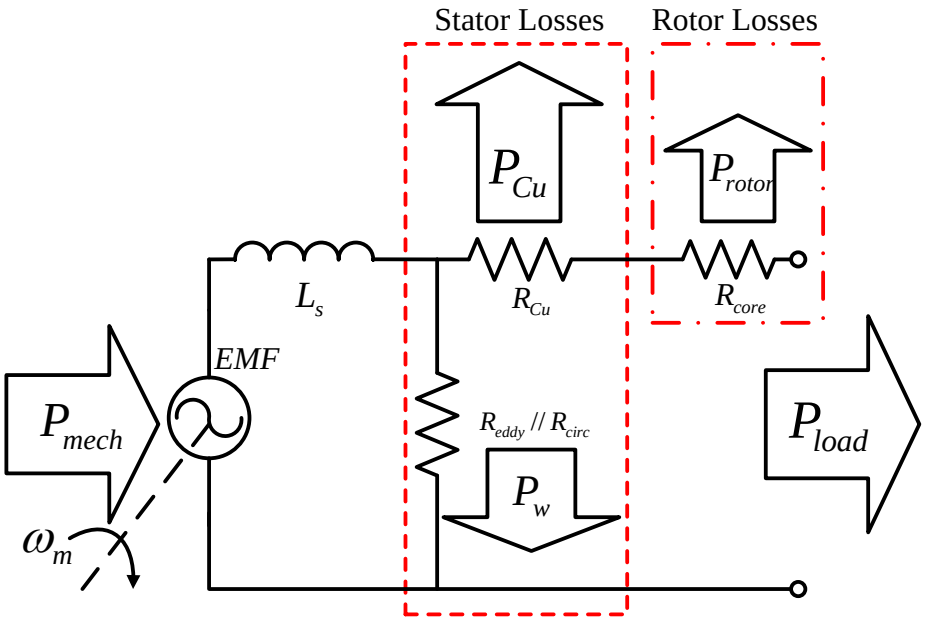

Figure A.1: Circuital representation of electrical losses in an air-cored machine

Method for Electrical Losses:

Eddy currents in the windings can be estimated analytically using the well-known Carters formula, Carter [1967] which is accurate at low electrical frequencies (i.e. $f \leq 50$ Hz), Wang and Kampar [2002]:

$$P_{eddy_{coils}} = \frac{\left(\pi^3 B_g^2 d_w^4 f^2 L_m N_t\right)}{4\rho_{Cu}(1 + \alpha_{Cu}\Delta T_{coil})} \tag{A.1}$$

Copper and rotor losses are calculated using:

$$P_{Cu} = 3I_{rms}^2 R_{Cu}^{amb}(1 + \alpha_{Cu}\Delta T_{coil}) \tag{A.2}$$

$$P_{rotor} = (3I_{rms}^2 R_{core})/(1 + \alpha_{core}\Delta T_{core}) \tag{A.3}$$

The core resistance R_{core} in Figure A.1 lumps together the magnets and iron losses. Since the thermal resistivity coefficients of the iron and Neodymium magnets are approximately 300 and 4000 times lower than the copper respectively (for the

thermal operating range of 0 to 120 ºC), the changes of resistivity in magnets and iron are neglected, and simply estimate rotor losses as $P_{rotor} \approx 3I_{rms}^2 R_{core}$.

Additionally, the phase current I_{rms} for a machine connected to a resistive load (R_{load}) is obtained from:

$$EMF^2 = \left(V_{load} + R_{eq} I_{rms}\right)^2 + (\omega_s L_s I_{rms})^2 \tag{A.4}$$

$$I_{rms} = \frac{EMF}{\sqrt{R_{load}^2 + 2R_{load}R_{eq} + R_{eq}^2 + (\omega_s L_s)^2}} \tag{A.5}$$

As $R_{eddy}//R_{circ} \gg \omega_e L_s$ from Figure A.1, the equivalent Thevenin resistance R_{eq} of the generator considering the thermal effect in the copper only is given by:

$$R_{eq} = R_{Cu}^{amb}(1 + \alpha_{Cu}\Delta T_{coil}) + R_{core} \tag{A.6}$$

Copper resistance can be easily estimated. However, the core resistance is obtained using can the locked-rotor test. As the machine is connected to a resistive load bank and the EMF has negligible harmonics, McDonald et al. [2011], the only relevant loss is induced by the 1st time harmonic component. The core resistance was measured using the direct-axis connection described in Mellor [1991], using a magnetic analyzer (Wayne Kerr Electronics, model 3260B), that gives the equivalent impedance in the locked-rotor test. The estimation is accurate in terms of aggregated losses. Segregation between iron and magnet losses is presented in Chong et al. [2014].

Eddy and circulating current losses were determined experimentally by the no-load tests from standstill to rated speed. Torque input and mechanical speed were measured at the shaft of the generator in steady state conditions. At low speed, the mechanical losses are linearly proportional to the rotational speed, whereas eddy and circulating current losses are directly proportional to the square of rotational speed. Mechanical and electrical losses are modelled using (A.7) and (A.8) respectively. The constants k_m, k_{eddy} are obtained by fitting the experimental data to a 2nd order polynomial as shown in Figure A.2. The circulating current coefficient k_{circ} is obtained from the segregation of losses.

For mechanical loss,

$$P_{mech-loss} = k_m \omega_m \tag{A.7}$$

For circulating and eddy current losses,

$$P_w = (k_{eddy} + k_{circ}){\omega_m}^2 \tag{A.8}$$

For no-load loss,

$$P_{no-load} = P_w + P_{mech-loss} \tag{A.9}$$

where k_m, k_{circ} and k_{eddy} are constants for mechanical, circulating and eddy current losses respectively. The values of these constants are given in the table below.

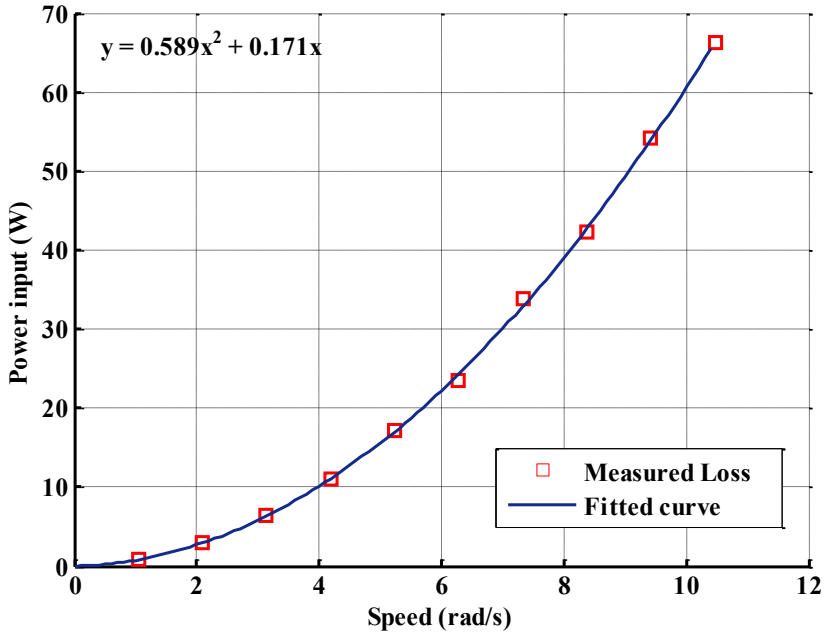

Figure A.2: No-load losses (disconnected coils) fitted to a 2nd order polynomial. The first coefficient (0.589) represents k_{eddy}, the second one (0.171) represents k_m.

Segregation between eddy and circulating current losses is done by performing the no-load test twice: coils with disconnected and parallel connections. Table A.1 summarizes the experimental constants and magnitudes for the no-load losses at 100 rpm. The eddy current loss using (A.1) shows good agreement compared to the measured value.

	Disconnected coils (no circulating loss)			Parallel Connection	
	k_m	k_{eddy}	k_{eddy} (Analytical)	k_{eddy}	k_{circ}
Constants at 21.8 ºC	0.171	0.589	0.583	0.589	1.980
Power Loss at 100 rpm (W)	1.8	64.7	63.9	64.7	217.5

Table A.1: Mechanical, Eddy, and Circulating Current Losses of the AFPM Generator at Rated Speed

Appendix B – Mesh Refinement Study and Convergence

Mesh refinement study

The objective of the CFD analysis was to determine the machine temperature rise for different inlet configuration at the rotor. As the stator and rotor are cooled by air passing over them and the air at the wall is heated by the wall temperature, the air temperature gradient perpendicular to the wall is high. Therefore, sufficient number of computational cells is required for the qualitative CFD analysis. The temperature and flow fields are computed on three grids as shown in Figure B.1. There are 31, 21 and 12 computational cells across the rotor-stator gap of the CFD model. Figure B.2, Figure B.3 and Figure B.4 indicate the resulting temperature rises of thermocouple A, thermocouple B, thermocouple C, coil mean temperature, magnet mean temperature and rotor mean temperature using the three grids. For each grid, the number of computational cells across the rotor-stator gap is normalised to the number of computational cells across the rotor-stator gap for the finest grid (i.e. Mesh 1). For instances, 31/31 gives 1 for Mesh 1, 31/21 gives 1.48 for Mesh 2 and 31/12 gives 2.58 for Mesh 3. Figure B.2, Figure B.3 and Figure B.4 show that the machine temperature rises vary with the grid spacing. However, the temperature difference between Mesh 1 and Mesh 2 is negligible. This indicates that mesh independent solutions have been reached. Hence, Mesh 1 is sufficient to calculate the conjugate heat transfer solution. The CFD results presented in Chapter 4 are obtained from Mesh 1.

Convergence

For each inlet configuration, the residuals of the CFD solution are monitored. Besides, the machine temperature and flow velocity passing through the ventilation holes are also monitored in order to confirm convergence of the CFD solution. Each solution was properly converged with respect to iterations as shown from Figure B.5 to Figure B.15.

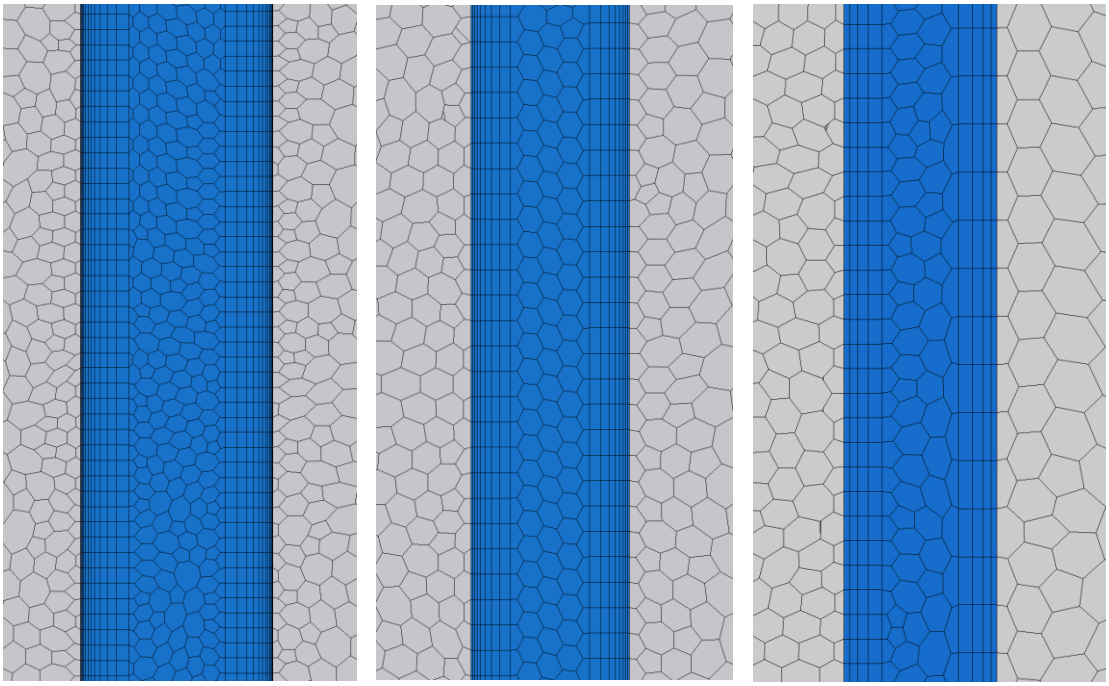

(a) Mesh 1 (b) Mesh 2 (c) Mesh 3

Figure B.1: Mesh in rotor-stator gap (blue region – air, grey region – stator/rotor)

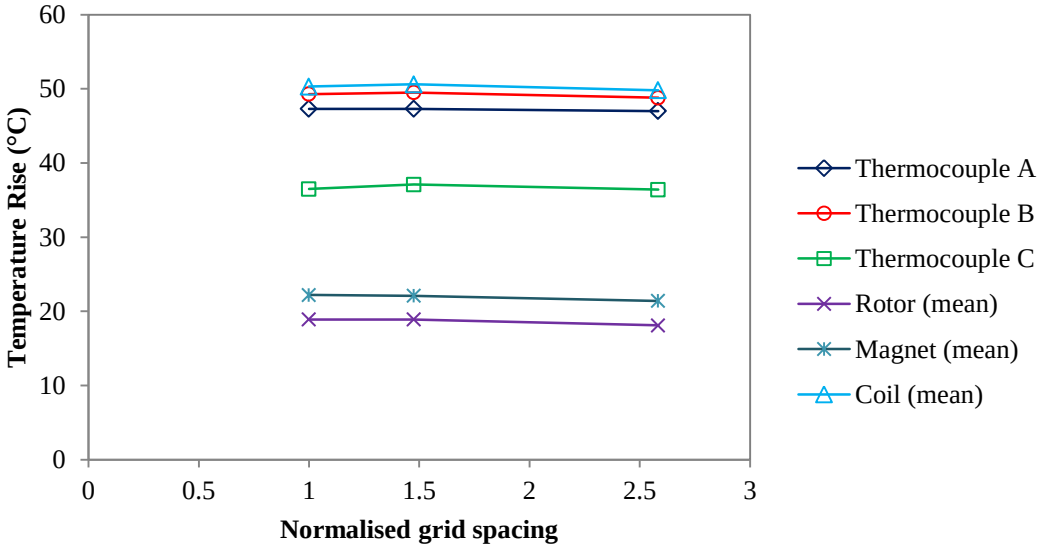

Figure B.2: Mesh refinement study for Case 1: Ventilation with radial and axial holes

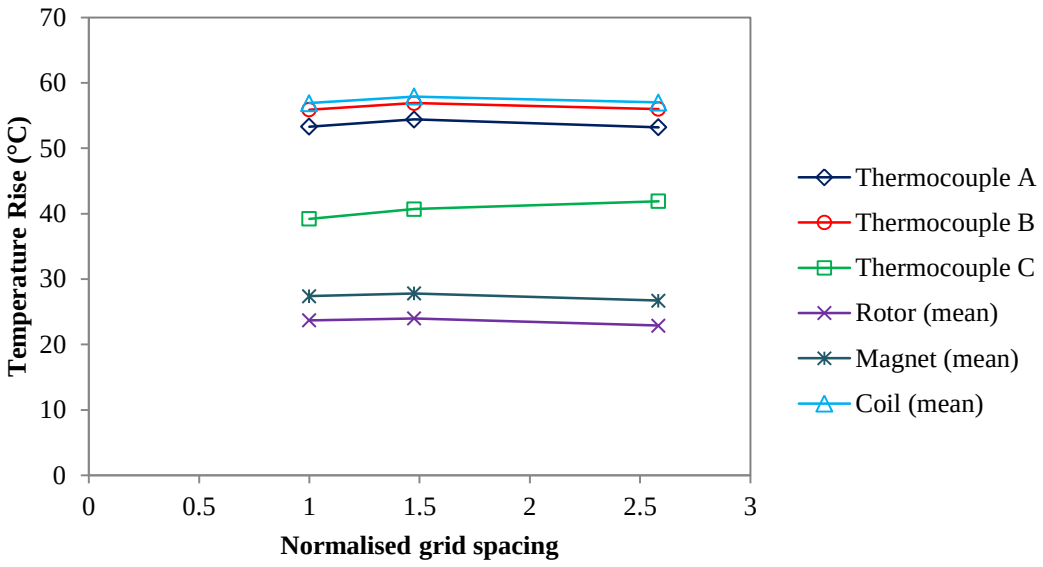

Figure B.3: Mesh refinement study for Case 2: Ventilation with radial holes only

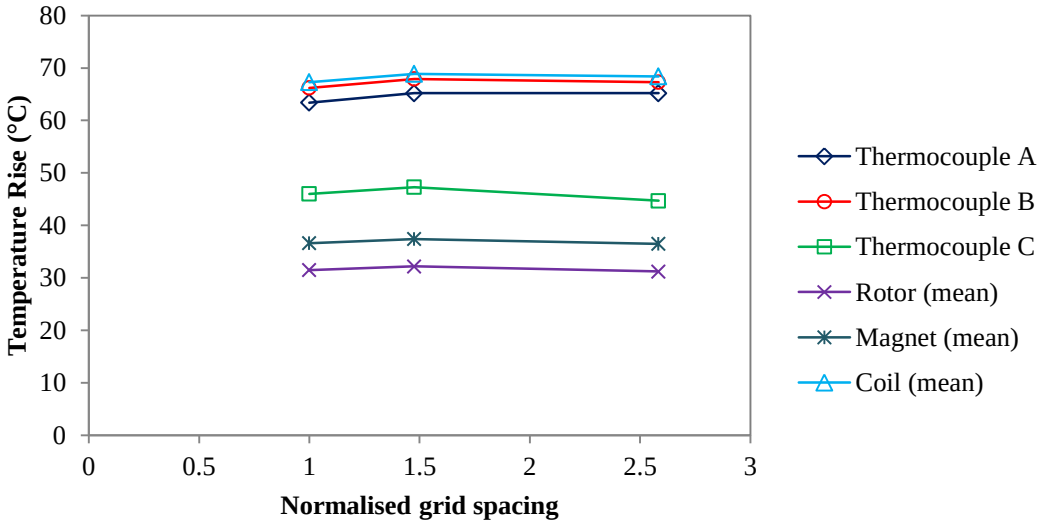

Figure B.4: Mesh refinement study for Case 3: Ventilation with axial holes only

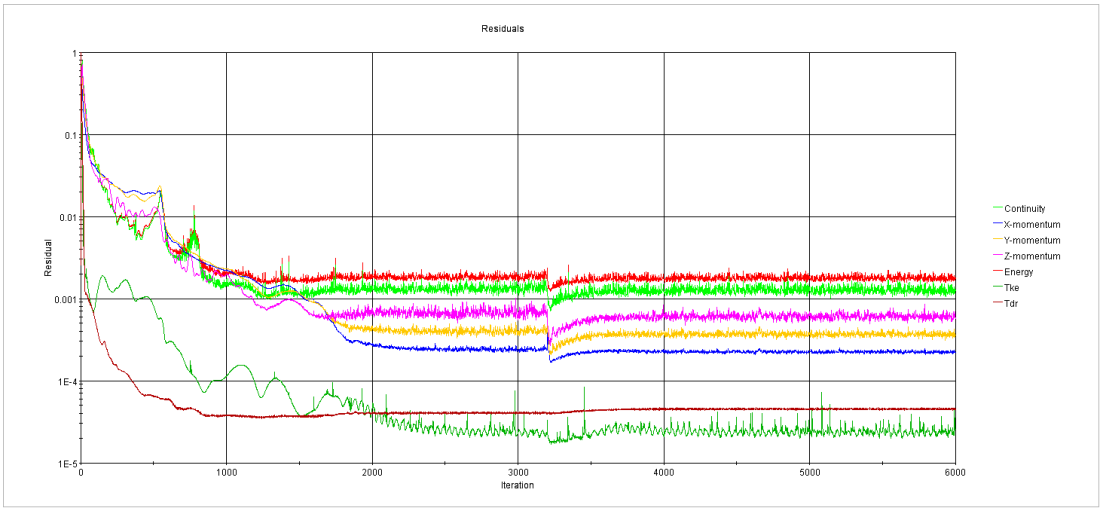

Figure B.5: Residuals for Case 1: Ventilation with radial and axial holes

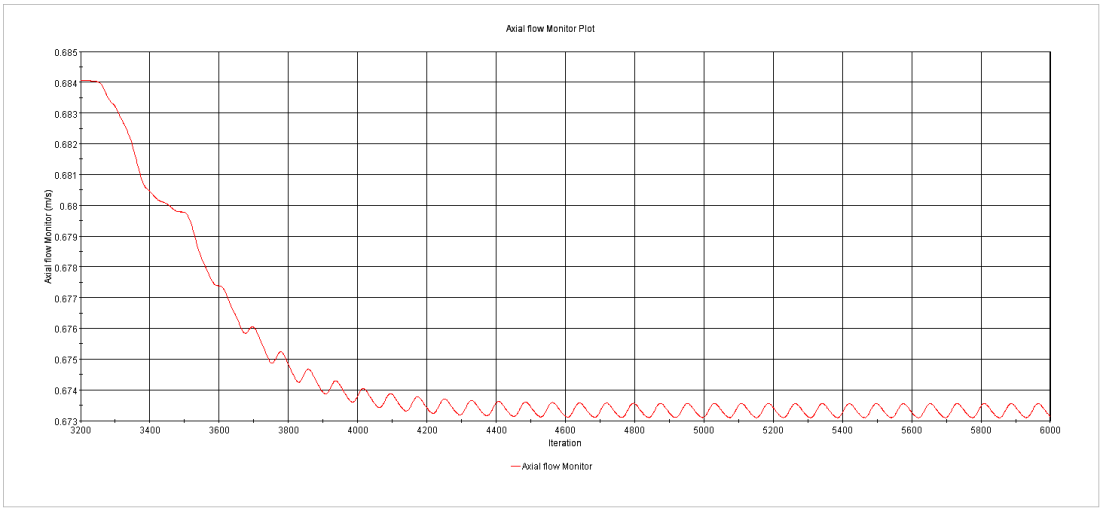

Figure B.6: Flow velocity in axial hole for Case 1: Ventilation with radial and axial holes

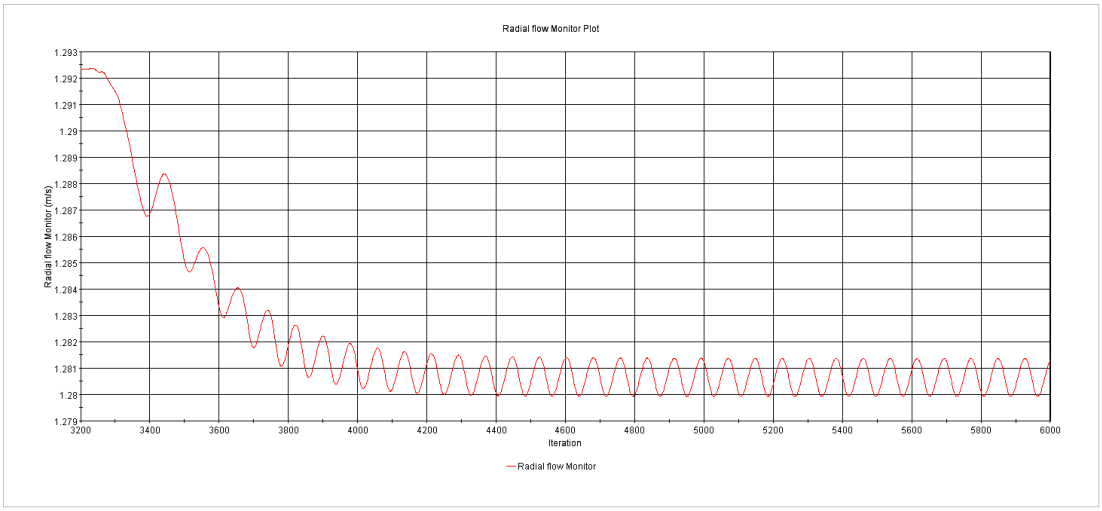

Figure B.7: Flow velocity in radial hole for Case 1: Ventilation with radial and axial holes

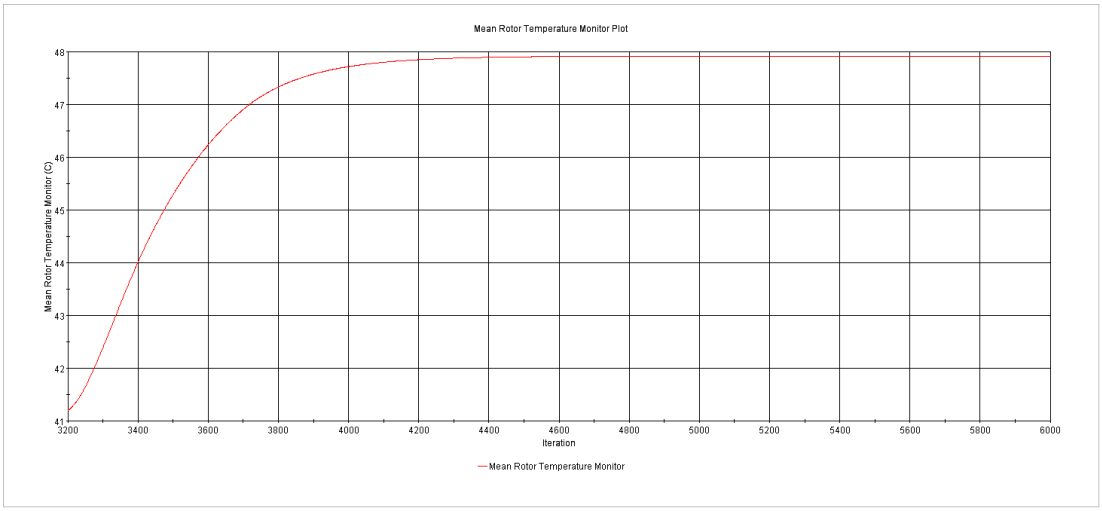

Figure B.8: Mean rotor temperature for Case 1: Ventilation with radial and axial holes

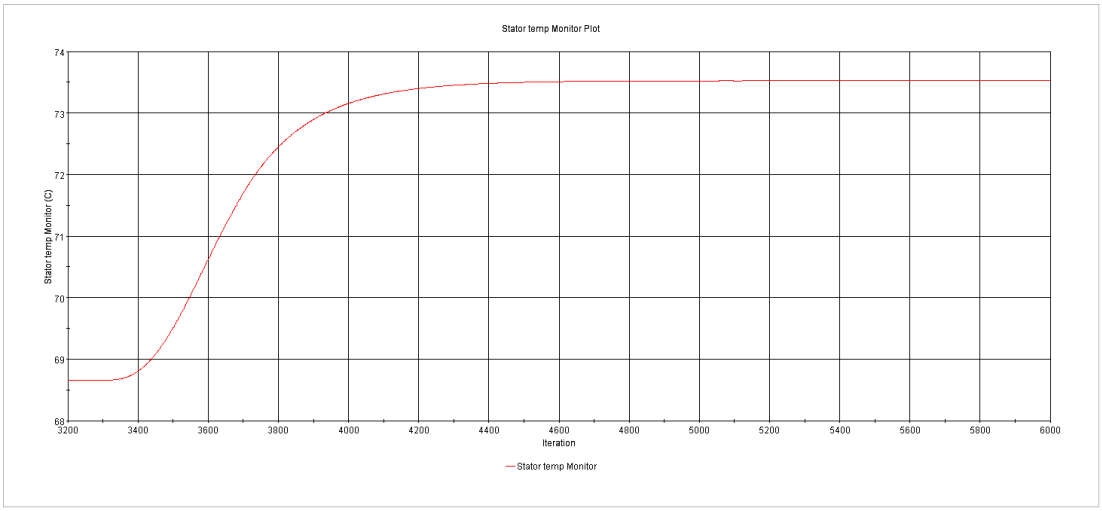

Figure B.9: Mean stator surface temperature for Case 1: Ventilation with radial and axial holes

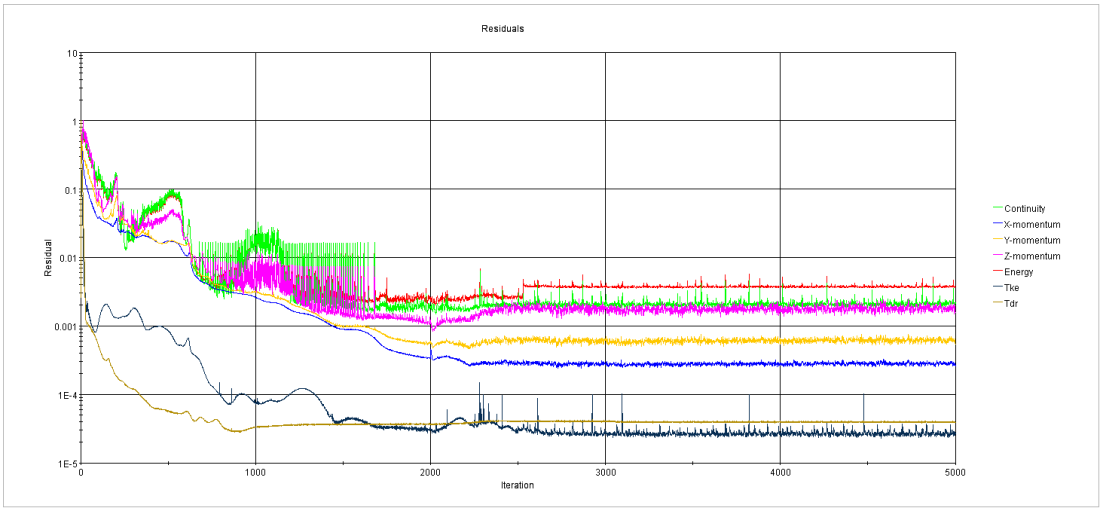

Figure B.10: Residuals for Case 2: Ventilation with radial holes only

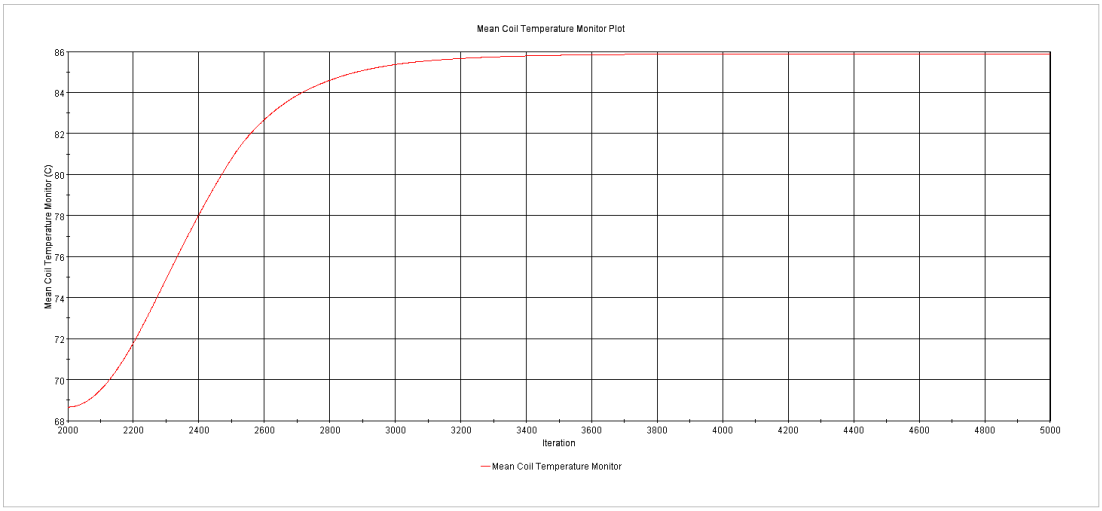

Figure B.11: Mean coil temperature for Case 2: Ventilation with radial holes only

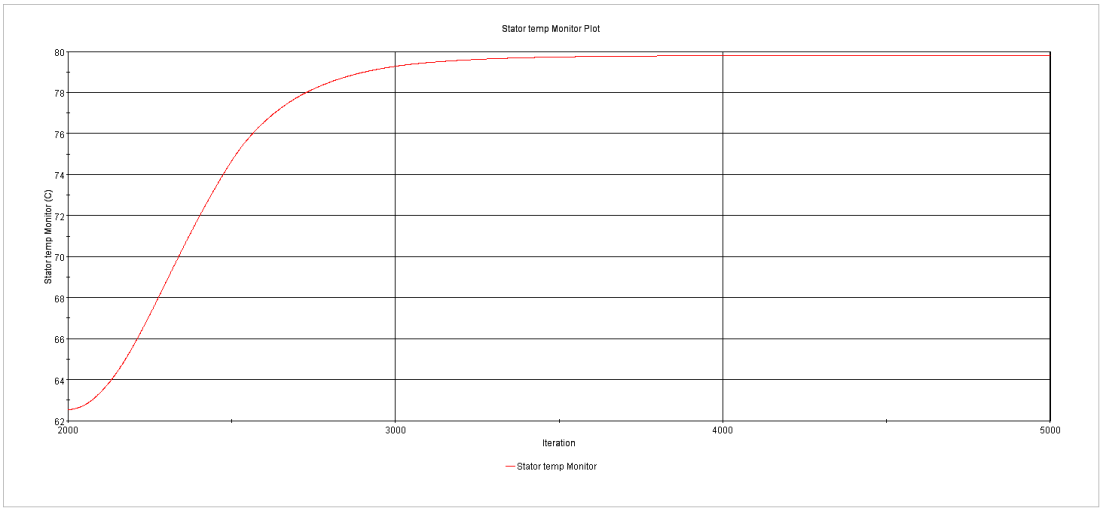

Figure B.12: Mean stator surface temperature for Case 2: Ventilation with radial holes only

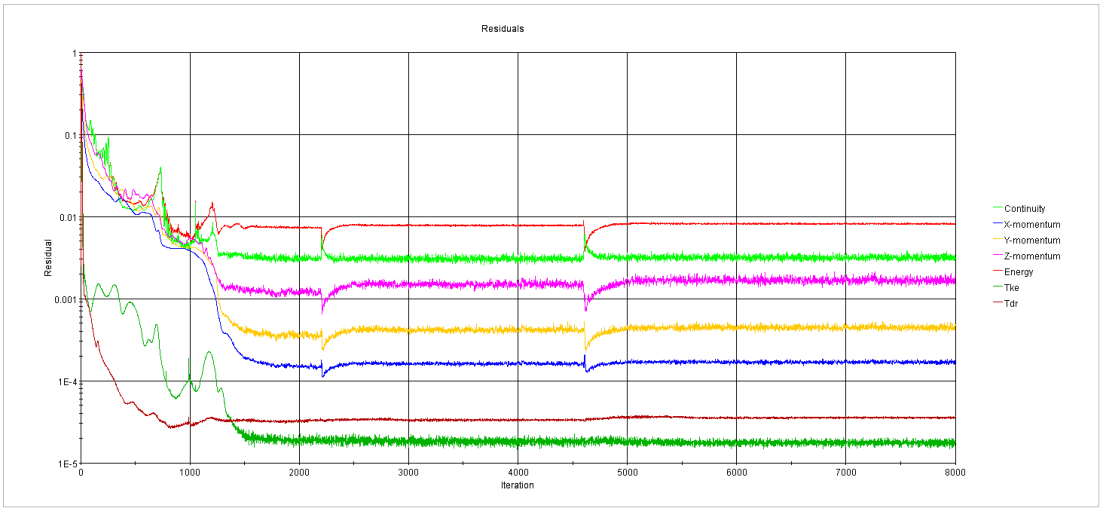

Figure B.13: Residuals for Case 3: Ventilation with axial holes only

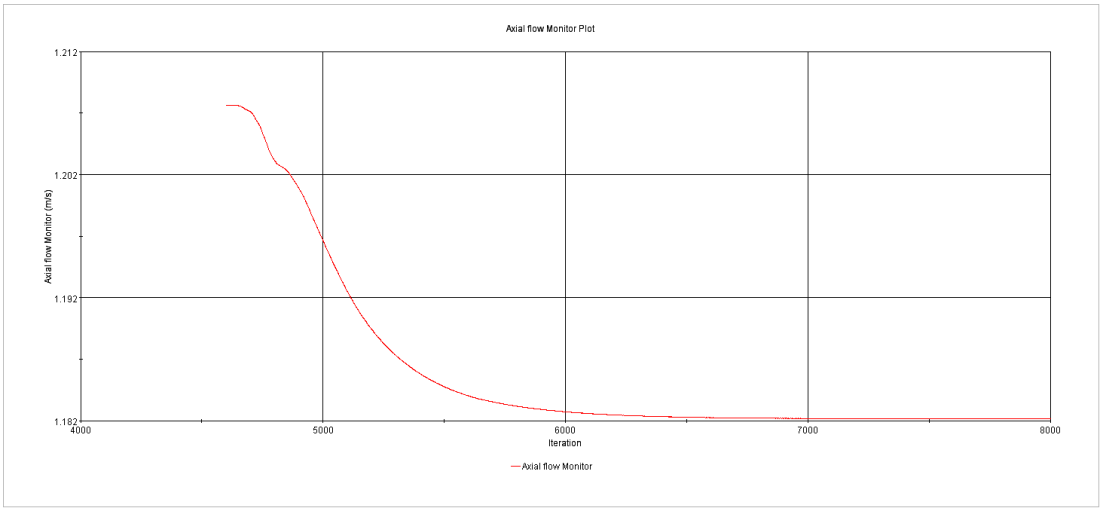

Figure B.14: Flow velocity in axial hole for Case 3: Ventilation with axial holes only

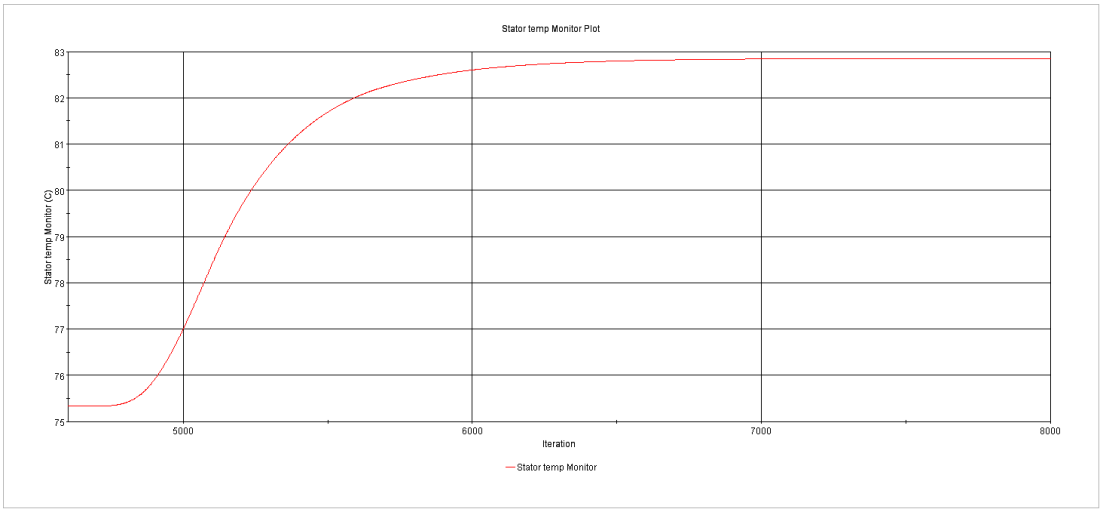

Figure B.15: Mean stator surface temperature for Case 3: Ventilation with axial holes only

Appendix C – CFD Field Functions

The electrical losses of the AFPM machine at 100 rpm for a single stage can be simplified and represented as functions of coil temperature rise. These linear relations are used to specify the losses of where the losses occur.

1. Winding Loss = copper loss + eddy current loss + circulating current loss

$$P_{Cu} = 618.9 + 1.869\Delta T_{coil} \quad \text{(C.1)}$$

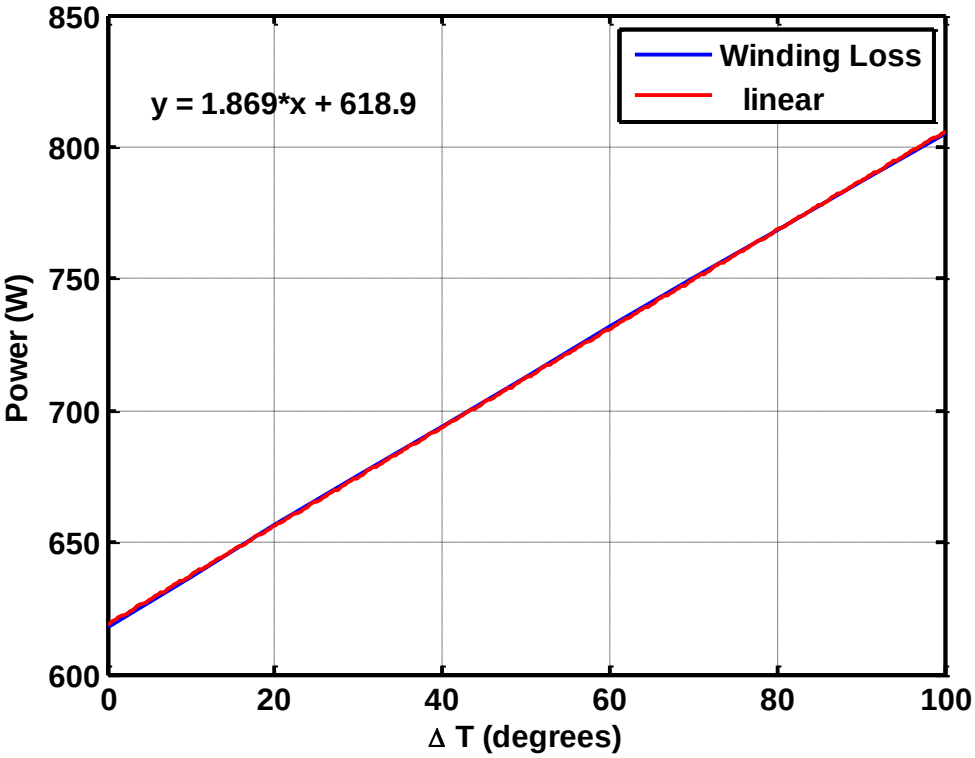

Figure C.1: The variation of winding loss with coil temperature rise

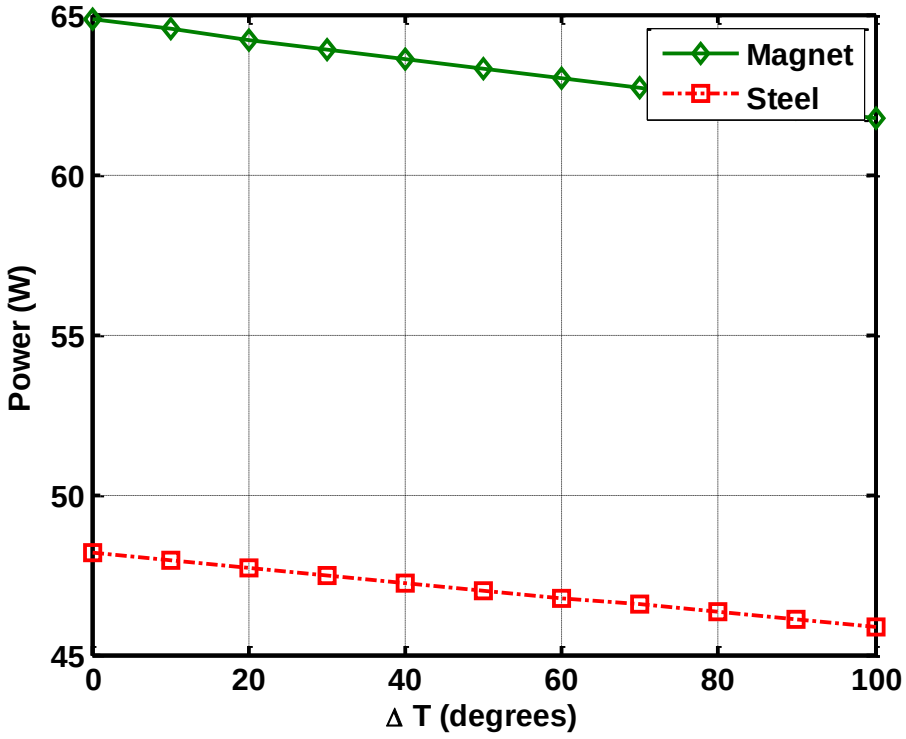

Figure C.2: The variation of rotor loss with coil temperature rise

2. For magnet loss,

$$P_{magnet} = 64.8 - 0.0306\Delta T_{coil} \quad \text{(C.2)}$$

3. For core-back iron loss,

$$P_{steel} = 48.1 - 0.0227\Delta T_{coil} \quad \text{(C.3)}$$

Appendix D – Liquid-cooled Heat Sink

Specification of the heat sink - Aavid Thermalloy [2007]

tube material: Copper, 9.5 mm (0.375”) O.D. × 1.24 mm (0.044”) wall

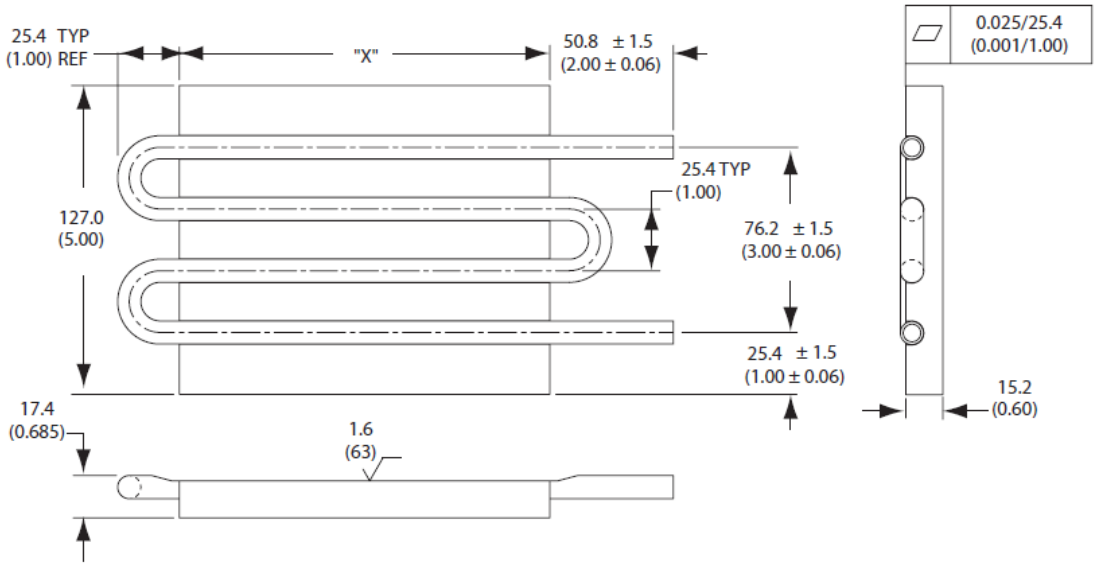

Figure D.1: Technical drawing of Hi-Contact™ Liquid Cold Plate 4 Pass Model, dimensions as shown are mm (inches), “X” dimension refers to 152 mm (6”) or 305 mm (12”) in Figure D.2.

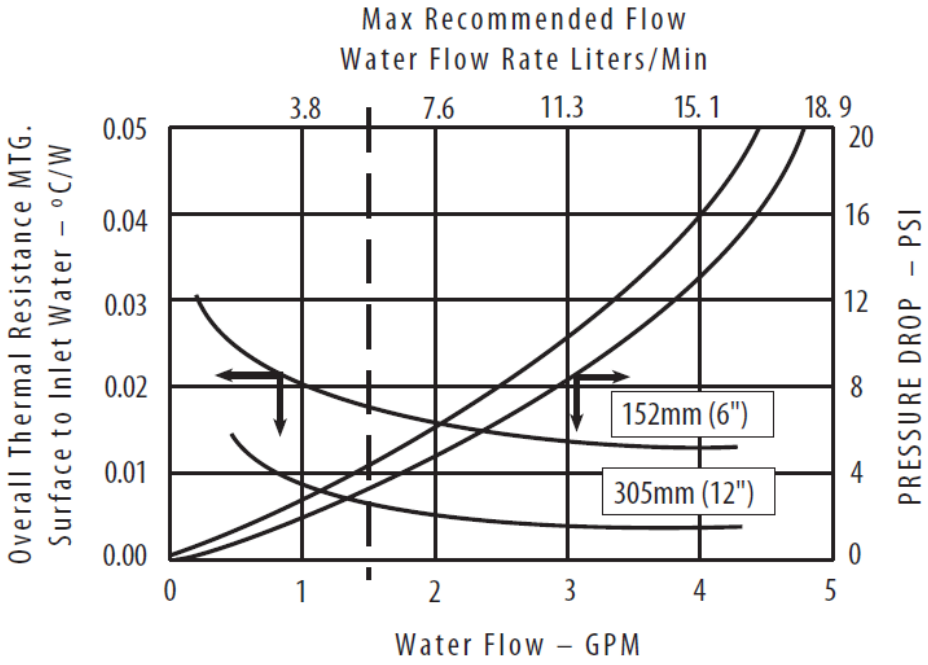

Figure D.2: The relationship of pressure drop and flow rate

Appendix E – Axial and Radial Dimensions of Al'Akayshee and Williams [2003] Machine

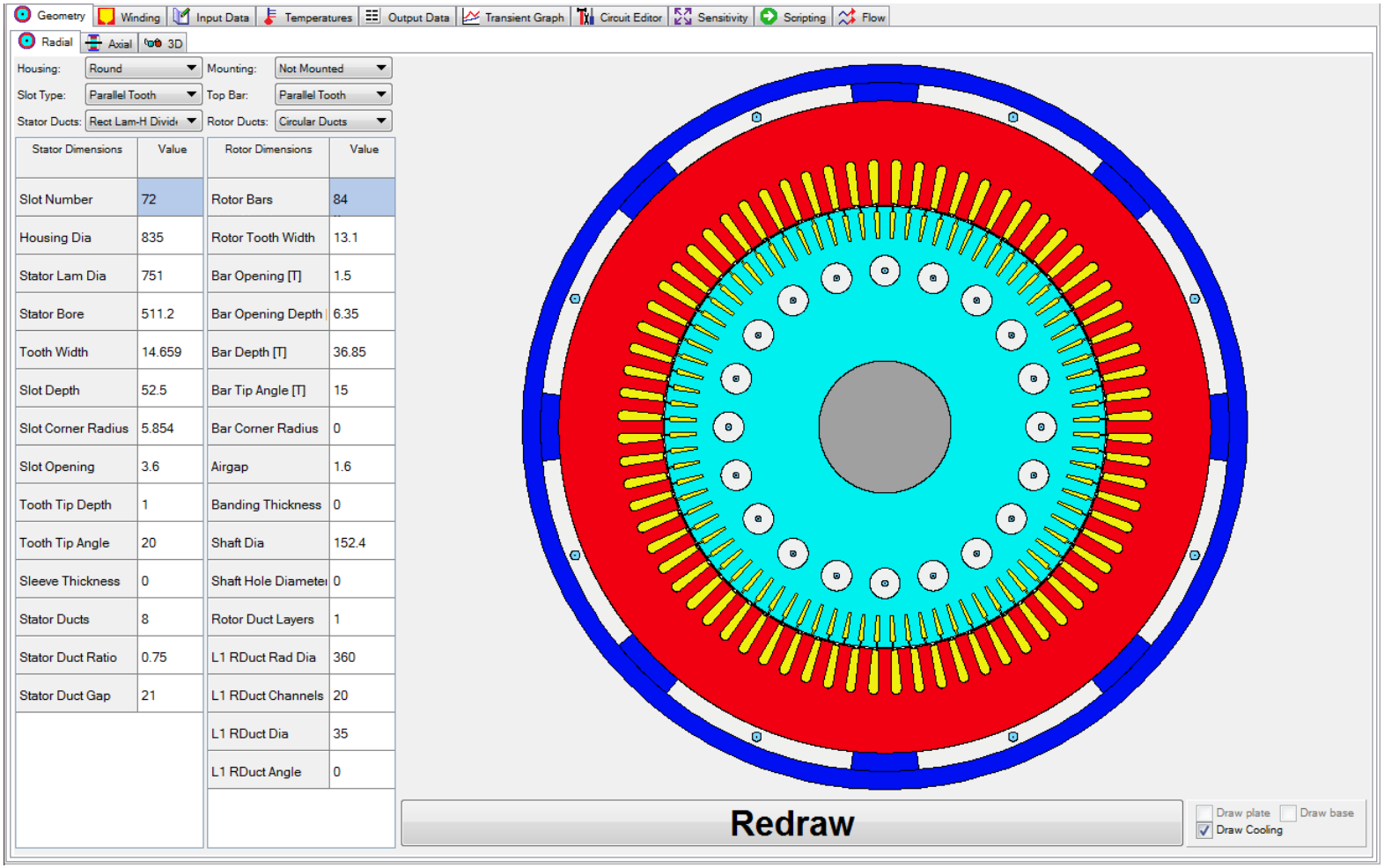

Figure E.1: Axial dimensions of Al'Akayshee and Williams [2003] machine

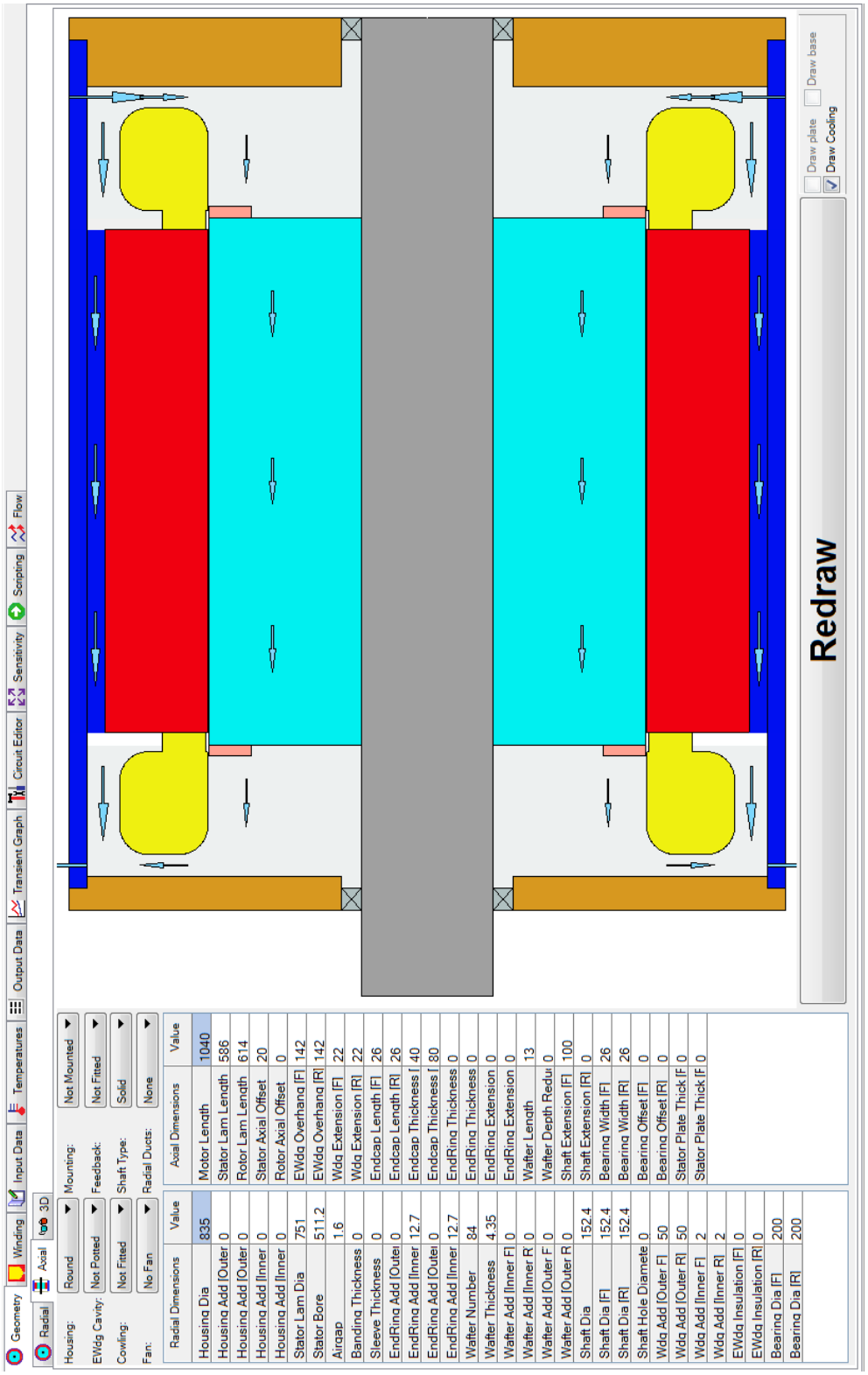

Figure E.2: Radial dimensions of Al'Akayshee and Williams [2003] machine

Appendix F – Mesh Refinement Study for Chapter 6

In Chapter 6, the aim of the CFD analysis was to determine the pressure drop for the input flow rate or the induced flow rate for the input pressure. Due to the effects of rotation, the pressure losses of air passing through circular ducts in rotor and rotor-stator gap are higher when compared to the stationary case. In the CFD model, rotation results in a high velocity gradient in the tangential direction in the rotor-stator gap. Consequently, mesh refinement study is performed for the maximum rotor speed for each test to ensure sufficient number of computational cells is allocated for the qualitative CFD analysis. The CFD analysis is run with four different grids on a single problem; one is finer than the grid used to obtain the CFD results presented in Chapter 6, but two are coarser. In order to compare the solutions obtained from the four different grids, the number of computational cells across the rotor-stator gap for each grid is normalised to the number of computational cells across the rotor-stator gap for the grid used to obtain the CFD results presented in Chapter 6. As a result, the normalised grid spacing is equal to 1 for the grid used to obtain the CFD results presented in Chapter 6, the normalised grid spacing is less than 1 for the finer grid, the normalised grid spacing is higher than 1 for the coarser grids.

Test A

The mesh in the airgap and rotor duct for different grids is shown in Figure F.1. As the difference between the resulting pressure drops, axial flow velocities in the airgap and rotor duct from the CFD solutions are negligible as shown in Figure F.2 and Figure F.3, the CFD results for Test A at 6000 rpm are mesh independent solutions. The mesh with the normalised grid spacing = 1.00 was also used for lower speed. Each solution was properly converged with respect to iterations.

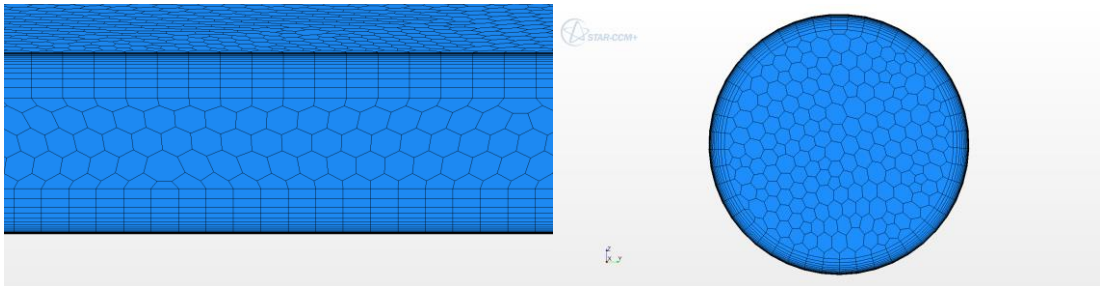

Mesh 1 (Normalised grid spacing = 1.00)

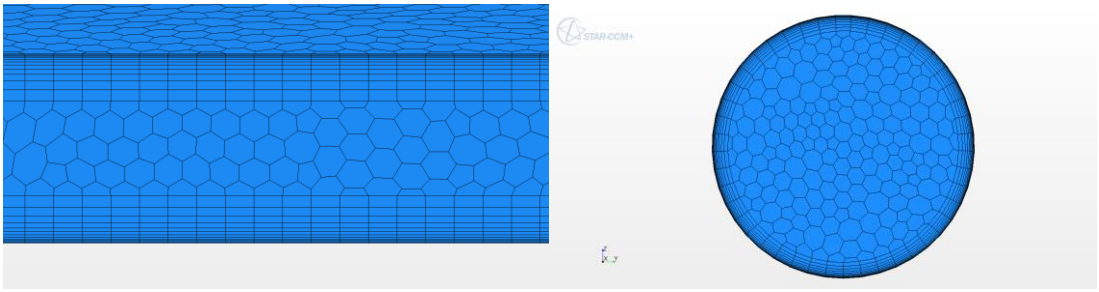

Mesh 2 (Normalised grid spacing = 1.28)

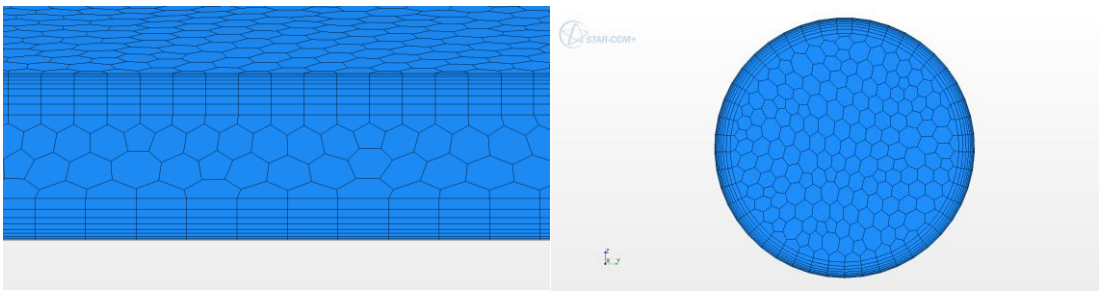

Mesh 3 (Normalised grid spacing = 1.85)

Figure F.1: Mesh in airgap (left) and rotor duct (right) for Test A

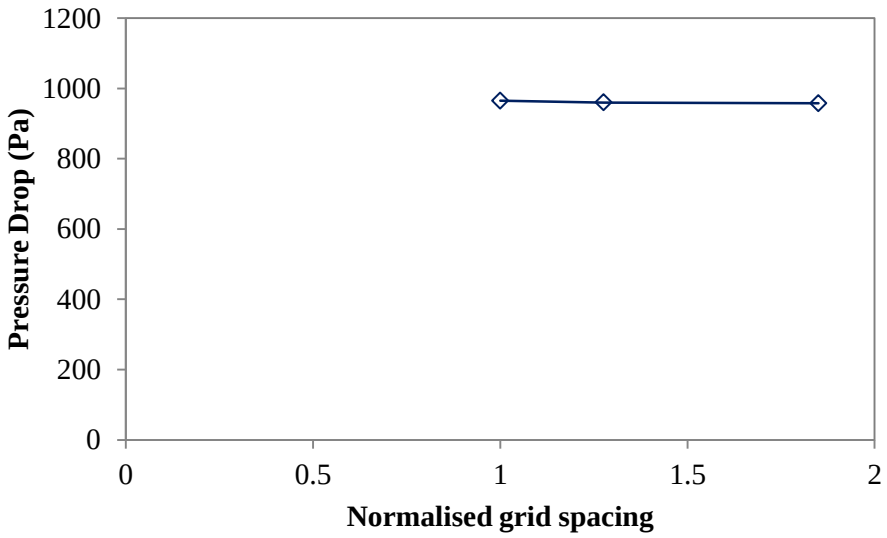

Figure F.2: The variation of pressure drop with normalised grid spacing for Test A at 6000 rpm

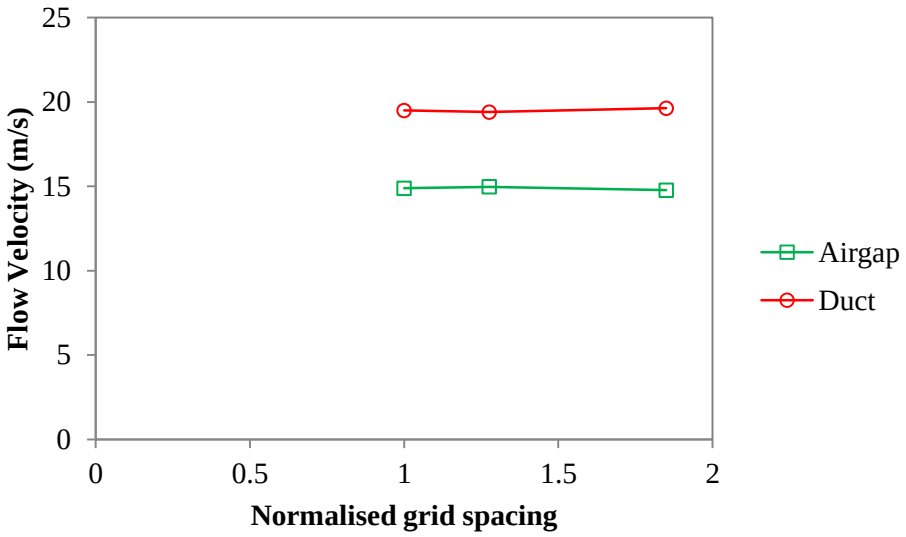

Figure F.3: The variation of airgap and duct axial flow velocities with normalised grid spacing for Test A at 6000 rpm

Test B

The mesh in the airgap and rotor duct for different grids is shown in Figure F.4. Since the CFD analysis is run with user input pressure and the flow rate passing through the system is predicted, the inlet flow velocities obtained from the four different grids is compared as shown in Figure F.5. Their differences are negligible. Therefore, for Test B at 6000 rpm, mesh independent solutions have been reached. The mesh with the normalised grid spacing = 1.00 was also used for lower speed. Each solution was properly converged with respect to iterations.

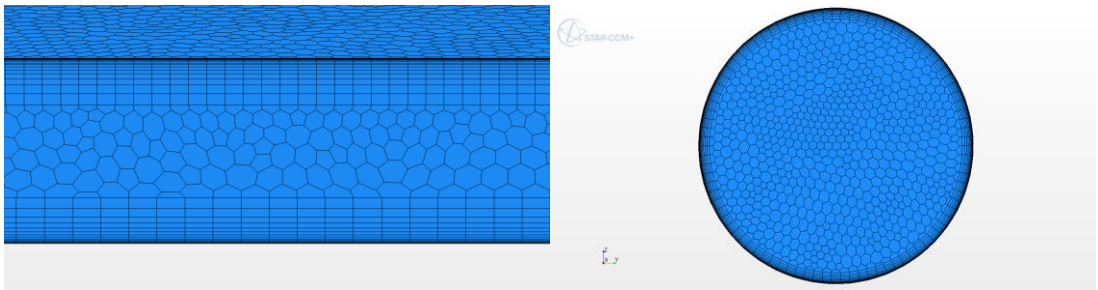

Mesh 1 (Normalised grid spacing = 0.81)

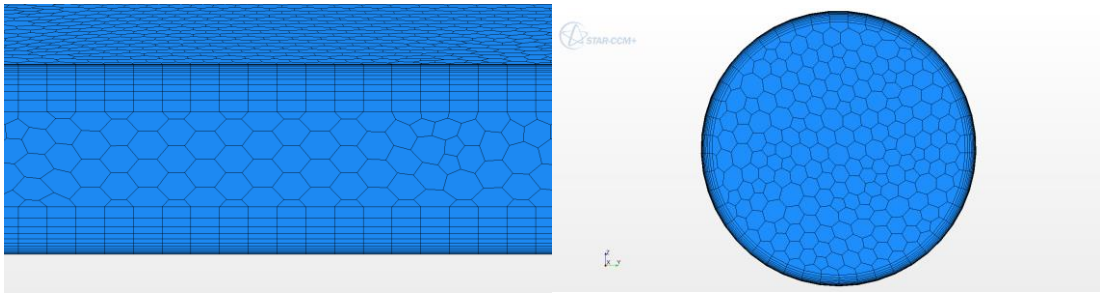

Mesh 2 (Normalised grid spacing = 1.00)

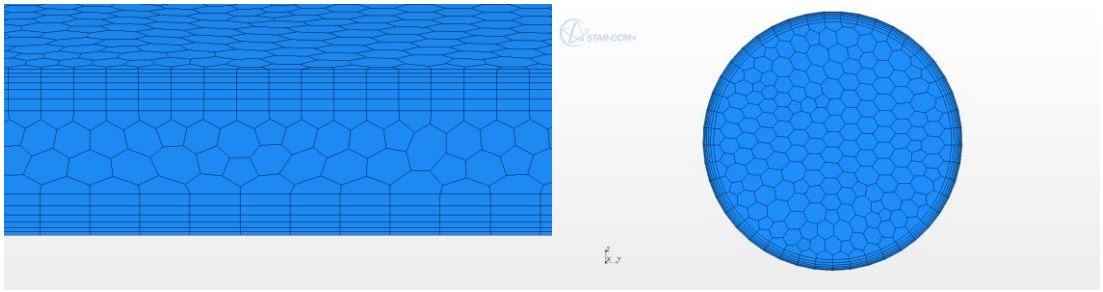

Mesh 3 (Normalised grid spacing = 1.81)

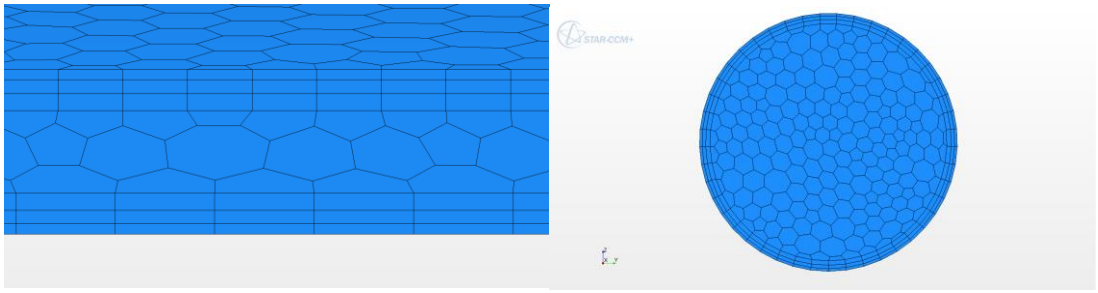

Mesh 4 (Normalised grid spacing = 3.22)

Figure F.4: Mesh in airgap (left) and rotor duct (right) for Test B

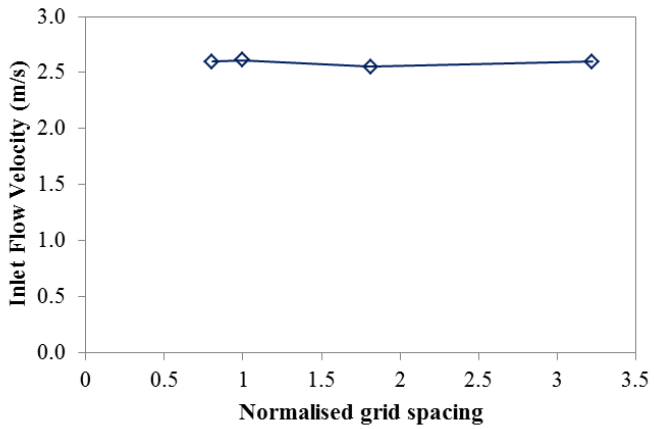

Figure F.5: The variation of inlet flow velocity with normalised grid spacing for Test B at 6000 rpm

Test C

The mesh in the airgap and rotor duct for different grids is shown in Figure F.6. Figure F.7 and Figure F.8 show that the resulting pressure drops, axial flow velocities in the airgap and rotor duct from the CFD solutions vary with the grid spacing. However, the results obtained from the mesh of normalised grid spacing = 1.00 is close to the results obtained from the finer mesh (normalised grid spacing = 0.75). Hence, the mesh of normalised grid spacing = 1.00 is sufficient to calculate the fluid flow problem at 3000 rpm. The same mesh was also used for lower speed. Each solution was properly converged with respect to iterations.

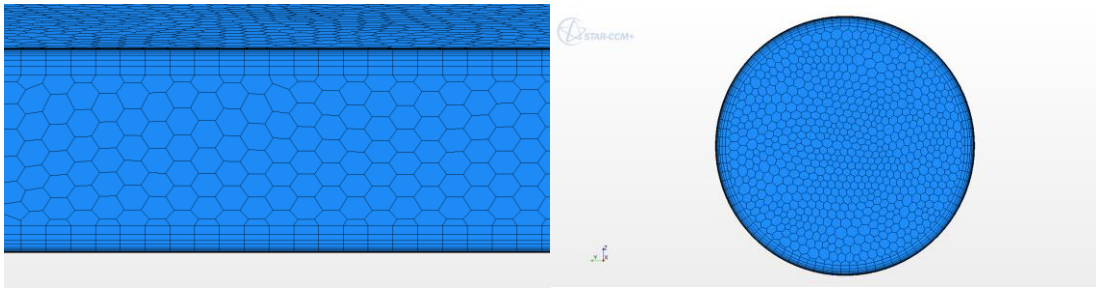

Mesh 1 (Normalised grid spacing = 0.75)

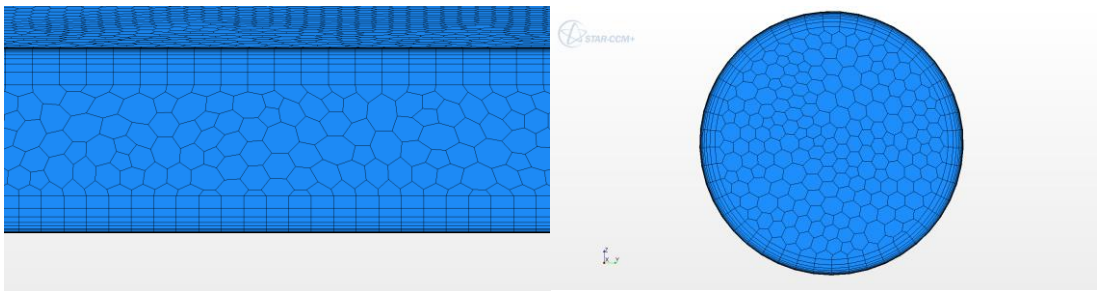

Mesh 2 (Normalised grid spacing = 1.00)

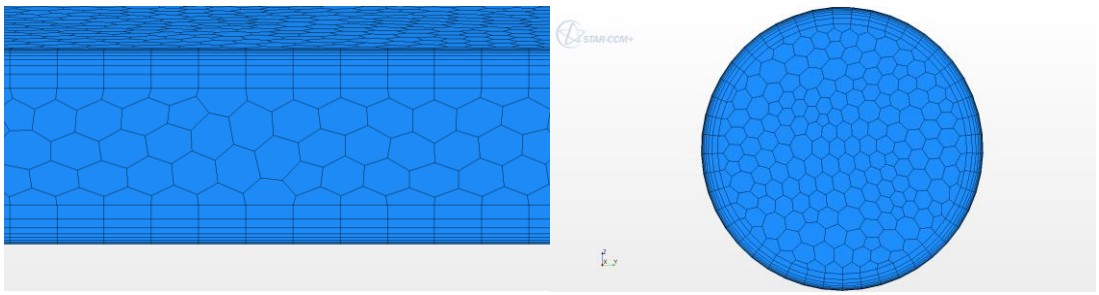

Mesh 3 (Normalised grid spacing = 1.43)

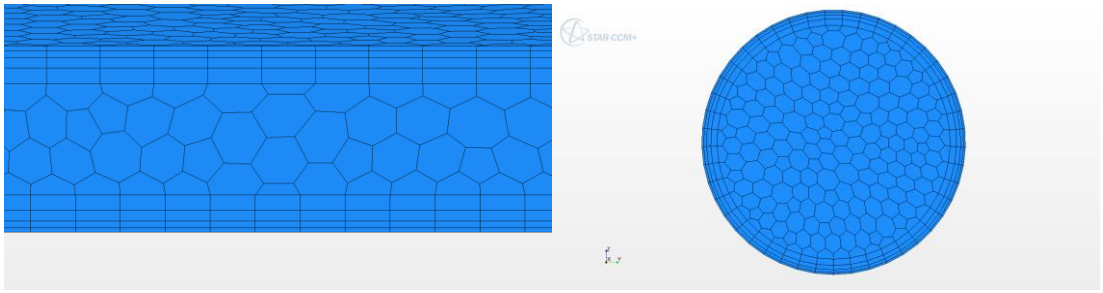

Mesh 4 (Normalised grid spacing = 2.50)

Figure F.6: Mesh in airgap (left) and rotor duct (right) for Test C

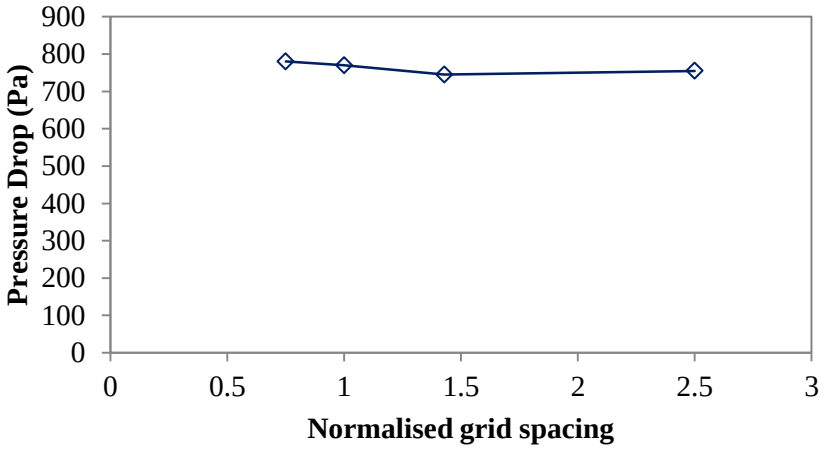

Figure F.7: The variation of pressure drop with normalised grid spacing for Test C at 3000 rpm

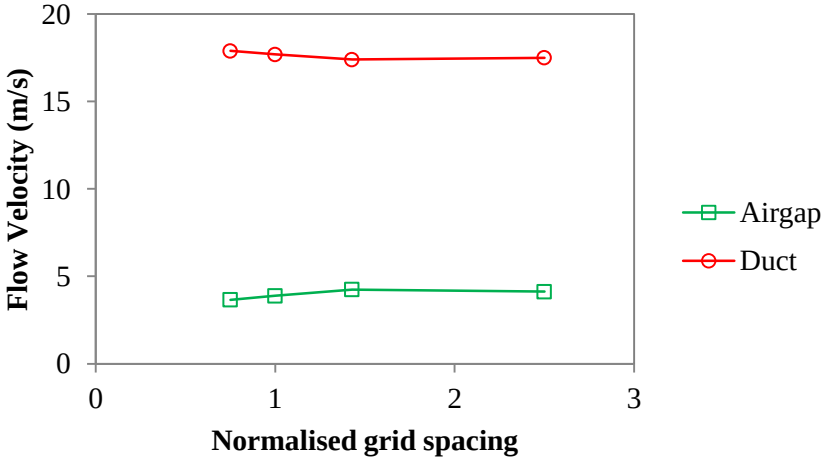

Figure F.8: The variation of airgap and duct axial flow velocities with normalised grid spacing for Test C at 3000 rpm

Test G

The mesh in the airgap and rotor duct for different grids is shown in Figure F.9. Figure F.10 and Figure F.11 show that the resulting pressure drops, axial flow velocities in the airgap and rotor duct from the CFD solutions vary with the grid spacing. However, the results obtained from the mesh of normalised grid spacing = 1.00 is close to the results obtained from the finer mesh (normalised grid spacing = 0.73). Hence, the mesh of normalised grid spacing = 1.00 is sufficient to calculate the fluid flow problem at 9000 rpm. The same mesh was also used for lower speed. Each solution was properly converged with respect to iterations.

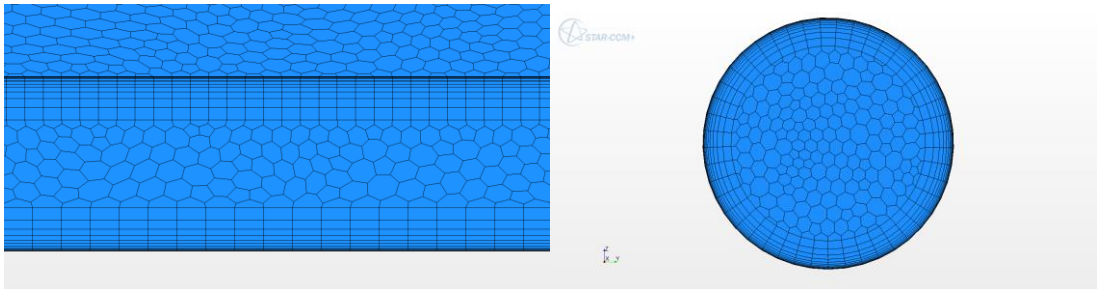

Mesh 1 (Normalised grid spacing = 0.73)

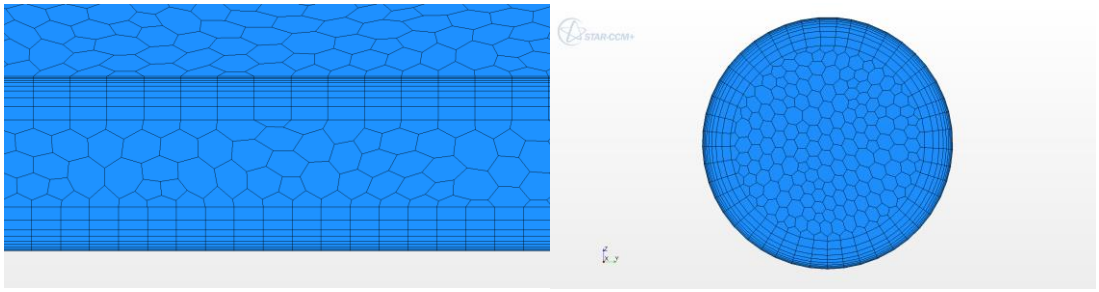

Mesh 2 (Normalised grid spacing = 1.00)

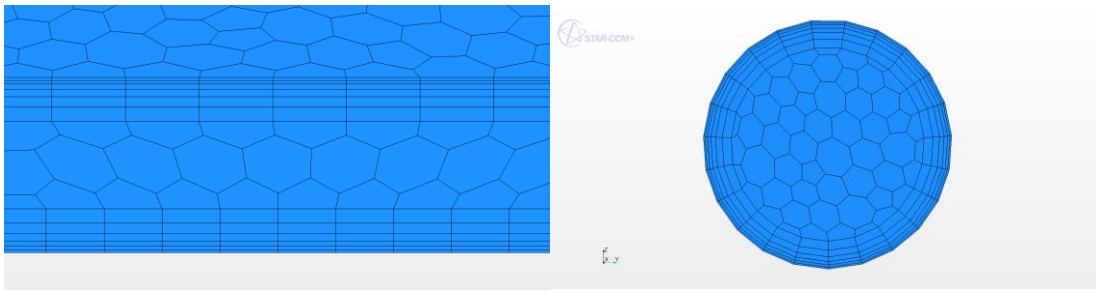

Mesh 3 (Normalised grid spacing = 1.47)

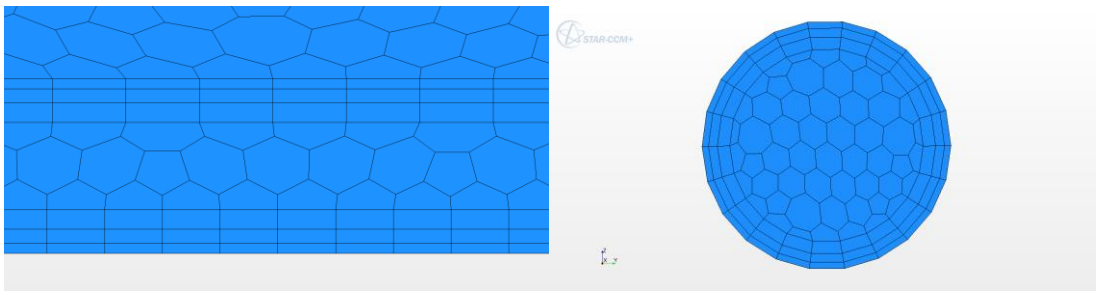

Mesh 4 (Normalised grid spacing = 2.44)

Figure F.9: Mesh in airgap (left) and rotor duct (right) for Test G

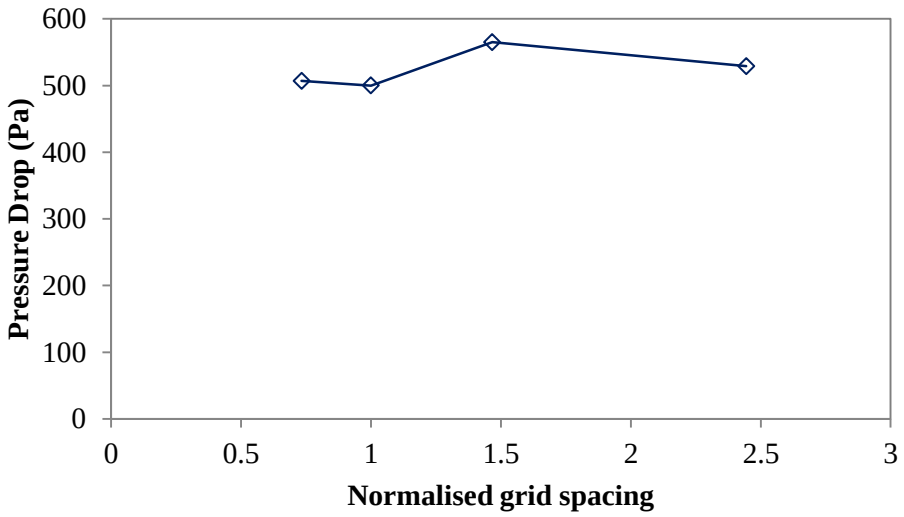

Figure F.10: The variation of pressure drop with normalised grid spacing for Test G at 9000 rpm

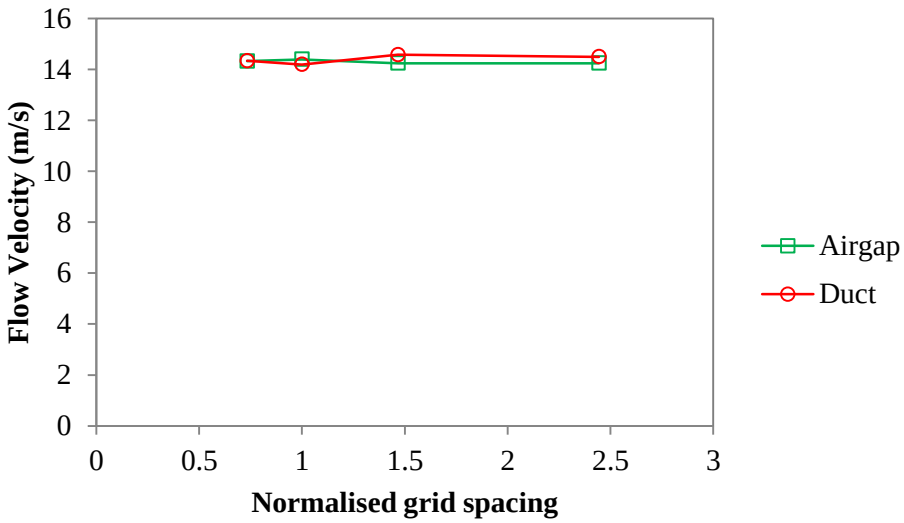

Figure F.11: The variation of airgap and duct axial flow velocities with normalised grid spacing for Test G at 9000 rpm

Test H

The mesh in the airgap is shown in Figure F.12. Mesh refinement study is performed for rotor speed at 6000 rpm and 12000 rpm for Test H. Figure F.13 and Figure F.14 show that the resulting pressure drops from the CFD solutions vary with the grid spacing. For 6000 rpm, the resulting pressure drop obtained from the mesh of normalised grid spacing = 2.18 is much higher than the finer meshes as shown in Figure F.13. For finer meshes, the differences in the resulting pressure drop are negligible. Therefore, for Test H at 6000 rpm, using the mesh of normalised grid spacing = 1.00, mesh independent solutions have been reached.

For 12000 rpm, the resulting pressure drop obtained from the mesh of normalised grid spacing = 1.41 and 2.18 are much higher than the finer meshes as shown in Figure F.14. For finer meshes (normalised grid spacing = 0.83 and 1.00), the differences in the resulting pressure drop are negligible. Therefore, for Test H at 12000 rpm, using the mesh of normalised grid spacing = 1.00, mesh independent solutions have been reached. The mesh with the normalised grid spacing = 1.00 was also used for lower speed. Each solution was properly converged with respect to iterations.

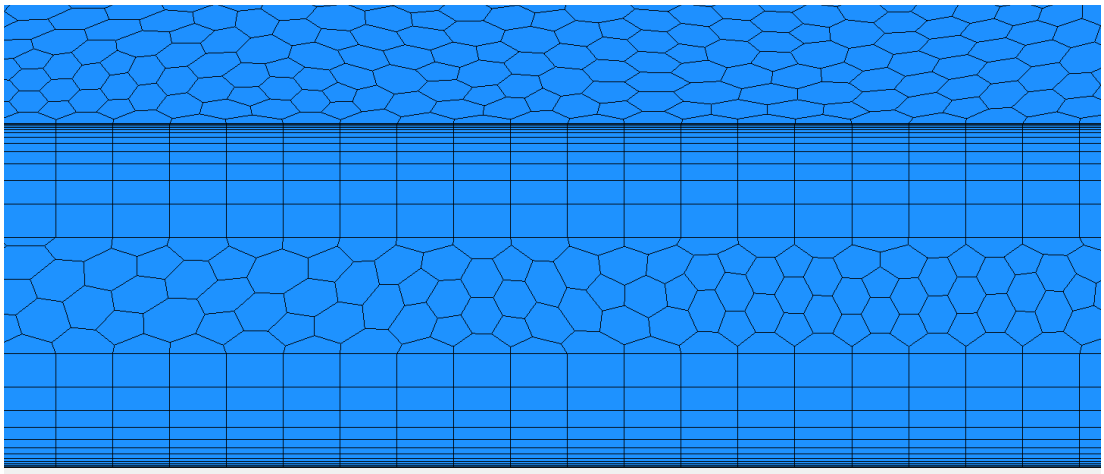

Mesh 1 (Normalised grid spacing = 0.83)

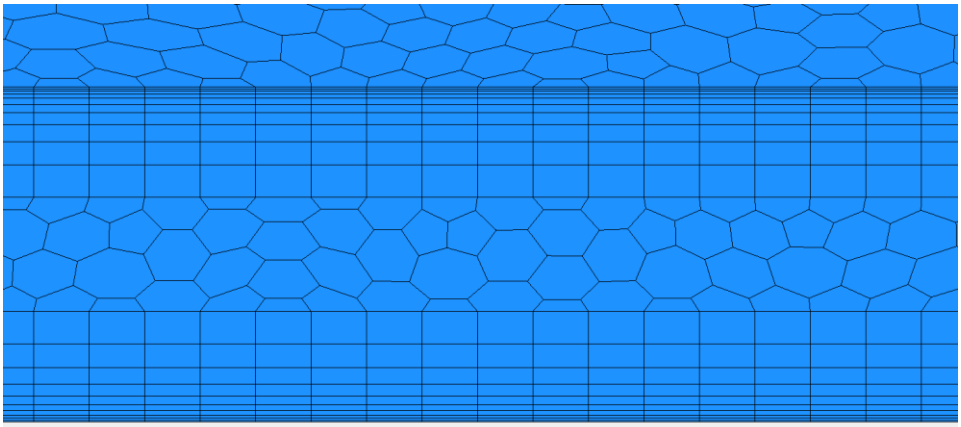

Mesh 2 (Normalised grid spacing = 1.00)

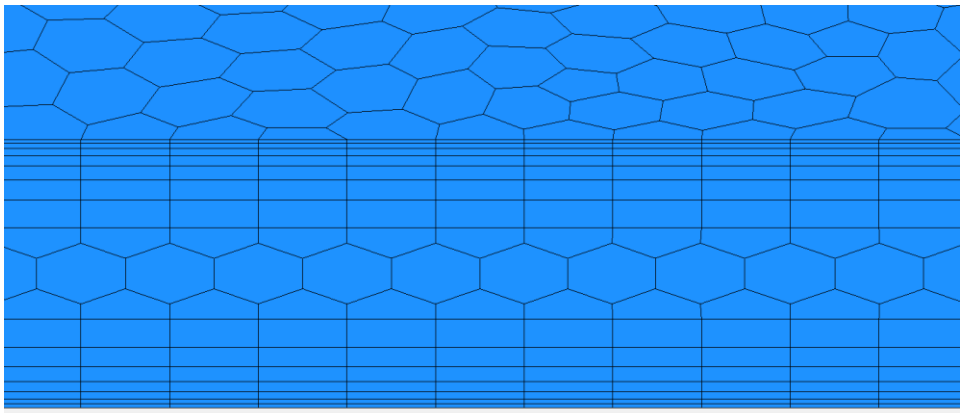

Mesh 3 (Normalised grid spacing = 1.41)

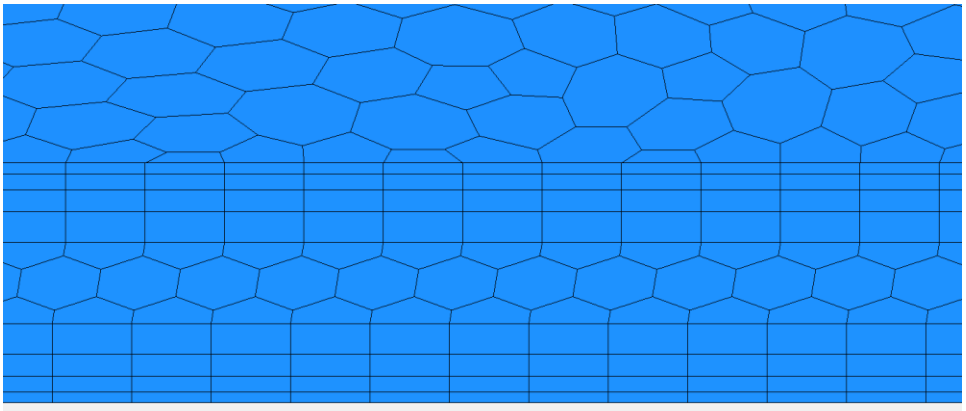

Mesh 4 (Normalised grid spacing = 2.18)

Figure F.12: Mesh in airgap for Test H

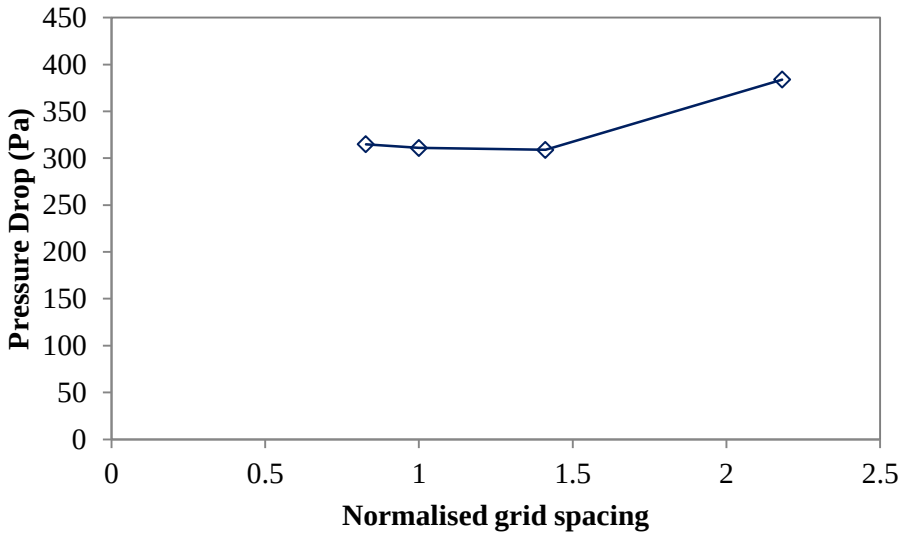

Figure F.13: The variation of pressure drop with normalised grid spacing for Test H at 6000 rpm

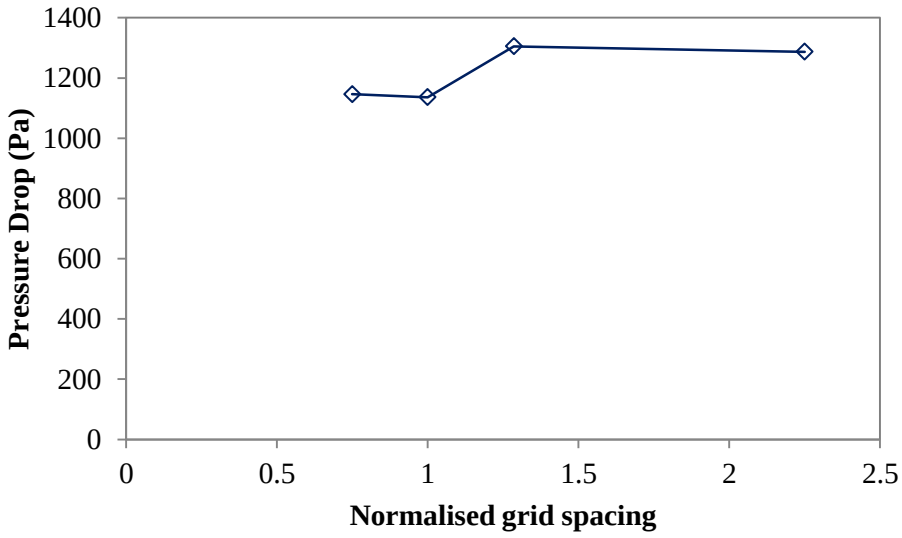

Figure F.14: The variation of pressure drop with normalised grid spacing for Test H at 12000 rpm

Appendix G – Comparison between CFD Solution and Power Law Velocity Profile

For fully developed turbulent flow, the velocity profile in a circular pipe can be represented using the empirical power law velocity profile. The power law velocity profile is used to check the velocity profile in the rotor duct of the CFD models for the investigation of combining flow loss. The length-to-diameter ratio of the rotor duct of Test B is 12*D* where *D* is the duct diameter. Therefore, for zero rotational speed cases, the comparisons are performed at 11.5*D* from the duct entrance of where a flow condition closes to the fully developed flow is achieved. The formula of power law velocity profile is expressed as:

$$\frac{u}{U_{max}} = \left(1 - \frac{r}{R}\right)^{\frac{1}{n}} \tag{G.1}$$

where u and U_{max} are local and maximum flow velocities of the velocity profile respectively. R is duct radius. *r* is a distance from duct central line of where the local velocity is calculated. *n* is the exponent of the power law velocity profile which is a function of Reynolds number. The value of *n* can be determined from Figure G.1. For inlet pressure = 952 Pa, the mean flow velocity *U* in the rotor duct is 31.89 m/s for CFD model without flow guard and is 31.82 m/s for CFD model with flow guard. Their resulting Reynold number is 39000 approximately. Thus, the exponent value of the power law velocity profile is 6.4. Besides, the central velocity U_{max} in the duct can be determined from the integration of the power law velocity profile. The relationship between U and U_{max} is given by:

$$\frac{U_{max}}{U} = \frac{(n+1)(2n+1)}{2n^2} \tag{G.2}$$

Based on this relationship, the maximum flow velocity is 1.247 times the mean flow velocity. The maximum flow velocities for the CFD model with and without the flow guard are 39.68 m/s and 39.77 m/s respectively. Since both velocities are similar, the power law velocity profile based on the maximum flow velocity of 39.77 m/s is only shown in Figure G.2. The velocity profiles obtained from CFD solutions with and without flow guard agree with the power law velocity profile as shown in Figure G.2.

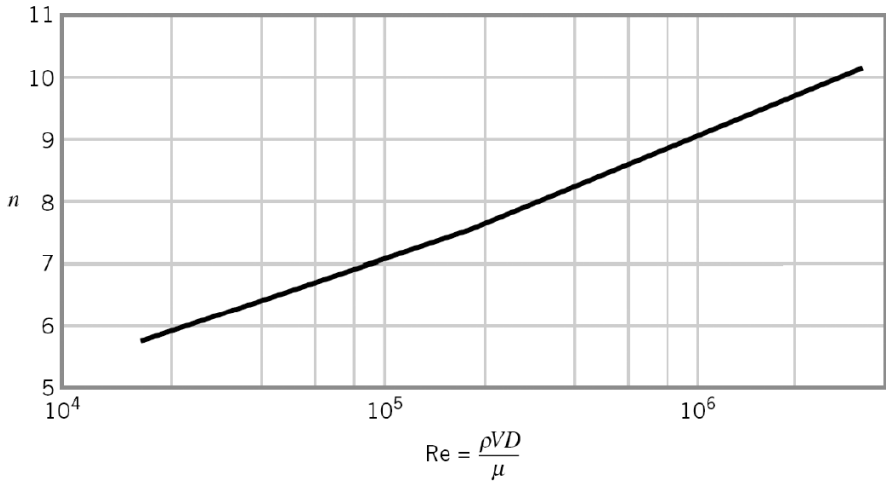

Figure G.1: The variation of exponent *n* of power law velocity profile with Reynolds number

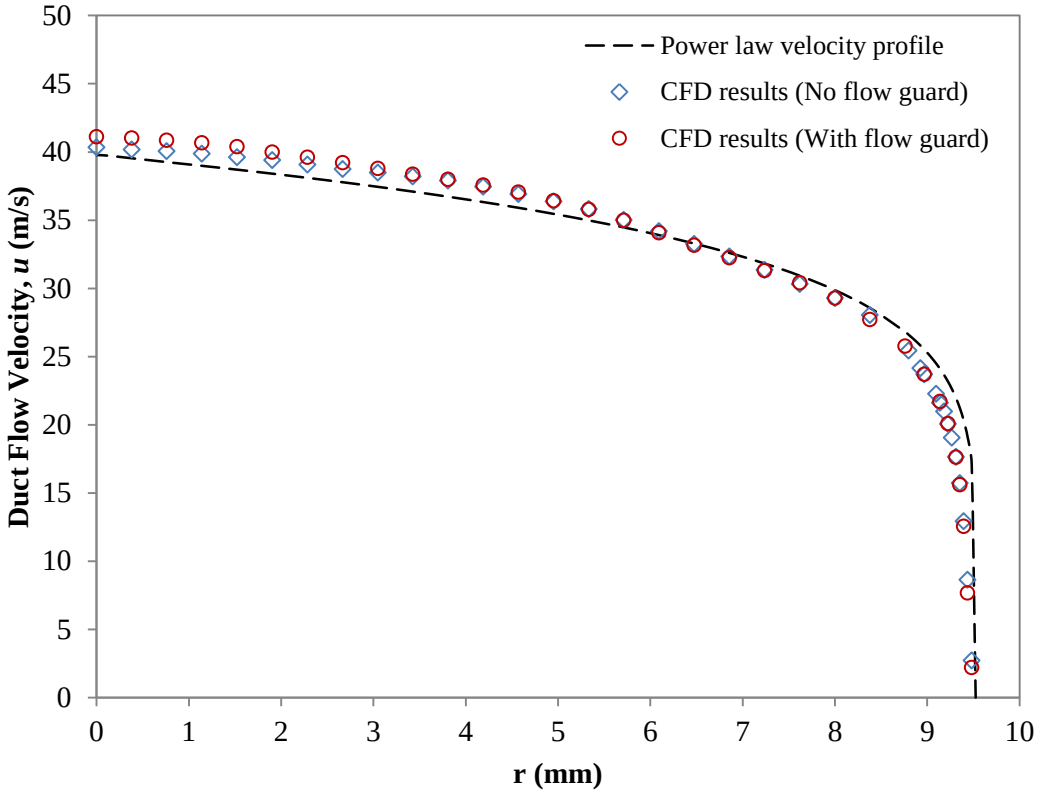

Figure G.2: The comparison between CFD obtained velocity profiles and power law velocity profile (Test B, duct diameter = 19.05 mm, Re = 39000)

Appendix H – Technical Drawings of Air Flow Test Rig

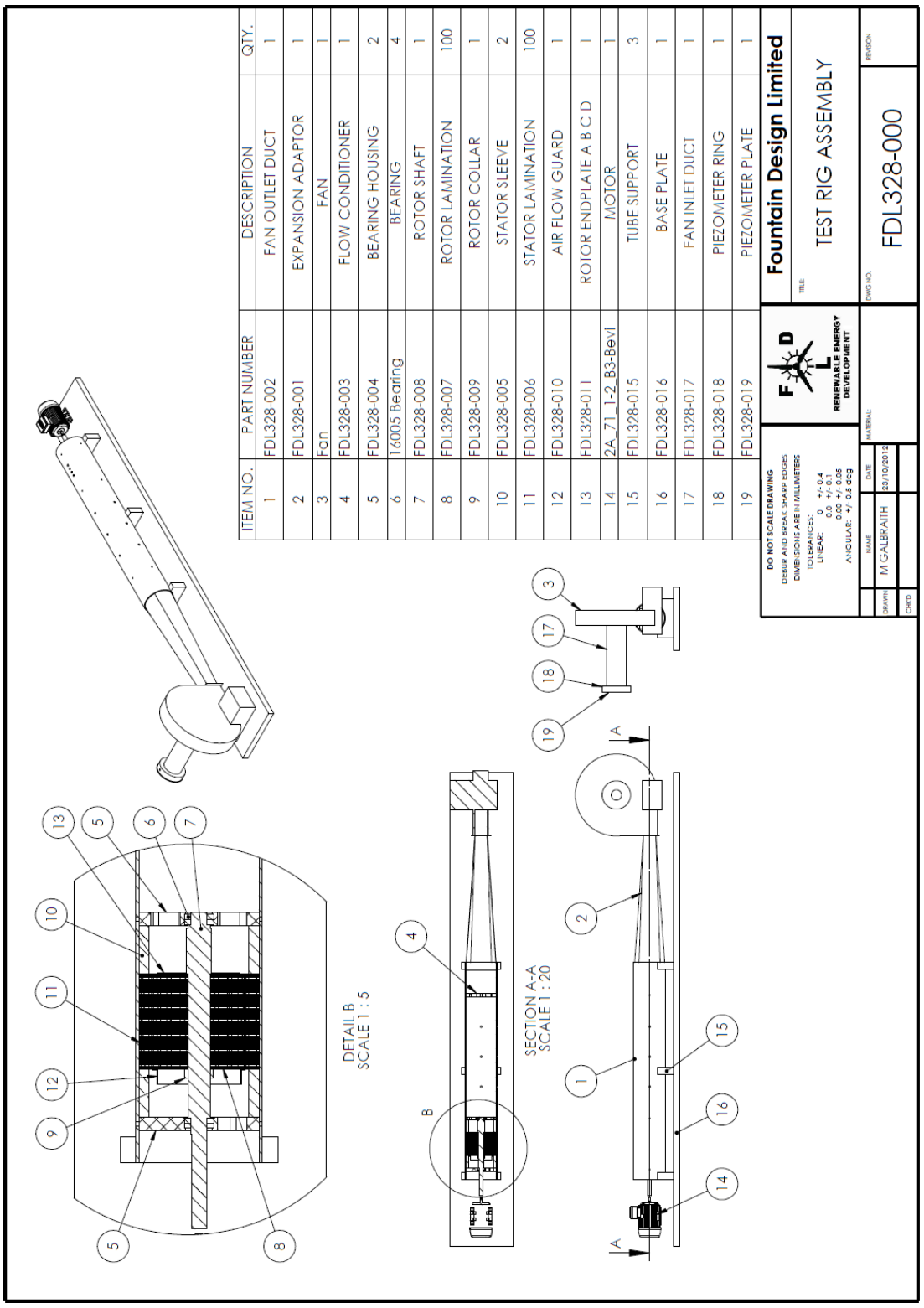
ITEM NO. | PART NUMBER | DESCRIPTION | QTY.
1 | FDL328-002 | FAN OUTLET DUCT | 1
2 | FDL328-001 | EXPANSION ADAPTOR | 1
3 | Fan | FAN | 1
4 | FDL328-003 | FLOW CONDITIONER | 1
5 | FDL328-004 | BEARING HOUSING | 2
6 | 16005 Bearing | BEARING | 4
7 | FDL328-008 | ROTOR SHAFT | 1
8 | FDL328-007 | ROTOR LAMINATION | 100
9 | FDL328-009 | ROTOR COLLAR | 1
10 | FDL328-005 | STATOR SLEEVE | 2
11 | FDL328-006 | STATOR LAMINATION | 100
12 | FDL328-010 | AIR FLOW GUARD | 1
13 | FDL328-011 | ROTOR ENDPLATE A B C D | 1
14 | 2A_71_1-2_B3-Bevi | MOTOR | 1
15 | FDL328-015 | TUBE SUPPORT | 3
16 | FDL328-016 | BASE PLATE | 1
17 | FDL328-017 | FAN INLET DUCT | 1
18 | FDL328-018 | PIEZOMETER RING | 1
19 | FDL328-019 | PIEZOMETER PLATE | 1
DETAIL B
SCALE 1 : 5
SECTION A-A
SCALE 1 : 20
DO NOT SCALE DRAWING
DEBUR AND BREAK SHARP EDGES
DIMENSIONS ARE IN MILLIMETERS
TOLERANCES:
LINEAR: .0 +/- 0.4
.00 +/- 0.1
.000 +/- 0.05
ANGULAR: +/- 0.5 deg
NAME
DRAWN M GALBRAITH
CHKD
DATE
23/10/2012
MATERIAL:
F D L RENEWABLE ENERGY DEVELOPMENT
Fountain Design Limited
TITLE:
TEST RIG ASSEMBLY
DWG NO.
FDL328-000
REVISION

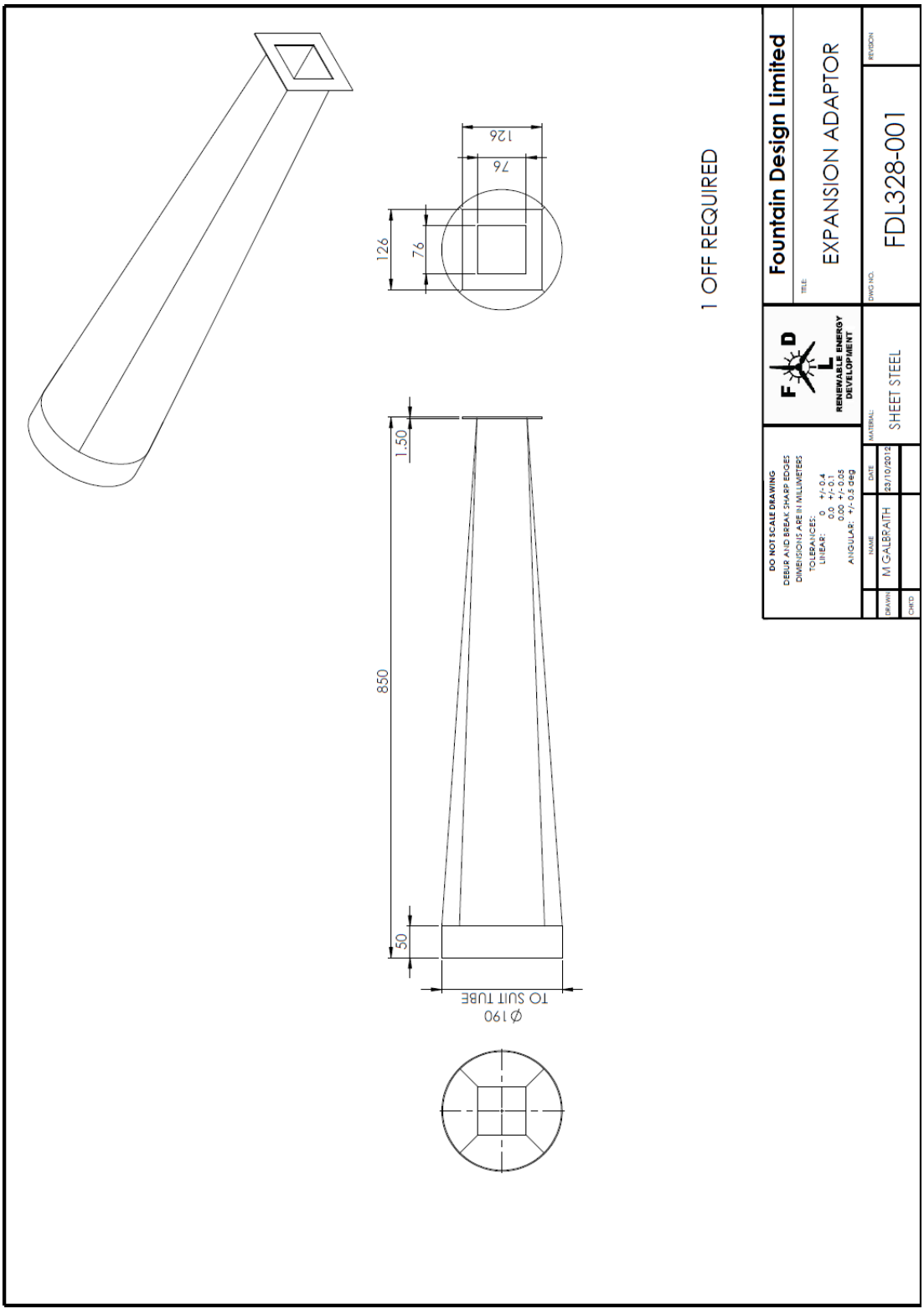
126
76
126
76
1.50
850
50
Ø190
TO SUIT TUBE
1 OFF REQUIRED
Fountain Design Limited
EXPANSION ADAPTOR
FDL328-001
SHEET STEEL
M GALBRAITH
29/10/2012
DO NOT SCALE DRAWING
DEBUR AND BREAK SHARP EDGES
DIMENSIONS ARE IN MILLIMETERS
RENEWABLE ENERGY DEVELOPMENT

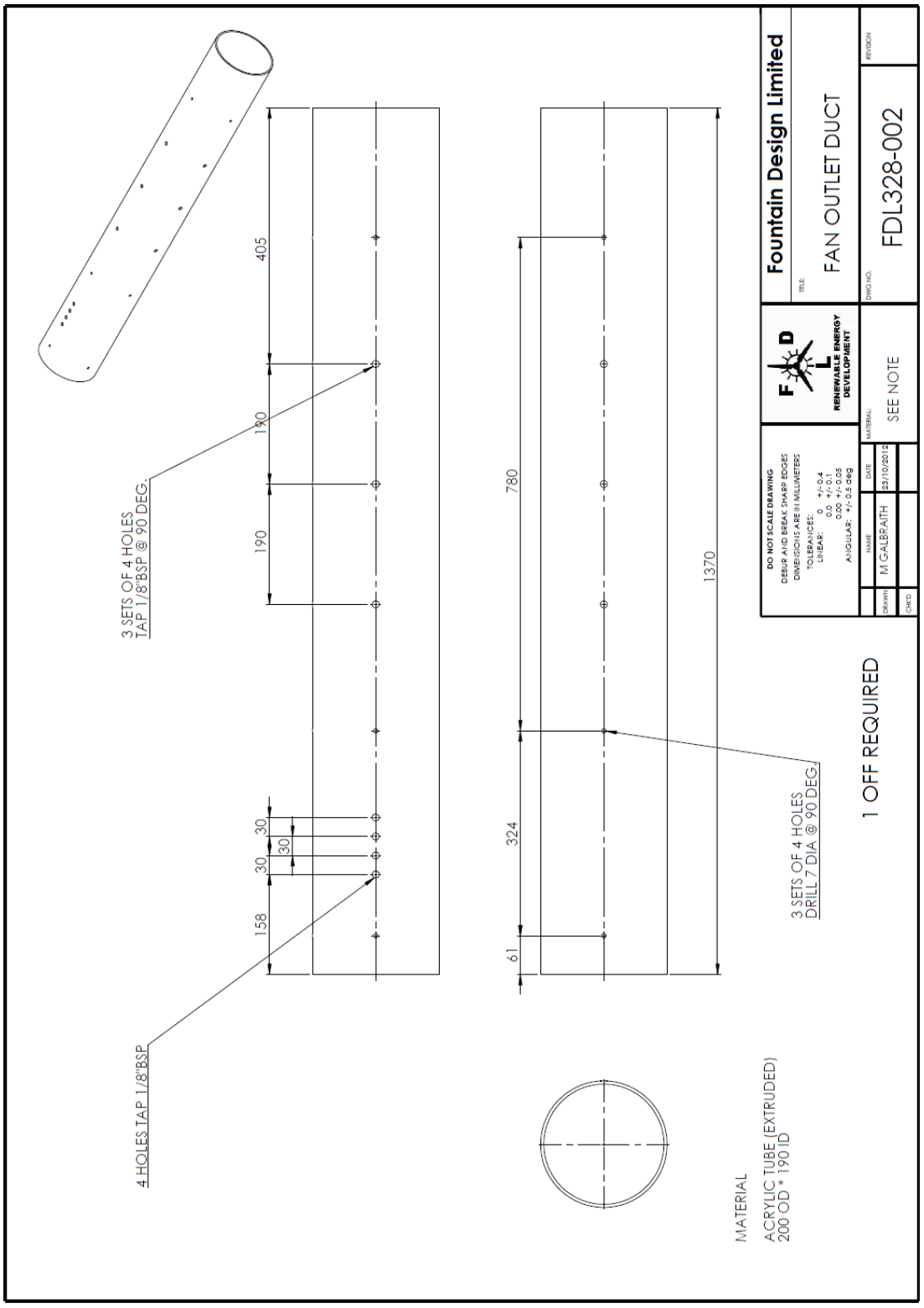
Fountain Design Limited
FAN OUTLET DUCT
FDL328-002
SEE NOTE
1 OFF REQUIRED
MATERIAL
ACRYLIC TUBE (EXTRUDED)
200 OD * 190 ID
3 SETS OF 4 HOLES
TAP 1/8"BSP @ 90 DEG.
4 HOLES TAP 1/8"BSP
3 SETS OF 4 HOLES
DRILL 7 DIA @ 90 DEG.
405
190
190
780
1370
324
61
158
30
30
30
DO NOT SCALE DRAWING
DEBUR AND BREAK SHARP EDGES
DIMENSIONS ARE IN MILLIMETERS
RENEWABLE ENERGY DEVELOPMENT

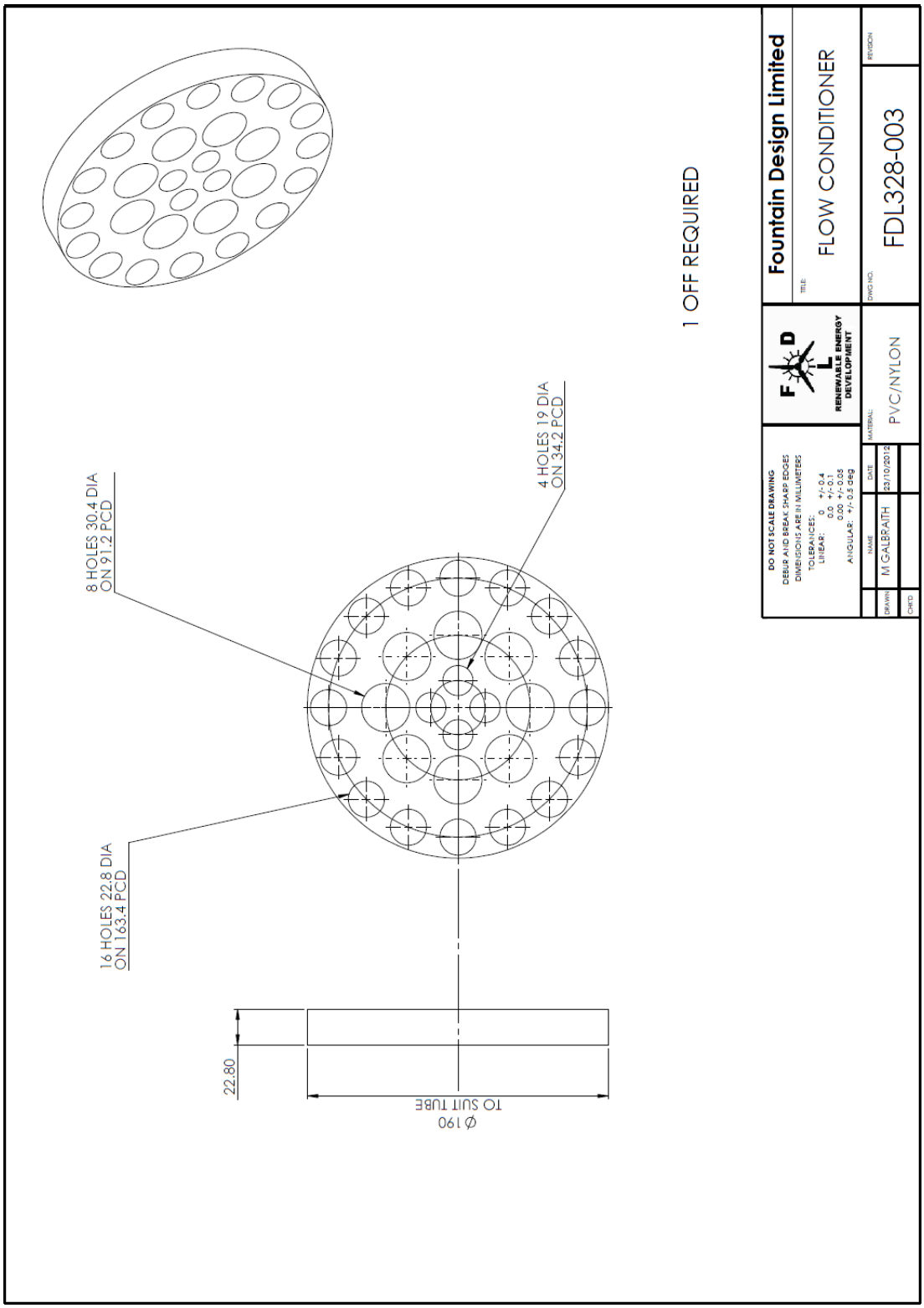
1 OFF REQUIRED
8 HOLES 30.4 DIA
ON 91.2 PCD
4 HOLES 19 DIA
ON 34.2 PCD
16 HOLES 22.8 DIA
ON 163.4 PCD
22.80
Ø 190
TO SUIT TUBE
DO NOT SCALE DRAWING
DEBUR AND BREAK SHARP EDGES
DIMENSIONS ARE IN MILLIMETERS
TOLERANCES:
LINEAR: 0 +/- 0.4
0.0 +/- 0.1
0.00 +/- 0.05
ANGULAR: +/- 0.5 deg
RENEWABLE ENERGY
DEVELOPMENT
Fountain Design Limited
TITLE:
FLOW CONDITIONER
NAME
DATE
MATERIAL:
PVC/NYLON
DRAWN
M GALBRAITH
23/10/2015
CHKD
DWG NO.
FDL328-003
REVISION

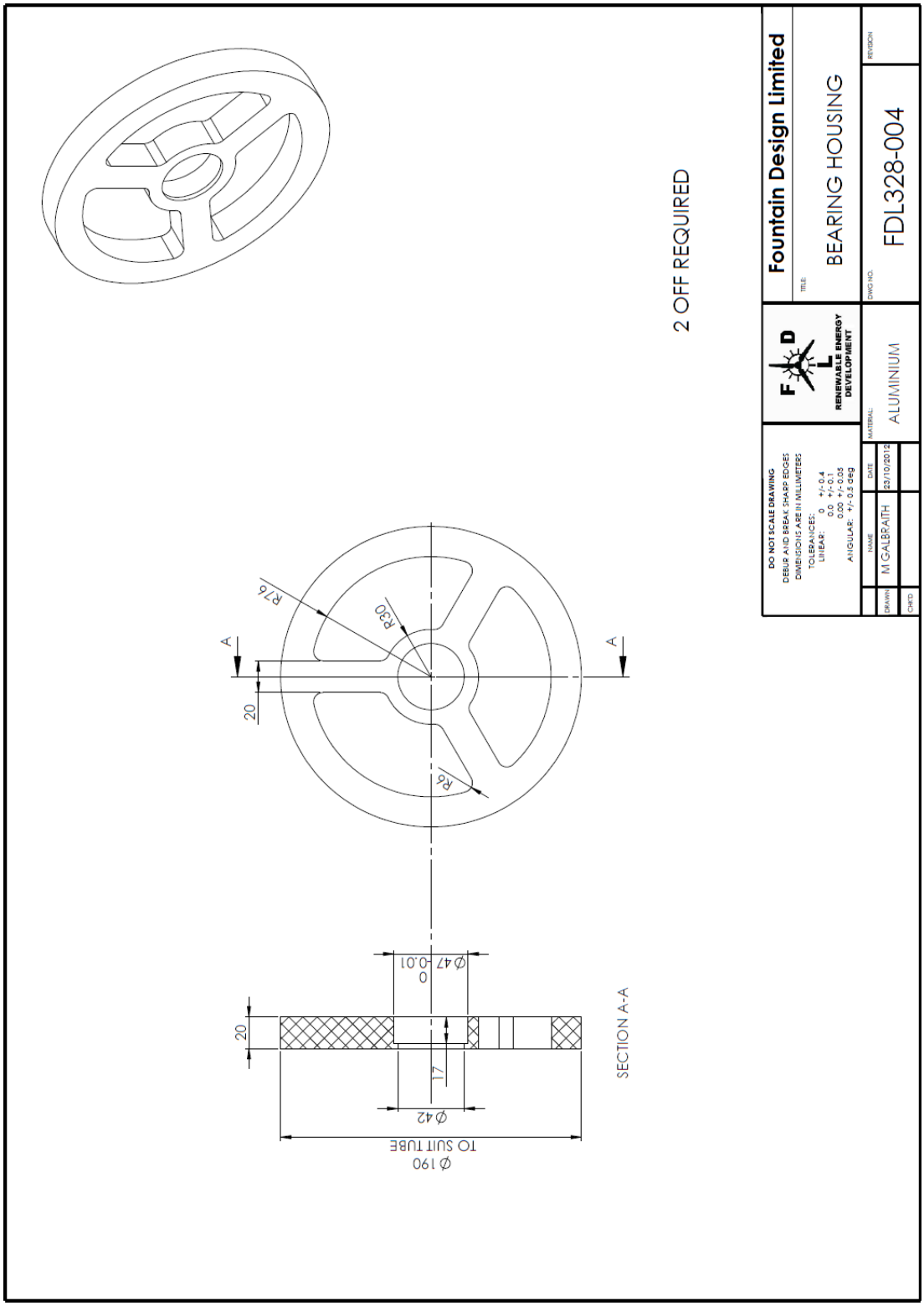
2 OFF REQUIRED
SECTION A-A
R76
R30
R6
20
A
A
Ø 190
TO SUIT TUBE
Ø 42
17
Ø 47 0 -0.01
DO NOT SCALE DRAWING
DEBUR AND BREAK SHARP EDGES
DIMENSIONS ARE IN MILLIMETERS
TOLERANCES:
LINEAR: 0 +/- 0.4
0.0 +/- 0.1
0.00 +/- 0.05
ANGULAR: +/- 0.5 deg
NAME
DATE
DRAWN
M GALBRAITH
23/10/2015
CHKD
MATERIAL:
ALUMINIUM
RENEWABLE ENERGY DEVELOPMENT
Fountain Design Limited
TITLE:
BEARING HOUSING
DWG NO.
FDL328-004
REVISION

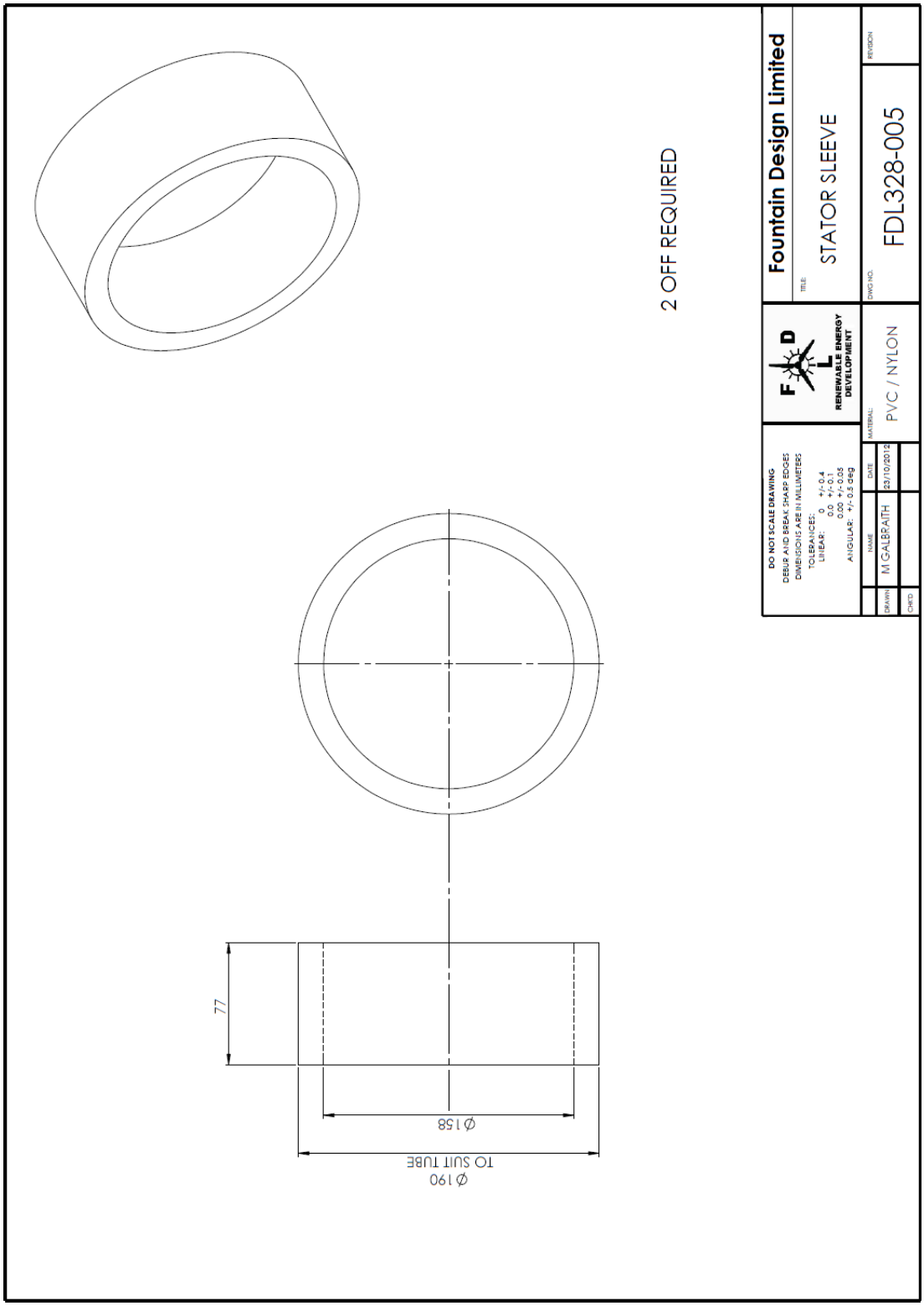
2 OFF REQUIRED
77
Ø 158
Ø 190
TO SUIT TUBE
DO NOT SCALE DRAWING
DEBUR AND BREAK SHARP EDGES
DIMENSIONS ARE IN MILLIMETERS
TOLERANCES:
LINEAR: 0 +/- 0.4
0.0 +/- 0.1
0.00 +/- 0.05
ANGULAR: +/- 0.5 deg
Fountain Design Limited
RENEWABLE ENERGY DEVELOPMENT
TITLE:
STATOR SLEEVE
DWG NO.
FDL328-005
REVISION
NAME
DATE
MATERIAL:
PVC / NYLON
DRAWN
M GALBRAITH
23/10/2012
CHKD

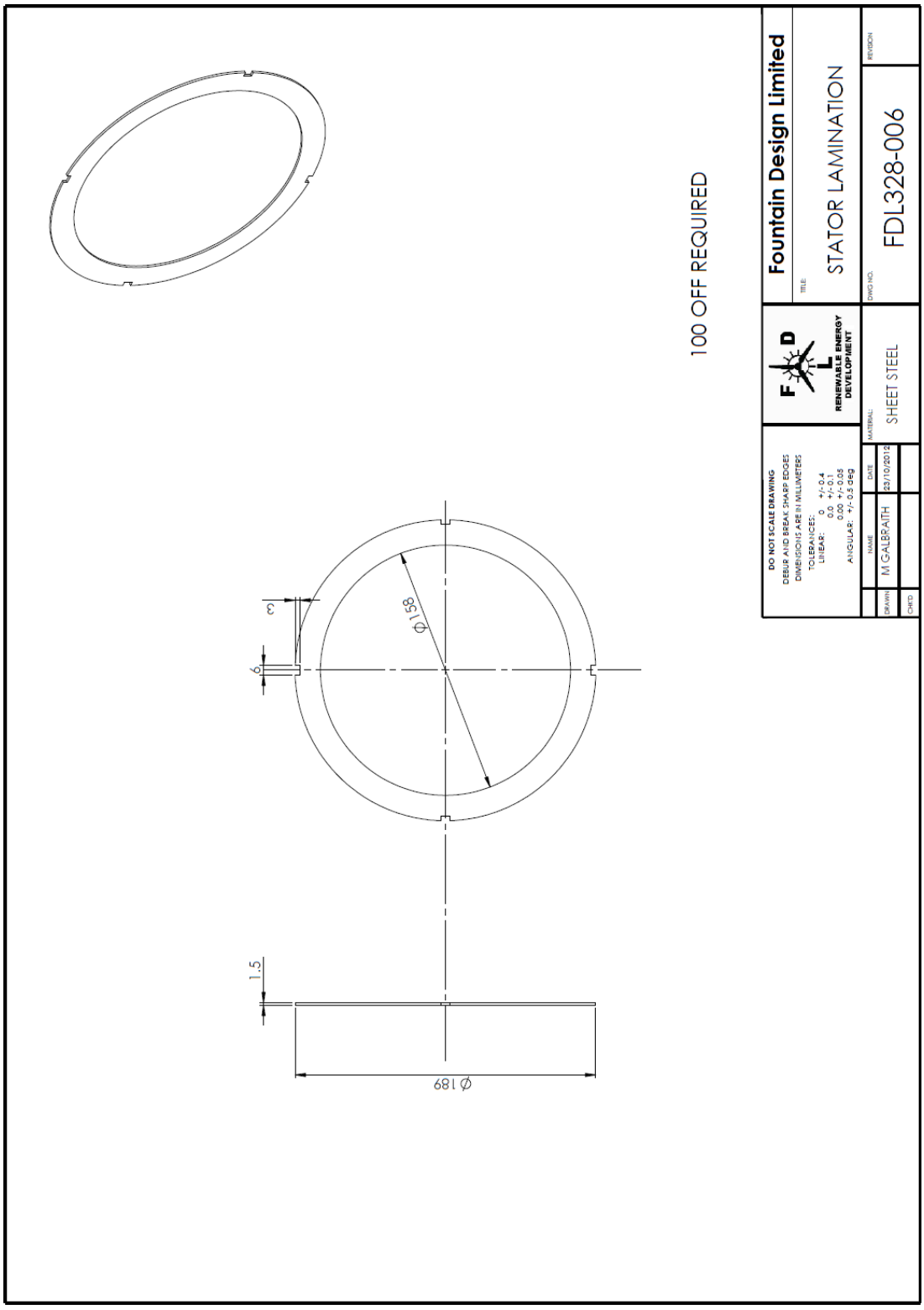
100 OFF REQUIRED
Fountain Design Limited
STATOR LAMINATION
FDL328-006
SHEET STEEL
RENEWABLE ENERGY DEVELOPMENT
DO NOT SCALE DRAWING
DEBUR AND BREAK SHARP EDGES
DIMENSIONS ARE IN MILLIMETERS
TOLERANCES:
LINEAR: 0 +/- 0.4
0.0 +/- 0.1
0.00 +/- 0.05
ANGULAR: +/- 0.5 deg
DRAWN
M GALBRAITH
23/10/2012
CHKD
3
6
ϕ158
1.5
ϕ189

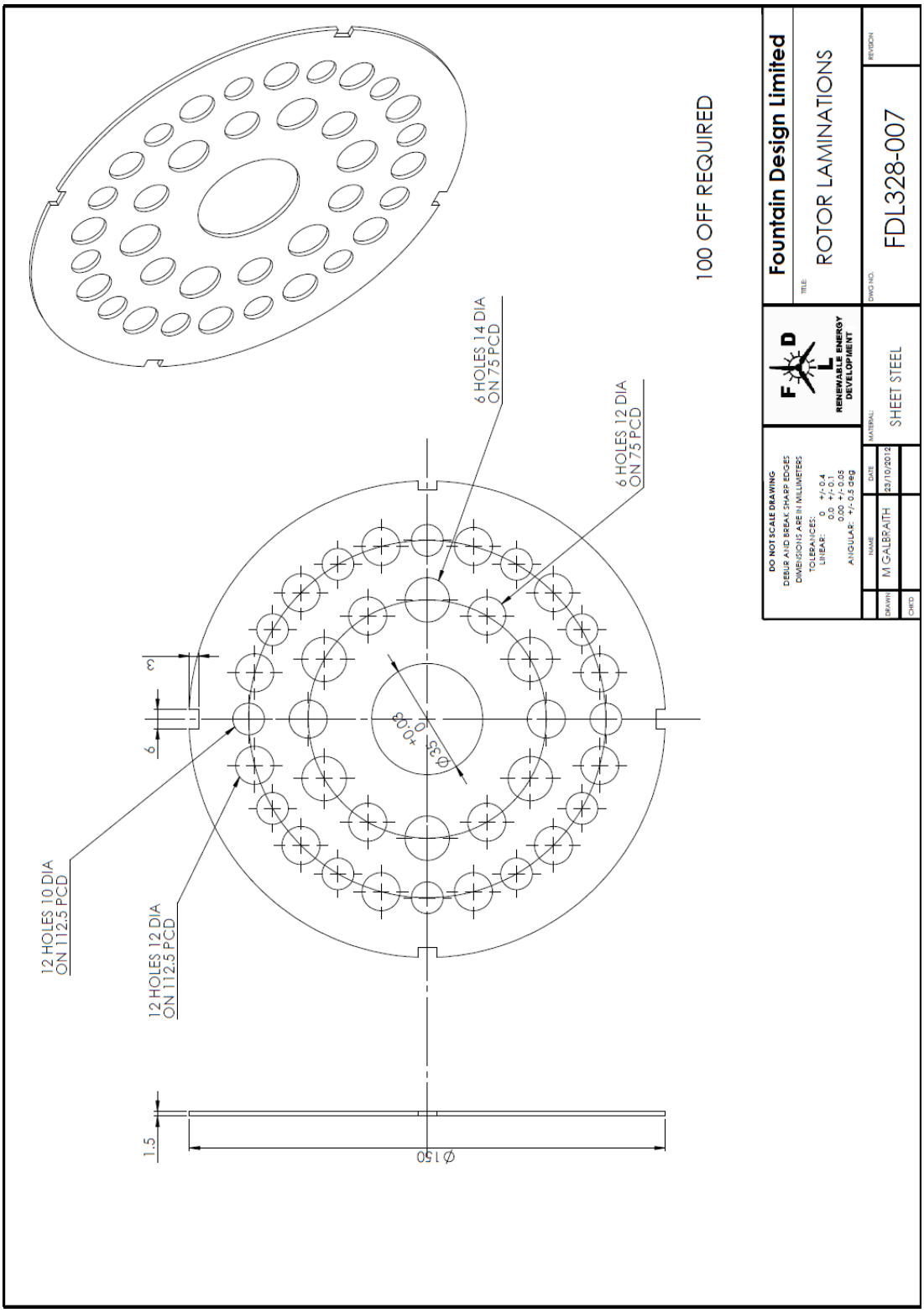
100 OFF REQUIRED
6 HOLES 14 DIA ON 75 PCD
6 HOLES 12 DIA ON 75 PCD
12 HOLES 10 DIA ON 112.5 PCD
12 HOLES 12 DIA ON 112.5 PCD
Ø35 +0.03 0
6
3
1.5
Ø150
DO NOT SCALE DRAWING
DEBUR AND BREAK SHARP EDGES
DIMENSIONS ARE IN MILLIMETERS
TOLERANCES:
LINEAR: 0 +/- 0.4
0.0 +/- 0.1
0.00 +/- 0.05
ANGULAR: +/- 0.5 deg
Fountain Design Limited
RENEWABLE ENERGY DEVELOPMENT
TITLE:
ROTOR LAMINATIONS
DWG NO.
FDL328-007
REVISION
NAME
DATE
MATERIAL:
DRAWN
M GALBRAITH
23/10/2012
SHEET STEEL
CHKD

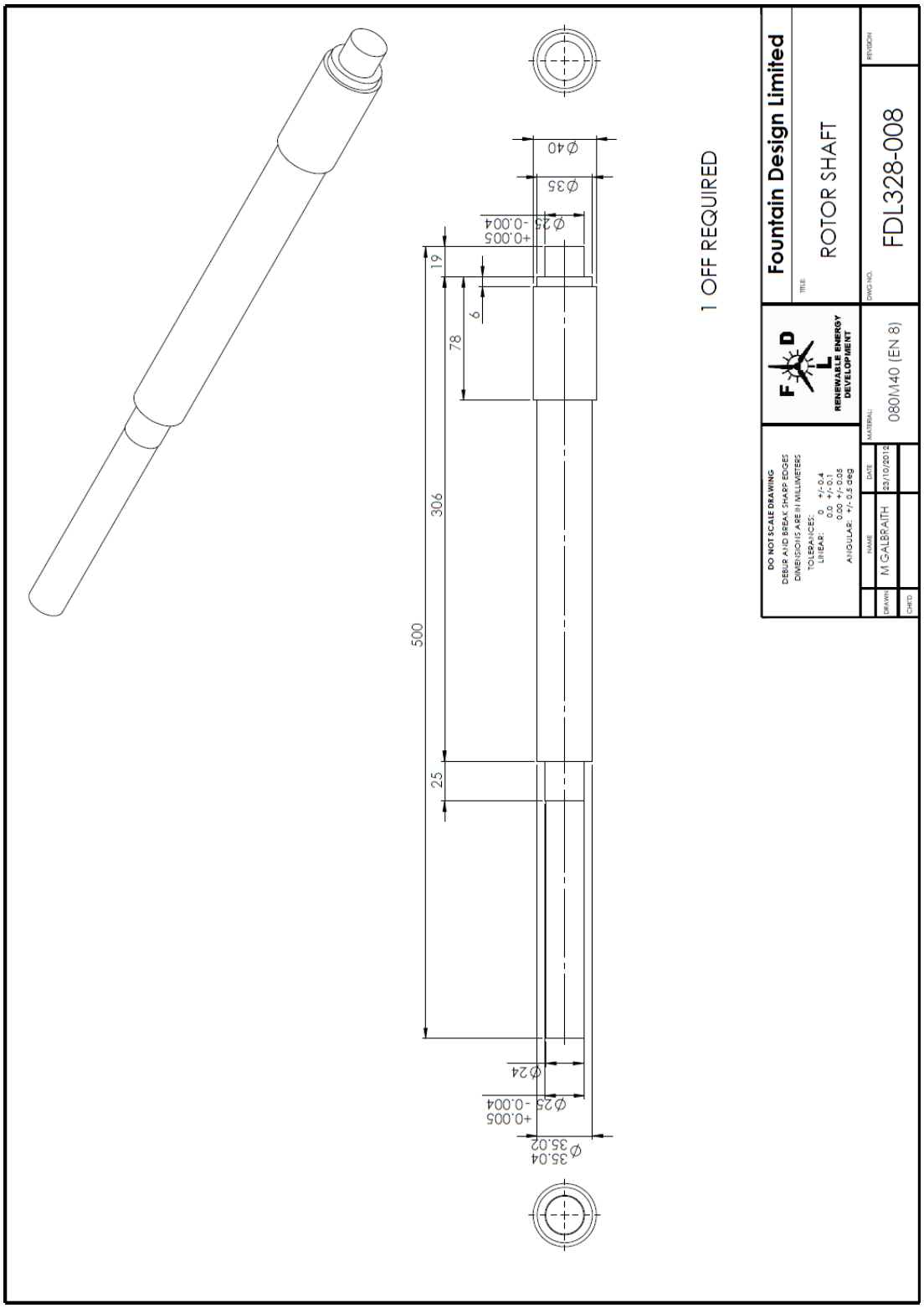
1 OFF REQUIRED
Ø40
Ø35
Ø25 +0.005 -0.004
19
6
78
306
500
25
Ø24
Ø25 +0.005 -0.004
Ø35.04 Ø35.02
Fountain Design Limited
TITLE:
ROTOR SHAFT
DWG NO.
FDL328-008
REVISION
F D L
RENEWABLE ENERGY DEVELOPMENT
MATERIAL:
080M40 (EN 8)
DO NOT SCALE DRAWING
DEBUR AND BREAK SHARP EDGES
DIMENSIONS ARE IN MILLIMETERS
TOLERANCES:
LINEAR: 0 +/- 0.4
00 +/- 0.1
0.00 +/- 0.05
ANGULAR: +/- 0.5 deg
NAME
DATE
DRAWN
M GALBRAITH
23/10/2012
CHKD

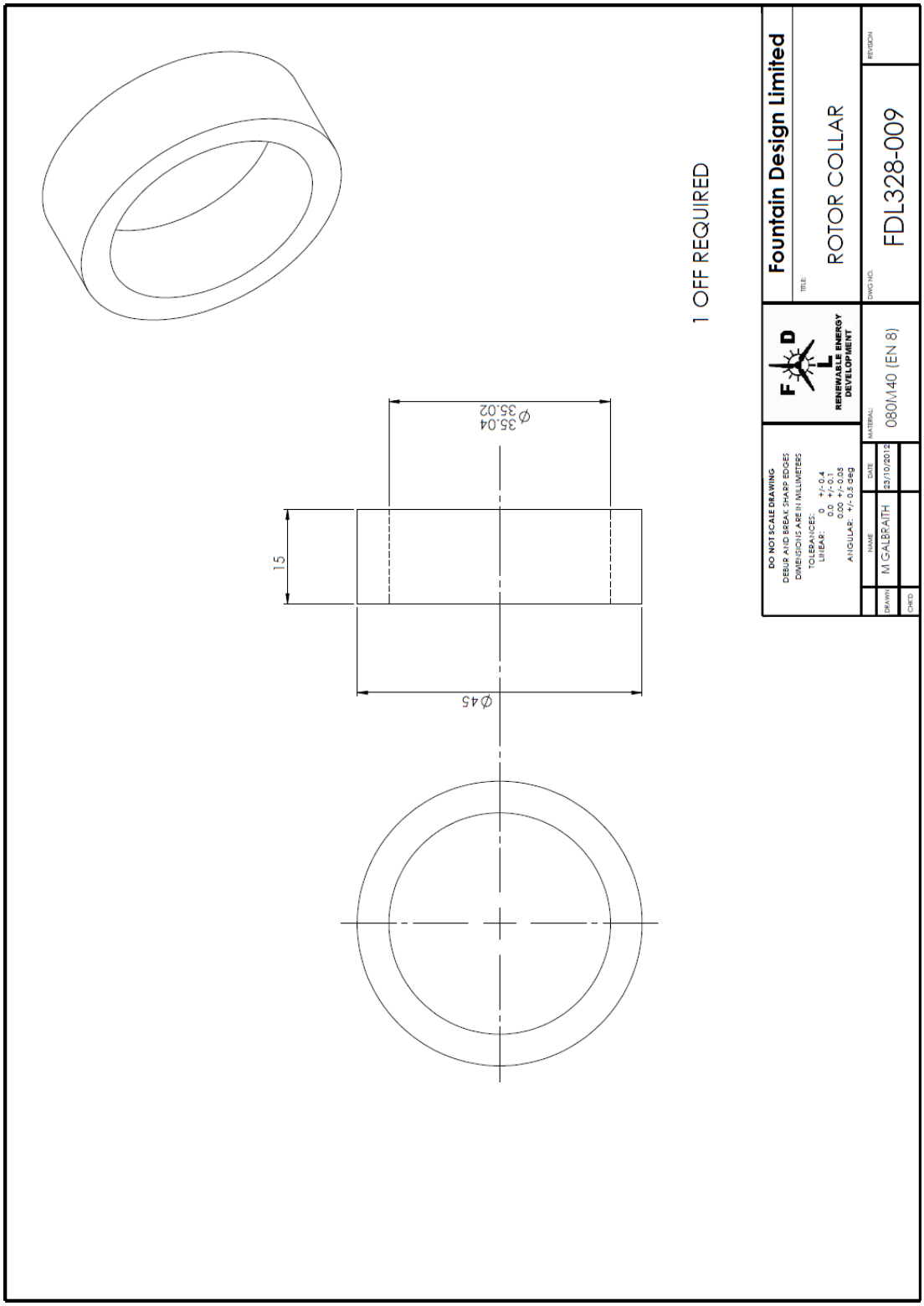
1 OFF REQUIRED
Ø35.04
Ø35.02
15
Ø45
Fountain Design Limited
TITLE:
ROTOR COLLAR
DWG NO.
FDL328-009
REVISION
RENEWABLE ENERGY DEVELOPMENT
MATERIAL:
080M40 (EN 8)
DO NOT SCALE DRAWING
DEBUR AND BREAK SHARP EDGES
DIMENSIONS ARE IN MILLIMETERS
TOLERANCES:
LINEAR: 0 +/- 0.4
0.0 +/- 0.1
0.00 +/- 0.05
ANGULAR: +/- 0.5 deg
NAME
DATE
DRAWN
M GALBRAITH
23/10/2015
CHKD

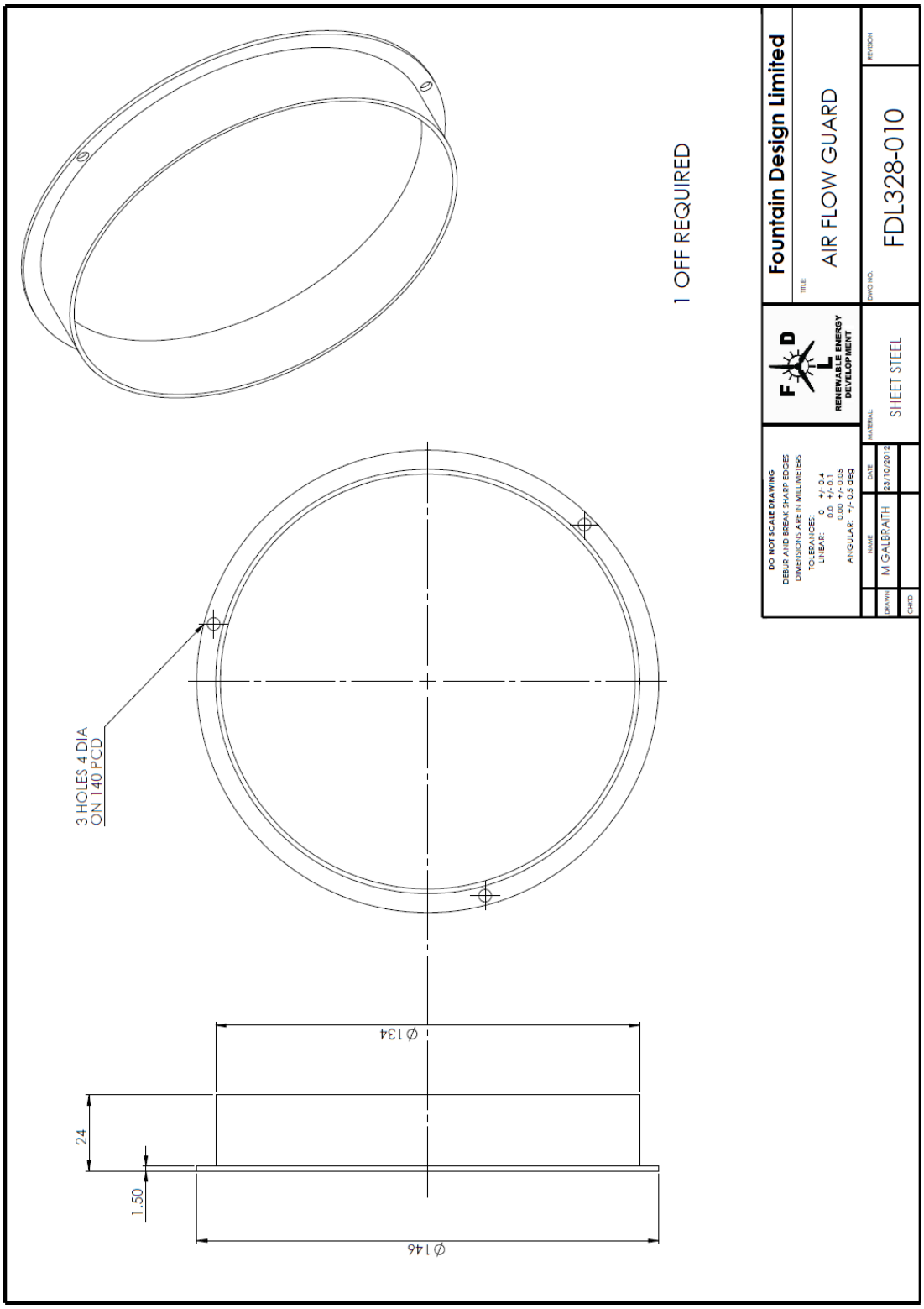
1 OFF REQUIRED
3 HOLES 4 DIA
ON 140 PCD
Ø134
Ø146
24
1.50
DO NOT SCALE DRAWING
DEBUR AND BREAK SHARP EDGES
DIMENSIONS ARE IN MILLIMETERS
TOLERANCES:
LINEAR: .0 +/- 0.4
.00 +/- 0.1
.000 +/- 0.05
ANGULAR: +/- 0.5 deg
RENEWABLE ENERGY DEVELOPMENT
Fountain Design Limited
TITLE:
AIR FLOW GUARD
DWG NO.
FDL328-010
REVISION
MATERIAL:
SHEET STEEL
DRAWN
M GALBRAITH
DATE
23/10/2012
CHKD

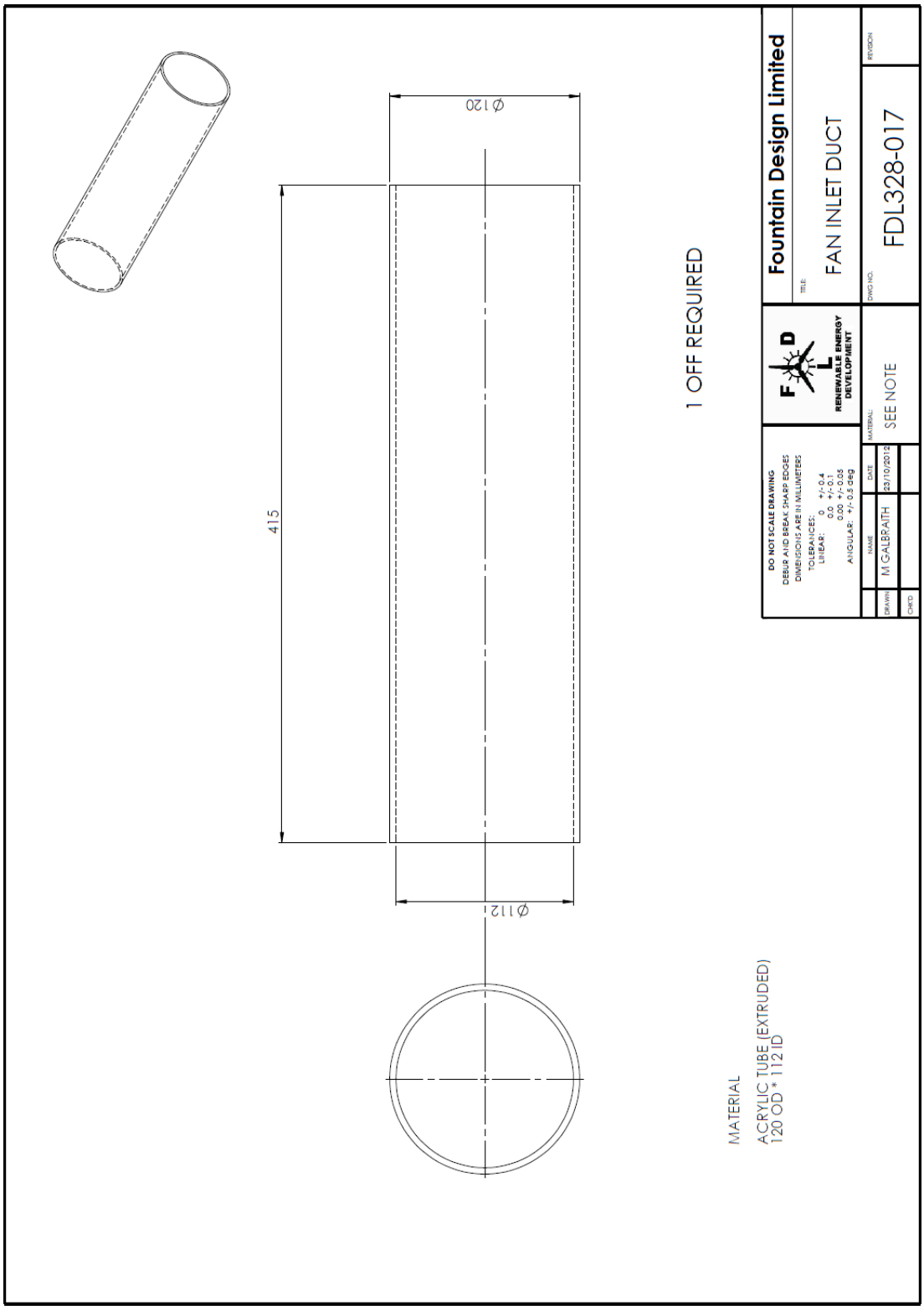
Ø120
415
Ø112
1 OFF REQUIRED
MATERIAL
ACRYLIC TUBE (EXTRUDED)
120 OD * 112 ID
Fountain Design Limited
TITLE:
FAN INLET DUCT
DWG NO.
FDL328-017
REVISION
MATERIAL:
SEE NOTE
DATE
23/10/2012
NAME
M GALBRAITH
DRAWN
CHKD
DO NOT SCALE DRAWING
DEBUR AND BREAK SHARP EDGES
DIMENSIONS ARE IN MILLIMETERS
TOLERANCES:
LINEAR: 0 +/- 0.4
0.0 +/- 0.1
0.00 +/- 0.05
ANGULAR: +/- 0.5 deg
RENEWABLE ENERGY DEVELOPMENT

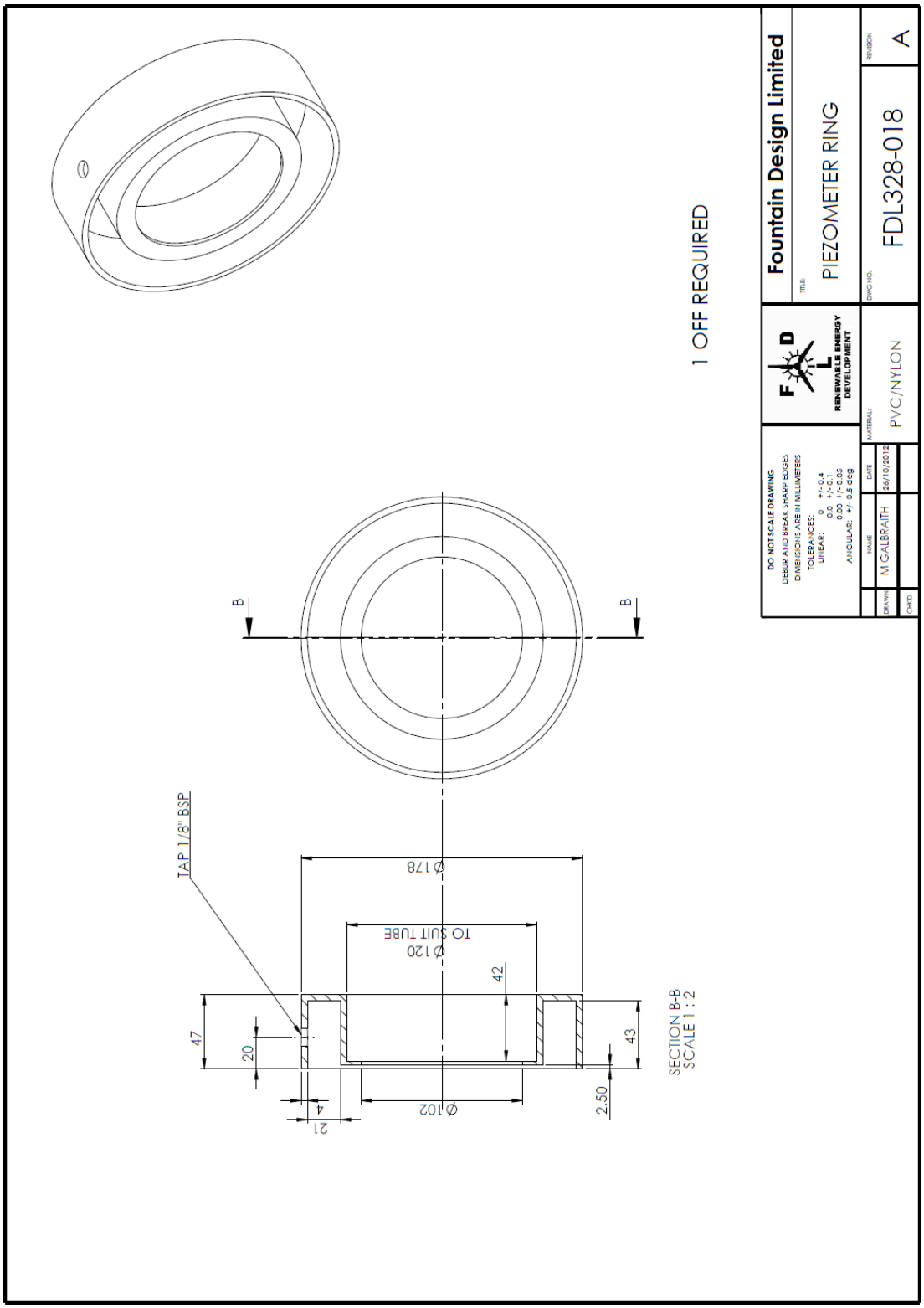
1 OFF REQUIRED
Fountain Design Limited
PIEZOMETER RING
FDL328-018
A
PVC/NYLON
M GALBRAITH
24/10/2012
RENEWABLE ENERGY DEVELOPMENT
DO NOT SCALE DRAWING
DEBUR AND BREAK SHARP EDGES
DIMENSIONS ARE IN MILLIMETERS
TOLERANCES:
LINEAR: 0 +/- 0.4
0.0 +/- 0.1
0.00 +/- 0.05
ANGULAR: +/- 0.5 deg
TAP 1/8" BSP
Ø178
TO SUIT TUBE
Ø120
Ø102
42
47
20
43
2.50
4
21
B
B
SECTION B-B
SCALE 1 : 2

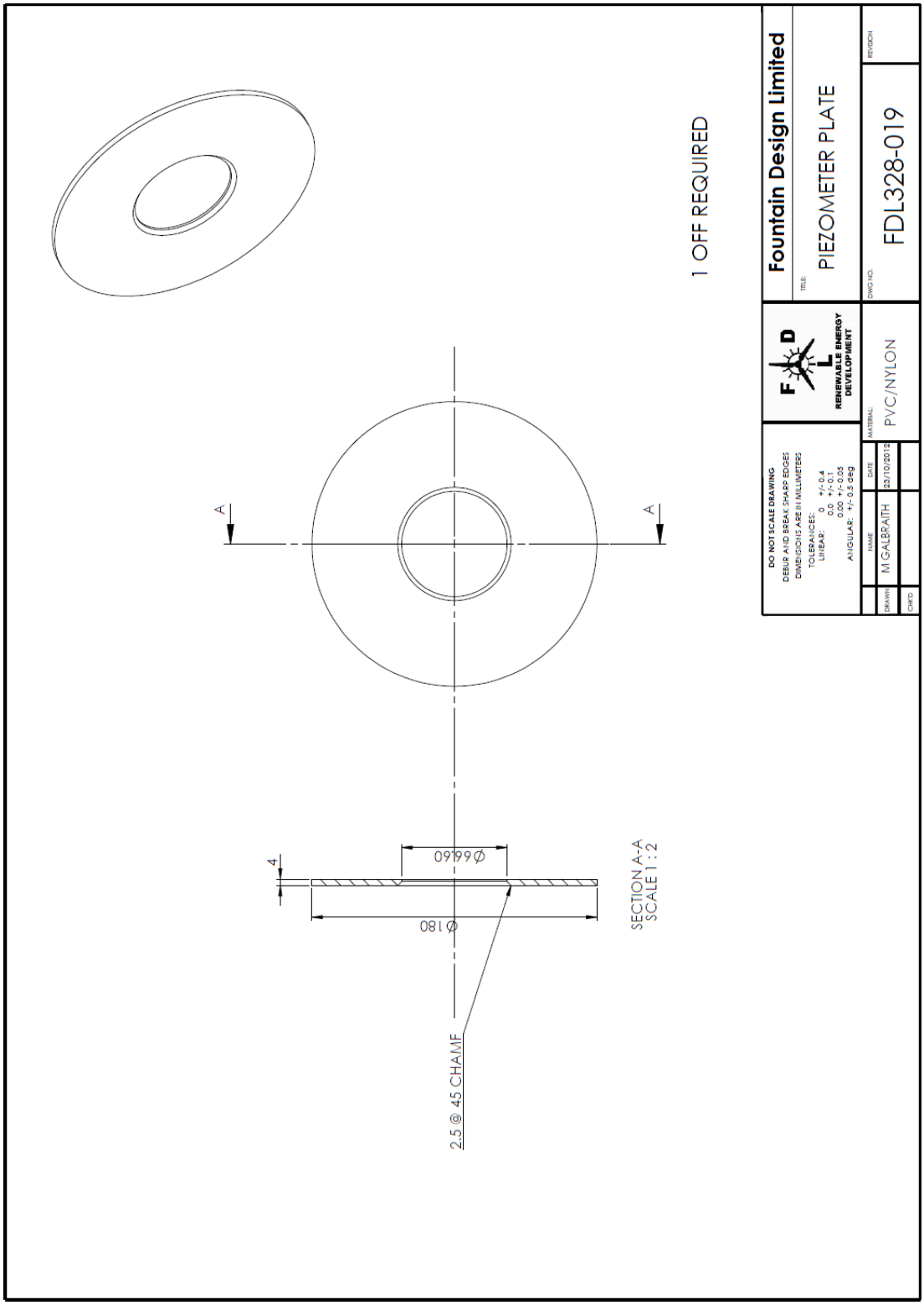
1 OFF REQUIRED
A
A
Ø66.60
4
Ø 180
2.5 @ 45 CHAMF
SECTION A-A
SCALE 1 : 2
DO NOT SCALE DRAWING
DEBUR AND BREAK SHARP EDGES
DIMENSIONS ARE IN MILLIMETERS
TOLERANCES:
LINEAR: 0 +/- 0.4
0.0 +/- 0.1
0.00 +/- 0.05
ANGULAR: +/- 0.5 deg
F D L
RENEWABLE ENERGY DEVELOPMENT
Fountain Design Limited
TITLE:
PIEZOMETER PLATE
DWG NO.
FDL328-019
REVISION
MATERIAL:
PVC/NYLON
NAME
DATE
DRAWN
M GALBRAITH
23/10/2012
CHKD

Appendix I – Centrifugal Fan (K-28-S)

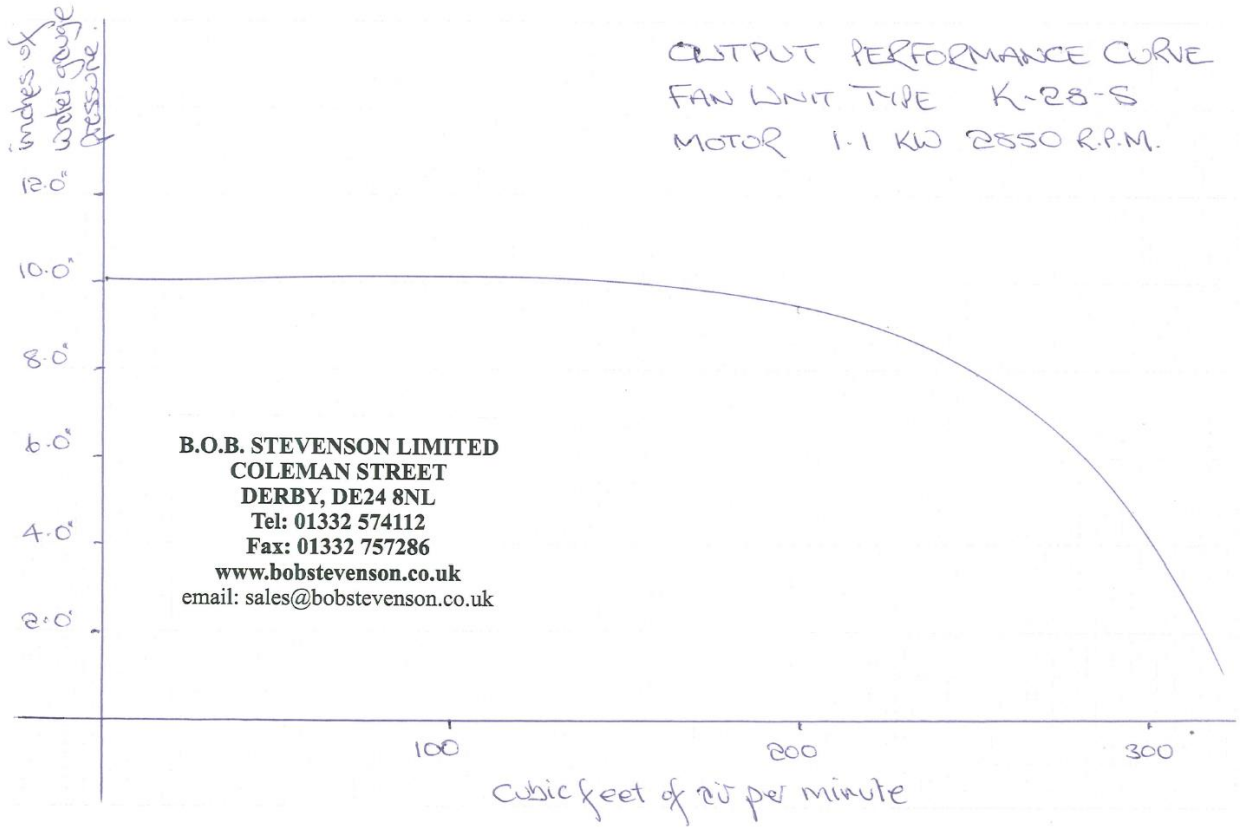

Figure I.1 Fan characteristic of K-28-S at 2850 rpm

Appendix J – Equivalent Flow Networks

The equivalent flow networks were constructed using the PORTUNUS Flow Library.

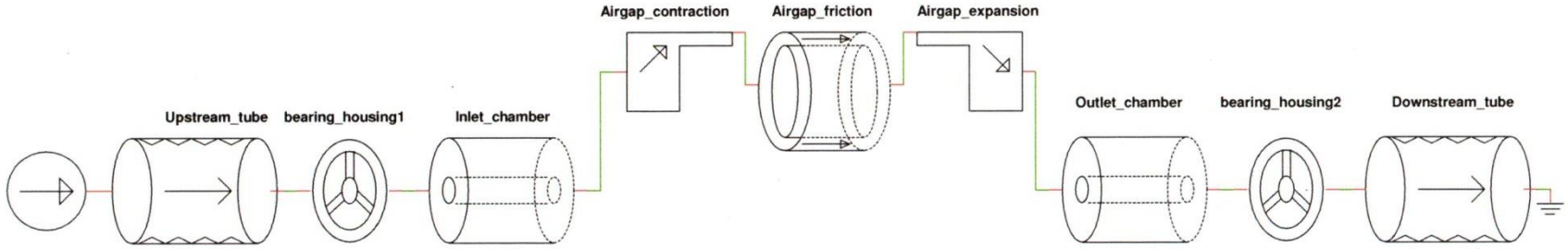

Figure J.1: Portunus flow network for the ventilation system with airgap, no flow guard and with stationary rotor

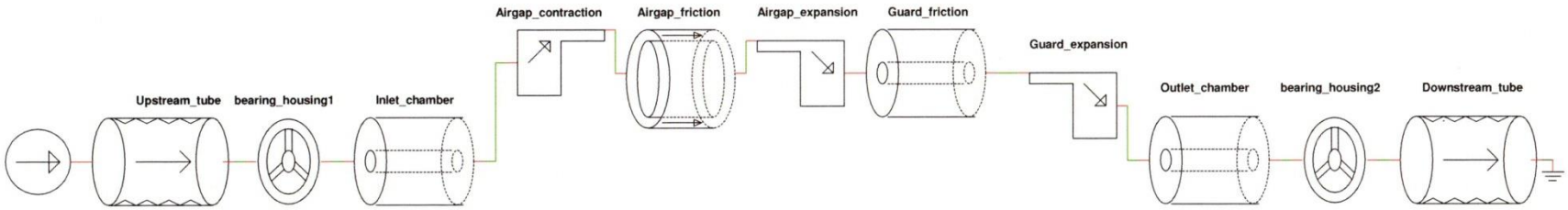

Figure J.2: Portunus flow network for the ventilation system with airgap, flow guard and stationary rotor

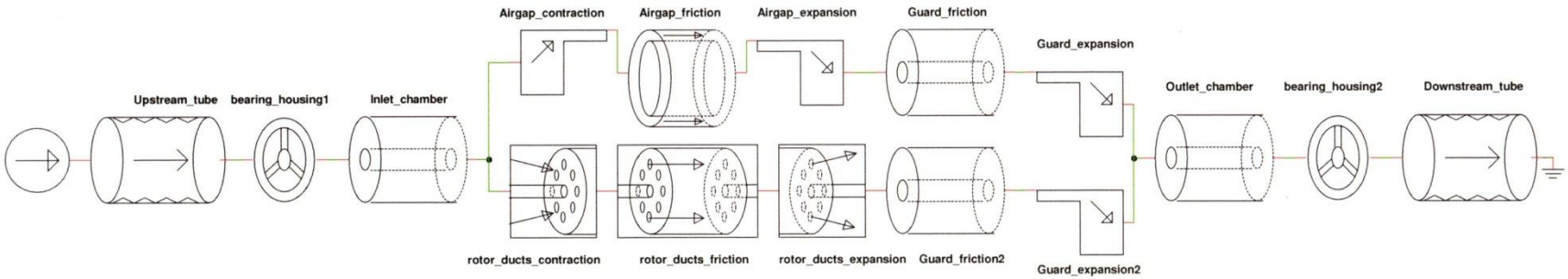

Figure J.3: Portunus flow network for the ventilation system with rotor ducts, airgap, flow guard and stationary rotor

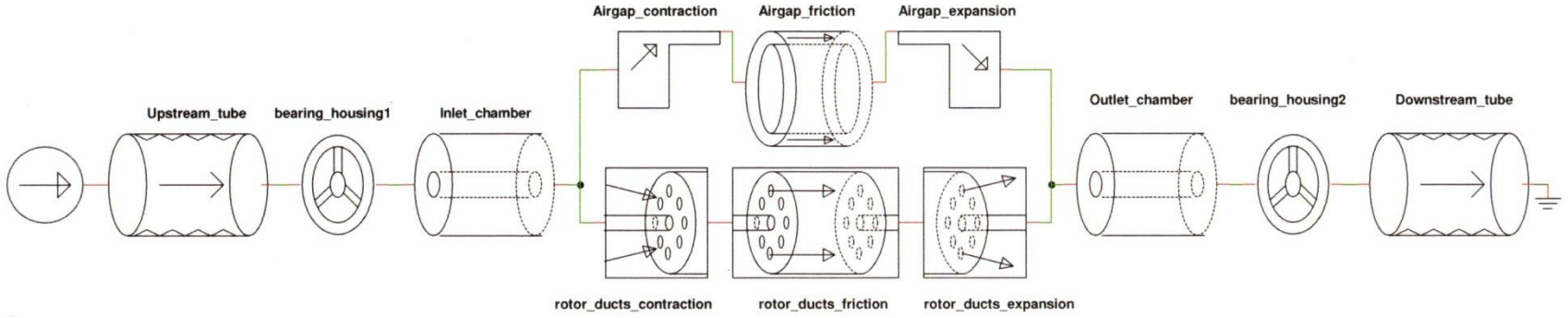

Figure J.4: Portunus flow network for the ventilation system with rotor ducts, airgap, no flow guard and with stationary rotor

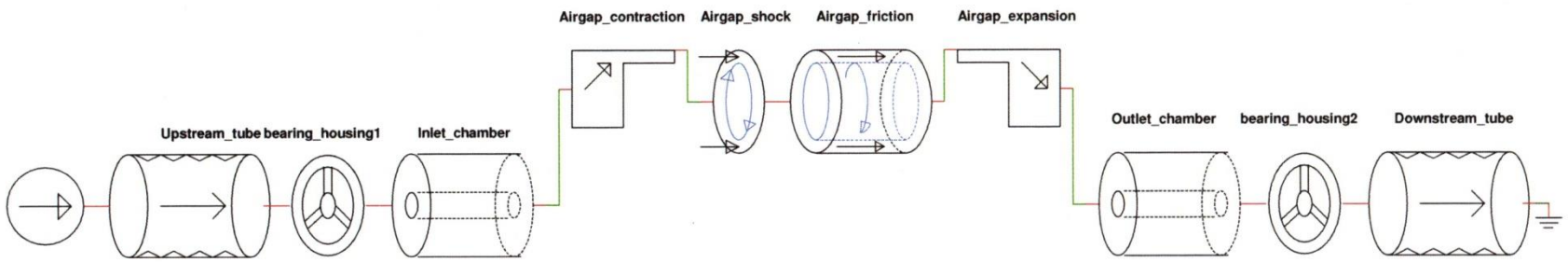

Figure J.5: Portunus flow network for the ventilation system with airgap, no flow guard and with rotating rotor

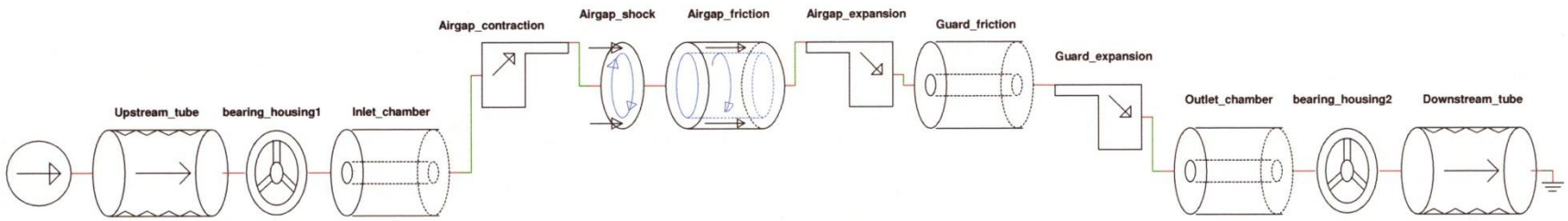

Figure J.6: Portunus flow network for the ventilation system with airgap, flow guard and rotating rotor

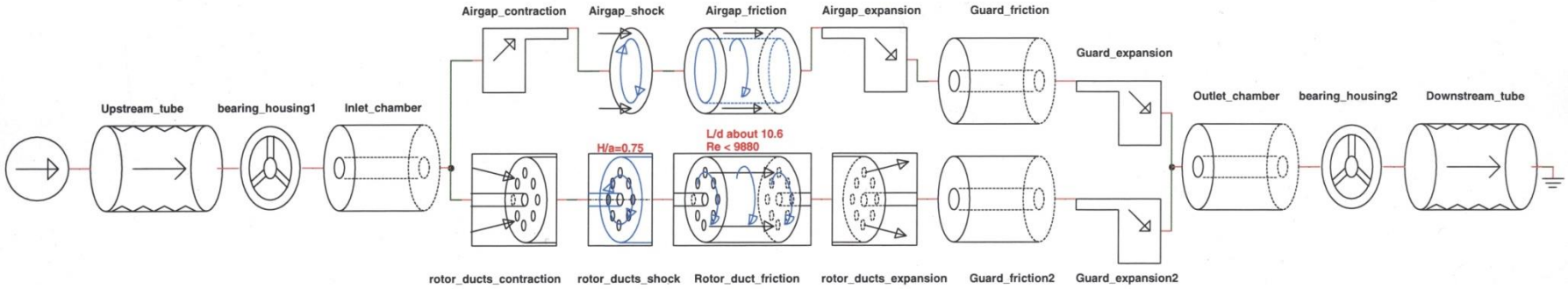

Figure J.7: Portunus flow network for the ventilation system with rotor ducts, airgap, flow guard and rotating rotor

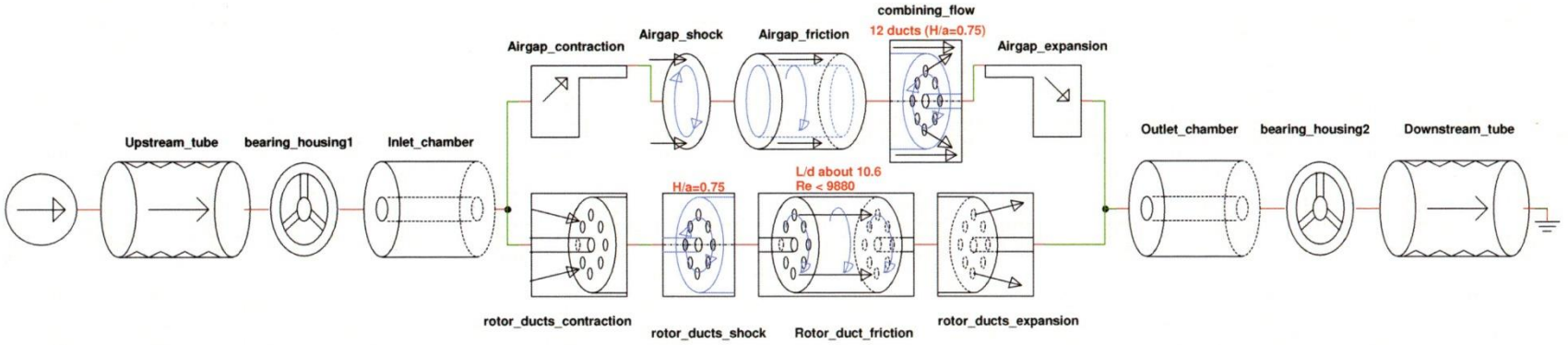

Figure J.8: Portunus flow network for the ventilation system with rotor ducts, airgap, no flow guard and with rotating rotor

Appendix K – Experimental Results for Stationary Tests with Rotor Ducts and Airgap

The comparison between the experimental results and the values predicted using the analytical flow network analysis is shown in Figure K.1 and Figure K.3. The contribution of pressure loss components of the rotor ducts in percentage from the Plane 3 to the outlet of the test rig is calculated from the experimentally validated flow networks. The total pressure loss for the cases of rotor ducts and airgap in Figure K.2 and Figure K.4 corresponds the pressure at Plane 3 for the given flow rate in Figure K.1 and Figure K.3 respectively.

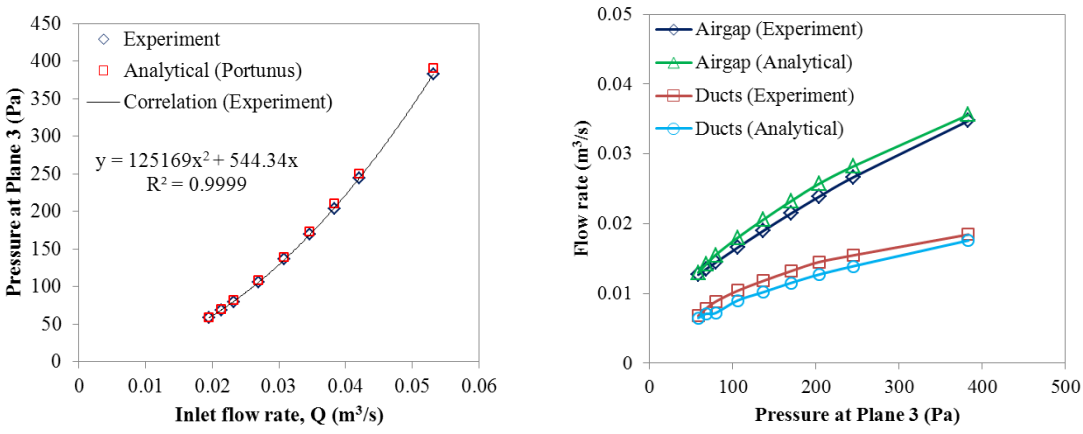

(a) *12 D10 PCD113*

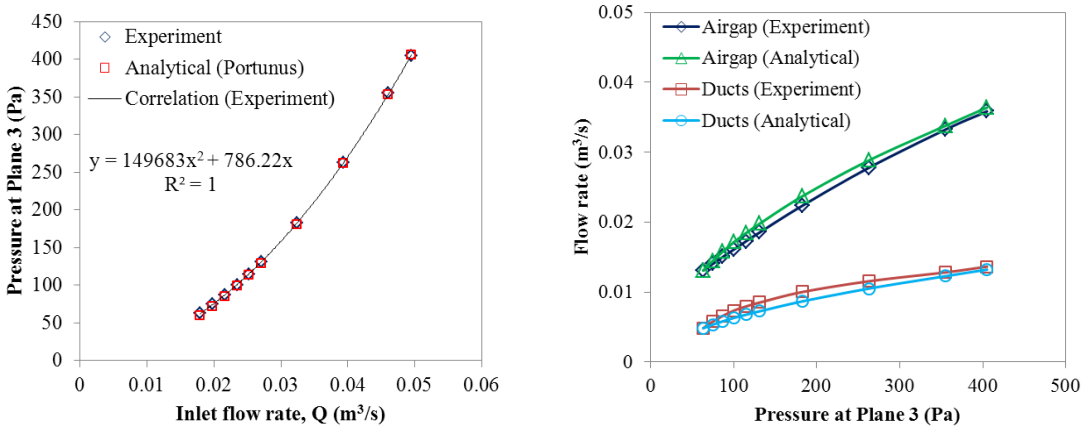

(b) *6 D12 PCD113*

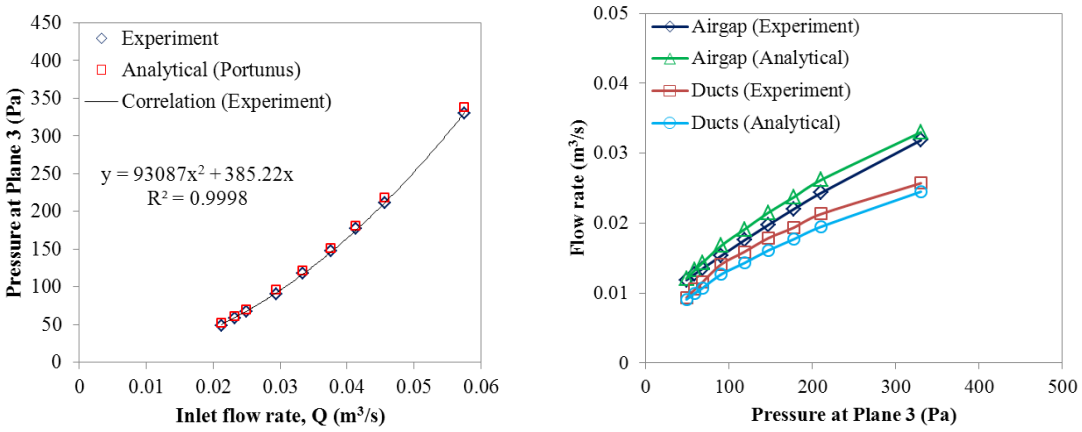

(c) *12 D12 PCD113*

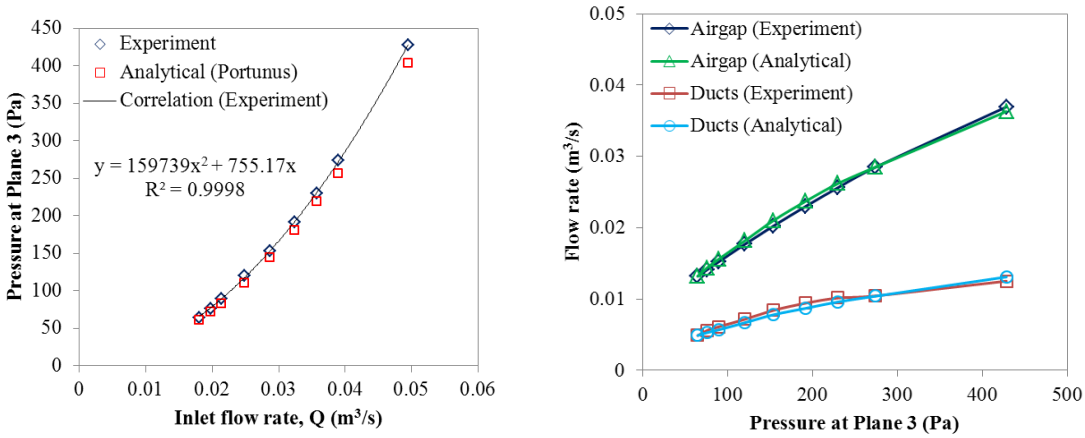

(d) *6 D12 PCD75*

Figure K.1:Pressure drop from the Plane 3 to the outlet versus inlet flow rate for ventilation with flow guard (left) and the flow distribution between rotor ducts and airgap (right)

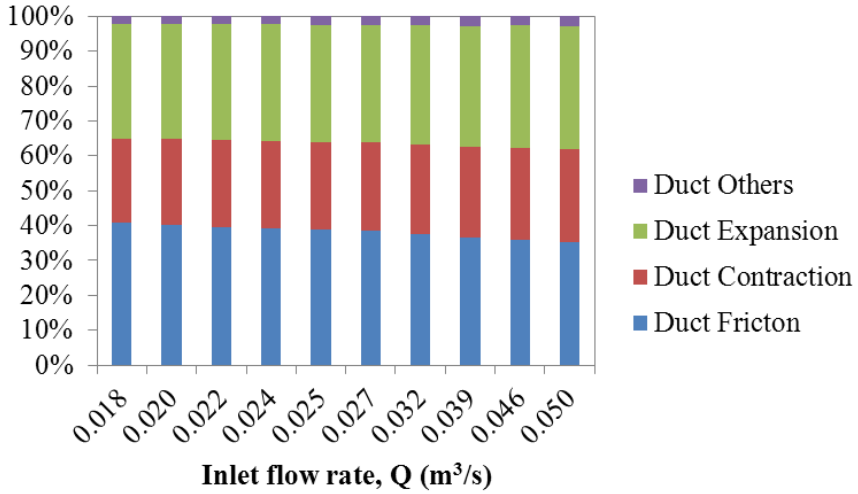

(a) *6 D12 PCD113*

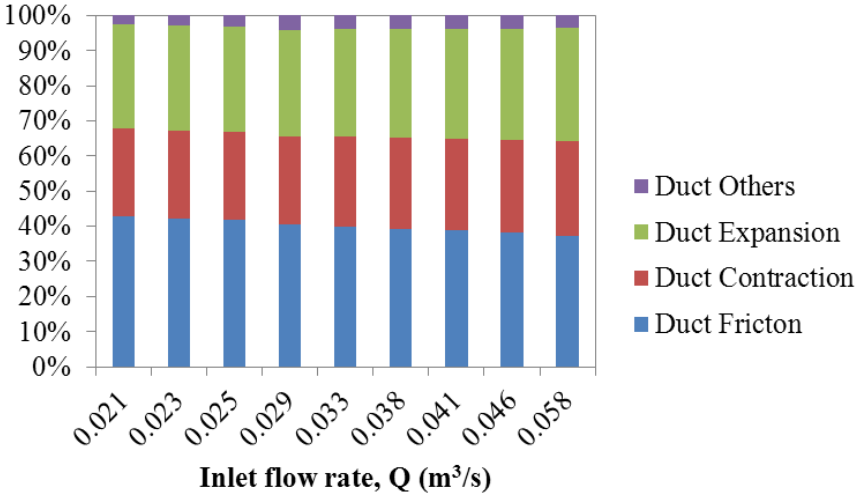

(b) *12 D12 PCD113*

Figure K.2:The contribution of pressure loss components of rotor ducts with flow guard determined using Portunus flow network analysis

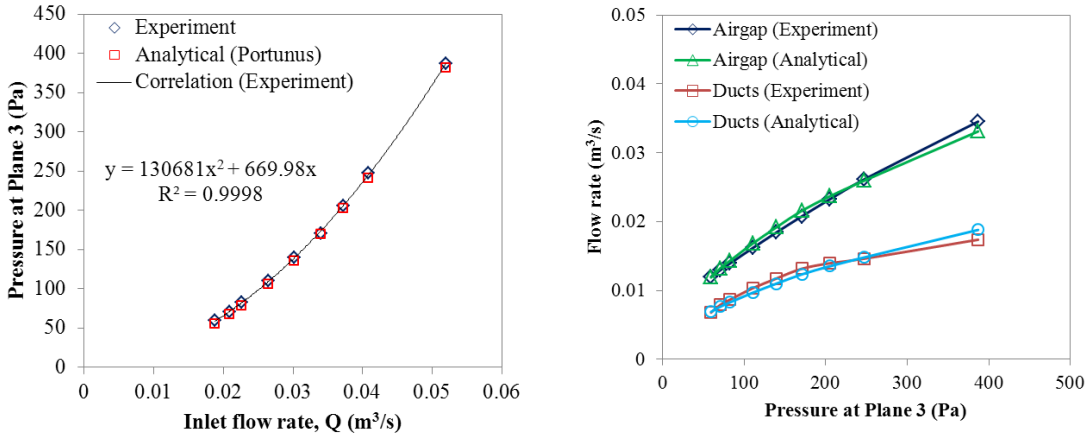

(a) *12 D10 PCD113*

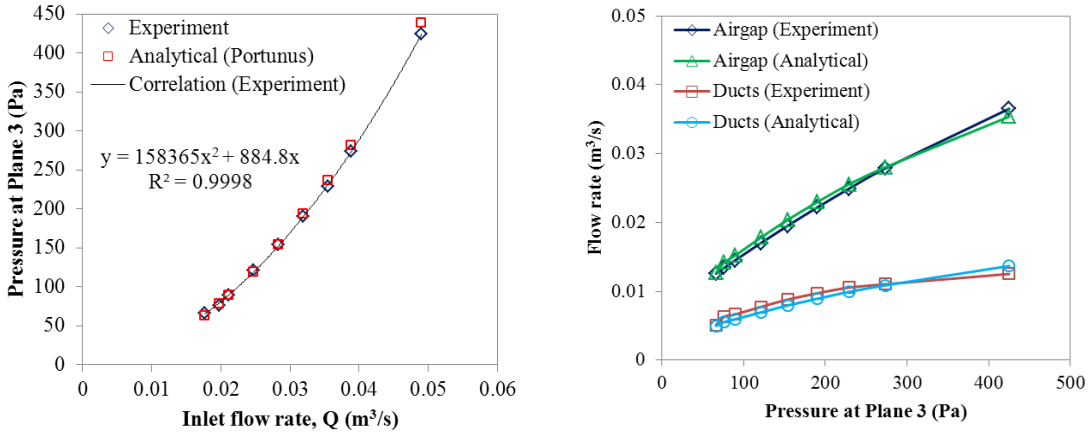

(b) *6 D12 PCD113*

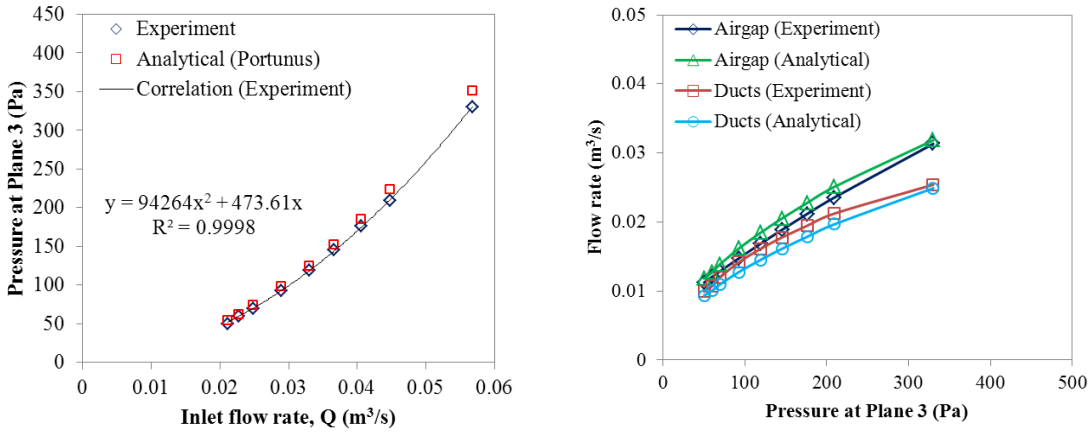

(c) *12 D12 PCD113*

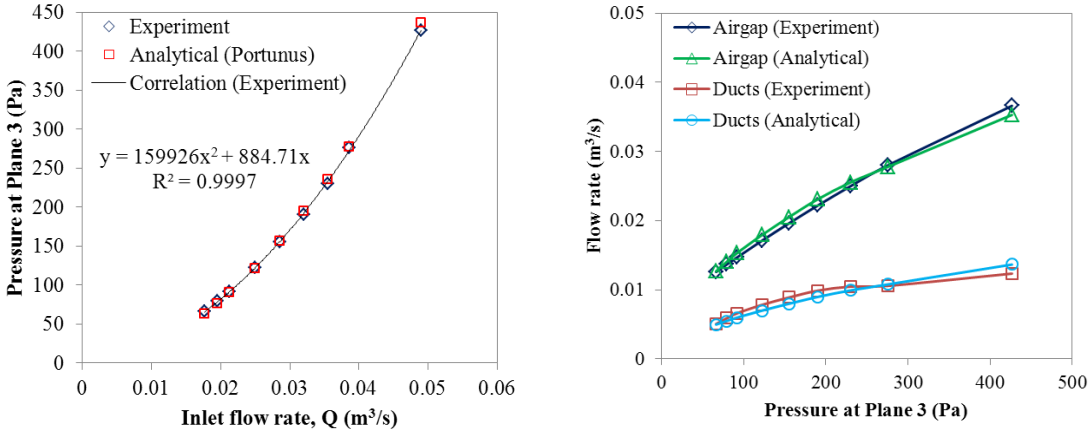

(d) *6 D12 PCD75*

Figure K.3: Pressure drop from the Plane 3 to the outlet versus inlet flow rate for ventilation without flow guard (left) and the flow distribution between rotor ducts and airgap (right)

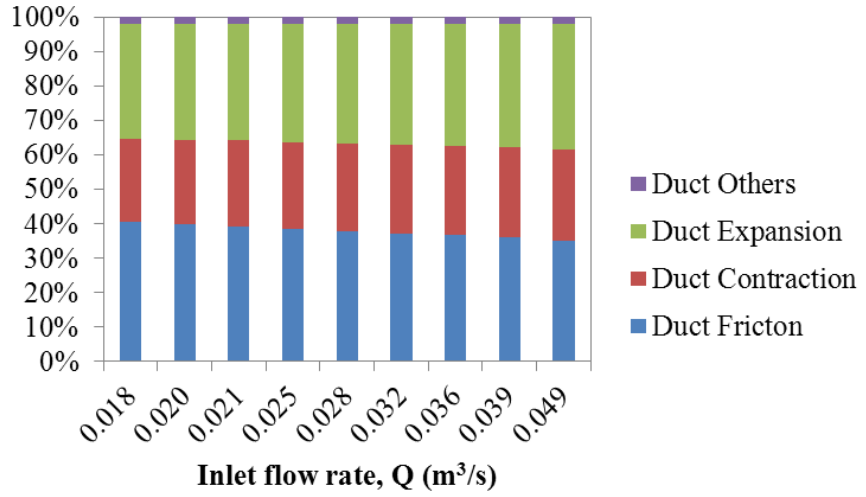

(a) *6 D12 PCD113*

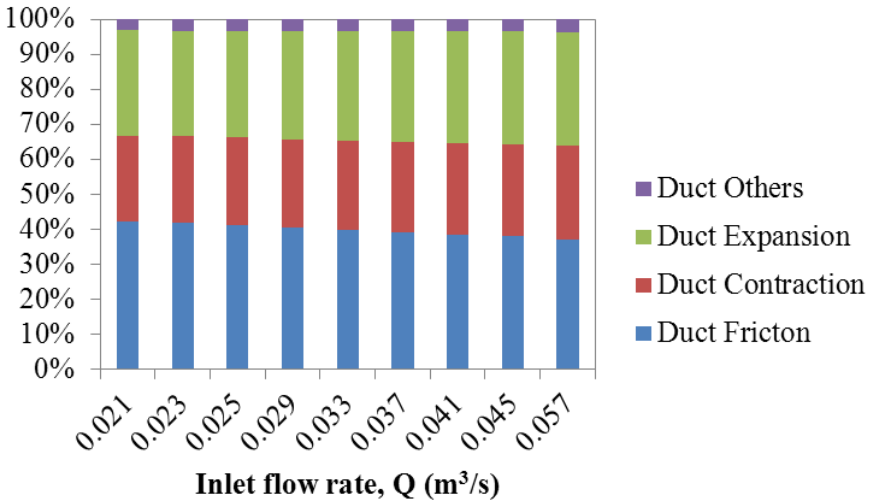

(b) *12 D12 PCD113*

Figure K.4: The contribution of pressure loss components of rotor ducts without flow guard determined using Portunus flow network analysis

Appendix L – Experimental Data for Ventilation with Airgap and Flow Guard

The equations (8.16) to (8.22) are limited by the fact that the input data, ΔP_3 needs to be within the range of the pressure. Therefore, interpretation of Q_{airgap} outside the range of the pressure of the equation is not recommended.

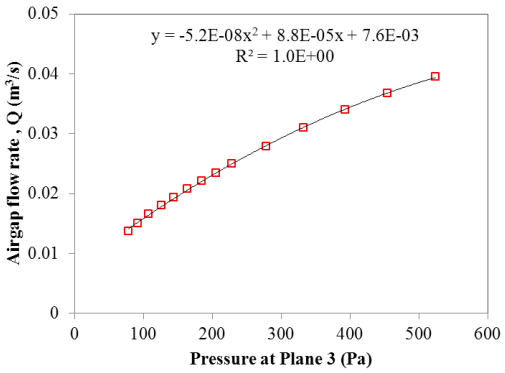

Rotor speed = 0 rpm

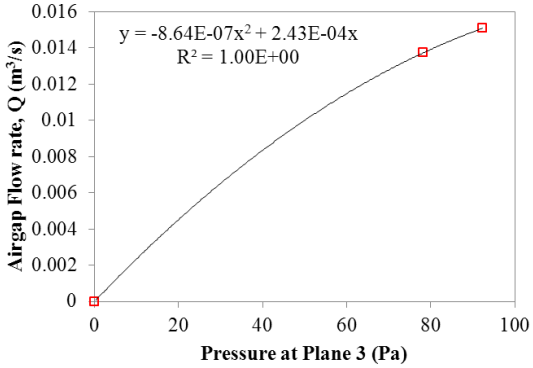

Rotor speed = 600 rpm

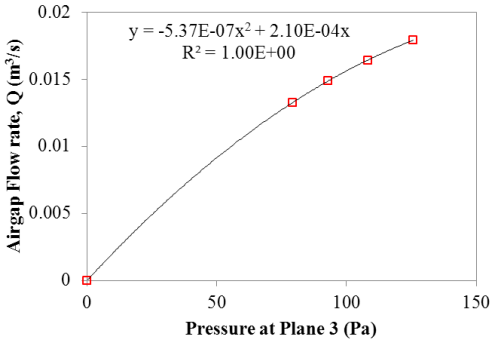

Rotor speed = 1200 rpm

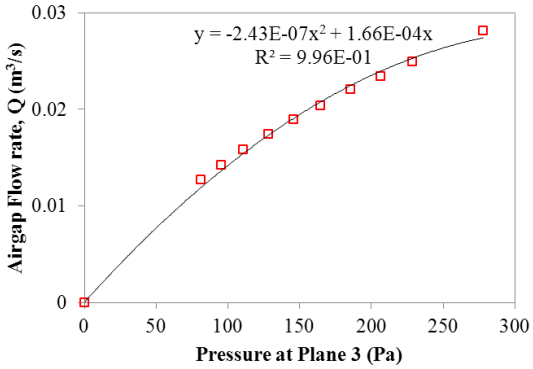

Rotor speed = 1800 rpm

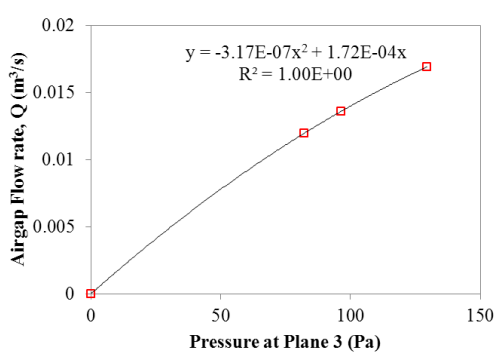

Rotor speed = 2100 rpm

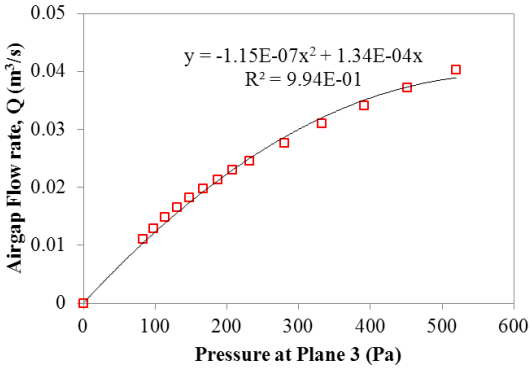

Rotor speed = 2400 rpm

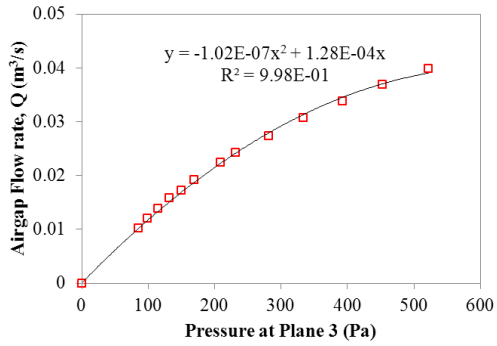

Rotor speed = 2700 rpm

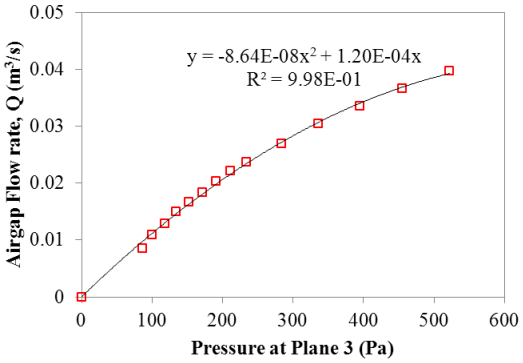

Rotor speed = 3000 rpm

Figure L.1: The airgap flow rate vs. pressure at Plane 3 for ventilation of airgap and flow guard

Appendix M – Experimental Results for Rotational Tests with Airgap only and Flow Guard

For the ventilation with airgap only and flow guard, the comparison between the experimental results and the values predicted using analytical flow network analysis is shown on the left hand side of Figure M.1. The comparison demonstrates that the flow network analysis is capable of predicting the pressure requirements for the flow passing through the airgap with rotor rotating at 1800 rpm, 2400 rpm and 3000 rpm. The contribution of pressure loss components obtained using the the experimentally validated flow network is illustrated on the right hand side of Figure M.1.

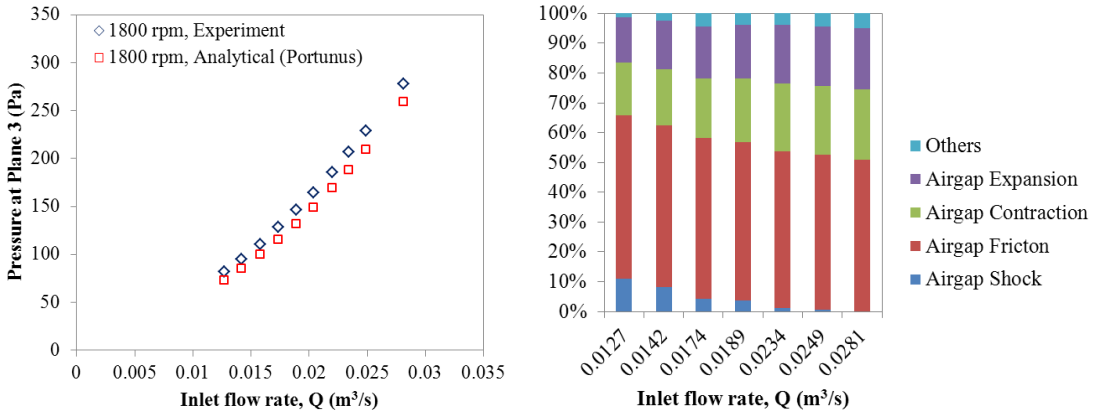

(a) Rotor speed = 1800 rpm

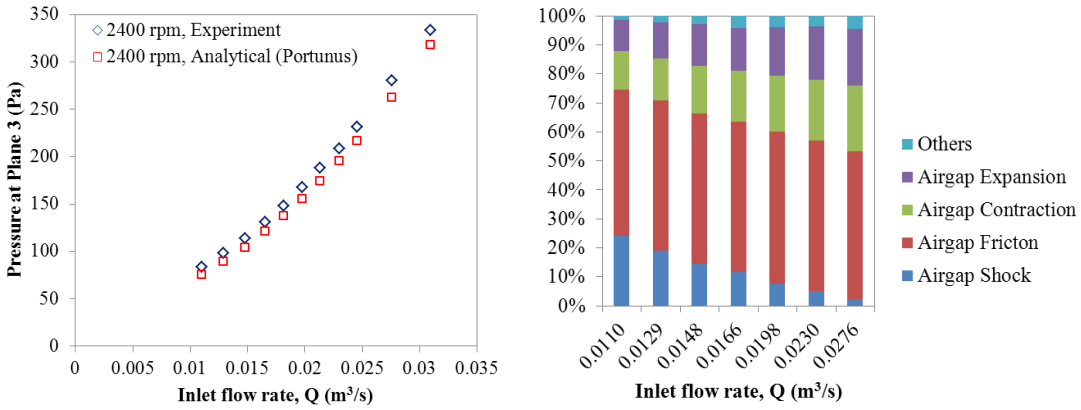

(b) Rotor speed = 2400 rpm

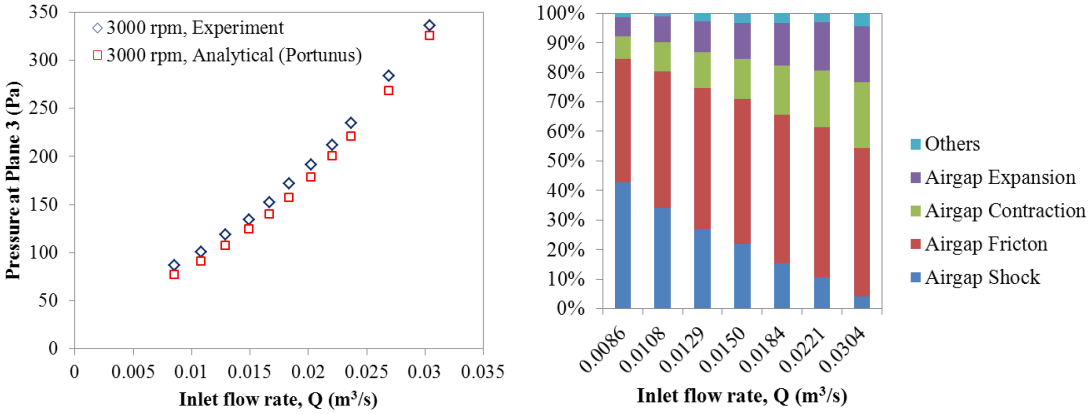

(a) Rotor speed = 3000 rpm

Figure M.1: Pressure drop from the Plane 3 to the outlet versus inlet flow rate for ventilation system of airgap with flow guard (left), and the contribution of pressure loss components determined using Portunus flow network analysis (right)

Appendix N – Experimental Results for Rotational Tests with Rotor Ducts, Airgap and Flow Guard

Figure N.1 shows the influence of rotation to system flow resistance curves of the case of rotor ducts and airgap in parallel, while Figure N.2 indicates the effects of rotation on flow distribution between the rotor ducts and airgap. In general, Q_{ducts} decreases for the increase in rotor speed.

Figure N.3 and Figure N.5 show the comparisons between the experimental results and the values predicted using analytical flow network analysis. Good agreements were achieved. In Figure N.4 and Figure N.6, the experimentally validated flow network was used to investigate the contribution of the main pressure loss components in percentage from Plane 3 to the outlet of the test rig.

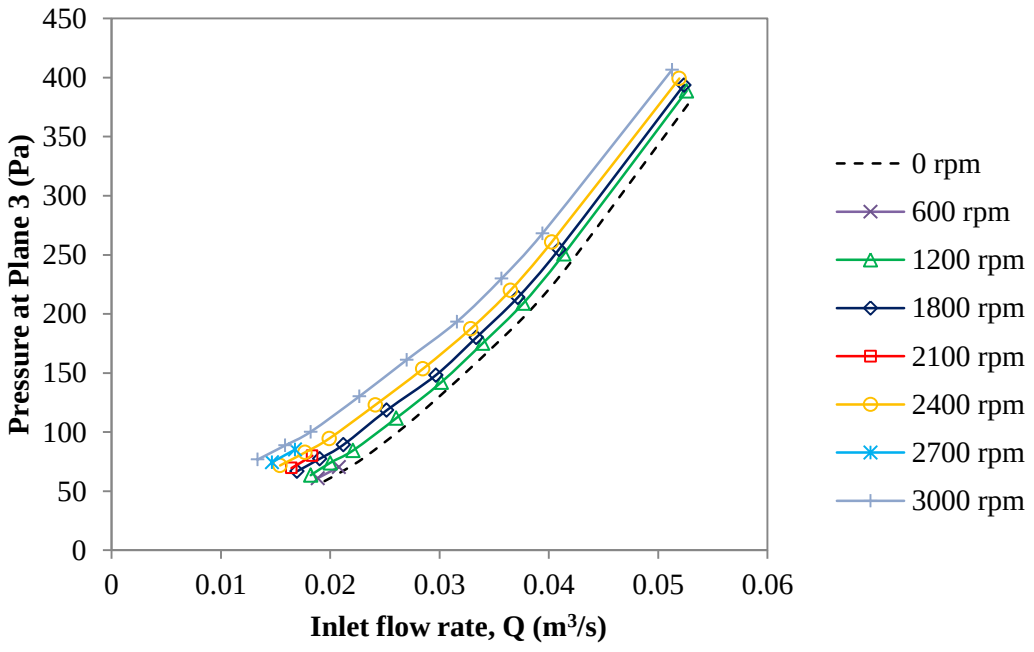

(a) *12 D10 PCD113*

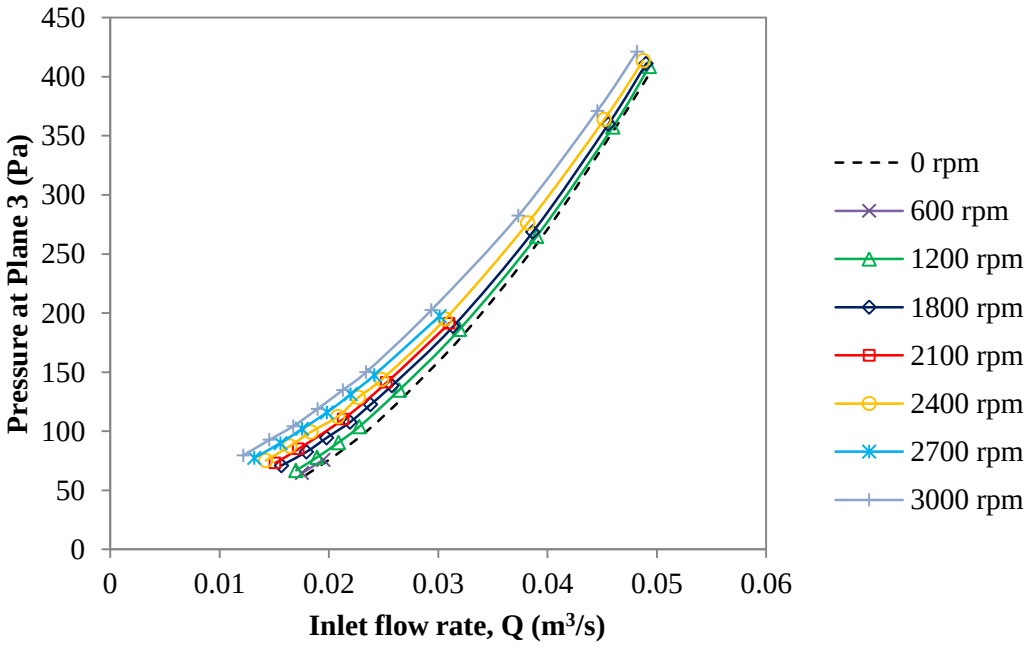

(b) *6 D12 PCD113*

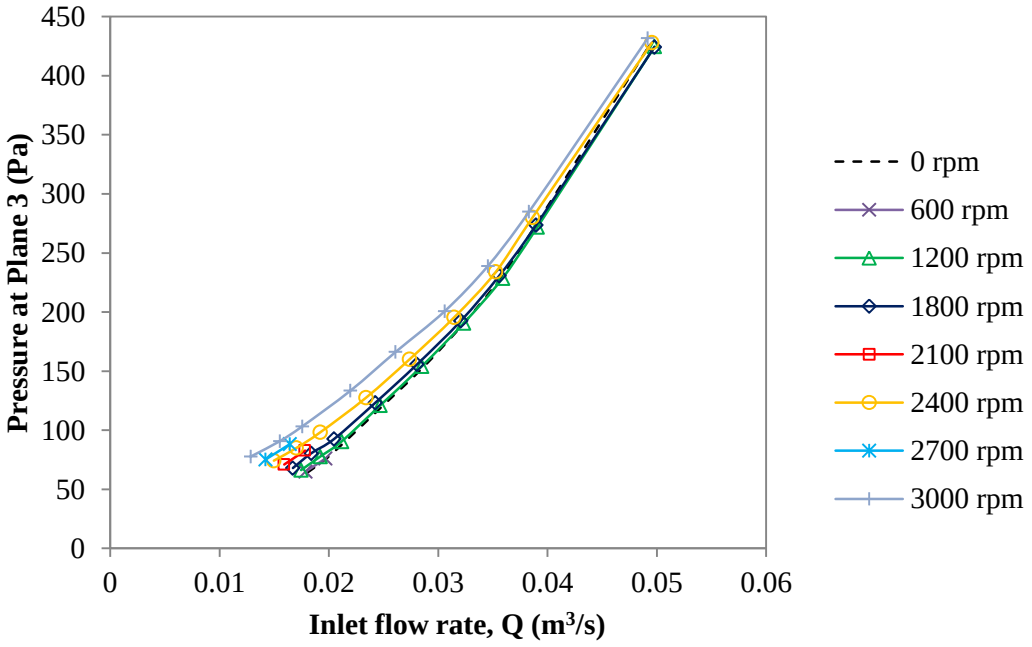

(c) *6 D12 PCD75*

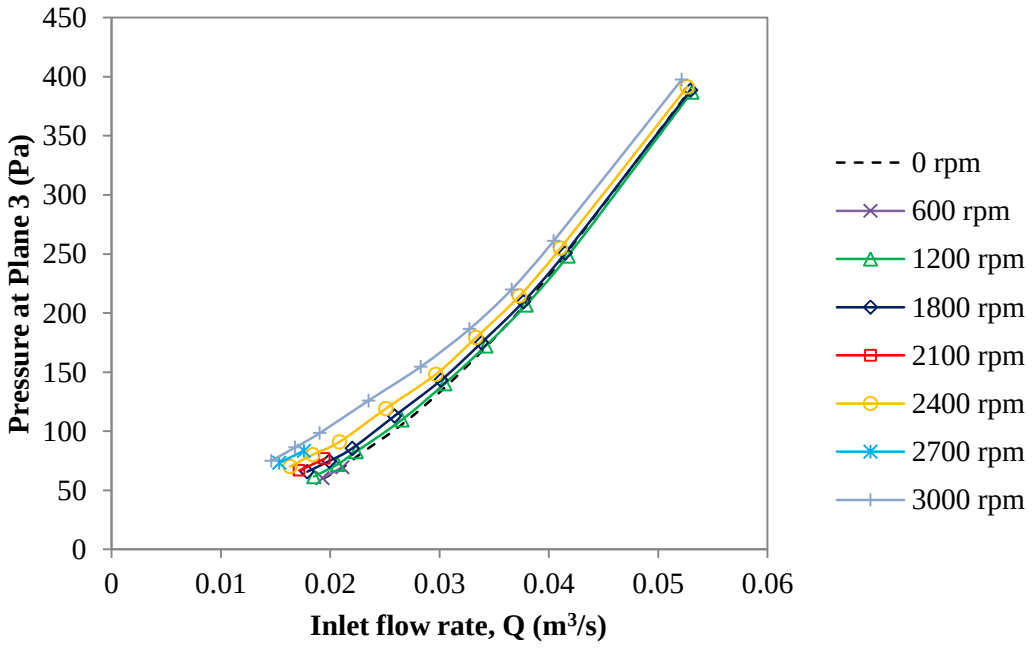

(d) *6 D14 PCD75*

Figure N.1: System flow resistance curves of ventilation with flow guard for rotor speed up to 3000 rpm

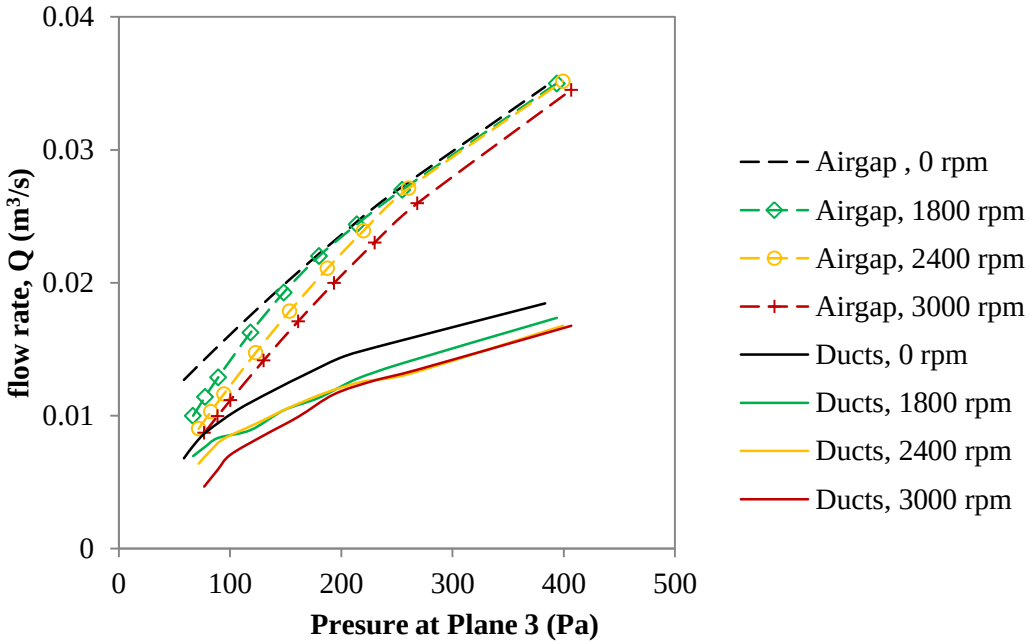

(a) *12 D10 PCD113*

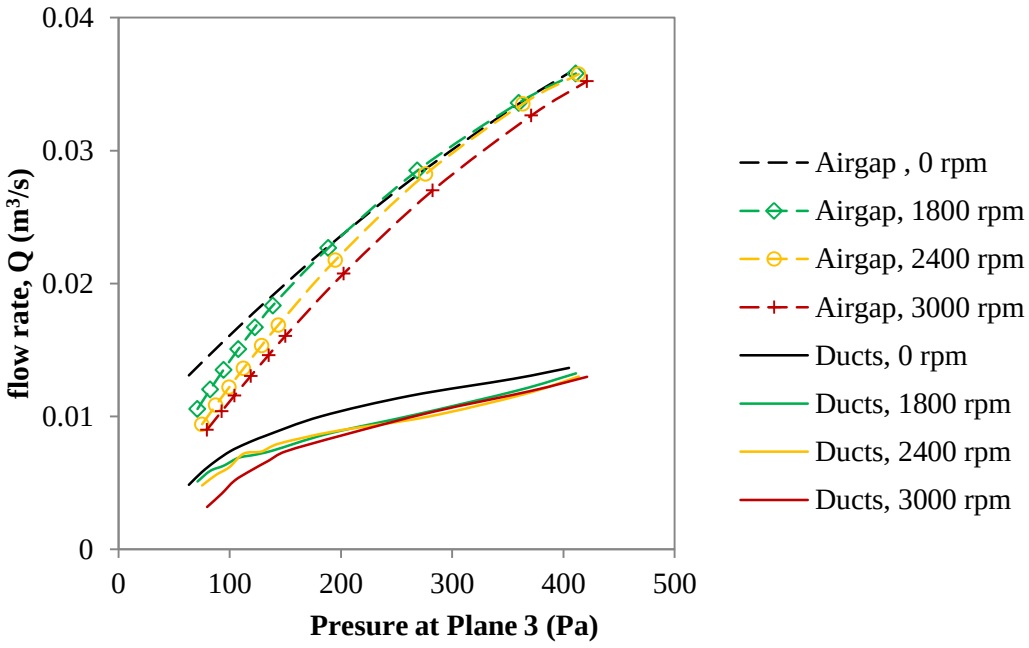

(b) *6 D12 PCD113*

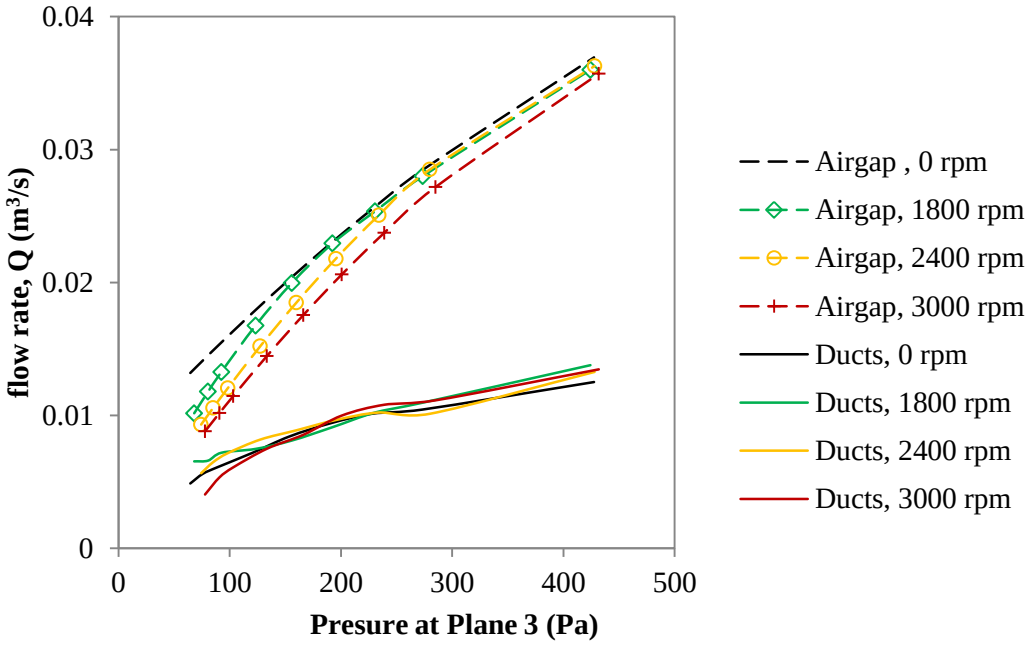

(c) *6 D12 PCD75*

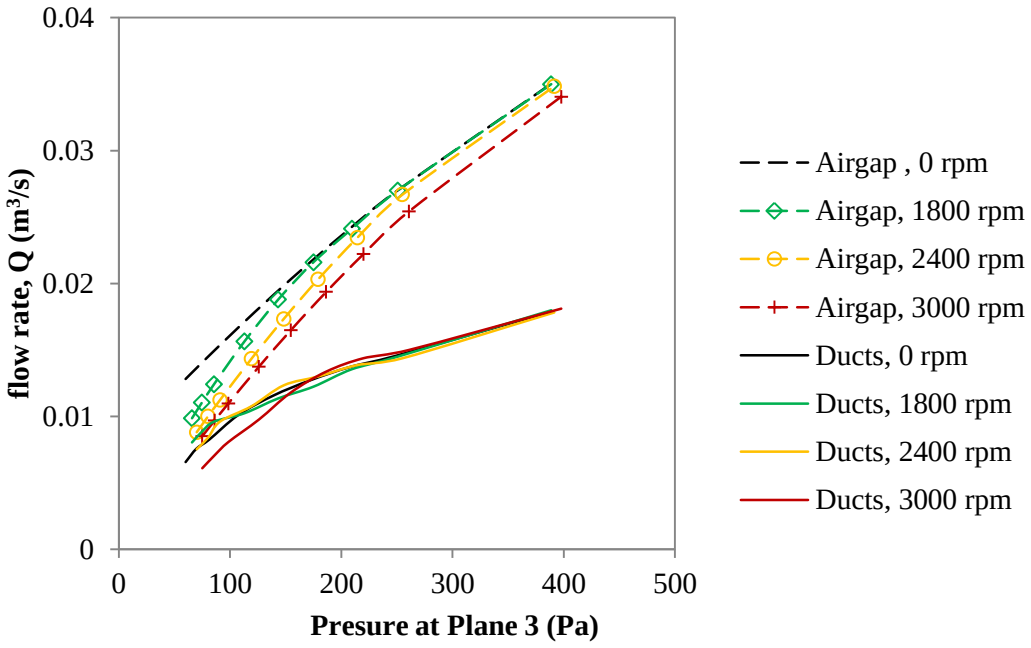

(d) *6 D14 PCD75*

Figure N.2: Flow distribution between airgap and rotor ducts with flow guard for rotor speed at 0 rpm, 1800 rpm, 2400 rpm and 3000 rpm

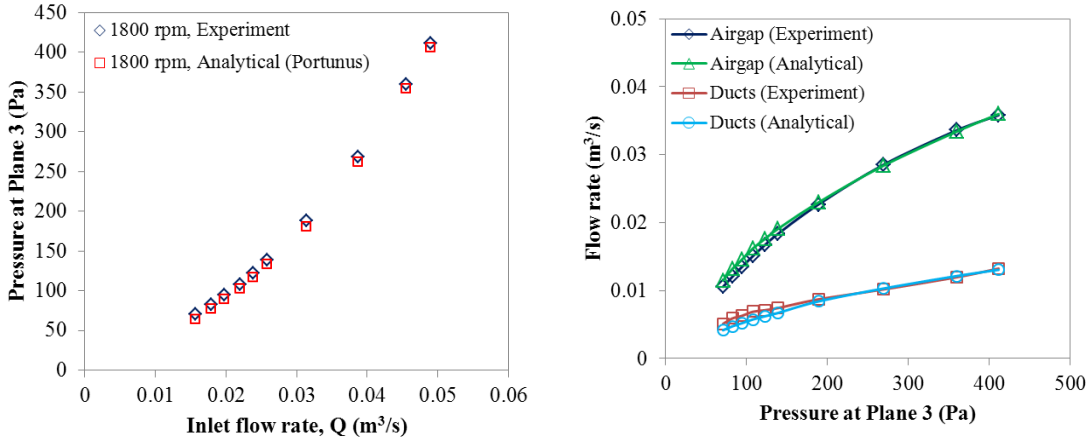

(a) Rotor speed = 1800 rpm

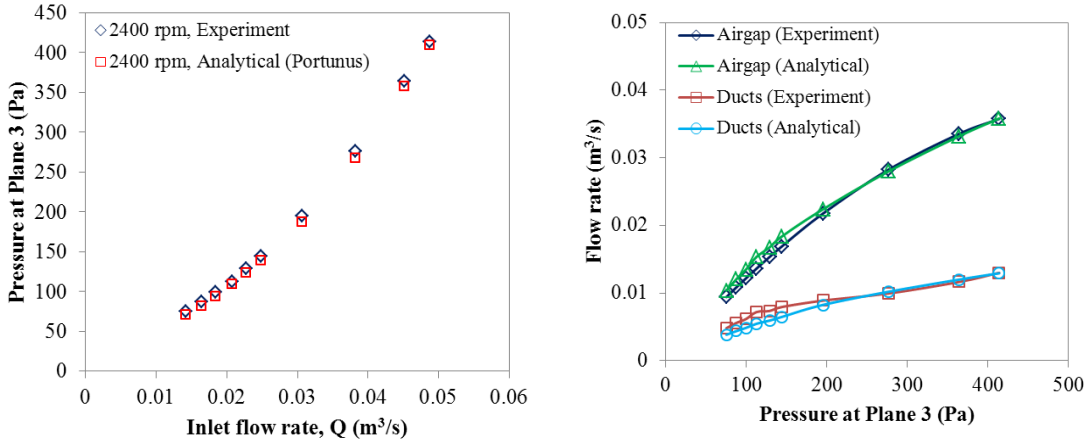

(b) Rotor speed = 2400 rpm

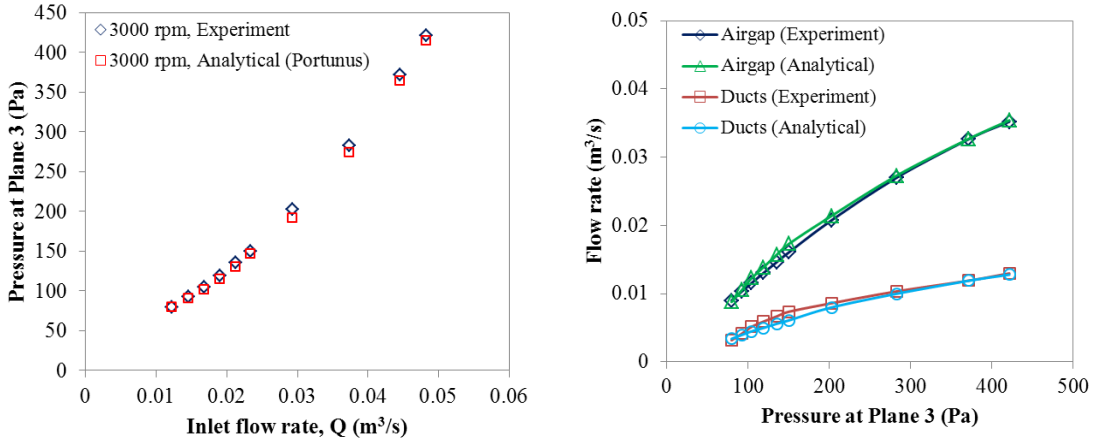

(c) Rotor speed = 3000 rpm

Figure N.3: Pressure drop from the Plane 3 to the outlet versus inlet flow rate for *6 D12 PCD113* (left) and the flow distribution between rotor ducts and airgap (right)

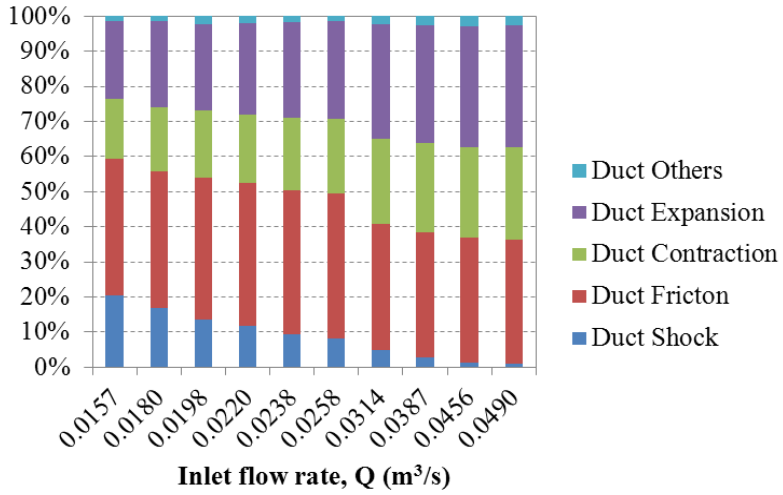

(a) Rotor speed = 1800 rpm

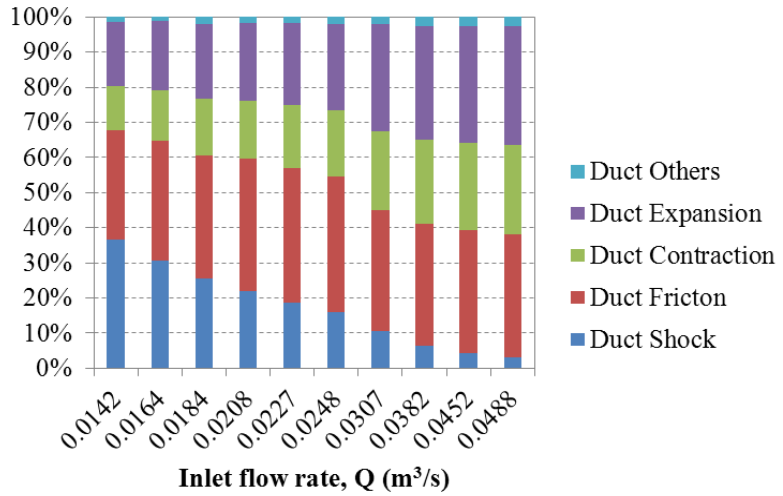

(b) Rotor speed = 2400 rpm

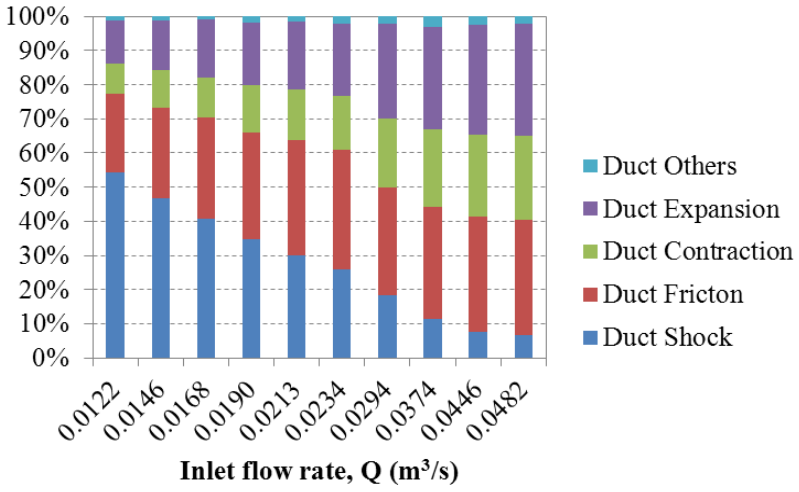

(c) Rotor speed = 3000 rpm

Figure N.4: The contribution of pressure loss components of rotor ducts for *6 D12 PCD113* obtained using Portunus flow network analysis

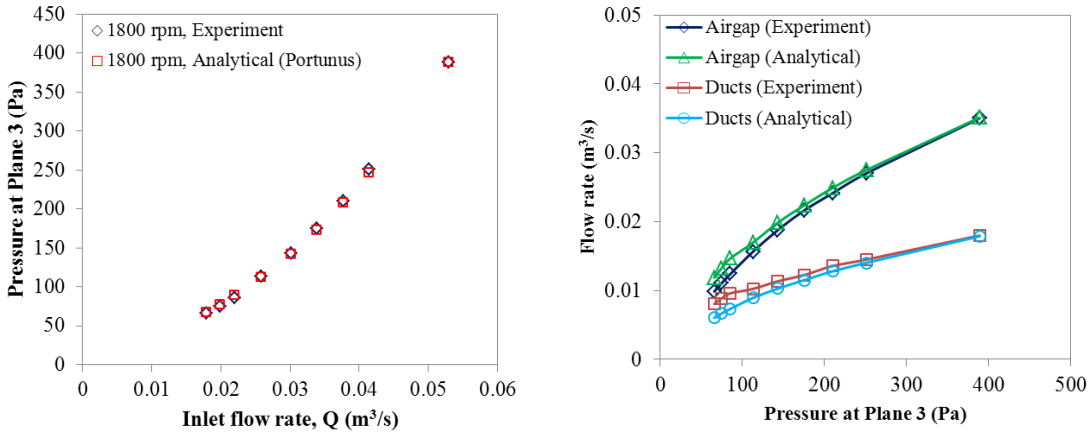

(a) Rotor speed = 1800 rpm

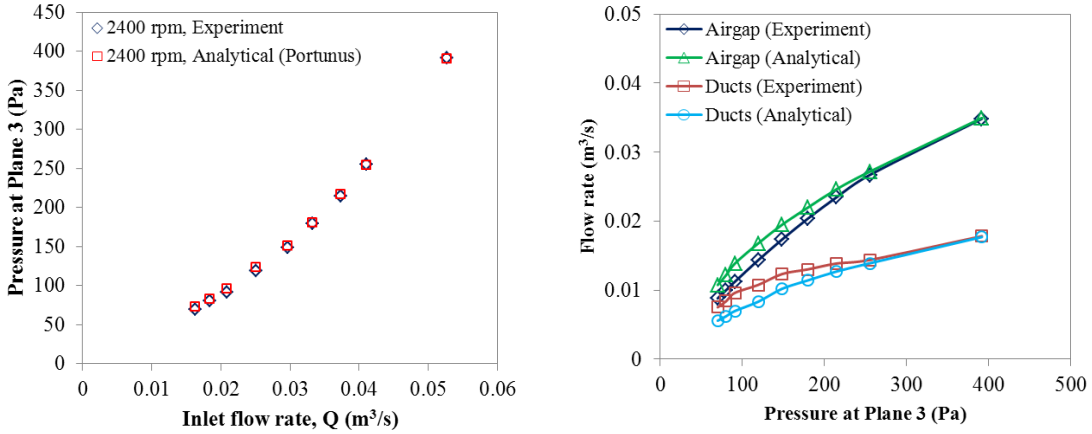

(b) Rotor speed = 2400 rpm

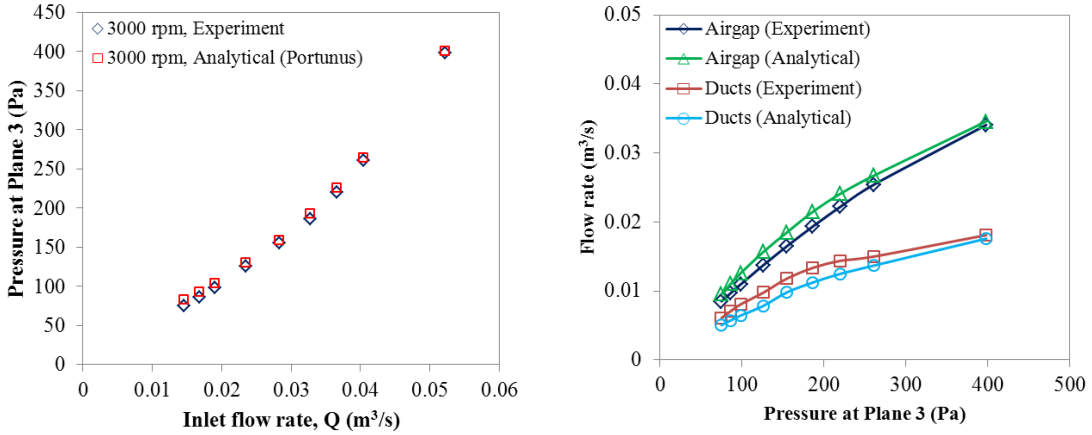

(c) Rotor speed = 3000 rpm

Figure N.5: Pressure drop from the Plane 3 to the outlet versus inlet flow rate for *6 D14 PCD75* (left) and the flow distribution between rotor ducts and airgap (right)

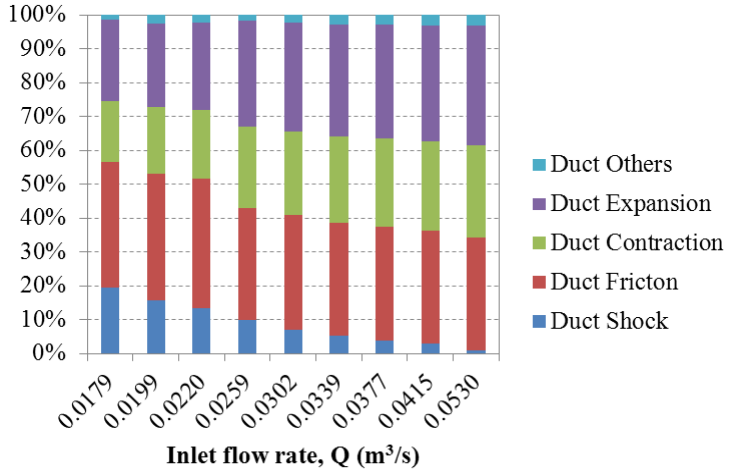

(a) Rotor speed = 1800 rpm

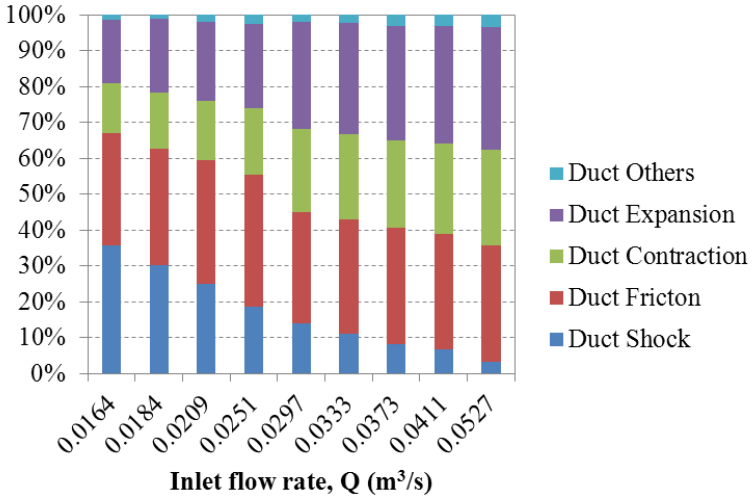

(b) Rotor speed = 2400 rpm

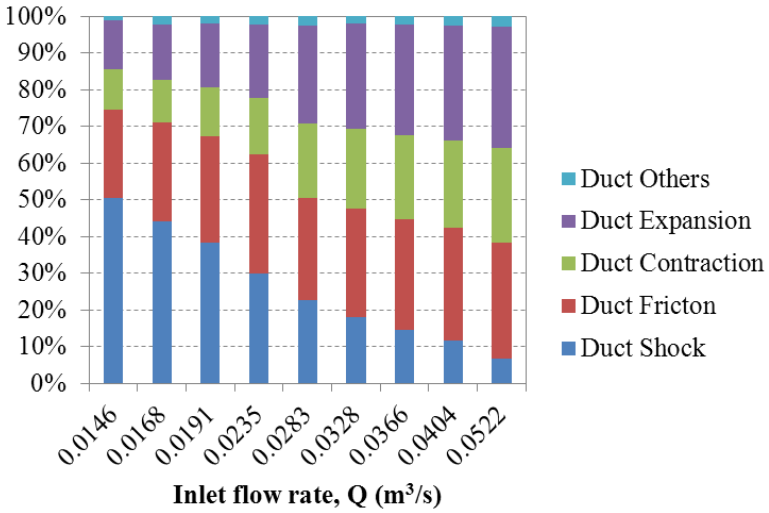

(c) Rotor speed = 3000 rpm

Figure N.6: The contribution of pressure loss components of rotor ducts for *6 D14 PCD75* obtained using Portunus flow network analysis

Appendix O – Experimental Data for Ventilation of Rotor Ducts, Airgap and Flow Guard

The equations (8.27) to (8.46) are limited by the fact that the input data, ΔP_3 needs to be within the range of the pressure. Therefore, interpretation of Q_{ducts} outside the range of the pressure of the equation is not recommended.

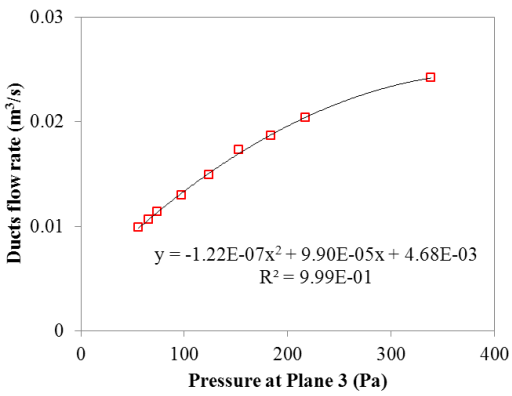

Rotor speed = 1200 rpm

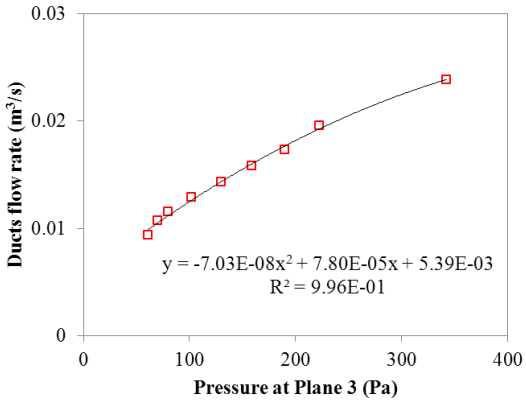

Rotor speed = 1800 rpm

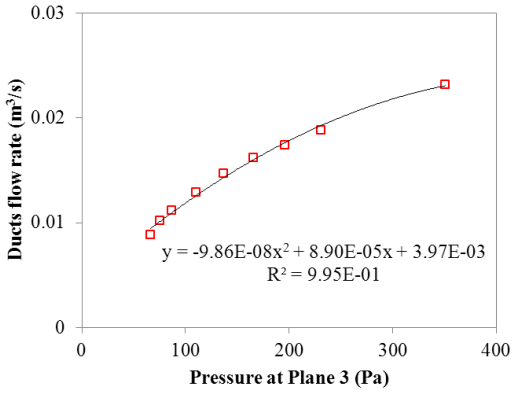

Rotor speed = 2400 rpm

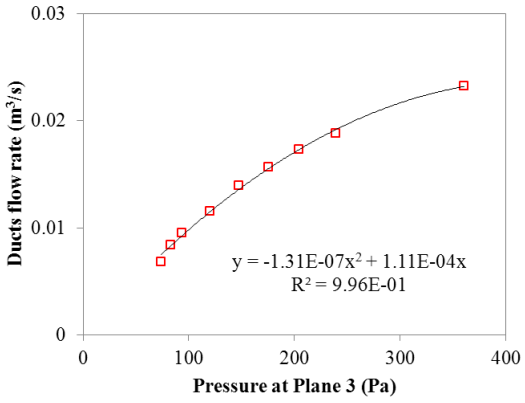

Rotor speed = 3000 rpm

Figure O.1: The rotor ducts flow rate vs. pressure at Plane 3 for *12 D12 PCD113*

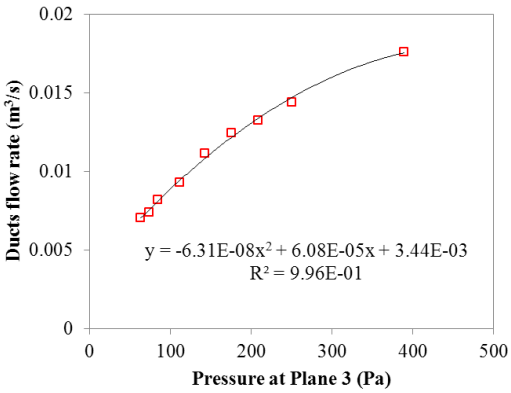

Rotor speed = 1200 rpm

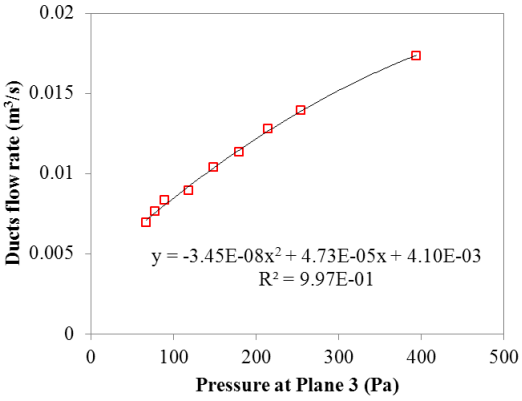

Rotor speed = 1800 rpm

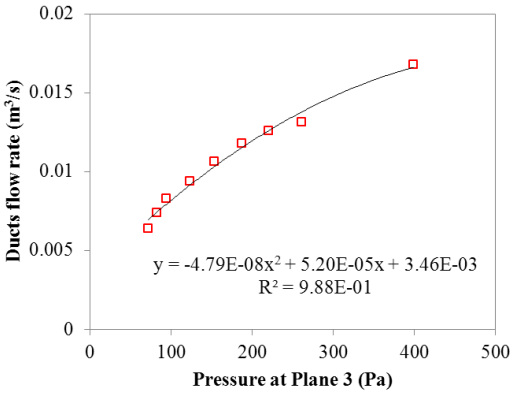

Rotor speed = 2400 rpm

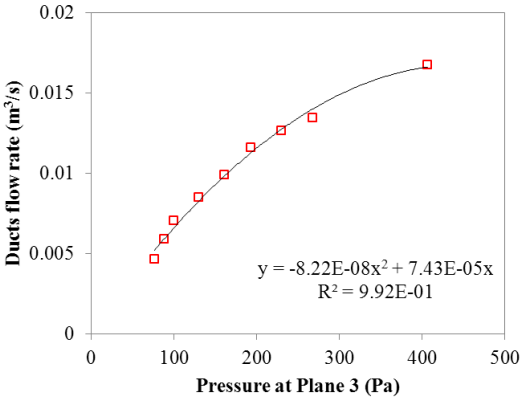

Rotor speed = 3000 rpm

Figure O.2: The rotor ducts flow rate vs. pressure at Plane 3 for *12 D10 PCD113*

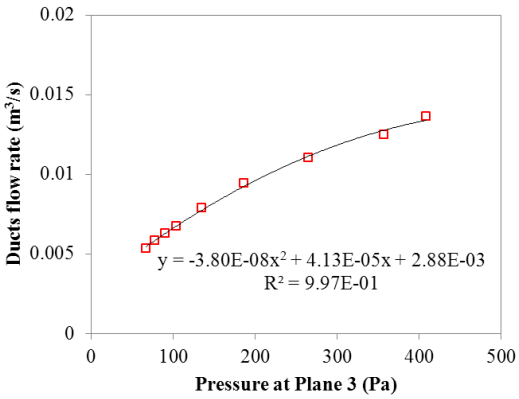

Rotor speed = 1200 rpm

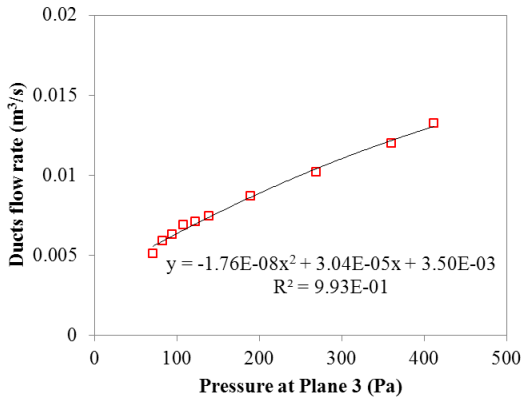

Rotor speed = 1800 rpm

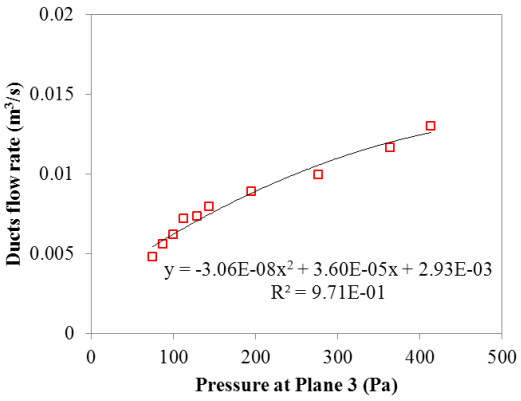

Rotor speed = 2400 rpm

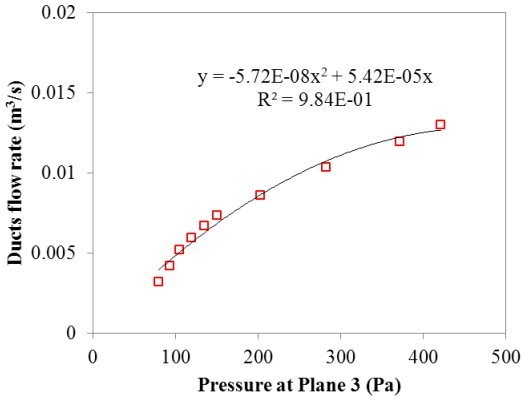

Rotor speed = 3000 rpm

Figure O.3: The rotor ducts flow rate vs. pressure at Plane 3 for *6 D12 PCD113*

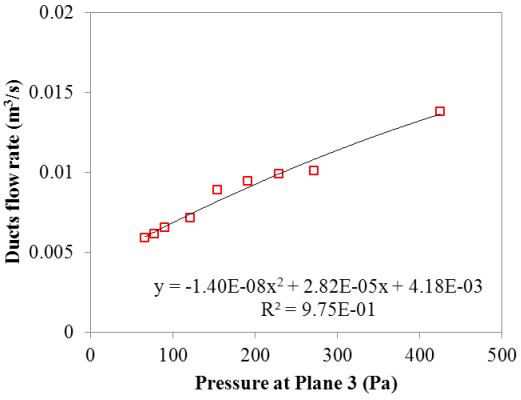

Rotor speed = 1200 rpm

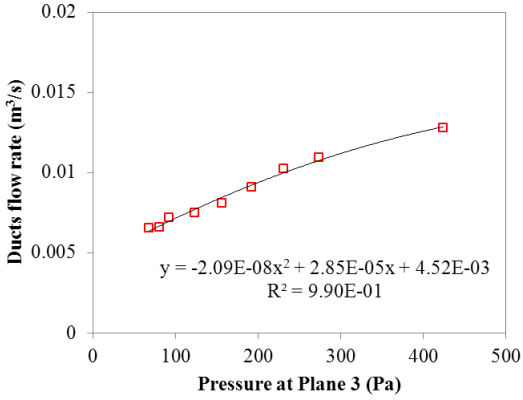

Rotor speed = 1800 rpm

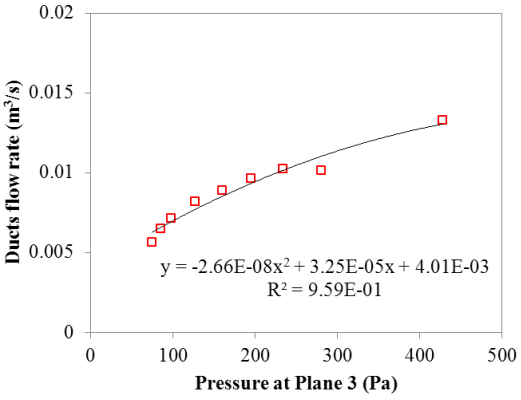

Rotor speed = 2400 rpm

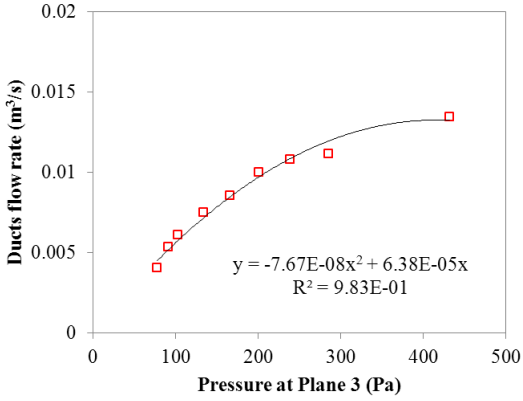

Rotor speed = 3000 rpm

Figure O.4: The rotor ducts flow rate vs. pressure at Plane 3 for *6 D12 PCD75*

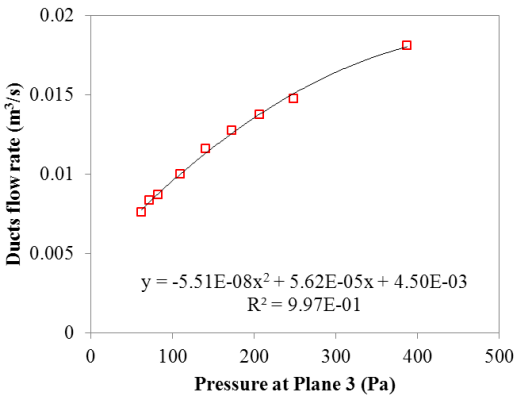

Rotor speed = 1200 rpm

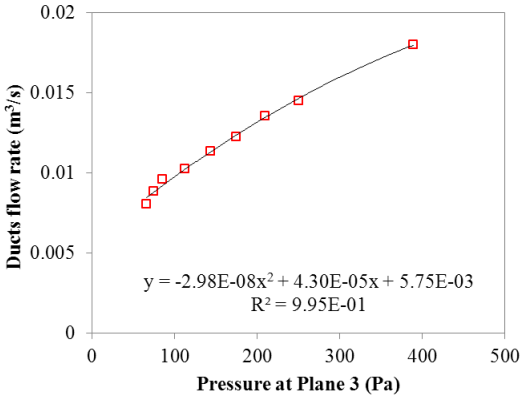

Rotor speed = 1800 rpm

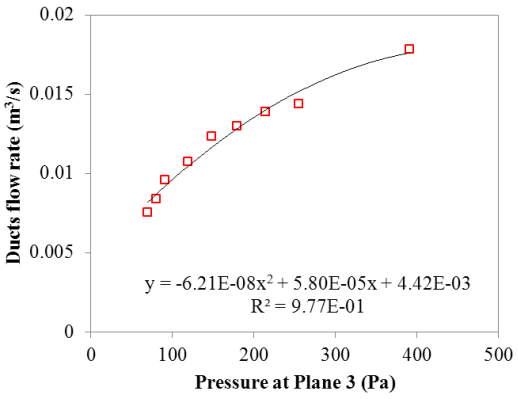

Rotor speed = 2400 rpm

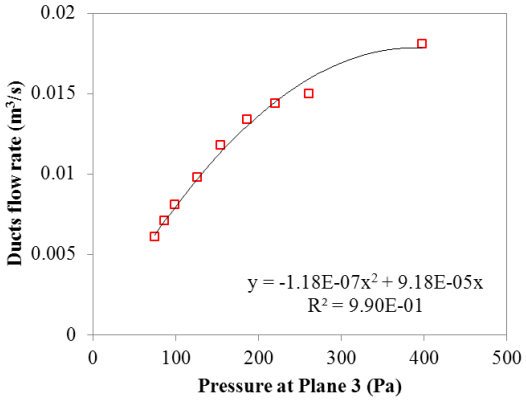

Rotor speed = 3000 rpm

Figure O.5: The rotor ducts flow rate vs. pressure at Plane 3 for *6 D14 PCD75*

Appendix P – Experimental Results for Rotational Tests with Rotor Ducts, Airgap and no Flow Guard

Figure P.1 shows the comparison between the system flow resistance curves for the case of rotor ducts and airgap with the flow guard (solid line) and without the flow guard (dashed line). The pressure losses were plotted against the inlet flow rate for rotor speed at 0, 1200, 2400 and 3000 rpm.

Figure P.2 illustrates the flow distribution between the rotor ducts and airgap for the cases without the flow guard. With rotation, when compared to the ventilation system with airgap only the flow rate passing through the airgap decreases further due to the combining flow loss.

Figure P.3 and Figure P.5 show the comparisons between the experimental results and the values predicted using analytical flow network analysis for *12 D12* PCD113 and *6 D12 PCD113* respectively. Good agreements were achieved. The experimentally validated flow network was used to investigate the contribution of the pressure loss components from the Plane 3 to the outlet of the test rig. In Figure P.4 and Figure P.6, the stacked columns display the percentage that the main flow components contribute to the total pressure loss over a range of inlet flow rate.

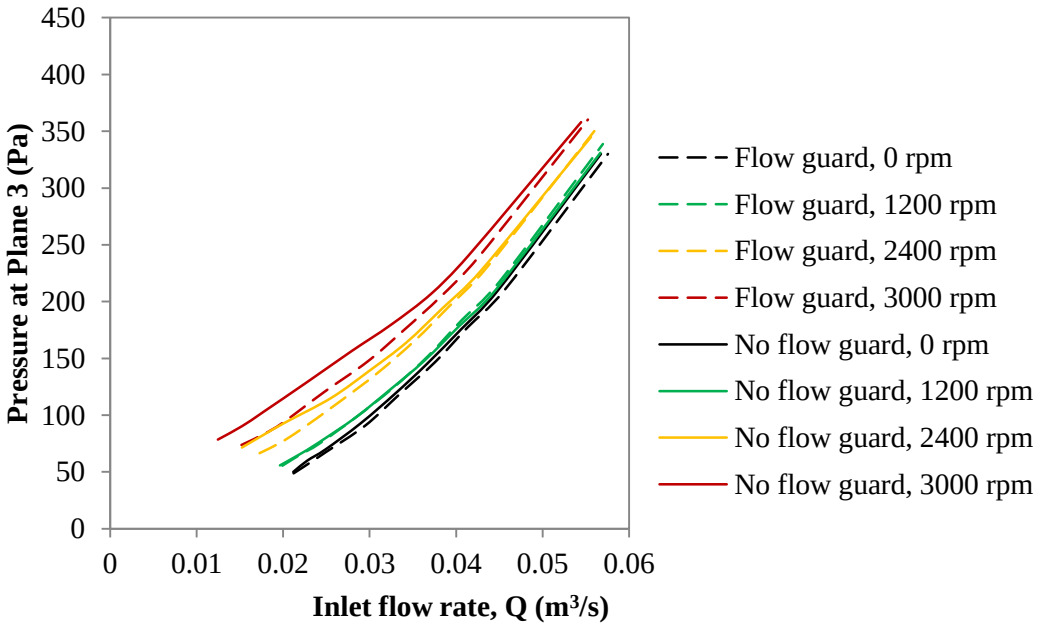

(a) *12 D12 PCD113*

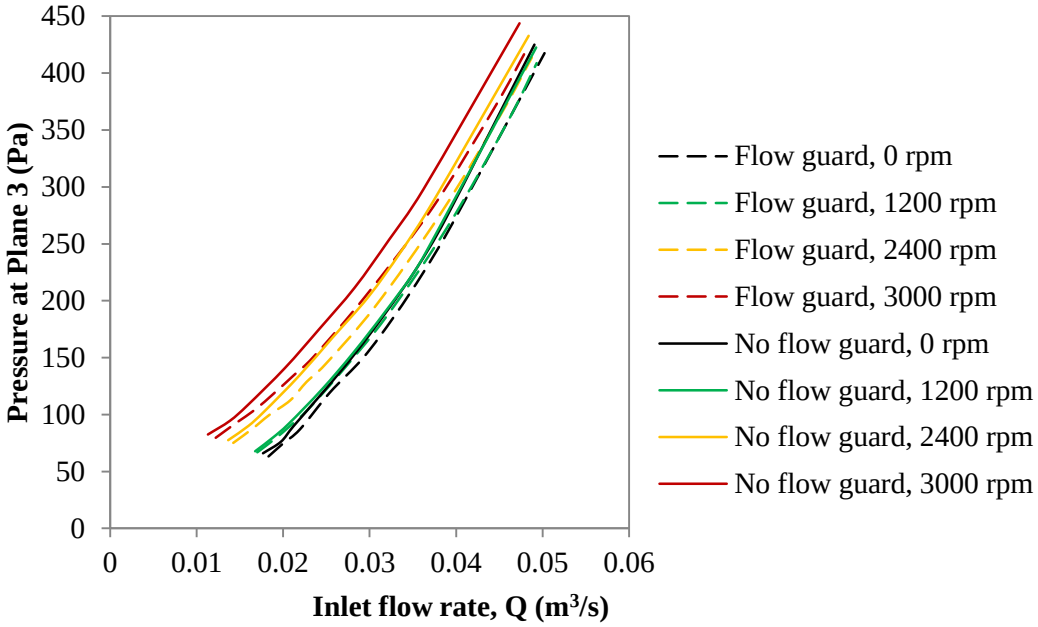

(b) *6 D12 PCD113*

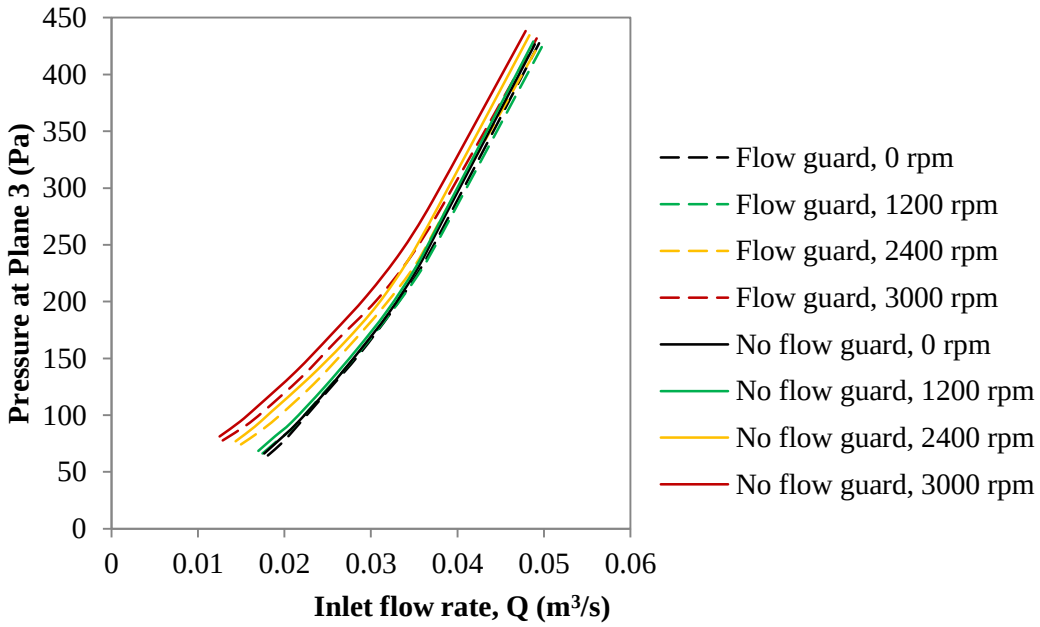

(c) *6 D12 PCD75*

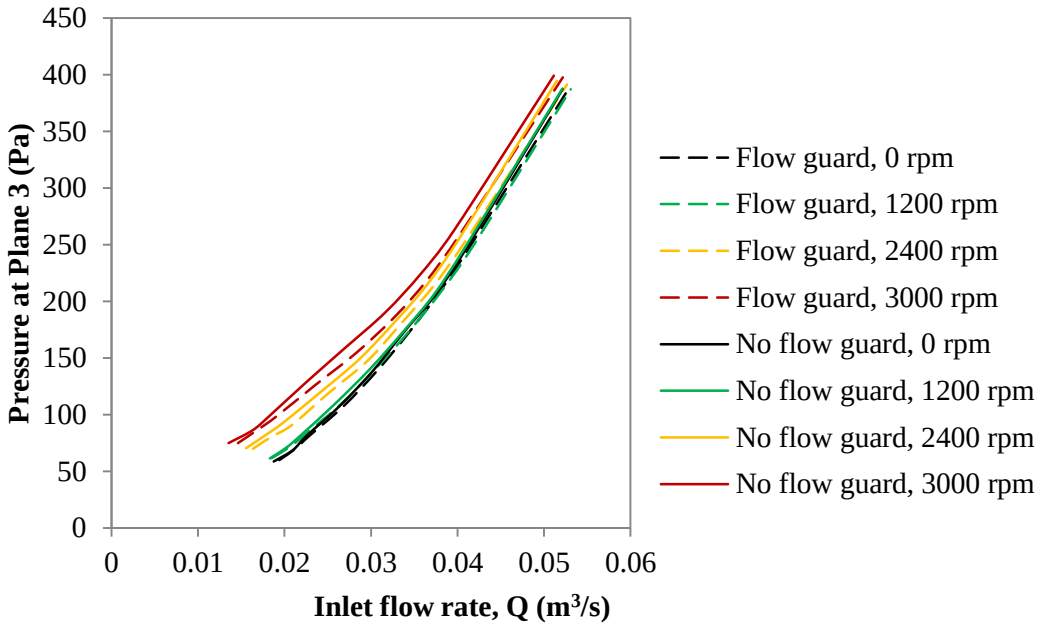

(d) *6 D14 PCD75*

Figure P.1: System flow resistance curves of ventilation with and without flow guard for rotor speed up to 3000 rpm

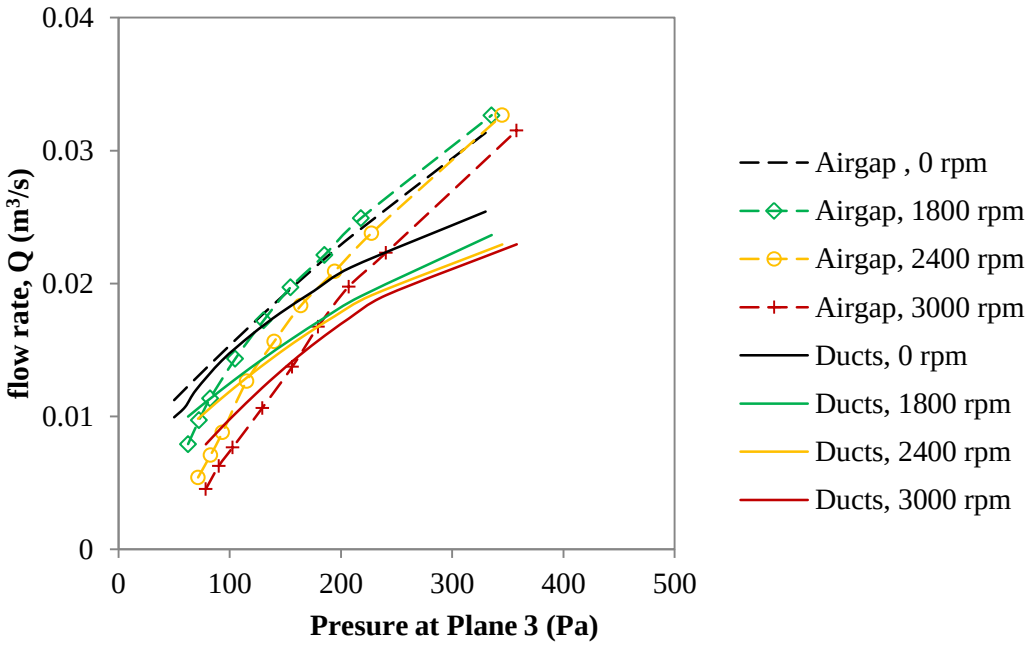

(a) *12 D12 PCD113*

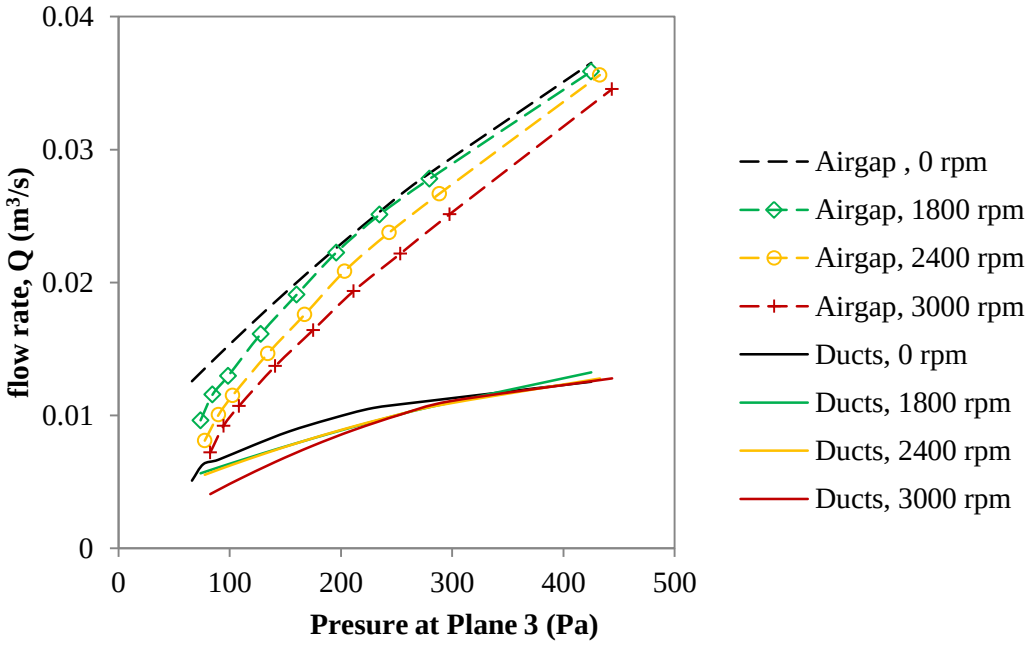

(b) *6 D12 PCD113*

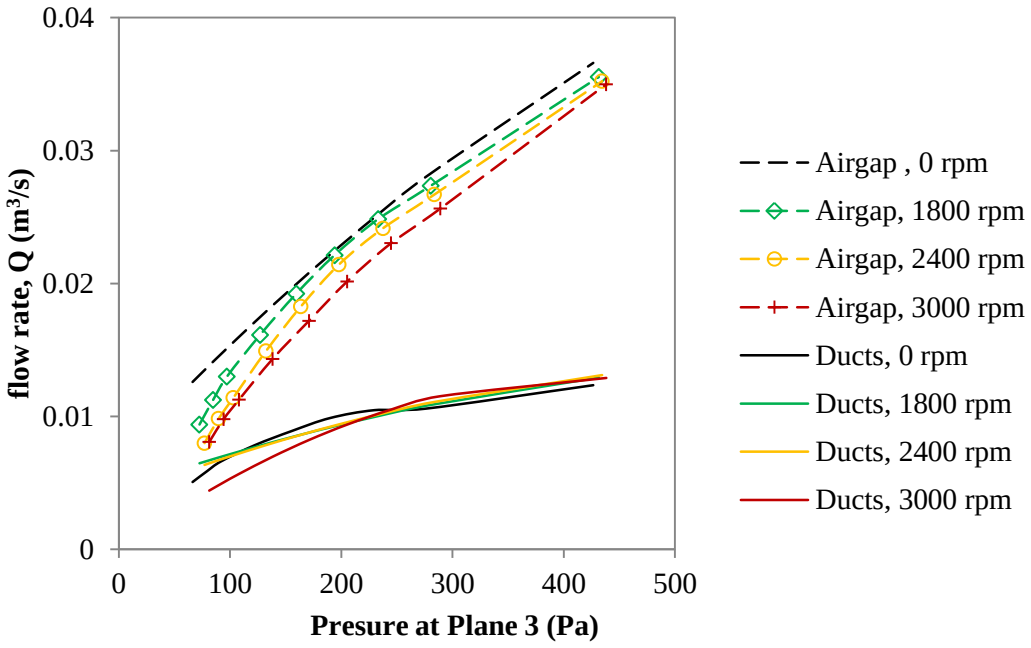

(c) *6 D12 PCD75*

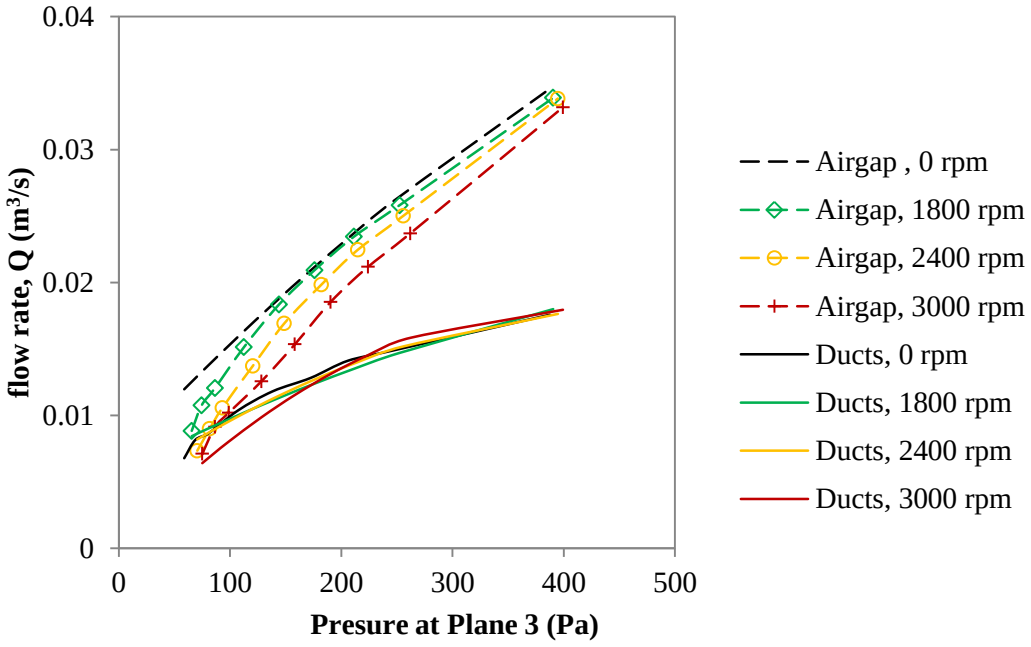

(d) *6 D14 PCD75*

Figure P.2: Flow distribution between airgap and rotor ducts without flow guard for rotor speed at 0 rpm, 1800 rpm, 2400 rpm and 3000 rpm

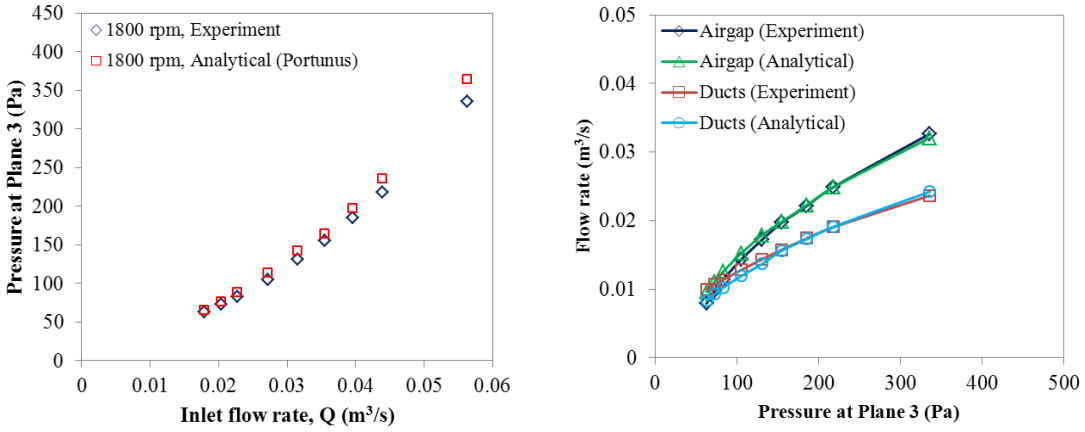

(a) Rotor speed = 1800

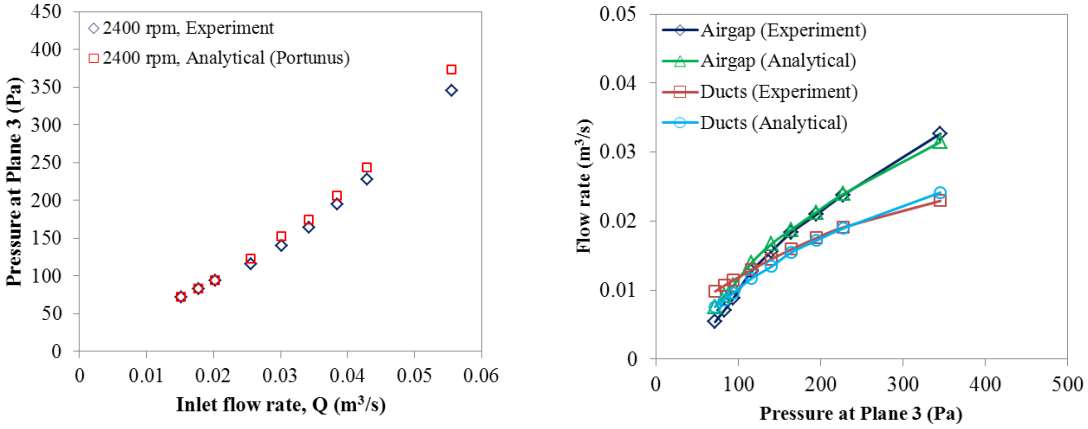

(b) Rotor speed = 2400

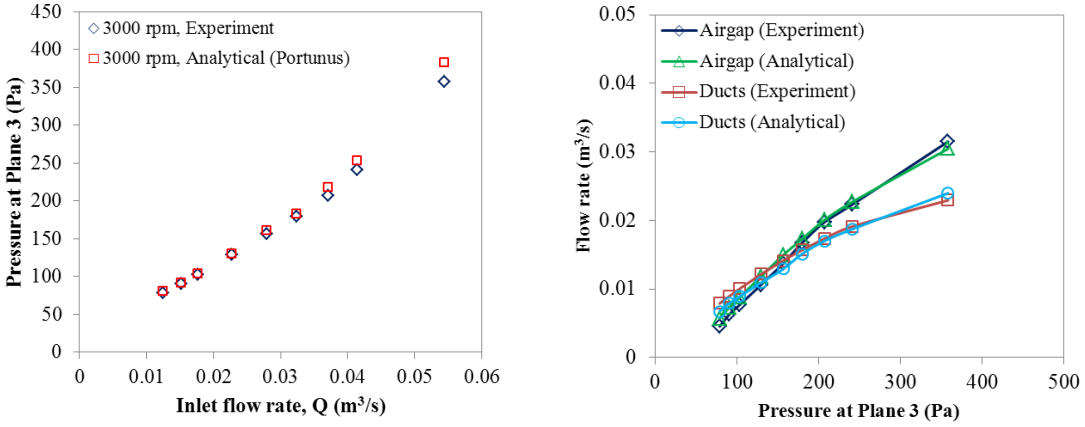

(c) Rotor speed = 3000

Figure P.3: Pressure drop from the Plane 3 to the outlet versus inlet flow rate (left) and the flow distribution between rotor ducts and airgap (right) for *12 D12 PCD113*

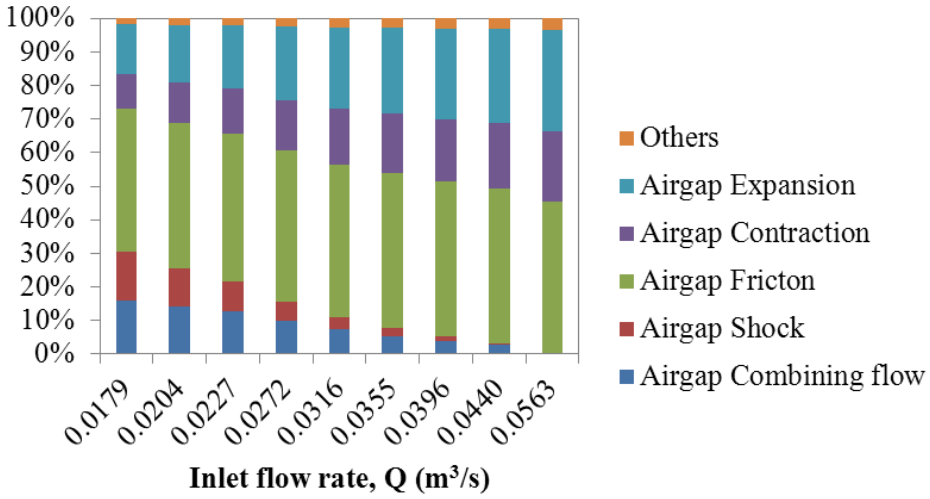

(a) Rotor speed = 1800

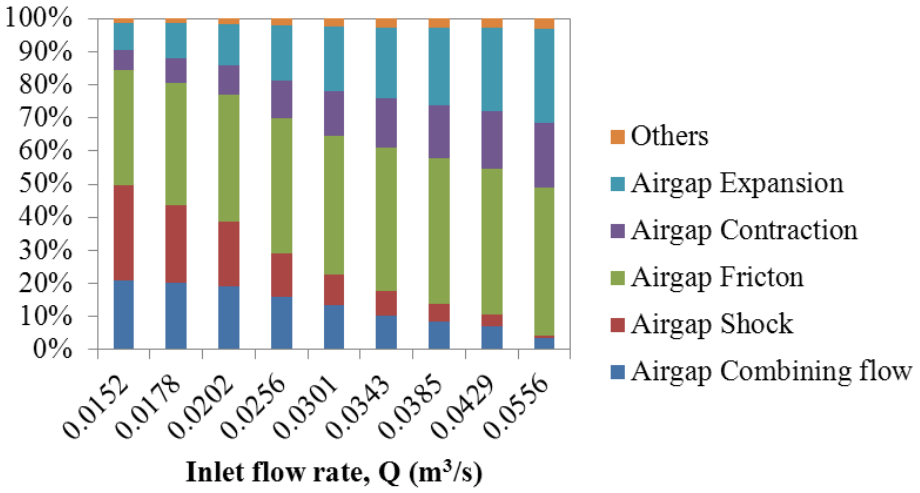

(b) Rotor speed = 2400

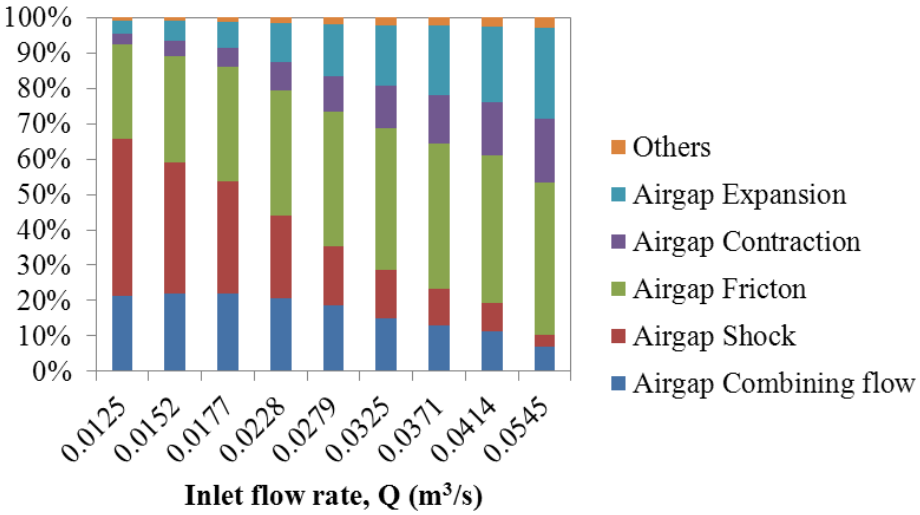

(c) Rotor speed = 3000

Figure P.4: The contribution of pressure loss components of rotor ducts for *12 D12 PCD113* obtained using Portunus flow network analysis

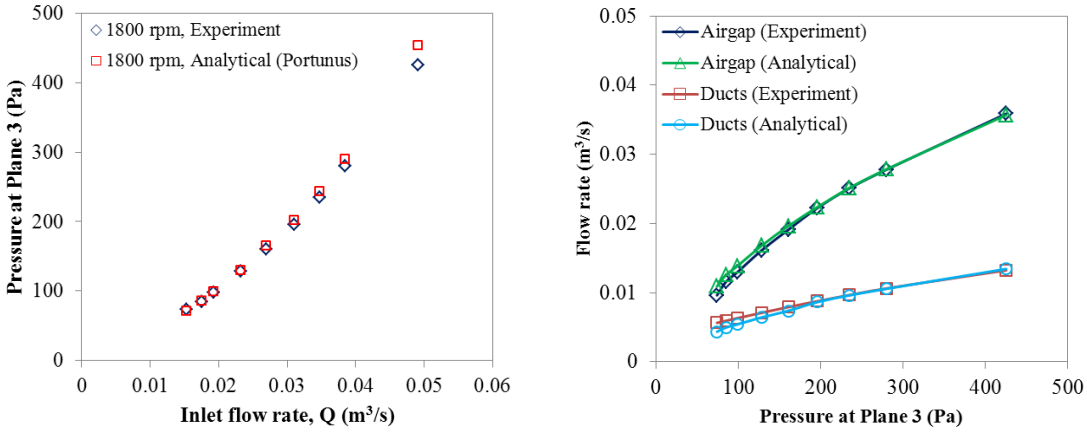

(a) Rotor speed = 1800

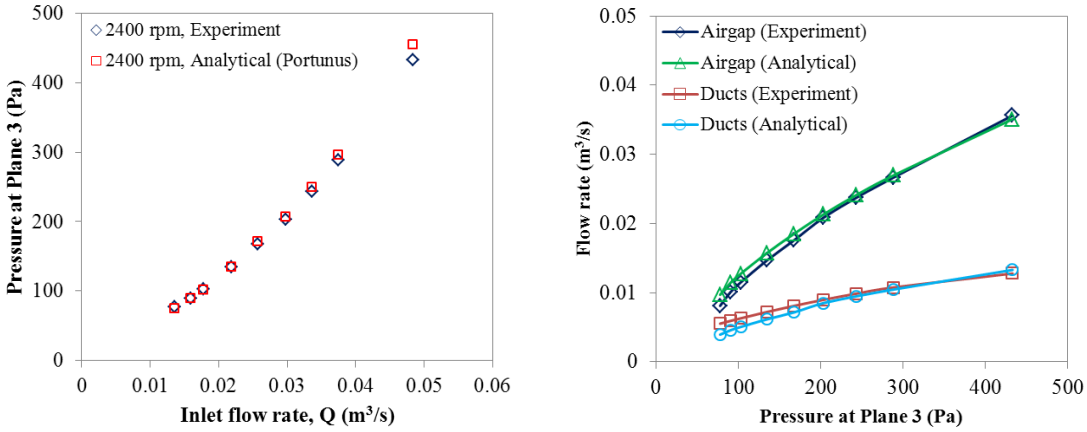

(b) Rotor speed = 2400

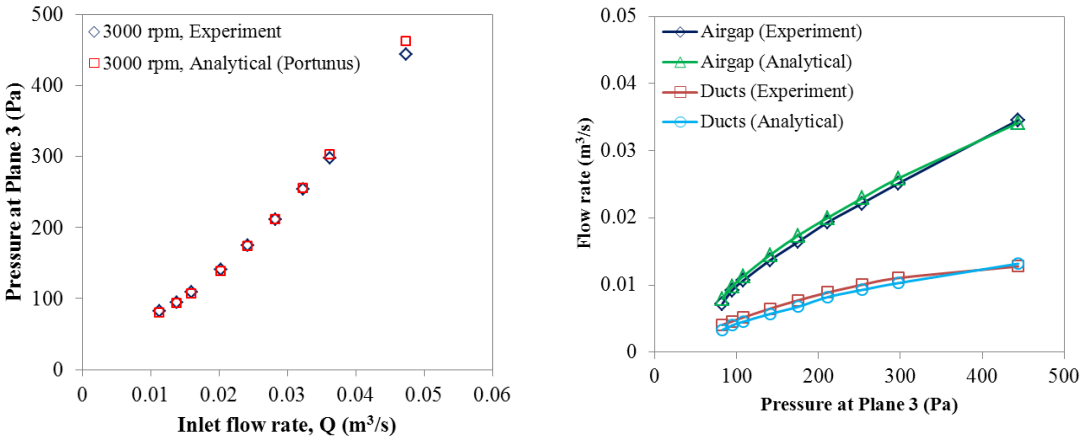

(c) Rotor speed = 3000

Figure P.5: Pressure drop from the Plane 3 to the outlet versus inlet flow rate (left) and the flow distribution between rotor ducts and airgap (right) for *6 D12 PCD113*

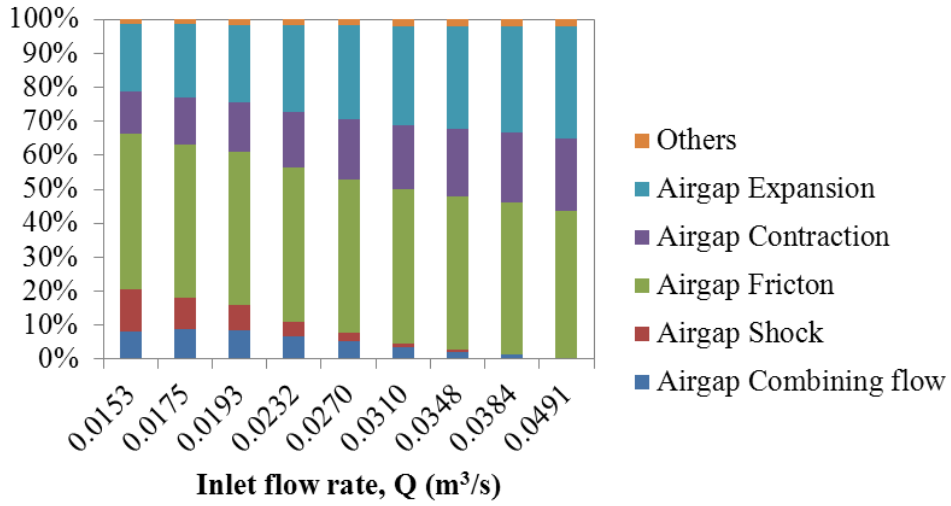

(a) Rotor speed = 1800

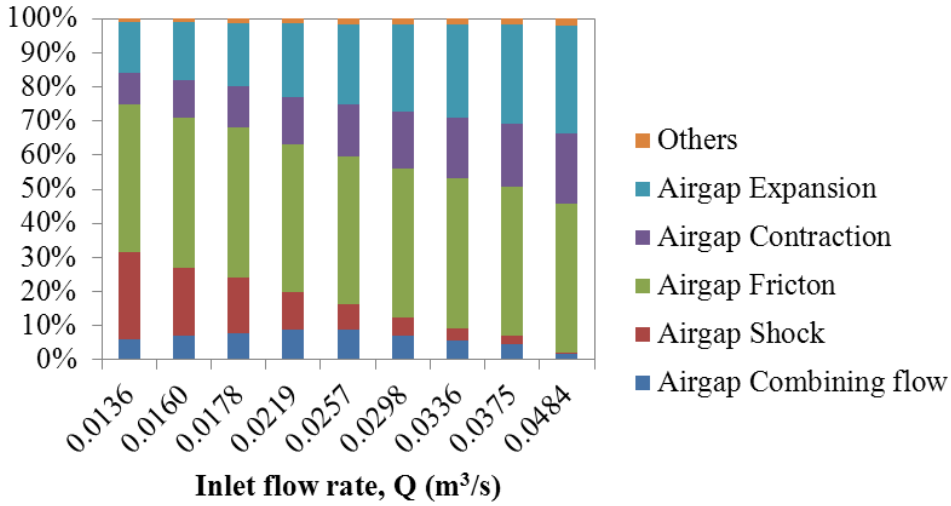

(b) Rotor speed = 2400

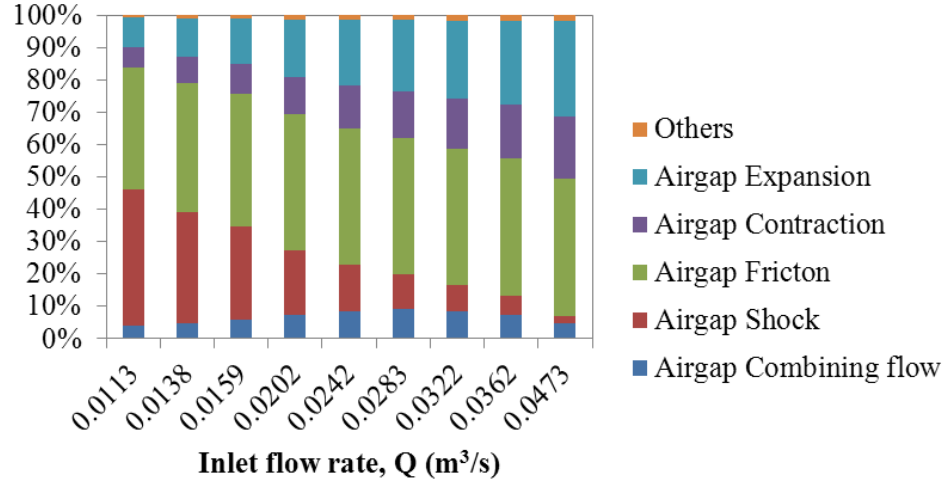

(c) Rotor speed = 3000

Figure P.6: The contribution of pressure loss components of rotor ducts for *6 D12 PCD113* obtained using Portunus flow network analysis